Fabian I. Ezema
Chandrakant D. Lokhande
Abhishek C. Lokhande *Editors*

Chemically Deposited Metal Chalcogenide-based Carbon Composites for Versatile Applications

Springer

Chemically Deposited Metal Chalcogenide-based Carbon Composites for Versatile Applications

Fabian I. Ezema • Chandrakant D. Lokhande •
Abhishek C. Lokhande
Editors

Chemically Deposited Metal Chalcogenide-based Carbon Composites for Versatile Applications

Springer

Editors
Fabian I. Ezema
Department of Physics & Astronomy
University of Nigeria, Nsukka
Nsukka, Nigeria

Chandrakant D. Lokhande
Centre for Interdisciplinary Research
D Y Patil University
Kolhapur, India

Abhishek C. Lokhande
Mechanical Engineering Department
Khalifa University of Science and
Technology
Abu Dhabi, United Arab Emirates

ISBN 978-3-031-23400-2 ISBN 978-3-031-23401-9 (eBook)
https://doi.org/10.1007/978-3-031-23401-9

This Springer imprint is published by the registered company Springer Nature Switzerland AG
The registered company address is: Gewerbestrasse 11, 6330 Cham, Switzerland

Preface

One of the innovative and useful materials now being researched for potential applications and prospects for value addition for ongoing quality and performance improvement is metal chalcogenide-based carbon composites. Numerous popular science and engineering databases, including Scopus and Web of Science, can be used to search through the vast body of engineering and science literature on metal chalcogenide-based carbon composites. However, reports of novel materials, processing methods, and structure-to-property and processing-to-property correlations are ongoing. Reviews are published in journals on a regular basis in ever-increasing numbers, yet the aim of having them all in one place is frequently defeated by their diversity and dispersion.

In this book, significant papers on the synthesis, characterizations, and applications of chemically deposited metal chalcogenide-based carbon composites for versatile applications are collected. This book has developed from our earlier one on "chemically produced nanocrystalline metal oxide thin films for a variety of applications."

It is clear that the book now available on chemically deposited metal chalcogenide-based carbon composites for energy conversion, storage, and sensing might assist the community in accessing the necessary resources in a single location. As a result, the book was designed to offer advice on chemically produced metal chalcogenide-based carbon composites for energy conversion (photovoltaic); chemically produced metal chalcogenide-based carbon composites for energy storage (supercapacitors and batteries); and chemically processed metal chalcogenide-based carbon composites for sensing, simulation, and modelling.

The first 8 chapters of this book, which has a total of 14 chapters, are devoted to providing general information on the development of solution-processed metal chalcogenide-based carbon composites, their properties and applications, their structural and electronic properties, and the insights gained from first-principles calculations on the properties derived from Chap. 13 of the book.

The subsequent five chapters thoroughly discuss the water-splitting and photovoltaic uses of carbon composites based on metal chalcogenides. Reviews on the subject's most recent developments in general as well as the advantages of metal

chalcogenide-based carbon composites for photovoltaic activity are covered. The chapters also cover photoelectrochemical cells, hydrogen production, and the use of carbon composites based on metal chalcogenides for photocatalysis.

Lithium ion batteries, supercapacitors, and other energy storage technologies are the subjects of the majority of this book's chapters, along with broader energy storage topics.

We are grateful to the authors who put their time and effort into creating this book, which would not have been possible without them. We really hope that the time and energy you invested in writing the chapters will assist to increase your profile as a specialist in science and engineering research. Working with the Springer Nature's editorial teams has been a delight, especially with Michel Luby, Zoe Kennedy, Brian Halm, and Praveena John. Thank you all, for your rapid assistance with editing and ideas that improved the book's presentation. In fact, it was a pleasure working together with the book's editors.

Finally, we would like to extend our sincere gratitude to you, the reader, and we really hope that reading this book was beneficial to you. We really hope that you enjoyed reading this book and found it useful.

Nsukka, Nigeria — Fabian I. Ezema
Kolhapur, India — Chandrakant D. Lokhande
Abu Dhabi, United Arab Emirates — Abhishek C. Lokhande

Contents

0D, 1D, 2D, and 3D Structured Chalcogenides for Supercapacitor Applications

Nikila Nair and Babasaheb R. Sankapal

Abbreviations

0D	Zero dimensional
1D	One dimensional
2D	Two dimensional
A g^{-1}	Ampere per gram
A°	Angstrom
ASC	Asymmetric supercapacitors
C g^{-1}	Coulomb per gram
CD	Charge-discharge
C_{DL}	Double-layer capacitance
CE	Counter electrode
CNT	Carbon nanotube
C_{sp}	Specific capacitance
CV	Cyclic voltammetry
E	Energy density
ECSA	Electrochemically active surface area
EDLCs	Electrical double-layer capacitors
EDS	Energy-dispersive X-ray spectroscopy
EES	Electrochemical energy storage
EIS	Electrochemical impedance spectroscopy

N. Nair
Department of Mechanical Engineering, Indian Institute of Science, Bangalore, Karnataka, India
e-mail: nikilanair@iisc.ac.in

B. R. Sankapal (✉)
Nanomaterials and Device Laboratory, Department of Physics, Visvesvaraya National Institute of Technology, Nagpur, Maharashtra, India
e-mail: brsankapal@phy.vnit.ac.in

F. I. Ezema et al. (eds.), *Chemically Deposited Metal Chalcogenide-based Carbon Composites for Versatile Applications*, https://doi.org/10.1007/978-3-031-23401-9_1

E_{pa}	Anodic peak current
E_{pc}	Cathodic peak current
ESR	Equivalent series resistance
ESS	Energy storage systems
EV	Electrical vehicles
$F\ g^{-1}$	Farad per gram
FESEM	Field emission scanning electron microscopy
FSS	Flexible symmetric solid
GCD	Galvanostatic charge-discharge
h	Hour
HRTEM	High-resolution transition electron microscopy
HSCs	Hybrid supercapacitors
I	Current density
IE	Ion exchange
IL	Ionic liquid
K_{sp}	Solubility product
LED	Light-emitting diodes
$m^2\ g^{-1}$	Meter square per gram
$mA\ cm^{-2}$	Milliampere per centimetre square
$mAh\ g^{-1}$	Milliampere hour per gram
$mF\ cm^{-2}$	Millifarad per centimetre square
$mV\ s^{-1}$	Millivolt per second
MWCNT	Multiwalled carbon nanotube
NF	Nickel foam
NWs	Nanowires
P	Power density
QD	Quantum dots
R_{ct}	Charge transfer resistance
RE	Reference electrode
R_s	Internal resistance
SCs	Supercapacitors
SEM	Scanning electron microscopy
SILAR	Successive ionic layer adsorption and reaction
SSA	Specific surface area
SWCNT	Single-walled carbon nanotubes
T_c	Charging time
T_d	Discharging time
TEM	Transmission electron microscopy
V	Potential
V_f	Final potential
V_i	Initial potential
V_{max}	Maximum potential
V_{min}	Minimum potential
$W\ kg^{-1}$	Watt per kilogram
WE	Working electrode
$Wh\ kg^{-1}$	Watt hour per kilogram

1 Introduction

Nature has provided mankind with all necessary things for survival, but his desire for an easy and fast world has motivated him to innovate. His aspiration has encouraged unrestrained utilization of fossil fuels, naturally available resources, nuclear energy, etc. Uncontrolled utilization of non-renewable resources has led to their extinction and an increase in their cost, to such an extent that it has compelled all world powers and scientific societies to find sustainable energy storage technology. An ample amount of energy can be retrieved from renewable resources, but their storage has been a matter of great concern. Intensive research has been directed towards alternative ways of energy production and energy storage. It is also being taken care that these substitutes should be cost-effective, exhibiting good performance with sustainability. These must also be environment-friendly and reliable. At present, the use of portable electronic gadgets with innovative features like flexibility, lightweight, and reduced size has made energy storage an essential need of the hour [1]. Inclination towards advanced technologies contributed to the sudden surge in energy storage systems (ESS). These devices can save ample amount of energy from various renewable resources like wind, solar power, etc. and release it when needed [2]. Depending on the function, response time, and duration of storage, these can be classified, but the most common method of classification is its energy storage mechanisms. Figure 1 gives a broader classification of the mechanisms by which the energy can be stored. These are categorized as electrical, mechanical, thermal, chemical, and electrochemical [3]. The energy storage devices are expected to be cost-effective, long lasting, durable, efficient, and trustworthy. The market potential of ESS is predicted to increase over the coming decades. However, a lot of emphasis and breakthrough research are reported in the field of electrochemical ways of energy storage. Figure 2 shows that after thermal energy storage, it is supercapacitors and batteries that have garnered major attention in the world for research scenarios.

Electrochemical energy storage (EES) systems have found inevitable importance in our daily life as they are being widely used for electronic gadgets, electrical vehicles (EVs), and power grids. EES systems displaying high energy density with unrestrained high-power density and better cycling life have posed an enormous challenge in front of world powers and scientific societies. Figure 3 shows different types of electrochemical energy storage devices inclusive of batteries, fuel cells, and electrochemical capacitors. The desirable amount of power required, charging requisite, and speed of the device determine the ESS to be utilized.

Batteries play a vital part in our lives as these are being used rigorously in cars, radios, mobile phones, watches, laptops, remote controls, etc. [4]. Although these are rechargeable and reusable, they have shown a lot of setbacks like their ability to store charge deteriorates over time and eventually needs to be disposed of when they can no longer hold a charge. Also, they have low power density with low charge-discharge time. These disadvantages associated with the batteries have been the cause of the development of fuel cells. Fuel cells incorporated with

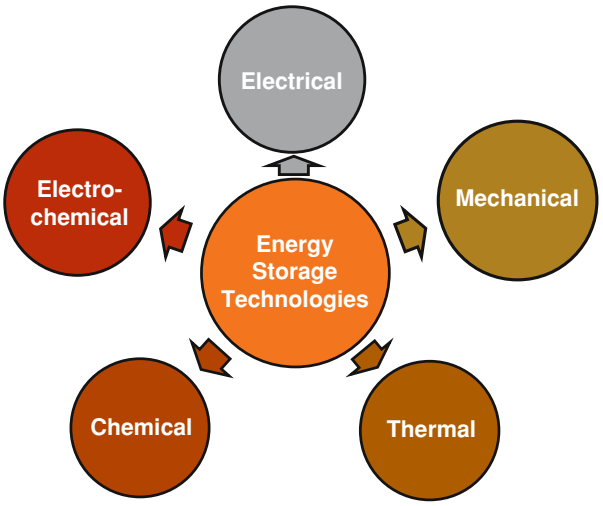

Fig. 1 Energy storage technologies

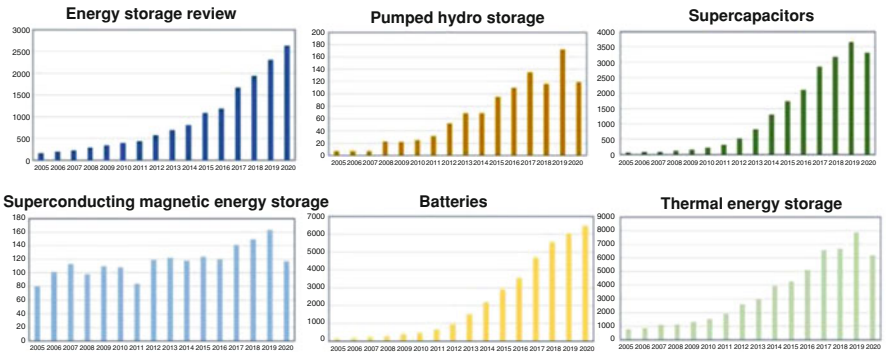

Fig. 2 Publications on different energy storage systems over the past 15 years [3]

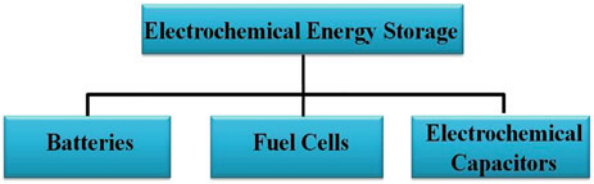

Fig. 3 Various electrochemical energy storage devices

hydrogen are being utilized in telecommunication and hybrid vehicles and for uninterrupted power supply, etc. as hydrogen is a non-hazardous and abundantly available resource. These cells are rechargeable and theoretically can provide continuous energy. However, their storage and handling are of great concern as they

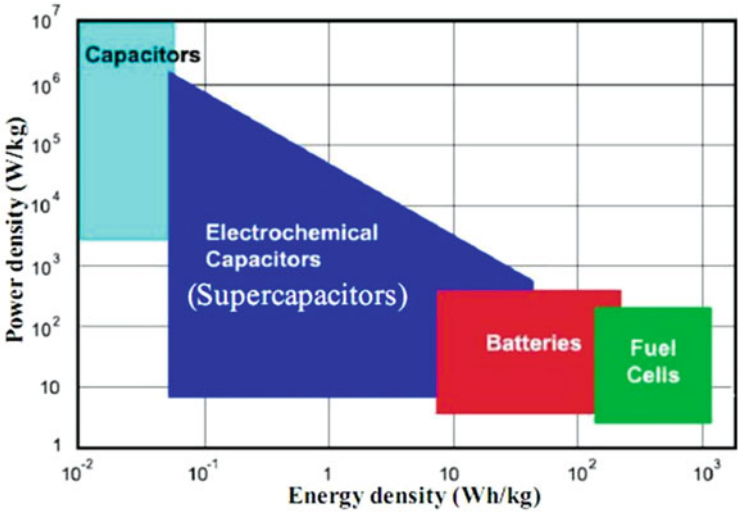

Fig. 4 Ragone plot for various energy storage devices [2]

require bulky and heavy tanks like CNG and complex insulating bottles, making the whole system massive [5]. Nevertheless, they have their constraints which prevent their exchange in each other's domain. These drawbacks of batteries and fuel cells lead to the invention of electrochemical capacitors, i.e. supercapacitors (SCs) which fill the gap between capacitors and batteries.

The Ragone plot shown in Fig. 4 quantitatively compares the performance of various electrochemical storage devices based on their power and energy density. SC falls within the batteries and conventional capacitors, where it shows the merits of both devices [6]. SCs, secondary energy storage systems, can exhibit high power density with a less negative impact on the environment when compared to batteries [7]. The capacitance and charge-discharge capability of SCs are much higher than that of any other conventional capacitors. The specific energy density (1–10 Wh kg^{-1}) associated with SCs is much lower than that of batteries but higher when compared to conventional capacitors. Similarly, the specific power density (> 10 kW kg^{-1}) of SCs is higher than the batteries but lower when compared to the capacitors [5, 6]. The equivalent series resistance (ESR) of SCs is low eventually increasing the power and minimum loss of energy during the operation [7]. Since no chemical reaction takes place during the charging or discharging process, it can be charged and discharged hundreds to thousands of times without any degradation, thus increasing the life span (> 10^5) [1, 6, 8–10]. Also, its efficiency is 90% with no maintenance, while that of currently used batteries is 80% [11–14]. Table 1 briefly articulates the merits of SC compared to batteries and conventional capacitors [15]. For high-power and high-energy-devices like mobiles and electric vehicles, SCs can be used in combination with rechargeable batteries [16].

Table 1 Comparison of battery, supercapacitor, and capacitor [17]

	Battery	Supercapacitor	Capacitor
Cycle life	1000	> 500,000	Almost infinite
Charging time	1 to 5 h	s to min	10^{-6} to 10^{-3} s
Discharge time	0.3 to 3 h	s to min	10^{-6} to 10^{-3} s
Charge storage	Faradaic	Non-faradaic/faradaic	Charge is stored in the dielectric material in an electrostatic field
Specific energy (Wh kg^{-1})	10–100	1–10	< 0.1
Specific power (W kg^{-1})	< 1000	500–10,000	≫10,000

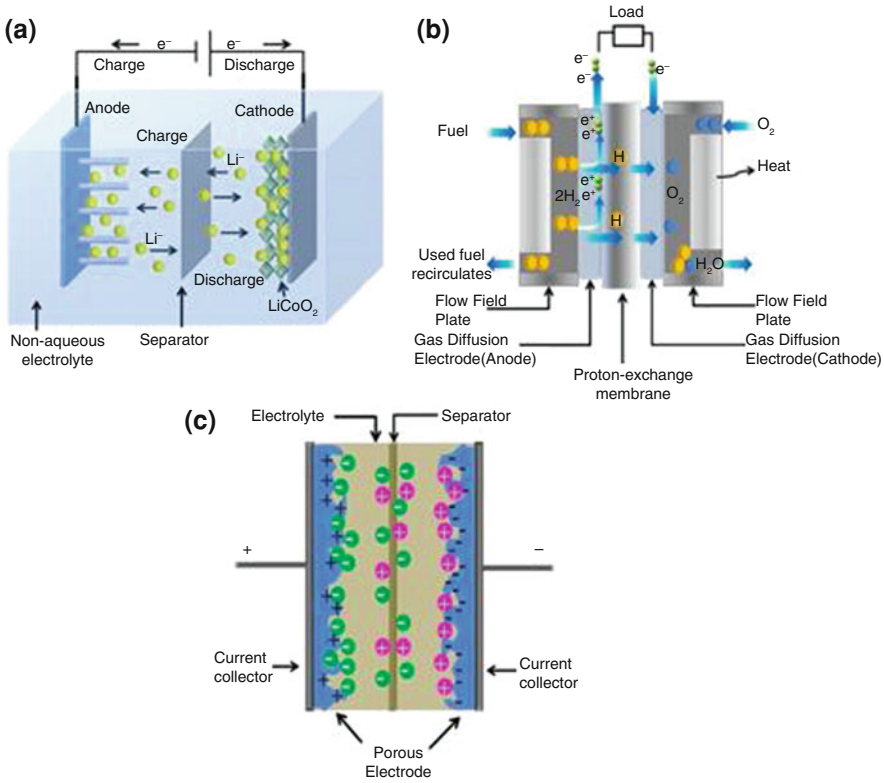

Fig. 5 Schematic representation of (**a**) intercalation/de-intercalation reaction mechanism in a rechargeable lithium-ion battery containing solid electrodes and a liquid electrolyte, (**b**) proton-exchange membrane fuel cell, and (**c**) two-electrode supercapacitor [18–20]

All three ESS (batteries, supercapacitors, and capacitors) have different energy storage behaviours. Figure 5 shows the schematic arrangement for (a) intercalation/de-intercalation mechanism of a lithium-ion battery with solid electrodes immersed in liquid electrolyte [18], (b) proton-exchange membrane fuel

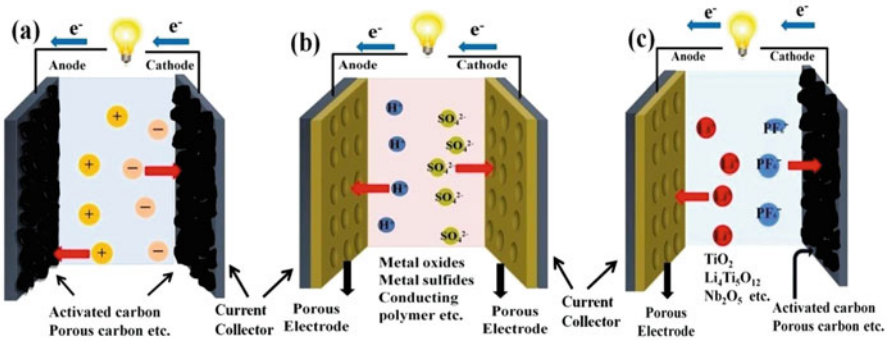

Fig. 6 Schematic showing the working mechanisms of (**a**) carbon-based electrical double-layer capacitor (EDLC), (**b**) pseudocapacitor, and (**c**) hybrid supercapacitor

cell [19], and (c) the two-electrode SC [20]. Analogous to batteries and fuel cells, SCs consist of one positive and one negative electrode with an electrolyte which can be in liquid or gel form and a separator to isolate the two electrodes electrically [21, 22]. Studies have shown that the electrode material and its morphology have an inevitable impact on the charge storage ability of the device. Electrodes with high surface area and porous structure can enhance the supercapacitive behaviour of the device to a large extent. Nanomaterials with their high surface-to-volume ratio characteristics have been able to establish a substantial impact on the field of energy storage systems. The electrochemical performance of the SC device is highly influenced by the specific surface area (SSA) of the electrode material as it decides the amount of charge to be stored, increasing the capacitance of the device. Along with SSA, pore size distribution, pore shape, structure, surface functionality, and electrical conductivity of the electrode material also contribute to the specific capacitance [23]. The morphology of electroactive material seems to improve the cycling performance of the device fabricated due to its ability to accommodate strain during ion insertion/removal [24]. Electrodes trigger charge accumulation at the electrode/electrolyte interface when they are placed in the electrolyte. Based on the charge accumulation mechanism and the active materials used for the electrodes, the electrochemical SCs are widely categorized under electrical double-layer capacitors (EDLCs), pseudocapacitors, and hybrid supercapacitors [5, 25]. Figure 6 shows the schematic representation of (a) carbon-based electrical double-layer capacitor (EDLC), (b) pseudocapacitor, and (c) hybrid supercapacitor [26, 27].

2 Electrical Double-Layer Capacitor

EDLCs store charges through the electrostatic method exhibiting no prominent oxidation or reduction peaks in cyclic voltammetry (CV). Due to this, the resulting

energy density of EDLC SCs is low (Fig. 6a) [28–30]. Materials prepared from carbon shows such behaviour where charges pile on the electrode and an equal but opposite charge develops in the electrolyte which provides charge neutrality. Charge accumulations on the surface of the electrode and in the electrolyte together form a double layer. Such accumulations can be explained based on the following theoretical models: (1) the Helmholtz model, (2) the Gouy-Chapman model, and (3) the Stern model [15]. The theoretical Helmholtz model is well depicted in Fig. 7a which predicts that the charges opposite to that on the surface of the electrode diffuse through the electrolyte and accumulate at the electrode/electrolyte interface when polarized, causing the formation of two layers parallel to each other termed as ‘electrical double layer (EDL)’, but there are certain disadvantages associated with this theory, such as it does not consider the diffusion of ion through the electrolyte. Dipole moment interaction of both electrode and electrolyte is neglected. According to the Gouy-Chapman model, as shown in the Fig. 7b, there is an exponential decrease in the potential as we move from the electrode surface to the bulk fluid. This model predicted a larger capacitance at the interface; as a result, this was not applicable for highly charged layers. Lastly, the Stern model (Fig. 7c) considered both the Helmholtz model and the Gouy-Chapman model. The inner region of ion distribution was considered as an adsorption area, and the region outside was considered as a diffusion region of distributed ionic charge. Thus, the total capacitance of an EDLC is given by

$$\frac{1}{C_{\mathrm{dl}}} = \frac{1}{C_{\mathrm{H}}} + \frac{1}{C_{\mathrm{diff}}} \quad (1)$$

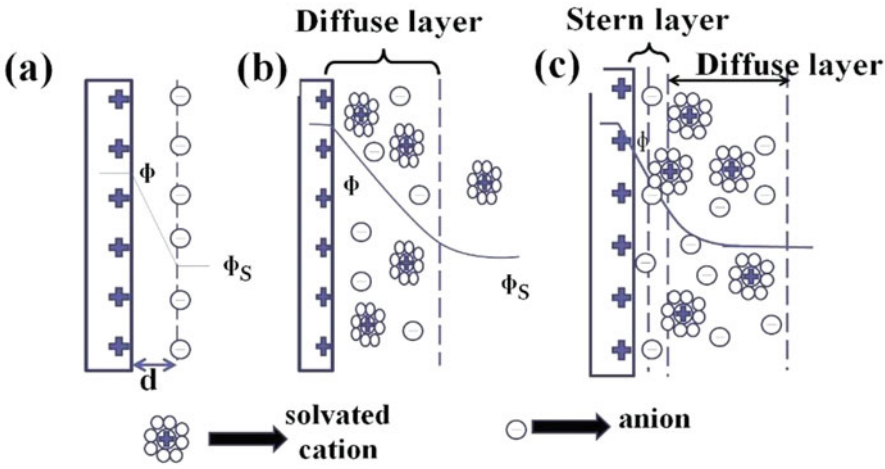

Fig. 7 Schematic representation of (**a**) Helmholtz model, (**b**) Gouy-Chapman model, and (**c**) Stern model [15]

Here C_{dl} represents the EDLC capacitance, C_H represents the capacitance of Stern type, and C_{diff} is the capacitance corresponding to the diffusion region [31]. The electric charge accumulated is relative to the number of ions adsorbed.

3 Pseudocapacitors

Pseudocapacitors, the second type of electrochemical SC, are made up of two electrodes with "two different" active materials having porous morphology (Fig. 6b). These SCs store energy by using one of the following processes: (a) ion electrosorption or adsorption (Fig. 8a), (b) surface redox process (Fig. 8b), or (c) intercalation process (Fig. 8c). The energy densities associated with these SCs are higher than those observed in EDLC. This is due to the highly reversible faradaic nature of the active material, used as an electrode in pseudocapacitors [32]. However, the energy stored in these types of SCs is less compared to other storage devices; hence there is a significant challenge in enhancing this property and employing it as a replacement for batteries [33]. The main difference between pseudocapacitor and EDLC is that in the case of EDLC, no ion-exchange (IE) process occurs between the electrode and the electrolyte, indicating that the electrolyte ions remain almost stable during electrochemical activity, while in the case of pseudocapacitors, it suffers from poor cyclic performance due to repetitive redox reactions and a large internal resistance caused by the poor electrical conductivity [26, 34].

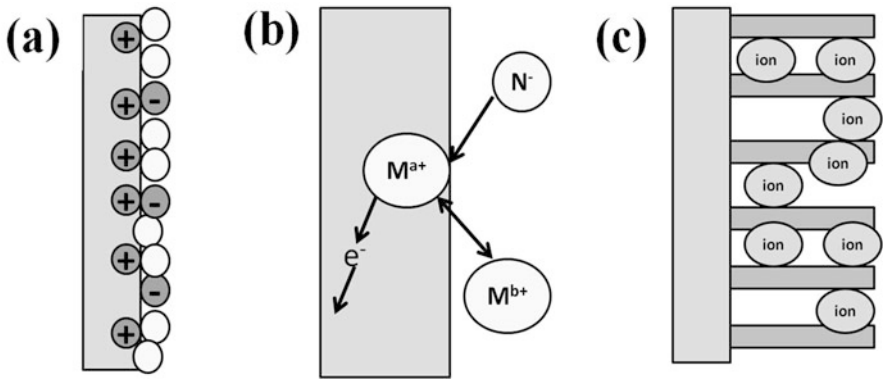

Fig. 8 Representation of (**a**) ion electrosorption or adsorption, (**b**) surface redox process, and (**c**) intercalation [32]

4 Hybrid Supercapacitor

Hybrid supercapacitors (HSCs) with high energy density values of approximately >50 Wh kg^{-1} and power density > 10 kW kg^{-1} with a stable cycle are considered to be an excellent energy storage system [26]. Figure 6c shows the utilization of porous material on one electrode and carbon-based material on another electrode. The first reported HSCs used battery-type electrolytes where Li ions intercalated into the porous anode and increased the energy density while the anions adsorbed onto the surface of the carbon-based cathode and resulted in high power density. However, the main issue with this type of energy storage is that the cation-intercalation kinetics is slower which caused an imbalance in the rate performance of each electrode.

5 Characteristic Behaviour of EDLC and Pseudocapacitors

Supercapacitors are mainly categorized based on their cyclic voltammetry (CV) and charge-discharge (CD) profile. Brief insight is given into the characteristic behaviour of both types of SCs.

5.1 Cyclic Voltammetry

Cyclic voltammetry (CV) yields basic information about the electrochemical cell such as the working potential window, charge storage capability, charge storage mechanism, and cycle life of the cell. The electrochemical cell utilized for analysis purposes consists of three electrodes, counter electrode (CE), reference electrode (RE) and the working electrode (WE), placed in a beaker filled with an appropriate amount of electrolyte. For CV measurements, a triangular-shaped potential, also called sweep voltage, as shown in Fig. 9a, is applied between the WE and RE while the response current is measured between the WE and CE. The output obtained will show a plot between the current and the voltage as shown in Fig. 9b. This study is termed as cyclic voltammetry since this can be continued for 'n' number of cycles. Here, we can also change the rate at which the electrode surface should be scanned.

The rate at which the voltage changes over time during each phase of the sweep voltage is termed as the scan rate of the experiment. The current response of EDLC and pseudocapacitor is different when voltage is applied. EDLC has almost a rectangular voltammetric shape, while pseudocapacitor shows redox peaks, one for oxidation and the other for reduction process (Fig. 10) [35]. During the initial forward scan, reduction of the active materials occurs, generating a cathodic current which keeps on increasing till it reaches a peak value termed as cathodic peak current (E_{pc}) where almost complete analyte is used up. After reaching the peak

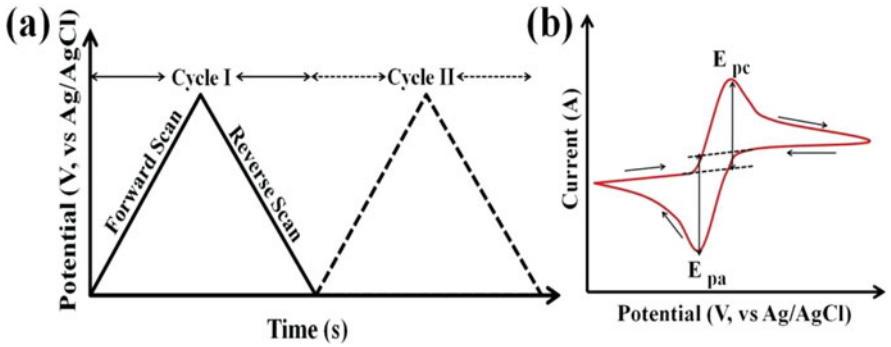

Fig. 9 (**a**) Sweep cycle provided by the potentiostat to the electrochemical cell and (**b**) output provided by the cell (cyclic voltammogram)

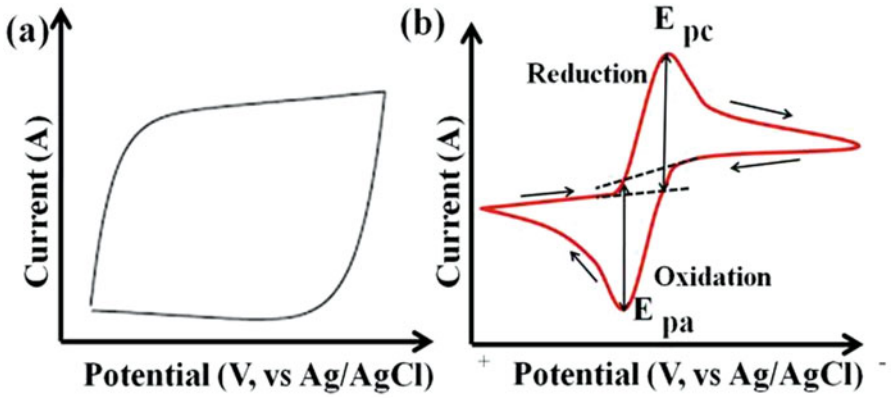

Fig. 10 Characteristic CV of (**a**) EDLC and (**b**) pseudocapacitor [35]

value, increasing the forward scan reduces the current. Now on a reverse scan, if the material is reversible, then oxidation of the material begins in such a way that the highest peak current is obtained in the reverse direction which is termed as anodic peak current (E_{pa}). A nearly rectangular-shaped CV curve of EDLC materials indicates that the capacitive behaviour of the active material is good and it provides a low contact resistance which can boost the charge transfer process at the interface [33]. However, in the case of a pseudocapacitive electrode, the peak current of the CV curve must vary linearly with the scan rate. Typically, CV is studied for different scan rates. If at each scan rate an identical curve is obtained, then it implies that the redox process of the electrode material is reversible and is reproducible. During a high scan rate, the superficial surface of the electrode is utilized, while in case of a lower scan rate, both the exterior and the interior of the active material participate actively. From the CV curve of the electrode, the specific capacitance (C_{sp}) can be calculated by using the formula [36]

$$C_{sp} = \frac{\int I\, dv}{m \times \frac{dv}{dt} \times (V_2 - V_1)} \tag{2}$$

Here response current (A) is denoted by 'I', 'm' total mass of the active material (g), $V_2 - V_1$ potential window of the CV curve (V), and $\frac{dv}{dt}$ the scan rate (V s^{-1}).

5.2 Galvanostatic Charge-Discharge Characteristics

The galvanostatic charge-discharge (GCD) process is studied by applying a constant current to the electrochemical cell [37]. It is a more versatile and accurate approach for characterizing the SC device. A constant current is applied to the cell which will be less than the maximum current obtained from the CV curve. The output obtained will be a plot between the potential (V) and time (s). The CD profile for both EDLC and a pseudocapacitor is distinct. EDLC shows an almost ideal capacitor profile as shown in Fig. 11a. The time taken for charging (T_c) will be almost equal to the time taken for discharging (T_d). If the curve appears non-linear, then the charge storage ability of the material will be pseudocapacitive in nature (Fig. 11b). A small IR drop usually appears in the case of pseudocapacitors; these may also appear in the case of EDLCs. This drop arises due to the internal resistance of the cell as well as due to the different rates of oxidation and reduction reactions occurring within the cell [38, 39]. The smaller the IR drop, the lesser will be the internal resistance of the device which implies that there is good adhesion between the active material and the substrate, improving the conductivity of the electrodes which is necessary for energy electrodes [36, 40]. A larger discharge time indicates that the charge storage capability of the material is good, i.e. the material can provide energy for a longer duration of time [41]. C_{sp} is calculated from the CD curve using the formula [42]

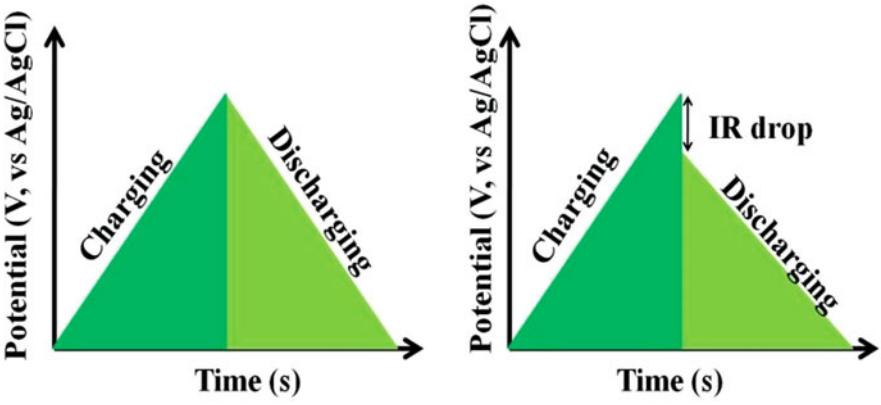

Fig. 11 Charge-discharge curves of (**a**) ideal supercapacitor and (**b**) pseudocapacitor

$$C_{\mathrm{sp}} = \frac{I \int V\, dt}{m \times V^2 \big|_{V_i}^{V_f}} \tag{3}$$

where 'I' represents current density, 'm' mass of the active material, $\int Vdt$ area under the experimental curve, and V_f and V_i the final potential and the initial potential of the active window. Energy and power density are two key attributes of a SC, where the former defines the quantity of energy that can be stored in the device, while the latter tells about how fast this can be released [43]. Energy stored by a SC is related to the charge accumulated at each of its various interfaces and on its active potential window (V). It is calculated from CV using the formula

$$E = \frac{0.5 \times C_{\mathrm{sp}} \times \left(V_{\mathrm{max}}^2 - V_{\mathrm{min}}^2\right)}{3.6} = \frac{1}{2 \times 3.6} \times C_{\mathrm{sp}} \times V^2 \tag{4}$$

where V_{max} and V_{min} represent the maximum and the minimum potential of the window in V and C_{sp} the specific capacitance in F g^{-1}. Power is related to energy density and discharge time using the formula

$$P = \frac{E \times 3600}{T_d} \tag{5}$$

where T_d is the discharge time in seconds.

5.3 Electrochemical Impedance Spectroscopy

Electrochemical impedance spectroscopy (EIS) is used to estimate the resistive properties of electrode. It measures the resistivity offered by any circuit to the flow of electric current through it. EIS can also be used to determine the different reaction processes occurring at the surface of the active material. It provides information regarding the electron transfer rate of any reaction. It plots the graph between the real and the imaginary part of the impedance value, termed as the 'Nyquist plot'. For measurement, a sinusoidal signal of certain frequency range is applied to the electrochemical cell. The Nyquist plot shows a semi-circle at higher frequency range, while at lower frequency range, it shows a 45° angle line as shown in Fig. 12. X-axis intercept of the semi-circle is termed as the internal resistance (R_s) or equivalent series resistance (ESR). ESR is the sum of various resistances exciting in the electrochemical cell. These includes the resistance at the interface of the active material and the current collector, the resistance offered by the electrolyte ions, and the intrinsic resistance of the active material [44]. It can also determine the rate at which the cell can be charged-discharged (power capability) [45]. Lesser value of R_s is beneficial for rapid ion transport from solution to the electrode [46]. Twice the radius of the semi-circle formed in the Nyquist plot provides the charge transfer resistance (R_{ct}) at the electrode/electrolyte interface. If the semi-circle at

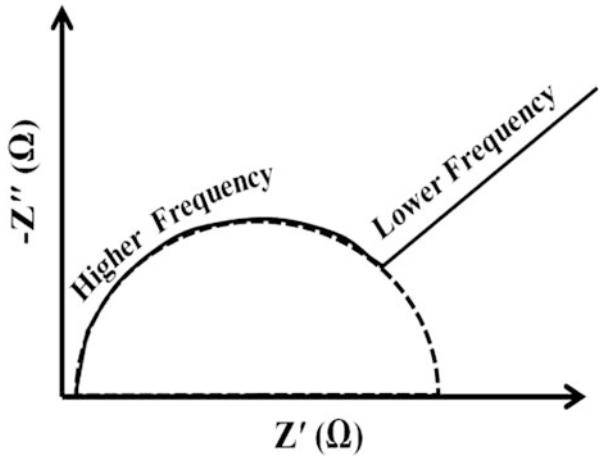

Fig. 12 EIS spectrum of an electrochemical cell

higher frequency is negligible, then it suggests that the resistance provided is due to the ion-diffusion process which is frequency dependent. Theoretically, the ESR estimated from the IR drop and that from the intercept must be the same, but it appears to vary in most of the cases. This is mainly because in charge-discharge analysis, the resistance offered is a sum of various constituents of the cell that includes the active material and the separator, while in the case of Nyquist plot, resistance is a function of frequency. Thus, ESR estimation through Nyquist plot is more accurate than the charge-discharge analysis [47]. The second part of Nyquist plot which is a 45° inclination line is called the Warburg resistance and is a result of ion diffusion/transport in the electrolyte [39]. If this line is nearly vertical at lower frequency, then the electrode is close to an ideal capacitor, i.e. the ion-diffusion path becomes short and the ion-diffusion resistance reduces [48].

5.4 Stability

An ideal SC must charge and discharge for an infinite number of cycles; however in actual conditions, the stability of SC is highly influenced by the mechanical and chemical stability of the electrode material [49]. Instability obtained during cycling process of SCs may be attributed to various facts such as (i) phase change of electrode material during oxidation-reduction process, (ii) dissolution of electrode material in electrolyte, or (iii) due to some other side reactions. During stability study, the material is subjected to continuous cycle of sweep potential and the corresponding current is studied, i.e. during stability analysis, continuous graph of CV or CD is taken for cycles $\geq$1000. The material with good stability will not show any significant loss, indicating less degradation of the electrode material [50].

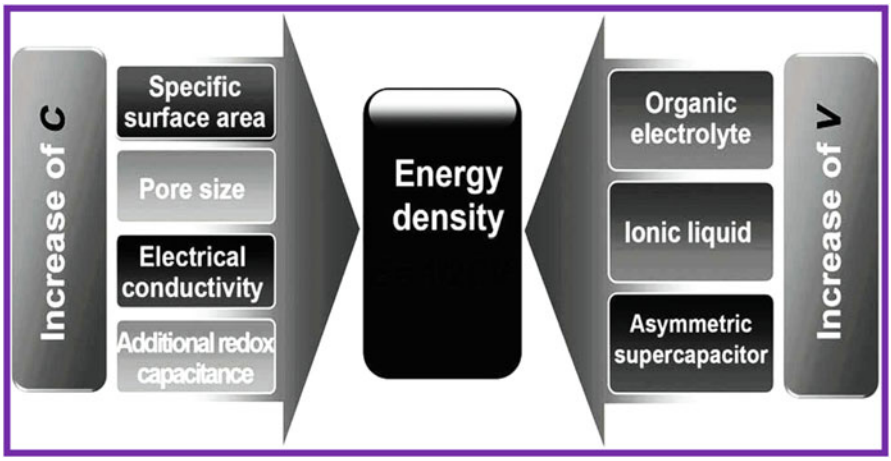

Fig. 13 Factors affecting the energy density of the supercapacitors [58]

6 Factors Affecting Supercapacitive Behaviour

Supercapacitors (SCs) are supposed to be the saviour for next-generation high energy demands [51, 52]. This can exhibit high capacitance with high power density, with low internal resistance, fast charge-discharge rate, and good stability with safe operations [53, 54]. These are low maintenance and lightweight devices which can be used in places were high current for short duration of time is a must [55]. Alas, with all such benefits, its moderate energy density value is one of the most crucial challenges that requires to be enhanced so that it can be a commercially viable primary power supply. Also, the fabrication processes for large-scale manufacturing continues to be the major challenge for its commercialization. Several other challenges faced by SCs apart from being low energy density device and surged cost in mass production are that its voltage output per unit cell is low and it has a high self-discharge trait [56].

In general, energy associated with an electrode or device can be calculated using the formula [57]

$$E = \frac{1}{2} \mathrm{CV}^2 \tag{6}$$

which indicates that it is proportional to the capacity and potential window within which the SC can actively exhibit higher capacitance. However, energy density calculated for the device is more compelling than that of the electrode alone since the capacitance typically reduces in device compared to the electrode. Figure 13 indicates the factors that can increase both capacitance and the potential window of SC [58].

6.1 Specific Surface Area

Increased specific surface area can provide more functioning sites for faradaic reactions [34]. However, Lu et al. [52] had stated that for high performance, materials with dimensions in nano-regime are not enough, but structures with high ionic accessibility play a dominant role. Such accessibility should be supported by materials even during fast charge-discharge process [52]. Carbon nanomaterials and their allotropes are advocated to be one such potential candidate for SC applications. Theoretically, the specific capacitance must increase with specific surface area (SSA) as $C = \varepsilon_0 \varepsilon_r \frac{A}{d}$. However, practically this relationship is not linear as it depends on the electrolyte entering through the micropores of the material surface [59].

6.2 Pore Size

Specific surface area, a key factor for increasing the capacitance, is a combination of highly interfused pores of macro (> 50 nm), meso (2–50 nm), and micro (< 2 nm) range. Each pore size has their own individual significance such as macro-pores can facilitate transportation of electrolyte ions into the internal parts of active materials, meso-pores provides transport conduits for the diffusion of electrolytes, while micropores allows accommodation of electrolyte ions through controlled diffusion and molecular sieve method [60]. Kondrat et al. [61] during their study about pore size and its influence on energy storage efficacy had stated that the ideal pore size that provides maximum energy density increases with the operating voltage and saturates at higher voltage [61]. Here, not only pore size but also its distribution, connectivity, and wettability have significant influence over the capacitance storage capability of the electrode. Interconnected pores with open and continuous path assist rapid ionic transport which are advantageous for attaining high specific capacitance and ultrahigh power density. Pore connectivity is more important than the size as it ensures fast interfacial faradaic reaction in compact electrodes. Highly wettable micropore reduces the system resistance and improves the power response of the electrode. It increases the contact surface between the electrolyte and the active material [60].

6.3 Electrical Conductivity

Besides pore size and its distribution, material conductivity also enhances the capacitance of SC as it highly favours the faradaic reactions [62]. Most of the transition metal oxides, sulphides, and hydroxides have low conductivities, while carbon-based materials have good electrical conductivity. So, a composite of such materials seems to increase the conductivity and reduce the internal resistance

drastically. Pandit et al. [63] could easily demonstrate the significant enhancement in the C_{sp} of the electrode when the conductivity was increased by anchoring silver (Ag) nanoparticles onto multiwalled CNT (MWCNT). Ag nanoparticles demonstrated a C_{sp} of 452 F g^{-1} at a scan rate of 2 mV s^{-1} which increased to 757 F g^{-1} in case of its composite with MWCNT. Similarly, the specific energy of the metal was found to be 27.8 W h kg^{-1} which improved to 60.7 W h kg^{-1} for same potential window of 0.9 V when combined with MWCNT [63, 64].

6.4 Additional Redox Capacitance

The charge storage capability of any electrode is higher if their existing redox peaks provides high current output. There are multiple ways to increase the redox peaks: (i) use of materials with multiple oxidation states, (ii) synthesis of bimetal or trimetal electrodes, and (iii) addition of redox materials to the electrolyte. Multivalent transition metals lead to high electrical conductivity which eventually has an impact over the SC behaviour. Similarly, induction of a material into a host will also render multiple oxidation states which eventually enhance the SC behaviour. Electrolytes are also considered to be another key factor for the better performance. Energy density is related to the decomposition voltage of the electrolyte, while power density is depended on the ionic conductivity of the electrolyte. Redox electrolyte consists of redox-active material which takes an active part during charge-discharge process and also facilitates the electron transfer while undergoing redox process [65–67].

6.5 Organic Electrolyte

An electrolyte not only provides ions for electrochemical activity in SC but also defines the cell voltage beyond which it decomposes, creating gases. Electrolytes used in SCs should provide wide working potential range with high conductivity, low viscosity, and chemical stability. These are also expected to be environmentally benign, easily available, and cheap. There exist three main types of electrolytes such as aqueous, organic, and ionic liquids, the properties of which are summarized in Table 2 [59].

Aqueous electrolytes have good ionic conductivity than organic or ionic liquid (IL) electrolyte. However, its restricted potential window with low decomposition potential refrains it from being an ideal electrolyte for high energy density SCs. In case of organic electrolytes, a wider voltage window of approximately 3 V is obtained, while in case of aqueous electrolytes, it is 1 V. Aqueous electrolytes are environmentally benign and composed of small anions and hydrated cations which can penetrate through micro-, meso-, and macro-pores of the electrode material. On the other hand, organic electrolytes suffer from high cost, poor ionic conductivity, and high toxicity, which would limit their application, though in case of non-

Table 2 Different types of electrolyte properties [59]

Electrolyte type	Electrochemical window	Ion size	Cost	Toxicity
Aqueous	≤ 1	0.37–0.26 nm	L	L
Organic	2.5~2.7	Solvated ~1.3–1.16 nm Bare cation ~0.67 nm bare anion ~0.48 nm	M/H	M/H
ILs	3–6	0.76×0.43, 0.8×0.3 nm	VH	L

aqueous electrolyte, its resistivity is more resulting into higher internal resistance (ESR). Accessing the active sites becomes easier with small electrolyte ions or with ions whose size is comparable to the pores of the electrode material [68]. Organic electrolytes can increase the potential window with higher decomposition voltage instead of aqueous electrolytes. But organic electrolytes are flammable and toxic which curtails its maximum utilization in SCs [69].

6.6 Ionic Liquid

Ionic liquids (ILs) are safe alternative to organic electrolyte, owing to their incombustible nature, wide working potential range, and more ionic conductivity with thermostability. ILs have two redox moieties which can undergo fast reversible redox reaction providing a high capacity, high rate of charge storage [60]. These contains bulky, asymmetric organic cation and weakly coordinating inorganic/organic anion which can deliver a wide range of working potential [65]. Despite the use of organic or ionic electrolytes, it is essential that the pore size of the electrode material should be compatible with the size of the electrolyte ions to enable easy diffusion [70]. Pure, eutectic, and ILs/organic solvent mixtures have been studied for SC applications. Even with many advantages, their application is limited, owing to their high viscosity, limited ionic conductivity at low temperature, and poor contact with the electrodes [71]. Still, IL-based solids or gel electrolytes are the most promising electrolytes for solid SCs [72].

6.7 Asymmetric Supercapacitors

Asymmetric SC (ASC) is reported to work in a wide potential range, and as energy density is directly related to it as per Eq. 6, it can be considered as a promising alternative. Here, one electrode will be of battery type which serves as energy source and another as capacitive type electrode which serves as a power source. ASCs combine the voltage window of the two electrodes working on different mechanisms, to increase the maximum operating voltage. In aqueous electrolyte, this can reach up to 2 V, eventually enhancing the energy density and power density of the device.

Innumerable materials are explored for the purpose of enhancing the supercapacitive properties. Besides pursuing for new materials and their various combinations, nanostructuring of materials has also been the major focus of scientific experts as it decides the active areas available for electrochemical activity.

7 Nanostructure Dimensions

0D, 1D, 2D, and 3D nanostructures propose different amounts of specific surface area for electrochemical activity. Same material with different morphologies can show different SC activity, so comparison in terms of nanostructures is not a sufficient method. Figure 14 shows various dimensions of nanomaterials that are

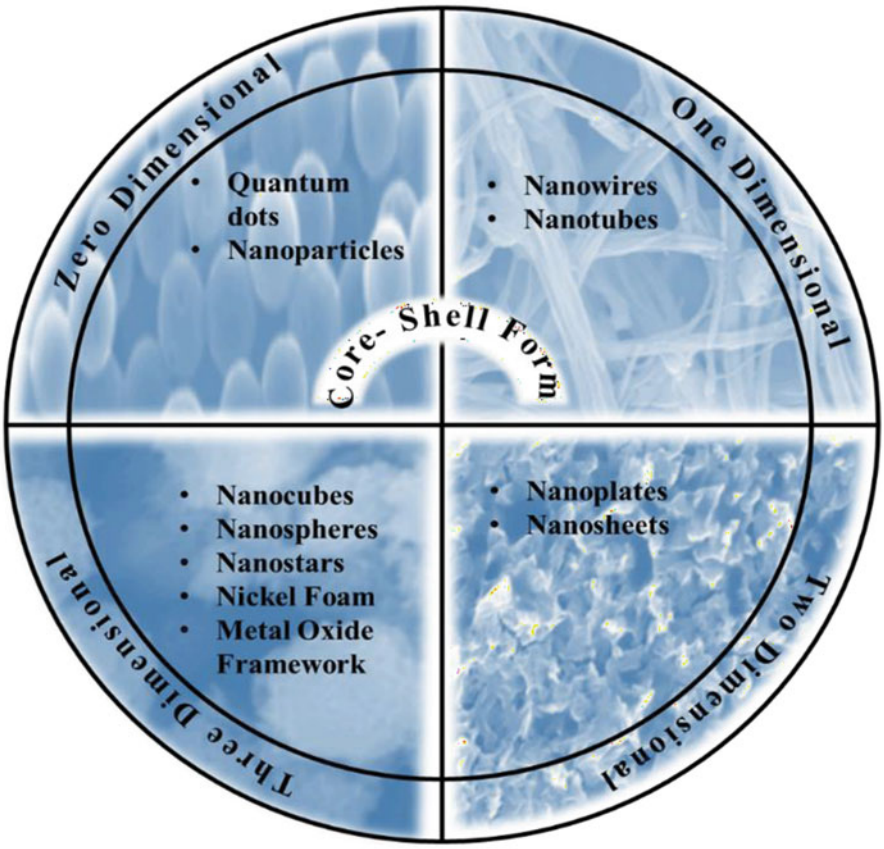

Fig. 14 Different possible dimensions of the nanomaterials with their examples

synthesized and classified, till now. Core-shell morphology in both 0D and 1D forms has also been evaluated.

7.1 Zero-Dimensional (0D) Nanostructure

Structures with their dimensions below nanometer level (100 nm) along their three sides are classified as zero-dimensional (0D) materials. Such structures have good specific surface area which can provide more functional surfaces for electrochemical activity [73]. As shown in Fig. 14, these include quantum dots and nanoparticles of shapes like cages, spheres, and onion. Hollowed and core-shell 0D structures have augmented the C_{sp} of SCs considerably.

Pandit et al. [63] used electroless method to deposit Ag nanoparticles on stainless steel substrate (SS). Figure 15(a,b) shows the FESEM images of Ag nanoparticles over SS substrate which exhibits nearly circular shape of Ag particles. HRTEM image shown in Fig. 15c depicts a morphology analogue to quantum dots. CV analysis of the material in 0.5 M NaOH electrolyte between −0.2 and −1.1 V as shown in Fig. 15d exhibits prominent redox peaks at each scan rates. It reached up to 452 F g^{-1} C_{sp} at a scan rate of 2 mV s^{-1}. GCD study shown in Fig. 15e indicates IR drop up to 0.6 V and then a linear behaviour. C_{sp} evaluated from GCD showed nearly half the value obtained through CV analysis, i.e. 247 F g^{-1} at 2 mA cm^{-2} current density. This is because the potential windows for both studies were different. The electrode showed specific energy and specific power density of

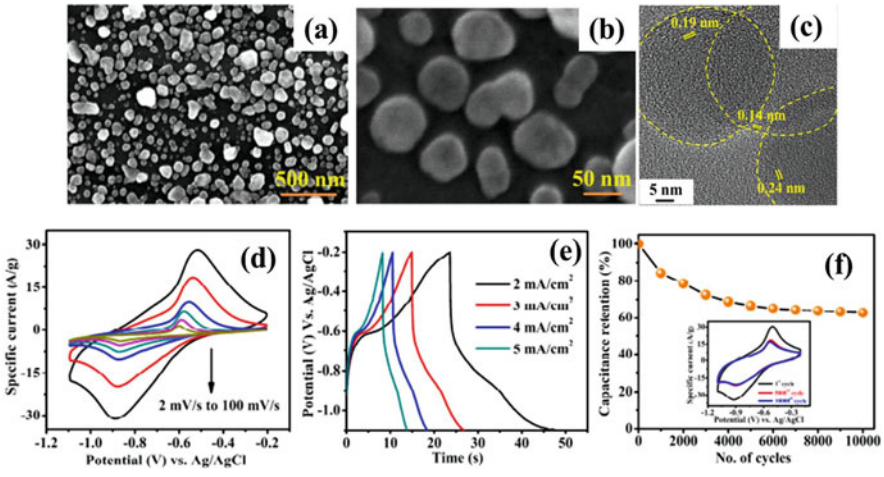

Fig. 15 (**a**, **b**) FESEM images of Ag nanoparticles at different magnifications, (**c**) HRTEM image of the nanoparticles showing size <100 nm, (**d**) CV analysis of the electrode material, (**e**) GCD profile of the material, and (**f**) retention test of the Ag nanoparticles. Inset showing CV of the electrode material at different cycles [63]

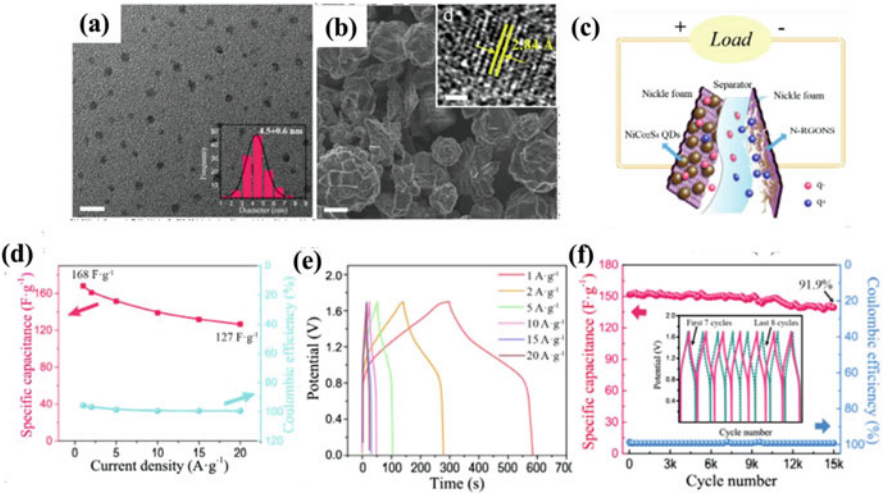

Fig. 16 (**a**) TEM image of $NiCo_2S_4$ QDs and the inset shows the histogram for particle size, (**b**) FESEM image of $NiCo_2S_4$ QD and inset showing the HRTEM image of single QD, (**c**) schematic of $NiCo_2S_4$//nitrogen doped reduced graphene oxide nanosheet device fabricated, (**d**) specific capacitance and coulombic efficiency of the device fabricated, (**e**) charge-discharge study of the device at different current density, and (**f**) capacitance and coulombic retention of the device with inset showing the CD cycles at different cycles [75]

27.8 Wh kg^{-1} and 4.1 kW kg^{-1}, respectively. With initial deterioration of 37%, the material could maintain 63% of its initial capacity up to 10,000 cycles (Fig. 15f). The bode plot analysis showed −72° phase angle which is nearer to the ideal −90° for capacitive behaviour [63]. Zhang et al. [74] fabricated graphene quantum dots of size less than 5 nm using hydrothermal method with nitric acid and obtained a C_{sp} of 296.7 F g^{-1} at a current density of 1 A g^{-1} in 2 M KOH. The GCD curves were symmetric indicating EDLC behaviour of the electrode. The electrode showed an energy density 41.2 W h kg^{-1} at a power density 500 W kg^{-1} within a working potential of −1 to 0 V. The electrode could maintain 97.6% of its initial potential even at 5000 CV cycles [74]. Chen et al. [75] stated that during material fabrication, there exist many internal dead zones that virtually do not participate in electrochemical activity. Apparently, the depth to which an electrolyte can diffuse is only 20 nm. So, to involve all such areas, it has been reported that quantum dot (QD) structures can provide the requisite small size with large specific surface area and rich pore structure essential for an enhanced SC behaviour. They prepared $NiCo_2S_4$ QDs through colloidal hot injection process and coated it over the nickel foam (NF) using binder. Figure 16a shows the TEM image of the QD with excellent monodispersity. From Fig. 16b, it is evident that the synthesized material has a spherical or ellipsoidal morphology. A comparative analysis of $NiCo_2S_4$, NiS_2, and CoS_2 quantum dots showed that $NiCo_2S_4$ encloses larger CV area in KOH electrolyte. The GCD analysis showed C_{sp} of bulk $NiCo_2S_4$, CoS_2, NiS_2, and $NiCo_2S_4$ to

be 177.2, 294.1, 308.9, and 987.2 C g^{-1}, respectively. Figure 16c represents schematic of device fabricated using $NiCo_2S_4$//nitrogen doped reduced graphene oxide nanosheets as cathode and anode electrodes, respectively. The highest C_{sp} obtained from the device was 168.1 F g^{-1} at a current density of 1 A g^{-1} (Fig. 16d). Very small potential drop can be seen from the GCD curves (Fig. 16e) with nearly symmetric branches of charge-discharge indicating good and reliable capacitance. Cyclic study of the device showed 91.9% stability at 15,000 cycles (Fig. 16f). The device was able to exhibit a maximum energy density of 67.5 W h kg^{-1} at power density of 850 W kg^{-1} [75].

7.2 One-Dimensional (1D) Nanostructures

One-dimensional (1D) nanowire (NW) has attracted great consideration due to their ease of synthesis and unidirectional route. Such morphology exposes more active interfaces between electrode and electrolyte. 1D structures have unique property of efficient charge transfer and fast strain relaxation during electrochemically driven volume expansion/contraction. They have unique chemical and physical features and promising applications in LED, lasers, field emitters, solar cells, and as electrode materials for energy storage devices [76]. As shown in Fig. 14, 1D includes nanowires and nanotubes which can also exist in core-shell form. TiO_2 is one of the oxides with higher stability, low cost, better safety, and environmental friendliness in comparison to other metal oxides. Its composite with 1D MWCNT is believed to deliver an enhanced electrochemical behaviour due to the synergetic effect of both the materials. Sankapal et al. [77] coated SS substrate with 1D MWCNT through dip-coating method followed by the deposition of TiO_2 nanodots through the chemical bath deposition method (CBD) (Fig. 17a). CBD method is a simple, low-cost, and binder-free approach for large-scale deposition of material on different substrates. This helps in pin-hole-free and uniform deposition of the electrode material. Figure 17b shows the FESEM image of TiO_2 _ coated MWCNT with entangled networks having larger pores enabling the accessibility of the active areas by the electrolyte ions. Figure 17c clearly shows the formation of TiO_2 nanodots over MWCNT. The CV analysis of the electrode shown in Fig. 17d has pseudocapacitive nature implicating that the charge storage is through redox mechanism. Redox peaks are obtained either through intercalation/de-intercalation of the electrolyte ion or through the adsorption of H^+ ions on the surface. A maximum specific capacitance of 329 F g^{-1} was obtained at a scan rate of 5 mV s^{-1} in 1 M H_2SO_4 within a potential frame of 0 to 0.9 V. As per Fig. 17e, the stability analysis showed a drop for the first 100 cycles; thereafter, it could retain 76% of its initial capacitance for the next 1500 cycles. At higher current density, GCD profile showed an almost linear relation between charging-discharging time and voltage, while at lower current densities, this behaviour changed to a non-linear

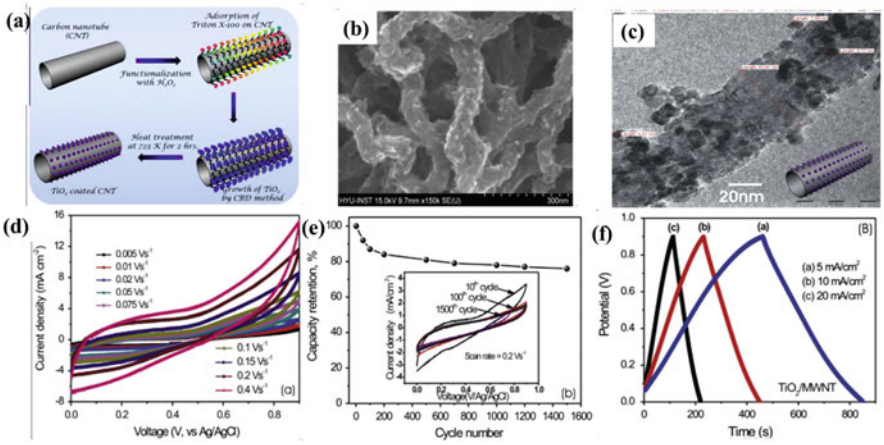

Fig. 17 (**a**) Pictorial representation showing the process of formation of TiO_2-coated CNT. (**b**) FESEM image of TiO_2-coated CNT. (**c**) HRTEM image showing TiO_2 nanoparticles over CNT. (**d**) CV analysis of the electrode material at different scan rates. (**e**) Stability study of the electrode. Inset showing the CV curves at 10th, 100th, and 1500th cycles. (**f**) Charge-discharge curve of the electrode at different current densities [77]

pattern. At current density of 5 mA cm^{-2}, the electrode showed a maximum specific capacitance of 312 F g^{-1} [77].

Raut et al. [78] fabricated vertically aligned arrays of TiO_2 nanotubes through anodization method on Ti foil. FESEM image shown in Fig. 18a depicts vertically aligned nanotubes which can provide a unidirectional path towards the substrate, reducing the internal resistance of the electrode. Such vertical alignment reduces the barriers and promotes easy flow of electrolyte ions enabling access to active areas within the hollow region of the nanotubes. The cross-sectional view of the material shown in Fig. 18b indicates a thickness of 3.2 μm. The nanotubes have an average length of 3 μm with diameter of approximately 96 nm. The TEM image in Fig. 18c clearly shows tube-like structure of the electrode material. The electrochemical behaviour of the electrode was analysed in various electrolytes like NaOH, KOH, and Na_2SO_4 within a potential window of 0 to −1 V. It was observed that in 1 M KOH, TiO_2 nanotubes showed largest C_{sp} of 153 F g^{-1}. As the radius of hydrated electrolyte ion K^+ is around 3.31 A° which is less than the diameter of the nanotube, it permits intercalation of electrolyte ions along the direction of the nanotube. The high ionic conductivity of K^+ is another factor that contributes to the larger specific capacitance of the electrode material. Figure 18d shows the CV analysis of TiO_2 electrode material at different scan rates. It has a maximum C_{sp} of 207 F g^{-1} at 5 mV s^{-1} scan rate which was maintained up to 153 F g^{-1} at 100 mV s^{-1}. Galvanostatic charge-discharge analysis (Fig. 18e) showed a non-linear behaviour with reduced IR drop. TiO_2 electrode could exhibit 27.8 W h kg^{-1} energy density corresponding to 1.42 kW kg^{-1} power density at 0.6 mA cm^{-2} current density. Stability analysis of the same showed 100% retention for the first

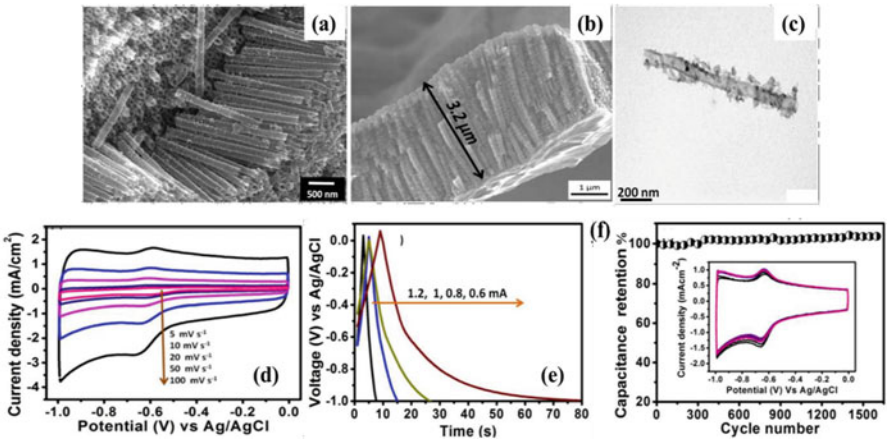

Fig. 18 (**a**) FESEM images of vertically aligned TiO_2 nanotubes, (**b**) cross-sectional view of TiO_2 nanotubes, (**c**) HRTEM image of the nanotube, (**d**) CV analysis of the TiO_2 nanotube at different scan rates, (**e**) charge-discharge analysis of the electrode material, and (**f**) stability analysis of the electrode material. Inset shows CV of the material during stability study [78]

300 cycles which slowly increased to 103% and remained constant up to 1500 cycles [78]. When comparing TiO_2 nanodots over MWCNT and TiO_2 arrays of nanotubes vertically aligned over the substrate, it can be inferred that the MWCNT increases the C_{sp} of the electrode material, while the vertically aligned material increases the stability of the electrode. Patil et al. [40] used the same CBD method for the deposition of cadmium hydroxide ($Cd(OH)_2$) NWs over SS substrate and studied its SC property. $Cd(OH)_2$ exhibited high energy density, long lifetime, and high discharge rates. Figure 19a shows ultralong, entangled nanowires of $Cd(OH)_2$. The electrochemical analysis in different molarity of NaOH electrolyte showed that in 1 M, the specific capacitance obtained was the highest. On further analysis with 1 M NaOH, it was observed that the electrode showed a specific capacitance of 267 F g^{-1} at 5 mV s^{-1} (Fig. 19b). The electrode exhibited specific energy of 23.61 W h kg^{-1} with a maximum power of 3269.23 W kg^{-1} for 1.87 A g^{-1} current density (Fig. 19c). Figure 19d shows 86% cyclic stability for $Cd(OH)_2$ electrode. Figure 19e shows the CV curve of symmetric supercapacitor with $Cd(OH)_2$//$Cd(OH)_2$ as the electrode and NaOH as the aqueous electrolyte. It exhibited a maximum C_{sp} of 51 F g^{-1} at 5 mV s^{-1} in −1.9 to 0 V potential window (Fig. 19f). The charge-discharge graph showed a sudden drop during discharging process, indicating the high internal resistance (Fig. 19g) with maximum energy density of 11.09 W h kg^{-1} and power density of 799 W kg^{-1} at 0.84 A g^{-1} current density (Fig. 19h). The device showed an increase in its capacitance by 17% till 500 cycles and maintained the same upto 1000 cycles [40].

In continuation, Patil et al. [79] prepared 1D core-shell morphology with $Cd(OH)_2$ as the core and $Cu(OH)_2$ as the shell. $Cd(OH)_2$ was deposited using CBD method and further converted into $Cu(OH)_2$ through ion-exchange (IE) method

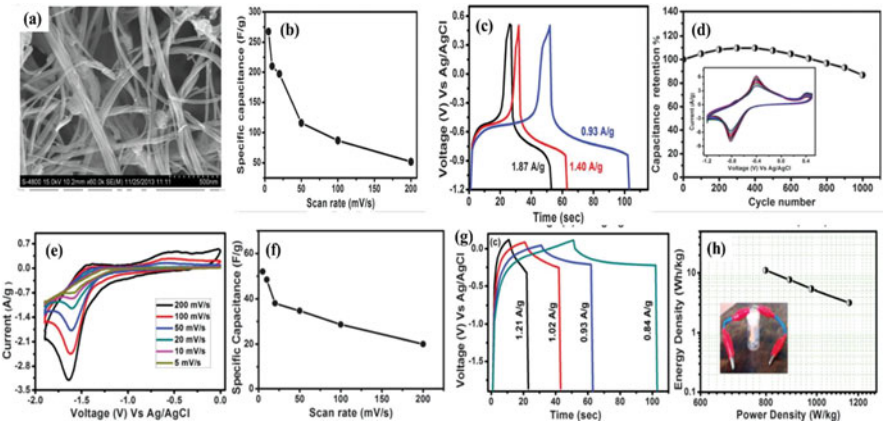

Fig. 19 (**a**) $Cd(OH)_2$ nanowires over stainless steel, (**b**) specific capacitance of the electrode in 1 M NaOH, (**c**) charge-discharge curve, and (**d**) stability of $Cd(OH)_2$ nanowires. Inset showing CV curve of the electrode in 1 M NaOH for different scan rates, (**e**) CV curve of symmetric supercapacitor device with $Cd(OH)_2$ as both the electrodes and the corresponding (**f**) specific capacitance, (**g**) charge-discharge curve, and (**h**) Ragone plot of the device. Inset shows the $Cd(OH)_2$//$Cd(OH)_2$ symmetric device with liquid electrolyte [40]

where the $Cd(OH)_2$ nanowire was placed in a Cu source [79]. IE method can generate shapes and morphologies in nano-dimensions, which are otherwise difficult to attain. A controlled procedure of such processes help in the formation of lightly doped nanoparticles, alloys, core-shells, and segmented rods. In nanoparticles, the surface-to-volume ratio is large; hence the IE process is much faster [80, 81]. Depending on the requisite type of material, IE can be of cationic or anionic form which is highly influenced by the thermodynamics and the activation barrier. The spontaneity of IE process is attributed to the lower activation barrier which allows diffusion of atoms in nanocrystalline solids when compared to the bulk phase [82]. The difference in the solubility product (K_{sp}) of the initial and the resultant material results in the IE process. The more negative the K_{sp}, the more will be the probability of conversion from parent material to the final without much alteration in the initial surface architecture [83, 84]. The free energy or solubility product (K_{sp}) of $Cu(OH)_2$ ($\sim 10^{-19}$) is more negative than the K_{sp} of cadmium hydroxide ($\sim 10^{-14}$), thus assisting the conversion process. Figure 20(a,b) shows the FESEM images of $Cu(OH)_2$ nanowires and $Cd(OH)_2$/$Cu(OH)_2$ core-shell nanowires, respectively. Figure 20c shows the TEM image of the synthesized sample. The image evidently shows the formation of small particles on the surface of the core nanowires. Figure 20d shows the CV analysis of core material $Cu(OH)_2$ prepared at different deposition time. It is evident from the image that the area enclosed by the curve increases as the deposition time increases. It increased till 15 min; thereafter it reduced due to the overdeposition of the shell material on the core which eventually hinders the smooth flow of electrolyte ions. Samples deposited for 15 min have been further used for electrochemical analysis. Figure 20e

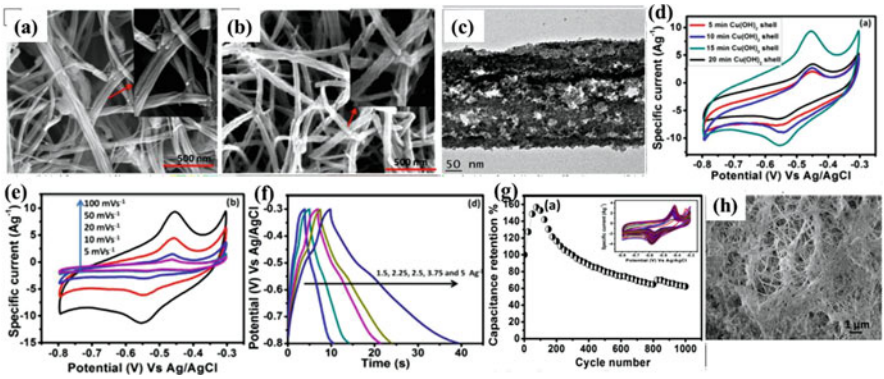

Fig. 20 FESEM images of (**a**) $Cd(OH)_2$ nanowires on stainless steel, (**b**) core-shell structure of $Cd(OH)_2/Cu(OH)_2$, (**c**) TEM image of $Cd(OH)_2/Cu(OH)_2$ core-shell structure, (**d**) CV analysis of different time duration for $Cu(OH)_2$ shell deposition, (**e**) CV analysis of $Cd(OH)_2/Cu(OH)_2$ core-shell nanowires in 1 M NaOH for different scan rates, (**f**) charge-discharge analysis for different current density, and (**g**) stability test of $Cd(OH)_2/Cu(OH)_2$ electrode. Inset showing CV of $Cd(OH)_2/Cu(OH)_2$ core-shell nanowire. (**h**) FESEM image of $Cd(OH)_2/Cu(OH)_2$ core-shell nanowire after the stability test [79]

depicts the CV of $Cd(OH)_2/Cu(OH)_2$ core-shell nanowire for different scan rates. Maximum C_{sp} obtained is 374 F g^{-1} for 5 mV s^{-1} scan rate. For different current densities, the sample showed a non-linear charge-discharge curve (Fig. 20f). C_{sp} calculated from charge-discharge curve was found to be 277 F g^{-1} for a current density of 1.5 A g^{-1}. Stability analysis showed that the capacitance increased for initial 100 cycles which was further retained up to 62% for 1000 cycles (Fig. 20g). Figure 20h shows the morphology of $Cd(OH)_2/Cu(OH)_2$ nanowire after stability test, and it shows that the morphology of the material remains almost intact [79].

Working on similar concept, Patil et al. [85] fabricated $Cd(OH)_2/Fe(OH)_2$ core-shell material through IE process. Figure 21a shows the C_{sp} of $Cd(OH)_2/Fe(OH)_2$ core-shell electrode material in various electrolytes. It is evident that for Na_2SO_4 electrolyte, the specific capacitance was high. Further analysis for the electrode was performed in 1 M Na_2SO_4 electrolyte where Fig. 21b shows the CV characteristic of the electrode. From Fig. 21c, the specific and areal capacitance of $Cd(OH)_2/Fe(OH)_2$ core-shell electrode was calculated to be 331 F g^{-1} and 82.80 mF cm^{-2} within working potential of 0.3 and − 0.9 V, respectively. Electrolyte ions at the surface of $Cd(OH)_2/Fe(OH)_2$ core-shell electrode practice two processes: surface adsorption and intercalation process. The surface adsorption mechanism reaction is as shown below:

$$Fe(OH)_2 + Na^+ + e^- \leftrightarrow Fe(OH)_2Na^+ \tag{7}$$

$$Cd(OH)_2 + Na^+ + e^- \leftrightarrow Cd(OH)_2Na^+ \tag{8}$$

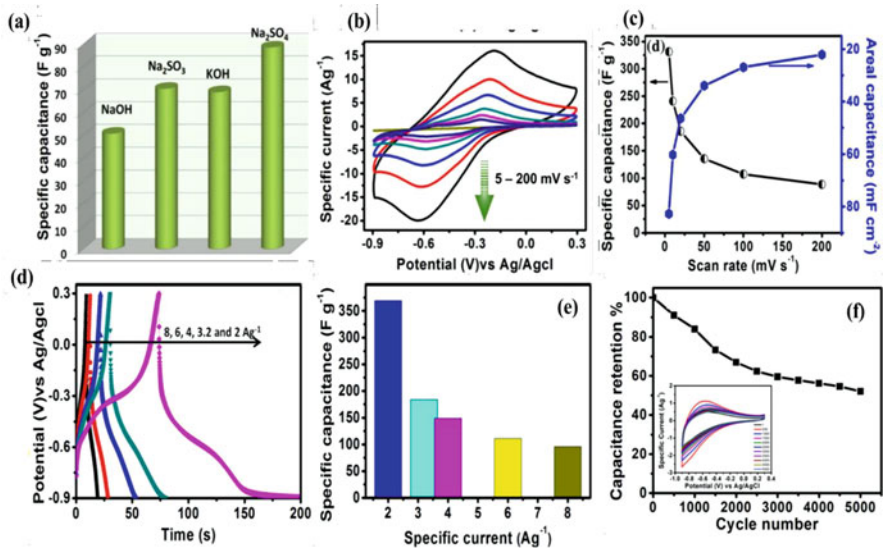

Fig. 21 (**a**) Specific capacitance of $Cd(OH)_2/Fe(OH)_2$ core-shell structure in different electrolytes, (**b**) $Cd(OH)_2/Fe(OH)_2$ core-shell material for different scan rates, (**c**) graph exhibiting both specific capacitance and areal capacitance, (**d**) charge-discharge curve for different current density, (**e**) specific capacitance of $Cd(OH)_2/Fe(OH)_2$ core-shell electrode for different current density, and (**f**) stability test of $Cd(OH)_2/Fe(OH)_2$ core-shell electrode material. Inset showing CV curve of $Cd(OH)_2/Fe(OH)_2$ core-shell electrode [85]

Intercalation process involves the following mechanism:

$$Fe(OH)_2 + Na^+ + e^- \leftrightarrow FeONa + H_2O \tag{9}$$

$$Fe(OH)_2 + Na^+ + e^- \leftrightarrow CdONa + H_2O \tag{10}$$

GCD analysis showed a maximum C_{sp} of 368 F g^{-1} at 2 A g^{-1} (Fig. 21(d,e)). Also, stability of 52% was obtained for over 5000 cycles at a scan rate of 50 mV s^{-1} [85].

Likewise, Nair et al. [86] synthesized CdS nanowire from $Cd(OH)_2$ nanowires using ion-exchange process and studied its electrochemical activity. Figure 22a shows schematic involving the synthesis of CdS nanowires. Initially, a compact layer of CdS was grown over SS followed by the growth of $Cd(OH)_2$ nanowire bundles using CBD method, and its further conversion to CdS nanowires through IE process was accomplished by placing the sample in a sulphide ion source. As solubility product (K_{sp}) of both parent and final products is different, such transformations are possible and visible through the naked eyes. The solubility product of $Cd(OH)_2$ is ~10^{-14}, and that of CdS is ~10^{-27}, resulting in the conversion of the host material. Figure 22b depicts the deposition of compact CdS over SS

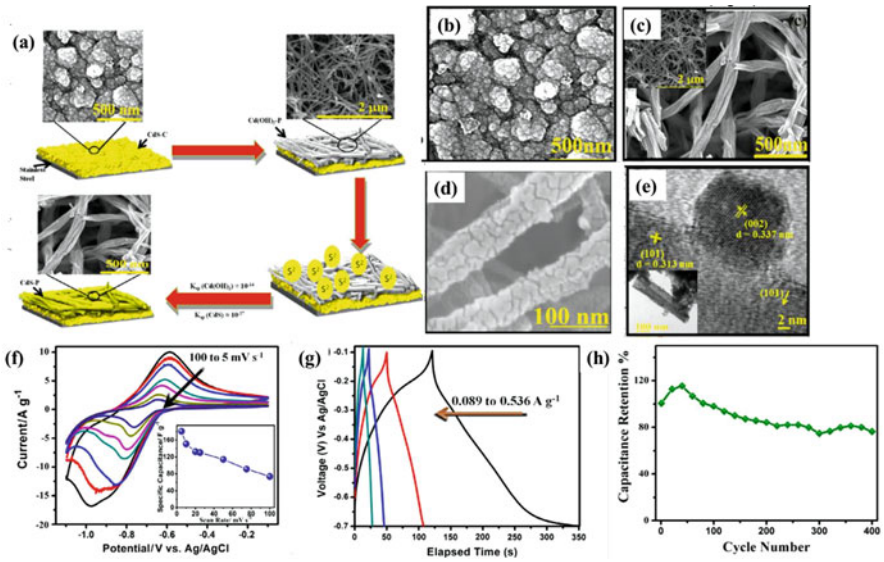

Fig. 22 (**a**) Schematic of the process undertaken for the growth of CdS nanowires. FESEM images of (**b**) CdS compact layer coated over the stainless steel substrate and (**c**) CdS nanowire bundles grown over the CdS compact at a magnification scale of 500 nm with inset at a magnification scale of 2 μm. (**d**) Porous surface of CdS nanowires at a magnification scale of 100 nm and (**e**) HRTEM image of CdS nanoparticles on the surface of CdS nanowire. Inset showing the image of CdS nanowire at a magnification of 100 nm (**f**) CV analysis of CdS nanowire bundle at different scan rates, (**g**) charge-discharge curves of CdS nanowires for different current densities, and (**h**) capacity retention of the material for 400 cycles [86]

substrate. Figure 22c shows the deposition of CdS nanowire bundles over the compact layer. Inset of the figure shows the FESEM image of the same material at magnification of 2 μm. Figure 22d shows the FESEM image of the porous CdS nanowire at a magnification of 100 nm. Such porous structure induces an enhanced surface area for electrochemical activity. Figure 22e shows the HRTEM image of CdS nanoparticles on CdS nanowire. The fabricated material was further scrutinized for electrochemical activity in different electrolytes of different molarity for different potential windows. It was observed that for 1 M Na_2SO_3 electrolyte, CdS showed the maximum specific capacitance. The CV curve showed in Fig. 22f had prominent oxidation-reduction peaks within a potential range of −1.1 to −0.1 V. These peaks correspond to the transformation of Cd^{2+} to Cd^0 and that of S^0. Redox peaks implicate a pseudocapacitive type of charge accumulation. C_{sp} of CdS nanowire was found to be 181 F g^{-1} at a scan rate of 5 mV s^{-1}. GCD showed a maximum specific capacity of 33.41 F g^{-1} at 89 mA g^{-1} current density (Fig. 22g). Energy density and power density of the electrode at same current density were calculated to be 1.72 Wh kg^{-1} and 27.14 W kg^{-1}, respectively. The stability analysis showed that the electrode specific capacitance increased initially and then remained constant up to 76% from 250 to 400 cycles (Fig. 22h) [86].

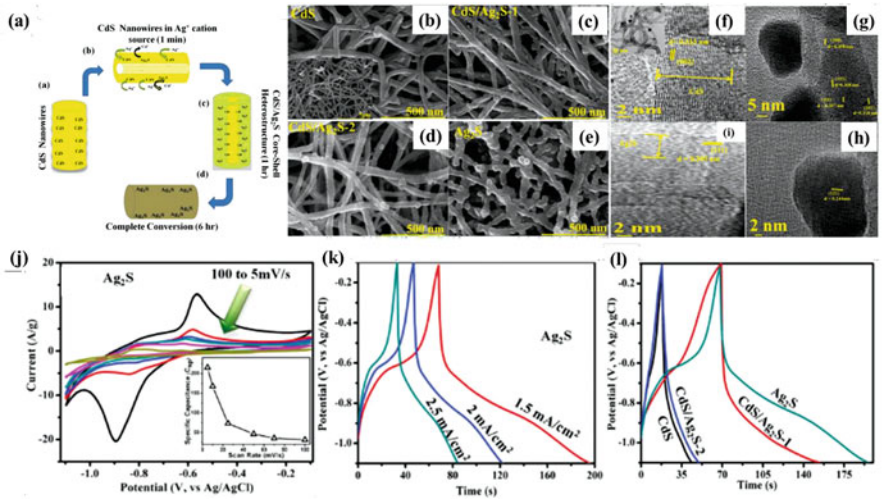

Fig. 23 (**a**) Graphical representation of the ion-exchange process during the immersion time. FESEM image of (**b**) CdS nanowires. Inset showing the ultralong structure of the CdS nanowire. FESEM images of the initial material after immersion in the cation source for (**c**) 1 min, (**d**) 1 h, and (**e**) 6 h. HRTEM images of (**f**) CdS, (**g**) CdS after 1 h of immersion in the cationic source, (**h**) Ag_2S precipitates formed on the surface of the nanowire, (**i**) Ag_2S nanowire after 6 h immersion, (**j**) CV of the Ag_2S material at different scan rates, (**k**) charge-discharge characteristics of Ag_2S at different current densities, and (**l**) charge-discharge curve of different samples prepared [87]

Further, study reported the conversion of CdS NWs into Ag_2S NWs by placing parent structure in Ag^+ ion source. As K_{sp} of Ag_2S (~ 10^{-50}) is more negative than that of CdS (~10^{-27}), IE process is spontaneous. To analyse the effect of cationic source, samples of different immersion time in the cationic source were prepared, and their electrochemical activity at each stage was evaluated. Figure 23a shows the schematic for the fabrication of sample. In Fig. 23b, initial CdS nanowire prepared can be seen. Inset of the figure shows a network of wire prepared. Three different immersion times (1 min, 1 h, and 6 h) in cationic source have been studied. Figure 23c–e shows the FESEM images of the samples for time durations 1 min, 1 h, and 6 h, respectively. The surface of initial nanowire was smooth; as the immersion time increased, the surface became rough. Figure 23f shows the HRTEM image of the CdS nanowire. Figure 23g depicts the HRTEM image of CdS nanowire after 1 h immersion in cationic source. Figure 23h shows precipitates of Ag_2S formed on the surface of CdS nanowire which is the cause for uneven surface of CdS samples, as observed in the FESEM image. On further increasing the time duration, the sample converted from CdS to Ag_2S as shown in Fig. 23i. Study revealed that at an intermediate stage, a core-shell heterostructure is formed due to the formation of precipitates on the surface of the CdS sample. Such process is an uncomplicated and facile method for the synthesis of core-shell heterostructure morphology. Electrochemical study of each sample showed that after complete

conversion into Ag_2S, the CV curve exhibited maximum current (Fig. 23j). The charge-discharge curve of Ag_2S in 1.5 M NaOH showed charging duration to be less compared to the discharge time (Fig. 23k). When comparing the charge-discharge curves of samples (Fig. 23l), CdS, CdS/Ag_2S-1 (1 min), CdS/Ag_2S-2 (1 h), and Ag_2S (6 h) showed that in case of Ag_2S, the IR drop is less compared to other samples. Also, their discharge time is less compared to other samples within the same potential window. This is attributed to the high electrical conductivity of silver. C_{sp} of CdS, CdS/Ag_2S-1 (1 min), CdS/Ag_2S-2 (1 h), and Ag_2S (6 h) at 1.5 mA cm^{-2} current density were found to be 41.46, 15.04, 56.84, and 268.47 F g^{-1}, respectively. It is evident from the C_{sp} analysis that the capacitance increases as the amount of conducting material increases. The specific energy density and specific power density of Ag_2S sample were found to be 44.74 W h kg^{-1} and 1278.43 W kg^{-1}, respectively [87].

A similar study on the formation of HgS on CdS nanowires by Nair et al. [90] showed that the core-shell morphology exhibited maximum C_{sp}. Figure 24a–d shows the schematic of the process involved during the fabrication of HgS electrode. Figure 24e–h shows the FESEM images of CdS, CdS immersed in the Hg^{+}source for 15, 30, and 60 min, respectively. It shows that although the nanowire morphology is maintained, but the surface is more uneven as the immersion time increases. HRTEM images show that such unevenness is because of the formation of HgS precipitates over the surface of the CdS nanowires (Fig. 24i, j). Figure 24k, l shows that before complete conversion to HgS, a core-shell heterostructure of CdS/HgS composite is formed. Figure 24m–o shows the CV graphs of CdS immersed in Hg^{+}source for different time durations. CV indicates that for core-shell heterostructure, the current output is more than other samples. The charge-discharge analysis of the same material as shown in Fig. 24p implicates very less IR drop compared to other samples. C_{sp} of HgS nanowire electrode was evaluated as 94.40 F g^{-1} at a current density of 2 mA cm^{-2} which is more than that of CdS (27.82 F g^{-1}) and HgS (19.08 F g^{-1}). Trasatti plot analysis (Fig. 24q, r) shows that the maximum contribution to the C_{sp} is from the inner surface of the electrode as compared to the outer surface. The intercept of linear plot between C_{total} and $\upsilon^{1/2}$ indicates the contribution from inner surface, while the intercept of linear plot between C_{total} and $\upsilon^{-1/2}$ gives the contribution from the outer surface. Stability analysis for 1250 cycles showed that core-shell heterostructure had approximately 87% of retention compared to other samples [88].

Transition materials with higher oxidation states and reversible nature are being explored for SC applications since these are capable to increase the C_{sp}. However, some of these materials exhibit poor electrical conductivity which restricts its wide-scale capability. To overcome such incongruity, highly conductive carbon materials like graphene, carbon nanotube (CNT), single-walled carbon nanotube (SWCNT), and multiwalled carbon nanotube (MWCNT) are used in conjunction with the high valent transition materials and utilized as an electrode material. Most of the metal deposition process involves two highly complex conventional methods like hydrothermal, electrostatic co-precipitation method and electrophoretic deposition to obtain a good quality transparent film.

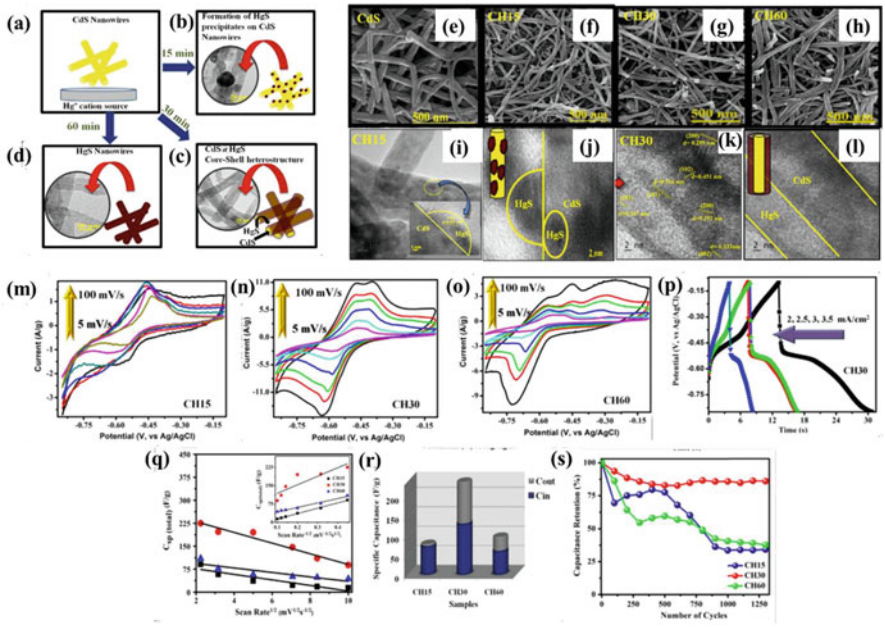

Fig. 24 (**a**–**d**) Schematic of the process undertaken for the fabrication of the electrode. FESEM images of (**e**) CdS. CdS placed in Hg source for (**f**) 15 min, (**g**) 30 min, and (**h**) 60 min. HRTEM images of CdS in Hg source for (i–j) 15 min and (k–l) 30 min; (**m**) CV analysis of CdS/HgS for 15 min, (**n**) CdS/HgS 30 min, (**o**) Hg 60 min, (**p**) charge-discharge curve of CdS/HgS 30 min, and (**q**) Trasatti plot for calculation of C_{sp} from total surface of the electrode. Inset showing Trasatti plot for outer surface of the electrode. (**r**) Contribution from both inner and outer surfaces of the electrode and (**s**) capacitance retention of the samples prepared [88]

Sankapal et al. [89] used low-cost 'dip and dry' process, SILAR, to deposit Co_3O_4 nanoparticles over MWCNT. Figure 25a, b shows the FESEM images of Co_3O_4/MWCNT electrode material at different magnifications. It is evident from the HRTEM image shown in Fig. 25c that Co_3O_4 nanoparticles form an encapsulation over MWCNT. CV analysis of Co_3O_4/MWCNT composite in 2 M KOH showed maximum C_{sp} of 685 F g^{-1} at 5 mV s^{-1} within a potential window of 0.2 to 0.5 V (Fig. 25c). The charge-discharge study as illustrated in Fig. 25e indicates a reduced or negligible IR drop with non-linear behaviour at lower current densities, indicating that the charge storage mechanism is solely of pseudocapacitive type. At higher current densities, this showed a linear behaviour indicating non-faradaic reaction. The maximum specific energy and specific power of the electrode material were found to be 16.41 W h kg^{-1} and 300 W kg^{-1}, respectively. Capacitance retention study showed 73% preservation for 5000 cycles (Fig. 25f) [89].

Pandit et al. [64] used electroless method to deposit Ag nanoparticles over MWCNT. Electroless process involves two steps as shown in Fig. 26a wherein the cationic precursor is first coated over MWCNT and later dipped in a reducing agent

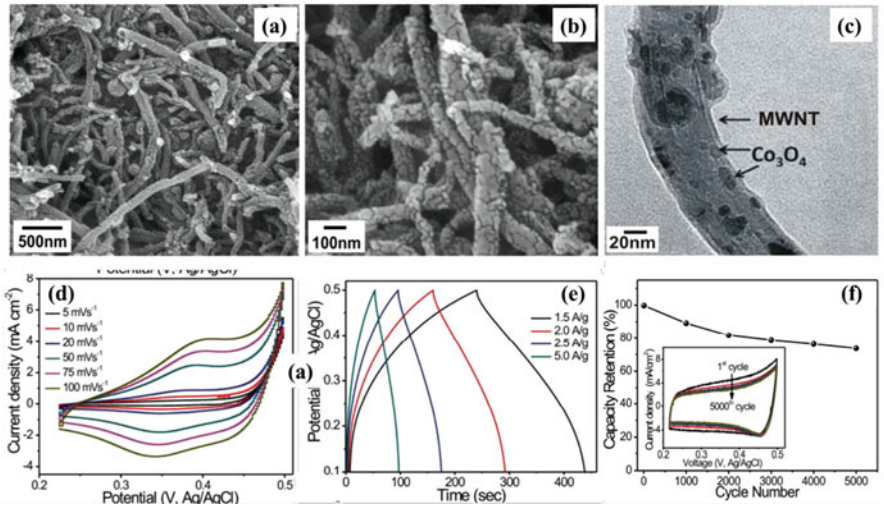

Fig. 25 FESEM images of Co_3O_4/MWCNT electrode material at (**a**) 500 nm and (**b**) 100 nm, (**c**) HRTEM image of the electrode material, (**d**) CV of the electrode material at different scan rates, (**e**) charge-discharge analysis of Co_3O_4/MWCNT electrode material, and (**f**) capacitance retention of the material. Inset shows CV cycles at different cycles [89]

like hydrazine to form the metal particles. FESEM image (Fig. 26b) of the material synthesized shows Ag nanoparticles evenly deposited over MWCNT.

When MWCNT-coated substrate was dipped into the cationic source, the van der Waals forces trigger adsorption of Ag^+ ions. Hydrazine reduces Ag^+ ions into metallic element as shown below:

$$4Ag^+ + N_2H_4 \rightarrow 4Ag \downarrow + N_2 \uparrow + 4H^+ \tag{11}$$

EDS plot shown in Fig. 26c indicates a sharp peak at 3 keV which validates the formation of Ag metal. Electrochemical study of the electrode in 0.5 M NaOH shows sharp oxidation and reduction peaks within a potential range of 0.9 V (−1.1 to −0.2 V) (Fig. 26d). Maximum C_{sp} obtained was equal to 757 F g^{-1} at 2 mV s^{-1} scan rate. GCD analysis showed a synergetic profile of both MWCNT which is a linear variation corresponding to EDLC and Ag NPs showing non-linear profile corresponding to faradaic behaviour (Fig. 26e). Through GCD, C_{sp} obtained was equal to 540 F g^{-1} at 2 mA cm^{-2} current density. Stability analysis showed 83% retention for 3000 cycles, implicating an excellent stable nature of the electrode material (Fig. 26f). The maximum specific energy and power of the composite electrode were calculated as 60.7 W h kg^{-1} and 3.3 kW kg^{-1}, respectively [64]. C_{sp} of Ag nanoparticles prepared by electroless method has been reported to exhibit 452 F g^{-1} at 2 mV s^{-1} [63]. On comparison of both Ag nanoparticles and its composite with MWCNT, the composite showed enhancement in the C_{sp}.

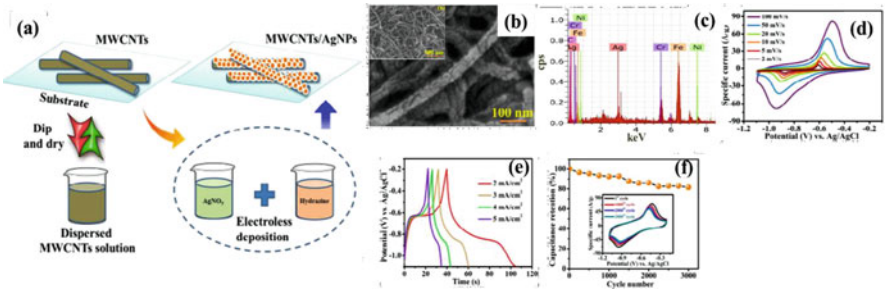

Fig. 26 (**a**) Schematic of the process involved in the electroless deposition of Ag nanoparticle over MWCNT. (**b**) FESEM image of the Ag nanoparticles over MWCNT. Inset showing the intertangled image of MWCNT. (**c**) EDS analysis of the electrode material. (**d**) CV analysis of the fabricated electrode. (**e**) Charge-discharge curve of the electrode. (**f**) Cyclic stability of the fabricated electrode [64]

Among other transition metals, vanadium has also gained quiet remarkable attention due to its multiple valence states. Vanadium oxide is a layered structure which helps in effortless intercalation/de-intercalation of the electrolyte ions. Mostly such structures are not ruptured during continuous cyclic process, implicating that such structures are able to sustain the volume expansion observed during the cyclic process.

Pandit et al. [90] encapsulated MWCNT with layered V_2O_5 using CBD method as shown in Fig. 27a. Figure 27b shows the FESEM image of V_2O_5 nanoflakes forming an interconnected layer over MWCNT. Inset of the Fig. 27b shows the EDAX spectra of the fabricated electrode. Figure 27c, d demonstrates the HRTEM images of the electrode. Figure 27e–g validates the existence of vanadium, carbon, and oxygen in the electrode material. Figure 27h shows the CV of MWCNT, V_2O_5, and V_2O_5/MWCNT where the specific current of V_2O_5/MWCNT is found to be maximum when compared to other samples. The CV profile of V_2O_5/MWCNT is analogues to that observed in EDLC and pseudocapacitor combination. This implies that the charge storage mechanism in the electrode is of both faradaic and electrostatic types (Fig. 27i). The CD curve shows an almost triangular profile with reduced IR drop in case of V_2O_5/MWCNT composite (Fig. 27j). It shows a maximum C_{sp} of 629 F g^{-1} at 2 A g^{-1} specific current in 2 M $LiClO_4$ within a working potential of 0 to 1 V. The stability study (Fig. 27k) initially showed reduction, and after 250 cycles, it showed 100% retention. This increases to 109% after 1200 cycles and again reduces slowly to 93% at 4000 cycles. A flexible solid-state SC (FSS-SSC) fabricated with V_2O_5/MWCNT and PVA-$LiClO_4$ exhibited an excellent reversibility even at lower scan rate as shown in Fig. 27l within a potential window of 1.8 V. CD curve showed an asymmetric curve in Fig. 27m, attributed to the reversible redox mechanism. The device showed a specific capacitance of 160 F g^{-1} at 1 A g^{-1} within a potential window of 1.8 V. The specific energy of the device could reach a maximum value of 72 W h kg^{-1} at 1 A g^{-1} with specific power of 2.3 kW kg^{-1}. The stability analysis showed decrease during initial cycles

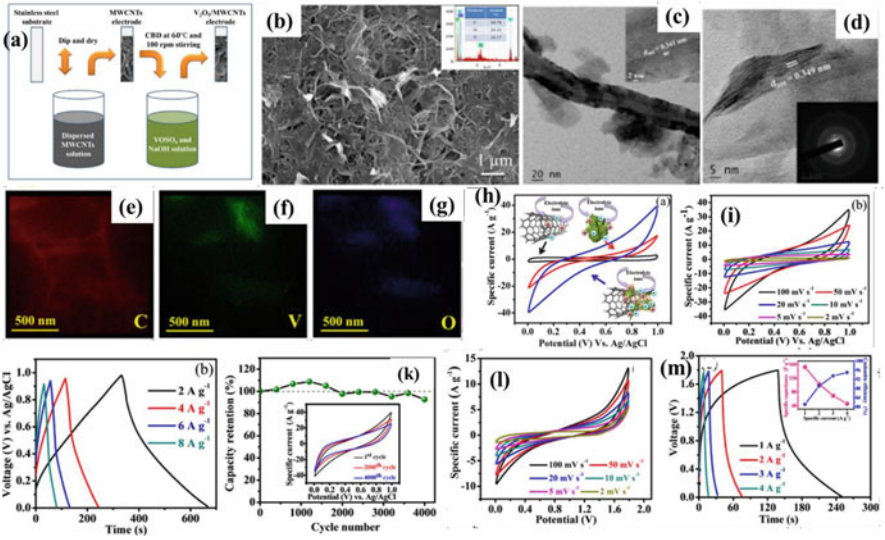

Fig. 27 (**a**) Schematic of the dip and dry method with chemical bath deposition process. (**b**) FESEM image of V_2O_{5-} encapsulated MWCNT. Inset showing the EDAX spectra of the electrode. (c–d) HRTEM of V_2O_5/MWCNT at different magnifications. Inset of (**c**) interplanar spacing of MWCNT. Inset of (**d**) SAED pattern of V_2O5/MWCNT. (**e**–**g**) Elemental mapping of the electrode showing carbon, vanadium, and oxygen. (**h**) CV curve of MWCNT, V_2O_5, and V_2O_5/MWCNT. (**i**) CV curve of V_2O_5/MWCNT at different scan rates. (**j**) CD curve of the electrode and (**k**) stability analysis of the electrode. Inset showing the CV cycles of the electrode at first, 2000th, and 4000th cycle. (**l**) CV curve of FSSC device. (**m**) CD curve of the fabricated device. Inset showing specific capacitance and coulombic efficiency with respect to the specific current [90]

which reached up to 105% retention after 1200 cycles. After 4000 cycles, it showed an excellent capacitance retention of 96% [90].

Adding to these studies, Pande et al. [91] attempted to extend the potential window of V_2O_5/MWCNT electrode device from 1.8 to 2 V since most of the typical devices require a minimum voltage of 1.5 V. The CV analysis of the symmetric device made with V_2O_5/MWCNT electrode in 2 M $LiClO_4$ aqueous electrolyte showed an extended potential window up to 2 V without compromising on its reversibility. For 2 V potential frame, the C_{sp} of the device reached up to 569.7 F g^{-1} for 2 mV s^{-1}. The GCD study of the device showed 111.7 F g^{-1} C_{sp} for a high current density of 3 mA cm^{-2}. The fabricated device retained 89% of the capacitance even after 4000 cycles. In aqueous electrolyte, the device was able to demonstrate maximum energy density of 62 W h kg^{-1} with a power density of 11.5 kW kg^{-1} [91].

Ceria is a reactive rare earth oxide that has played a vital role in various emerging technologies. Nevertheless, its two oxidation states Ce^{3+} and Ce^{4+} can help to boost the supercapacitance profoundly. Deng et al. [92] fabricated CeO_2/MWCNT nanocomposite electrode through hydrothermal method and found that for mole

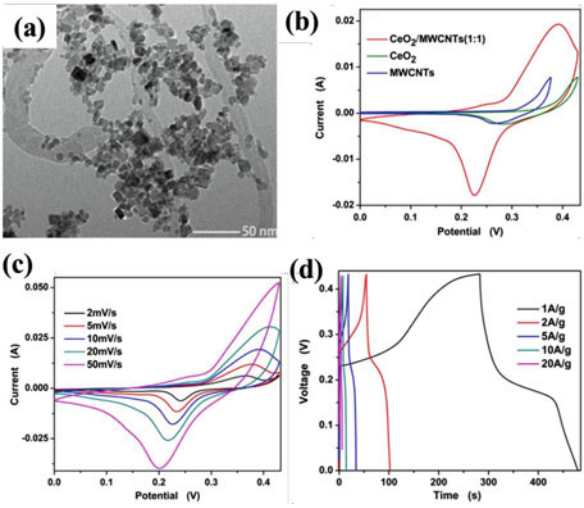

Fig. 28 (**a**) TEM image of CeO_2/MWCNT nanocomposite. (**b**) CV curves of MWCNT, CeO_2, and CeO_2/MWCNT nanocomposite. (**c**) CV curve of CeO_2/MWCNT nanocomposite at different scan rates. (**d**) Charge-discharge curves of CeO_2/MWCNT nanocomposite [92]

ratio of 1:1 the electrode exhibited maximum C_{sp} of 455.6 F g^{-1} at 1 A g^{-1} current density. TEM analysis (Fig. 28a) shows a rectangular-shaped CeO_2 on the surface of MWCNT. CV analysis of MWCNT, CeO_2, and CeO_2/MWCNT is shown in Fig. 28b; it implicates that the nanocomposite formed by CeO_2 and MWCNT produces more current output as compared to other samples. Its further electrochemical analysis in KOH of 6 M within a potential range of 0 to 0.43 V at different scan rates (Fig. 28c) showed a redox peak, characteristic of pseudocapacitance. The charge-discharge analysis (Fig. 28d) showed maximum C_{sp} of 455.7 F g^{-1} for CeO_2/MWCNT at 1 A g^{-1} which was 246% and 518% more than the C_{sp} of MWCNT and CeO_2, respectively. The capacitance retention study of CeO_2/MWCNT electrode showed 81.1% stability for 2000 cycles for 10 A g^{-1} current density [92].

Similarly, Pandit et al. [93] fabricated CeO_2 on MWCNT but by using CBD method. Figure 29a shows the FESEM image of CeO_2/MWCNT where CeO_2 nanoparticles appear to encapsulate the outer surface of MWCNT offering well-established conductive network. Such encapsulation reduces the charge transfer resistance and increases the access to the functioning surface. HRTEM image shown in Fig. 29b is in full agreement of FESEM image where the CeO_2 is anchored on the surface of MWCNT. Electrochemical analysis of the electrode is shown in Fig. 29c which has a redox peak corresponding to the reversible redox reaction:

$$Ce^{iv}O_2 + OH^- \leftrightarrow Ce^{III}O_2OH + e^- \tag{12}$$

within a potential window of −0.5 to −1.1 V when tested in 0.5 M NaOH. Compared to CeO_2 and MWCNT, CeO_2/MWCNT composite showed maximum capacitance of 1215.7 F g^{-1} at a scan rate of 2 mV s^{-1}. Charge-discharge curve of CeO_2/MWCNT (Fig. 29d) incorporates EDLC and pseudocapacitive behaviours.

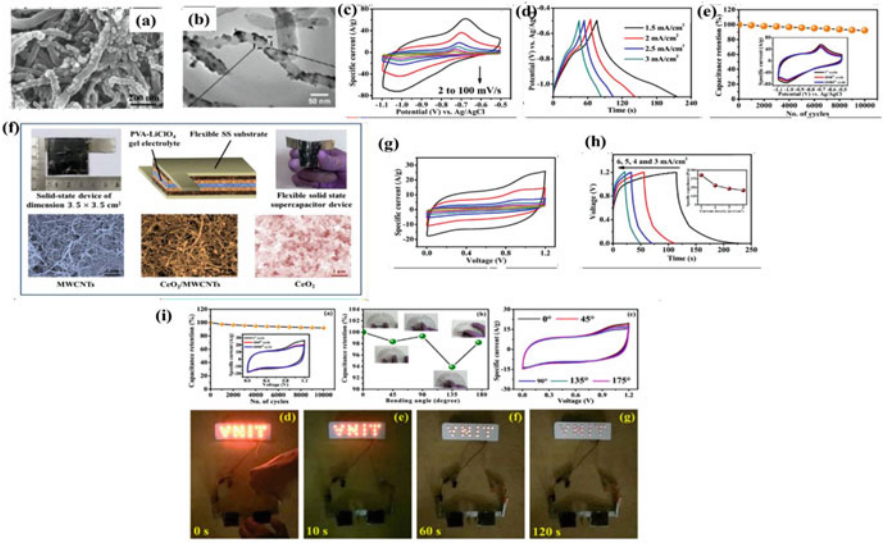

Fig. 29 (**a**) FESEM image on stainless steel substrate. (**b**) HRTEM image of CeO_2/MWCNT thin film. (**c**) CV curve in 0.5 M NaOH electrolyte. (**d**) Charge-discharge curve at different current density. (**e**) Stability test of electrode. (**f**) Schematic representation of the fabricated device with CeO_2/MWCNT as electrode and PVA-$LiClO_4$ gel electrolyte. (**g**) CV curve of the fabricated device at different scan rates. (**h**) Charge-discharge curve of the device at different current density. (i:a) Stability study of the device, (i:b) capacitance retention at different bending angles, (i:c) CV curve at different bending angles, and (i:d–g) working model demonstration of the device fabricated [93]

Through charge storage mechanism, the electrode exhibited a maximum C_{sp} of 1044.2 F g^{-1} at 1.5 mA cm^{-2}. The electrode showed C_{sp} retention of 92.3% for 10,000 cycles (Fig. 29e). They also calculated the real and imaginary capacitance with respect to frequency and obtained maxima for imaginary component at 20.6 Hz frequency with the relaxation time as 48.5 ms. The Bode plot analysis showed a phase angle of −77°, suggesting good capacitive response. Figure 29f shows the flexible symmetric solid-state SC device fabricated from CeO_2/MWCNT with PVA-$LiClO_4$ electrolyte. CV curve of the device shown in Fig. 29g displayed C_{sp} of 486.5 F g^{-1} at a scan rate of 2 mV s^{-1} within 1.2 V potential. Figure 29h depicts the CD curve of the fabricated device at different current densities. Device displayed a maximum specific energy of 85.7 Wh kg^{-1} with a power density of 2.6 kW kg^{-1}. Power density value was enhanced to 5 kW kg^{-1} as the energy density changed to 41.9 Wh kg^{-1}. Stability study of the device showed a sudden drop for initial 1000 cycles which stabilized after 2000 cycles up to 10,000 cycles with excellent retention of 92.1% (Fig. 29i:a).

Figure 29i:b, c shows the study of the device bending effect (0–175°) on the C_{sp}, and it was able to retain 98.2% of its initial capacitance. Figure 29i:d–g demonstrates the working model of the device [93].

7.3 Two-Dimensional (2D) Nanostructures

Two-dimensional (2D) nanostructures are thin films or layers where two sides are in nanometer range. These normally include nanosheet or nanoplate morphologies. Such morphology can expose more functional surfaces for electrochemical activity. Layered structure with dimensions of few atomic ranges can also be classified under this. It allows easy penetration of electrolyte ions which increases the C_{sp} of the electrode.

Raut et al. [94] compared the electrochemical behaviour of Fe_2O_3 and its composite with MWCNT, prepared by SILAR method. Figure 30a, b shows the FESEM images of Fe_2O_3 agglomerated nanoparticles and Fe_2O_3 encapsulated MWCNT, respectively. Due to the formation of agglomeration on MWCNT, many active surfaces are available for the electrolyte to store the charges. Figure 30c shows the HRTEM image of Fe_2O_3/MWCNT composite material. Comparing CV of MWCNT, Fe_2O_3 and Fe_2O_3/MWCNT showed that the current output of the composite was more when compared to other samples in 1 M Na_2SO_3 (Fig. 30d). The charge storage scope of Fe_2O_3/MWCNT is more when compared to other samples; this is due to the synergetic effect of both materials wherein MWCNT exhibits rectangular shape, while Fe_2O_3 induces the redox peaks. The CV analysis of the composite material for different scan rates is shown in Fig. 30e, and from the graph, the C_{sp} of the electrode material is evaluated to be 431 F g^{-1} at 5 mV s^{-1} within a potential frame of −0.8 to 0 V. Figure 30f indicates the GCD profile of the composite electrode at different current densities. This shows low internal resistance and excellent conductivity with 437.5 F g^{-1} C_{sp} at 1 A g^{-1}. Electrode exhibited an energy density of 38.89 W h kg^{-1} and power density of 800 W kg^{-1} at 2 A g^{-1} current density. Retention study of the electrode showed 48% for 500 cycles

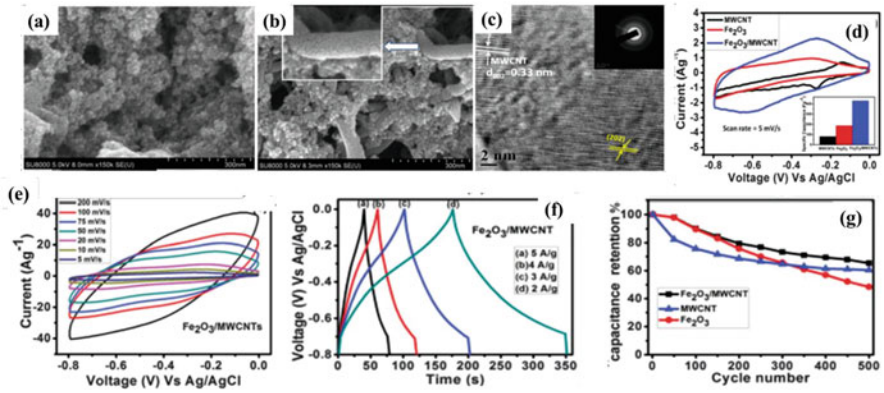

Fig. 30 FESEM images of (**a**) Fe_2O_3 and (**b**) Fe_2O_3/MWCNT. (**c**) HRTEM image of Fe_2O_3/MWCNT. (**d**) CV analysis of MWCNT, Fe_2O_3, and Fe_2O_3/MWCNT at 5 mV s^{-1} scan rate. (**e**) CV analysis of Fe_2O_3/MWCNT at different scan rates. (**f**) Charge-discharge profile of Fe_2O_3/MWCNT. (**g**) Stability study of MWCNT, Fe_2O_3, and Fe_2O_3/MWCNT [94]

in case of Fe_2O_3, while in case of Fe_2O_3/MWCNT, it was 65% [94]. In extension to above work in 2021, Raut et al. [95] prepared solid-state symmetric SC device by assembling Fe_2O_3/MWCNT as both electrodes and PVA-$LiClO_4$ gel as both separator and gel electrolyte. The fabricated device was able to extend the potential window to 1 V and display a specific capacitance of 70.16 F g^{-1} at 0.57 A g^{-1} current density. The device had specific energy and power of 9.74 W h kg^{-1} and 487.24 W kg^{-1}, respectively, with a coulombic efficiency of 69.23%. Under different folding angles from 0° to 140°, the device could maintain 95% of the initial capacitance indicating its great flexibility. During stability analysis, the device for initial 400 cycles showed 155% enhancement in the capacitance which reduced to 75% for the next 900 cycles. The fifth day analysis of the device showed only 7% decay in the capacitance. The device was further studied for series and parallel combinations, and it was observed that for parallel conditions, the current value increased four times when compared to single device, while for series combination, enhancement in the potential window to 2 V has been observed but compromising its current output value [95].

Raut et al. [97] used SILAR method to fabricate thin film of mixed transition metal oxide $ZnFe_2O_4$ on SS substrate. The morphology of the fabricated electrode showed nanoparticles of $ZnFe_2O_4$ over nanoplates. The electrochemical study of the material gave a maximum specific capacitance of 471 F g^{-1} at 5 mV s^{-1} in 1 M NaOH. The curve showed reversible redox peaks corresponding to Zn-O to Zn-O-OH or Fe-O to Fe-O-H, implicating that the charge storage mechanism is the same as that found in pseudocapacitors. GCD analysis at different current densities showed there was an initial drop in the current which further exhibited a linear behaviour within the potential frame of 0 to −1 V. Energy density was calculated to be 53.22 W h kg^{-1}, while power density was found to be 1.87 kW kg^{-1}. The electrode could maintain 72% of its initial capacitance over 1000 cycles. A flexible solid-state symmetric SC device fabricated with $ZnFe_2O_4$ as the electrodes and PVA-$LiClO_4$ as gel electrolyte had a C_{sp} of 26 F g^{-1}. GCD analysis of the device showed a C_{sp} of 32.22 F g^{-1} with energy density 4.47 Wh kg^{-1} and power density of 277.78 W kg^{-1}. The device could retain 66% of its capacitance over 1000 cycles. 34% of capacitance loss was attributed to the degradation of $ZnFe_2O_4$ and the gel electrolyte [96]. Composite of $ZnFe_2O_4$ material with CNT enhanced the characteristics of the $ZnFe_2O_4$ SCs with a specific capacity of 217 mAh g^{-1} at 5 mV s^{-1} scan rate in a potential frame of −1 to 0 V. Symmetric solid-state device with $ZnFe_2O_4$/CNT as the electrodes and PVA-LiCl as the gel electrode showed a shift in the potential window to 0–1 V. Their CV analysis showcased an almost symmetric rectangular profile for different scan rates. GCD showed almost negligible IR drop with 92.2 F g^{-1} C_{sp} at 0.35 A g^{-1} current density. Corresponding specific energy was calculated to be 12.8 Wh kg^{-1} with a specific power of 377.86 W kg^{-1}. For 2000 cycles, the device showed a capacitive retention of 70%. They analysed the Nyquist and bode plot of the device before and after 2000 cycles and found that there was very minute change in the Nyquist plot, while the bode plot remained almost the same, indicating the good cyclic stability of the device [97]. Raut et al. [98] investigated the effect of replacing Fe with Co

in $ZnFe_2O_4$ material. Mesoporous 2D nanoflake structured $ZnCo_2O_4$ material was synthesized through SILAR method. It showed a C_{sp} of 675 F g^{-1} in 1 M KOH for a potential window of 0 to 0.5 V. Symmetric device fabricated with this material as both cathode and anode electrodes and PVA-KOH as the electrolyte exhibited a C_{sp} of 69.56 F g^{-1} at 1.07 A g^{-1} with specific energy of 9.67 W h kg^{-1} and specific power of 1.45 kW kg^{-1}. The device could exhibit 68% of its original capacitance for 2000 cycles [98].

Selenium, one of the chalcogens, has been already being extensively considered for solar cells, optoelectronics, and light-emitting diodes. Pawar et al. [99] used CdSe microspheres as electrode material for electrochemical application. They used one-pot CBD method for the synthesis of CdSe, wherein cadmium sulphate was initially reduced to cadmium hydroxide, and further Na_2SeSO_3 was added to form CdSe. They varied the deposition time on FTO substrate from 2, 4, 6, 8, to 10 h keeping the solution at a temperature of 70 °C. As the time duration increased, a more even and denser film was observed with larger microspheres since the material deposition increased with time. For 8 h reaction, the microsphere size was found to be 600 nm. On further increasing the deposition time, it distorted the sphere shape and formed a 2D layer over the substrate. The charge transfer resistance of the sample during electrochemical analysis showed a decrease as the deposition time increased. Along with this, the electrochemical cell resistance also reduced till 8 h beyond which the resistances increased again due to the flattening and peeling of the electrode material. CdSe showed a highest areal capacitance of 1.285 mF cm^{-2} in 0.1 M H_2SO_4 electrolyte within a potential frame of −0.2 to 0.8 V at 10 mV s^{-1} scan rate. The energy density of the electrode was calculated to be 4.015 W h kg^{-1} with a capacitance loss of 12.5% for initial 1000 cycles and later 3.8% for the next 1000 cycles [99].

Kavyashree et al. [100] fabricated $Sr(OH)_2$ thin film over SS substrate by SILAR method at room temperature. Figure 31a shows the schematic deposition procedure of $Sr(OH)_2$ film using SILAR method. They obtained a dendrite morphology (Fig. 31b, c) with high porosity which reduces the diffusion path of the electrolyte ion and increases its specific capacitance. They found that for 20 SILAR cycles, a more prominent and reversible oxidation-reduction peaks were visible in optimized 1 M NaOH electrolyte. Figure 31d shows the CV analysis of $Sr(OH)_2$ thin film in 1 M NaOH electrolyte within a potential window of 0 to −0.8 V. Peaks observed in CV curve are related to the reduction of Sr(II) to Sr(0) and oxidation of Sr(0) to Sr(II). The highest specific capacity obtained for $Sr(OH)_2$ thin film is 308 C g^{-1} at 5 mV s^{-1} (Fig. 31e). Figure 31f shows the CD analysis of $Sr(OH)_2$ thin film wherein the initial drop signifies the internal resistance; later there is a linear variation of double-layer capacitance due to the charge separation at the interface and finally the pseudocapacitive behaviour due to the adsorption and desorption process at the interface. The highest specific capacity of the thin film from CD curve was evaluated to be 413 F g^{-1} at 2 A g^{-1} with energy density and power density of 45.95 W h kg^{-1} and 2.6 W kg^{-1}, respectively. It is evident from the stability graph that as cycle increases, the specific capacity declines by ~35% up to 5000 cycles (Fig. 31g) [100].

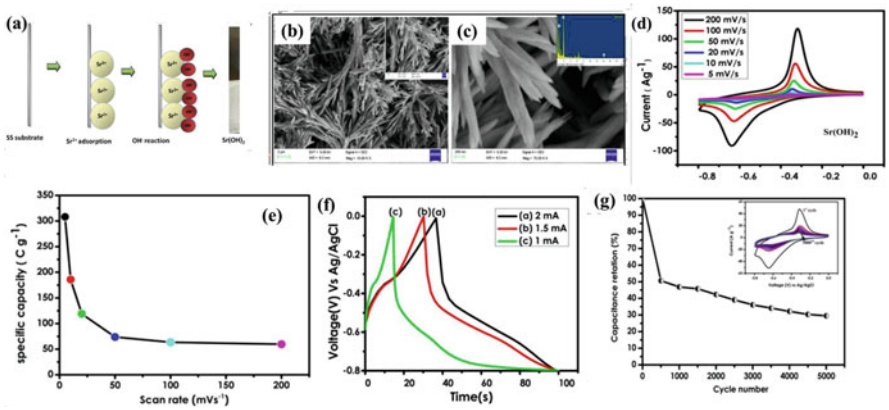

Fig. 31 $Sr(OH)_2$ thin film: (**a**) Schematic diagram. (**b**) FESEM image (**c**) FESEM image at higher magnification. Inset shows the EDS pattern. (**d**) CV in 1 M NaOH. (**e**) Specific capacity at different scan rates. (**f**) Charge-discharge curve. (**g**) Capacitance retention of the film. Inset showing the CV characteristics [100]

Kavyashree et al. [101] further tried to increase the specific capacity and cyclic stability of $Sr(OH)_2$ sample by doping it with 1%, 2%, and 3% of copper since cationic doping has the ability to enhance the electrical conductivity of the sample. Applying the same SILAR method they deposited, Cu doped $Sr(OH)_2$ thin film over SS substrate. They obtained similar tuberose structure for undoped $Sr(OH)_2$ as earlier which on further increasing the concentration of dopant formed flake-like structure over the tuberose morphology $Sr(OH)_2$ with 2% doping exhibited very high current output within a potential window of −0.8 to 0. The maximum specific capacities of 2 and 3% Cu-doped $Sr(OH)_2$ are found to be 303 and 442 C g^{-1}, respectively. Nevertheless on increasing the scan rate, the specific capacity of 2% Cu-doped $Sr(OH)_2$ is more when compared to other doped samples. On analyzing the charge-discharge behaviour of Cu-doped $Sr(OH)_2$ in 1 M Na_2SO_4, it was observed that the peak current is proportional to the square root of the scanning rate which is a characteristic of battery-type electrode. The specific capacities of 2% and 3% Cu-doped $Sr(OH)_2$ were found to be 554 and 817 C g^{-1} for 0.4 mA cm^{-1} charge density, respectively. They analysed that the IR drop in the CD curve reduced as the doping concentration increases, indicating that the conductivity of the electrode increased with the doping concentration. Also, it was observed that the charging time reduced while the discharging time increased as the doping concentration increased. The capacity retention of the electrode increased initially with the doping concentration up to 2% which on further increasing the concentration reduced the retention percentage. For 2% Cu doping, the retention was about 71%, while for 3% doping, this value reduced to 45% for 6000 cycles [101]. Similarly, they tried to dope $Sr(OH)_2$ sample with 0.1, 0.5, and 1% of Fe using the same SILAR method and found that for 1 M Na_2SO_4 electrolyte within a potential window of −1.1 to 0 V, specific capacity varied as 685, 776, and 653 C g^{-1} at a scan rate of 5 mV s^{-1}.

For 0.5% doping of Fe in $Sr(OH)_2$, the specific capacity calculated from charge-discharge curve was found to be 871 C g^{-1} at 1.2 mA cm^{-2} which is greater than the values obtained for 0.1 and 1% doping concentration. High capacity retention of about 79% has been observed in case of 0.5% doping for 800 cycles [102]. This study reveals that the doping process does not impact the primary structure of the material, but additional surfaces are added which eventually increases the area available for electrochemical activity, enhancing the specific capacity, potential window, and the stability of the material considerably.

Bismuth is another material which has found importance in the field of SCs. Bismuth oxide has wide band gap, high refractive index, dielectric permittivity, ionic conductivity, and photoconductivity. Raut et al. [103] successfully fabricated interconnected needle-like structure of Bi_2O_3 through SILAR method and studied its electrochemical analysis. In 1 M Na_2SO_4 electrolyte, Bi_2O_3 film showcased maximum current response displaying specific capacitance of 329.6 F g^{-1} at 5 mV s^{-1} scan rate within a potential window of −0.8 to 2 V. The CD analysis initially showed IR drop which later showed a non-linear behaviour indicating that the charge storage mechanism is moreover redox type rather than capacitive type. At 5.17 A g^{-1} current density, the C_{sp} was calculated to be 399.6 F g^{-1} within the potential window of −0.8 to 0.3 V. Bi_2O_3 material also showed a capacitance retention of 72% for 3000 cycles before which at initial 200 cycles the C_{sp} increased. The FESEM analysis of the sample after 3000 cycles shows collapsing of the nanoneedle-like structure which is supposed to be the reason for the decrease in the specific capacitance of the electrode [103].

Vanadium can exist in multiple oxidation states like +2, +3, +4, and + 5, and its oxide in 1D morphology has shown C_{sp} of 165 F g^{-1} [90]. So, Pandit et al. [104] worked on the fabrication of 2D morphology of vanadium oxide (V_2O_5) as it can expose more areas for electrochemical activity and found that the C_{sp} increased to 735 F g^{-1} at 1 mV s^{-1} scan rate, implying that the morphology of the electrode material plays a major role in assigning capacitance to the SC. As shown in Fig. 32a, they obtained 2D nanoflakes of V_2O_5 through CBD method. Figure 32b shows the HRTEM image of the nanoflakes obtained. The CV study of the material in 2 M $LiClO_4$ shows a non-EDLC behaviour within a potential window of 0 to 1 V with an areal capacitance of 0.40 F cm^{-2} (Fig. 32c). Inset of Fig. 32c shows the oxidation-reduction peaks of CV profile and also the specific and areal capacitance at different scan rates. The GCD study showed in Fig. 32d indicates IR drop for initial potentials and then a non-linear behaviour of the electrode material due to the reversible redox reaction of the intercalation/deintercalation of Li^+ ions in the electroactive sites of the material. GCD showed a C_{sp} of 222 F g^{-1} at a current density of 1 A g^{-1}. The electrode showed capacitance retention of 71% at 1000 cycles for 20 mV s^{-1} scan rate (Fig. 32e). A flexible all-solid-state symmetric device with V_2O_5 as electrode material and PVA-$LiClO_4$ as gel electrolyte (Fig. 32f) showed a C_{sp} of 358 F g^{-1} and areal capacitance of 0.38 F cm^{-2} for a potential window of 1.8 V. Figure 32g shows the CV response of the device for various potential windows. From the GCD study in Fig. 32h, it can be inferred that the device initially showed an IR drop which

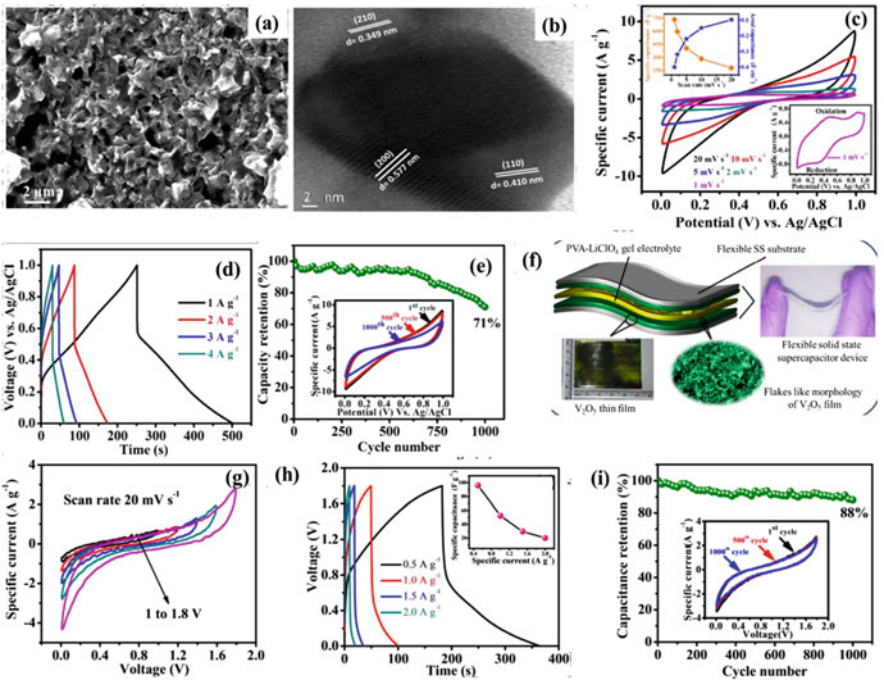

Fig. 32 (**a**) FESEM image of V_2O_5 thin film. (**b**) HRTEM image of V_2O_5 thin film. (**c**) CV of V_2O_5 thin film in 2 M $LiClO_4$ electrolyte. Inset showing the oxidation-reduction curve of the film at 1 mvV s_{-}^{-1} scan rate and the graph showing the areal and specific capacitance. (**d**) Charge-discharge profile of V_2O_5 thin film. (**e**) Stability test of V_2O_5 thin film electrode. (**f**) Schematic of the flexible symmetric solid SC device (FSS). (**g**) CV of the fabricated device in different potential windows. (**h**) Charge-discharge curve of the device. Inset showing the specific capacitance of the device. (**i**) Capacitance retention of the device. Inset showing the CV of the device at first, 500th, and 1000_{th} cycle [104]

further formed a non-linear behaviour. The C_{sp} of the electrode was evaluated to be 96 F g^{-1} for 0.5 A g^{-1} current density. The device could show a capacitance stability of 88% for 1000 cycles (Fig. 32i). Bending the device from 0° to 175° showed 91% retention of capacitance for potential window of 1.8 V. The device showed specific energy of 43 Wh kg^{-1} with specific power of 900 W kg^{-1} [104].

Since bismuth and vanadium have shown good $C_{sp,}$ Bommineedi et al. [105] fabricated orthorhombic $BiVO_4$ material with spongy morphology through SILAR process over SS substrate. Figure 33a shows the schematic process for the synthesis of $BiVO_4$ material. Figure 33b, c shows the FESEM images of the material at different magnifications. It shows that $BiVO_4$ forms nano-pebbles with spiky surface increasing the surface area of the electrode material. Figure 33d shows the CV analysis of the material in 1 M KCl. It clearly indicates the presence of oxidation and reduction peaks of Bi and V. It could attain a C_{sp} of 707 A g^{-1} at a scan rate of

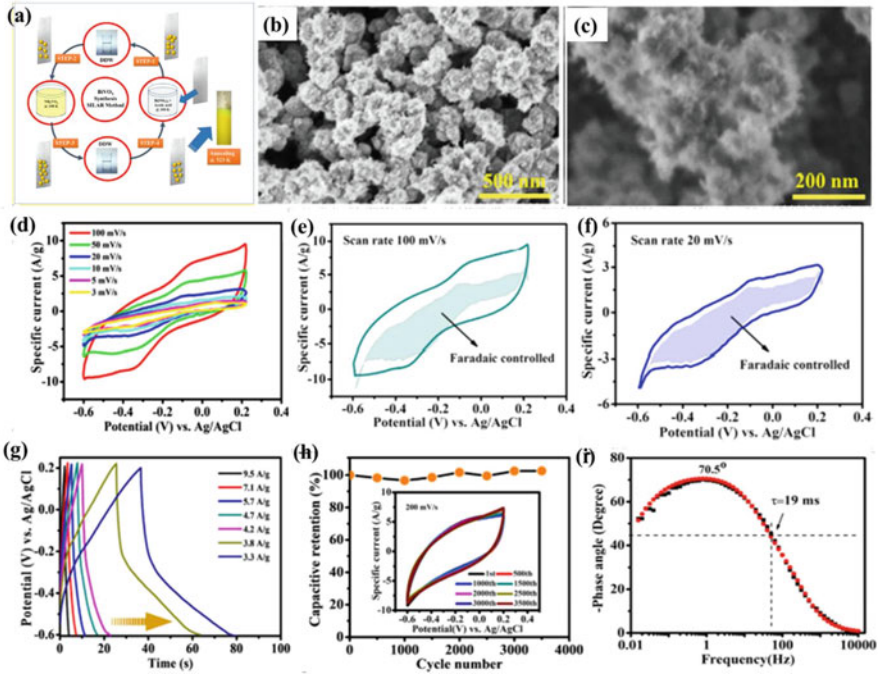

Fig. 33 (**a**) Schematic of the work undertaken for the fabrication of $BiVO_4$. (**b–c**) FESEM images of $BiVO_4$ at different magnifications. (**d**) CV analysis of $BiVO_4$ at different scan rates. (e–f) Contributions from faradaic and capacitive methods at two different scan rates, 100 and 20 mV s_{-}^{1}, respectively. (**g**) CD analysis of the electrode at different current density. (h) Stability study of the material. Inset showing CV of the electrode at every 500th cycle. (i) Bode phase plot [105]

3 mV s^{-1}. They also calculated the electrochemically active surface area using CV for two different scan rates. Here they have used the formula

$$\mathrm{ECSA} = \mathrm{C_{DL}}/\mathrm{C_s} \tag{13}$$

where C_{DL} represents the double-layer capacitance obtained from the CV curve corresponding to the non-faradaic region, whereas C_s represents the C_{sp} of electrochemical double layer. C_{DL} is evaluated from the slope of the I_{DL}-V graph where I_{DL} is evaluated from the formula $I_{DL} = C_{DL} \times \upsilon$. Here, υ denotes the scan rate and the C_s is approximated to be 40 mF cm^{-2}. The calculated electrochemically active surface area of $BiVO_4$ was 87.1 m^2 g^{-1}. The GCD analysis (Fig. 33g) showed non-linear behaviour which was in accordance with the CV studies. From GCD study, the C_{sp} was calculated to be 199 F g^{-1} at 3.3 A g^{-1} current density. Capacitance retention showed 102% at 3500 cycles wherein it reduced to 98% during initial 1000 cycles. The relaxation time obtained from frequency vs. capacitance graph

was 20 ms which was closer to the 19 ms obtained from the Bode phase plot at 45° phase angle. Reduced relaxation time indicates high power delivering capacity of an ideal SC [105].

Although 2D materials have shown their importance in the field of SCs, the SCs mainly require an increased surface area for the enhancement in the capacitive value. However, a uniform repeatable deposition of 2D structures like nanosheets is still a great challenge.

7.4 Three-Dimensional (3D) Nanostructures

3D structure facilitates large surface area and short diffusion path. These includes nanocubes, nanostars, nickel foam, and metal oxide frames. Yan et al. [106] fabricated thin film of MnO_2 over 3D Ni foam through hydrothermal process. Figure 34a shows the FESEM image of intertwined nanosheets of length 100–200 nm formed on the surface of Ni foam. Such structures make certain that more area is exposed to the electrolytes for the reaction purpose as the pore sizes were found to be ~20 nm. CV curve (Fig. 34b) showed nearly a rectangular curve with no redox peaks within a potential frame of 0 to 1 V in 1 M Na_2SO_4 at 2 mV s^{-1} scan rate. GCD study (Fig. 34c) shows a linear and symmetric curve indicating reversible behaviour. At 1 A g^{-1} current density, the thin film showed C_{sp} of 241 F g^{-1}. Stability analysis showed loss in capacitance at initial 300 cycles, and later, there was only 10% loss up to 1000 cycles [106].

Zhu et al. [107] used 2D nanosheets of V_2O_5 as the building blocks for the construction of 3D architecture with high surface area, ultrathin thickness, and porous architecture. Figure 35a shows the schematic of the fabrication process undertaken for the formation of 3D V_2O_5.FESEM image of 3D V_2O_5 shown in Fig. 35b clearly displays that the 3D structure is formed of numerous interconnected nanosheets. This morphology is formed by freeze drying V_2O_5 nanosheets. They compared the 3D V_2O_5 with its bulk and stacked structures. Figure 35c shows that the C_{sp} of 3D V_2O_5 is 521 F g^{-1} which is more than that observed in case of bulk and stacked structures. Also, the charge-discharge analysis of different morphologies showed that in case of 3D V_2O_5, the discharge time is more and

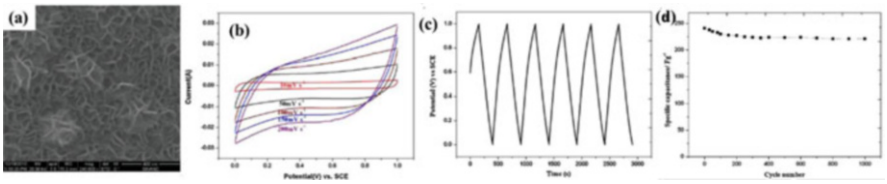

Fig. 34 (**a**) FESEM image of 3D MnO_2 film over the Ni foam. (**b**) CV analysis of MnO_2 film. (**c**) Charge-discharge profile. (**d**) Stability study of the film [106]

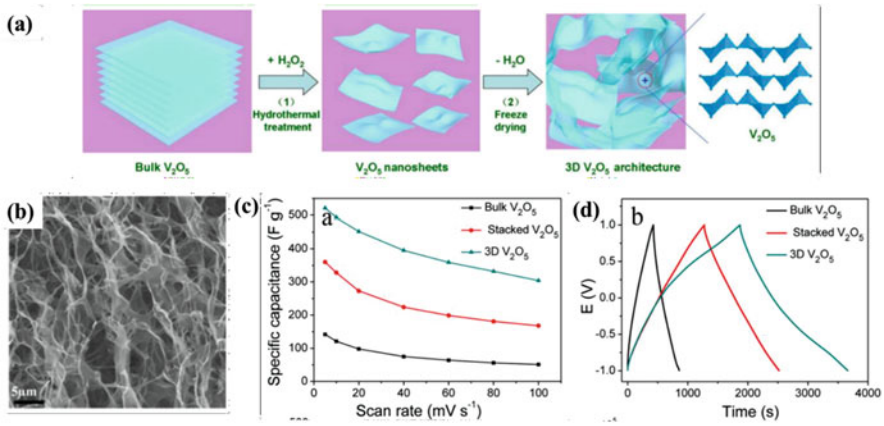

Fig. 35 (**a**) Schematic of the fabrication process involved for 3D V_2O_5 architecture. (**b**) FESEM image of 3D V_2O_5. (**c**) Specific capacitance of bulk, stacked, and 3D V_2O_5. (**d**) Charge-discharge profile of bulk, stacked, and 3D V_2O_5 [107]

the slope is less, indicating higher electrochemical activity. In 1 M aqueous Na_2SO_4 electrolyte, 3D morphology showed a maximum specific capacitance of 451 F g^{-1} at 0.5 A g^{-1} current density within a potential window of −1 to 1 V. It showed that the proposed structure gave an energy density of 247.9 W h kg^{-1} and power density of 497.1 W kg^{-1}. This architecture was also able to exhibit a capacitance retention of ~90% after 4000 cycles [107].

Metal organic frameworks (MOFs) are famous for their extraordinary porosity and surface area which can be tuned through the selection of appropriate linkers and metal nodes [108]. Wang et al. [109] fabricated Ni-based MOFs and co-doped it with different weights of Co. Figure 36a–d show the SEM and TEM images of Ni-MOF and Co-doped Ni-MOF prepared through hydrothermal method. The image corresponding to Ni-MOF shows microspheres with nanoribbon-like morphology on the surface. On co-doping with Co, this shows microspheres of reduced diameter with interconnected and enlarged nanoribbons forming a 3D flower-like morphology. The CV analysis with different amounts of Co shows that for Co_2-Ni-MOF, the C_{sp} was larger compared to others. The CV analysis of Co_2-Ni-MOF in 6 M KOH shown in Fig. 36e indicates oxidation-reduction peaks due to the ion exchange of OH^- ions and the oxidation states of Ni and Co. Microsphere morphology with interconnected nanoribbons facilitates the intercalation and de-intercalation of the electrolyte ions. Co_2-Ni-MOF showed the maximum C_{sp} of 1300 F g^{-1} at 1 A g^{-1} with extended discharge time indicating its ability to store charges (Fig. 36f). Capacitance retention showed 59% and 71% of initial C_{sp} value for both Ni-MOF and Co_2-Ni-MOF, respectively. Hybrid supercapacitor device fabricated with Co_2-Ni-MOF as one electrode and AC as another electrode showed CV as depicted in Fig. 36g with redox peaks indicating faradaic behaviour. The GCD (Fig. 36h) shows almost symmetric curves indicating excellent electrochemical stability. The device

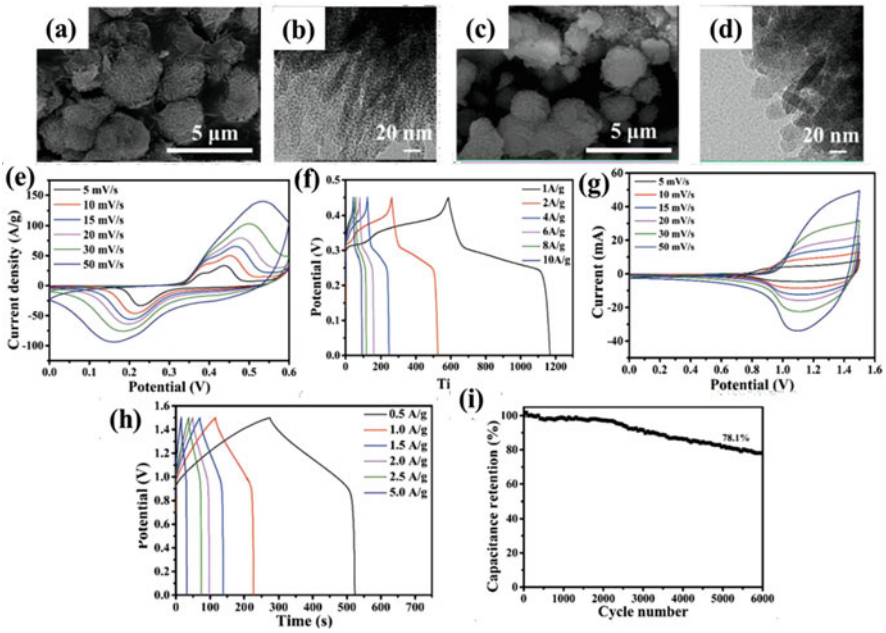

Fig. 36 SEM and TEM images of (**a**–**d**) Ni-MOF and (**c**, **d**) Co_2-MOF. (**e**) CV plot of Co_2-Ni-MOF. (**f**) CD profile of CO_2-Ni-MOF, asymmetric SC fabricated with Co_2-MOF//AC electrodes. (**g**) CV curve. (**h**) CD profile. (**i**) Capacitance retention of the device [109]

could retain about 78.1% of the capacitance even after 6000 cycles (Fig. 36i). The energy density of the device was found to be 25.92 W h kg^{-1} with power density of 375 W kg^{-1} [109]. Table 3 tabulates the literature survey for 0D, 1D, 2D and 3D nanostructured materials for SC application.

8 Summary and Conclusions

This chapter gives a brief outlook on various architectures of electrode materials which have been utilized for supercapacitors. Nanomaterials with 0D, 1D, 2D, and 3D morphologies have found to have an impact on the capacitive behaviour of the supercapacitors. Each morphology exposes different amounts of active area for electrochemical activity as a result the specific capacitance offered by them is different. As for energy density, devices in which materials with maximum active area exposed to the electrolyte provided a wider potential window eventually enhancing the supercapacitors. Most of the morphologies encompass large amount of dead zones or areas not accessible by the electrolyte ions. The main aspect of varying the morphology is to allow areas to be exposed for the electrolyte dissociation, although no exact configuration of the material morphology can be claimed to provide the

Table 3 Literature survey of 0D, 1D, 2D, and 3D nanostructured materials for supercapacitor application

Material	Morphology	Liquid/solid	Specific capacitance	Potential window	ED	PD	Stability	References
Ag	Nanoparticles	–	452 F g^{-1} at 2 mV s^{-1}	−1.1 to −0.2	27.8	4.1 k	63%at 10,000	[63]
Graphene	Quantum dot	–	296.7 F g^{-1} at 1 A g^{-1}	-1 to 0	41.2	500	97.6%at 5000	[74]
$NiCo_2S_4$	Quantum dots	Liquid	168.1 F g^{-1} at 1 A g^{-1}	0 to 1.5	67.5	850	99.2%at 15000	[75]
TiO_2/MWCNT	Nanodots over nanowires		329 F g^{-1} at 5 mV s^{-1}	0 to 0.9	–	–	76%at 1500	[77]
TiO_2	Vertically aligned nanotube		207 F g^{-1} at 5 mV s^{-1}	-1 to 0	27.8	1.42 k	103%at 1500	[78]
$Cd(OH)_2//^{Cd}(OH)_2$	Nanowire	Liquid	51 F g^{-1} at 5mV s^{-1}	−1.9 to 0	11.09	799	17%at 1000	[40]
$Cd(OH)_2/^{Cu}(OH)_2$	Core-shell nanowires	Liquid	277 F g^{-1} at 1.5 A g^{-1}	−0.3 to −0.8	–	–	62%at 1000	[79]
$Cd(OH)_2$/$Fe(OH)_2$	Core-shell nanowires	Liquid	368 F g^{-1} at 2 A g^{-1}	−0.9 to 0.3	–	–	52%at 5000	[85]
CdS	Nanowires		181 F g^{-1} at 5 mV s^{-1}	−1.1 to −0.1	1.72	27.14	76%at 400	[86]
CdS/Ag_2S	Nanoparticles over nanowires		15.04 F g^{-1} at 1.5 mA cm^{-2}	−0.1 to −1.1 V	2.5	107.17	–	[87]
CdS/Ag_2S	Core-shell heterostructure		56.84 at 1.5mA cm^{-2}	−0.1 to −1.1 V	9.47	1070.1	–	
Ag_2S	Nanowire		268.47 at 1.5 mA cm^{-2}	−0.1 to −1.1 V	44.74	1278.43	–	
CdS/HgS	Core-shell heterostructure nanowire		94.40 F g^{-1} at 2 mA cm^{-2}	−0.1 to −1.1 V	–	–	87% at 1250	[88]
HgS	Nanowire		19.08 F g^{-1} at 2 mA cm^{-2}	−0.1 to −1.1 V	–	–	~30% at 1250	
Co_3O_4/MWCNT	Nanoparticles over MWCNT		685 F g^{-1} at5 mV s^{-1}	0.2 to 0.5 V	16.41	300	73%at 5000	[89]
Ag/MWCNT	Nanoparticles on MWCNT		757 F g^{-1} at 2 mV s^{-1}	−1.1 to −0.2	60.7	3.3 k	83%at 3000	[64]
V_2O_5/MWCNT	Nanoflakes over MWCNT	Solid	160 F g^{-1} at 1 A g^{-1}	0 to 1.8	72	2.3 k	96% at 4000	[90]
V_2O_5/MWCNT	Nanoflakes over MWCNT	Liquid	569.7 F g^{-1} at 2 mV s^{-1}	0 to 2	62	11.5 k	89.2%at 4000	[91]
CeO_2/MWCNT	Nanoparticles on MWCNT		455.6 F g^{-1} at 1 A g^{-1}	0 to 0.43			~81.1% at 2000	[92]
CeO_2/MWCNT/ /CeO_2/MWCNT	Nanoparticles over MWCNT	Solid	486.5 F g^{-1} at 2 mV s^{-1}	0 to 1.2	85.7	2.6 k	92.1%at 2000	[93]
Fe_2O_3	Agglomerated nanoparticles		180 F g^{-1} at 2 A g^{-1}	−0.8 to 0	16	800	48%at 500	[94]

(continued)

Table 3 (continued)

Material	Morphology	Liquid/solid	Specific capacitance	Potential window	ED	PD	Stability	References
Fe_2O_3/MWCNT	Nanoparticles over nanowire		437.5 F g^{-1}at 2 A g^{-1}	−0.8 to 0	33.33	1200	65%at 500	
Fe_2O_3/MWCNT// Fe_2O_3/MWCNT	Nanoparticles over nanowire	Solid	70.16 F g^{-1} at 0.57 A g^{-1}	0 to 1	9.74	487	75%at 1500	[95]
$ZnFe_2O_4$//$ZnFe_2O_4$	Nanoparticles on nanoplates	Solid	26 F g^{-1} at 2mV s^{-1}	0 to 1	4.47	277	66%at 1000	[96]
$ZnFe_2O_4$/CNT// $ZnFe_2O_4$/CNT	Nanoparticles over nanowire	Solid	92.2 F g^{-1} at 0.35 A g^{-1}	0 to 1	12.8	377.86	70% at 2000	[97]
$ZnCo_2O_4$//$ZnCo_2O_4$	Nanoflakes	Solid	69.65 F g^{-1} at 1.07 A g^{-1}	0 to 1	9.67	1451	68%at 2000	[98]
CdSe	Nanospheres	–	1.285 F cm-2 at 10 mV s^{-1}	−0.2 to 0.8	4.015		~16.3% at 2000	[99]
$Sr(OH)_2$	Thin film (tuberose)		413 C g^{-1} at2 A g^{-1}	−0.8 to 0	45.95	2.6	~ 35% at 5000	[100]
Cu:$Sr(OH)_2$ (1%)	Thin film (tuberose with flakes)		467 C g^{-1} at0.4 mA cm^{-1}	−0.8 to 0			68% at 6000	[101]
Cu:$Sr(OH)_2$ (2%)	Thin film (tuberose with flakes)		554 C g^{-1} at0.4 mA cm^{-1}	−0.8 to 0	–	–	71% at 6000	
Cu:$Sr(OH)_2$ (3%)	Thin film (tuberose with flakes)		817 C g^{-1} at0.4 mA cm^{-1}	−0.8 to 0	–	–	45% at 6000	
Fe:$Sr(OH)_2$ (0.1%)	Thin film (tuberose with fibres on surface)		375C g^{-1} at1.2 mA cm^{-2}	−1.1 to 0			65%at 800	[102]
Fe:$Sr(OH)_2$ (0.5%)	Thin film (tuberose with fibres on surface)		790C g^{-1} at1.2 mA cm^{-2}	−1.1 to 0			79%at 800	
Fe:$Sr(OH)_2$ (1%)	Thin film (tuberose with fibres on surface)		871 C g^{-1} at1.2 mA cm^{-2}	−1.1 to 0			66%at 800	
Bi_2O_3	Nanoneedles	–	399.6 F g^{-1} at 5.17 A g^{-1}	−0.8 to 0.3	–	–	72%at 3000	[103]
	Nanoflakes	Solid	358 F g^{-1} at1 mV s^{-1}	0 to 1.8	43	900	88%at 1000	[104]
$BiVO_4$	Nano-pebbles		707 F g^{-1} at3 mV s^{-1}	−0.6 to 0.2	–	–	102%at 3500	[105]
MnO_2	Interconnected nanosheets		241 F g^{-1} at1 A g^{-1}	0 to 1	–	–	~90%at 1000	[106]
V_2O_5	Interconnected nanosheets	–	451 F g^{-1} at0.5 A g^{-1}	−1.0 to 1.0	247.9	497.1	~ 90%at 4000	[107]
	Stacked		314 F g^{-1} at0.5 A g^{-1}	−1.0 to 1.0	172	–	–	
	Bulk		108 F g^{-1} at0.5 A g^{-1}	−1.0 to 1.0	58	–	–	
Co_2-Ni-MOF//AC	Microspheres with interconnected nanoribbons		1300 F g^{-1}at 1 A g^{-1}(of electrode)	0 to 1.5	25.92	375	78.1% at 6000	[109]

'//' means device fabricated
'/' means coating
':' means doping

utmost electrochemical behaviour. The literature review identifies interconnected morphologies like nanowires and metal organic frameworks of highly conducting materials have shown an increased life span and high specific capacitance. In the present literature survey, Co_2-Ni-MOF have shown the highest specific capacitance with a moderate energy density and excellent cyclic stability. For energy density of supercapacitors, vanadium oxide with interconnected nanosheets have shown an excellent value.

Nowadays hollow structures have found more complex features to enhance the electrocapacitive performance as both inner and outer surfaces can provide active sites for electrochemical activity. Besides the contemporary fabrication of nanowires and core-shell structures, more different types of morphologies like star-shaped, square-shaped, hollow spheres, and hollow cube shapes are being explored for the electrochemical enhancement.

9 Future Scope

Ample amount of work has been testified for supercapacitors wherein different materials with different morphologies have been explored. However, there exists still disparity in case of its energy density. Increase in specific capacitance does not guarantee a remarkable presentation of energy density. Hence, there exists still a wide scope pertaining to the energy density of the devices fabricated from the published materials. Besides all these studies have been carried out at laboratory level where the environment is under extreme control. A large-scale fabrication and practical implementation of such devices in our daily chores need to be investigated.

References

1. Q. Wang, X. Wang, B. Liu, G. Yu, X. Hou, D. Chen, G. Shen, J. Mater. Chem. A **1**, 2468–2473 (2013)
2. S. Koohi-Fayegh, M.A. Rosen, J. Energy Storage **27**, 101047 (2020)
3. Z. Zhang, T. Ding, Q. Zhou, Y. Sun, M. Qu, Z. Zeng, Y. Ju, L. Li, K. Wang, F. Chi, Renew. Sust. Energ. Rev. **148**, 111263 (2021). https://doi.org/10.1016/j.rser.2021.111263
4. X. Ma, W. Luo, M. Yan, L. He, L. Mai, Nano Energy **24**, 165–188 (2016)
5. P. Simon, Y. Gogotsi, Nat. Mater. **7**, 845–854 (2008)
6. D.P. Dubal, P.G. Romero, B.R. Sankapal, R. Holze, Nano Energy **11**, 377–399 (2015)
7. R. Vellacheri, A.A. Haddad, H. Zhao, W. Wang, C. Wang, Y. Lei, Nano Energy **8**, 231–237 (2014)
8. G.Q. Zhang, H.B. Wu, H.E. Hoster, M.B.C. Park, X.W. Lou, Energy Environ. Sci. **5**, 9453–9456 (2012)
9. H. Cheng, A.D. Su, S. Li, S.T. Nguyen, L. Lu, C.Y.H. Lim, H.M. Duong, Chem. Phys. Lett. **601**, 168–173 (2014)

10. V.S. Kumbhar, A.C. Lokhande, N.S. Gaikwad, C.D. Lokhande, Chem. Phys. Lett. **645**, 112–117 (2016)
11. Q. Zhang, W. Deng, S. Zhang, J. Wu, J. Control Sci. Eng. **2016**, 1–17 (2016)
12. X. Lu, Y. Qu, Y. Wang, C. Qin, G. Liu, Energy Convers. Manag. **171**, 1273–1291 (2018)
13. M.A. Hannan, M.M. Hoque, A. Mohamed, A. Ayob, Renew. Sust. Energ. Rev. **69**, 771–789 (2017)
14. Z. Bououchma, J. Sabor, H. Aitbouh, Mater. Today Proc. **13**, 688–697 (2019)
15. A. González, E. Goikolea, J. Andoni, R. Mysyk, Renew. Sust. Energ. Rev. **58**, 1189–1206 (2016)
16. J.H. Kim, S.H. Kang, K. Zhu, J.Y. Kim, N.R. Neale, A.J. Frank, Chem. Commun. **47**, 5214–5216 (2011)
17. A. Gonzalez, E. Goikolea, J.A. Barrena, R. Mysyk, Renew. Sust. Energ. Rev. **58**, 1189–1206 (2016)
18. P. Roy, S.K. Srivastava, CrystEngComm **7**, 7801–7815 (2015)
19. http://www.ballard.com/files/images/aboutballard/How-a-fuel-cell-works.jpg
20. T. Chen, L. Dai, J. Mater. Chem. A **2**, 10756–10775 (2014)
21. G. Wang, L. Zhang, J. Zhang, Chem. Soc. Rev. **41**, 797–828 (2012)
22. X. Rui, H. Tan, Q. Yan, Nanoscale **6**, 9889–9924 (2014)
23. M. Nehra, N. Dilbaghi, G. Marrazza, A. Kaushik, R. Abolhassani, Y.K. Mishra, K.H. Kim, S. Kumar, Nano Energy **76**, 104991 (2020)
24. D.P. Dubal, G.S. Gund, C.D. Lokhande, R. Holze, Energ. Technol. **2**, 401–408 (2014)
25. P. Lamba, P. Singh, P. Singh, P. Singh, A. Bharti, M.G. Kumar, Y. Kumar, J. Energy Storage **48**, 103871 (2022)
26. E. Lim, C. Jo, J. Lee, Nanoscale **8**, 7827–7833 (2016)
27. K. Jost, G. Dion, Y. Gogotsi, J. Mater. Chem. A **2**, 10776–10787 (2014)
28. G.S. Gund, D.P. Dubal, S.S. Shinde, C.D. Lokhande, ACS Appl. Mater. Interfaces **6**, 3176–3188 (2014)
29. A. Ramadoss, G.S. Kim, S.J. Kim, CrystEngComm **15**, 10222–10229 (2013)
30. M. Sevilla, R. Mokaya, Energy Environ. Sci. **7**, 1250–1280 (2014)
31. L.L. Zhang, X.S. Zhao, Chem. Soc. Rev. **38**, 2520–2531 (2009)
32. P. Justin, G. Ranga Rao, Int. J. Hydrog. Energy **35**, 9709–9715 (2010)
33. A. Bello, O.O. Fashedemi, J.N. Lekitima, M. Fabiane, D.D. Arhin, K.I. Ozoemena, Y. Gogotsi, A.T. Charlie Johnson, N. Manyala, AIP Adv. **3**, 082118-1–9 (2013)
34. X. Li, L. Jiang, C. Zhou, L. Jinping, H. Zeng, NPG Asia Mater. **7**, e165 (2015)
35. Y. Wang, Y. Song, Y. Xia, Chem. Soc. Rev. **45**, 5925–5950 (2016)
36. P. Li, Y. Yang, E. Shi, Q. Shen, Y. Shang, S. Wu, ACS Appl. Mater. Interfaces **6**, 5228–5234 (2014)
37. R. Ramya, R. Sivasubramanian, M.V. Sangaranarayanan, Electrochim. Acta **101**, 109–129 (2013)
38. A.K. Singh, D. Sarkar, G.G. Khan, K. Mandal, J. Mater. Chem. A **1**, 12759 (2013)
39. D.P. Dubal, G.S. Gund, R. Holze, C.D. Lokhande, J. Power Sources **242**, 687–698 (2013)
40. S. Patil, S. Raut, R. Gore, B.R. Sankapal, New J. Chem. **39**, 9124–9131 (2015)
41. J. Kim, H. Ju, A.I. Inamdar, Y. Jo, J. Han, H. Kim, H. Im, Energy **70**, 473–477 (2014)
42. S. Roldan, D. Barreda, M.B. Granda, R. Menendz, R. Santamarıía, C. Blanco, Phys. Chem. Chem. Phys. **17**, 1084 (2015)
43. Z. Fan, J. Yan, T. Wei, L. Zhi, G. Ning, T. Li, F. Wei, Adv. Funct. Mater. **21**, 2366–2375 (2011)
44. T. Peng, T. Zhao, Q. Zhou, H. Zhou, J. Wang, J. Liu, Q. Liu, CrystEngComm **17**, 7583–7591 (2015)
45. M.D. Stoller, S. Park, Y. Zhu, J. An, R.S. Ruoff, Nano Lett. **8**, 3498–3502 (2008)
46. X. Zhang, D. Zhao, Y. Zhao, P. Tang, Y. Shen, C. Xu, H. Li, Y. Xiao, J. Mater. Chem. A **1**, 3706–3712 (2013)
47. B. Abdulhakeem, B. Farshad, M. Damilola, T. Fatemeh, F. Mopeli, D. Julien, M. Ncholu, RSC Adv. **4**, 39066–39072 (2014)

48. H. Wei, H. Gu, J. Guo, S. Wei, Z. Guo, J. Electrochem. Soc. **160**, 3038–3045 (2013)
49. Z. Yu, L. Tetard, L. Zhai, J. Thomas, Energy Environ. Sci. **8**, 702–730 (2015)
50. A. Bello, F. Barzegar, M.J. Madito, D.Y. Momodu, A.A. Khaleed, T.M. Masikhwa, J.K. Dangbegnon, N. Manyala, Electrochim. Acta **213**, 107–114 (2016)
51. Q. Lu, J.G. Chen, J.Q. Xiao, Angew. Chem. Int. Ed. **52**, 1882–1889 (2013)
52. X. Lu, M. Yu, G. Wang, T. Zhai, S. Xie, Y. Ling, Y. Tong, Y. Li, Adv. Mater. **25**, 267–272 (2013)
53. G.A. Snook, P. Kao, A.S. Best, J. Power Sources **196**, 1–12 (2011)
54. X. Cao, Z. Yin, H. Zhang, Energy Environ. Sci. **7**, 1850–1865 (2014)
55. M. Yu, W. Wang, C. Li, T. Zhai, X. Lu, Y. Tong, NPG Asia Mater. **6**, e129 (2014). https://doi.org/10.1038/am.2014.78
56. D.P. Dubal, G.S. Gund, C.D. Lokhande, R. Holze, ACS Appl. Mater. Interfaces **5**, 2446–2454 (2013)
57. T.E. Balaji, H.T. Das, T. Maiyalagan, ChemElectroChem **8**, 1–25 (2021)
58. J. Yan, Q. Wang, T. Wei, Z. Fan, Adv. Energy Mater. **4**, 1300816 (2014). https://doi.org/10.1002/aenm.201300816
59. C.M. Wang, C.Y. Wen, Y.C. Che, J.Y. Chang, C.H. Ho, K.S. Kao, W.C. Shih, C.M. Chiu, Y.A. Shen, The influence of specific surface area on the capacitance of the carbon electrodes supercapacitor, in *Proceedings of the 3rd International Conference on Industrial Application Engineering*, (2015), pp. 28–31
60. C. Liu, X. Yan, F. Hu, G. Gao, G. Wu, X. Yang, Adv. Mater. **30**, e1705713 (2018). https://doi.org/10.1002/adma.201705713
61. S. Kondrat, C.R. Perez, V. Presser, Y. Gogotsi, A.A. Kornyshev, Energy Environ. Sci. **5**, 6474–6479 (2012)
62. K.B. Xu, W.Y. Li, Q. Liu, B. Li, X.J. Liu, L. An, Z.G. Chen, R.J. Zou, J.Q. Hu, J. Mater. Chem. A **2**, 4795–4802 (2014)
63. B. Pandit, V.S. Devika, B.R. Sankapal, J. Alloys Compd. **726**, 1295–1303 (2017)
64. B. Pandit, B.R. Sankapal, New J. Chem. **41**, 10808–10814 (2017)
65. L. Zhang, S. Yang, J. Chang, D. Zhao, J. Wang, S. Yang, B. Cao, Front. Chem. **8**, 413 (2020)
66. Y. Teng, E. Liu, R. Ding, K. Liu, R. Liu, L. Wang, Electrochem. Acta **194**, 394–404 (2016)
67. J. Lee, B. Kruner, A. Tolosa, S. Sathyamoorthy, D. Kim, S. Chaudhary, Energy Environ. Sci. **9**, 3392–3398 (2016)
68. M. Lu, *Supercapacitors: Materials, Systems, and Applications* (John Wiley & Sons, 2013)
69. S. Pan, M. Yao, J. Zhang, B. Li, C. Xing, X. Song, P. Su, H. Zhang, Recognition of ionic liquids as high-voltage electrolytes for supercapacitors. Front. Chem. **8**(261) (2020)
70. X. Wang, Y. Li, F. Lou, M.E. Melandsø Buan, E. Sheridan, D. Chen, RSC Adv. **7**, 23859–23865 (2017)
71. A. Balducci, W.A. Henderson, M. Mastragostino, S. Passerini, P. Simon, F. Soavi, Electrochim. Acta **50**, 2233–2237 (2005)
72. X.H. Lu, M.H. Yu, G.M. Wang, Y.X. Tong, Y. Li, Energy Environ. Sci. **7**, 2160–2181 (2014)
73. Y. Ma, X. Xie, W. Yang, Z. Yu, X. Sun, Y. Zhang, X. Yang, H. Kimura, C. Hou, Z. Guo, W. Du, Adv. Compos. Hybrid Mater. **4**, 906–924 (2021)
74. S. Zhang, L. Sui, H. Dong, W. He, L. Dong, L. Yu, ACS Appl. Mater. Interfaces **10**, 12983–12991 (2018)
75. W. Chen, X. Zhang, L. Mo, Y. Zhang, S. Chen, Chem. Eng. J. **388**, 124109 (2020)
76. G. Zhou, L. Xu, G. Hu, L. Mai, Y. Cui, Chem. Rev. **119**, 11042–11109 (2019)
77. B.R. Sankapal, H.B. Gajare, D.P. Dubal, R.B. Gore, R.R. Salunkhe, H. Ahn, Chem. Eng. J. **247**, 103–110 (2014)
78. S.S. Raut, G.P. Patil, P.G. Chavan, B.R. Sankapal, J. Electroanal. Chem. **780**, 197–200 (2016)
79. S.L. Patil, S.S. Raut, B.R. Sankapal, Thin Solid Films **692**, 137584 (2019)
80. X. Yan, X. Tong, L. Ma, Y. Tian, Y. Cai, C. Gong, Mater. Lett. **124**, 133–136 (2014)
81. S. Gupta, S.V. Kershaw, A.L. Rogach, Adv. Mater. **25**, 6923–6944 (2013)
82. S. Kuder, L. Carbone, M.F. Cacule, R. Cingolani, A. Falqui, E. Snoeck, W. Parak, L. Manna, Nano Lett. **5**, 445–449 (2005)

83. S.L. Patil, R.S. Chaudhari, R.D. Ladhe, P.K. Baviskar, B.R. Sankapal, J. Sci. Rev. **2**, 91–95 (2010)
84. N.B. Sonawane, K.V. Gurav, R.R. Ahire, J.H. Kim, B.R. Sankapal, Sensors Actuators A Phys. **216**, 78–83 (2014)
85. S. Patil, S. Raut, B. Pandit, S.N. Pandey, S.A. Pande, B. Sankapal, J. Mater. Sci. Mater. Electron. **32**, 22472–22480 (2021)
86. N. Nair, S. Majumder, B.R. Sankapal, Chem. Phys. Lett. **659**, 105–111 (2016)
87. N. Nair, B.R. Sankapal, New J. Chem. **40**, 10144–10152 (2016)
88. N. Nair, B.R. Sankapal, Nano-Struct. Nano-Objects **10**, 159–166 (2017)
89. B.R. Sankapal, H.B. Gajare, S.S. Karade, D.P. Dubal, RSC Adv. **5**, 48426–48432 (2015)
90. B. Pandit, D.P. Dubal, P. Gómez-Romero, B.B. Kale, B.R. Sankapal, Sci. Rep. **7**, 43430 (2017)
91. S.A. Pande, B. Pandit, B.R. Sankapal, Mater. Des. **182**, 107972 (2019)
92. D. Deng, N. Chen, Y. Li, X. Xing, X. Liu, X. Xiao, Y. Wang, Phys. E Low Dimens. Syst. Nanostruct. **86**, 284–291 (2017)
93. B. Pandit, B.R. Sankapal, M. Koinkar, Sci. Rep. **5**(5892–1), 13 (2019)
94. S.S. Raut, B.R. Sankapal, New J. Chem. **40**, 2619–2627 (2016)
95. S.S. Raut, L.K. Bommineedi, S. Pande, B.R. Sankapal, Synth. Met. **271**, 116629 (2021)
96. S.S. Raut, B.R. Sankapal, Electrochim. Acta **198**, 203–211 (2016)
97. S.S. Raut, B.R. Sankapal, M.S.A. Hossain, S. Pradhan, R.R. Salunkhe, Y. Yamauchi, Eur. J. Inorg. Chem. **2018**, 137–142 (2018)
98. S.S. Raut, B.R. Sankapal, J. Colloid Interface Sci. **487**, 201–208 (2017)
99. S.A. Pawar, D.S. Patil, J.C. Shin, Mater. Today Chem. **4**, 164–171 (2017)
100. S. Kavyashree, S.S. Raut, B.R. Sankapal, S.N. Pandey, Electrochim. Acta **258**, 34–42 (2017)
101. S. Kavyashree, S. Raut, S. Parveen, B.R. Sankapal, S.N. Pandey, ChemElectroChem **5**, 4021–4028 (2018)
102. S. Kavyashree, S. Parveen, S.S. Raut, M.K. Tiwari, B.R. Sankapal, S.N. Pandey, J. Alloys Compd. **781**, 831–841 (2019)
103. S.S. Raut, O. Bisen, B.R. Sankapal, Ionics (Kiel) **23**, 1831–1837 (2017)
104. B. Pandit, D.P. Dubal, B.R. Sankapal, Electrochim. Acta **242**, 382–389 (2017)
105. L.K. Bommineedi, B. Pandit, B.R. Sankapal, Int. J. Hydrog. Energy **46**, 25586–25595 (2021)
106. D. Yan, Z. Guo, G. Zhu, Z. Yu, H. Xu, A. Yu, J. Power Sources **199**, 409–412 (2012)
107. J. Zhu, L. Cao, Y. Wu, Y. Gong, Z. Liu, H.E. Hoster, Y. Zhang, S. Zhang, S. Yang, Q. Yan, P.M. Ajayan, R. Vajtai, Nano Lett. **13**, 5408–5413 (2013)
108. A.E. Baumann, D.A. Burns, B. Liu, V.S. Thoi, Commun. Chem. **2**(1), 1–14 (2019)
109. J. Wang, Q. Zhong, Y. Xiong, D. Cheng, Y. Zeng, Y. Bu, Appl. Surf. Sci. **483**, 1158–1165 (2019)

1D, 2D, and 3D Structured Metal Chalcogenides for Supercapacitor Application

S. S. Kumbhar, S. J. Marje, V. V. Patil, S. B. Bhosale, S. S. Pujari, J. L. Gunjakar, C. D. Lokhande, and U. M. Patil

Abbreviations

1D	One dimensional
2D	Two dimensional
3D	Three dimensional
AB	Acetylene black
CBD	Chemical bath deposition
CC	Carbon cloth
CV	Cyclic voltammetry
EDLC	Electric double-layer capacitor
EIS	Electrochemical impedance spectroscopy
FESEM	Field emission scanning electron microscopy
GCD	Galvanostatic charge-discharge
GO	Graphene oxide
NG	N-doped graphene
NMC	Nitrogen-doped mesoporous carbon
NWs	Nanowires
PANI	Polyaniline
Pt	Platinum
rGO	Reduced graphene oxide
TEM	Transmission electron microscopy

S. S. Kumbhar · S. J. Marje · V. V. Patil · S. B. Bhosale · S. S. Pujari · J. L. Gunjakar
C. D. Lokhande · U. M. Patil (✉)
Centre for Interdisciplinary Research, D. Y. Patil Education Society, Kolhapur, India

F. I. Ezema et al. (eds.), *Chemically Deposited Metal Chalcogenide-based Carbon Composites for Versatile Applications*, https://doi.org/10.1007/978-3-031-23401-9_2

1 Introduction

The developing global economic system raises social and ecological issues such as fossil fuel degradation and destruction of environmental health, which are the important reasons to increase the need development of clean and renewable power resources [1–6]. However, the storage of energy supplied by renewable energy sources is the main problem that can be solved by developing efficient electrical energy storage devices. Among them, supercapacitors attract more attention due to the many attractive features at the advanced industry levels such as fast charging-discharging; high specific power, i.e.,>10 kW kg^{-1}; high cyclic stability, i.e.,100,000 cycles; and eco-friendly behavior [7–9].

In rural areas, public grids are not readily available and are complicated to reach due to the requirement of high-cost wiring to supply electricity. In these areas, supercapacitors are helpful; also, they are used in portable electronic devices like digital cameras, mobile phones, laptops, etc., because of their flexibility and lightweight. Also, the supercapacitor's high-power density makes it suitable for use in hybrid and electric vehicles, which is required for quick acceleration after braking, which saves energy and protects the batteries from the higher frequency fast charge-discharge processing.

The performance of different energy storage devices is plotted in the Ragone plot and presented in Fig. 1. In a comparative study, it seems that the supercapacitor is an intervening stage between the conventional capacitor and batteries. The gap between the low-power batteries and low-energy capacitors is fulfilled by supercapacitors offering higher power than a battery and higher energy than capacitors. The supercapacitors store charges in the range of 100–1000 F for each device which is higher than conventional capacitors (μF to mF) [10, 11].

Supercapacitors are classified into three types depending on their charge storage mechanisms: electric double-layer capacitor (EDLC), pseudocapacitor, and hybrid capacitor. The materials (carbon-based) like carbon nanotubes, activated carbon, graphene, etc., considered EDLC materials, store charges electrostatically. The metal hydroxide/oxides, chalcogenides, conducting polymers, etc. commonly exhibited pseudocapacitive performance by storing charges via redox reaction [12, 13]. The charges are stored by both mechanisms in a hybrid capacitor.

Up to now, numerous materials have been studied for supercapacitor application, but they have not fulfilled the requirements of supercapacitor electrode material, like low preparation cost, high capacitance, and durability. The performance of supercapacitors is based on the properties of active materials. So, tremendous efforts are taken by researchers to improve the capacitive performance of material via increasing specific surface area and conductivity. The manipulating or downscaling of the microstructures of the active materials in 1D, 2D, and 3D is the most authentic approach to increase the conductivity and surface area of the active material, which ultimately enhances supercapacitive performance in terms of energy density and power density. Among all types of materials, the metal chalcogenides (metal selenides, sulfides, tellurides, etc.) catch much attention because of their unique

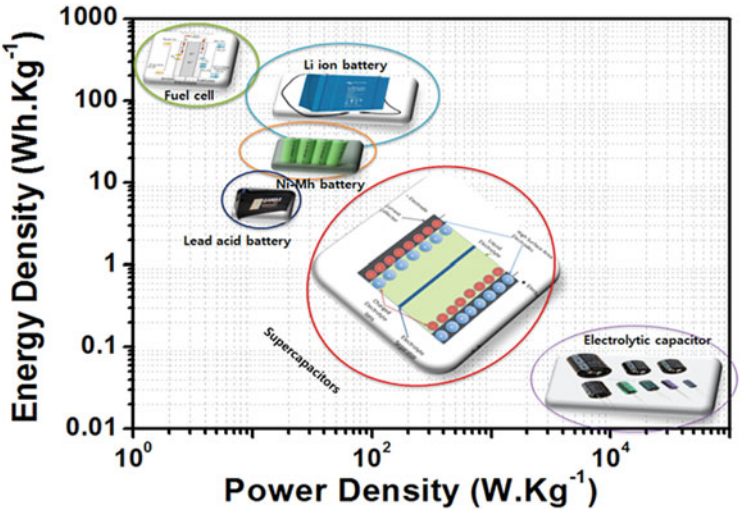

Fig. 1 Ragone plots for different energy storage devices with their energy and power densities

physicochemical features and are used for different applications [14]. Therefore, the morphological structures (1D, 2D, and 3D) and strategies used to enhance the electrochemical performance of metal chalcogenides are summarized in this chapter.

2 Fundamentals of Supercapacitors

The electric double-layer charge storage technology was well known in the nineteenth century, but its first practical use in double-layer capacitor was patented by H. I. Becker in 1957 using carbon electrodes in aqueous electrolyte [15]. Furthermore, B. E. Conway in 1975–1985 developed a new charge storage principle that replaced coin cell batteries in memory backup systems. The fast and reversible redox reaction in bulk electrode material, i.e., pseudocapacitive material used for the storage mechanism like ruthenium oxide (RuO_2), and this invention opened new trends in energy storage development [16]. From 1990, the research world concentrated on developing high-performance supercapacitor devices to replace battery technology. Now, numerous companies all over the world manufacture supercapacitor devices for commercial applications. Based on recent research and development trends, supercapacitors are divided into three classes as follows: electric double-layer capacitors (EDLCs), pseudocapacitors, and hybrid capacitors.

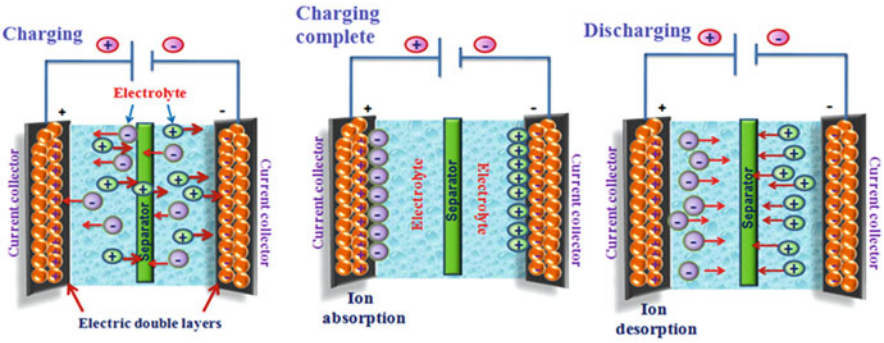

Fig. 2 Schematic representation of charge storage mechanism of electric double-layer capacitor

2.1 Electric Double-Layer Capacitors (EDLCs)

The EDLCs are prepared by combining two carbon electrodes, an electrolyte, and a separator, and charges are stored electrostatically (non-faradaically), similar to conventional capacitors [21–24]. So, there is no net charge transfer between electrode and electrolyte. In charging, electrons externally move towards the positive electrode from the negative electrode via an external loop, and in an electrolyte, ions move in the direction of oppositely charged electrodes and are adsorbed on the surface of the electrode (Fig. 2a). The double layer of ions forms at the surface of each electrode (Fig. 2b. The reverse direction movement of the electrons and ions occurs in discharging process (Fig. 2c) [26–27].

In a non-faradic reaction, no net charge transfer between electrode and electrolyte avoids phase transformation of material and offers high reversibility in charge storage that the main reason for the higher cyclic stability of EDLCs. The materials based on carbon-like carbon nanotubes, carbon aerogels, activated carbon, and graphene are generally applied to increase the performance of EDLC.

2.2 Pseudocapacitors

In a faradic process, oxidation and reduction (redox) reactions take place in between electrolyte and electrode interface by the charge transfer; pseudocapacitors stored charges by faradaic mechanism. The capacity of charge storage in pseudocapacitive materials is larger than EDLC materials because of the involvement of less number of ions in the formation of double layer than in the process of ion exchange because of the utilization of more surface area of active material for the reaction. Other factors also play a key to boost the performance of the pseudocapacitors, such as materials' conductivity, particle size, and the usage of electrolytes. The schematic representation of the charge storage mechanism in the pseudocapacitor

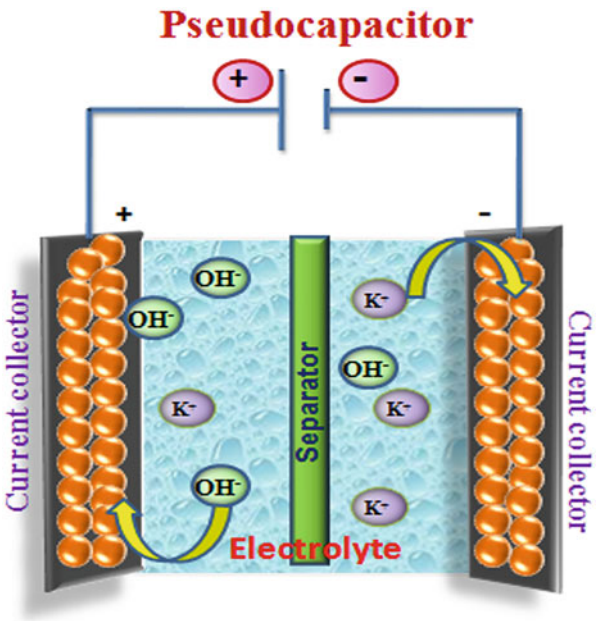

Fig. 3 Schematic representation of charge storage mechanism of pseudocapacitor

is shown in Fig. 3. The process of intercalation/deintercalation, redox reaction, and electrosorption between the de-solvated ions and electrode surface are labeled as pseudocapacitors [20]. Generally, conducting polymers, metal oxides/hydroxides, metal chalcogenides, etc. are employed as pseudocapacitive materials [17–19]. Pseudocapacitors are further categorized into three groups depending on the charge storage mechanisms: (a) intrinsic pseudocapacitor (on or near material surface faradaic reactions), (b) intercalation-type pseudocapacitor (charge stored in tunnels or layers of materials), and (c) extrinsic pseudocapacitor (faradaic reaction at the surface of nano-sized battery materials).

2.3 Hybrid Capacitors

The EDLC offers high specific surface area but low specific capacitance, and on the other hand, pseudocapacitor offers high specific capacitance but limited cyclic life due to faradaic reactions. Thus, the hybridization of EDLC and pseudocapacitors is an effective path to solving the problems related to both systems [28–32]. Therefore, the hybrid capacitors developed by the amalgamation of EDLC and pseudocapacitor store charges through both a faradic and a non-faradic reaction mechanism, a charge storage mechanism schematically presented in Fig. 4. In such type of system, pseudocapacitors offer higher capacitance that provides high energy density,

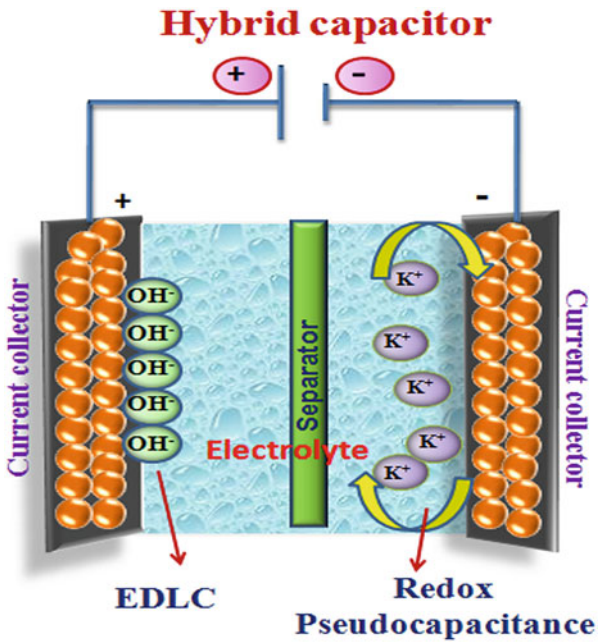

Fig. 4 Schematic representation of charge storage mechanism of hybrid capacitor

although EDLCs provide high power density. So, the hybrid capacitors achieve higher energy density, power density, and cyclic stability than their individual counterparts. Generally, the combination of carbon-based materials with pseudocapacitive materials enhances the contact between materials and electrolyte and charge storing ability. This combination offers high energy of batteries and power like a capacitor with improved cycle life. These devices may be capable of bridging the gap between batteries and supercapacitors. Therefore, the coupling between carbon-based materials with pseudocapacitive materials has obtained enormous interest due to the large enhancement in the total capacitance of the device.

3 Metal Chalcogenides

The Group 16 of the periodic table is identified as chalcogen; it is also familiar as the oxygen family. The oxygen (O), polonium (Po), tellurium (Te), selenium (Se), and livermorium (Lv) elements exist in this group. Among them, polonium and livermorium are radioactive and synthetic elements, respectively. The chemical behavior of oxygen is different from selenium, sulfur, polonium, and tellurium. The chalcogens are lighter and have relatively low atomic radii, and they have -2, $+2$, $+4$, and $+$ 6 common oxidation states [33]. In Group 16 elements, selenium

and tellurium are metalloids, oxygen and sulfur are nonmetals, and polonium is metal under typical conditions. The chemical compounds consisting of at least one chalcogen anion are referred to as chalcogenides and are used in various applications. In particular, metal-based sulfides, tellurides, and selenides are used in various applications such as optoelectronic sensors, ionic sensors, solar cells, fuel cells, batteries, and supercapacitors.

3.1 Metal Sulfides

The tenth commonly available element in the universe is sulfur which has multiple oxidation states -2, -1, 0, $+1$, $+2$, $+3$, $+4$, $+5$, and $+$ 6 [34]. Sulfur associated with metal cations provides extensive tunable physical, chemical, and electrochemical properties in metal sulfides. Also, metal sulfides are cheap and abundant in nature. Many of them have various valence states showing multiple redox transitions and are good conductors. Furthermore, the metal sulfide offers a high theoretical capacity (1672 mAh g^{-1}) and specific energy (2567 Wh kg^{-1}) with an environmentally friendly nature. The metal sulfides are considered a capable aspirant for the high-performing supercapacitor application owned by their cost-effectiveness, good electrical conductivity, lower electronegativity, and redox behavior. The different metal sulfides such as NiS, CoS, CoS_2, CuS, NiS, NiS_2, etc., as well as their composites, have been prepared and investigated for supercapacitor applications.

3.2 Metal Selenides

Selenium, present in the same group of sulfur, and the identical valence electrons and oxidation states are shown as sulfur [35]. So, it offers similar chemical and electrochemical properties like metal sulfide. The attractive physical and chemical properties of metal selenide allow its application in various fields and their high refractive index with photoconductive nature useful for photodetectors and sensor applications [36]. The low volume effect, high bulk density, good reversibility, and rate capability make them potential electrode material for batteries (lithium and sodium-ion batteries). Also, they catch a lot of interest as a capable aspirant for supercapacitor applications because of their rich redox behavior, thermal and mechanical stability, and good electronic conductivity. The various metal selenides like NiSe, CoSe, $CoSe_2$, Cu_3Se_2, $NiSe_2$, etc. and their composites have been synthesized for supercapacitor applications.

3.3 Metal Tellurides

Tellurium (Te) has attracted great attention due to its nonlinear optical, thermoelectrical, gas sensing, and electrochemical properties. Te is a p-type semiconductor that has 0.35 eV bandgap [37]. Te has −2, +2, +4, and + 6 oxidation states, and its association with metal cations is referred to as metal tellurides. Due to the metallic structure and unique morphology, metal tellurides have high electrical conductivity, high specific surface area, and higher active sites for electrochemical reaction. The above excellent properties make them a favorable candidate for numerous applications, like solar cells, fuel cells, lithium-ion batteries, electrocatalysis, supercapacitors, etc. [38]. Also, their strong spin-orbit coupling induces large nonsaturating magnetoresistance, which makes them a potential candidate for spintronic and magnetic memory devices [39, 40]. The numerous single metals and their composites of selenides like TaTe, CoTe, NiTe, GaTe, $CoTe_2$, etc. were synthesized for supercapacitor applications.

3.4 1D Structured Metal Chalcogenides

A large assortment of materials with different nanostructures studied for supercapacitor application in recent years, nanostructured one-dimensional (1D) materials, including conducting polymers, carbon, metal oxides/hydroxides, nitrides, and chalcogenides, etc., show innovative advantages like proficient 1D electron transfer, higher specific area, and tremendous mechanical strength, which makes capable them beneficial for flexible devices [41–46]. The 1D nanostructures which include nanorods, nanotubes, nanofibers, nanowires, etc. can provide shorter path lengths for charge transportation with higher conductivity that offers more efficient contact between the electrode and electrolytic ions and more electroactive sites, consequently improving the rate of charging-discharging even at higher current densities [47–49]. Various methods for the preparation of 1D structured chalcogenide materials such as hydrothermal, electrodeposition, solvothermal, chemical bath deposition (CBD), reflux, etc. are summarized in Table 1 with their corresponding morphologies, specific capacitance, electrolyte, energy density, power density, and cyclic stability [50–75].

Table 1 displays various preparation methods of 1D structured chalcogenide materials having different morphologies and electrochemical performances. Subhadarshini et al. [63] prepared 1D NiSe-Se by chemical method, i.e., CBD method, nanotubes of NiSe-Se deposited on Ni-foam by the chemical reaction of $NiCl_2$, HCl, LiCl, SeO_2 in deionized water at 85°C temperature for 5 h. The schematic illustration of the synthesis process is shown in Fig. 5a, after 5 h reaction NiSe-Se layer was deposited over the Ni-foam, and the FE-SEM images of NiSe-Se are presented in Fig. 5b.

Table 1 Literature study of 1D structured chalcogenide materials

Sr. no.	Material	Method	Morphology	Electrolyte	Energy density Wh kg^{-1}	Power density W kg^{-1}	Specific capacitance (F g^{-1}) at current density (A g^{-1})	Cycles/capacitive retention	Ref.
1.	Ni_3S_2@NiS	One-step in situ growth	Nanorods	2 M KOH	–	–	516 at 0.5		[50]
	Ni_3S_2@Co_9S_8				–	–	925 at 0.5 [1]		
	NiS@$NiSe_2$				–	–	1412 at 0.5		
2.	$Ni_{0.8}$ $Cu_{0.2}S$	Hydrothermal	Nanorods	6 M KOH	–	–	~1092 at 15 mA g^{-1}	3000 (80%)	[51]
	NiS						575 at 15 mA g^{-1}	–	
	Cu_9S_5						70 at 15 mA g^{-1}	–	
3.	Ni-co sulfide	Hydrothermal	Nanowires	1 M KOH	25	3.57 k	2415 at 2.5 mA cm^{-2}	3000 (78.5%)	[52]
4.	$NiCo_2S_4$	Sacrificial template	Nanotubes	6 M KOH	–	–	933 at 1	1000 (63%)	[53]
5.	CoS	Hydrothermal	Nanowires	3 M KOH	34	–	508 at 2.5 mA cm^{-2}	500 (81.2%)	[54]
6.	Cobalt sulfide	Hydrothermal	Nanotubes	6 M KOH	–	–	285 at 0.5	1000 (86.5%)	[55]
7.	$CuCo_2S_4$	Hydrothermal	Nanorods	2 M KOH	50.56	4.6 k	515 at 1	10,000 (~93.3%)	[56]
8.	Bi_2S_3-rGO	Hydrothermal	Nanorods	2 M KOH	–	–	396 at 1	100 (75%)	[57]
9.	GO/strontium sulfide	Hydrothermal	Nanorods	2 M KOH	10.55	294.35	1831.14 at 3 mA cm^{-2}	–	[58]
10.	NiSe	Hydrothermal	Nanowires	2 M KOH	–	–	1790 at 5	1000 (70%)	[59]
11.	NiSe	Hydrothermal	Nanorods	6 M KOH	38.8	629	6.81 F cm^{-2} at 5 mA cm^{-2}	–	[60]

(continued)

Table 1 (continued)

Sr. no.	Material	Method	Morphology	Electrolyte	Energy density Wh kg^{-1}	Power density W kg^{-1}	Specific capacitance (F g^{-1}) at current density (A g^{-1})	Cycles/capacitive retention	Ref.
12.	Ni@NiSe	Solvothermal	Nanowires	2 M KOH	–	–	42 at 1		[61]
	Ni@$Ni_{0.8}Co_{0.2}Se$				17	1526.8	86 at 1		
	Ni@$Ni_{0.6}Co_{0.4}Se$				–	–	39 at 1		
	Ni@Co_9Se_8				16.9	1685.1	66 at 1		
13.	PANI@$NiSe_2$	Chemical oxidative polymerization	Nanotubes	6 M KOH	38.33	308	275.6 mAh g^{-1} at 1	1000 (66%)	[62]
14.	NiSe-se	CBD	Nanotubes	1 M KOH	29.90	594.46	2447.46 at 1	10,000 (95.09%)	[63]
15.	$Ni_{0.5}Co_{0.5}Se_2$	Selenization	Nanowires	6 M KOH	37.5	22.2 k	524 C g^{-1} at 1	3500 (91%)	[64]
16.	$NiCoSe_2$	Solvothermal	Nanorods	1 M KOH	50.66	160.12	1.4 mAh cm^{-2} at 3 mA cm^{-2}	5000 (83.7%)	[65]
17.	$NiCo_2Se_4$	Hydrothermal	Nanotubes	6 M KOH	25	490	461 at 1	5000 (93%)	[66]
18.	Se/rGO	Reflux	Nanorods	1 M KOH	–	–	390 at 5 mV s^{-1}	5000 (~90%)	[67]
19.	CoSe-se	CBD	Nanotubes	1 M KOH	37.394	475.30	1750.81 at 1	4000 (95%)	[68]
20.	WSe_2	Hydrothermal	Microrods	0.5 M KOH	–	–	10.41 at 10 mV s^{-1}	–	[69]
21.	Te-carbon cloth	Electrosynthesis	Nanorods	–	73.62	15,000	235.6 at 2.5 mA cm^{-2}	10,000 (89%)	[70]
22.	Te nanowires	Electrodeposition	Nanowires	0.5 Na_2SO_4	–	–	24 at 25 mV s^{-1}	1000	[71]
23.	CoTe	Hydrothermal	Nanowires	3 M KOH	32.9	800.27	643.6 at 1	5000 (76.9%)	[72]
24.	La_2Te_3	CBD	Cinnamon-like	1 M KOH	~126	2.5 k	469 at 2 mV s^{-1}	1000 (74%)	[73]
25.	$Ni_{0.33}Co_{0.67}Te$	Solvothermal	Nanotubes	6 M KOH	54	918	131.2 mAh g^{-1} at 1	5000 (90%)	[74]
26.	Sm_2Te_3	One-step chemical route	Barley-like	1 M $LiClO_4$-propylene carbonate	25.60	14.18 k	207 at 5 mV s^{-1}	1000 (78%)	[75]

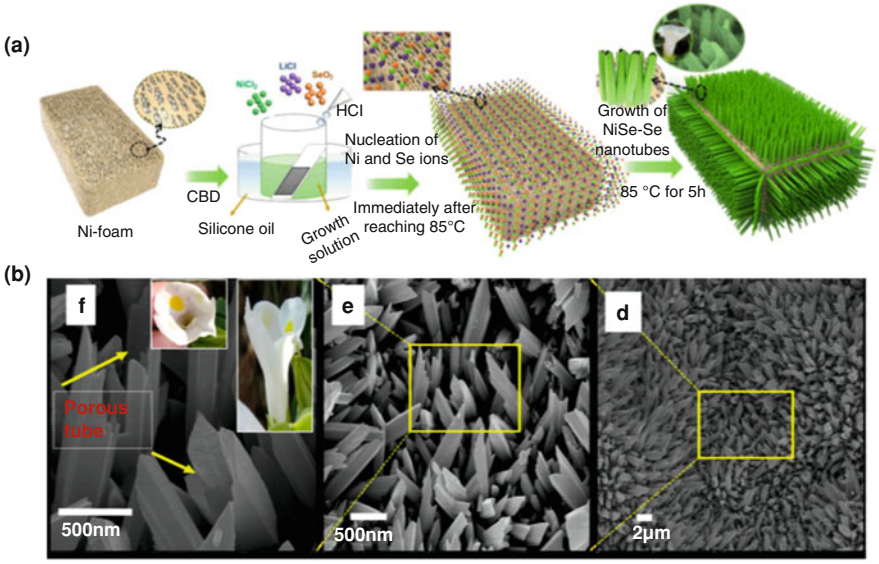

Fig. 5 (**a**) Schematic representation of the preparation of nanotubes of NiSe-Se by a chemical bath deposition method. (**b**) SEM images of NiSe-Se nanotubes at different magnifications [63]. (Reproduced with permission from American Chemical Society, Copyright © 2020)

The electrochemical performance of NiSe-Se was investigated in 1 M KOH electrolyte using a half-cell system, where Ag/AgCl, Pt, and NiSe-Se is used as a reference electrode, counter electrode, and working electrode, respectively. The electrochemical performance of NiSe-Se electrode with cyclic stability is presented in Fig. 6a–e. The NiSe-Se exhibits a maximum specific capacitance of 2447.46 F g^{-1} at a current density of 1 A g^{-1} (Fig. 6 (d)) with 95.09% capacitive retention after 10,000 GCD cycles (Fig. 6e). Also, the hybrid supercapacitor device was also fabricated, which achieves a maximum 29.90 Wh kg^{-1} energy density at 594.46 W kg^{-1} power density. Furthermore, chemically deposited nanotubes of NiSe-Se over Ni-foam enhance the electrode's total electroactive area, which increases electroactive sites for electrolytic ions adsorption and diffusion; also the space between the sheets acts as ion pools; therefore, it shows good electrochemical performance.

Yanhong et al. [52] synthesized Ni-Co sulfide by hydrothermal method and obtained nanowire-like morphology for Ni-Co sulfide after 12 h reaction at 90°C temperature. In the synthesis process, the same molar ratio of nickel and cobalt was used, and Ni-foam was used as a conducting substrate for binder-free synthesis. The nanowires of Ni-Co sulfide obtained a higher capacitance of 2415 F g^{-1} at the current density of 2.5 mA cm^{-2} with good (78.5%) capacitive retention for 3000 cycles. The practical applicability of Ni-Co sulfide was tested by fabricating an asymmetric supercapacitor device, which delivers 25 Wh kg^{-1} energy density at a high power density (3.57 kW kg^{-1}).

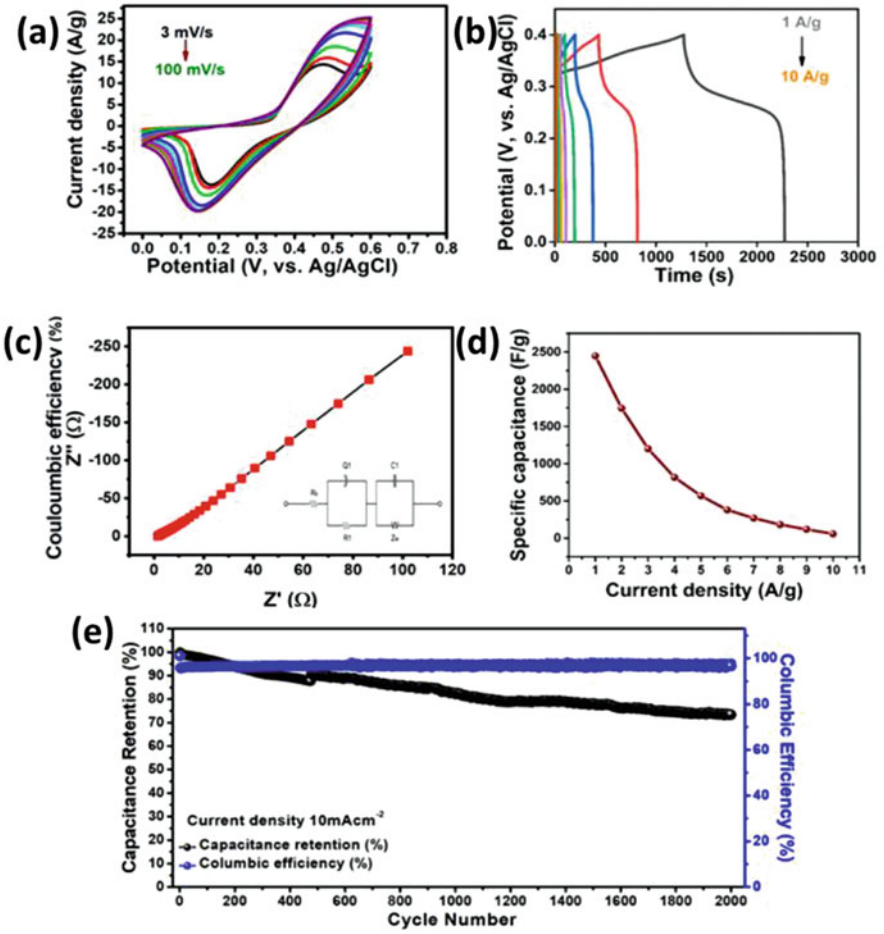

Fig. 6 (**a**) The CV curves, (**b**) galvanostatic charge-discharge curves, and (**c**) EIS study of NiSe-Se nanotubes; (**d**) plot of specific capacitance at various current densities; and (**e**) cyclic stability of NiSe-Se electrode at 10 mA cm^{-2} current density [63]. (Reproduced with permission from the American Chemical Society, Copyright © 2020)

Narthana et al. [51] prepared binary and ternary compounds of sulfides, and the effect of composition variation on morphology and electrochemical performances have been studied. The binary and ternary sulfides (NiS, Cu_9S_5, and $Ni_{0.8}Cu_{0.2}S$) were prepared hydrothermally with nanorod-like morphology. The pseudocapacitive nature of ternary and binary sulfides was observed in electrochemical study. The ternary compound exhibited higher specific capacitance higher than binary compounds. The nanorods of $Ni_{0.8}Cu_{0.2}S$ achieved maximum capacitance of 1092 F g^{-1} at 15 mA g^{-1}, higher than Cu_9S_5 (70 F g^{-1}) and NiS (575 F g^{-1}) binary

compounds. Also, $Ni_{0.8}Cu_{0.2}S$ showed lower charge transfer resistance (R_{ct}) as compared to Cu_9S_5 and NiS and 80% capacitive retention after 3000 CGD cycles.

Cobalt selenide and selenium-enriched cobalt selenide (CoSe-Se) were prepared by Subhadarshini et al. [68] using the CBD method. In this work, only nickel precursor was replaced by the cobalt precursor, i.e., $CoCl_2.6H_2O$, and followed the same synthesis process of NiSe-Se for the preparation of CoSe-Se. The reaction time and temperature were varied in the synthesis process to study the impact of preparative parameters on morphologies and corresponding performance. The maximum specific capacitance obtained for CoSe-Se was 1750.81 F g^{-1} at 1 A g^{-1} current density.

The selenium-rich nanotube-like architecture of NiSe synthesized by the CBD method offers a higher electrochemical response than the other single and composite chalcogenides. In addition, the high specific surface area, mechanical strength, and efficient pathway for both electrons and ions offered by 1D nanostructures are advantageous for flexible devices. The overall study demonstrates that the self-standing 1D material exhibits superior electrochemical capacity and is a promising aspirant for high-performance supercapacitor applications.

3.5 2D Structured Metal Chalcogenides

The 2D structured materials owned much interest due to their exceptional mechanical properties, like strength and Young's modulus, with lower weight and ultrathin structure as compared to their bulk counterpart. Other characteristics such as flexibility, chemical stability, transparency, etc. enhance their usage in various applications [76]. The unique physiochemical properties for ultrathin layered 2D materials were obtained at single or few atomic thicknesses. The essential advantages offered by 2D materials for the future generation of energy storage are as follows: (i) their thin nanosheet-like structure offers a high active surface area for the reaction because of the whole contact of surface atoms, (ii) their edges are more reactive in chemical reaction than the basal planes, and the gaps between the sheets (open van der Waals gap) provide more intercalation of electrolytic ions, and (iii) high flexibility and mechanical strength due to single atomic thickness boost their application in wearable electronics [77]. The literature survey on the 2D structured chalcogenide materials, mostly sheetlike morphology obtained using different methods, morphologies, and respective electrochemical performances, is tabulated in Table 2 [78–100].

Iqbal et al. [78] prepared graphene oxide (GO) based on Al_2S_3 by hydrothermal method on Ni-foam substrate. The GO-based Al_2S_3 obtained nanowall-like morphology after 4 h reaction at 120° C temperature. The higher specific capacitance was achieved for GO-based Al_2S_3 nanowalls of 2362.15 F g^{-1} at scan rate of 2 mV s^{-1} than the pristine Al_2S_3 (1097.88 F g^{-1}). The GO-based Al_2S_3 nanowalls exhibit higher specific capacitance of 2373.51 F g^{-1} at 3 mA cm^{-2} current density than the pristine Al_2S_3 (1108.25 F g^{-1}).

Table 2 Literature study of 2D structured chalcogenide materials

Sr. no.	Material	Method	Morphology	Electrolyte	Energy density Wh kg^{-1}	Power density W kg^{-1}	Specific capacitance (F g^{-1}) at current density (A g^{-1})	Cycles/capacitive retention	
1.	Al_2S_3	Hydrothermal	Nanowalls	2 M KOH	74.73	2663.58	2373.51 at 3 mA cm^{-2}	1300 (45%)	[78]
2.	Ag@MoS_2/WO_3	Hydrothermal	Nanosheet	2 M KOH	19.63	1859	95.61 mAh g^{-1} at 1	4000 (90%)	[79]
3.	CuS/acetylene black	Solvothermal	Nanosheet	6 M KOH	–	–	2981 at 1	600 (92%)	[80]
4.	Graphene-C_3N_4/CoS	Solvothermal	Nanosheet	3 M KOH	18.5	99.8	668 at 2	5000	[81]
5.	MoS_2/GO	Electrophoretic deposition	Nanosheet	1 M Na_2SO_4	23	17 k	613 at 25 mV s^{-1}	–	[82]
6.	Ni-Co sulfide	Micelle-confined growth and sulfuration	Nanosheet	6 M KOH	41.4	414	1304 at 2	6000 (936.5%)	[83]
7.	Carbon sponge-$NiCo_2S_4$	Hydrothermal	Nanosheet	3 M KOH	–	–	1093 at 0.5	8000 (83%)	[84]
8.	NiCoS	Solvothermal	Nanosheet	2 M KOH	40	379	1653 at 1	3000 (84%)	[85]
9.	Ni-Co-S	Electrodeposition	Nanosheet	1 M KOH	60	1.8 k	1418 at 5	–	[86]
10.	CC/H-Ni@Al-Co-S	Template-assisted	Nanosheet	2 M KOH	65.7	765.3	2434 at 1	10,000 (94.8%)	[87]
11.	Ni@Ni-CoS	Electrodeposition	Nanosheet	6 M KOH	18.4 mWh cm^{-3}	254.5 mW cm^{-3}	392.8 C cm^{-3} at 0.5 A cm^{-3}	10,000 (90.5%)	[88]
12.	Ni-Co-Mn-S	Electrodeposition	Nanosheet	2 M KOH	94.07	5.24 k	2717 at 1	1000 (80%)	[89]

13.	$Bi_{18}SeO_{29}$/BiSe	Hydrothermal	Lamella-like	2 M KOH	24.2	871.2	471.3 at 0.5	5000 (93%)	[90]
	$Co_{0.85}Se$		Flower-like nanosheet		–	–	255 at 0.5	–	
14.	$CoSe_2$	Hydrothermal	Nanosheet	2 M KOH	–	–	951 at 10 mV s^{-1}	2500 (42%)	[91]
	$CoTe_2$						360 at 5 mV s^{-1}	2500 (52%)	
15.	$NiSe_2$	Plasma-assisted dry exfoliation	Nanosheet	1 M KOH	–	–	383 at 5 mV s^{-1}	1000 (76.2%)	[92]
16.	$NiSe_2$	Hydrothermal	Hexapod-like	1 M KOH	–	–	75 at 2 mV s^{-1}	5000 (94%)	[93]
17.	$NiSe_2$@CNT	Microwave process	Lamellar	6 M KOH	25.61	810	980.5 at 1	9000 (82%)	[94]
18.	N and Se Co-doped graphene aerogel	Hydrothermal	Nanosheet	1 M Na_2SO_4	26.3	900	302.9 at 1	12,000 (94.1%)	[95]
19.	NiSe/NiO	Hydrothermal	Nanosheet	1 M KOH	–	–	83.5 at 2 mV s^{-1}	5000 (94%)	[96]
20.	WO_3/Se	Hydrothermal	Nanorectangular 2D particles	0.1 M H_2SO_4	47 mWh kg^{-1}	345 mW kg^{-1}	564 at 6	2000 (98%)	[97]
21.	GaTe	Probe sonication	Nanosheet	3 M KCl	–	–	23 at 0.5	10,000 (96%)	[98]
22.	CoTe	Hydrothermal	Nanosheet	3 M KOH	67	~793.5	622.8 at 1	1000 (88.9%)	[99]
23.	$TaTe_2$	Microwave-assisted	Nanosheet	0.5 M KOH	–	–	4.09 at 5 mV s^{-1}	400	[100]

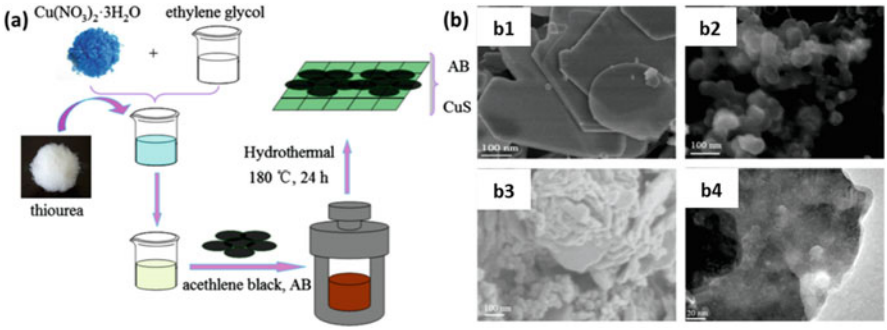

Fig. 7 (**a**) Schematic representation of preparation of nanotubes of CuS/AB by hydrothermal method and (**b**) (b1 and b3) SEM and (b2 and b4) TEM images of CuS/AB nanosheets [80]. (Reproduced with permission from Elsevier, Copyright © 2015)

Haung et al. [80] solvothermally prepared acetylene black (AB)-incorporated nanosheets of copper sulfide, using ethylene glycol, copper nitrate trihydrate, and thiourea solution, heated at 150°C for 24 h in stainless steel autoclave. The schematic presentation of the synthesis process for CuS/AB nanosheets is shown in Fig. 7a. The SEM and TEM images are given in Fig. 7b. The stacked plate-like morphology was obtained for CuS material in SEM and TEM analysis. The sheets have irregular thicknesses with an irregular diameter of less than 20 nm. The electrochemical study of AB, CuS, and CuS/AB was compared in this study and given in Fig. 8a–e. The comparative CV and GCD plots of AB, CuS, and CuS/AB electrodes are presented in Fig. 8a–c, respectively.

The CuS/AB electrode exhibited high electrochemical response than the other, so the CV (at different scan rates) and GCD (at different current densities) studies of CuS/AB electrodes were tested and displayed in Fig. 8b–d, respectively.

The highest specific capacitance obtained by CuS/AB electrode of 2981 F g^{-1} at 1 A g^{-1} current density in aqueous (6 M KOH) electrolyte is higher than copper sulfide/acetylene black flower-like morphology [80]. Also, the CuS/AB electrode displays good cyclic stability (92%). Sahoo et al. [89] synthesized nanosheets of quaternary material of nickel-cobalt-manganese sulfide by electrodeposition method on Ni-foam. The nanosheet-like architecture of Ni-Co-Mn-S confirms from transmission electron microscopy (TEM), and the average size was found to be 10–12 nm. The electrochemical study studied an aqueous (2 M KOH) electrolyte that shows a specific capacitance of 2717 F g^{-1} at 1 A g^{-1} current density with 80% capacitive retention.

The electrodeposited nanosheets of Ni-Co-Mn-S deliver the highest capacitive performance than the other composites. The 2D structured materials only offer a contact of surface area than the bulk material that improves the usage of the active material in the electrochemical performance of supercapacitors. The overall investigation suggested that the 2D architecture of material offers high electrochemical

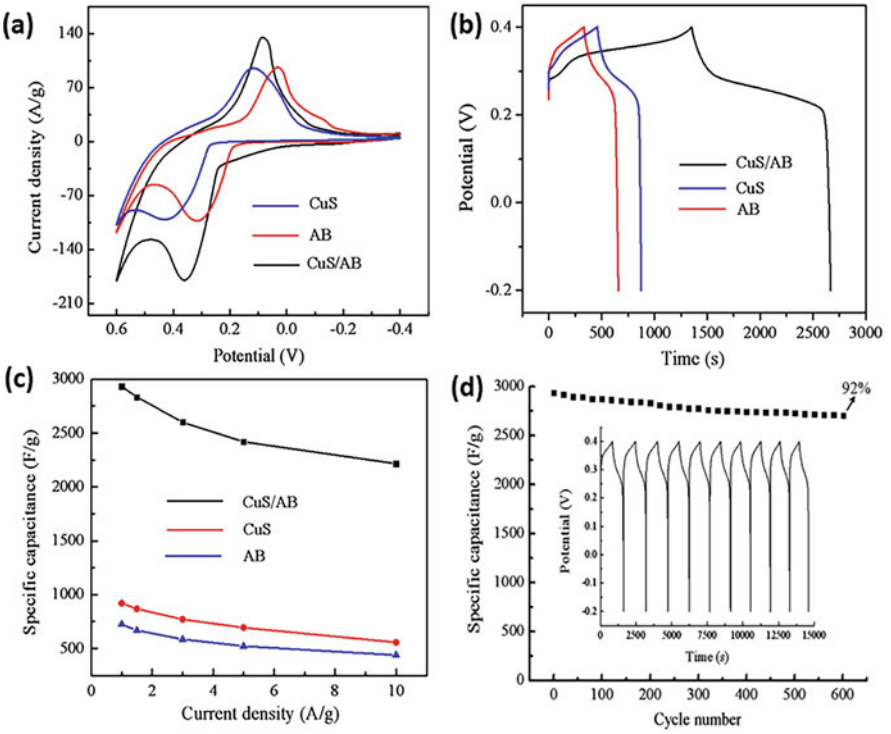

Fig. 8 (**a**) CV curves of CuS, AB, and CuS/AB; (**b**) GCD curves of CuS, AB, and CuS/AB; (**c**) specific capacitance with current density of CuS, AB, and CuS/AB, and (**d**) cyclic stability of CuS/AB [80]. (Reproduced with permission from Elsevier, Copyright © 2015)

performance due to high active electrochemical area; also, it allowed flexibility and lightweight.

4 3D Structured Metal Chalcogenides

The 3D structure of active material provides 3D interconnected porosity, proper interlayer spacing, and maximum surface area. The porous 3D structure with pores is favorable for quick diffusion and easy access to electrolytic ions. In a 3D structure, an open network offers maximum theoretical surface area, leading to improved capacitive performance [101–103]. Generally, 3D structured electrodes are prepared using templates of metal foam or the active material combined with 3D nanostructures. The recent study on 3D structured chalcogenides is tabulated in Table 3 with respective synthesis methods, morphology, and supercapacitive performance [104–126].

Table 3 Literature study of 3D structured chalcogenide materials

Sr. no.	Material	Method	Morphology	Electrolyte	Energy density Wh kg^{-1}	Power density W kg^{-1}	Specific capacitance (F g^{-1}) at current density (A g^{-1})	Cycles/capacitive retention	Ref.
1.	$CoS_{1.097}$	Solvothermal	Flower-like	2 M KOH	–	–	555 at 5 mA cm^{-2}	2500 (97.4%)	[104]
2.	CoS	Electrodeposition	Nanosheet-arrays	1 M KOH	0.174 Wh m^{-2}	212.745 W m^{-2}	410 mF cm^{-2} at 1 mA cm^{-2}	10,000 (86.8%)	[105]
3.	CoS	A rapid and ambient chemical route	3D-hexagonal	2 M KOH	301.4	1400	1173 at 1 mV s^{-1}	1500 (99%)	[106]
4.	CoS/G	Chemical bath	Nanoparticles/ nanosheets	6 M KOH	–	–	2423.3 at 5 mV s^{-1}	–	[107]
5.	Ni_9S_8	CBD	Nanoparticles	1 M KOH	51.11	2.66 k	2055 at 2	–	[108]
6.	$Ni_{0.75}Co_{0.25}S_2$	Hydrothermal	Nanoparticles	2 M KOH	54.9	1515.4	2141.9 at 2	3000 (75.3%)	[109]
7.	$Ni_xCo_{1-x}S_{1.097}$-rGO	Hydrothermal	Microspheres	2 M KOH	–	–	1152 at 0.5	–	[110]
8.	Mn-co-S	Hydrothermal	Pinecone-like	3 M NaOH	–	–	992 at 1	5500 (102.35%)	[111]
9.	MoS_2/NG	Hydrothermal	Flower-like	1 M KOH	–	–	245 at 0.25	1000 (91.3%)	[112]
10.	RuS_2	Sonochemical	Nanoparticles	0.5 M H_2SO_4	–	–	85 at 0.5 mA cm^{-2}	5000 (96.15%)	[113]
11.	SnS_2-Ni_3S_2	Hydrothermal	Flake-like	2 M KOH	–	–	272 mAh g^{-1} at 4 mA cm^{-2}	3000 (91%)	[114]
12.	ZnS/G	Solvothermal	Nanoparticles	6 M KOH	–	–	197.1 at 5 mV s^{-1}	2000 (89.2%)	[115]

13.	Se-(CoFe)S_2	Sulfurization-selenization	Nanoboxes	2 M KOH	–	–	1329 at 0.5	5000 (82%)	[116]
14.	Ni_3Se_2	Electrochemical deposition	Cauliflower-like	1 M KOH	32.8	677.03	119.6 mAh g^{-1} at 2	5000	[117]
15.	NiSe	Solvothermal	Microspheres	2 M KOH	–	–	492 at 0.5	200 (84.6%)	[118]
16.	$NiSe_2$	Hydrothermal	Truncated cube-like	4 M KOH	44.8	969.7	1044 at 3	2000 (67%)	[119]
17.	$NiSe_2$@Fe_3Se_4	CBD	Layered-like $NiSe_2$, flake-like Fe_3Se_4	6 M KOH	52	398	6.05 C cm^{-2} at 6 mA cm^{-2}	10,000 (92%)	[120]
18.	$Ni_{0.34}Co_{0.66}Se_2$	Hydrothermal	Nanorod-arrays	1 M KOH	0.47 mWh cm^{-3}	37.5 mW cm^{-3}	2.61 F cm^{-2} at 4 mA cm^{-2}	6000 (92.6%)	[121]
19.	NiCoSe	Hydrothermal	Spear-shaped	3 M KOH	61.24	800	211 mAh g^{-1} at 1	5000 (90.31%)	[122]
20.	Cu_3Se_2	CBD	Hexagons	1 M KOH	62	989	1285 at 0.5	3000 (92%)	[123]
21.	G-$MnSe_2$	Hydrothermal	Cubes	0.5 M H_2SO_4	1.84 mWh cm^{-2}	19.9 mW cm^{-2}	93.3 mF cm^{-2} at 1 mV s^{-1}	–	[124]
22.	NiTe@$NiCoSe_2$	Hydrothermal	Nanorods and nanoparticles	3 M KOH	59.8	800	560.6 mAh g^{-1} at 0.5	5000 (98.6%)	[125]
23.	Te/NMC	Intercalation	3D bi-continuous structure	6 M KOH	–	–	197 at 0.5	1000 (95%)	[126]
24.	NiTe:Co	Hydrothermal	Flake-shaped	3 M KOH	36.8	–	1645.6 at 1	1000 (85%)	[127]

The 3D metal chalcogenide materials were prepared by different chemical methods such as CBD, hydrothermal, solvothermal, electrodeposition, etc., which have obtained different morphologies and supercapacitive performance. In 3D metal chalcogenide, the literature study shows better performance by changing the method of preparation of materials. Some material shows excellent specific performance, good cyclic stability, and better energy density and power density.

Gao et al. [110] prepared 3D microspheres of $Ni_xCo_{1-x}S_{1.097}$-rGO by hydrothermal method. The supercapacitive performance of $Ni_xCo_{1-x}S_{1.097}$-rGO was measured in an aqueous (2 M KOH) electrolyte and achieved a specific capacitance of 1152 F g^{-1} at a current density of 0.5 A g^{-1}. Xie et al. [109] used the solvothermal-hydrothermal method for the synthesis of $Ni_{1-x}Co_xS_2$, cobalt successfully doped in NiS_2 at 200°C temperature after 14 h chemical reaction. The hollow spheres observed for pristine NiS_2 material (Fig. 9a) and cobalt doping in NiS_2 change the morphology. The hollow spheres break gradually after cobalt is doped into the NiS_2 and the seldom intact hollow spheres are observed for $Ni_{0.75}Co_{0.25}S_2$ (Fig. 9b), and the nanoparticle-like nature is observed for CoS_2 material (Fig. 9c). Similar results were observed from TEM analysis, after doping of cobalt in NiS_2 hollow spheres converted into nanoparticles. The electrochemical characterization of $Ni_{1-x}Co_xS_2$ electrodes was carried out in an aqueous (2 M KOH) electrolyte. The CV curves of $Ni_{1-x}Co_xS_2$ electrodes at 10 mV s^{-1} scan rate are presented in Fig. 9d. The highest current response was obtained for $Ni_{0.75}Co_{0.25}S_2$ electrode than the other electrodes. The CV curves of $Ni_{0.75}Co_{0.25}S_2$ at different scan rates are recorded and presented in Fig. 9e. The GCD analysis of $Ni_{0.75}Co_{0.25}S_2$ electrode was carried out within 0–0.4 V vs SCE potential window at various current densities and given in Fig. 9f, representing higher kinetics and ideal battery-like behavior. The GCD analysis used for the specific capacitance calculation and calculated capacitance of $Ni_{1-x}Co_xS_2$ electrodes are presented in Fig. 9g. The $Ni_{0.75}Co_{0.25}S_2$ electrode exhibited a maximum capacitance of 2141.9 F g^{-1} at 2 A g^{-1} current density which is higher than the pristine NiS_2 electrode (1542.6 F g^{-1}).

The surface of $Ni_{0.75}Co_{0.25}S_2$ is rough, allowing the maximum contact among electrolytic ions and electrode material at the time of the charging and discharging process, which is responsible for high electrochemical performance. The asymmetric supercapacitor device fabricated using activated carbon (negative electrode) and $Ni_{0.75}Co_{0.25}S_2$ (positive electrode) delivers 54.9 Wh kg^{-1} energy density at 1515.4 W kg^{-1} power density with 81% capacitive retention after 4000 cycles. Shaikh et al. [106] synthesized CoS at ambient conditions via a rapid chemical route method. The 3D hexagonal CoS obtained capacitance of 1173 F g^{-1} at 1 mV s^{-1} with 99% capacitive retention after 1500 cycles. The CoS and CoS-G showed maximum specific capacitance of 2100.0 F g^{-1} and 2423.3 F g^{-1}, respectively, at the scan rate of 5 mV s^{-1}.

The composite of nanoparticles of CoS with graphene sheets exhibits highest specific capacitance 2423.3 F g^{-1} at 5 mV s^{-1} scan rate [107]. In addition, the 3D architecture of composite material exhibits higher supercapacitive performance than

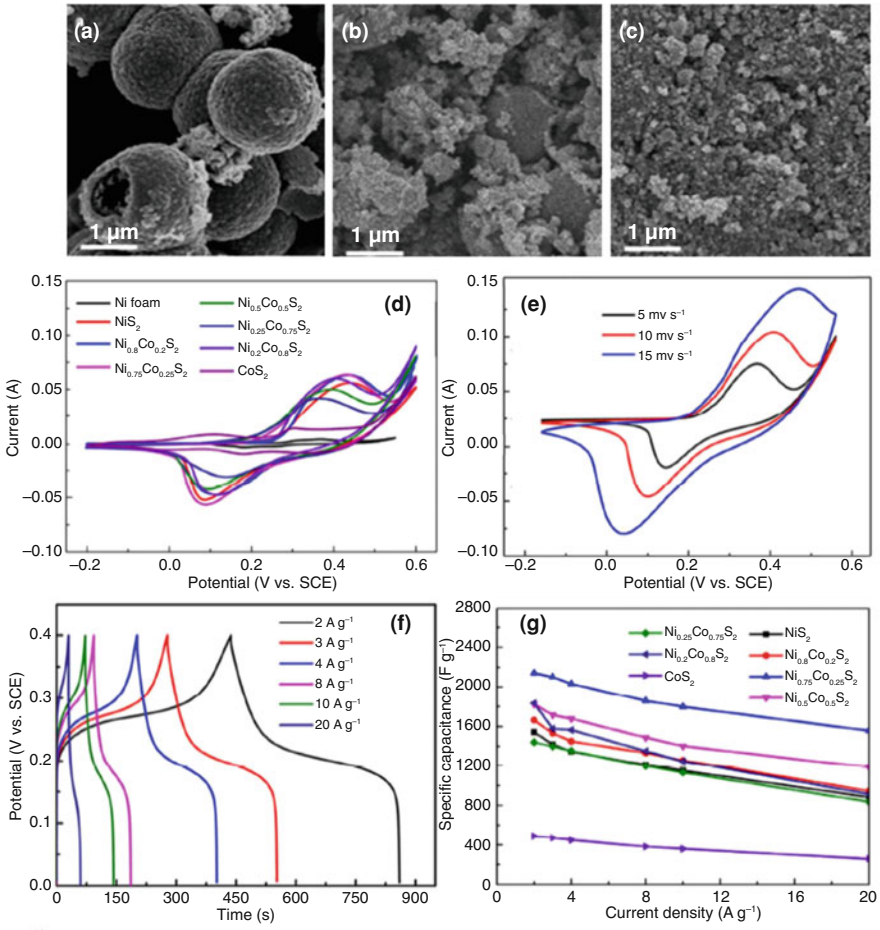

Fig. 9 SEM images of (**a**) NiS_2, (**b**) $Ni_{0.75}Co_{0.25}S_2$, and (**c**) CoS_2. (**d**) CV curves of $Ni_{1-x}Co_xS_2$ at 10 mV s^{-1} scan rate. (**e**) CV and (**f**) GCD curves of $Ni_{0.75}Co_{0.25}S_2$ at different scan rates and current densities. (**g**) Specific capacitance at various current densities of $Ni_{1-x}Co_xS_2$ electrodes [110]. (Reproduced with permission from Royal Society of Chemistry, Copyright © 2014)

the pristine due to higher specific surface area for electrochemical reaction and easy paths for ion transportation with high mechanical stability.

5 Conclusions and Future Perspectives

This chapter briefly summarized the preparation of 1D, 2D, and 3D structured metal chalcogenide materials and their performance in supercapacitor application.

The precise attention was rewarded, illustrating the properties of chalcogenides materials. The present study is concentrated on the progress of metal chalcogenide materials using different synthesis methods that allow variety in the dimensions of morphologies. In 1D structured metal chalcogenide materials, the different kinds of morphologies were obtained such as nanowires, nanorods, nanotubes, etc. by different methods like hydrothermal, electrodeposition, CBD, reflux, etc. The structure or morphology of the materials was changed with a change in preparation methods, preparative parameters, etc. In 2D metal structured chalcogenide materials, mostly nanosheets were obtained and reported. The 3D structured metal chalcogenide materials contained morphologies like nanoboxes, nanotubes, nanoparticles, microspheres, flower-like etc. It is found that different structures of chalcogenide materials exhibit distinct electrochemical properties in supercapacitor application. A possible future trend is to fabricate composite material, which is the combination of various dimensionalities or core-shell structures (1D over 2D or 3D structures) that may offer high surface area, efficient charge transport, specific capacitance, and cyclic stability. These composite or core-shell structured materials can be a combination of EDLC (high cyclic stability) and pseudocapacitive properties (high specific capacitance) to achieve further high supercapacitive performance.

Acknowledgments The authors are thankful to the Department of Science and Technology, India-Innovation in Science Pursuit for Inspired (DST-INSPIRE), for financial support through research project sanction no. DST/INSPIRE/04/2016/000260. Also, the authors are thankful to the Science and Engineering Research Board (DST-SERB), New Delhi, India, for financial support through research project sanction no. CRG/2019/005730.

References

1. P. Liu, J. Zhao, Z. Dong, Z. Liu, Y. Wang, Interwoving polyaniline and a metal-organic framework grown in situ for enhanced supercapacitor behavior. J. Alloys Compd. **854**, 157181 (2021). https://doi.org/10.1016/j.jallcom.2020.157181
2. D. Prakash, S. Manivannan, Unusual battery type pseudocapacitive behaviour of graphene oxynitride electrode: High energy solid-state asymmetric supercapacitor. J. Alloys Compd. **854**, 156853 (2021). https://doi.org/10.1016/j.jallcom.2020.156853
3. M. Sethi, U. Shenoy, D. Bhat, Simple solvothermal synthesis of porous graphene-NiO nanocomposites with high cyclic stability for supercapacitor application. J. Alloys Compd. **854**, 157190 (2021). https://doi.org/10.1016/j.jallcom.2020.157190
4. Z. Sun, F. Li, Z. Ma, Q. Wang, F. Qu, Battery-type phosphorus doped FeS_2 grown on graphene as anode for hybrid supercapacitor with enhanced specific capacity. J. Alloys Compd. **854**, 157114 (2021). https://doi.org/10.1016/j.jallcom.2020.157114
5. Y. Wang, M. Qiao, M. Mamat, Nitrogen-doped macro-meso-micro hierarchical ordered porous carbon derived from ZIF-8 for boosting supercapacitor performance. Appl. Surf. Sci. **540**, 148352 (2021). https://doi.org/10.1016/j.apsusc.2020.148352
6. G. Zan, T. Wu, H. Chen, F. Dong, Q. Wu, $BiVO_4$ nanocoral superstructures and their excellent electrical/optical dual-functions. J. Alloys Compd. **852**, 157035 (2021). https://doi.org/10.1016/j.jallcom.2020.157035
7. D. Dubal, O. Ayyad, V. Ruiz, P. Gomez-Romero, Hybrid energy storage: The merging of battery and supercapacitor chemistries. Chem. Soc. Rev. **44**, 1777–1790 (2015). https://doi.org/10.1039/C4CS00266K

8. M. Wu, J. Gao, S. Zhang, A. Chen, Synthesis and characterization of aerogel-like mesoporous nickel oxide for electrochemical supercapacitors. J. Porous. Mater. **13**, 407–412 (2006). https://doi.org/10.1007/s10934-006-8038-x
9. H. Hwang, D. Shin, T. Kim, S. Park, T. Yeo, W. Choi, Tunable fabrication of coreshell Ni-MnO_2 hybrid foams through structure-guided combustion waves for binderfree high-performance supercapacitor electrodes. J. Mater. Chem. A **6**, 22998–23009 (2018). https://doi.org/10.1039/C8TA08110G
10. M. Winter, R. Brodd, What are batteries, fuel cells, and supercapacitors? Chem. Rev. **104**, 4245–4270 (2004). https://doi.org/10.1021/cr020730k
11. J. Chmiola, G. Yushin, Y. Gogotsi, C. Portet, P. Simon, P. Taberna, Anomalous increase in carbon at pore sizes less than 1 nanometer. Science **313**, 1760–1763 (2006). https://doi.org/10.1126/science.1132195
12. K. Ghosh, S. Srivastava, Superior supercapacitor performance of Bi_2S_3 nanorod/reduced graphene oxide composites. Dalton Trans. **49**, 16993–17004 (2020). https://doi.org/10.1039/D0DT03594G
13. Q. Zhang, E. Uchaker, S. Candelaria, G. Cao, Nanomaterials for energy conversion and storage. Chem. Soc. Rev. **42**, 3127–3171 (2013). https://doi.org/10.1039/C3CS00009E
14. Y. Zhang, Q. Zhou, J. Zhu, Q. Yan, S. Dou, W. Sun, Nanostructured metal chalcogenides for energy storage and electrocatalysis. Adv. Funct. Mater. **27**, 1702317 (2017). https://doi.org/10.1002/adfm.201702317
15. Low Voltage Electrolytic Capacitors: H. I. Becker, U.S. Patent 2800616 1957
16. S. Hadz¯i-Jordanov, H. Angerstein-Kozlowska, M. Vukovič, B. Conway, Reversibility and growth behavior of surface oxide films at ruthenium electrodes. J. Electrochem. Soc. **125**, 1471 (1978). https://doi.org/10.1149/1.2131698
17. Z. Wen, W. She, Y. Li, R. Che, Paramecium-like α-MnO_2 hierarchical hollow structures with enhanced electrochemical capacitance prepared by a facile dopamine carbon-source assisted shell-swelling etching method. J. Mater. Chem. A **2**, 20729–20738 (2014). https://doi.org/10.1039/C4TA04312J
18. L. Xing, K. Huang, L. Fang, Preparation of layered graphene and tungsten oxide hybrids for enhanced performance supercapacitors. Dalton Trans. **45**, 17439–17446 (2016). https://doi.org/10.1039/C6DT03719D
19. J. Xu, T. Xiao, X. Tan, P. Xiang, L. Jiang, D. Wu, J. Li, S. Wang, A new asymmetric aqueous supercapacitor: Co_3O_4//Co_3O_4@polypyrrole. J. Alloys Compd. **706**, 351–357 (2017). https://doi.org/10.1016/j.jallcom.2017.02.253
20. W. Li, K. Xu, G. Song, X. Zhou, R. Zou, J. Yang, Z. Chen, J. Hu, Facile synthesis of porous $MnCo_2O_{4.5}$ hierarchical architectures for high-rate supercapacitors. Cryst. Eng. Comm. **16**, 2335–2339 (2014). https://doi.org/10.1039/C3CE42581A
21. X. Du, L. Wang, W. Zhao, Y. Wang, T. Qi, C. Li, Preparation of hierarchical porous carbon from waste printed circuit boards for high performance electric double-layer capacitors. J. Power Sources **223**, 166–173 (2016). https://doi.org/10.1016/j.jpowsour.2016.05.054
22. M. Tokita, N. Yoshimoto, K. Fujii, M. Morita, Degradation characteristics of electric double-layer capacitors consisting of high surface area carbon electrodes with organic electrolyte solutions. Electrochim. Acta **209**, 210–218 (2016). https://doi.org/10.1016/j.electacta.2016.05.041
23. X. Zhang, W. Wang, J. Lu, L. Hu, J. Heng, Reversible heat of electric double-layer capacitors during galvanostatic charging and discharging cycles. Thermochim. Acta **636**, 1–10 (2016). https://doi.org/10.1016/j.tca.2016.04.014
24. J. Long, D. Bélanger, T. Brousse, W. Sugimoto, M. Sassin, O. Crosnie, Asymmetric electrochemical capacitors-stretching the limits of aqueous electrolytes. MRS Bull. **36**, 513–522 (2011). https://doi.org/10.1557/mrs.2011.137
25. F. Shi, L. Li, X. Wang, C. Gu, J. Tu, Metal oxide/hydroxide-based materials for supercapacitors. RSC Adv. **4**, 41910–41921 (2014). https://doi.org/10.1039/C4RA06136E
26. G. Wang, L. Zhang, J. Zhang, A review of electrode materials for electrochemical supercapacitors. Chem. Soc. Rev. **41**, 797–828 (2012). https://doi.org/10.1039/C1CS15060J

27. N. Chodankar, H. Pham, A. Nanjundan, J. Fernando, K. Jayaramulu, D. Golberg, Y. Han, D. Dubal, True meaning of pseudocapacitors and their performance metrics: Asymmetric versus hybrid supercapacitors. Small **16**, 2002806–2002841 (2020). https://doi.org/10.1002/smll.202002806
28. X. Zhao, L. Zhang, S. Murali, M. Stoller, Q. Zhang, Y. Zhu, R. Ruoff, Incorporation of manganese dioxide within Ultraporous activated graphene for high-performance electrochemical capacitors. ACS Nano **6**, 5404–5412 (2012). https://doi.org/10.1021/nn3012916
29. C. Hsieh, W. Lee, C. Lee, H. Teng, Electrochemical capacitors fabricated with tin oxide/graphene oxide nanocomposites. J. Phys. Chem. C **118**, 15146–15153 (2014). https://doi.org/10.1021/jp502958w
30. T. Chen, Y. Elabd, Hybrid-capacitors with polyaniline/carbon electrodes fabricated via simultaneous electrospinning/electrospraying. Electrochim. Acta **229**, 65–72 (2017). https://doi.org/10.1016/j.electacta.2017.01.140
31. T. Nguyen, M. Boudard, M. Carmezim, M. Montemor, $Ni_xCo_{1-x}(OH)_2$ nanosheets on carbon nanofoam paper as high areal capacity electrodes for hybrid supercapacitor. Energy J. **126**, 208–216 (2017). https://doi.org/10.1016/j.energy.2017.03.024
32. W. Shaheen, M. Warsi, M. Shahid, M. Khan, M. Asgharb, Z. Ali, M. Sarfraz, H. Anwar, M. Nadeem, I. Shakir, Carbon coated MoO_3 nanowires/graphene oxide ternary nanocomposite for high-performance supercapacitors. Electrochim. Acta **219**, 330–338 (2016). https://doi.org/10.1016/j.electacta.2016.09.069
33. M. Jackson, *Periodic table advanced* (Bar Charts Inc., 2002) ISBN 978-1-57222-542-8
34. X. Cui, Z. Shan, L. Cui, J. Tian, Enhanced electrochemical performance of sulfur/carbon nanocomposite material prepared via chemical deposition with a vacuum soaking step. Electrochim. Acta **105**, 23–30 (2013). https://doi.org/10.1016/j.electacta.2013.04.156
35. Y. Sun, X. Tian, B. He, C. Yang, Z. Pi, Y. Wang, S. Zhang, Studies of the reduction mechanism of selenium dioxide and its impact on the microstructure of manganese electrodeposit. Electrochim. Acta **56**, 8305–8310 (2011). https://doi.org/10.1016/j.electacta.2011.06.111
36. S. Park, J. Choi, Y. Lee, J. Park, H. Song, Formation of metal selenide and metal–selenium nanoparticles using distinct reactivity between selenium and Noble metals. Chem. Asian J. **10**, 1452–1456 (2015). https://doi.org/10.1002/asia.201500191
37. M. Manikandan, S. Dhanuskodi, N. Maheshwari, G. Muralidharan, C. Revathi, R. Kumar, G. Rao, High performance supercapacitor and non-enzymatic hydrogen peroxide sensor based on tellurium nanoparticles. Sens. Bio-Sens. Res. **13**, 40–48 (2017). https://doi.org/10.1016/j.sbsr.2017.02.001
38. D. Jamwal, S. Mehta, Metal telluride nanomaterials: Facile synthesis, properties and applications for third generation devices. ChemistrySelect **4**, 1943–1963 (2019). https://doi.org/10.1002/slct.201803680
39. D. Futaba, K. Hata, T. Yamada, T. Hiraoka, Y. Hayamizu, Y. Kakudate, O. Tanaike, H. Hatori, M. Yumura, S. Iijima, Shape-engineerable and highly densely packed single-walled carbon nanotubes and their application as super-capacitor electrodes. Nat. Mater. **5**, 987–994 (2006). https://doi.org/10.1038/nmat1782
40. J. Xu, K. Wang, S.Z. Zu, B.H. Han, Z. Wei, Hierarchical nanocomposites of polyaniline nanowire arrays on graphene oxide sheets with synergistic effect for energy storage. ACS Nano **4**, 5019–5026 (2010). https://doi.org/10.1021/nn1006539
41. J. Zhi, W. Zhao, X. Liu, A. Chen, Z. Liu, F. Huang, Highly conductive ordered mesoporous carbon based electrodes decorated by 3D graphene and 1D silver nanowire for flexible supercapacitor. Adv. Funct. Mater. **24**, 2013–2019 (2014). https://doi.org/10.1002/adfm.201303082
42. Z. Chen, V. Augustyn, J. Wen, Y. Zhang, M. Shen, B. Dunn, Y. Lu, High-performance supercapacitors based on intertwined CNT/V_2O_5 nanowire nanocomposites. Adv. Mater. **23**, 791–795 (2011). https://doi.org/10.1002/adma.201003658
43. J. Xu, Q. Wang, X. Wang, Q. Xiang, B. Liang, D. Chen, G. Shen, Flexible asymmetric Supercapacitors based upon Co_9S_8 nanorod//Co_3O_4@RuO_2 nanosheet arrays on carbon cloth. ACS Nano **7**, 5453–5462 (2013). https://doi.org/10.1021/nn401450s

44. X. Lu, T. Liu, T. Zhai, G. Wang, M. Yu, S. Xie, Y. Ling, C. Liang, Y. Tong, Y. Li, Improving the cycling stability of metal–nitride supercapacitor electrodes with a thin carbon Shell. Adv. Energy Mater. **4**, 1300994 (2014). https://doi.org/10.1002/aenm.201300994
45. B. Wang, T. Zhu, H. Wu, R. Xu, J. Chen, X. Lou, Porous Co_3O_4 nanowires derived from long $Co(CO_3)_{0.5}(OH)\cdot 0.11H_2O$ nanowires with improved supercapacitive properties. Nanoscale **4**, 2145–2149 (2012). https://doi.org/10.1039/C2NR11897A
46. C. Chen, S. Wang, X. Luo, W. Gao, G. Huang, Y. Zeng, Z. Zhu, Reduced $ZnCo_2O_4$@$NiMoO_4\cdot H_2O$ heterostructure electrodes with modulating oxygen vacancies for enhanced aqueous asymmetric supercapacitors. J. Power Sources **409**, 112–122 (2019). https://doi.org/10.1016/j.jpowsour.2018.10.066
47. W. Chen, R. Rakhi, H. Alshareef, Facile synthesis of polyaniline nanotubes using reactive oxide templates for high energy density pseudocapacitors. J. Mater. Chem. A **1**, 3315–3324 (2013). https://doi.org/10.1039/C3TA00499F
48. J. Jiang, J. Liu, S. Peng, D. Qian, D. Luo, Q. Wang, Z. Tian, Y. Liu, Facile synthesis of α-MoO3 nanobelts and their pseudocapacitive behavior in an aqueous Li_2SO_4 solution. J. Mater. Chem. A **1**, 2588–2594 (2013). https://doi.org/10.1039/C2TA01120D
49. D. Guo, L. Lai, A. Cao, H. Liu, S. Dou, J. Ma, Nanoarrays: Design, preparation and supercapacitor applications. RSC Adv. **5**, 55856–55869 (2015). https://doi.org/10.1039/C5RA09453D
50. W. Wei, L. Mi, Y. Gao, Z. Zheng, W. Chen, X. Guan, Partial Ion-exchange of nickel-sulfide-derived electrodes for high performance supercapacitors. Chem. Mater. **26**, 3418–3426 (2014). https://doi.org/10.1021/cm5006482
51. K. Narthana, G. Durai, P. Kuppusami, J. Theerthagiri, S. Sujatha, S. Lee, M. Choi, One-step synthesis of hierarchical structured nickel copper sulfide nanorods with improved electrochemical supercapacitor properties. Int. J. Energy Res. **45**, 9983–9998 (2021). https://doi.org/10.1002/er.6492
52. Y. Li, L. Cao, L. Qiao, M. Zhou, Y. Yang, P. Xiao, Y. Zhang, Ni–Co sulfide nanowires on nickel foam with ultrahigh capacitance for asymmetric supercapacitors. J. Mater. Chem. A **2**, 6540–6548 (2014). https://doi.org/10.1039/c3ta15373h
53. H. Wan, J. Jiang, J. Yu, K. Xu, L. Miao, L. Zhang, H. Chen, Y. Ruan, $NiCo_2S_4$ porous nanotubes synthesis via sacrificial templates: High-performance electrode materials of supercapacitors. CrystEngComm **15**, 7649–7651 (2013). https://doi.org/10.1039/C3CE41243A
54. S. Bao, C. Li, C. Guo, Y. Qiao, Biomolecule-assisted synthesis of cobalt sulfide nanowires for application in supercapacitors. J. Power Sources **180**, 676–681 (2008). https://doi.org/10.1016/j.jpowsour.2008.01.085
55. H. Wan, X. Ji, J. Jiang, J. Yu, L. Miao, L. Zhang, S. Bie, H. Chen, Y. Ruan, Hydrothermal synthesis of cobalt sulfide nanotubes: The size control and its application in supercapacitors. J. Power Sources **243**, 396–402 (2013). https://doi.org/10.1016/j.jpowsour.2013.06.027
56. S. Guo, W. Chen, M. Li, J. Wang, F. Liu, J. Chen, Effect of reaction temperature on the amorphous-crystalline transition of copper cobalt sulfide for supercapacitors. Electrochim. Acta **271**, 498–506 (2018). https://doi.org/10.1016/j.electacta.2018.03.189
57. G. Nie, X. Lu, J. Lei, L. Yang, C. Wang, Facile and controlled synthesis of bismuth sulfide nanorods-reduced graphene oxide composites with enhanced supercapacitor performance. Electrochim. Acta **154**, 24–30 (2015). https://doi.org/10.1016/j.electacta.2014.12.090
58. M. Iqbal, M. Ashiq, A. Razaq, G. Murtza, B. Parven, M. Hassan, Excellent electrochemical performance of graphene oxide based strontium sulfide nanorods for supercapacitor applications. Electrochim. Acta **273**, 136–144 (2018). https://doi.org/10.1016/j.electacta.2018.04.014
59. C. Tang, Z. Pu, Q. Liu, A. Asiri, X. Sun, Y. Luo, Y. He, In situ growth of NiSe nanowire film on nickel foam as an electrode for high-performance supercapacitors. ChemElectroChem **2**, 1903–1907 (2015). https://doi.org/10.1002/celc.201500285
60. Y. Tian, Y. Ruan, J. Zhang, Z. Yang, J. Jiang, C. Wang, Controllable growth of NiSe nanorod arrays via one-pot hydrothermal method for high areal-capacitance supercapacitors. Electrochim. Acta **250**, 327–334 (2017). https://doi.org/10.1016/j.electacta.2017.08.084

61. K. Guo, S. Cui, H. Hou, W. Chen, L. Mi, Hierarchical ternary Ni-Co-Se nanowires for high-performance supercapacitor device design. Dalton Trans. **45**, 19458–19465 (2016). https://doi.org/10.1039/C6DT03863H
62. T. Hao, Y. Liu, G. Liu, C. Peng, B. Chen, Y. Feng, J. Ru, J. Yang, Insight into faradaic mechanism of polyaniline@$NiSe_2$ core-shell nanotubes in high performance supercapacitors. Energy Storage Mater. **23**, 225–232 (2019). https://doi.org/10.1016/j.ensm.2019.05.011
63. S. Subhadarshini, E. Pavitra, G. Raju, N. Chodankar, D. Goswami, Y. Han, Y. Huh, N. Das, One-dimensional NiSe-Se hollow nanotubular architecture as a binder-free cathode with enhanced redox reactions for high-performance hybrid supercapacitors. ACS Appl. Mater. Interfaces **12**, 29302–29315 (2020). https://doi.org/10.1021/acsami.0c05612
64. X. Song, C. Huang, Y. Qin, H. Li, H. Chen, Hierarchical hollow, sea-urchin-like and porous $Ni_{0.5}Co_{0.5}Se_2$ as advanced battery material for hybrid supercapacitors. J. Mater. Chem. A **6**, 16205–16212 (2018). https://doi.org/10.1039/C8TA05037F
65. X. Shi, H. Wang, S. Ji, V. Linkov, F. Liu, R. Wang, $CoNiSe_2$ nanorods directly grown on Ni foam as advanced cathodes for asymmetric supercapacitors. Chem. Eng. J. **364**, 320–327 (2019). https://doi.org/10.1016/j.cej.2019.01.156
66. S. Li, Y. Ruan, Q. Xie, Morphological modulation of $NiCo_2Se_4$ nanotubes through hydrothermal selenization for asymmetric supercapacitor. Electrochim. Acta **356**, 136837 (2020). https://doi.org/10.1016/j.electacta.2020.136837
67. Z. Ghouri, M. Motlak, S. Afaq, N. Barakat, A. Abdala, Template-free synthesis of Se-nanorods-rGO nanocomposite for application in supercapacitors. Nanotechnol. Rev. **8**, 661–670 (2019). https://doi.org/10.1515/ntrev-2019-0057
68. S. Subhadarshini, E. Pavitra, G. Raju, N. Chodankar, A. Mandal, S. Roy, S. Mandal, M. Rao, D. Goswami, Y. Huh, N. Das, One-pot facile synthesis and electrochemical evaluation of selenium enriched cobalt selenide nanotube for supercapacitor application. Ceram. Int. **47**, 15293–15306 (2021). https://doi.org/10.1016/j.ceramint.2021.02.093
69. D. Chakravarty, D. Late, Microwave and hydrothermal synthesis of WSe_2 micro/nanorods and its application in Supercapacitor. RSC Adv. **5**, 21700–21709 (2015). https://doi.org/10.1039/C4RA12599A
70. S. Manoharan, K. Krishnamoorthy, V. Mariappan, D. Kesavan, S. Kim, Electrochemical deposition of vertically aligned tellurium nanorods on flexible carbon cloth for wearable supercapacitors. Chem. Eng. J. **421**, 129548 (2021). https://doi.org/10.1016/j.cej.2021.129548
71. H. Tsai, A. Yaghoubi, T. Chan, C. Wang, W. Liu, C. Liao, S. Lu, L. Chen, Y. Chueh, Electrochemical synthesis of ultrafast and gram-scale surfactant-free tellurium nanowires by gas-solid transformation and its applications on supercapacitor electrode and P-doping of graphene transistor. Nanoscale **7**, 7535–7539 (2015). https://doi.org/10.1039/C5NR00876J
72. M. Xiao, Y. Su, M. Zhao, B. Du, Synthesis of CoTe nanowires: A new electrode material for supercapacitor with high-stability and high-performance. Nanotechnology **31**, 055706 (2019). https://doi.org/10.1088/1361-6528/ab4dbf
73. S. Patil, B. Patil, R. Bulakhe, C. Lokhande, Electrochemical performance of a portable asymmetric supercapacitor device based on cinnamon-like La_2Te_3 prepared by a chemical synthesis route. RSC Adv. **4**, 56332–56341 (2014). https://doi.org/10.1039/c4ra09124h
74. S. Zhang, D. Yang, M. Zhang, Y. Liu, T. Xu, J. Yang, Z. Yu, Synthesis of novel bimetallic nickel cobalt telluride nanotubes on nickel foam for high-performance hybrid supercapacitors. Inorg. Chem. Front. **7**, 477–486 (2020). https://doi.org/10.1039/C9QI01395D
75. V. Kumbhar, A. Lokhande, N. Gaikwad, C. Lokhande, One-step chemical synthesis of samarium telluride thin films and their supercapacitive properties. Chem. Phys. Lett. **645**, 112–117 (2016). https://doi.org/10.1016/j.cplett.2015.12.042
76. J. Kim, J. Jeong, N. Kim, R. Joshi, G. Lee, Mechanical properties of two-dimensional materials and their applications. J. Phys. D. Appl. Phys. **52**, 083001 (2019). https://doi.org/10.1088/1361-6463/aaf465
77. K. Kumar, N. Choudhary, Y. Jung, J. Thomas, Recent advances in two-dimensional nanomaterials for Supercapacitor electrode applications. ACS Energy Lett. **3**, 482–495 (2018). https://doi.org/10.1021/acsenergylett.7b01169

78. M. Iqbal, M. Ashiq, M. Hassan, R. Nawaz, A. Masood, A. Razaq, Excellent electrochemical behavior of graphene oxide based aluminum sulfide nanowalls for supercapacitor applications. Energy **159**, 151–159 (2018). https://doi.org/10.1016/j.energy.2018.06.123
79. M. Poudel, H. Karki, H. Kim, Silver nanoparticles decorated molybdenum sulfide/tungstate oxide nanorods as high performance supercapacitor electrode. J. Energy Storage **32**, 101693 (2020). https://doi.org/10.1016/j.est.2020.101693
80. K. Huang, J. Zhang, Y. Jia, K. Xing, Y. Liu, Acetylene black incorporated layered copper sulfide nanosheets for high-performance supercapacitor. J. Alloys Compd. **641**, 119–126 (2015). https://doi.org/10.1016/j.jallcom.2015.04.075
81. D. Jiang, Q. Xu, S. Meng, C. Xia, M. Chen, Construction of cobalt sulfide/graphitic carbon nitride hybrid nanosheet composites for high performance supercapacitor electrodes. J. Alloys Compd. **706**, 41–47 (2017). https://doi.org/10.1016/j.jallcom.2017.02.204
82. U. Patil, M. Nam, S. Kang, J. Sohn, H. Sim, S. Kang, S. Jun, Fabrication of ultra-high energy and power asymmetric supercapacitors based on hybrid 2D MoS_2/graphene oxide composite electrodes: A binder-free approach. RSC Adv. **6**, 43261–43271 (2016). https://doi.org/10.1039/C6RA00670A
83. X. Li, Q. Li, Y. Wu, M. Rui, H. Zeng, Two-dimensional, porous nickel-cobalt sulfide for high-performance asymmetric supercapacitors. ACS Appl. Mater. Interfaces **7**, 19316–19323 (2015). https://doi.org/10.1021/acsami.5b05400
84. X. Liang, K. Nie, X. Ding, L. Dang, J. Sun, F. Shi, H. Xu, R. Jiang, X. He, Z. Liu, Z. Lei, Highly compressible carbon sponge supercapacitor electrode with enhanced performance by growing nickel-cobalt sulfide nanosheets. ACS Appl. Mater. Interfaces **10**, 10087–10095 (2018). https://doi.org/10.1021/acsami.7b19043
85. T. Liu, J. Liu, L. Zhang, B. Cheng, J. Yu, Construction of nickel cobalt sulfide nanosheet arrays on carbon cloth for performance-enhanced supercapacitor. J. Mater. Sci. Technol. **47**, 113–121 (2020). https://doi.org/10.1016/j.jmst.2019.12.027
86. W. Chen, C. Xia, H. Alshareef, One-step electrodeposited nickel cobalt Sulfide Nanosheet arrays for high-performance asymmetric Supercapacitors. ACS Nano **8**, 9531–9541 (2014). https://doi.org/10.1021/nn503814y
87. J. Huang, J. Wei, Y. Xiao, Y. Xu, Y. Xiao, Y. Wang, L. Tan, K. Yuan, Y. Chen, When Al-doped cobalt-sulfide nanosheets meet nickel nanotube arrays: A highly efficient and stable cathode for asymmetric supercapacitors. ACS Nano **12**, 3030–3041 (2018). https://doi.org/10.1021/acsnano.8b00901
88. S. Xu, C. Su, T. Wang, Y. Ma, J. Hu, J. Hu, N. Hu, Y. Su, Y. Zhang, Z. Yang, One-step electrodeposition of nickel cobalt sulfide nanosheets on Ni nanowire film for hybrid supercapacitor. Electrochim. Acta **259**, 617–625 (2018). https://doi.org/10.1016/j.electacta.2017.11.027
89. S. Sahoo, R. Mondal, D. Late, C. Rout, Electrodeposited nickel cobalt manganese based mixed sulfide nanosheets for high performance supercapacitor application. Microporous Mesoporous Mater. **244**, 101–108 (2017). https://doi.org/10.1016/j.micromeso.2017.02.043
90. G. Ma, F. Hua, K. Sun, E. Fenga, H. Peng, Z. Zhang, Z. Lei, Nanostructure selenium compounds as pseudocapacitive electrodes for high-performance asymmetric supercapacitor. R. Soc. Open Sci. **5**, 171186 (2018). https://doi.org/10.1098/rsos.171186
91. K. Bhat, S. Shenoy, H. Nagaraja, K. Sridharan, Porous cobalt chalcogenide nanostructures as high performance pseudo-capacitor electrodes. Electrochim. Acta **248**, 188–196 (2017). https://doi.org/10.1016/j.electacta.2017.07.137
92. A. Chang, C. Zhang, Y. Yu, Y. Yu, B. Zhang, Plasma-assisted synthesis of $NiSe_2$ ultrathin porous nanosheets with selenium vacancies for supercapacitor. ACS Appl. Mater. Interfaces **10**, 41861–41865 (2018). https://doi.org/10.1021/acsami.8b16072
93. N. Arul, J. Han, Facile hydrothermal synthesis of hexapod-like two dimensional dichalcogenide $NiSe_2$ for supercapacitor. Mater. Lett. **181**, 345–349 (2016). https://doi.org/10.1016/j.matlet.2016.06.065
94. Y. Zheng, Y. Tian, S. Sarwar, J. Luo, X., Zhang carbon nanotubes decorated $NiSe_2$ nanosheets for high-performance supercapacitors. J. Power Sources **452**, 227793 (2020). https://doi.org/10.1016/j.jpowsour.2020.227793

95. J. Chen, C. Lin, M. Zhang, T. Jin, Y. Qian, Constructing nitrogen, selenium co-doped graphene aerogel electrode materials for synergistically enhanced capacitive performance. ChemElectroChem **7**, 3311–3318 (2020). https://doi.org/10.1002/celc.202000635
96. K. Bhat, H. Nagaraja, Effect of oxygen substitution and phase on nickel selenide nanostructures for supercapacitor applications. Mater. Res. Express **5**, 105504 (2018). https://doi.org/10.1088/2053-1591/aadac2
97. R. Barik, A. Kumar, Y. Yadav, S. Jha, D. Bhattacharyya, P. Ingole, Two-dimensional tungsten oxide/selenium nanocomposite fabricated for flexible supercapacitors with higher operational voltage and their charge storage mechanism. ACS Appl. Mater. Interfaces **13**, 8102–8119 (2021). https://doi.org/10.1021/acsami.0c15818
98. S. Siddique, C. Gowda, R. Tromer, S. Demiss, A. Gautam, O. Femi, P. Kumbhakar, D. Galvao, A. Chandra, C. Tiwary, Scalable synthesis of atomically thin gallium telluride Nanosheets for Supercapacitor applications. ACS Appl. Nano Mater. **4**, 4829–4838 (2021). https://doi.org/10.1021/acsanm.1c00428
99. B. Ye, C. Gong, M. Huang, Y. Tu, X. Zheng, L. Fan, J. Lin, J. Wu, Improved performance of a CoTe//AC asymmetric supercapacitor using a redox additive aqueous electrolyte. RSC Adv. **8**, 7997–8006 (2018). https://doi.org/10.1039/C7RA12919J
100. D. Chakravarty, P. Kumar, V. Ugale, D. Late, Microwave-assisted synthesis of few-layered $TaTe_2$ and its application as Supercapacitor. Eur. J. Inorg. Chem. **2015**, 1598–1603 (2015). https://doi.org/10.1002/ejic.201403220
101. Z. Yu, L. Tetard, L. Zhai, J. Thomas, Supercapacitor electrode materials: nanostructures from 0 to 3 dimensions. Energy Environ. Sci. **8**, 702–730 (2015). https://doi.org/10.1039/C4EE03229B
102. H. Jiang, P. Lee, C. Li, 3D carbon based nanostructures for advanced supercapacitors. Energy Environ. Sci. **6**, 41–53 (2013). https://doi.org/10.1039/C2EE23284G
103. S. He, W. Chen, 3D graphene nanomaterials for binder-free supercapacitors: Scientific design for enhanced performance. Nanoscale **7**, 6957–6990 (2015). https://doi.org/10.1039/C4NR05895J
104. Q. Wang, L. Jiao, H. Du, J. Yang, Q. Huan, W. Peng, Y. Si, Y. Wang, H. Yuan, Facile synthesis and superior supercapacitor performances of three-dimensional cobalt sulfide hierarchitectures. CrystEngComm. **13**, 6960–6963 (2011). https://doi.org/10.1039/C1CE06082A
105. Y. Liu, S. Guo, W. Zhang, W. Kong, Z. Wang, W. Yan, H. Fan, X. Hao, G. Guan, Three-dimensional interconnected cobalt sulfide foam: Controllable synthesis and application in supercapacitor. Electrochim. Acta **317**, 551–561 (2019). https://doi.org/10.1016/j.electacta.2019.05.121
106. S. Shaikh, M. Rabinal, Rapid ambient growth of copper sulfide microstructussres: Binder free electrodes for supercapacitor. J. Energy Storage **28**, 101288 (2020). https://doi.org/10.1016/j.est.2020.101288
107. R. Ramachandran, S. Felix, M. Saranya, C. Santhosh, V. Velmurugan, B. Ragupathy, S. Jeong, A. Grace, Synthesis of Cobalt Sulfide–Graphene (CoS/G) Nanocomposites for Supercapacitor Applications. IEEE Trans. Nanotechnol. **12**, 985–990 (2013). https://doi.org/10.1109/TNANO.2013.2278287
108. U. Patil, P. Katkar, S. Marje, C. Lokhande, S. Jun, Hydrous nickel sulphide nanoparticle decorated 3D graphene foam electrodes for enhanced supercapacitive performance of an asymmetric device. New J. Chem. **42**, 20123–20130 (2018). https://doi.org/10.1039/C8NJ04228D
109. S. Xie, J. Gou, B. Liu, C. Liu, Synthesis of cobalt-doped nickel Sulfide nanomaterials with rich edge sites as high-performance supercapacitor electrode materials. Inorg. Chem. Front. **5**, 1218–1225 (2018). https://doi.org/10.1039/C8QI00172C
110. Y. Gao, S. Cui, L. Mi, W. Wei, F. Yang, Z. Zheng, H. Hou, W. Chen, Double metal ions synergistic effect in hierarchical multiple sulfide microflowers for enhanced Supercapacitor performance. ACS Appl. Mater. Interfaces **7**, 4311–4319 (2015). https://doi.org/10.1021/am508747m

111. Y. Zhao, Z. Shi, H. Li, C. Wang, Designing pinecone-like and hierarchical manganese cobalt sulfides for advanced supercapacitor electrode. J. Mater. Chem. A **6**, 12782–12793 (2018). https://doi.org/10.1039/C8TA02438C
112. B. Xie, Y. Chen, M. Yu, T. Sun, L. Lu, T. Xie, Y. Zhang, Y. Wu, Hydrothermal synthesis of layered molybdenum sulfide/N-doped graphene hybrid with enhanced supercapacitor performance. Carbon **99**, 35–42 (2016). https://doi.org/10.1016/j.carbon.2015.11.077
113. K. Krishnamoorthy, P. Pazhamalai, S. Kim, Ruthenium sulfide nanoparticles as a new pseudocapacitive material for supercapacitor. Electrochim. Acta **227**, 85–94 (2017). https://doi.org/10.1016/j.electacta.2016.12.171
114. B. Pant, G. Ojha, M. Park, One-pot synthesis, characterization, and electrochemical studies of tin-nickel sulfide hybrid structures on nickel foam for supercapacitor applications. J. Energy Storage **32**, 101954 (2020). https://doi.org/10.1016/j.est.2020.101954
115. R. Ramachandran, M. Saranya, P. Kollu, B. Raghupathyc, S. Jeong, A. Grace, Solvothermal synthesis of zinc sulfide decorated graphene (ZnS/G) nanocomposites for novel Supercapacitor electrodes. Electrochim. Acta **178**, 647–657 (2015). https://doi.org/10.1016/j.electacta.2015.08.010
116. Y. Song, X. Zhao, Z. Liu, Surface selenium doped hollow heterostructure/defects co-Fe sulfide nanoboxes for enhancing oxygen evolution reaction and supercapacitors. Electrochim. Acta **374**, 137962 (2021). https://doi.org/10.1016/j.electacta.2021.137962
117. G. Nagaraju, S. Cha, S. Sekhar, J. Yu, Metallic layered polyester fabric enabled nickel selenide nanostructures as highly conductive and Binderless electrode with superior energy storage performance. Adv. Energy Mater. **7**, 1601362 (2016). https://doi.org/10.1002/aenm.201601362
118. K. Guo, F. Yang, S. Cui, W. Chen, L. Mi, Controlled synthesis of 3D hierarchical NiSe microspheres for high-performance supercapacitor design. RSC Adv. **6**, 46523–46530 (2016). https://doi.org/10.1039/C6RA06909F
119. S. Wang, W. Li, L. Xin, M. Wu, Y. Long, H. Huang, X. Lou, Facile synthesis of truncated cube-like $NiSe_2$ single crystals for high-performance asymmetric supercapacitors. Chem. Eng. J. **330**, 1334–1341 (2017). https://doi.org/10.1016/j.cej.2017.08.078
120. R. Manikandan, C. Raj, G. Nagaraju, R. Velayutham, S. Moulton, J. Puigdollers, B. Kim, Selenium enriched hybrid metal chalcogenides with enhanced redox kinetics for high-energy density supercapacitors. Chem. Eng. J. **414**, 128924 (2021). https://doi.org/10.1016/j.cej.2021.128924
121. P. Xu, W. Zeng, S. Luo, C. Ling, J. Xiao, A. Zhou, Y. Sun, K. Liao, 3D Ni-Co selenide nanorod array grown on carbon fiber paper: Towards high-performance flexible supercapacitor electrode with new energy storage mechanism. Electrochim. Acta **241**, 41–49 (2017). https://doi.org/10.1016/j.electacta.2017.04.121
122. H. Liu, H. Guo, N. Wu, W. Yao, R. Xue, M. Wang, W. Yang, Rational design of nickel-cobalt selenides derived from multivariate bimetal metal-organic frameworks for high-performance asymmetric supercapacitor. J. Alloys Compd. **856**, 156535 (2021). https://doi.org/10.1016/j.jallcom.2020.156535
123. D. Malavekar, S. Kale, V. Lokhande, U. Patil, J. Kim, C. Lokhande, Chemically synthesized Cu_3Se_2 film based flexible solid-state symmetric Supercapacitor: Effect of reaction Bath temperature. J. Phys. Chem. C **124**, 28395–28406 (2020). https://doi.org/10.1021/acs.jpcc.0c08454
124. B. Balamuralitharan, S. Karthick, S. Balasingam, K. Hemalatha, S. Selvam, J. Raj, K. Prabakar, Y. Jun, H. Kim, Hybrid reduced graphene oxide/$MnSe_2$ cubes: A new electrode material for supercapacitors. Energ. Technol. **5**, 1953–1962 (2017). https://doi.org/10.1002/ente.201700097
125. B. Ye, S. Xiao, X. Cao, J. Chen, A. Zhou, Q. Zhao, W. Huang, J. Wang, Interface engineering for enhancing performance of additive-free NiTe@$NiCoSe_2$ core/shell nanostructure for asymmetric supercapacitors. J. Power Sources **506**, 230056 (2021). https://doi.org/10.1016/j.jpowsour.2021.230056

126. C. Kim, J. Ji, M. Aftabuzzaman, H, Kim, three-dimensional tellurium and nitrogen co doped mesoporous carbons for high performance supercapacitors. RSC Adv. **11**, 8628–8635 (2021). https://doi.org/10.1039/D0RA10374H
127. B. Ye, M. Huang, L. Fan, J. Lin, J. Wu, Co ions doped NiTe electrode material for asymmetric supercapacitor application. J. Alloys Compd. **776**, 993–1001 (2019). https://doi.org/10.1016/j.jallcom.2018.10.358

Chemically Deposited Iron Chalcogenide-Based Carbon Composites for Supercapacitor Applications

Shreelekha N. Khatavkar, Swarda N. Khatavkar, and Shrikrishna D. Sartale

Abbreviations

ACC	Activated carbon cloth
ALD	Atomic layer deposition
Ac	Areal capacitance
CC	Carbon cloth
CBD	Chemical bath deposition
CMC	Carboxymethyl cellulose
CF	Coffee filter
CFP	Carbon fiber paper
CP	Carbon paper
CNTs	Carbon nanotubes
CNFs	Carbon nanofibers
CNP	Carbon nanotube paper
CTAB	Cetrimonium bromide
CD	Current density
CV	Cyclic voltammetry
CVD	Chemical vapor deposition
CS	Cyclic stability
EC	Electrochemical
ECS	Energy conversion and storage
ED	Energy density

S. N. Khatavkar · S. D. Sartale (✉)
Thin Films and Nanomaterials Laboratory, Department of Physics, Savitribai Phule Pune University, Pune, India
e-mail: sdsartale@physics.unipune.ac.in

S. N. Khatavkar
Department of Education and Extension, Savitribai Phule Pune University, Pune, India

F. I. Ezema et al. (eds.), *Chemically Deposited Metal Chalcogenide-based Carbon Composites for Versatile Applications*, https://doi.org/10.1007/978-3-031-23401-9_3

EDL	Electric double layer
EDLC	Electric double layer capacitor
EDTA	Ethylenediaminetetraacetic acid
FCC	Face-centered cubic
FE-SEM	Field emission scanning electron microscopy
FSS-SC	Flexible solid-state supercapacitor
FTO	Fluorine-doped tin oxide
GCD	Galvanostatic charge-discharge
GA	Graphene aerogel
GF	Graphite foam
GP	Graphene oxide paper
HRTEM	High-resolution TEM
IS	Impedance spectroscopy
ITO	Indium tin oxide
LIBs	Lithium ion batteries
LPD	Liquid phase deposition
MCs	Metal chalcogenides
MWNT	Multi-walled carbon nanotube
NF	Nanoflakes
NP	Nanoparticles
NR	Nanorods
NRA	Nanorod arrays
NS	Nanosheets
NT	Nanotubes
NW	Nanowires
1D	One dimensional
PIHCs	Potassium ion hybrid capacitors
PEDOT	Poly(3,4-ethylenedioxythiophene)
PEG	Polyethylene glycol
PET	Polyethylene terephthalate
PD	Power density
PTFE	Polytetrafluoroethylene
PVA	Polyvinyl alcohol
rGO	Reduced graphene oxide
SAED	Selected area electron diffraction
SEM	Scanning electron microscopy
SC	Supercapacitor
Sc	Specific capacitance
SILAR	Successive ionic layer adsorption and reaction
SP	Supercapacitive performance
SS	Stainless steel
TEM	Transmission electron microscopy
2D	Two dimensional
3D	Three dimensional
VACNTs	Vertically aligned carbon nanotube arrays

1 Supercapacitors

Problems like changing climate, exhausting fossil fuels and storage of energy produced by solar and wind power can be solved by providing highly capable, inexpensive, and environment-friendly electrical energy storage devices [1]. Today's energy demands can be fulfilled with the help of advanced energy conversion and storage (ECS) devices [2] which include SCs.

In today's market, the SC industry is in high demand [3]. Also, SCs are a significant part of the emerging energy storage technology [4]. The demand for flexible and wearable microelectronic devices is increasing day by day due to the need and development in different fields [5–10].

As shown in Fig. 1, SCs consist of three classes: electric double layer capacitor (EDLC), pseudocapacitor, and hybrid capacitor [12, 13]. Each category is based on different charge storage mechanisms. These mechanisms are governed by non-faradic and/or faradic processes. The EDLC's charge storage mechanism is based on a non-faradic process [14], and there is no transfer of charge at the electrode-electrolyte interface [12, 15]. EDLC's performance can be enhanced depending on the electrolyte type used. Generally, carbon materials are used to prepare electrodes for EDLCs [11]. The pseudocapacitor's charge storage mechanism is based on a faradic process [16]. The pseudocapacitor stores the charge electrostatically, and the faradic charge transfer occurs at the electrode-electrolyte interface. The electrode materials include conducting polymers and/or metal chalcogenides (MCs) [12]. The pseudocapacitance may be intrinsic or extrinsic. Generally, the charge storing

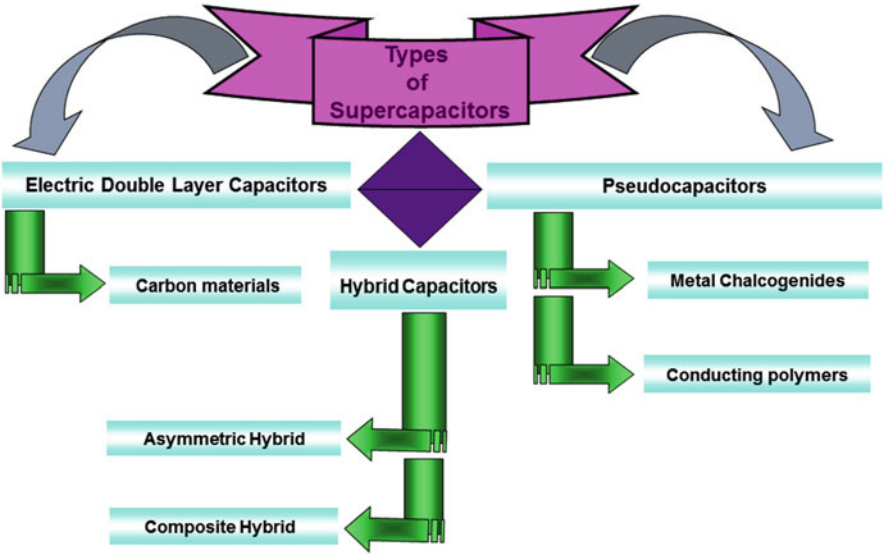

Fig. 1 Classification of SCs and the associated electrode materials. (Adapted from Ref. [11])

capacity of the pseudocapacitive electrode is higher than that of the EDLC electrode. This is because the number of ions involved in charge separation is much smaller as compared to the number of protons exchanged between the electrode surface and electrolyte. The reasons for the variation in the performance of the pseudocapacitor are conductivity of the active material, the specific surface area of the electrode, particle size, category of the electrolyte, and the design of the device. Moreover, the charge storing capacity of the pseudocapacitive electrode is very high (high Sc) as compared to that of the EDLC electrode, but these electrodes have limited CS and low PD due to phase change and faradic reactions [11].

To overcome the drawbacks, hybrid SC is constructed, which is a combination of both EDLC and pseudocapacitor. In hybrid SC, one electrode is of EDLC type, and other is of pseudocapacitor type. These SCs work with various storage mechanisms, and in various electrodes' potential ranges, the hybrid devices can accomplish an extensive potential window, which results in the rise in ED while retaining their high PD [17]. The scheme, optimization, and fabrication of the proper electrode material are crucial challenges to gain high EC performance of the hybrid devices for energy storage [15].

Current collectors (2), electrode material, electrolyte, and separator are the main components of any type of SC. The quality of SC is dependent on the choice of each of these (including working potential window). While choosing the electrode material, the preference is given to the properties of the material such as multiple oxidation states, good electrical conductivity, high surface area, porosity and chemical stability, good surface wettability, EC activity (how freely electrolyte ions can interact with the electrode surface), long cycle stability, and thermodynamic stability for extensive working potential window [18, 19]. For electrode materials, researchers are always in search of materials with low cost, high efficiency, and outstanding properties. MCs are extensively used as electrode materials [20]. MCs for SC electrode material application include metal oxides [21–24], metal sulfides [25, 26], metal selenides [27], and metal tellurides [28]. As compared to bulk, nanostructured MCs are advantageous for energy devices due to new physicochemical properties (quantum size effect) [29], high specific surface area [1, 26], and stability [30–32]. Carbon materials comprising activated carbon, carbon nanotubes (CNTs), and graphene are extensively useful due their high conductivity and higher surface area [15, 35–46]. Among these hybrid materials MC-based carbon composites have numerous advantages for SC applications.

To suppress the shortcoming and to enhance their usual properties, hybrid MCs are formed by loading/combining them with other materials like carbon materials, noble metals, metal oxides, and conductive polymers, by fabricating mixed metal chalcogenides, or by doping heteroatoms [30, 33, 34].

2 Thin Film SC Electrode Materials

Preparation of electrode using binder to coat powder on the conducting substrate has drawbacks of poor adhesion and electrical contacts. One of the promising ways

to have good EC properties is to develop binder-free electrodes. The binder-free electrodes have the benefits of complete utilization of the electroactive material [47]. Therefore, in order to improve the performance, the material is deposited in the form of thin film, which gives better adhesion and electrical contact. While choosing a certain deposition method, one has to know about the electroactive material, the substrate's nature, morphology, and thickness for a particular application [48].

Chemical deposition methods cost less in comparison with physical deposition methods. Under chemical methods, solution-based deposition methods are one of the bottom-up approaches as chemical reactions occur in solutions resulting in precipitation, which gets deposited in thin film form on the substrate kept in solution [49]. Neither a special instrument nor a vacuum is needed. The basic things needed are chemicals, beakers, hot plate and stirrer, etc. [50]. Any type of substrate, whether it is conducting or nonconducting or has a flat or complex shape, can be used for chemical deposition. Moreover, oxidation or corrosion is avoided due to the low-temperature deposition process. For large area deposition, chemical methods can be easily scaled up.

The formation of nuclei and successive growth are the two main factors leading to film formation in the chemical deposition. Parameters that control the growth of the film are precursor concentration, stirring rate, pH, complexing agent, and temperature. Microcrystalline structures with varying grain sizes up to 100 nm are observed in chemically deposited MC thin films depending on deposition conditions. Depending on application, the required morphology of the film differs. This can be obtained by the variation in the precursor and/or complexing agent [51]. High-quality MC thin films have been deposited by solution-based chemical methods. Table 1 gives a short description of various chemical methods that have been used for deposition of MC thin films.

3 Iron Chalcogenide Thin Film Supercapacitor Electrodes

After silicon, iron is the most abundant element in the Earth's crust. High theoretical capacitance, environmentally friendly, less cost, and more availability on earth are the main reasons due to which iron chalcogenides are thought as one of the important electrode materials for SCs. During an EC process, iron chalcogenide (iron oxide, iron sulfide, iron selenide, and iron telluride) materials exhibit multiple valence states like Fe^{3+}, Fe^{2+}, and Fe^{0}. Hence, they offer redox sites that include Fe^{0}/Fe^{2+}, Fe^{0}/Fe^{3+}, and Fe^{2+}/Fe^{3+}, which enhance the performance of energy storage device.

Important shortcomings of the iron-based materials' electrode are poor conductivity and CS. This can be overcome by development of nanomaterials. Different iron-based 1D, 2D, and 3D nanostructures have been developed [53]. In the following sections, we summarize the available literature dealing with iron chalcogenide thin films for SC applications.

Table 1 Description of various chemical deposition methods used for MC thin film electrodes

Sr.no.	Deposition method	Factors affecting film formation	Advantages	Disadvantages
1	Hydrothermal/solvothermal	(a) Temperature (b) Time (c) Concentration (d) pH (e) Pressure (volume of the solution) in autoclave	(a) Large-scale production (b) High purity products (c) No toxic chemicals involved	(a) Requirement of high temperature and pressure (b) Not possible to obtain intermediate phases at different deposition times
2	CBD	(a) pH (b) Concentration (c) Temperature (d) Additives	(a) Large area deposition (b) Different morphologies (c) Doping	(a) Material wastage in the form of precipitation (b) Hydroxide formation (c) Time-dependent composition and morphology
3	LPD	(a) Precursor concentration (b) Scavenging agent (c) Deposition time and temperature	(a) Additive/binder-free method (b) No use of toxic chemicals (c) Reproducibility is high	(a)Wastage of material due to precipitation in the solution (b) Slow process
4	SILAR	(a) Adsorption time (b) Reaction time (c) Rinsing time (d) Precursor concentration (e) Number of growth cycles (f) Temperature	(a) Wastage of material is avoided (b) Precise control on thickness (c) Multilayer deposition	(a) Time-consuming process
5	Spray pyrolysis	(a) Substrate temperature (b) Gas flow rate (c) Distance between atomizer and substrate	(a) Good crystallinity (b) Large-area and high-quality films of uniform thickness	(a) High temperature (b) Limitation on substrate selection (c) Evolution of harmful gases as by-products

6	Sol-gel	(a) Surfactants (b) Solvents (c) Reaction time (d) Temperature	(a) Large-scale production (b) High purity materials (c) Low temperature (d) Easy and low cost	(a) Multistep process
7	Spin coating	(a) Rotation speed (b) Ramp (c) Drop size (d) Concentration and viscosity of the solution (e) Spinning time	(a) Time-saving method (b) Deposition of multiple layers	(a)Wastage of solution (b) Limitation on large-area deposition
8	EC deposition	(a) Deposition time (b) Deposition temperature (c) Concentration of the electrolyte (d) Strength and type (static/pulsed) of current/potential	(a) Uniform morphology (b) One-step synthesis (c) Well-adherent film deposition	(a) Conducting substrate is required (b) Large-scale production is difficult

Adapted from Ref. [52]

4 Iron Oxides

There are many reports available on the cathode materials of SCs, but the study of anode materials is rarely reported. Iron oxide is among the best suitable anode materials for aqueous SCs. Owing to high stability (thermodynamically) and abundant availability, hematite (α-Fe_2O_3) phase has many applications [54] along with SCs [55]. α-Fe_2O_3 is considered a capable material for anode in SC application (particularly asymmetric) because of the following: large negative potential window, less cost, high redox activity, and environmentally friendly [56]. So far, theoretical high capacitance value does not match with the practical EC performance. The stability and ED of iron oxides are low. Poor electrical conductivity is one of the reasons. The carbon based composite material has sufficient conductivity from the carbon to transport the electron back and forth from the iron oxide structure [57].

Wu et al. anodically electrodeposited nanostructured iron oxide onto nickel substrate in aqueous solution at room temperature and at 300 °C annealing done for 1 h. A film deposited at a 0.125 $mAcm^{-2}$ higher CD was highly porous in structure with randomly distributed NS, and that at a 0.05 $mAcm^{-2}$ lower CD it was also porous but with smaller pores, i.e., aggregated NR. At 3 Ag^{-1} discharge, the Sc of the film was 173 Fg^{-1} deposited at 0.125 $mAcm^{-2}$, and that of film was 120 Fg^{-1} deposited at 0.05 $mAcm^{-2}$. This is because electrochemically larger pores are accessed earlier than small pores [58].

By implementing simple and low-cost anodization method, highly ordered α-Fe_2O_3 NT arrays on an iron foil were prepared by Xie et al. In Fig. 2a, a nanotubular structure (with an average pore diameter of ~100 nm, a thickness of wall of ~ 20 nm, and a length of ~3 μm) can be visualized. From Fig. 2b, tubular structure of single α-Fe_2O_3 NT after annealing is confirmed. Insets of Fig. 2b SAED and HRTEM (top and bottom) prove that nanotubes are crystallized in a hematite structure. Because there were fast transport of ions and large surface area of these unique nanostructures, the electrode showed high Sc (138 Fg^{-1} at 1.3 Ag^{-1}) and good CS (89% after 500 cycles) [59].

Lokhande et al. electrodeposited Fe_2O_3 thin films on SS plates with varying precursor concentrations. The estimated maximum Sc was 540 Fg^{-1} at 2.5 Ag^{-1} in 1 M KOH [60]. This electrode was annealed at various temperatures for various time durations. For 40 min of annealing at 300 K, the electrode showed a maximum Sc of 487 Fg^{-1} at 20 mVs^{-1} [61]. It is well known that annealing can cause changes in morphology, phase/structure, and other properties, but the effect of annealing on EC properties was not studied by the authors. Sarma et al. observed the effect of annealing temperature on the supercapacitive properties of α-Fe_2O_3 NT electrodes. Figure 3 shows the effect of annealing on morphology. The preparation of electrodes was carried out using a pure Fe substrate by EC anodization, and thereafter, they were annealed between 200 and 700 °C. The temperature used for annealing is highly responsible for the supercapacitive behavior. The electrode for which annealing was done at 300 °C was found to show superior supercapacitive performance at 20 $mVs^{-1}$of 187 $mFcm^{-2}$ [62] (Fig. 4a). The electrodes made

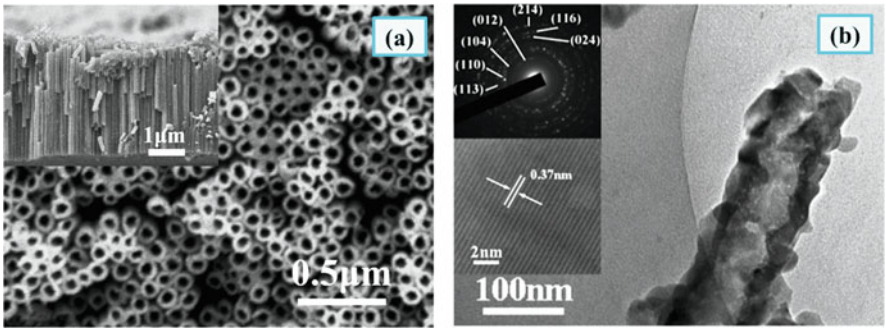

Fig. 2 (**a**) FE-SEM image of the top view of as-anodized α-Fe_2O_3 NT arrays on an iron foil with cross-section in inset and (**b**) TEM of single α-Fe_2O_3 NT after annealing. The insets (top and bottom) are of SAED pattern of NT and HRTEM, respectively [59]

using a similar procedure were annealed in different gas atmospheres: air, argon, nitrogen, and oxygen. The EC behavior of these electrodes was studied by doing CV, GCD, CS, and IS. The highest Sc obtained was 298 $mFcm^{-2}$ at 3 $mAcm^{-2}$ for the electrode annealed in Ar atmosphere (Fig. 4b). The improvement in EC performance was due to the more electrical conductivity through the formation of a more quantity of the Fe_3O_4, which resulted in increment of oxygen vacancies [63].

Huang et al. directly grew α-Fe_2O_3 NS on Ni foam by a hydrothermal method and heat treatment. Nickel foam has a 3D structure with high electrical conductivity; hence, there is increase in the charge transfer, and internal resistance is reduced by keeping a rapid reaction. The EC performance of the α-Fe_2O_3 electrode was analyzed in 1 M Li_2SO_4, Na_2SO_4, and KOH electrolytes. At 0.36 Ag^{-1}, the α-Fe_2O_3 NS electrode displayed highest Sc as 147 Fg^{-1} in Li_2SO_4 electrolyte [64].

α-Fe_2O_3 NT were developed on fabric of carbon by Yang et al. through a template-accelerated hydrolysis method. The areal capacitance (Ac) of the α-Fe_2O_3 electrode obtained was 180.4 $mFcm^{-2}$ at a CD of 1 $mAcm^{-2}$. The Sc at an equivalent CD of 1.4 Ag^{-1} corresponded to 257.8 Fg^{-1} [65]. Lee et al. demonstrated vertically aligned mixed iron (III) oxyhydroxide/oxide NS grown on iron foils by an oxidation chemically. The EC characterizations were tested in KOH, Na_2SO_4, and Na_2SO_3 electrolytes. The Ac of the electrode was highest in Na_2SO_3, 312 $mFcm^{-2}$ at 10 mVs^{-1} [66]. Among the various hematite nanostructured morphologies like nanoparticles (NP), nanoflakes (NF), nanoflowers, NS, NT, nanorods (NR), nanocorals, nanowires (NW), nanocubes, and nanofibers, NF are promising for photoelectrochemical and SC devices. Different studies show that synthesizing hematite NF is very much time-consuming and also requires binder in some cases. Liu et al. prepared ultrathin hematite NF with a binder-free and less time-consuming process. First, akaganeite (β-FeOOH) NR were synthesized by a seed-assisted hydrothermal method. Following annealing in tube furnace, it was converted to hematite NR. Electrochemically induced morphological transformation from hematite NR to hematite NF was done by applying −1.2 V vs. Ag/AgCl. From an EC study, at the CD of 1 $mAcm^{-2}$, the Ac calculated was 145.9 $mFcm^{-2}$ [67].

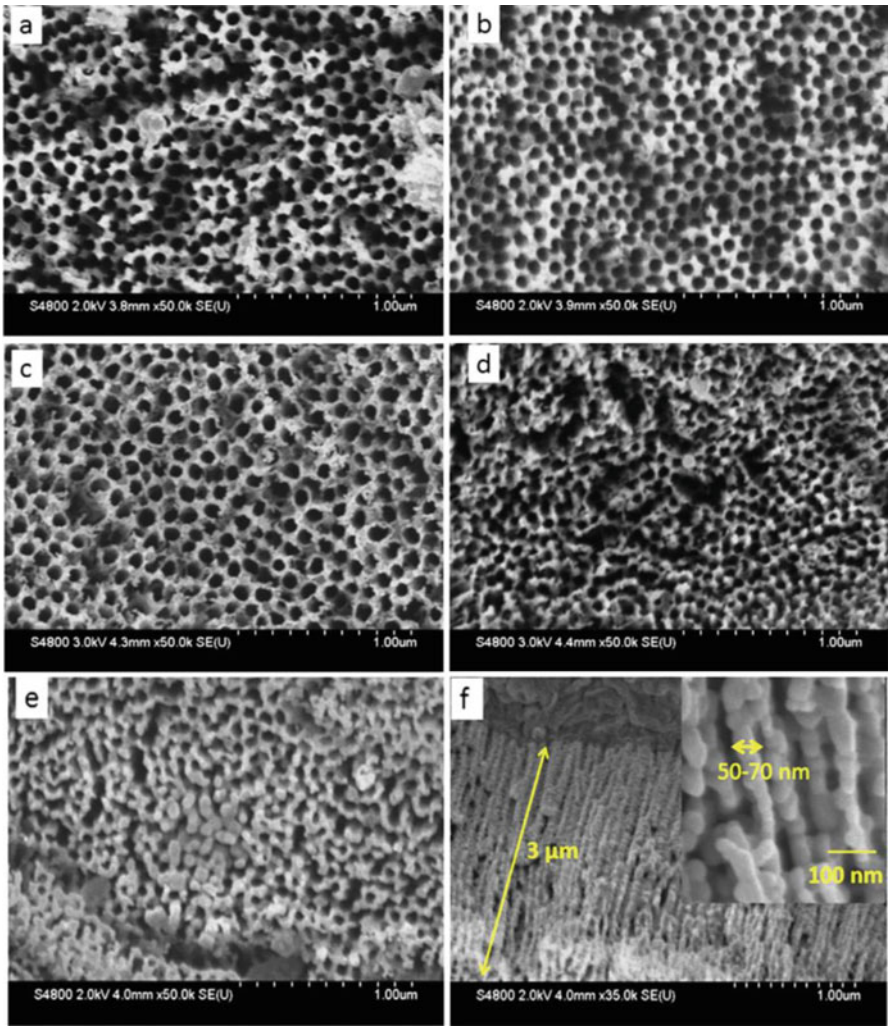

Fig. 3 Images of the α-Fe_2O_3 NT after annealing for 2 h at (**a**) 200, (**b**) 300, (**c**) 400, (**d**) 500, and (**e**) 600 °C and (**f**) transformed NR at 600 °C (cross-sectional view) [62]

Gund et al. synthesized α-Fe_2O_3 NP on flexible SS by implementing the SILAR method [68]. 0.1 M NaOH (at 333 K) and 0.05 M $FeSO_4$ were used as anionic and cationic sources, respectively. After 100 SILAR cycles, the α-Fe_2O_3 NP grown substrate was washed and dried at 353 K for 5 h. This electrode showed uniform casing of a highly porous microstructure comprised of fine interconnected NP of about ~20 nm diameter on an SS sheet (Fig. 5a, b). Diffusion and ion transport are supported through the electrode due to its porous microstructures. The highest calculated value of Sc of this electrode at 5 mVs^{-1} was 283 Fg^{-1}. An asymmetric

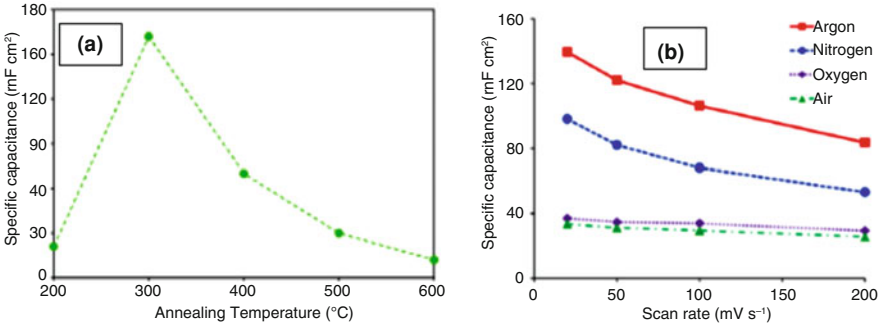

Fig. 4 (**a**) Variation in Sc against the annealing temperature [62] and (**b**) variation in Sc versus scan rate for the α-Fe_2O_3 NT annealed in various atmospheres [63]

FSS-SC device was fabricated (MnO_2//Fe_2O_3). The estimated maximum Sc was 92 Fg^{-1} at 5 mVs^{-1}, and the decrease after 3000 CV cycles was 91%. Chodankar et al. reported α-Fe_2O_3 on SS by SILAR. These α-Fe_2O_3 thin films were prepared at 313 K by 100 SILAR cycles, in which 0.05 M $FeCl_3$ was used as a cationic precursor whereas 0.1 M NaOH was used as an anionic precursor. As seen in Fig. 5c, d, the morphological study reflected the formation of NP of irregular size and shape. Also, the substrate was densely covered by randomly oriented NP. This electrode at 5 mVs^{-1} showed Sc 339 Fg^{-1} and 360 Fg^{-1} at a CD of 1 $mAcm^{-2}$. The MnO_2//Fe_2O_3 asymmetric cell revealed a high Sc of 145 Fg^{-1} with an ED of 41 $Whkg^{-1}$ and a PD of 2.1 $kWkg^{-1}$ [69]. Shinde et al. also prepared Fe_2O_3 thin films on flexible SS by SILAR. For this synthesis procedure, solutions of 0.01 M $FeCl_3$ and 1 M NaOH were used as cationic and anionic precursors. 120 SILAR cycles were carried for the uniform deposition on substrate. The FE-SEM images (Fig. 5e, f) revealed the formation of highly porous surface morphology comprising NP that are decorated on the surface of the substrate. This provides insertion and de-insertion of electrolyte. The EC performance revealed maximum Sc at 5 mVs^{-1} of 275 Fg^{-1} (CV) and at 5 $mAcm^{-2}$ of 350 Fg^{-1} (GCD). Also, a α-Fe_2O_3/α-Fe_2O_3 symmetric device was being fabricated. Its maximum Sc at 5 mVs^{-1} was 21.5 Fg^{-1} and 11 Fg^{-1} at 0.5 $mAcm^{-2}$. A fabricated asymmetric (CuO//Fe_2O_3) SC device at 2 $mAcm^{-2}$ showed an Sc of 79 Fg^{-1} (2.0 V potential range). The ED and PD of 23 $Whkg^{-1}$ and 19 $kWkg^{-1}$ were calculated for asymmetric SC. Moreover, it demonstrated the exceptional flexibility with 89% retention at a bending angle of 180° [70].

Hydrothermally homogenous α-Fe_2O_3 NW (diameter, about 10 nm) were grown on a CFP by Tang et al. At 2 Ag^{-1}, a high Sc of 908 Fg^{-1} was achieved along with a superb efficiency of 90% retention till 10 Ag^{-1} in an extensive negative potential range of 0 to −1.35 V [71]. Nan et al. made a sequence of 3D porous spinous α-Fe_2O_3 on a flexible iron foil by a simple wet chemical method and annealing at 400 °C in air for 4 h (Fig. 6). Effects of temperature, precursors' concentration, and

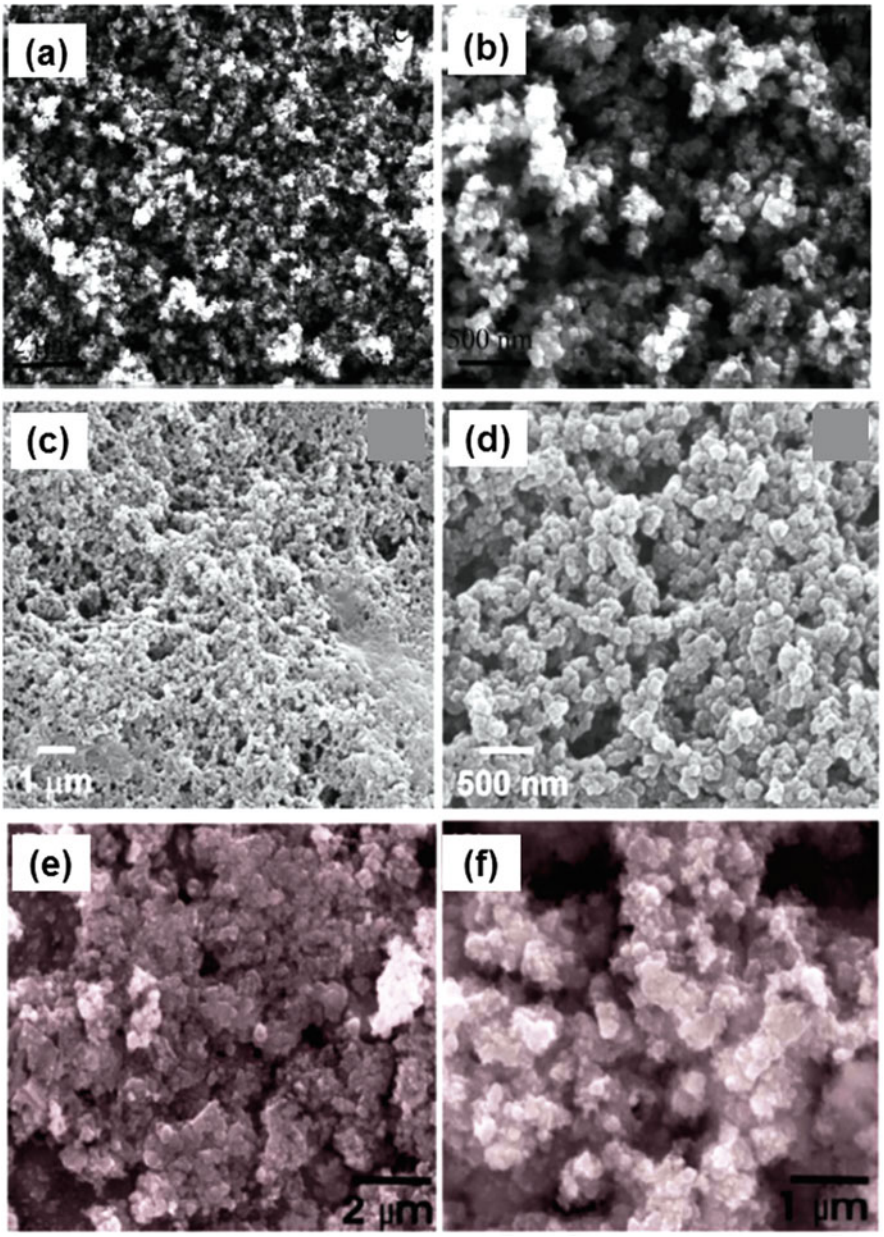

Fig. 5 FE-SEM of α-Fe_2O_3 electrodes prepared through SILAR at two different scales: (**a**) 2 μm and (**b**) 500 nm reported by Gund et al. [68]; (**c**) 1 μm and (**d**) 500 nm reported by Chodankar et al. [69] and (**e**) 2 μm and (**f**) 1 μm reported by Shinde et al. [70]

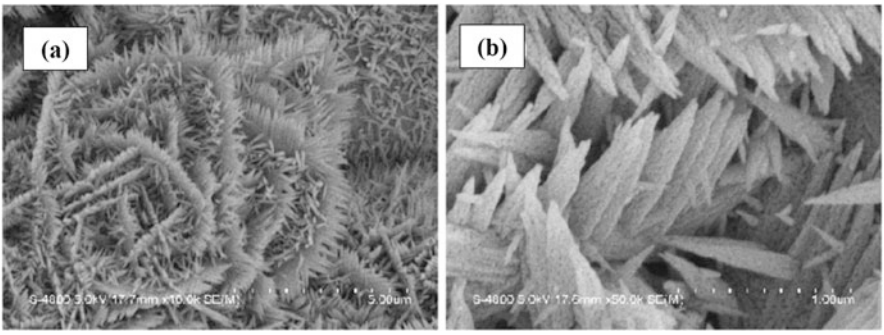

Fig. 6 FE-SEM images with two different magnifications of the porous spinous α-Fe_2O_3 annealed at 400 °C in air for 4 h [72]

reaction time on morphology were studied. From GCD at 1 Ag^{-1}, the highest Sc determined was 524.6 Fg^{-1} [72].

Kadam et al. carried out electrodeposition (cathodic) to deposit α-Fe_2O_3 on SS. A morphological study revealed that the film surface was well covered with irregular shaped grains. At 5 mVs^{-1}, the observed Sc was 135 Fg^{-1} in the 0.5 M Na_2SO_4 electrolyte. CS showed 4–5% decrement after 1000 cycles [73]. Due to the less electrical conductivity ($\sim 10^{-14}$ S/cm) of the α-Fe_2O_3 electrode, there is problem of low PD and ED. This problem can be resolved by combining it with carbon-based materials, metals, etc. But instead of searching other materials to combine with α-Fe_2O_3, Tang et al. tried and scrutinized a heterostructure of iron ferrite@iron oxide core-shell NRAs. From CVs at 5 mVs^{-1}, a 1206 Fcm^{-3} (231.9 Fg^{-1}) volumetric capacitance was revealed, higher than the individual electrodes of Fe_3O_4 (315 Fcm^{-3}) and α-Fe_2O_3 (595 Fcm^{-3}) [74]. Along with the capacitance, rate capability was also noticeably improved.

Peng et al. grew hematite nanocrystals on a CC by a hydrothermal method. It displayed at 2 $mAcm^{-2}$ a high Ac of 1.66 Fcm^{-2} (1660 Fg^{-1}) and an admirable CS of 5000 cycles and a retention of 88.6% at higher CDs. After fabrication of the symmetric FSS-SC device, at 2 $mAcm^{-2}$, the 16.82 Fcm^{-3} volumetric capacitance for the Fe_2O_3/CC//Fe_2O_3/CC device from GCD was noted. Also this device proved outstanding under various conditions [75].

Zhang et al. synthesized, α-Fe_2O_3 NR on CC using the hydrothermal method delivered Ac of 500 $mFcm^{-2}$ at 4 $mAcm^{-2}$ from GCD. Also, an asymmetric device was fabricated with NiO NS on nickel foam and α-Fe_2O_3 NR on CC, which showed the maximum Ac and Sc values 228.8 $mFcm^{-2}$ and 57.2 Fg^{-1} at CD 4 mA cm^{-2}. This asymmetric SC in solid state revealed large PDs and EDs of 312 Wkg^{-1} at 12.4 $Whkg^{-1}$ and 951 W kg^{-1} at 3.64 $Whkg^{-1}$ [76].

In order to enhance the capacitive efficiency of Fe_2O_3 anodes, Liang et al. carried out novel phosphine plasma activation. This effectually altered the defect concentration, active surface area, and conductivity without changing the bulk phase of Fe_2O_3. Hence, a fivefold improvement in Ac was accomplished for the

plasma functionalized Fe_2O_3 (Fe_2O_3-P). An asymmetric device made up of MnO_2 and Fe_2O_3-P attained a high ED of 57.3 $Whkg^{-1}$ at a PD of 1404 Wkg^{-1} [77]. Zheng et al. reported the preparation of spinous α-Fe_2O_3 on Ni foam through a hydrothermal method. Their EC properties from GCD at 1 $mAcm^{-2}$ showed a high discharge Ac of 681 $mFcm^{-2}$ and a CS of 76.1% when compared to initial Ac after 6000 cycles. The outstanding supercapacitive conductivity is due to its distinctive spatial structures, which provided enormous numbers of active sites [78].

Nanomaterials of carbon are costly and unsuited for the environment since hazardous liquids (conc. H_2SO_4, N_2H_4, N-Methyl-2-pyrrolidone, etc.) that prominently hamper their applications may be used in synthesis. In such scenario, silver NW (AgNW) are used in flexible electrode materials due to their good antioxidation property, simple synthesis, flexibility, and conductivity. Chen et al. reported a conductive, cheap, and environmentally compatible current collector in which porous coffee-filter (CF) sheets behave like frame and networks like conductive structures of silver NW are formed due to H-bonding among them. AgNW were grown on CF by dip coating, and then Fe_2O_3 NR were grown on this AgNW/CF by a hydrothermal method. The Fe_2O_3 NR/AgNW/CF electrode revealed reversible charging and discharging with an exceptional Sc, 287.4 Fg^{-1} at PD 18 $kWkg^{-1}$ and ED 64.6 $Whkg^{-1}$. The Fe_2O_3 NR/AgNW/CF electrode showed 5000 cycles CS. This electrode suggested an innovative opening for researchers to make biosensing devices constructed on 3D hierarchical materials [79].

We deposited α-Fe_2O_3 on flat SS by LPD and studied the EC behavior of it. The nature of the α-Fe_2O_3 film on SS (flat) was porous (Fig. 7a). In 0.5 M, which was the optimized concentration of Na_2SO_3, the maximum value noted of Sc at 5 mVs^{-1} was 582 Fg^{-1} from CV. At 2 $mAcm^{-2}$, the highest value 179 Fg^{-1} of Sc was observed from the charge-discharge curve. LPD is a low-cost method, and hence, the electrodes fabricated by this method are affordable [80]. Similarly, using an LPD method, α-Fe_2O_3 was deposited on SS mesh. It was observed from SEM (Fig. 7b, c) that the mesh fibers were well covered with α-Fe_2O_3. The morphology showed a porous nature compact film that covered all fibers of SS mesh (Fig. 7d).

The highest Sc of α-Fe_2O_3 films on the mesh of SS estimated from GCD at 4 $mAcm^{-2}$ was 960 Fg^{-1} in 0.5 M Na_2SO_3, and that from CV at 5 mVs^{-1} was 548 Fg^{-1}. Figure 8a, b reveals the strong increase in Sc of the α-Fe_2O_3 thin film by altering the substrate. Hence, the α-Fe_2O_3 on SS mesh was more capable and flexible for SC with the high surface area [81]. Therefore, SS mesh was chosen in the fabrication of the α-Fe_2O_3/α-Fe_2O_3 FSS-SC device. The maximum Sc of the device obtained from CV at 5 mVs^{-1} was 1.6 Fg^{-1} [82].

Kang et al. synthesized the α-Fe_2O_3 electrode with abundant oxygen vacancies and uniformly aligned it on a carbon cloth through a hydrothermal method. By altering the temperature of reaction, the morphology can be adjusted. At 100–180 °C, reaction was performed, and the study revealed the optimized reaction temperature as 160 °C. Oxygen vacancies introduced into this optimized α-Fe_2O_3 (α-Fe_2O_3-Vo) electrode commendably increased the number of active sites that improved Sc along with the pseudocapacitive contribution. The maximum Ac and Sc of the α-Fe_2O_3-Vo electrode at 1 $mAcm^{-2}$ were 862.12 $mFcm^{-2}$ (~354.05 Fg^{-1}), which is 5.88 times

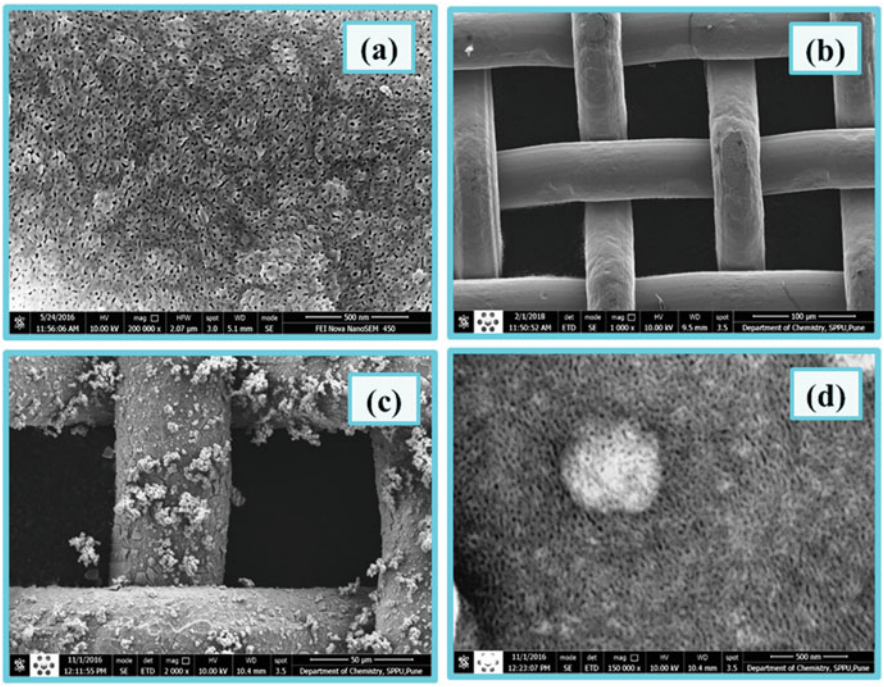

Fig. 7 FE-SEM of (**a**) α-Fe_2O_3 film on the flat SS substrate at 200,000×, (**b**) SS mesh at 1000×, (**c**) and (**d**) α-Fe_2O_3 mesh of SS at two magnifications: 2000× and 1,50,000×, respectively [80, 81]

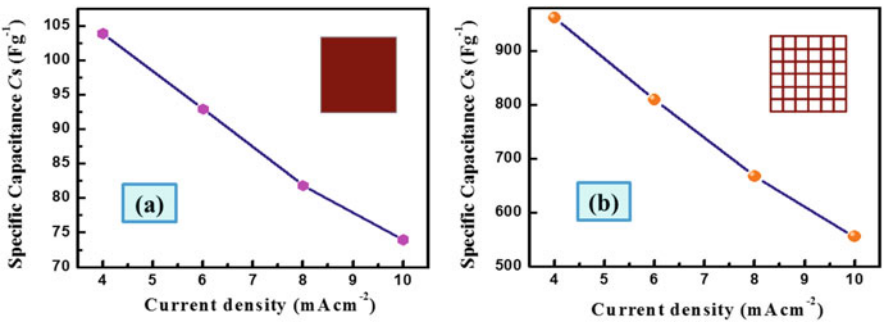

Fig. 8 Variation of Sc obtained by GCD versus CD of the α-Fe_2O_3 electrode on (**a**) flat and (**b**) mesh SS [81]

more than that of the α-Fe_2O_3 electrode (146.5 $mFcm^{-2}$). α-Fe_2O_3-Vo electrode exhibited CS with 51.23% retention after 2500 cycles. From Fig. 9, it can be seen that the capacitive-controlled process contributing to α-Fe_2O_3 is significantly greater than the α-Fe_2O_3-Vo electrode, indicating the dominant diffusion-controlled charge-storage mechanism for the α-Fe_2O_3-Vo. It can be noted that the surface-

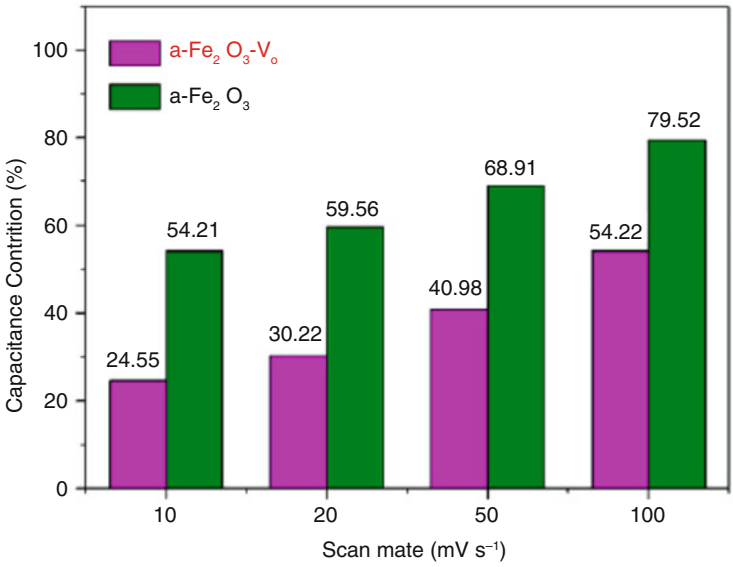

Fig. 9 The capacitance contribution at different scan rates for α-Fe_2O_3-Vo and α-Fe_2O_3 electrodes [83]

controlled Sc contributions lead the total Sc as the scan rate increases and the inner contribution decreases [83].

Yadav et al. reported the preparation of the iron oxyhydroxide film (ASD) by reduction using nitrate applying cathodic potential. Post-deposition annealing treatment at 300 and 500 °C in Ar (300-Ar and 500-Ar) and air environments (300-Air and 500-Air) converted γ-FeOOH to α-Fe_2O_3. Along with the phase, there was transformation of the structure from layered to rhombohedral. Observed morphology was of flake-like NS. From the EC tests, an Sc of 79.57 Fg^{-1} was detected for the phase with oxygen deficiency of α-Fe_2O_3 in the 0.5 M Na_2SO_4 electrolyte, in which pseducapacitive contribution was 45.1% and EDL contribution was 54.9% (Fig. 10). The enhanced Sc was 161.02 Fg^{-1} in 0.5 M Na_2SO_3 [84]. Table 2 represents the summary of the SP of the α-Fe_2O_3 electrode based on CV/GCD measurements in the three-electrode system.

Table 3 compiles the reported SP of the α-Fe_2O_3 symmetric device based on CV/GCD measurements. The enhancement in EC performance of Fe_2O_3 (as anode) can be achieved by making chemical modifications by varying the structure and improving the conductivity by means of several forms of carbon [92]. To increase the charge storage and transmission capabilities, core-shell is formed from metals and α-Fe_2O_3 [55, 93].

Zhao et al. applied low temperature hydrothermal and spray deposition (on copper foils) for the flexible nanostructured hybrid SC based on thin film MWNT formation as cathode and composite anode of α-Fe_2O_3/MWNT. The randomly

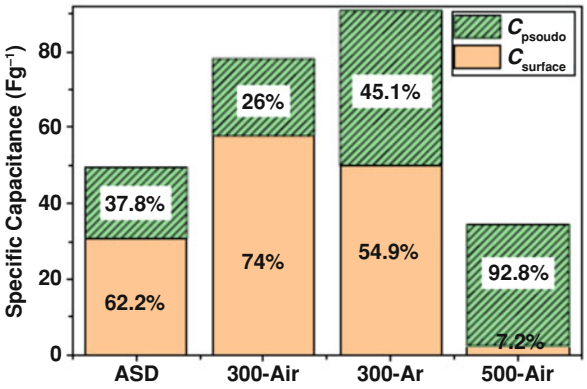

Fig. 10 Charge storage contribution obtained from Trasatti method of γ-FeOOH and air and argon annealed (α-Fe_2O_3) thin films [84]

oriented separate MWNTs showed an interconnected nanoporous structure (Fig. 11a) that proposed the accessibility of a high concentration of mixed ionic/electronic conducting routes. The α-Fe_2O_3 particles were spherical (diameter, ~100 nm) with narrow diameter distribution (SEM). In the presence of MWNTs, the size and shape of the α-Fe_2O_3 particles did not change (Fig. 11b, c). The CTAB has a major role in the preparation of monodisperse α-Fe_2O_3 particles. The α-Fe_2O_3/MWNT composite was formed by the hydrothermal method without CTAB showing a change from spherical to cuboidal or polyhedral morphology and a broadening of sizes (Fig. 11d, e). EC characterizations revealed the high Sc of 100 Fg^{-1} of the MWNT-α-Fe_2O_3 SC. From charge-discharge studies (potential range, 0–2.8 V), a high ED of 50 $Whkg^{-1}$ at a PD of 1000 Wkg^{-1} was observed. Insertion of MWNT penetrating inside networks of the monodisperse α-Fe_2O_3 nanosphere containing a film was the reason for this excellent EC performance [94].

Zhang et al. fabricated the α-Fe_2O_3/graphene nanocomposite by a solvothermal method and later gave treatment of annealing. The superb combination of small homogeneous crystalline α-Fe_2O_3 nanoparticles (~35–40 nm) and interconnected graphene sheets offers ion transport and fast electronic, which made this composite extraordinarily potential for fast energy storage. The maximum Sc calculated at 5 mVs^{-1} was 2310 Fg^{-1} [95].

Guan et al. reported iron oxide NP decorated on a 3D ultrathin graphite foam-carbon NT forest substrate (GF-CNT@Fe_2O_3). The graphite foam-CNT (GF-CNT) forest was prepared via a CVD method and iron oxide by ALD on the GF-CNT. The 3D graphite foam is covered by wire-shaped structures (Fig. 12a). The high magnified image inside inset (a) displays that after the ALD coating, the foam structure is maintained. From a magnified image (Fig. 12b, c), it was seen that CNTs were coated uniformly with NP and without aggregation. At CD 20 $mAcm^{-2}$, the maximum Ac was ~470.5 $mFcm^{-2}$, which was ~4 times greater than that of GF-CNT (~93.8 $mFcm^{-2}$). Also, excellent stability for 50,000 cycles for the electrode

Table 2 Summary of the SP of the α-Fe_2O_3 electrode (binder-free) based on CV/GCD measurements in the three-electrode system

Sr. no.	Deposition method	Morphology	Substrate	Electrolyte	Scan rate/CD	Maximum Ac/Sc	Ref.
1	Hydrothermal	1D NR	Carbon cloth	3 M LiCl	10 mVs^{-1}	64.5 Fg^{-1}	[85]
2	Cathodic electrodeposition	Irregular shaped grains	SS	0.5 M Na_2SO_4	5 mVs^{-1}	135 Fg^{-1}	[73]
3	Anodic deposition	NS	Nickel	1 M Li_2SO_4	5 mVs^{-1}	146 Fg^{-1}	[86]
4	Hydrothermal	Porous sheets	Nickel foam	1 M Li_2SO_4	0.36 Ag^{-1}	147 Fg^{-1}	[64]
5	Cathodic electrodeposition	Flake-like NS	SS foil	0.5 M Na_2SO_3	10 mVs^{-1}	161.02 Fg^{-1}	[84]
6	Electrodeposition	Porous NS	Nickel foil	1 M Li_2SO_4	3 Ag^{-1}	173 Fg^{-1}	[58]
7	SILAR	Porous irregular shaped grains	SS	1 M NaOH	5 mVs^{-1}	178 Fg^{-1}	[87]
8	SILAR	NP	SS	1 M Na_2SO_3	5 mVs^{-1}	187 Fg^{-1}	[88]
9	LPD	Porous	Flat SS	0.5 M Na_2SO_3	5 mVs^{-1}	202 Fg^{-1}	[80]
10	Electrodeposition	Fe_3O_4@Fe_2O_3 core-shell NRA	Titanium	1 M Na_2SO_4	5 mVs^{-1}	231.9 Fg^{-1}	[74]
11	Electrospin	Fibers	Nickel	1 M LiOH	1 mVs^{-1}	256 Fg^{-1}	[89]
12	Hydrolysis method	Fe_2O_3 NT	Carbon fabric	5 M LiCl	1.4 Ag^{-1}	257.8 Fg^{-1}	[65]
13	SILAR	Porous microstructure	SS	1 M Na_2SO_4	5 mVs^{-1}	283 Fg^{-1}	[68]
14	SILAR	Irregular size and shape NP	SS	1 M Na_2SO_4	5 mVs^{-1}	339 Fg^{-1}	[69]
15	Spray processing	Hollow porous micro-rods	SS	0.5 M Na_2SO_3	2 mVs^{-1}	346 Fg^{-1}	[90]
16	SILAR	Porous NP	SS	1 M Na_2SO_4	5 $mAcm^{-2}$	350 Fg^{-1}	[70]

17	Hydrothermal	Microspheres	Carbon cloth	1 M Na_2SO_4	1 $mAcm^{-2}$	862.12 $mFcm^{-2}$ (~354.05 Fg^{-1})	[83]
18	Spin coating	NW	FTO	0.5 M Na_2SO_3	5 mVs^{-1}	354.3 Fg^{-1}	[91]
19	Electrodeposition	Porous nano-crystalline	SS	1 M KOH	5 mVs^{-1}	487 F g^{-1}	[61]
20	Wet chemical process	Porous spinous	Iron foil	1 M Na_2SO_4	1 Ag^{-1}	524.6 Fg^{-1}	[72]
21	Electrodeposition	Semiporous	SS	1 M KOH	2.5 Ag^{-1}	540 Fg^{-1}	[60]
22	Seed-assisted hydrothermal	NF	Carbon cloth	1 M NaOH	1 $mAcm^{-2}$	145.9 $mFcm^{-2}$	[67]
23	Potentiostatic anodization	NT	Iron foil	1 M Li_2SO_4	20 mVs^{-1}	187 $mFcm^{-2}$	[62]
24	Potentiostatic anodization	NT	Iron foil	1 M Li_2SO_4	3 $mAcm^{-2}$	298 $mFcm^{-2}$	[63]
25	Chemical oxidation method	NS	Iron foil	1 M Na_2SO_3	10 mVs^{-1}	312 $mFcm^{-2}$	[66]
26	Hydrothermal (additional plasma treatment)	NR	Carbon cloth	1 M Na_2SO_4	1 $mAcm^{-2}$	340 $mFcm^{-2}$	[77]
27	Hydrothermal	Carbon cloth	Carbon cloth	1 M KOH	4 $mAcm^{-2}$	500 $mFcm^{-2}$	[76]
28	Hydrothermal	Nickel foam	Nickel foam	1 M LiOH	1 $mAcm^{-2}$	681 $mFcm^{-2}$	[78]
29	Hydrothermal	CFP	CFP	2 M KOH	2 Ag^{-1}	908 Fg^{-1}	[71]
30	LPD	SS mesh	SS mesh	0.5 M Na_2SO_3	4 $mAcm^{-2}$	960 Fg^{-1}	[81]
31	Hydrothermal	Carbon cloth	Carbon cloth	1 M Na_2SO_4	2 $mAcm^{-2}$	(1660 Fg^{-1})	[75]

Table 3 SP of the α-Fe_2O_3 symmetric device based on CV/GCD measurements

Sr. No.	Method for deposition of electrodes of the symmetric device	Electrolyte	Substrate	Maximum Ac/Sc	Scan rate/CD	CS (%)	ED and PD	Ref.
1	LPD	PVA-KOH	Mesh SS	1.6 Fg^{-1}	5 mVs^{-1}	76 (1000 cycles)	0.063 $Whkg^{-1}$ and 225 Wkg^{-1}	[82]
2	SILAR	CMC-Na_2SO_4	Flexible SS	21 Fg^{-1}	5 mVs^{-1}	88 (1000 cycles)	~8 $Whkg^{-1}$ and ~10 $KWkg^{-1}$	[70]
3	Hydrothermal	(PVA)-H_3PO_4	Carbon cloth	16.82 Fcm^{-3}	2 $mAcm^{-2}$	–	8.74 $mWhcm^{-3}$ and 27.6 $mWcm^{-3}$	[75]

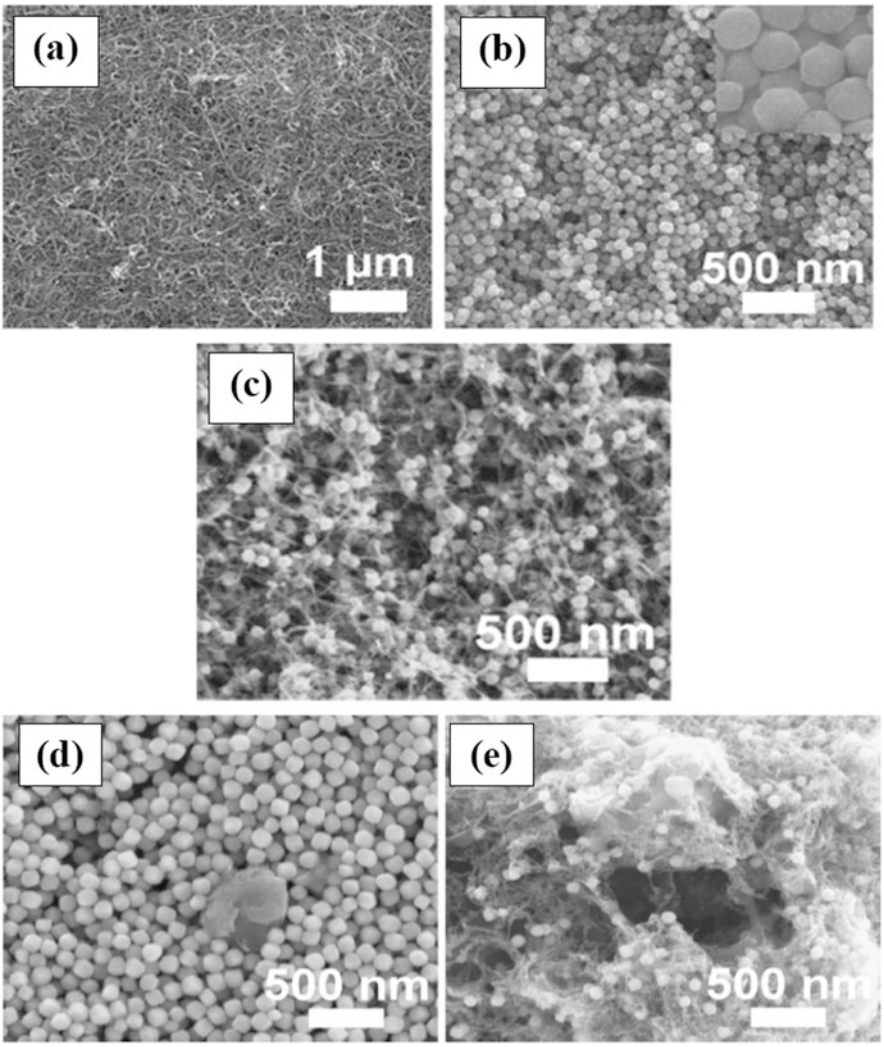

Fig. 11 SEM of the spray-deposited top surface of (**a**) a purified MWNT film, (**b**) α-Fe_2O_3 film, and (**c**) α-Fe_2O_3/MWNT composite film; (**d**) α-Fe_2O_3 and (**e**) α-Fe_2O_3/MWNT composite synthesized by the hydrothermal method without CTAB [94]

was recorded. The GF-CNT has advantages due to its good mechanical stability, flexibility, lightweight, and conductivity. Moreover, ALD is effective in emerging uniform material. This is particularly for substrates having complex morphology and high aspect ratio [96].

In portable electronic devices, electrodes need to withstand deformations maintaining their functioning. Hence, flexible electrodes play an important role in this respect. Cheng et al. prepared a 3D CNT@Fe_2O_3 sponge electrode with a porous

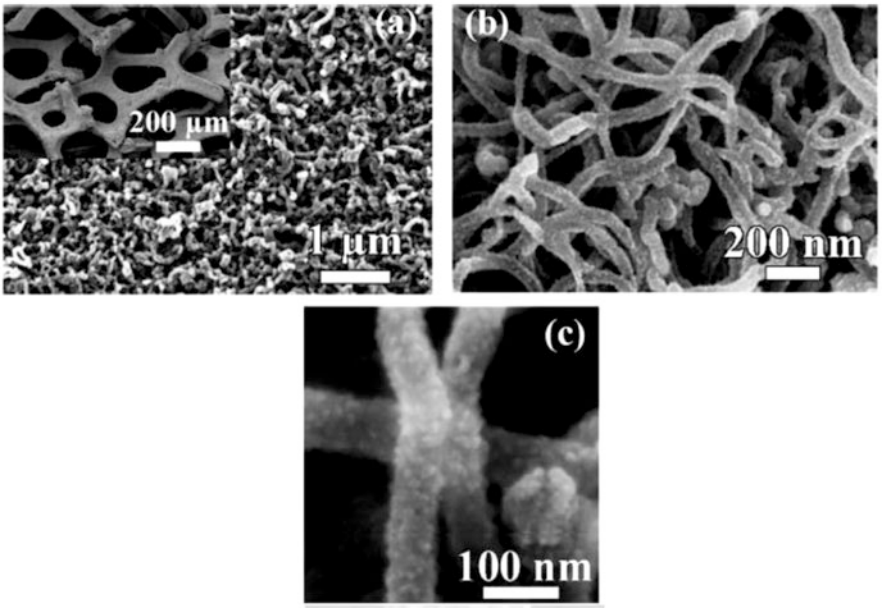

Fig. 12 SEM of GF-CNT@Fe_2O_3 at three different scales (**a**–**c**) [96]

structure by a hydrothermal method. This comprised a conductive CNT network, with coating of Fe_2O_3 nano-horns. The highest Sc from CV for the CNT@Fe_2O_3 sponge at 5 mVs^{-1} is about 296.3 Fg^{-1} obtained. The CNT@Fe_2O_3 sponge in deformed state maintained higher than 90% of the original Sc under a 70% compressive strain [97]. Raut et al. studied preparation of MWNTs, Fe_2O_3, and Fe_2O_3/MWNTs on SS. The coating method of "dip and dry" was carried out for MWNTs and the SILAR for deposition of Fe_2O_3. Uniform interconnected porous morphology was observed for MWNTs; aggregation of Fe_2O_3 NP was seen for the Fe_2O_3 thin film and porous nature with Fe_2O_3 NP decorated on MWNT uniformly for the Fe_2O_3/MWNT hybrid thin film. Scs of MWNTs, Fe_2O_3, and Fe_2O_3/MWNT electrodes calculated from CV at 5 mVs^{-1} revealed values of 81, 187, and 431 Fg^{-1}, respectively. From this, it confirmed that the Fe_2O_3/MWNT electrode showed the highest Sc. Also this hybrid electrode presented a high ED of 38 $Whkg^{-1}$ with a PD of 800 Wkg^{-1} [88]. Li et al. synthesized α-Fe_2O_3 porous nanospheres on the cloth of ACC (α-Fe_2O_3@ACC) through a hydrothermal method. The α-Fe_2O_3@ACC composite electrode at 1 $mAcm^{-2}$ displayed an Sc of about 2775 $mFcm^{-2}$ and at 2 mVs^{-1} about 4755 $mFcm^{-2}$. The symmetric device fabricated from two pieces of the α-Fe_2O_3@ACC electrodes showed a wide (0–1.8 V) potential window. A maximum Ac found at 1 $mAcm^{-2}$ was about 1565 $mFcm^{-2}$ and revealed good CS with 95% retention after 4000 cycles. This symmetric device delivered a volumetric energy density of 9.2 $mWhcm^{-3}$ at a PD of 12 $mWcm^{-3}$ and an ED of 4.5 $mWhcm^{-3}$ at a PD of 204 $mWcm^{-3}$ [98].

Due to chemical stability, high specific surface area, and high conductivity, VACNTs are considered to be perfect for electrode materials. Moreover, CNTs in the arrays promote abundantly of 1D conductive paths well-orientated to move the electrons in the similar direction. They also promote the transport of intermediate reactants and electrolyte ions. Zhang et al. synthesized Fe_2O_3-decorated millimeter-long VACNT anode materials for asymmetric SC by using two steps: impregnation using supercritical CO_2 and then annealing. Fe_2O_3/VACNT composites revealed a high Sc of 248 Fg^{-1} at 8 Ag^{-1}. Asymmetric SC is fabricated with NiO/VACNTs as cathode and Fe_2O_3/VACNTs as anode in 2 M KOH (aqueous). This device showed ED and PD of 137.3 $Whkg^{-1}$ and 2.1 $kWkg^{-1}$, respectively. It retained with ED and PD of 102.2 $Whkg^{-1}$ and 39.3 $kWkg^{-1}$, respectively. After 5000 cycles, Cs was 89.2% at 8 Ag^{-1} [99].

Huang et al. reported the Fe_2O_3 network of nanosized wires with a transparent film (FNW-TF) made at the interface of water-air through a bioinspired gas-liquid diffusion method. It was observed that the film was transparent with a large-area porous NW structure. Moreover, it can be moved onto any substrate of interest. To improve the EC stability, Fe_2O_3 NW were enveloped in shells of graphene (FNW@Gr-TF) for use as transparent electrodes due to the distinguishing graphene properties. Electrode material's stability is significantly increased in KOH reported 92.3% initial capacitance after 10,000 cycles. Due to the graphene coating, the electro-active material is prevented from getting dissolved in the electrolyte. The Ac of the symmetric device from CV was 3.3 $mFcm^{-2}$ at 10 mVs^{-1}, which was minimum hundred times greater than transparent devices with TF based on planar CVD graphene. Moreover, the symmetric device has a PD of 191.3 Wcm^{-3}, which was more than electrolytic capacitors, and an ED of 8 $mWhcm^{-3}$, which was similar to that of thin-film lithium-ion batteries [100]. The developed α-Fe_2O_3/graphene oxide paper (GP) negative electrode for high energy SCs was reported by Xie et al. This electrode was made by an exfoliation method. The Ac of α-Fe_2O_3/GP from GCD at 5 $mAcm^{-2}$ was 3.08 Fcm^{-2}, which was almost 14 times of the Fe_2O_3/CP (0.22 Fcm^{-2}). Ninety-five percent of initial capacitance was retained even after 5000 cycles for the α-Fe_2O_3/GP hybrid electrode [101].

Pourfarzad et al. synthesized α-Fe_2O_3/graphene hydrothermally on nickel foam as negative electrode for supercapacitive energy storage application [102]. The EC characterizations in the three-electrode system were measured in 3 M KOH. From the charging-discharging studies, it was confirmed that storage of charge was due to quasi-capacitive reactions (battery and pseudocapacitive type of materials can be differentiated with the help of EC signatures and kinetics analysis quantitatively [103]). For this composite, the calculated Sc was 420 Fg^{-1} at 1 Ag^{-1}. The maximum PD and ED were 91.5 $kWkg^{-1}$ and 101 $Whkg^{-1}$, respectively, with a CS of 82.5% capacitance retention after 5000 cycles. Tables 4 and 5 summarize the SP of the carbon-based α-Fe_2O_3 thin film electrode based three electrode and symmetric SC device measured by CV/GCD measurements.

Recently, Fe_3O_4 is becoming a more interesting SC electrode material due to its moderate electrical conductivity, high Sc, earth abundance, and environmental friendliness [104]. Chung et al. carried out the novel synthesis of highly crystalline

Table 4 SP of the carbon-based α-Fe_2O_3 thin film electrode in the three-electrode system based on CV/GCD measurements

Sr. no.	Deposition method	Substrate	Material and morphology	Electrolyte	Scan rate/CD	Maximum Ac/Sc	Ref.
1	Air-solution interface reactions	ITO/PET	FNW@Gr-TF	2 M KOH	50 mVs^{-1}	5 $mFcm^{-2}$	[100]
2	EC oxidation (exfoliation)	CP	Fe_2O_3/CP	–	5 $mAcm^{-2}$	0.22 Fcm^{-2}	[101]
3	EC oxidation (exfoliation)	GP	Fe_2O_3/GP	–	5 $mAcm^{-2}$	3.08 Fcm^{-2}	[101]
4	Hydrothermal	CNT sponge	CNT@Fe_2O_3 nano-horns	2 M KCl	5 mVs^{-1}	296.3 Fg^{-1}	[97]
5	Hydrothermal	Nickel foam	Fe_2O_3/graphene	3 M KOH	1 Ag^{-1}	420 Fg^{-1}	[102]
6	(Dip + dry) and SILAR	SS	Fe_2O_3/MWCNT	1 M Na_2SO_3	5 mVs^{-1}	431 Fg^{-1}	[88]
7	Solvothermal	Ni foam	α-Fe_2O_3 (NP)/graphene (NS)	6 M KOH	5 mVs^{-1}	2310 Fg^{-1}	[95]
8	CVD and ALD	GF-CNT	GF-CNT@Fe_2O_3 nanocrystalline	2 M KOH	20 $mAcm^{-2}$	470.5 $mFcm^{-2}$	[96]
9	Hydrothermal	ACC	Porous Fe_2O_3@ACC nanospheres	3 M $LiNO_3$	2 mVs^{-1}	4755 $mFcm^{-2}$	[98]

Table 5 SP of the carbon-based α-Fe_2O_3 symmetric device based on CV/GCD measurements

Sr. no.	Deposition methods for electrodes of the symmetric device	Material and Substrate	Electrolyte	Scan rate/CD	Maximum Ac/Sc	ED and PD	CS (%)	Ref.
1	Hydrothermal and spray deposition	(α-Fe_2O_3)/MWNT and copper foil	1 M $LiClO_4$ in ethylene carbonate/dimethyl carbonate	2 mVs^{-1}	100 Fg^{-1}	50 $Whkg^{-1}$ and 1000 Wkg^{-1}	600 cycles	[94]
2	Air-solution interface reactions	FNW@Gr-TF and ITO/PET	PVA/PAAS/KOH gel	10 mVs^{-1}	3.3 $mFcm^{-2}$	8 $mWhcm^{-3}$ and 191.3 $mWcm^{-3}$	78.2% (5000 cycles)	[100]
3	Hydrothermal	Fe_2O_3@ACC	3 M $LiNO_3$ aqueous	1 $mAcm^{-2}$	1565 $mFcm^{-2}$	9.2 $mWhcm^{-3}$ and 12 $mWcm^{-3}$	95% (4000 cycles)	[98]

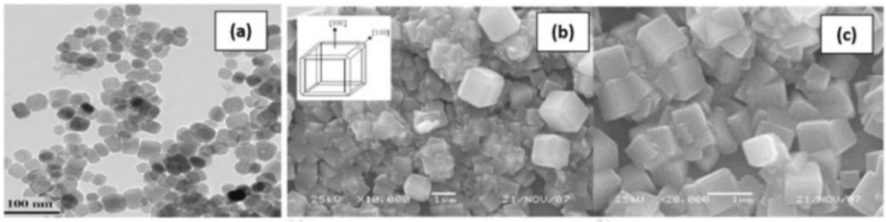

Fig. 13 (**a**) TEM of the as-prepared particles, (**b**) and (**c**) SEM images of the Fe_3O_4 film with different magnifications [106]

and pure in cellular nanoform Fe_3O_4 thin film through EC green rust deposition and later oxidation. This method made the Fe_3O_4 thin film on the Pt substrate with 350–950 nm mean pore diameter, 30–150 nm mean wall thickness, and ~3 μm film thickness. The maximum Sc obtained from EC studies at 20 mVs^{-1} was 105 Fg^{-1} [105]. Chen et al. prepared the Fe_3O_4 film on an SS foil by a hydrothermal process. The dense Fe_3O_4 film comprised octadecahedron (average diameter, ~500 nm) morphology (Fig. 13). The typical pseudocapacitive behavior was observed in a CV study in 1 M Na_2SO_3 solution. The Sc value was 118.2 Fg^{-1} at the 6 mA current with a capacity retention of 88.75% after 500 cycles [106].

Pang et al. fabricated electrodes of magnetite thin films in nanoform. First, the co-precipitation method was used to prepare the stable colloidal suspension of Fe_3O_4 NPs. Then thin films were made by drop coating on SS plates. After this, the films were subjected to calcination at different temperature and atmosphere. From a morphological study, it was seen that a nanoparticulate with porous nature films exhibited a particle size of 5–31 nm. EC properties were checked for these films in 1 M Na_2SO_4 solution. The highest Sc (at 50 mVs^{-1}) calculated of thin films made under optimized conditions (magnetite loading of 0.4 $\mu mol/cm^2$ and calcined at 300 °C in nitrogen) was 82 Fg^{-1} [107].

Hydrothermal method followed by post-annealing was used by Li et al. for synthesizing the Fe_3O_4 NR film on a Ti foil. For CV analysis, a 2.5 M Li_2SO_4 (aqueous) electrolyte was used. Sc determined at 0.5 mVs^{-1} was 191.35 Fg^{-1}. The process of Fe_3O_4 in Li_2SO_4 was related to inserting of Li^+ ion in spinel Fe_3O_4 to form $Li_xFe_3O_4$ based on the use of the Fe^{2+}/Fe^{3+} redox couple. The Li^+ insertion into Fe_3O_4 was tested by examining the XRD pattern and XPS spectrum. From the CVs (Fig. 14), it was concluded that for a moderate scan rate, Li^+ insertion is almost half of the stored charge is not capacitive. At a fast or slow scan rate, the charge storage difference for two different mechanisms is more noticeable due to the quick charge/discharge features related with capacitive processes. The quantitative analysis disclosed the fact that both diffusion-controlled contribution (Li^+ insertion) and capacitive are responsible for the charge storage. It was believed that pseudocapacitive electrodes are responsible for storing charge on surface and nearby area. In contradiction to this, it was proved in this work that the Fe_3O_4 NR film stored energy through uptake of Li in more large amount at high scan rates,

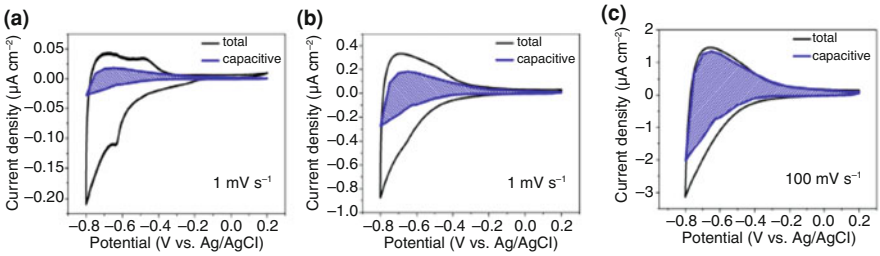

Fig. 14 CV of Fe_2O_3 NR film tested in 2.5 M Li_2SO_4 at different scan rates with the shaded area signifying the curve containing capacitive contribution [108]

which related conversion (topotactic) to $Li_xFe_3O_4$ without change in phase [108]. Table 6 shows the comparison of SP of Fe_3O_4 in the form of thin film electrode based on CV/GCD measurements in the three-electrode system.

Shi et al. prepared Fe_3O_4/reduced graphene oxide nanocomposites. Here, a solvothermal method was used for growing iron ferrite NP and rGO in one step. In this nanocomposite, Fe_3O_4 NP were decorated on rGO sheets. Further, this nanocomposite was sprayed on a carbon paper. In the 1 M KOH electrolyte, EC characterizations were performed. As compared to rGO and Fe_3O_4 NP, their nanocomposite showed higher Sc. Also, different Fe_3O_4:rGO weight ratios in Fe_3O_4/rGO nanocomposites were studied. The highest Sc found for the Fe_3O_4/rGO nanocomposites with 73.5 wt% Fe_3O_4 NP was 480 Fg^{-1} at 5 Ag^{-1} from GCD. The analogous ED was 67 $Whkg^{-1}$ at a PD of 5506 Wkg^{-1}. Interestingly, Fe_3O_4/rGO composites in nanoform exhibited no decrease in Sc after 1000 cycles [109].

Using a two-step technique, nanoporous ultrathin Fe_3O_4-CNS was reported by Liu et al., which shows a high surface area of 229 m^2g^{-1}. A high Sc of 163.4 Fg^{-1} at 1 Ag^{-1} of NS electrodes was obtained due to their distinctive morphology. The charge transfer increases significantly for the porous interconnected structure due to larger interfaces and considerably decreases the ion/electron diffusion pathways due to the thickness of ultra-small NS. Also, carbon nanopillars between NS layers contribute to high conductivity [110]. Fu et al. reported an outstanding "necklace" structure in which Fe_3O_4 spherulite "beads" were strung along carbon nanofibers (CNF) by a hydrothermal method (Fig. 15). This necklace was sprayed on SS substrates to fabricate electrodes. CNFs confirm the electrons flow to the current collector in the electrode and along the strings of the necklace. Good strain tolerance and high surface area were noted for CNFs decorated with Fe_3O_4 beads with <300 nm dimension. Fe_3O_4 is completely utilized as its bead on CNF is from its center itself. The SC electrodes at 1 Ag^{-1} showed a high Sc of 225 Fg^{-1} [111].

O'Neill et al. synthesized mesoporous composite electrodes of 1D Fe_3O_4/FeOOH nanowires by spray deposition on SS, which were entangled with MWNT. The Sc calculated was 300 Fg^{-1}, in aqueous Na_2SO_3 at 2 mVs^{-1} [112]. Sun et al. fabricated the C@Fe_3O_4 electrode, which was used as negative electrode for flexible fiber-shaped asymmetric SC. This electrode was synthesized via a two-

Table 6 SP of the Fe_3O_4 thin film electrode based on CV/GCD measurements in the three-electrode system

Sr. no.	Deposition method	Substrate	Morphology	Electrolyte	Scan rate/CD	Maximum Sc (Fg^{-1})	Ref.
1	Co-precipitation Drop coating	SS plates	NP and porous	1 M Na_2SO_4	50 mVs^{-1}	82	[107]
2	EC deposition	Pt	Nanosized cellular	1 M Na_2SO_4	20 mVs^{-1}	105	[105]
3	Hydrothermal	SS foil	Octadecahedron	1 M Na_2SO_3	6 mA	118.2	[106]
4	Hydrothermal	Ti	NR	2.5 M Li_2SO_4	0.5 Vs^{-1}	191.35	[108]

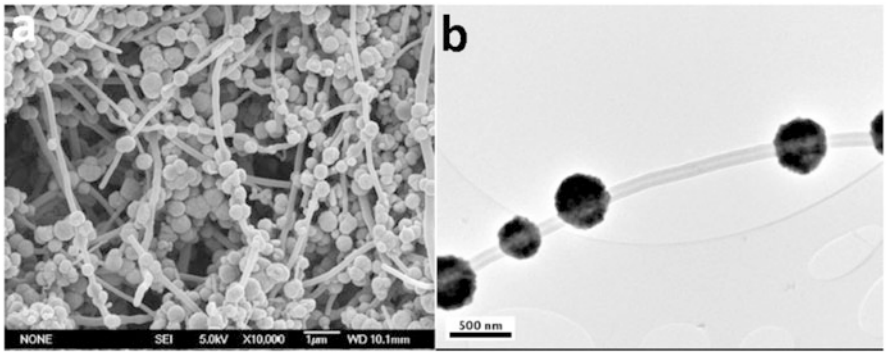

Fig. 15 SEM (**a**) and TEM (**b**) images of the as-prepared Fe_3O_4/CNF necklaces [111]

step electrodeposition followed by heating. In the first step, the Fe_3O_4 precursor was electrodeposited directly on the SS fiber, which revealed an NS structure. The second step consists of electrodeposition of PEDOT and heat treatment. Hence, a carbon layer was uniformly coated on Fe_3O_4 NS. The EC performance in the three-electrode system with 1 M LiCl (aqueous) provided an Sc of 127 $mFcm^{-2}$ for 1 mA from GCD [113]. Table 7 compares SP of the C-based Fe_3O_4 electrode as thin film based on CV/GCD measurements in the three-electrode system.

5 Iron Sulfide

Among the seven types of iron sulfides (cubic FeS, pyrrhotite, mackinawite, greigite, troilite, marcasite, and iron pyrite), the most stable phase and abundant is pyrite. Pyrite includes Fe^{2+} and S^{2-} and it is FCC in structure. Mostly for applications of battery and photovoltaics this phase is studied. Troilite and greigite have applications for energy storage. For pseudocapacitor applications, there is less literature on FeS as cathode electrodes.

In lithium primary and secondary batteries, iron sulfides are tested due to low cost and availability in nature [114]. Also iron sulfide with carbon composite (FeS/C) has potential application as anode material in LIBs [115].

When iron sulfide is considered as electrode material for SCs, there are very few reports. Karade et al. synthesized for the first time iron sulfide (FeS) by SILAR on SS substrates and the fabricated flexible symmetric SC device [116]. Recently, layered and tunnel structures have attracted great attention for the high performance of pseudocapacitors. Charge storage of electrodes is enhanced when such structures are used ,which provide better channel for extraction and ion insertion. Javed et al. synthesized CP-supported FeS_2 by a hydrothermal method. This electrode without binder exhibited an Sc of 852.3 Fg^{-1} in the LiCl liquid electrolyte from CV at 10 mVs^{-1} with admirable stability. The fabricated solid-state symmetric flexible

Table 7 SP of the carbon-based Fe_3O_4 thin film electrode based on CV/GCD measurements in the three-electrode system

Sr. no.	Deposition method	Substrate	Material and morphology	Electrolyte	Scan rate/CD	Maximum Sc ($F\ g^{-1}$)	Ref.
1	Solvothermal	–	Fe_3O_4-carbon NS Ultrathin, nanoporous	1 M Na_2SO_3	1 Ag^{-1}	163.4	[110]
2	Hydrothermal	SS	Fe_3O_4/CNF necklace structure	3 M KOH	1 Ag^{-1}	225	[111]
3	Spray deposition	SS	Fe_3O_4/FeOOH NW	0.5 M Na_2SO_3	2 mVs^{-1}	300	[112]
4	Solvothermal and spray deposition	Carbon paper	Fe_3O_4/rGO NP on NS	1 M KOH	5 Ag^{-1}	480	[109]

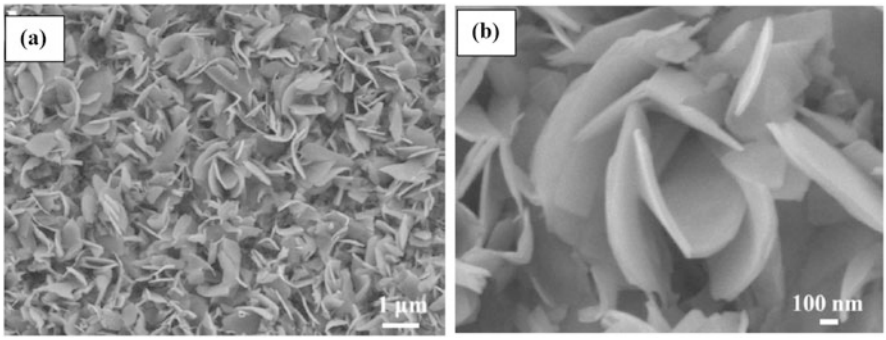

Fig. 16 FE-SEM images of (**a**) the rGO/FeS composite on an iron foil and (**b**) enlarged image of it [119]

device showed highest Sc of 484 Fg^{-1} from CV at 5 mVs^{-1}. FeS_6 octahedrons are arranged in a network-like structure, which forms a FeS_2 orthorhombic structure, where six S atoms surround the central Fe atom. This offers fast transmission of electrons and diffusion channel required for ion de-intercalation and intercalation provided by tunnels along the c direction during GCD. Hence, excellent EC performance was observed in this work [117].

Upadhyay et al. synthesized iron sulfide for 4, 7, and 12 h by a hydrothermal method on SS. Morphology of the material and EC performance were dependent on synthesis time. Synthesis time of 4 h showed formation of randomly oriented nanowires, 7 h as porous cuboidal and 12 h as smooth/dense cuboidal morphology, respectively. The EC tests performed between 0 and −0.95 V showed a maximum Ac of 730 $mFcm^{-2}$ from GCD at 1 $mAcm^{-2}$ for the electrode material synthesized for 7 h. This material exhibited very good CS, with 95% of the Sc retention after 2000 GCD cycles [118]. Zhao et al. reported the synthesis of the porous composite of rGO and iron sulfide on an iron foil by a hydrothermal method. In this synthesized electrode, a Fe foil was the iron source of FeS, the reductant of GO, and also the current collector. The morphology observed was a porous structure resembling a rose and between FeS interconnections (Fig. 16), which considerably enhanced large area and the speedy transport and ion diffusion of ions and electron transport. The electrode of rGO-iron sulfide revealed a high Sc of 900 $mFcm^{-2}$ (300 Fg^{-1}) at 10 $mAcm^{-2}$ and a higher CS of 97.5% capacity retention after 2000 cycles (in 2 M KOH). Ac found at a charging-discharging CD of 20 $mAcm^{-2}$ was 711.11 $mFcm^{-2}$ for rGO/FeS, which was higher than that for pure FeS on a Fe foil (344.44 $mFcm^{-2}$) [119].

6 Iron Selenide

In comparison with iron oxides and iron sulfides, iron selenides' EC performance is superior. This is because selenium has lower electronegativity than oxygen and sulfur. The weaker electronic and chemical bonding between selenium atoms due to these electronic states may change, allowing for more active performance in the EC reaction. Iron selenides $FeSe_2$ and Fe_7Se_8 are applied in sodium-ion batteries [120]. When solid-state SC applications are considered, there is very limited literature on iron selenide as electrode material. Two phases are present for iron diselenide, $FeSe_2$ and α-FeSe, and its purity after synthesis is challenging.

Santoshkumar et al. reported a submicron-sized flower-like iron selenide ($FeSe_2$) nanostructure synthesized using a KCl-templated solvothermal method and inert atmosphere used for calcination. From Fig. 17, it can be seen that the as-prepared sample's nature is cubic (a and b), which changed to flower-like nanostructures of 2D NF consisting of irregular platelets (c and d). This contained hollow cavities giving porosity that provided adhesion, which resulted in high stability. Figure 17e, f shows that even after 12 h of ultra-sonication, morphology was retained, indicating the stability of the material. This $FeSe_2$ electrode proved to be an excellent anode material for LIBs and SCs [121]. This flower-like $FeSe_2$ nanostructure showed an excellent Sc of 362.1 Fg^{-1} at 1 Ag^{-1} from GCD along with good CS after 5000 cycles.

Pandit et al. synthesized iron selenide with a porous NF surface through SILAR. This iron selenide electrode exhibited highest Sc of 671.7 Fg^{-1} at 2 mVs^{-1} from CV, 434.6 Fg^{-1} at 2 $mAcm^{-2}$ from GCD analysis and 91.9% CS for 4000 cycles (in 0.5 M NaOH electrolyte). Also, a bendable symmetric solid-state SC cell was fabricated, which showed a remarkable PD of 5.1 kW kg^{-1}. Along with very good tolerance for deformation, a demonstration of practical of running a small fan indicated ability for advanced energy storage applications. The best capacitance found for this cell was 65.3 Fg^{-1} at 2 mVs^{-1} [122]. Tian et al. fabricated the iron selenide/graphene aerogel ($FeSe_2$/GA) anode by a facile solvothermal method. Morphology of the $FeSe_2$/GA composite showed a structure comprising $FeSe_2$ NP uniformly dispersed in GA NS, which effectively forms an efficient conducting network of $FeSe_2$ nanoparticles. The EC testing exhibited a maximum Sc of 940 Fg^{-1} from GCD at 1 Ag^{-1} in 1 M KOH [123].

7 Iron Telluride

Bommineedi et al. prepared iron telluride-based mixed phase thin films on SS by SILAR. Structural studies indicated the growth of mixed phase of FeTe: Fe_2TeO_5. Surface morphology of iron telluride revealed uniform distribution of spherical nanopebbles with mean particle size distribution calculated as 30 nm. The EC characterizations depicted an Sc of 591 Fg^{-1} (166 $mFcm^{-2}$) at 3 mVs^{-1} from CV

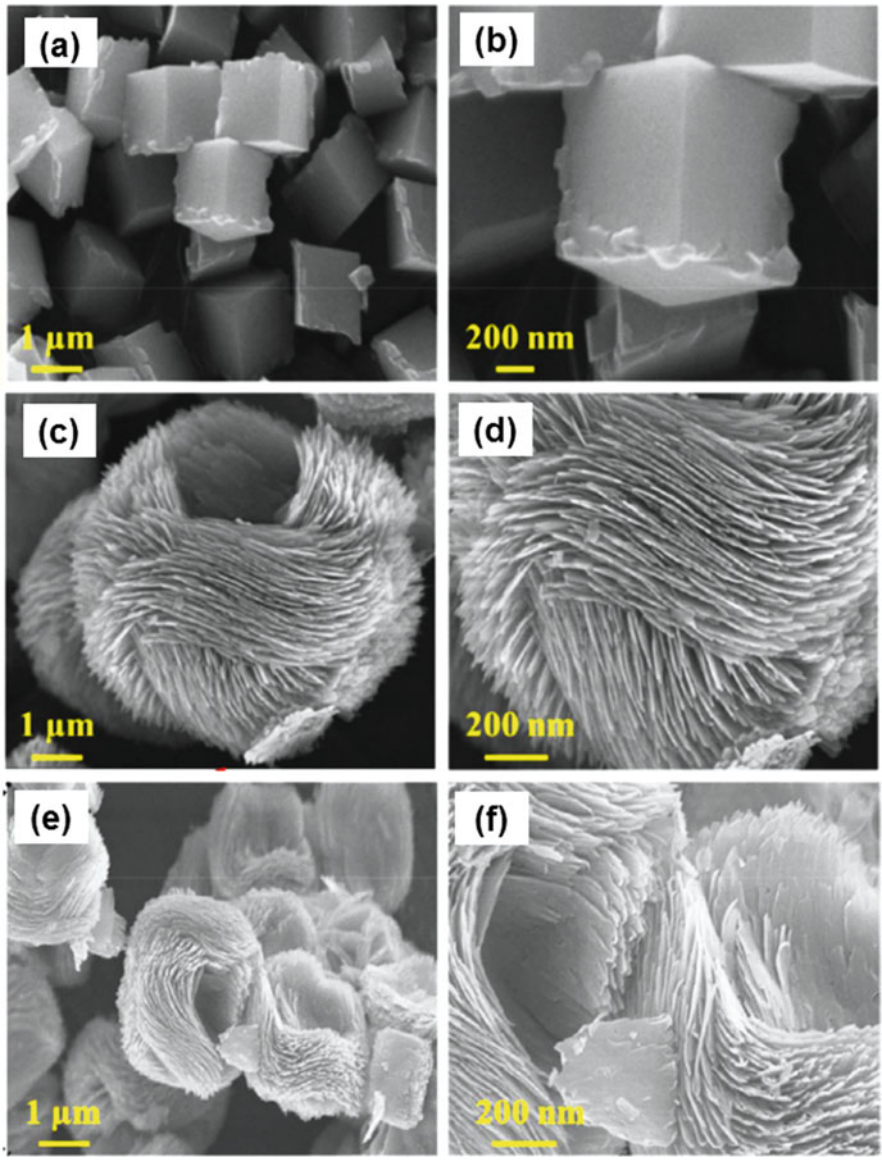

Fig. 17 FE-SEM images of flower-like FeS_2 nanostructures at low and high magnification of as prepared (**a**) and (**b**); after calcination (**c**) and (**d**) and after ultra-sonication (**e**) and (**f**), respectively [121]

and 107 Fg^{-1} (30 $mFcm^{-2}$) at 0.4 $mAcm^{-2}$ from GCD in the NaCl electrolyte. The electrode's EC stability study showed 66% capacitive retention at 100 mVs^{-1} for 2000 CV cycles [124].

8 Summary and Future Outlook

Wet chemical methods are more useful due to their economical and ecological nature and ability for large-scale manufacturing with low cost when compared to physical methods. Hence, chemically deposited iron chalcogenides are very much useful as electrode materials in the fabrication of SCs. Among iron chalcogenides, iron oxides form a huge and important class of electrode materials. In the future, there is a vast scope in fabricating and developing electrode materials using iron chalcogenides. For this, iron chalcogenides have to be deposited with advanced growth mechanisms. New strategies can be applied for changes in deposition methods in order to achieve various outstanding morphologies that can uplift the EC performance of electrode materials. Novel materials can be prepared by combining iron chalcogenides with the new emerging carbon materials to improve the efficiency of SCs. The combination of such novel materials can be tried on different types of flexible substrates to increase the flexibility of the fabricated SC device. Other approach can be the use of many electrolytes for superior stability and good charge transport.

References

1. R. Liu, J. Duay, S.B. Lee, Heterogeneous nanostructured electrode materials for electrochemical energy storage. Chem. Commun. (Camb.) **47**(5), 1384–1404 (2011)
2. M.A. Desai et al., An investigation of chemical and electrochemical conversion of SILAR grown Mn_3O_4 into MnO_2 thin films. J. Environ. Manag. **299**, 113564 (2021)
3. M.A. Desai et al., SILAR grown K^+ and Na^+ ions preinserted MnO_2 nanostructures for supercapacitor applications: A comparative study. Energy Fuel **35**(5), 4577–4586 (2021)
4. A. Afif et al., Advanced materials and technologies for hybrid supercapacitors for energy storage – A review. J. Energy Storage **25**, 100852 (2019)
5. A. Basu et al., CO_2 laser direct written MOF-based metal-decorated and heteroatom-doped porous graphene for flexible all-solid-state microsupercapacitor with extremely high cycling stability. ACS Appl. Mater. Interfaces **8**(46), 31841–31848 (2016)
6. D.P. Dubal et al., Towards flexible solid-state supercapacitors for smart and wearable electronics. Chem. Soc. Rev. **47**(6), 2065–2129 (2018)
7. C.V.V. Muralee Gopi et al., Recent progress of advanced energy storage materials for flexible and wearable supercapacitor: From design and development to applications. J. Energy Storage **27**, 101035 (2020)
8. S. Palchoudhury et al., Flexible supercapacitors: A materials perspective. Front. Mater. **5** (2019)
9. K. Jost, G. Dion, Y. Gogotsi, Textile energy storage in perspective. J. Mater. Chem. A **2**(28), 10776 (2014)
10. W. Zeng et al., Fiber-based wearable electronics: A review of materials, fabrication, devices, and applications. Adv. Mater. **26**(31), 5310–5336 (2014)
11. A. González et al., Review on supercapacitors: Technologies and materials. Renew. Sust. Energ. Rev. **58**, 1189–1206 (2016)
12. S.M. Chen et al., Recent advancements in electrode materials for the high-performance electrochemical supercapacitors: A review. Int. J. Electrochem. Sci. **9**(8), 4072–4085 (2014)

13. S.A. Haladkar et al., Assessment of ecologically prepared carbon-nano-spheres for fabrication of flexible and durable supercell devices. J. Mater. Chem. A **6**(16), 7246–7256 (2018)
14. B.E. Conway, *Electrochemical Supercapacitors: Scientific Fundamentals and Technological Applications* (Springer US, 1999)
15. F. Yao, D.T. Pham, Y.H. Lee, Carbon-based materials for lithium-ion batteries, electrochemical capacitors, and their hybrid devices. ChemSusChem **8**(14), 2284–2311 (2015)
16. A. Burke, Ultracapacitors: Why, how, and where is the technology. J. Power Sources **91**(1), 37–50 (2000)
17. N.S. Padalkar et al., Mesoporous nanohybrids of 2D Ni-Cr-layered double hydroxide nanosheets pillared with polyoxovanadate anions for high-performance hybrid supercapacitor. Adv. Mater. Interfaces **9**(1), 2101216 (2021)
18. J. Theerthagiri et al., Recent advances in metal chalcogenides (MX; X = S, Se) nanostructures for electrochemical supercapacitor applications: A brief review. Nanomaterials (Basel) **8**(4) (2018)
19. B.K. Kim et al., Electrochemical supercapacitors for energy storage and conversion, in *Handbook of Clean Energy Systems*, (Wiley, Chichester, 2015), pp. 1–25
20. Y. Dahiya et al., Modified transition metal chalcogenides for high performance supercapacitors: Current trends and emerging opportunities. Coord. Chem. Rev. **451**, 214265 (2022)
21. C.D. Lokhande, D.P. Dubal, O.S. Joo, Metal oxide thin film based supercapacitors. Curr. Appl. Phys. **11**(3), 255–270 (2011)
22. C. An et al., Metal oxide-based supercapacitors: Progress and prospectives. Nanosc. Adv. **1**(12), 4644–4658 (2019)
23. Y. Ma et al., Recent advances in transition metal oxides with different dimensions as electrodes for high-performance supercapacitors. Adv. Compos. Hybrid Mater. **4**(4), 906–924 (2021)
24. S.N. Khatavkar, S.D. Sartale, Superior supercapacitive performance of grass-like CuO thin films deposited by liquid phase deposition. New J. Chem. **44**(17), 6778–6790 (2020)
25. R. Barik, P.P. Ingole, Challenges and prospects of metal sulfide materials for supercapacitors. Curr. Opin. Electrochem. **21**, 327–334 (2020)
26. C.-H. Lai, M.-Y. Lu, L.-J. Chen, Metal sulfide nanostructures: Synthesis, properties and applications in energy conversion and storage. J. Mater. Chem. **22**(1), 19–30 (2012)
27. S.D. Tao Lu, C. Zhang, L. Zhang, G. Cui, Fabrication of transition metal seleniedes and their applications in energy storage. Coord. Chem. Rev. **330**, 75–99 (2016)
28. H. Fan et al., *Recent Advances of Metal Telluride Anodes for High-Performance Lithium/Sodium-Ion Batteries* (Mater Horiz, 2021)
29. C. Burda et al., Chemistry and properties of nanocrystals of different shapes. Chem. Rev. **105**(4), 1025–1102 (2005)
30. M.R. Gao et al., Nanostructured metal chalcogenides: Synthesis, modification, and applications in energy conversion and storage devices. Chem. Soc. Rev. **42**(7), 2986–3017 (2013)
31. K. Mensah-Darkwa et al., Recent advancements in chalcogenides for electrochemical energy storage applications. Energies **15**(11) (2022)
32. Y. Zhang et al., Nanostructured metal chalcogenides for energy storage and electrocatalysis. Adv. Funct. Mater. **27**(35) (2017)
33. Y. Li et al., MoS_2 nanoparticles grown on graphene: an advanced catalyst for the hydrogen evolution reaction. J. Am. Chem. Soc. **133**(19), 7296–7299 (2011)
34. H. Wang et al., Co1−xS-graphene hybrid: A high-performance metal chalcogenide electrocatalyst for oxygen reduction. Angew. Chem. **123**(46), 11161–11164 (2011)
35. O.H. Arie Borenstein, R. Attias, S. Luski, T. Brousse, D. Aurbach, Carbon-based composite materials for supercapacitor electrodes: A review. J. Mater. Chem. A **5**, 12653 (2017)
36. W.K. Chee et al., Flexible graphene-based supercapacitors: A review. J. Phys. Chem. C **120**(8), 4153–4172 (2016)
37. K. Chen et al., Structural design of graphene for use in electrochemical energy storage devices. Chem. Soc. Rev. **44**(17), 6230–6257 (2015)

38. R.A. Fisher, M.R. Watt, W.J. Ready, Functionalized carbon nanotube supercapacitor electrodes: A review on pseudocapacitive materials. ECS J. Solid State Sci. Technol. **2**(10), M3170–M3177 (2013)
39. Y. Gao, Graphene and polymer composites for supercapacitor applications: A review. Nanoscale Res. Lett. **12**(1), 387 (2017)
40. Q. Ke, J. Wang, Graphene-based materials for supercapacitor electrodes – A review. J. Mater. **2**(1), 37–54 (2016)
41. E.E. Miller, Y. Hua, F.H. Tezel, Materials for energy storage: Review of electrode materials and methods of increasing capacitance for supercapacitors. J. Energy Storage **20**, 30–40 (2018)
42. A.G. Pandolfo, A.F. Hollenkamp, Carbon properties and their role in supercapacitors. J. Power Sources **157**(1), 11–27 (2006)
43. Q. Wang, J. Yuan, Z. Fan, Carbon materials for high volumetric performance supercapacitors: Design, progress, challenges and opportunities. Energy Environ. Sci. **9**, 729 (2016)
44. L.L. Zhang, X.S. Zhao, Carbon-based materials as supercapacitor electrodes. Chem. Soc. Rev. **38**(9), 2520–2531 (2009)
45. N.S.U. Shaikh, S.B. Mane, V.J. Shaikh, J.S. Lokhande, V.C. Praserthdam, S. Lokhande, C.D. Kanjanaboos, Pongsakorn, Novel electrodes for supercapacitor: Conducting polymers, metal oxides, chalcogenides, carbides, nitrides, MXenes, and their composites with graphene. J. Alloys Compd. **893**, 161998 (2022)
46. A.S. Vedpathak et al., Green strategy for the synthesis of K^+ pre-inserted MnO_2/rGO and its electrochemical conversion to Na-MnO_2/rGO for high-performance supercapacitors. Energy Fuel **36**(8), 4596–4608 (2022)
47. V.K. Mariappan et al., Nanostructured ternary metal chalcogenide-based binder-free electrodes for high energy density asymmetric supercapacitors. Nano Energy **57**, 307–316 (2019)
48. S.N. Khatavkar, S.D. Sartale, Liquid phase deposition of nanostructured materials for supercapacitor applications, in *Chemically Deposited Nanocrystalline Metal Oxide Thin Films: Synthesis, Characterizations, and Applications*, ed. by F.I. Ezema, C.D. Lokhande, R. Jose, (Springer, Cham, 2021), pp. 725–763
49. H. Cai et al., Synthesis and emerging properties of 2D layered III–VI metal chalcogenides. Appl. Phys. Rev. **6**(4), 041312 (2019)
50. C.D. Lokhande, Chemical deposition of metal chalcogenide thin films. Mater. Chem. Phys. **27**(1), 1–43 (1991)
51. S. Sengupta, R. Aggarwal, Y. Golan, The effect of complexing agents in chemical solution deposition of metal chalcogenide thin films. Mater. Chem. Front. **5**(5), 2035–2050 (2021)
52. R.S. Kate, S.A. Khalate, R.J. Deokate, Overview of nanostructured metal oxides and pure nickel oxide (NiO) electrodes for supercapacitors: A review. J. Alloys Compd. **734**, 89–111 (2018)
53. S. Yu et al., Synthesis and application of iron-based nanomaterials as anodes of lithium-ion batteries and supercapacitors. J. Mater. Chem. A **6**(20), 9332–9367 (2018)
54. A.M. Jubb, H.C. Allen, Vibrational spectroscopic characterization of hematite, maghemite, and magnetite thin films produced by vapor deposition. ACS Appl. Mater. Interfaces **2**(10), 2804–2812 (2010)
55. Q. Xia et al., Nanostructured iron oxide/hydroxide-based electrode materials for supercapacitors. ChemNanoMat **2**(7), 588–600 (2016)
56. V.D. Nithya, N.S. Arul, Review on α-Fe_2O_3 based negative electrode for high performance supercapacitors. J. Power Sources **327**, 297–318 (2016)
57. V.C. Lokhande, A.C. Lokhande, C.D. Lokhande, Nanostructured metal chalcogenide/oxide films based supercapacitors, in *Progress and Prospects in Nanoscience Today*, ed. by S. Pawar, (Nova Science Publishers, Inc, New York, 2020), pp. 179–208
58. M.S. Wu et al., Nanostructured iron oxide films prepared by electrochemical method for electrochemical capacitors. Electrochem. Solid-State Lett. **12**(1), A1–A4 (2009)
59. K. Xie et al., Highly ordered iron oxide nanotube arrays as electrodes for electrochemical energy storage. Electrochem. Commun. **13**(6), 657–660 (2011)

60. B.J. Lokhande et al., Concentration-dependent electrochemical supercapacitive performance of Fe_2O_3. Curr. Appl. Phys. **13**(6), 985–989 (2013)
61. B.J. Lokhande, R.C. Ambare, S.R. Bharadwaj, Thermal optimization and supercapacitive application of electrodeposited Fe_2O_3 thin films. Measurement **47**, 427–432 (2014)
62. B. Sarma et al., Influence of annealing temperature on the morphology and the supercapacitance behavior of iron oxide nanotube (Fe-NT). J. Power Sources **272**, 766–775 (2014)
63. B. Sarma et al., Electrochemical capacitance of iron oxide nanotube (Fe-NT): Effect of annealing atmospheres. Nanotechnology **26**(26), 265401 (2015)
64. J.C. Huang et al., Fe_2O_3 sheets grown on nickel foam as electrode material for electrochemical capacitors. J. Electroanal. Chem. **713**, 98–102 (2014)
65. P. Yang et al., Low-cost high-performance solid-state asymmetric supercapacitors based on MnO_2 nanowires and Fe_2O_3 nanotubes. Nano Lett. **14**(2), 731–736 (2014)
66. K.K. Lee et al., Vertically aligned iron (III) oxyhydroxide/oxide nanosheets grown on iron substrates for electrochemical charge storage. Mater. Lett. **118**, 150–153 (2014)
67. T. Liu et al., Investigation of hematite nanorod–nanoflake morphological transformation and the application of ultrathin nanoflakes for electrochemical devices. Nano Energy **12**, 169–177 (2015)
68. G.S. Gund et al., Low-cost flexible supercapacitors with high-energy density based on nanostructured MnO_2 and Fe_2O_3 thin films directly fabricated onto stainless steel. Sci. Rep. **5**, 12454 (2015)
69. N.R. Chodankar et al., Bendable all-solid-state asymmetric supercapacitors based on MnO_2 and Fe_2O_3 thin films. Energy Technol. **3**(6), 625–631 (2015)
70. A.V. Shinde et al., Highly energetic flexible all-solid-state asymmetric supercapacitor with Fe_2O_3 and CuO thin films. RSC Adv. **6**(63), 58839–58843 (2016)
71. Q. Tang, W. Wang, G. Wang, The perfect matching between the low-cost Fe_2O_3 nanowire anode and the NiO nanoflake cathode significantly enhances the energy density of asymmetric supercapacitors. J. Mater. Chem. A **3**(12), 6662–6670 (2015)
72. H. Nan et al., Flexible superior electrode architectures based on three-dimensional porous spinous alpha-Fe_2O_3 with a high performance as a supercapacitor. Dalton Trans. **44**(20), 9581–9587 (2015)
73. S.L. Kadam, et al., *Electrodeposition of Fe_2O_3Nanoparticles and Its Supercapacitive Properties*. (2016), Vol. 1249, p. 020113
74. X. Tang et al., Hierarchical Fe(3)O(4)@Fe(2)O(3) Core-Shell Nanorod Arrays as High-Performance Anodes for Asymmetric Supercapacitors. ACS Appl. Mater. Interfaces **7**(49), 27518–27525 (2015)
75. S.M. Peng et al., Low-cost superior solid-state symmetric supercapacitors based on hematite nanocrystals. Nanotechnology **27**(50), 505404 (2016)
76. S. Zhang et al., Super long-life all solid-state asymmetric supercapacitor based on NiO nanosheets and α-Fe_2O_3 nanorods. Chem. Eng. J. **306**, 193–203 (2016)
77. H. Liang et al., Phosphine plasma activation of α-Fe_2O_3 for high energy asymmetric supercapacitors. Nano Energy **49**, 155–162 (2018)
78. X. Zheng et al., Spinous alpha-Fe_2O_3 hierarchical structures anchored on Ni foam for supercapacitor electrodes and visible light driven photocatalysts. Dalton Trans. **45**(16), 7094–7103 (2016)
79. Y.-C. Chen et al., Synthesis of Fe_2O_3 nanorods/silver nanowires on coffee filter as low-cost and efficient electrodes for supercapacitors. J. Electroanal. Chem. **801**, 65–71 (2017)
80. S.N. Khatavkar, S.D. Sartale, α-Fe_2O_3 thin films by liquid phase deposition: low-cost option for supercapacitor. J. Solid State Electrochem. **21**(9), 2555–2566 (2016)
81. S.N. Khatavkar, S.D. Sartale, α-Fe_2O_3 thin film on stainless steel mesh: A flexible electrode for supercapacitor. Mater. Chem. Phys. **225**, 284–291 (2019)
82. S.N. Khatavkar, S.D. Sartale, Fabrication and evaluation of symmetric flexible solid state supercapacitor device based on α-Fe_2O_3 thin films by LPD. AIP Conf. Proc. **2335**, 040008 (2021)

83. M. Kang et al., Facile fabrication of oxygen vacancy-rich α-Fe_2O_3 microspheres on carbon cloth as negative electrode for supercapacitors. Electrochim. Acta **338**, 135820 (2020)
84. J. Yadav et al., Role of oxidation states of iron on the super-capacitive behaviour of iron oxide films. Appl. Phys. A **128**(4) (2022)
85. X. Lu et al., Oxygen-deficient hematite nanorods as high-performance and novel negative electrodes for flexible asymmetric supercapacitors. Adv. Mater. **26**(19), 3148–3155 (2014)
86. M.S. Wu, R.H. Lee, Electrochemical growth of iron oxide thin films with nanorods and nanosheets for capacitors. J. Electrochem. Soc. **156**(9), A737–A743 (2009)
87. P.M. Kulal et al., Chemical synthesis of Fe_2O_3 thin films for supercapacitor application. J. Alloys Compd. **509**(5), 2567–2571 (2011)
88. S.S. Raut, B.R. Sankapal, Comparative studies on MWCNTs, Fe_2O_3 and Fe_2O_3/MWCNTs thin films towards supercapacitor application. New J. Chem. **40**(3), 2619–2627 (2016)
89. G. Binitha et al., Electrospun α-Fe_2O_3 nanostructures for supercapacitor applications. J. Mater. Chem. A **1**(38), 11698 (2013)
90. C. Fu, A. Mahadevegowda, P.S. Grant, Production of hollow and porous Fe_2O_3 from industrial mill scale and its potential for large-scale electrochemical energy storage applications. J. Mater. Chem. A **4**(7), 2597–2604 (2016)
91. J. Liu et al., Ultra-high capacitance hematite thin films with controlled nanoscopic morphologies. Nanoscale **6**(18), 10643–10649 (2014)
92. Z. Wang, C.-J. Liu, Preparation and application of iron oxide/graphene based composites for electrochemical energy storage and energy conversion devices: Current status and perspective. Nano Energy **11**, 277–293 (2015)
93. Y. Li, N. Hu, Modification of the elemental composition of iron(III) oxide as an asymmetric supercapacitor anode: A minireview. Instrum. Sci. Technol. **48**(6), 637–666 (2020)
94. X. Zhao, C. Johnston, P.S. Grant, A novel hybrid supercapacitor with a carbon nanotube cathode and an iron oxide/carbon nanotube composite anode. J. Mater. Chem. **19**(46), 8755 (2009)
95. H. Zhang et al., Solvothermally induced α-Fe_2O_3/graphene nanocomposites with ultrahigh capacitance and excellent rate capability for supercapacitors. J. Mater. Chem. A **3**(44), 22005–22011 (2015)
96. C. Guan et al., Iron oxide-decorated carbon for supercapacitor anodes with ultrahigh energy density and outstanding cycling stability. ACS Nano **9**(5), 5198–5207 (2015)
97. X. Cheng et al., Three-dimensional α-Fe_2O_3/carbon nanotube sponges as flexible supercapacitor electrodes. J. Mater. Chem. A **3**(42), 20927–20934 (2015)
98. J. Li et al., Porous Fe_2O_3 nanospheres anchored on activated carbon cloth for high-performance symmetric supercapacitors. Nano Energy **57**, 379–387 (2019)
99. W. Zhang et al., Fe_2O_3-decorated millimeter-long vertically aligned carbon nanotube arrays as advanced anode materials for asymmetric supercapacitors with high energy and power densities. J. Mater. Chem. A **4**(48), 19026–19036 (2016)
100. X. Huang, H. Zhang, N. Li, Symmetric transparent and flexible supercapacitor based on bio-inspired graphene-wrapped Fe_2O_3 nanowire networks. Nanotechnology **28**(7), 075402 (2017)
101. S. Xie et al., Advanced negative electrode of Fe_2O_3/graphene oxide paper for high energy supercapacitors. Mater. Res. Bull. **96**, 413–418 (2017)
102. H. Pourfarzad et al., Synthesis of Ni–Co-Fe layered double hydroxide and Fe_2O_3/Graphene nanocomposites as actively materials for high electrochemical performance supercapacitors. Electrochim. Acta **317**, 83–92 (2019)
103. N.R. Chodankar et al., True Meaning of pseudocapacitors and their performance metrics: Asymmetric versus hybrid supercapacitors. Small **16**(37), e2002806 (2020)
104. Y. Zeng et al., Iron-based supercapacitor electrodes: Advances and challenges. Adv. Energy Mater. **6**(24) (2016)
105. K.W. Chung et al., Novel synthesis and electrochemical characterization of nano-sized cellular Fe_3O_4 thin film. Electrochem. Solid-State Lett. **8**(5), A259–A262 (2005)

106. J. Chen, K.L. Huang, S.Q. Liu, Hydrothermal preparation of octadecahedron Fe_3O_4 thin film for use in an electrochemical supercapacitor. Electrochim. Acta **55**(1), 1–5 (2009)
107. S.C. Pang, W.H. Khoh, S.F. Chin, Nanoparticulate magnetite thin films as electrode materials for the fabrication of electrochemical capacitors. J. Mater. Sci. **45**(20), 5598–5604 (2010)
108. R. Li, J. Liu, Mechanistic investigation of the charge storage process of pseudocapacitive Fe_3O_4 nanorod film. Electrochim. Acta **120**, 52–56 (2014)
109. W. Shi et al., Achieving high specific charge capacitances in Fe_3O_4/reduced graphene oxide nanocomposites. J. Mater. Chem. **21**(10), 3422 (2011)
110. D. Liu et al., Ultrathin nanoporous Fe_3O_4–carbon nanosheets with enhanced supercapacitor performance. J. Mater. Chem. A **1**(6), 1952 (2013)
111. C. Fu, A. Mahadevegowda, P.S. Grant, Fe_3O_4/carbon nanofibres with necklace architecture for enhanced electrochemical energy storage. J. Mater. Chem. A **3**(27), 14245–14253 (2015)
112. L. O'Neill, C. Johnston, P.S. Grant, Enhancing the supercapacitor behaviour of novel Fe_3O_4/FeOOH nanowire hybrid electrodes in aqueous electrolytes. J. Power Sources **274**, 907–915 (2015)
113. J. Sun et al., A high performance fiber-shaped PEDOT@MnO_2//C@Fe_3O_4 asymmetric supercapacitor for wearable electronics. J. Mater. Chem. A **4**(38), 14877–14883 (2016)
114. C.Z. Xu, Y. Rui, X. Xiao, N. Zhu, J. Zhang, W. Chen, J. Liu, W. Tan, H. Hng, H.H. Yan, Controlled soft-template synthesis of ultrathin C@FeS nanosheets with high-Li-storage performance. ACS Nano **6**(6), 4713–4721 (2012)
115. Y.L. Xu, W. Zhang, F. Zhang, X. Zhang, W. Lee, C.-S. Tang, Yongbing, In situ incorporation of FeS nanoparticles/carbon nanosheets composite with an interconnected porous structure as a high-performance anode for lithium ion batteries. J. Mater. Chem. A **4**(10), 3697–3703 (2016)
116. S.S. Karade et al., First report on a FeS-based 2 V operating flexible solid-state symmetric supercapacitor device. Sustain. Energy Fuels **1**(6), 1366–1375 (2017)
117. M.S. Javed et al., A high-performance flexible solid-state supercapacitor based on Li-ion intercalation into tunnel-structure iron sulfide. Electrochim. Acta **219**, 742–750 (2016)
118. K.K. Upadhyay et al., Pseudocapacitive behaviour of FeSx grown on stainless steel up to 1.8 V in aqueous electrolyte. J. Energy Storage **26**, 100949 (2019)
119. C. Zhao et al., One-pot hydrothermal synthesis of RGO/FeS composite on Fe foil for high performance supercapacitors. Electrochim. Acta **246**, 497–506 (2017)
120. H. Tan et al., Metal chalcogenides: Paving the way for high-performance sodium/potassium-ion batteries. Small Methods **4**(1), 1900563 (2019)
121. P. Santhoshkumar et al., Hierarchical iron selenide nanoarchitecture as an advanced anode material for high-performance energy storage devices. Electrochim. Acta **356**, 136833 (2020)
122. B. Pandit et al., Combined electrochemical and DFT investigations of iron selenide: A mechanically bendable solid-state symmetric supercapacitor. Sustain. Energy Fuels **5**(19), 5001–5012 (2021)
123. Z. Tian et al., A high-performance asymmetric supercapacitor-based (CuCo)Se_2/GA cathode and $FeSe_2$/GA anode with enhanced kinetics matching. Nanoscale **13**(13), 6489–6498 (2021)
124. L.K. Bommineedi, T.K. Shivasharma, B.R. Sankapal, Mixed phase FeTe: Fe_2TeO_5 nanopebbles through solution chemistry: Electrochemical supercapacitor application. Ceram. Int. **48**(1), 137–147 (2022)

Nanostructure Design for Supercapacitor Application

Vaibhav C. Lokhande, Vikas J. Mane, A. C. Lokhande, C. D. Lokhande, and Taeksoo Ji

1 Introduction

Current energy needs have risen exponentially and so has the demand for energy storage systems. Energy harvested from renewable sources is infamous for its intermittency and unreliability. These issues are efficiently tackled with an effective and robust energy storage system. Batteries are currently the main option for energy storage. They are not always suitable as certain applications demand faster charging-discharging energy storage systems. With high power density and cyclic stability, supercapacitors can be employed in power-intense applications.

Supercapacitors, also known as ultracapacitors or electrochemical capacitors, are a new class of energy storage, which have risen to prominence due to fast-rising demand and advancements in electric vehicles and portable electronics. The ability to charge-discharge at a very high rate and deliver power at such an unprecedented level of magnitude makes it the ideal energy storage system. The only parameter in which supercapacitors trail batteries is the energy density. Apart from energy density, supercapacitors surpass batteries in stability, power density, lifetime, and rate capability. Supercapacitors' ability to withstand a high amount of load without sustaining any damage makes them the ideal candidate for energy storage devices.

V. C. Lokhande · T. Ji (✉)
Department of Electronics Engineering, Chonnam National University, Gwangju, South Korea
e-mail: tji@jnu.ac.kr

V. J. Mane · C. D. Lokhande
Centre for Interdisciplinary Research, D. Y. Patil Education Society (Deemed to be University), Kolhapur, Maharashtra, India

A. C. Lokhande
Department of Mechanical Engineering, Khalifa University of Science and Technology (KUST), Abu Dhabi, United Arab Emirates

F. I. Ezema et al. (eds.), *Chemically Deposited Metal Chalcogenide-based Carbon Composites for Versatile Applications*, https://doi.org/10.1007/978-3-031-23401-9_4

Supercapacitors are classified as an electrochemical double-layer capacitors (EDLC), pseudocapacitors, or hybrid capacitors. The classification is based on the charge storage mechanism. EDLC stores charge via ion adsorption at the electrode-electrolyte interface. The electrostatic attraction between the electrolyte ions and electrode leads to the formation of an electrochemical double layer. The double-layer capacitance is expressed as (1)

$$C = \frac{\in_r \in_o A}{D} \tag{1}$$

where $\in_r$ is the electrolyte dielectric constant, $\in_o$ is the dielectric constant of the vacuum, A is the electrode surface area, and d is the effective thickness of the double layer (charge separation distance). Thus, it is obvious that area (electrode surface area) is an important factor in determining the capacitance of the electrode material.

Pseudocapacitive materials due to their multiple oxidation states and fast surface redox reaction can imitate the performance of EDLC materials. The charge storage mechanism is a result of faradaic reactions involving charge transfer between electrolyte ions and the electrode material. Theoretically, pseudo-capacitance is controlled by thermodynamics according to which the extent of a reaction (q) that stems from Faradaic charge-transfer processes is a continuous function of the applied potential (V), so that a derivative, dq/dV, arises, which is equivalent to capacitance and is expressed as (2) [1].

$$C = \frac{\delta(\Delta q)}{\delta(\Delta V)} \tag{2}$$

The effective surface area influences the reaction kinetics. The larger the effective surface area, greater the electrolyte coverage and penetration. With increased effective surface area, more electroactive sites are exposed and are easily accessible. This increases the electrochemical performance of the material and influences parameters such as capacitance, energy density, and power density of the material.

A hybrid-type capacitor is made of asymmetric electrodes, one of which is pseudocapacitive and the other is EDLC type. In some cases, battery electrodes are also used in tandem with supercapacitor electrodes to fabricate a hybrid capacitor. The main criterion for the hybrid capacitor is that electrodes exhibit different charge storage mechanisms.

Nanoscale research has unlocked potential avenues for enhancing the performance of supercapacitors by synthesizing nanostructured electrode materials. Owing to the easy transport of ions through nanomaterials, a large number of electroactive sites and electrode-electrolyte interfaces are available which inevitably enhance the electrochemical performance. Even the properties of the nanomaterial deviate from the bulk and can be used to amplify the performance. Nanocomposite materials offer even better avenues for designing advanced electrodes. Such materials exhibit the synergetic effect of individual materials.

2 Nanotechnology and Nanomaterials

The word "nano" is a deviation of the Latin word "nanus" and the Greek word "νανς" both meaning dwarf. The International System (SI) of units describes nano as 10^{-9} parts of a unit. Nanotechnology is the general term for technology, which allows a controllable way to synthesize and manipulate nanomaterials [2]. Nanotechnology is defined as "a science, engineering, and technology conducted at the nanoscale (1 to 100 nm), where unique phenomena enable novel applications in a wide range of fields, from chemistry, physics, and biology, to medicine, engineering, and electronics" [3]. According to the definition, nanotechnology is related to the scale and size of the structures as well as to their application. Due to their small size, nanomaterials exhibit some interesting properties, and nanotechnology relates to taking advantage of such properties for their novel application.

The history of nanotechnology does not have a universally accepted and well-established time span. The ambiguity arises due to the use of nanotechnology in distant times without the awareness of it being used. For thousands of years BC, humans knew and mastered the art of making fabrics [4–6]. The fabrics through processing developed a network of pores with a size of 1–20 nm. The nanoporous material (fabric) was able to absorb sweat quickly and effectively and dry out much quicker as well. Another example of the use of nanotechnology is the Ayurveda medicines [7, 8]. Ayurveda is an ancient branch of medicine that has various examples, which would argue about the knowledge of nanotechnology. Description of processes similar to modern-day pyrolysis can be found to synthesize "bhasmas." Bhasmas (burnt powders) of gold, copper, iron, lead, etc. have been actively used in the treatment of various illnesses and diseases [9–11]. The use of nanotechnology in paints by the Maya civilization is another example, which proves that the use of nanomaterials was quite widespread [12]. Maya blue and yellow paint pigments are made by embedding coloring pigments in local phyllosilicate clay (palygorskite). The process of making such pigments allowed them to create different colors with the same ingredients by just controlling the size [13–15] (Fig. 1).

Through his famous talk "There's Plenty of Room at the Bottom," Richard Feynman promoted the concept of nanotechnology and nanomaterials into the limelight [16]. Feynman questioned "Why can't we write the entire 24 volumes of the Encyclopedia Britannica on the head of a pin?", and then went on to elaborate on a vision of using machines to build smaller machines down to the molecular level. Feynman's ideas to demonstrate the hypothesis have come to pass, and for these reasons, he is regarded as the father of modern nanotechnology. Norio Taniguchi at a conference in 1974 used the term nanotechnology for the first time to define and describe semiconductor processes [4]. K. Eric Drexler further popularized nanotechnology with the book "Engines of Creation: The Coming Era of Nanotechnology" [17]. In this first-ever book on nanotechnology, he describes complex machines from an atomic level that can independently manipulate other atoms and molecules into nanostructures. In 1991, Drexler, Peterson, and Pergamit published a book entitled "Unbounding the Future: the Nanotechnology Revolution"

Fig. 1 Gold bhasma (**a**) and Maya blue color (**b**) as examples of the use of nanotechnology in ancient times

wherein they intrigued the readers' interest through nanobots and assemblers for medicinal purposes, thereby coining the term nanomedicine.

The progress of modern nanotechnology has some significant milestones. After Feynman's lecture, work in this field took off. Physicists G. Binnig and H. Rohrer invented a new type of microscope now known as the scanning tunneling microscope (STM). A sharp tip moves very close to the test surface, thereby affecting the electron wave functions of the atoms in the tip and the test surface. Upon application of high voltage, the electrons jump through the vacuum gap. The electron signal is processed further to obtain the STM image. They received a Nobel Prize for the design of STM in 1986, and their work led to the development of other techniques such as atomic force microscope (AFM) and scanning probe microscopes (SPM) which are still used by researchers and scientists. During the same period, the synthesis of nanomaterials was budding. In 1985, R. Cur, H. Kroto, and R. Smalley discovered stable spherical structures of carbon (C60 and C70) also known as fullerenes. A few years later, carbon nanotubes (CNTs) were observed by Iijima et al. Nanotechnology was garnering a lot of attention due to its numerous applications. In 2000, President Clinton earmarked 490 million US$ for research in nanotechnology. In 2003, President George W. Bush signed the twenty-first century Nanotechnology Research and Development Act and paved the way for the National Nanotechnology Initiative (NNI) [3]. With this, research in nanotechnology became a national priority. This sparked interest of many scientists and the synthesis of nanostructured materials kick-started. In the past two decades, different nanostructures have been successfully synthesized. The number of nanostructures increased at such a great pace that it became essential to distinguish them categorically. A few attempts were made. Gleiter in 1995 gave the first classification which was further improved upon by Skorokhod in 2000. The updated classification still failed to consider all the nanostructures. Pokropivny and Skorokhod modified

the classification scheme for NSMs, in which all nanostructures (0D, 1D, 2D, and 3D) were included [18]. They argued that nanostructures should be separated from nanostructured materials because the nanostructures are characterized by form and dimensionality while then nanostructured materials by composition in addition. The detailed classification is summarized in Fig. 2.

3 Synthesis Methods

These synthesis or manufacturing methods are classified into two categories: top-down and bottom-up. Each of which differs in the quality of nanostructures, synthesis time, and cost. The top-down method is in essence breaking the bulk material into smaller nano-sized particles. The breakdown processes such as mechanical, optical, thermal, sputtering, chemical etching, etc. are employed to break the bulk material into smaller particles. These methods are not suitable for the preparation of uniformly shaped nanoparticles. Imperfections or variations of the surface structures of the particles have a significant impact on the physical and chemical properties of the nanomaterials. The bottom-up approach, on the other hand, refers to building up material from the bottom: atoms, molecules, and clusters. This route is utilized more in the preparation of nanoscale materials with uniform shape sizes and surface structures. This approach also employs mainly chemical methods. The self-assembly of the atoms or molecules into ordered materials is the key factor in the bottom-up approach. There are, however, other techniques such as positional assembly and templating, in which atoms, molecules, or clusters can be positioned specifically. Methods for fabricating nanoparticles can be further divided as physical or chemical. Figure 3 illustrates the schematic approach for the top-down and bottom-up approaches.

3.1 Physical Methods

Mechanical Milling Milling powder in a mill to break down the particles into smaller size or blending into new phases is the underlying concept of mechanical milling. The mechanical attrition of the coarse particles is achieved with the use of suitable balls (zirconia, agate, stainless steel, etc.). The balls are either let to roll down the surface of the chamber or fall freely or rotated in the chamber with arms attached to rotating central shaft. The kinetics of the milling process is dependent on the transfer of energy from the milling medium to the powder. Factors such as size of balls, rotating speed, temperature, time, and dry or wet conditions affect the final size of the nanomaterials. There are multiple types of ball milling available, for example, attrition ball milling, vibrating ball milling, low-energy tumbling, planetary ball milling, and high-energy ball milling.

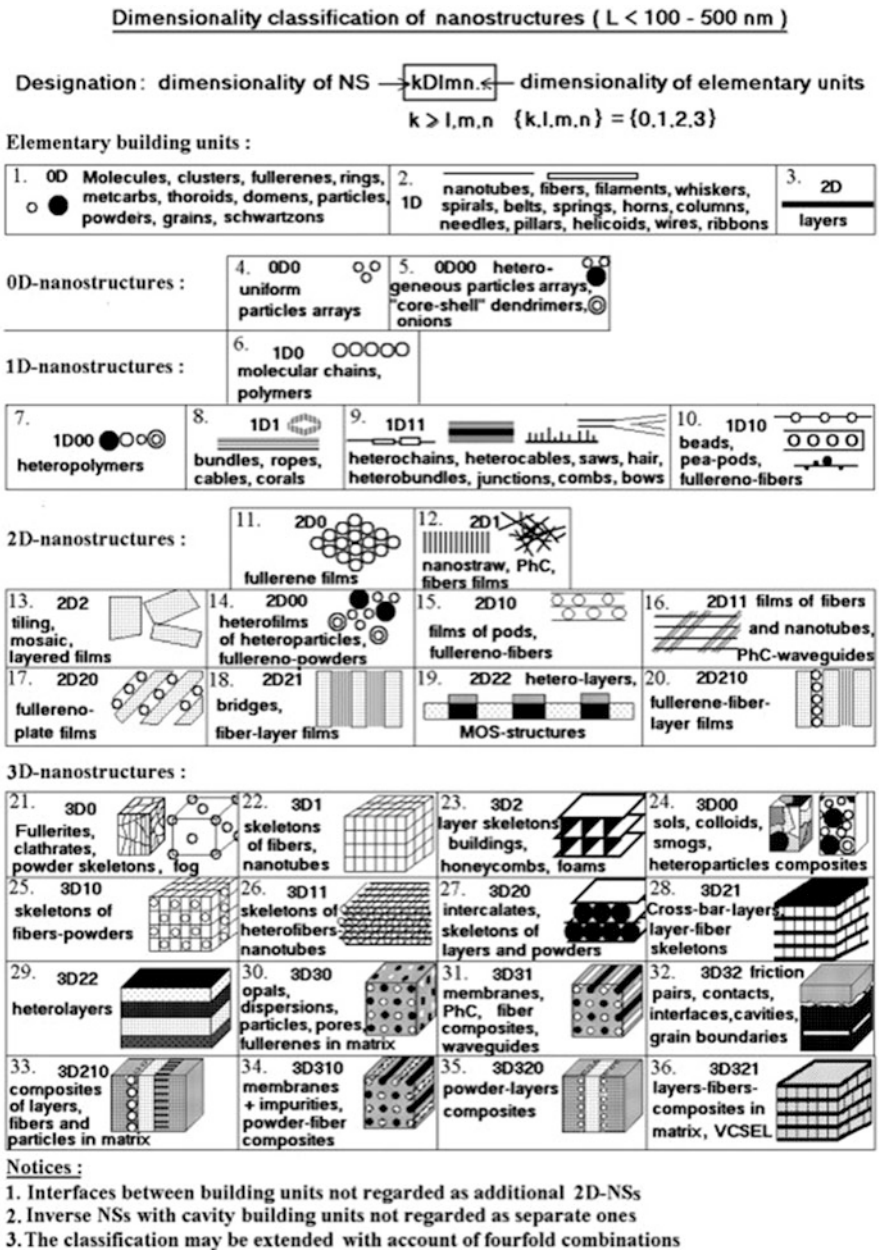

Fig. 2 Classification of nanostructures according to Pokropivny and Skorokhod et al. (Published with permission)

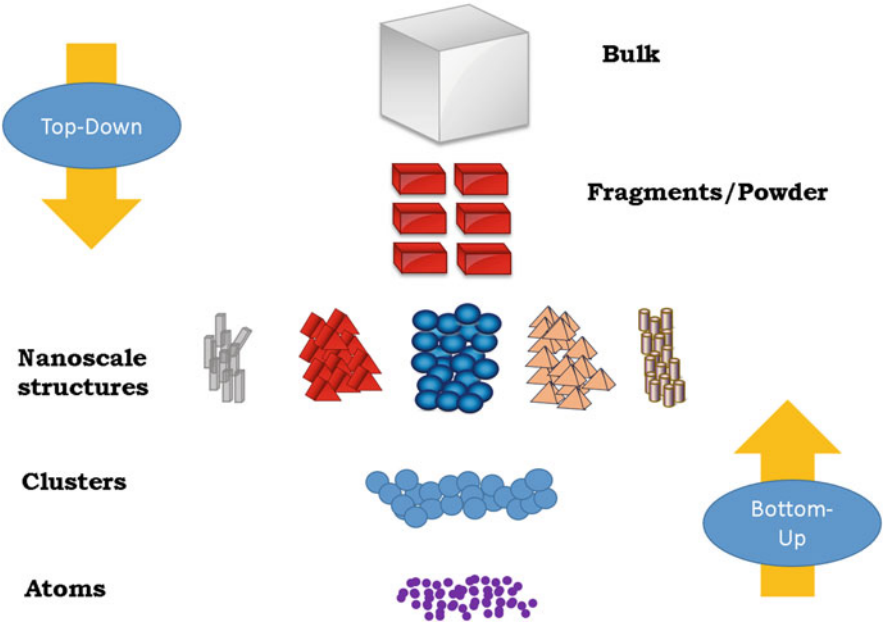

Fig. 3 Schematic representation of top-down and bottom-up approaches for synthesis of nanoparticles

Mechanical milling has drawbacks such as nonuniform shapes, surface structures and size distribution, contamination, and no control over the shape of the nanostructure.

Gas Phase Methods The gas phase method is based on homogeneous nucleation, condensation, and coagulation. Gas phase methods can be classified into chemical or physical methods and are one of the best methods for thin film deposition. The physical vapor deposition (PVD) is a collective set of processes, which employ the same underlying principle in a different way. The fundamental steps involved in PVD are as follows:

1. Vaporization of the material from a solid source.
2. Transportation of the vapor.
3. Condensation onto the substrate.

The general schematic diagram of gas phase method is shown in Fig. 4.

Laser Ablation In this technique, as seen in Fig. 5, a high-power laser beam strikes the target in a vacuum chamber generating plasma. It then converts the target material into colloidal solution of nanoparticles, which is carried by the carrier gas to the collector positioned downstream. The vapor condenses and deposits on the collector. The quality of the nanomaterials produced depends upon the type of laser, number of pulses, pulsing time, laser power and wavelength, temperature, pressure,

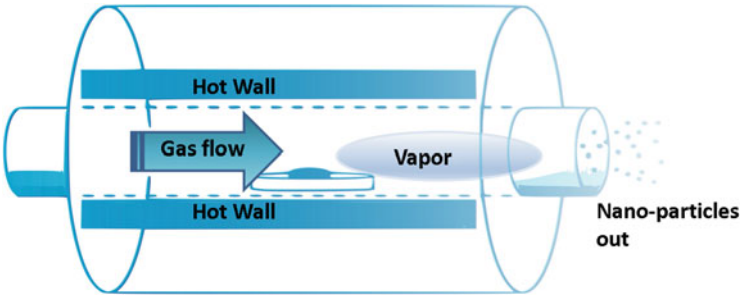

Fig. 4 Schematic of gas phase method illustrating the steps involved in the synthesis of nanoparticles

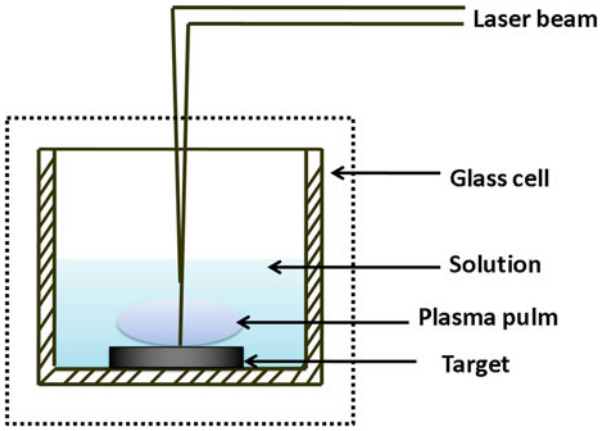

Fig. 5 Schematic of laser ablation method

type of inert gas, and catalysts. This technique can also be used for liquid phase as an efficient way to exfoliate material into their 2D forms. Solvent and fluid dynamics near the target play important role in thickness, shape, and size of the nanomaterial.

Sputtering Sputtering is a physical process. The solid-state target is vaporized and converted into the gas phase by bombardment with high energy ions (mainly noble gas ions). During sputtering, the energy of a plasma (partially ionized gas) pulls the atoms from the surface of a target (cathode) and deposits them on the substrate. The amount of material is controlled to achieve desirable thickness. Sputter deposition is a commonly used technique to deposit thin films. There are many types of sputtering: DC sputtering, RF sputtering, magnetron sputtering, and reactive sputtering, each with its advantages and disadvantages. Basic schematics of sputtering is shown in Fig. 6.

Thermal Evaporation Thermal evaporation is a method in which the source material is heated to high temperature under a vacuum, causing it to evaporate. The

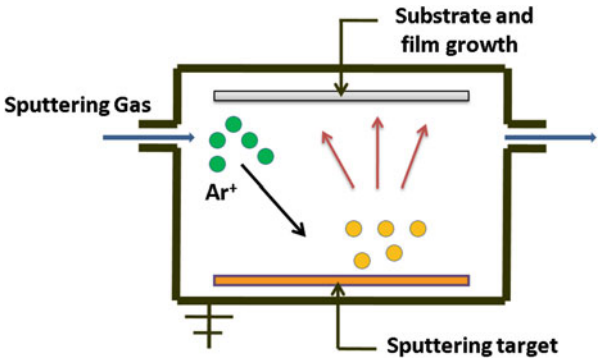

Fig. 6 Schematic diagram of sputtering process used in the synthesis and deposition of nanoparticles

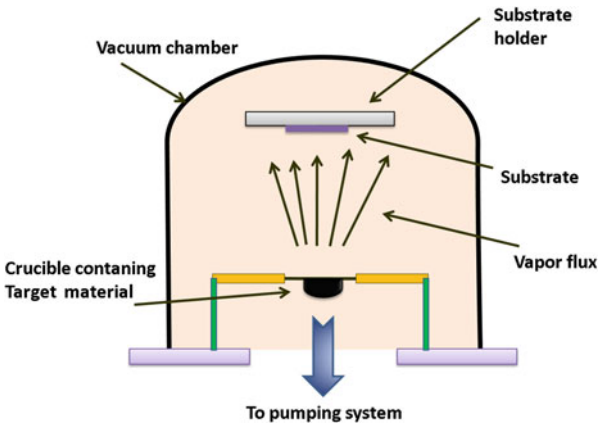

Fig. 7 Schematic drawing of thermal evaporation process

vapor particles move towards the substrate, where these vapors cool and change to a solid state. Figure 7 depicts the basic working of sputtering. The advantages of thermal evaporation are high deposition rates, low cost, and simplicity.

Templating Templating method is used to synthesize nanomaterial with uniform morphology or to mimic the morphology of the known material. In this method, the desired morphology is achieved via reactive deposition or dissolution or etching. The template material is coated on the substrate and acts as the platform for further deposition of the target material. The size and shape of the nanomaterial can be controlled by adjusting the morphology of the template. Numerous template materials were discovered and studied in the last few decades. With the use of a template, uniform and well-ordered nanostructures can be created on a large area. The problem with the method is that the removal of the templates after synthesis may become complicated.

3.2 Chemical Methods

Sol-Gel Method The sol-gel process is a chemical method used for the synthesis of various metal oxide nanoparticles with different nanostructures. In this method, precursors (metal alkoxide) are dissolved in a solvent to form a colloidal solution (sol). The colloidal solution is then heated to make a gel. The obtained gel is usually wet and dried to remove excess solvent. The rate at which solvent is evaporated determines the pore distribution in the gel. After the drying stage, the produced gels are ground and calcined. This method is highly cost-effective and used to produce materials for different applications (Fig. 8).

Hydrothermal and Solvothermal Method A hydrothermal or solvothermal method is a closed vessel reaction in which precursors react with each other or decompose in the presence of a solvent (solvothermal) or water (hydrothermal). The reaction happens at high temperatures and pressure. By application of heat (energy) to the system, autogenic pressure is generated that is a function of the percentage fill of the vessel and concentration of dissolved precursors. These methods are used to synthesize and deposit material. It is possible to synthesize a wide variety of nanostructures with simple control of parameters. Temperature, time, the concentration of precursors, pH, solvent, and percentage fill can be controlled to produce any type of structure and thermodynamically stable products (Fig. 9).

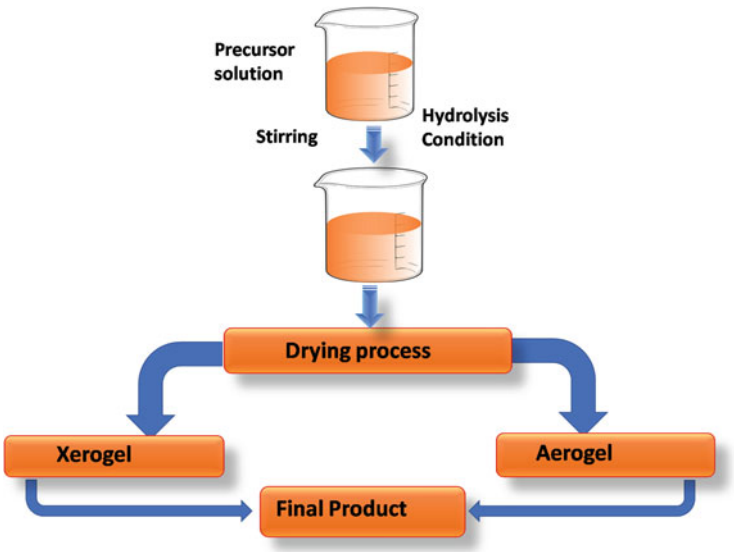

Fig. 8 Schematic drawing of sol-gel synthesis process

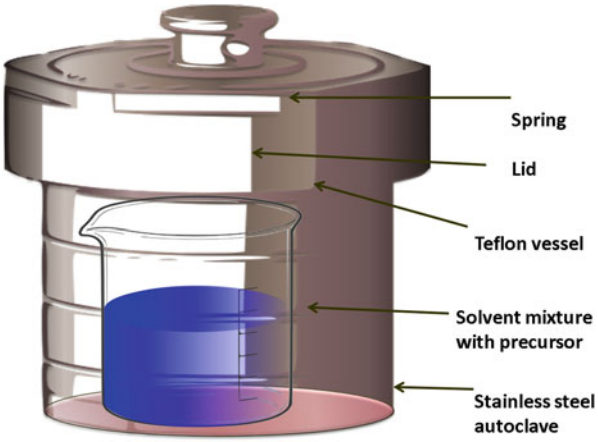

Fig. 9 Illustration of hydrothermal/solvothermal equipment used in the synthesis of nanoparticles

Sonochemical Method The sonochemical process is a powerful method to enhance chemical reactions and synthesize material. Ultrasonic radiations (20 kHz to 10 MHz) of fixed frequency are passed through a precursor solution. The alternating waves of expansion and compression cause cavities to form, grow, and implode. This is called acoustic cavitation and is primarily responsible enhanced rate of reaction. According to some researchers, the bubble formation and collapse can raise the local temperature up to 5000–25,000 k for less than a nanosecond and is followed by a very high cooling rate. A sonochemical method is simple and allows easy control of the size of nanoparticles by controlling the concentration of precursors and ultrasound radiation power. This method has proved useful in the synthesis of metal and metal oxide nanoparticles (Fig. 10).

4 Quantum Confinement Effect

The quantum size effect describes the physics of electron properties in solids where the particle size reduces significantly. Particles measuring in the range of 10–100 nm exhibit size effect, whereas quantum size effects are demonstrated by nanocrystallites measuring less than 10 nm. This effect becomes dominant when the nanometer size range/scale is reached. To understand quantum confinement, it is important to first understand the underlying phenomenon of quantum dots (QDs). QDs are extremely small semiconductor crystals of nanometer size. The electron in semiconductor materials is stimulated from the valence band to the conduction band. A "hole" is left behind in the valence band, which can be supposed as a particle with individual charge (+1) and effective mass. The electron-hole pairs are considered quasiparticles and are also known as "exciton." The spatial confinement

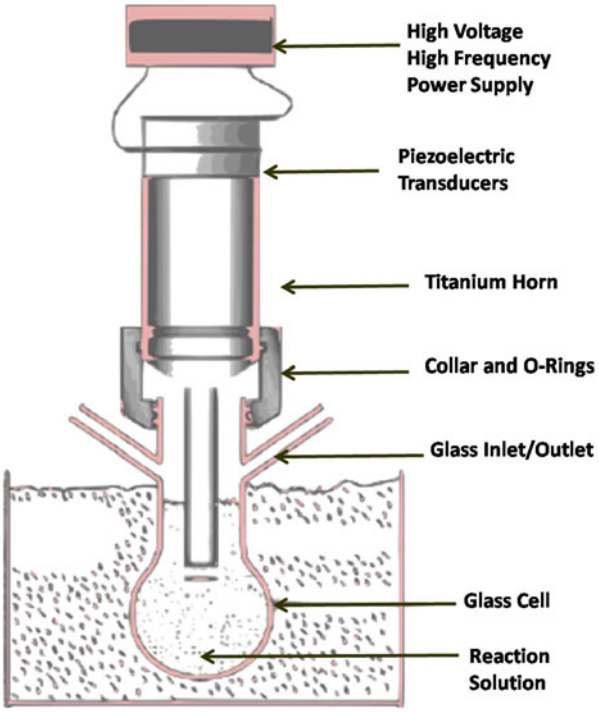

Fig. 10 Schematic drawing of sonochemical synthesis of nanomaterials

of excitons (electron-hole pairs) in one or more dimensions is quantum confinement. Due to the confinement of electronic wave function to the physical dimensions, the electronic energy levels become discrete. Quantum confinement happens when the radius of the quantum dots becomes smaller or equal to the Bohr exciton radius. The motion of electrons and holes is spatially confined to the physical dimensions of the quantum dot. Similarly, the restriction of the mobility of electrons and holes in the crystal dimensionality happens when the energy difference between two levels of quantum dots exceeds KBT (KB is the Boltzmann constant). Depending on the size, the QDs exhibit size-dependent optoelectronic properties with discrete electronic transitions. The physicochemical properties of QD particles also differ from the bulk materials. Due to the small particle size, the surface-to-volume ratio increases which affects their properties such as magnetic and electronic and also their interaction. The Quantum confinement effect in QDs results in discrete electronic states and hence the emergence of size-dependent properties (Fig. 11).

Based on the structure, the following classification is made concerning the quantum confinement in Table 1.

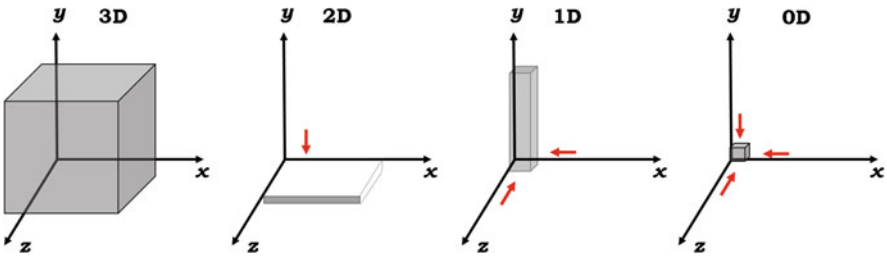

Fig. 11 Classification of nanoscale dimensions

Table 1 Classification of quantum-confined structures

Structure	Quantum confinement	Number of free dimension
3D	0	3
2D	1	2
1D	2	1
0D	3	0

5 Nanostructures

0D Structures 0D nanostructures are the simplest building block and can be utilized for building other nanostructures. 0D NSMs such as quantum dots, core-shell quantum dots, hollow spheres, etc. are some examples of 0D nanostructures. These nanostructures have numerous applications and have been successfully employed in LED, solar cells, lasers, and biosensors. 0D structures for supercapacitor electrodes are a lucrative prospect. The small size is desirable for electrode material. Electrochemical double-layer capacitors store charge based on electrostatic attraction, while pseudocapacitors store charge through surface redox reactions. Small size maximizes the effective surface area that is directly correlated to specific capacitance. Thus, it would be advantageous to use 0D nanostructured electrode material for supercapacitor application. 0D nanostructured materials are several thousand atoms and are spherical in shape. The main problem with using 0D materials is twofold. Synthesis of 0D materials in large quantities is not easy, and when it comes to scalability, the large quantity production leads to coalescence and aggregation of particles, which alters their chemical and physical properties.

Carbon quantum dots (CQD), graphene quantum dots (GQD), carbon nanospheres, and activated carbon are the prominent 0D nanostructured materials used as electrode materials for EDLC. Small size is favorable for increasing surface area, which enables large ionic adsorption. CQD are a new class of carbon materials with particle size less than 10 nm with a nanocrystalline core enveloped by the amorphous shell. The shell contains surface functional groups that are responsible for ion adsorption. CQD reported by Athika et al. [19] exhibited a specific capacitance of 95 Fg^{-1} with coulombic efficiency of almost 100%. The CQD were synthesized from denatured milk by hydrothermal method. Once the

CQD applicability as electrode material was established, researchers started to pair the CQD with other carbon materials to boost its performance. CQD was paired with rGO to yield a composite electrode. In their study, Zhao et al. [20] synthesized CQD-decorated interconnected rGO. The electrode exhibited a specific capacitance of 308 Fg^{-1} and showed excellent stability and efficiency. Hoang et al. [21] demonstrated that 3D porous rGO/CQD composite has superior specific capacitance of 374 Fg^{-1} with reasonable stability of 93% over 10,000 cycles. Similar to CQD, GQD are also garnering attention of researchers. Due to its excellent conductivity, high surface area, and nontoxicity, GQD are potential candidate for electrode material in energy storage device. Liu et al. [22] fabricated GQD//GQD symmetric micro-capacitor of 534.7 $\mu F\ cm^{-2}$ and the energy density of 0.074 $\mu Wh\ cm^{-2}$. The excellent electrochemical performances of micro-supercapacitors are the result of large specific surface area, ample active sites, and accessible edges. Zhang et al. [23] synthesized GQD with uniform sizes of less than 5 nm by a novel top-down strategy. They implemented the strategy via sonication and hydrothermal processes. GQD electrode material shows an ideal electric double-layer capacitance behavior with a high specific capacitance of 296.7 Fg^{-1}, an energy density of 41.2 W h kg^{-1} at 1 Ag^{-1}, a low internal resistance, and excellent cycling stability. Chen et al. electrodeposited GQD onto 3D graphene to obtain a novel supercapacitor electrode. The composite electrode had a specific capacitance of 268 Fg^{-1}, a 90% increase over the pure 3D graphene electrode. The increase in the electrochemical charge storage performance can be attributed to the increase in surface area and pore size distribution. The presence of microspores with a diameter less than 2 nm increased after GQD deposition. This was mainly due to the formation of new interstices between deposited GQDs on the 3D graphene scaffold. Due to their large inner pore volume and high specific surface area, carbon nanospheres and its various forms have been synthesized and used in supercapacitors as a high-performance electrode material.

Pseudocapacitive electrode materials usually exhibit better energy density than carbonaceous materials. However, the power density is relatively low. Nanocrystalline metal oxides have shown better discharge capacity, resulting in improved power density. Pseudocapacitive materials like transitional metal oxides and sulfides have their performance limited due to low surface area and reaction kinetics. Nanoparticles especially quantum dots have an extremely small size which increases the surface area as well as the surface reaction rate. Metal oxide quantum dots (RuO_2, SnO_2, MnO_2, CoO_x, NiO_x, Nb_2O_5, WO_3, etc.) have been reported as supercapacitor electrode materials with improved performance [24]. Geng et al. [25] synthesized SnO_2 quantum dots (4–6 nm) by microwave-assisted hydrothermal method. The BET analysis revealed a high surface area of 285.5 m^2g^{-1} which contributed to high specific capacitance of 315 Fg^{-1}. Zhao et al. [26] synthesized ruthenium oxide (RuO_2) quantum dots on reduced graphene oxide (rGO) surface by rapid microwave-assisted hydrothermal method. The composite material exhibited specific capacitance of 1120 Fg^{-1} with excellent rate and cyclic stability. RuO_2 is a popular pseudocapacitor with numerous reports; however, in this report, the performance of RuO_2 quantum dots approached the theoretical limit in terms of specific

capacitance. Thus, it is apparent that as the size becomes smaller, the surface area increases and enables better performance. Cong et al. [27] prepared 1.6 nm WO_3 quantum dots demonstrating improvement in electrochemical properties compared to bulk counterparts. The quantum dots showed an increase in capacitance and shift in redox peaks, indicating improved reversibility. To ascertain the reversibility of the redox reactions, the potential difference between the oxidation and reduction peak potential ($E_O - E_R$) is an important parameter. WO_{3-x} QD has 0.12 V, but the bulk counterpart has a 0.25 V potential difference, suggesting the improved reversibility in the case of quantum dots.

1D Structures 1D nanostructures have a certain aspect ratio, that is, length/diameter. According to these values, the nanostructures exhibit different structures such as nanorods, nanotubes, nanowires, and nanoribbons. 1D nanostructures maximize the surface area, provide an efficient pathway for electron transfer, and facilitate deep electrolyte penetration. The electrochemical performance is influenced by the choice and synergistic effect of the component materials and the proper arrangement of the materials. Isacfranklin et al. [28] directly grew one-dimensional carbon nanorods on stainless steel plate by chemical vapor deposition. The electrochemical performance revealed specific capacitance of 198 Fg^{-1} for the free-standing carbon nanorods. Wu et al. [29] reported N-doped carbon nanorods synthesis by one-step pyrolysis of melamine formaldehyde and cellulose nanocrystals. The nanorods had a high surface area of 564.2 m^2g^{-1} which resulted in a specific capacitance of 352 Fg^{-1}. The well-developed porous structure was critical for augmenting the EDLC and stimulating the pseudocapacitance effect. Polyaniline-derived carbon nanotubes were synthesized in bulk with a yield of 300 g in single preparation. Polyaniline nanorods were synthesized by oxidative polymerization of aniline and then converted to carbon nanorods through carbonization under inert atmosphere. The carbon nanorods possessed large specific surface area of 2246 $m^2\,g^{-1}$. The EDLC fabricated from such electrodes exhibited capacitance of 32 Fg^{-1} at 10 Ag^{-1}. Zhao et al. [30] designed binder-free electrode by depositing boron- and nitrogen-doped carbon nanowires onto carbon paper substrate. The electrode material had specific surface area of 1024 m^2g^{-1} and exhibited specific capacitance of 504 Fg^{-1}. Hu et al. [31] reported 1D carbon nanowires with specific capacitance of 258 Fg^{-1} at a current density of 1 Ag^{-1}.

Balamuralitharan et al. [32] synthesized V_2O_5 nanorods by hydrothermal method. The controlling factor was the pH of the solution, which enabled control over the size of nanorods. The 50–10 nm V_2O_5 nanorods provided excellent electron pathways, which improves electrical conductivity and provides a large number of reactive sites for redox reactions. The electrode displayed a high areal specific capacitance of 417.3 mF cm^{-2} in 0.5 M. Cyclic stability of 80% over 5000 cycles suggests that there is still scope for improvement. Similarly, Joseph et al. [33] successfully prepared Bi_2S_3 nanorods through hydrothermal synthesis. These nanorods offer large spaces between each other, which offers better ion intercalation, and electron transport through the structure and facilitate high electrochemical performance. The Bi_2S_3 exhibits a high specific capacity of

134.66 Cg^{-1} at 1 Ag^{-1} current density and a long cycle life of over 5000 cycles. $NiMoO_4$ nanorod electrodes were directly synthesized onto the Ni foam. The binder-free, nanostructured electrode exhibits a high specific capacity of 1320 Cg^{-1}. Saini et al. [34] demonstrated the effect of pH on the size of nanoparticles in the synthesis of hexagonal WO_3. They synthesized nanorods with a specific capacitance of 741 Fg^{-1}. Shinde et al. [35] also reported a specific capacitance of 694 Fg^{-1} for nanorods and nanoneedle-shaped WO_3. Similarly, 1D nanostructures of RuO_2, NiO, MoO_3, MnO_2, TiO_2, etc. have been synthesized and tested as supercapacitor electrode materials [36, 37].

2D Structures 2D nanostructures radically change surface reaction rates, and the structure provides efficient pathways for electrical transport throughout the material, leading to significant improvement in the performance of the electrode. Governed by quantum mechanics, electrons can freely move in the two-dimensional plane, but the motion is constrained in the third direction. Layered 2D materials have asserted dominance in materials science due to their extraordinary electrical, electrochemical, mechanical, and optoelectronic properties. Graphene and its derivatives are well known for their layered morphologies. Its 2D structure provides a large surface area that provides an extensive platform for ion adsorption. High electronic conductivity of graphene enhances power and energy density, while the superior mechanical property enables the fabrication of highly flexible and stable electrodes. Table 2 summarizes the electrochemical performance of graphene and its derivatives as a supercapacitor electrode.

MXenes were developed recently in 2011. They belong to a family of 2D inorganic compounds generally known as MAX. where M denotes the transition metal (V, Mo, W, Nb, Ti, Cr, etc.), X is nitrogen and/or carbon, and A element is tin, aluminum, or silicon. MXene is a novel category of materials that are produced through selective etching of an element from its precursors. These are generally transition metal nitrides, carbides, and carbonitrides, There are several examples of MXene, which have proven to be good electrode materials for supercapacitors. They store the charges through pseudocapacitive mechanisms (reactive metal sites) as well as EDL mechanism due to their high specific surface area.

Transition metal dichalcogenides (TMDs) are layered compounds with MX_2 configuration, in which M is a transition metal element and the term X can be any chalcogenide elements such as S, Se, and Te. The weak van der Waals force is responsible for holding the monolayers in place to form a layered structure. Each constituent layer comprises of three atomic sublayers, in which a transition metal layer is sandwiched in between the two-chalcogen sheets. TMDs have garnered a lot of interests as electrode materials for supercapacitor due to their large surface area, high chemical activity, low cost, high chemical and mechanical stability, and ease of synthesis through facile preparation methods. Table 3 summarizes the electrochemical charge storage performance of different 2D MXenes.

3D Structures 3D materials possess three dimensions, namely, length, width, and height. Unlike 2D materials, 3D materials possess an extra dimension, i.e., thickness

Table 2 Summary of different 2D nanostructured materials and their electrochemical performance

Electrode material	Surface area m^2g^{-1}	Specific capacitance	Synthesis method	References
Porous graphene nanoribbons	1062	223.0 Fg^{-1} at 1.0 Ag^{-1}	Thermal exfoliation under H2-plasma	[38]
N-doped porous reduced graphene	179.60	230 Fg^{-1} at 1 Ag^{-1}	Hydrothermal	[39]
Graphene sheets	862	269 Fg^{-1}	Chemical reduction	[40]
Graphene	520.08	130 Fg^{-1} at 5 mVs^{-1}	Laser irradiation	[41]
$Ni(OH)_2$/graphene	–	537 Fg^{-1}	Filtration-assisted layer-by-layer self-assembly	[42]
MnO_2/graphene	142.01	389 Fg^{-1}	Vacuum filtration	[43]
PANI/graphene	267	1046 Fg^{-1}	In situ polymerization	[44]

Table 3 Summary of different 2D nanostructure material MXenes and metal chalcogenides and their electrochemical performance

Electrode material	Electrolyte	Specific capacitance	References
Ti_3C_2Tx	1 M KOH	140 Fg^{-1}	[45]
V_4C_3	1 M H_2SO_4	268.5 Fg^{-1}	[46]
Ti_3C_2/rGO	1 M H_2SO_4	494.8 Fg^{-1}	[47]
W_2N	1 M KOH	700 Fcm^{-3}	[48]
VN	1 M KOH	1340 Fg^{-1}	[49]
Nb_4N_5	1 M H_2SO_4	225.8 mF cm^{-2}	[50]
TiN	1 M KOH	150 Fg^{-1}	[51]
WS_2	1 M Na_2SO_4	70 Fg^{-1}	[52]
$CuWS_2$	1 M Li_2SO_4	2666.6 Fg^{-1}	[53]
MoS=/rGO	1 M KOH	1071 Fg^{-1}	[54]
$CuSbS_2$	1 M LiOH	120 Fg^{-1}	[55]
$SnSe_2$	6 M KOH	228 Fg^{-1}	[56]
VS_2	$BMIMBF_4$-PVA	4760 μFcm^{-2}	[57]

or depth. 3D nanostructured electrode materials have a high specific surface area, and due to the virtue of their nanostructure, they exhibit good stability (chemical and mechanical). The ordered macroporous structure is responsible for high interfacial area (electrode-electrolyte) and enables efficient ion diffusion and electron transfer within the materials. Ramesh et al. [58] investigated the fabrication of hierarchical 3D nanostructures with different metal oxides and highly porous graphene as support. 3D flower-like nanostructure of Co_3O_4@MnO_2 on nitrogen-doped graphene oxide scaffold showed significant specific capacitance of 347 Fg^{-1} at 0.5 Ag^{-1}. Feng et al. [59] demonstrated self-assembled 3D hierarchical $MnMoO_4$/$NiWO_4$ microspheres for high-performance supercapacitor. The microspheres were synthesized using the hydrothermal method, and the electrode exhibited a high capacitance of 598 Fg^{-1} at a current density of 1 Ag^{-1}. Similarly, 3D MnO_2 nanoparticles decorated on graphene hydrogel showed a maximum capacitance of 242 Fg^{-1} [60]. Dong et al. [61] synthesized 3D graphene foam and loaded Co_3O_4 onto it to fabricate a high capacitance composite. The 3D graphene scaffold provided a platform for the growth of cobalt oxide nanowires. The composite electrode had a high surface area which contributed to a specific capacitance of 1100 Fg^{-1}. Li et al. fabricated 3D honeycomb-like CoN-Ni_3N/N-C nanosheets on carbon cloth via a mild solvothermal method [62]. The electrodes had an areal capacitance of 1.2 F cm^{-2}.

6 Conclusion

Supercapacitor technology has systematically evolved over the last decade. Their current state has benefited from the overall research focused on them. Electrode

material research has greatly improved the electrochemical performance of supercapacitors. Composite electrode materials with compatible components can improve the overall electrochemical performance, but to make the devices commercially viable, a more significant development is necessary. Nanostructured electrode material has proven to be an efficient way to enhance electrochemical performance. 0D nanoparticles generally lead to superior powder density at a high rate, owing to short ion diffusion paths, while 1D structures provide efficient electron-ion transport. In 2D structures, due to the high aspect ratio, electron transfer and movement are unrestricted. This reduces the overall internal resistance of the electrode material. 3D structures with macroporous surfaces are famous for high ion diffusion and electron transfer. Nanostructures have an exceptionally high surface area, which is a vital attribute for electrode material. High surface area ensures deep electrolyte penetration, exposure to a large number of active redox sites, and increase in ion diffusivity and electron conductivity. All these factors directly influence electrochemical performance. When dealing with nanoparticles, the quantum effect also plays an important role in defining the material properties. Synthesis of nanoparticles with different sizes and shapes can enable the designing of electrode materials more suitable for supercapacitor application.

Acknowledgments This work was supported by Basic Science Research Program through the National Research Foundation of Korea (NRF) funded by the Ministry of Education under Grant 2021R1F1A104994711.

References

1. B.E. Conway, B.E. Conway, The electrochemical behavior of ruthenium oxide (RuO2) as a material for electrochemical capacitors. Electrochem. Supercapacitors (1999). https://doi.org/10.1007/978-1-4757-3058-6_11
2. About Nanotechnology | National Nanotechnology Initiative. (n.d.). https://www.nano.gov/about-nanotechnology. Accessed 30 June 2022
3. About the NNI | National Nanotechnology Initiative. (n.d.). https://www.nano.gov/about-nni. Accessed 30 June 2022
4. S. Bayda, M. Adeel, T. Tuccinardi, M. Cordani, F. Rizzolio, The history of nanoscience and nanotechnology: From chemical-physical applications to nanomedicine. Molecules **25** (2020). https://doi.org/10.3390/MOLECULES25010112
5. S. Bruni, C.M. Cellamare, P. Di Lazzaro, A. Gessi, G. Marghella, L. Stante, Analysis of an archaeological linen cloth: The shroud of Arquata. Radiat. Phys. Chem. **167**, 108248 (2020). https://doi.org/10.1016/j.radphyschem.2019.03.052
6. A. Melelli, D.U. Shah, G. Hapsari, R. Cortopassi, S. Durand, O. Arnould, V. Placet, D. Benazeth, J. Beaugrand, F. Jamme, A. Bourmaud, Lessons on textile history and fibre durability from a 4,000-year-old Egyptian flax yarn. Nat. Plants **79**(7), 1200–1206 (2021). https://doi.org/10.1038/s41477-021-00998-8
7. D. Rajput, B. Patgiri, OA01.02. Literary study on heavy metal poisoning and ayurveda with special reference to Naga Bhasma (Calcined Lead). Anc. Sci. Life **32**, 2 (2012). https://doi.org/10.4103/0257-7941.111959
8. (16) (PDF) Sikata varga (Silicate-containing-compounds) in ayurvedic medicine: An updated review. (n.d.). https://www.researchgate.net/publication/351915047_Sikata_varga_Silicate-containing-compounds_in_Ayurvedic_Medicine_An_Updated_Review. Accessed 30 June 2022

9. S.S. Savrikar, B. Ravishankar, Introduction to "Rasashaastra" the iatrochemistry of ayurveda. Afr. J. Tradit. Complement. Altern. Med. **8**, 66–82 (2011). https://doi.org/10.4314/ajtcam.v8i5S.1
10. Rasashastra – Wikipedia. (n.d.). https://en.wikipedia.org/wiki/Rasashastra. Accessed 30 June 2022
11. L.C. (Lakshmi C. Mishra), *Scientific Basis for Ayurvedic Therapies* (Routledge, 2004), p. 626
12. M.S. Del Río, A. Doménech, M.T. Doménech-Carbó, M.L.V. De Agredos Pascual, M. Suárez, E. García-Romero, The Maya blue pigment. Dev. Clay Sci. **3**, 453–481 (2011). https://doi.org/10.1016/B978-0-444-53607-5.00018-9
13. Y. Lu, A. Wang, From structure evolution of palygorskite to functional material: A review. Microporous Mesoporous Mater. **333** (2022). https://doi.org/10.1016/j.micromeso.2022.111765
14. L. Li, G. Zhuang, M. Li, P. Yuan, L. Deng, H. Guo, Influence of indigo-hydroxyl interactions on the properties of sepiolite-based Maya blue pigment. Dyes Pigments **200** (2022). https://doi.org/10.1016/j.dyepig.2022.110138
15. E. Ruiz-Hitzky, P. Aranda, A. Álvarez, J. Santarén, A. Esteban-Cubillo, Advanced materials and new applications of sepiolite and palygorskite. Dev. Clay Sci. **3**, 393–452 (2011). https://doi.org/10.1016/B978-0-444-53607-5.00017-7
16. There's Plenty of Room at the Bottom – Caltech Magazine. (n.d.). http://calteches.library.caltech.edu/1976/. Accessed 30 June 2022
17. K.E. Drexler, *Engines of Creation: The Coming Era of Nanotechnology* (Anchor Books, 1986), p. 320
18. V.V. Pokropivny, V.V. Skorokhod, Classification of nanostructures by dimensionality and concept of surface forms engineering in nanomaterial science. Mater. Sci. Eng. C **27**, 990–993 (2007). https://doi.org/10.1016/J.MSEC.2006.09.023
19. A. Prasath, M. Athika, E. Duraisamy, A.S. Sharma, P. Elumalai, Carbon-quantum-dot-derived nanostructured MnO2 and its symmetrical supercapacitor performances. ChemistrySelect. **3**, 8713–8723 (2018). https://doi.org/10.1002/SLCT.201801950
20. X. Zhao, M. Li, H. Dong, Y. Liu, H. Hu, Y. Cai, Y. Liang, Y. Xiao, M. Zheng, Interconnected 3 D network of graphene-oxide nanosheets decorated with carbon dots for high-performance supercapacitors. ChemSusChem **10**, 2626–2634 (2017). https://doi.org/10.1002/CSSC.201700474
21. V.C. Hoang, V.G. Gomes, High performance hybrid supercapacitor based on doped zucchini-derived carbon dots and graphene. Mater. Today Energy **12**, 198–207 (2019). https://doi.org/10.1016/J.MTENER.2019.01.013
22. W. Liu, X. Yan, J. Chen, Y. Feng, Q. Xue, Novel and high-performance asymmetric micro-supercapacitors based on graphene quantum dots and polyaniline nanofibers. Nanoscale **5**, 6053–6062 (2013). https://doi.org/10.1039/C3NR01139A
23. S. Zhang, L. Sui, H. Dong, W. He, L. Dong, L. Yu, High-performance supercapacitor of graphene quantum dots with uniform sizes. ACS Appl. Mater. Interfaces **10**, 12983–12991 (2018). https://doi.org/10.1021/ACSAMI.8B00323
24. V.C. Lokhande, A.C. Lokhande, C.D. Lokhande, J.H. Kim, T. Ji, Supercapacitive composite metal oxide electrodes formed with carbon, metal oxides and conducting polymers. J. Alloys Compd. **682**, 381–403 (2016). https://doi.org/10.1016/J.JALLCOM.2016.04.242
25. J. Geng, C. Ma, D. Zhang, X. Ning, Facile and fast synthesis of SnO2 quantum dots for high performance solid-state asymmetric supercapacitor. J. Alloys Compd. **825**, 153850 (2020). https://doi.org/10.1016/J.JALLCOM.2020.153850
26. J. Zhao, J. Zhang, H. Yin, Y. Zhao, G. Xu, J. Yuan, X. Mo, J. Tang, F. Wang, Ultra-fine ruthenium oxide quantum dots/reduced graphene oxide composite as electrodes for high-performance supercapacitors. Nanomater **12**, 1210 (2022). https://doi.org/10.3390/NANO12071210
27. S. Cong, Y. Tian, Q. Li, Z. Zhao, F. Geng, S. Cong, Y.Y. Tian, Q.W. Li, Z.G. Zhao, F.X. Geng, Single-crystalline tungsten oxide quantum dots for fast pseudocapacitor and electrochromic applications. Adv. Mater. **26**, 4260–4267 (2014). https://doi.org/10.1002/ADMA.201400447

28. M. Isacfranklin, R. Yuvakkumar, P. Senthil Kumar, V. Thirumal, G. Ravi, D. Velauthapillai, Hydrogen free direct growth carbon nanorod as a promising electrode in symmetric supercapacitor applications. Prog. Org. Coat. **158**, 106379 (2021). https://doi.org/10.1016/J.PORGCOAT.2021.106379
29. X. Wu, Z. Shi, R. Tjandra, A.J. Cousins, S. Sy, A. Yu, R.M. Berry, K.C. Tam, Nitrogen-enriched porous carbon nanorods templated by cellulose nanocrystals as high performance supercapacitor electrodes. J. Mater. Chem. A **3**, 23768–23777 (2015). https://doi.org/10.1039/C5TA07252B
30. Z. Zhao, Y. Xie, Electrochemical supercapacitor performance of boron and nitrogen co-doped porous carbon nanowires. J. Power Sources **400**, 264–276 (2018). https://doi.org/10.1016/J.JPOWSOUR.2018.08.032
31. Z. Hu, S. Li, P. Cheng, W. Yu, R. Li, X. Shao, W. Lin, D. Yuan, N,P-co-doped carbon nanowires prepared from bacterial cellulose for supercapacitor. J. Mater. Sci. **51**, 2627–2633 (2016). https://doi.org/10.1007/S10853-015-9576-X/FIGURES/6
32. B. Balamuralitharan, I.H. Cho, J.S. Bak, H.J. Kim, V2O5 nanorod electrode material for enhanced electrochemical properties by a facile hydrothermal method for supercapacitor applications. New J. Chem. **42**, 11862–11868 (2018). https://doi.org/10.1039/C8NJ02377H
33. N. Joseph, C. Raj, A. Chandra Bose, Hydrothermally synthesized Bi2S3 nanorod for supercapacitor electrode application. AIP Conf. Proc. **2265**, 030607 (2020). https://doi.org/10.1063/5.0017546
34. S. Saini, P. Chand, Effect of aqueous electrolytes on h-WO3 nanorods as an electrode material for supercapacitor application. Chem. Phys. Lett. **802**, 139760 (2022). https://doi.org/10.1016/J.CPLETT.2022.139760
35. P.A. Shinde, A.C. Lokhande, N.R. Chodankar, A.M. Patil, J.H. Kim, C.D. Lokhande, Temperature dependent surface morphological modifications of hexagonal WO3 thin films for high performance supercapacitor application. Electrochim. Acta **224**, 397–404 (2017). https://doi.org/10.1016/J.ELECTACTA.2016.12.066
36. R.S. Devan, R.A. Patil, J.H. Lin, Y.R. Ma, One-dimensional metal-oxide nanostructures: Recent developments in synthesis, characterization, and applications. Adv. Funct. Mater. **22**, 3326–3370 (2012). https://doi.org/10.1002/ADFM.201201008
37. Y. Ma, X. Xie, W. Yang, Z. Yu, X. Sun, Y. Zhang, X. Yang, H. Kimura, C. Hou, Z. Guo, W. Du, Adv. Compos. Hybrid Mater. **44**(4), 906–924 (Recent advances in transition metal oxides with different dimensions as electrodes for high-performance supercapacitors, 2021). https://doi.org/10.1007/S42114-021-00358-2
38. M. Torabi, R. Karimi Shervedani, A. Amini, High performance porous graphene nanoribbons electrodes synthesized via hydrogen plasma and modified by Pt-Ru nanoclusters for charge storage and methanol oxidation. Electrochim. Acta **290**, 616–625 (2018). https://doi.org/10.1016/J.ELECTACTA.2018.09.082
39. S.K. Singh, V.M. Dhavale, R. Boukherroub, S. Kurungot, S. Szunerits, N-doped porous reduced graphene oxide as an efficient electrode material for high performance flexible solid-state supercapacitor. Appl. Mater. Today **8**, 141–149 (2017). https://doi.org/10.1016/J.APMT.2016.10.002
40. Y. Si, E.T. Samulski, Exfoliated graphene separated by platinum nanoparticles. Chem. Mater. **20**, 6792–6797 (2008). https://doi.org/10.1021/CM801356A
41. D. Yang, C. Bock, Laser reduced graphene for supercapacitor applications. J. Power Sources **337**, 73–81 (2017). https://doi.org/10.1016/J.JPOWSOUR.2016.10.108
42. M. Li, Z. Tang, M. Leng, J. Xue, Flexible solid-state supercapacitor based on graphene-based hybrid films. Adv. Funct. Mater. **24**, 7495–7502 (2014). https://doi.org/10.1002/ADFM.201402442
43. B.G. Choi, M. Yang, W.H. Hong, J.W. Choi, Y.S. Huh, 3D macroporous graphene frameworks for supercapacitors with high energy and power densities. ACS Nano **6**, 4020–4028 (2012). https://doi.org/10.1021/NN3003345/SUPPL_FILE/NN3003345_SI_001.PDF
44. J. Yan, T. Wei, B. Shao, Z. Fan, W. Qian, M. Zhang, F. Wei, Preparation of a graphene nanosheet/polyaniline composite with high specific capacitance. Carbon N.Y. **48**, 487–493 (2010). https://doi.org/10.1016/J.CARBON.2009.09.066

45. S. Xu, G. Wei, J. Li, Y. Ji, N. Klyui, V. Izotov, W. Han, Binder-free Ti3C2Tx MXene electrode film for supercapacitor produced by electrophoretic deposition method. Chem. Eng. J. **317**, 1026–1036 (2017). https://doi.org/10.1016/J.CEJ.2017.02.144
46. X. Wang, S. Lin, H. Tong, Y. Huang, P. Tong, B. Zhao, J. Dai, C. Liang, H. Wang, X. Zhu, Y. Sun, S. Dou, Two-dimensional V4C3 MXene as high performance electrode materials for supercapacitors. Electrochim. Acta **307**, 414–421 (2019). https://doi.org/10.1016/J.ELECTACTA.2019.03.205
47. Q. Yang, Z. Xu, B. Fang, T. Huang, S. Cai, H. Chen, Y. Liu, K. Gopalsamy, W. Gao, C. Gao, MXene/graphene hybrid fibers for high performance flexible supercapacitors. J. Mater. Chem. A **5**, 22113–22119 (2017). https://doi.org/10.1039/C7TA07999K
48. S. Ouendi, K. Robert, D. Stievenard, T. Brousse, P. Roussel, C. Lethien, Sputtered tungsten nitride films as pseudocapacitive electrode for on chip micro-supercapacitors. Energy Storage Mater. **20**, 243–252 (2019). https://doi.org/10.1016/J.ENSM.2019.04.006
49. D. Choi, G.E. Blomgren, P.N. Kumta, Fast and reversible surface redox reaction in nanocrystalline vanadium nitride supercapacitors. Adv. Mater. **18**, 1178–1182 (2006). https://doi.org/10.1002/ADMA.200502471
50. H. Cui, G. Zhu, X. Liu, F. Liu, Y. Xie, C. Yang, T. Lin, H. Gu, F. Huang, H. Cui, G. Zhu, F. Liu, Y. Xie, C. Yang, T. Lin, H. Gu, F. Huang, X. Liu, Niobium nitride Nb4N5 as a new high-performance electrode material for supercapacitors. Adv. Sci. **2**, 1500126 (2015). https://doi.org/10.1002/ADVS.201500126
51. X. Zhou, C. Shang, L. Gu, S. Dong, X. Chen, P. Han, L. Li, J. Yao, Z. Liu, H. Xu, Y. Zhu, G. Cui, Mesoporous coaxial titanium nitride-vanadium nitride fibers of core-shell structures for high-performance supercapacitors. ACS Appl. Mater. Interfaces **3**, 3058–3063 (2011). https://doi.org/10.1021/AM200564B/ASSET/IMAGES/LARGE/AM-2011-00564B_0007.JPEG
52. S. Ratha, C.S. Rout, Supercapacitor electrodes based on layered tungsten disulfide-reduced graphene oxide hybrids synthesized by a facile hydrothermal method. ACS Appl. Mater. Interfaces **5**, 11427–11433 (2013). https://doi.org/10.1021/AM403663F/SUPPL_FILE/AM403663F_SI_001.PDF
53. P. Pazhamalai, K. Krishnamoorthy, S. Sahoo, V.K. Mariappan, S.J. Kim, Copper tungsten sulfide anchored on Ni-foam as a high-performance binder free negative electrode for asymmetric supercapacitor. Chem. Eng. J. **359**, 409–418 (2019). https://doi.org/10.1016/J.CEJ.2018.11.153
54. R.N. Bulakhe, V.H. Nguyen, J.J. Shim, Layer-structured nanohybrid MoS2@rGO on 3D nickel foam for high performance energy storage applications. New J. Chem. **41**, 1473–1482 (2017). https://doi.org/10.1039/C6NJ02590K
55. K. Ramasamy, R.K. Gupta, H. Sims, S. Palchoudhury, S. Ivanov, A. Gupta, Layered ternary sulfide CuSbS 2 nanoplates for flexible solid-state supercapacitors. J. Mater. Chem. A **3**, 13263–13274 (2015). https://doi.org/10.1039/C5TA03193A
56. C. Zhang, H. Yin, M. Han, Z. Dai, H. Pang, Y. Zheng, Y.Q. Lan, J. Bao, J. Zhu, Two-dimensional tin selenide nanostructures for flexible all-solid-state supercapacitors. ACS Nano **8**, 3761–3770 (2014). https://doi.org/10.1021/NN5004315/SUPPL_FILE/NN5004315_SI_001.PDF
57. J. Feng, X. Sun, C. Wu, L. Peng, C. Lin, S. Hu, J. Yang, Y. Xie, Metallic few-layered VS2 ultrathin nanosheets: High two-dimensional conductivity for in-plane supercapacitors. J. Am. Chem. Soc. **133**, 17832–17838 (2011). https://doi.org/10.1021/JA207176C/SUPPL_FILE/JA207176C_SI_001.PDF
58. S. Ramesh, K. Karuppasamy, H.S. Kim, H.S. Kim, J.H. Kim, Hierarchical flowerlike 3D nanostructure of Co3O4@MnO2/N-doped graphene oxide (NGO) hybrid composite for a high-performance supercapacitor. Sci. Rep. **81**(8), 1–11 (2018). https://doi.org/10.1038/s41598-018-34905-7
59. X. Feng, Y. Huang, M. Chen, X. Chen, C. Li, S. Zhou, X. Gao, Self-assembly of 3D hierarchical MnMoO4/NiWO4 microspheres for high-performance supercapacitor. J. Alloys Compd. **763**, 801–807 (2018). https://doi.org/10.1016/J.JALLCOM.2018.06.025

60. S. Wu, W. Chen, L. Yan, Fabrication of a 3D MnO2/graphene hydrogel for high-performance asymmetric supercapacitors. J. Mater. Chem. A **2**, 2765–2772 (2014). https://doi.org/10.1039/C3TA14387B
61. X.C. Dong, H. Xu, X.W. Wang, Y.X. Huang, M.B. Chan-Park, H. Zhang, L.H. Wang, W. Huang, P. Chen, 3D graphene-cobalt oxide electrode for high-performance supercapacitor and enzymeless glucose detection. ACS Nano **6**, 3206–3213 (2012). https://doi.org/10.1021/NN300097Q/SUPPL_FILE/NN300097Q_SI_001.PDF
62. K. Li, B. Zhao, H. Zhang, H. Lv, J. Bai, H. Ma, P. Wang, W. Li, J. Si, X. Zhu, Y. Sun, 3D porous honeycomb-like CoN-Ni3N/N-C nanosheets integrated electrode for high-energy-density flexible supercapacitor. Adv. Funct. Mater. **31**, 2103073 (2021). https://doi.org/10.1002/ADFM.202103073

Emerging Electrode Materials for Li-Ion Capacitor

A. C. Lokhande and D. Choi

Abbreviations

AC	Activated carbon
CMC	Carboxymethylcellulose
C	Carbon
CNTs	Carbon nanotubes
CV	Cyclic voltammetry
GCD	Galvanostatic charge-discharge
DC	Diethyl carbonate
ED	Energy density
EDLC	Electric double-layer capacitance
EC	Ethylene carbonate
FEC	Fluoroethylene carbonate
GG	Guar gum
GO	Graphene oxide
HCl	Hydrochloric acid
HF	Hydrofluoric acid
ICE	Initial coulombic efficiency
LICs	Lithium-ion capacitors
LIBs	Lithium-ion batteries
LTO	$Li_4Ti_5O_{12}$
LFP	$LiFePO_4$
LiDFP	Lithium difluorophosphate
lacOCA	Lactic acid O-carboxyanhydride

A. C. Lokhande (✉) · D. Choi (✉)
Department of Mechanical Engineering, Khalifa University of Science and Technology, Abu Dhabi, United Arab Emirates
e-mail: abhshek.lokhande@ku.ac.ae; daniel.choi@ku.ac.ae

F. I. Ezema et al. (eds.), *Chemically Deposited Metal Chalcogenide-based Carbon Composites for Versatile Applications*, https://doi.org/10.1007/978-3-031-23401-9_5

LiFOB	Lithium difluoro(oxalato)borate
MEMP-DFOB	Mesylethyl-methyl-pyrrolidinium
NMP	N-methyl-2-pyrrolidone
NACA	N-acetylcaprolactam
N	Nitrogen
1D	One dimensional
PVDF	Polyvinylidene fluoride
PD	Power density
PCN	Porous carbon nanofiber
PDMS	Polydimethylsiloxane
PVA	Polyvinyl alcohol
PAA	Polyacrylic acid
PR	Polyrotaxane
PFPI	Pentafluorophenyl isocyanate
SCs	Supercapacitors
C_s	Specific capacitance
SiO_2	Silicon dioxide
SA	Sodium alginate
DFEC	Trans-difluoroethylene carbonate
TFPC	Trifluoropropylene carbonate
0D	Zero dimensional

1 Introduction

Renewable energy sources such as tidal, wind, and solar energy have gained significant attention in recent years as an effective alternative to traditional energy sources (wood, coal, petroleum, etc.) due to their clean and abundant nature [1]. However, these energy sources' erratic nature results in uncertainties regarding noncontinuous power generation and utilization. As a result, energy storage systems play an important role in overcoming these drawbacks by providing the desired energy needs. Various energy storage systems such as thermal and hydropower energy storage, flow batteries, electrochemical batteries, flywheel, and compressed air energy have been reported [2]. Out of these, electrochemical energy storage has emerged as a reliable and well-established technology for satisfying ever-rising energy demands.

Electrochemical energy storage systems consist of lithium-ion batteries (LIBs) and supercapacitors. These energy storage devices occupy a very crucial status in the electronic industry such as electric vehicles and portable electronics. Typically, LIBs exhibit high energy density (100–150 Wh/kg) but suffer from poor power density (<1 kW/kg) and lower cyclic stability (<4000 cycles) [3]. On the contrary, supercapacitors exhibit high power density (>10 kW/kg) and high cyclic stability but suffer from low energy density (10–20 Wh/kg) [4]. These combined drawbacks result in very limited applications of LIBs and supercapacitors in commercial

systems where simultaneous high energy and high power densities are required. The employed electrode plays a significant role in tuning the electrochemical performance of these energy storage devices. Usually, the electrodes used in LIBs exhibit a charge storage mechanism based on slow redox reactions (faradic reactions). On the other hand, the supercapacitor electrode exhibits a charge storage mechanism, that is, electric double-layer capacitance (EDLC) based on rapid surface capacitive reactions. So far, numerous research attempts have been made to improve the energy density of supercapacitors by developing high surface area carbon-based electrodes and the power density of LIBs by enhancing the reaction kinetics at the electrode-electrolyte interface. However, the performance attained by these energy storage devices is still not satisfactory.

Commercial electrical systems usually require high energy and high power density for operation [5]. However, none of the energy storage devices such as batteries and supercapacitors are competent enough to provide the desired energy requirements. Thus, there is a great need to develop an energy storage system that integrates the combined advantages of batteries (high energy density) and supercapacitors (high power density). In this regard, hybrid lithium-ion capacitors (LICs) consisting of battery-type anode (redox) and supercapacitive-type cathode (EDLC) have emerged as reliable energy storage devices for commercial systems [6]. LICs exhibit enhanced energy and power densities with higher cyclic stability. As a result, LICs form a bridge between the traditional batteries and capacitors, which can be used in a variety of commercial electronic applications (Fig. 1). The concept of LIC was first demonstrated in 2001 by Amatucci et al. [7] by fabricating a device based on $Li_4Ti_5O_{12}$ (LTO) redox anode and activated carbon (AC) EDLC

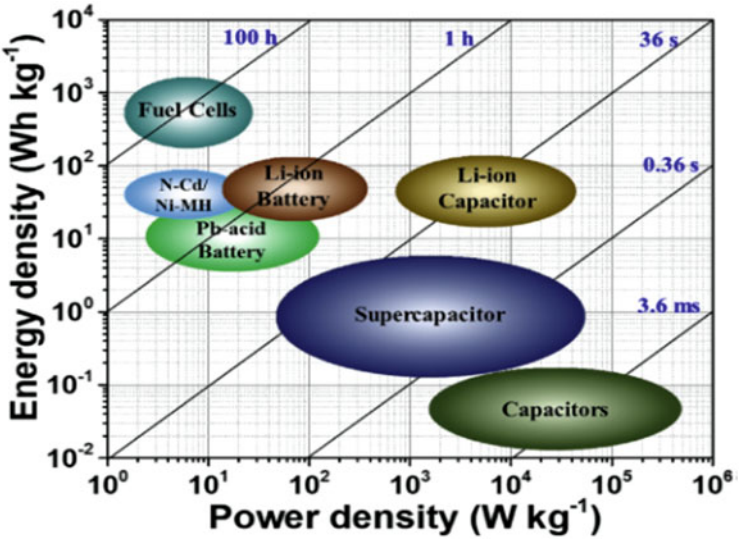

Fig. 1 The reported various energy storage systems. (Reprinted with copyright permission from Ref. [2])

cathode. Since then, numerous research attempts have been made to develop high-performance LICs. LICs' performance is mostly influenced by the properties of electrode materials [8]. One of the major challenges associated with LICs is the kinetic imbalance between the sluggish reaction-based anode and the rapid surface reaction-based cathode [9]. Therefore, developing the anode property by making it kinetically compatible with the cathode is the possible solution for attaining high-performance LICs. The strategies involved in improving the anode properties generally include the modifications of the electrode material's structural, electrical, and chemical properties. Additionally, exploring and developing novel electrode materials are the key to achieving improved LICs' performance. Therefore, in this chapter, we aim to discuss the fundamental idea of LIC along with the selection criteria for electrode materials, current developments, drawbacks, and future scope of LICs.

2 Architecture, Fabrication, and Performance Evaluation of LIC

The typical LIC device structure is shown in Fig. 2.

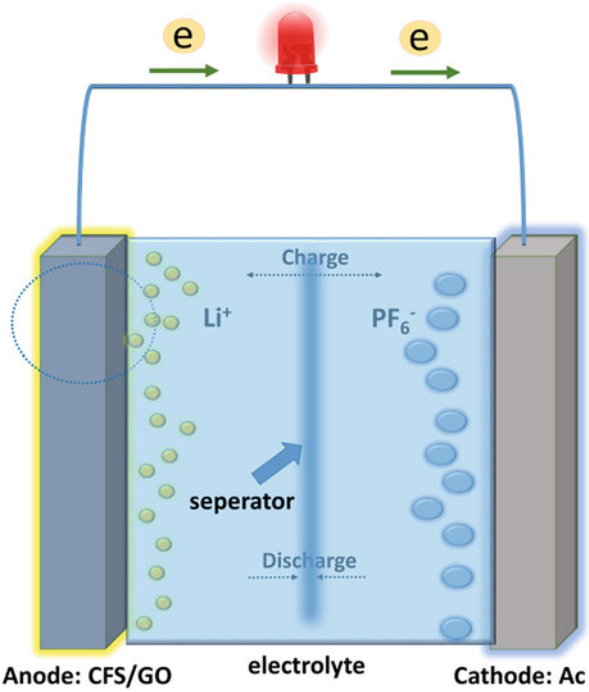

Fig. 2 The schematic structure of the lithium-ion capacitor (LIC)

As seen, LIC is composed of four components, namely, anode, cathode, electrolyte, and separator. The anode is the redox-type electrode in which the charge storage mechanism is accomplished through the intercalation/de-intercalation reactions of Li ions. The cathode is based on EDLC material where the charge storage mechanism is accomplished through surface adsorption reactions. Generally, high surface area carbon materials are usually employed as cathodes. A high charge capacity is obtained in cathodes due to efficient charge separation in the Helmholtz double layer at the electrolyte-electrode interface [10]. Both the electrodes (anode and cathode) are placed in an electrolyte containing Li salts. The electrolyte is composed of three main components, namely, the lithium salt which acts as the charge carrier, the additives that improve the physical and chemical properties, and the solvent that is used to dissolve the Li salt and additives (Fig. 3). The LIC electrolytes can be classified as aqueous and nonaqueous (organic) [11]. The aqueous electrolytes have low viscosity and high ionic mobility. As a result, they exhibit high power density and high rate capacity. Some of the commonly aqueous electrolytes are alkaline nitrates ($LiNO_3$), sulfates (Li_2SO_4), and hydrates (LiOH). However, the aqueous electrolytes exhibit the disadvantage of the low operating potential (up to 1.2 V) [12]. Due to this, the aqueous electrolytes exhibit low energy density. On the contrary, the nonaqueous electrolytes exhibit a wide operating potential of up to 3 V for organic electrolytes and 4 V for ionic liquids [13]. As a result, ultra-high energy densities are attained for the nonaqueous electrolytes. However, the low ionic mobility of these nonaqueous electrolytes due to high viscosity results in lower power density. Generally, $LiPF_6$ salt dissolved in an

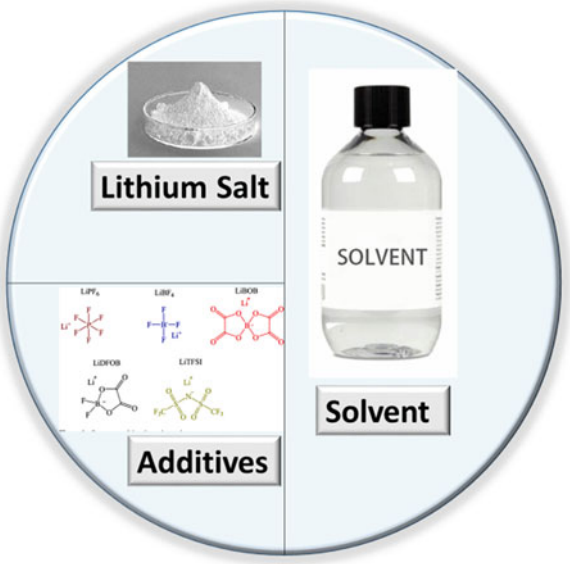

Fig. 3 The components of the Li-ion-based electrolyte

equal mixture of ethylene carbonate (EC) and diethyl carbonate (DC) is used as the organic electrolyte. The organic electrolyte is highly moisture sensitive, and thus, the LIC device fabrication is done in an inert environment (Ar) inside the glovebox. The separator used is a polypropylene, ceramic, or glass fiber membrane. The separator promotes the efficient travel of electrolyte ions to the electrodes. During charging, the Li^{+} ions intercalate into the anode, and the PF^{6-} ions adsorb on the cathode. During discharging, these ions revert into the electrolyte. Thus, the motion of these ions from the electrolyte to electrodes and vice versa results in charging-discharging cycles.

The process of LIC fabrication is similar to that of the LIBs. The electrode materials are fabricated using the "conventional slurry-coating" approach. In electrode fabrication, the active material is mixed with a binder and conductive carbon material in a solvent to form a slurry. The slurry is then coated on the conducting substrate using the drop-casting or doctor-blade method and dried to form the active electrode. Polyvinylidene fluoride (PVDF) and N-methyl-2-pyrrolidone (NMP) are the commonly used binder and solvent, respectively. Carbon black, super-P, or activated carbon (AC) is used as the conductive carbon material. The ratio of the active material/binder/conducting carbon material is generally kept as 75:10:15, respectively. For the anode and the cathode fabrication, the slurry is coated on copper and aluminum foil, respectively, for efficient charge extraction. The drawback of this conventional slurry-coating approach is that it is a time-consuming and complex method. Additionally, the use of binders reduces the capacity of the electrodes as it significantly raises the "dead weight" and introduces high electrical resistance [14]. Thus, the possible solution to restore the capacity is to fabricate "binder-free" electrodes. The binder-free electrodes can be fabricated using the "wet filtration technique" [15]. In this technique, a homogeneous dispersion of active electrode material and carbon nanotubes (CNTs) is obtained in an aqueous medium (water + ethanol) and then vacuum filtration followed by air drying (80 °C – 2 h) to form the active electrode (Fig. 4). The electrochemical contribution of the CNTs is negligible as it only acts as the support structure (substrate) for the active material. Most of the charge generation/storage is exclusively contributed by the active material. Vacuum filtration is advantageous as it allows the easy escape of solvent between composite channels, enabling the formation of a uniform and dense stacking-like composite structure. Additionally, vacuum filtration enables the formation of a binder-free

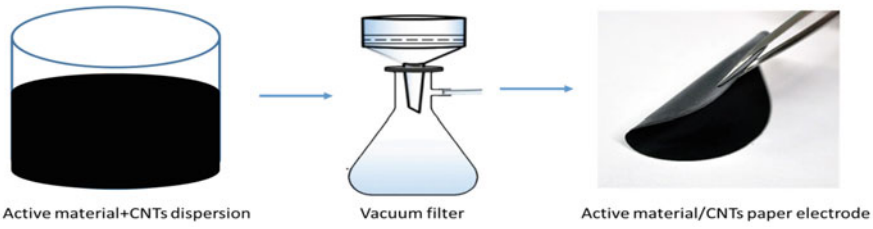

Fig. 4 The schematics of the wet filtration technique

electrode in the form of thin paper or membrane (buckypaper) that can be directly used for energy storage applications.

The LIC performance is evaluated using standard electrochemical techniques such as cyclic voltammetry (CV), galvanostatic charge-discharge (GCD), and electrochemical impedance spectroscopy (EIS) under ambient conditions. The specific capacitance (C_s), energy density (E), and power density (P) of the LIC device are calculated from the GCD analysis using the following equations:

$$C_s = \frac{I \times T_d}{(V_2 - V_1) \times m} \tag{1}$$

$$E = \frac{0.5 \times C_s \times (V_2 - V_1)^2}{3.6} \tag{2}$$

$$P = \frac{E \times 3600}{T_d} \tag{3}$$

Here, the discharging time is in seconds (s), E is the energy density, and P is the power density. Furthermore, as the LIC device structure is hybrid (anode and cathode are different), the specific capacity of the electrodes is different. Therefore, systematic mass balancing (anode/cathode) is required to match the reaction kinetics of the electrodes. The mass balancing is attained using the equation below:

$$Q_+ = Q_- \, (Q = C \times V \times m) \tag{4}$$

C, V, and m are the capacitance, operating voltage, and mass of the active material, respectively. The significance of mass balancing is that it results in proper and equal utilization of the electrodes during charging/discharging processes, thereby resulting in higher capacity with longer cyclic stability. If mass balancing is not achieved, either of the electrodes (anode or cathode) will be over/underutilized, eventually leading to significant performance deterioration.

3 Electrodes of LIC

The performance of LICs is exclusively governed by the properties of the electrodes. Hence, major emphasis is given to the development of advanced electrodes to achieve the desired efficient performance. Various anode materials based on metalloids (Si/C, Sn/C) [16], transition metal compounds (TiO_2, Nb_2O_5, Fe_2O_3, LTO) [17–19], polyanions (TiP_2O_7/C, $TiNb_2O_7$/C) [20, 21], and graphite [22] in combination with EDLC-type cathode based on the carbonaceous materials

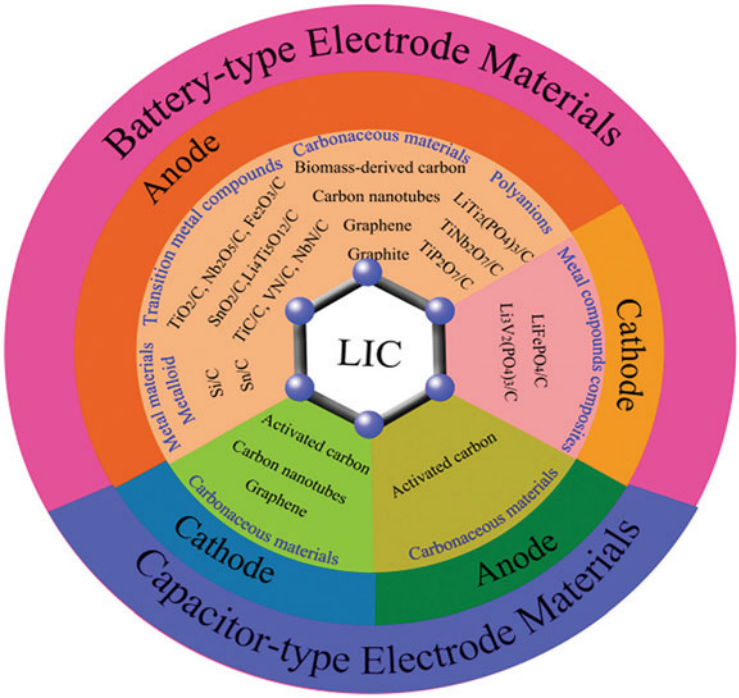

Fig. 5 The various reported electrode materials for LICs. (Reprinted with copyright permission from Ref. [84])

(graphene and Ac) have been reported as electrodes for LICs (Fig. 5). Based on the involved charge storage mechanism, these electrodes are classified into three types, namely, (a) insertion type, (b) conversion type, and (c) alloying type [23]. The insertion-type electrodes such as graphite, LTO, $LiCrTiO_4$, TiO_2, TiP_2O_7, and $LiTi_2(PO_4)_3$ are structurally stable and hence exhibit high cyclic stability [19, 20, 24–26]. However, their high de-intercalation potential (1.5 V vs. Li/Li^+) limits the output voltage, resulting in lower energy density. In addition, the lower electrical conductivity, as well as the lower theoretical capacity (140 mAh/g for LTO and 372 mAh/g for graphite) of these materials, also results in reduced performance. The conversion-type electrodes such as V_2O_5, VN, Nb_2O_5, Fe_2O_3, and MnO exhibit high energy capacity and high-rate capability due to efficient redox activity [27–31]. However, these electrodes suffer from volume expansion issues that result in gradual capacity loss after subsequent cycling. The third type of electrodes based on the alloying mechanism (Cu/Si, Sn, B-Si, SiO_2) [32, 33] even exhibits higher energy capacity than the conversion-type electrodes, but suffers from rapid capacity loss during successive cycles due to significantly high volume expansion issues (300 times for Si) [34]. In addition, the kinetic charge imbalance between the redox-type anode and the EDLC-type cathode also results in restricted electrochemical

performance. Hence, there is a great need to explore and develop novel anode electrodes that overcome these existing problems and deliver efficient performance in LICs for commercial applications. In this chapter, we tend to discuss the most commonly reported electrodes for LIC application. The electrodes based on sulfides [35–41], oxides [42–57], silicon [58–77], two-dimensional (2D) structured MXene [78–83], and carbon [84–92] materials are discussed in this chapter.

3.1 Sulfide-Based Electrodes for LIC

Metal sulfides have emerged as the ideal material for energy storage applications due to their numerous advantages such as low cost, easy processability, high natural abundance, high electrical conductivity, high theoretical capacity, low electronegativity, and superior redox activity [35–37]. Metal sulfides based on multiple atoms (binary sulfides) have also been used as reliable electrode materials due to their rich oxidation states. The metal-sulfur (M-S) bonding is weak, and as a result, the structure can be easily polarized, thereby leading to high redox activity (high charge generation) [38–41]. Metal sulfides such as MoS_2, SnS, CoS, MnS, Cu_2SnS_3, etc. have been reported for LIC application [35–41]. The MoS_2 is a transition metal sulfide and exhibits a structure analogous to graphite (layered structure). Recently, MoS_2 has emerged as a suitable electrode material in LIB and LIC applications due to its captivating properties such as high ionic conductivity, high theoretical capacity (669–1675 mAh/g), and wider interatomic layer spacing (0.62 nm) [35, 36]. The MoS_2 structure is composed of three atomic layers in which the Mo layer is sandwiched between two S layers and interacted with a weak van der Waals force. As a result, the interatomic layer spacing can be easily varied, resulting in easy and resistance-free Li-ion intercalation/de-intercalation. Additionally, the layered structure of the MoS_2 provides double-layer capacitance that is highly beneficial for obtaining superior rate capabilities. Ju et al. [35] fabricated a MoS_2-based porous carbon nanofiber (PCN) composite electrode for LIC. The PCN/MoS_2 composite was fabricated in a two-step process in which the PCNs were initially synthesized using the electrospinning method and then the MoS_2 nanosheets were fabricated on the PCNs using a carbonization pretreatment followed by the hydrothermal method (Fig. 6a). The fabricated PCN/MoS_2 composite exhibited a unique structure in which the MoS_2 nanoflake-flowerballs were uniformly deposited on PCNs. The combination of one-dimensional (1D) PCNs and 3D MoS_2 nanoflake-flowerballs resulted in the formation of a porous hierarchical structure with a high surface area (81.67 m^2/g) (Fig. 6b). The LIC device fabricated with the PCN/MoS_2 composite anode and AC as cathode delivered a high performance with a maximum energy density (ED) of 75.5 Wh/kg and a power density (PD) of 25.5 kW/kg. The obtained performance was attributed to the synergistic effect of the evenly distributed 3D structured MoS_2 nanoflake-flowerballs that provided stupendous electro-active sites for Li-ion storage and the PCNs that provided the least resistance conductive pathways for ionic diffusion. Additionally, the PCNs also avoided the aggregation

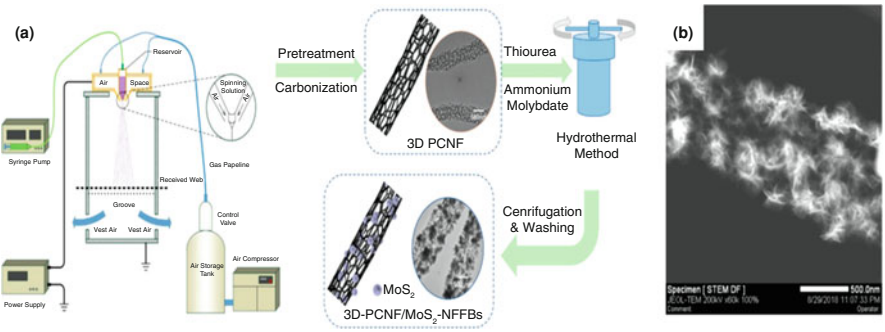

Fig. 6 (**a**) The schematics of the multistep fabrication process of the MoS_2 nanosheets and (**b**) the FESEM image of the composite porous carbon nanofiber (PCNF)/MoS_2 nanosheets. (Reprinted with copyright permission from Ref. [35])

of MoS_2 nanostructures during electrochemical cycles, thereby restoring their active electrosites. However, the LIC device exhibited low cyclic stability of 78% for 5000 cycles which could be ascribed to the volume expansion issues and the polysulfide diffusion effect of the MoS_2 nanostructures.

Wang et al. [36] attempted to solve these issues of MoS_2 nanostructures and improve the electrochemical performance by utilizing a novel structural strategy. The strategy was based on the encapsulation of MoS_2 nanostructures with RGO nanosheets and introducing a conductive carbon layer between MoS_2 layers using a one-step hydrothermal method followed by the carbonization process (Fig. 7a). The RGO encapsulation significantly buffered the volume expansion of MoS_2 nanostructures, increased the surface area for maximum Li-ion interaction, and enhanced the electrical conductivity and charge transfer kinetics. Furthermore, the RGO encapsulation provided numerous anchoring sites for immobilized polysulfides, resulting in a restricted polysulfide diffusion effect. The conductive carbon layer increased the interlayer distance of MoS_2 layers from 0.63 to 0.99 nm, thereby resulting in maximum accommodation of Li ions (Fig. 7b, c). Such synergistic effects of RGO encapsulation and the interplanar carbon layer improved the electrochemical performance. The LIC device fabricated using MoS_2-C-RGO anode and AC cathode exhibited a high ED of 188 Wh/Kg, PD of 40 kW/kg, and 80% cyclic stability for 10,000 cycles. The enhanced electrochemical performance was also recognized by the attainment of triangular GCD profiles for the LIC device at varied current densities (1–20 A/g) due to the optimized mass ratio of the electrodes (anode/cathode, 1/2) (Fig. 7d).

Yin et al. [37] also demonstrated the improved performance of the $Ti_3C_2T_x$ MXene electrode by increasing their interlayer distance using $MoSe_2$ nanoparticles. A self-standing $MoSe_2/Ti_3C_2T_x$ MXene composite electrode film was fabricated using a vacuum filtration technique (Fig. 8a). The vacuum filtration resulted in the formation of the binder-free flexible composite electrode film in which the $MoSe_2$ nanoparticles were embedded between the layers of $Ti_3C_2T_x$ MXene nanosheets

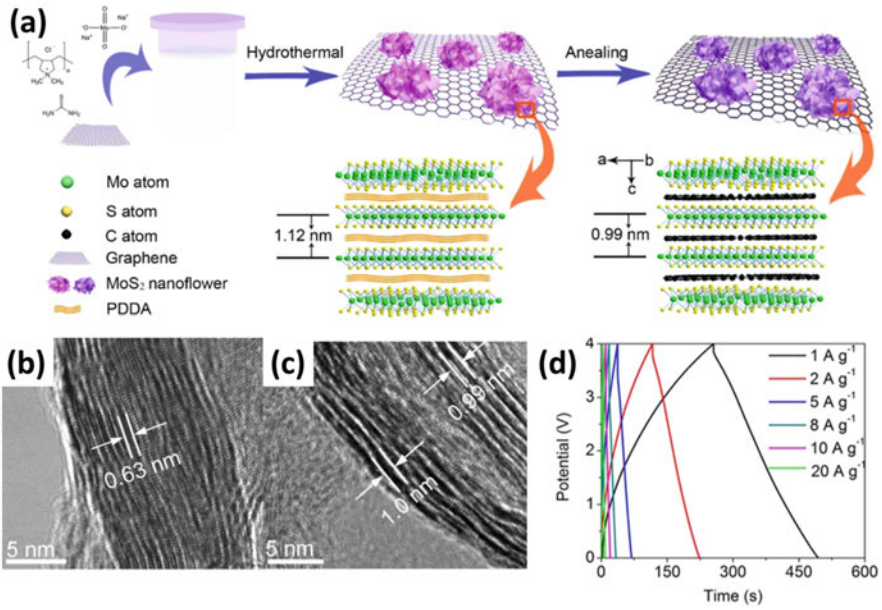

Fig. 7 (**a**) The schematics of the multistep fabrication process of MoS_2 nanosheets and (**b**, **c**) the interplanar lattice distance of the pristine MoS_2 and the conductive carbon layer-based MoS_2 nanosheets, respectively, and (**d**) the galvanostatic charge-discharge (GCD) curves of the LIC device based on MoS_2-C-RGO anode and AC cathode at varied current densities. (Reprinted with copyright permission from Ref. [36])

(Fig. 8b, c). The $MoSe_2$ nanoparticles act as a spacer between the $Ti_3C_2T_x$ MXene nanosheets and prevent them from restacking. As a result of this unique arrangement, the active electrode surface area is restored, and maximum electroactive sites are exposed for efficient Li-ion interaction and transport. The composite electrode demonstrated a high ED of 110.1 Wh/kg and PD of 4.76 kW/kg.

Huang et al. [38] adopted an approach to improve the electrochemical performance of the alloy-type SnS nanosheets by encapsulation of nitrogen-doped porous carbon layer (NPC). A two-step process consisting of freeze-drying of the metallic precursors followed by the carbonization process (600 °C- 2 h in argon) was adopted to fabricate the SnS/NPC composite electrode (Fig. 9).

The freeze-drying resulted in the formation of 3D structured morphology of the electrode, highly suitable for electrochemical application. The SnS/NPC composite electrode delivered a high initial discharge capacity of 1399.7 mAh/g in the half-cell configuration and exhibited a high ED of 155.5 Wh/kg and PD of 0.213 kW/kg with cyclic stability of 86% for 3000 cycles in LIC device configuration. The obtained higher performance was ascribed to the NPC coating on the SnS nanosheets that resulted in improved electrical and charge transfer properties. Additionally, the NPC coating resulted in a three-time improvement in the surface area of the composite electrode (210.55 m^2/g) than the pristine SnS electrode (74.32 m^2/g). Likewise,

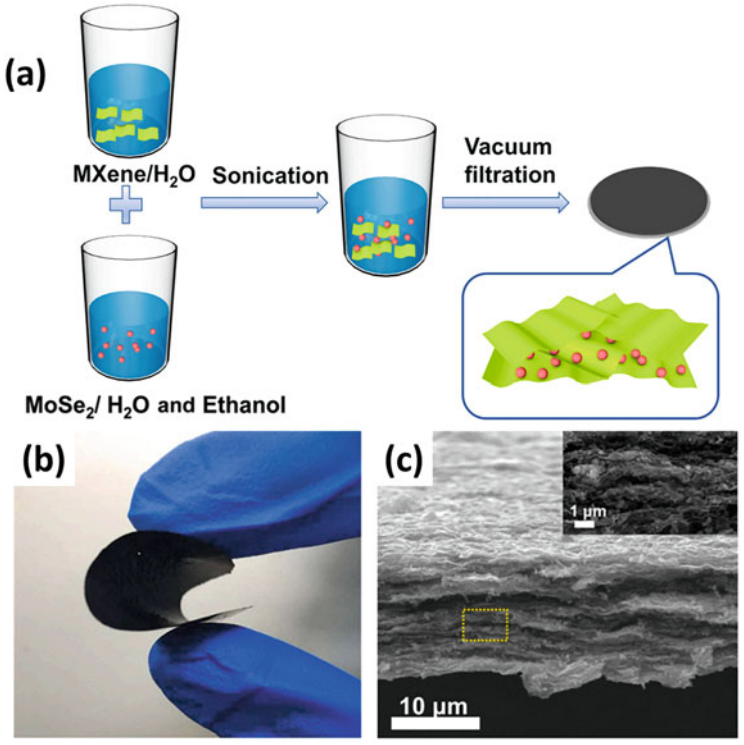

Fig. 8 (**a**) The schematics of the fabrication $MoSe_2$/MXene composite using the vacuum filtration technique, (**b**, **c**) the photo image and the corresponding cross-section FESEM image fabricated flexible $MoSe_2$/MXene composite electrodes, respectively. (Reprinted with copyright permission from Ref. [37])

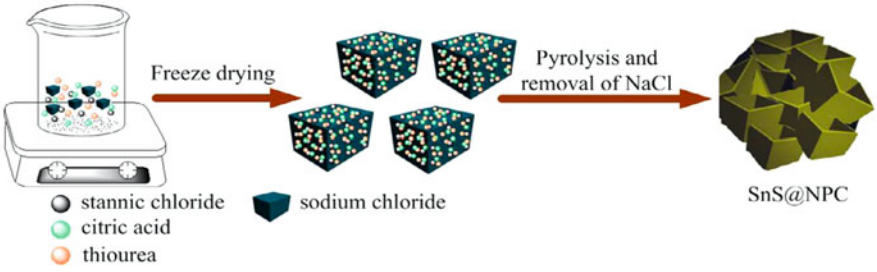

Fig. 9 The schematics of the fabrication of SnS-based nitrogen-doped porous carbon layer (NPC) composite electrode. (Reprinted with copyright permission from Ref. [38])

Lokhande et al. [39] demonstrated the improved electrochemical performance of the "conversion-alloy"-type Cu_2SnS_3 (CTS) electrode using CNTs' encapsulation. The CNTs' encapsulation improved the microstructural, electrical, and structural properties which were reflected through the generation of high-density electro-active

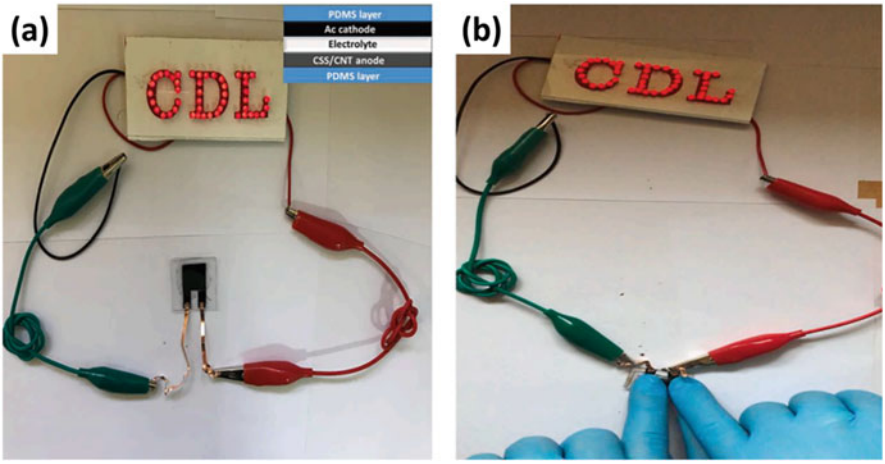

Fig. 10 (**a**) The photograph of the fabricated LIC device using the CTS/CNT anode and AC cathode in the (**a**) unbent and (**b**) bent conditions. (Reprinted with copyright permission from Ref. [39])

sites, buffering of volume expansion, enhanced reaction kinetics, and increased electrical conductivity. The theoretical analysis using density functional theory (DFT) further revealed that the Li ions exhibited favorable interactive features with the CTS/CNT composite electrode than the pristine CTS electrode in terms of higher valence charge transfer and higher binding energy. As a result, improved charge storage capacity, rate capability, and cyclic stability were obtained for the CTS/CNT composite electrode. The LIC device fabricated using CTS/CNT anode and AC cathode with the optimized mass balanced ratio (1:5.5) exhibited an ultra-high ED of 158.77 Wh/kg, PD of 12.5 kW/kg, and more than 80% cyclic stability for 10,000 cycles. To further demonstrate the practical applicability of the LIC device, a flexible LIC device was fabricated using polydimethylsiloxane (PDMS) support layers. The performance of the LIC device was unaffected in the twisted and unbend conditions, reflecting its possible applicability in wearable systems (Fig. 10).

Xing et al. [40] reported a LIC device based on an anode containing multiple metal sulfides (MnS, Co_4S_3, and Ni_3S_2) supported with carbon nanofibers exhibited a high ED of 182 Wh/kg at the PD of 0.21 kW/kg. The obtained higher ED was attributed to the synergistic effect of multiple charge storage mechanisms and restricted particle aggregation provided by the multiple metal sulfides and carbon nanofibers, respectively. Thus, from the above literature reports, it is clear that carbon encapsulation on metal sulfides results in improved electrochemical properties. Carbon encapsulation provides numerous advantages such as high electrical conductivity, high surface area, buffering of volume expansion, poly-sulfide adsorption, avoiding particle aggregation, and enhanced reaction kinetics. Surprisingly, some electrode materials perform well even in the absence of carbon encapsulation. The “conversion-type” 3D CoS electrode fabricated by Wang et al.

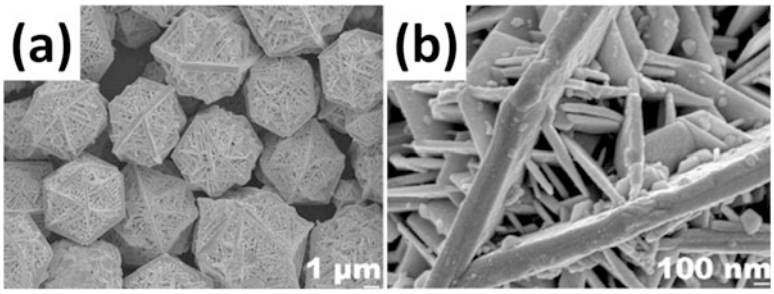

Fig. 11 (**a**, **b**) The low and high magnification FESEM images of CoS microspheres, respectively. (Reprinted with copyright permission from Ref. [41])

Table 1 The electrochemical performance of the reported metal sulfides for LIC application

Anode	Energy density (Wh/kg)	Power density (kW/kg)	Cyclic stability	References
MoS_2/porous carbon nanofiber (PCNF)	75.5	25.5	78% for 5000 cycles	[35]
$MoSe_2$/MXene	110.1	4.76	60% for 1000 cycles	[37]
MoS_2/C/RGO	188	40	60% for 10,000 cycles	[36]
SnS/N-doped porous carbon	155.5	0.213	86% for 3000 cycles	[38]
Cu_2SnS_3 (CTS)/CNT	158.77	12.50	84% for 10,000 cycles	[39]
MnS/Co_4S_3,/Ni_3S_2	182	0.121	79% for 2000 cycles	[40]
CoS	125.2	6.4	81.75% for 40,000 cycles	[41]

[41] exhibited an impressive performance with a high ED of 125.2 Wh/kg and ultra-high cyclic stability of 81.75% for 40,000 cycles. The superior performance was ascribed to the combined effect of higher electrical conductivity and the 3D structured morphology of CoS electrode. The higher electrical conductivity led to enhanced reaction kinetics by promoting rapid charge transport, while the unique 3D structured morphology (Fig. 11) (open flake-like assembly with porous structure) provided numerous high-density electro-active sites with lower cross-plane ionic diffusion. Thus, the electrode intrinsic properties also play a vital role in influencing electrochemical performance. Further enhanced electrochemical properties could be expected if CoS is encapsulated with carbon material.

By summarizing the results in Table 1, it is shown that metal sulfides exhibit a great scope in LICs due to their high attainable specific capacity and enhanced rate capability. However, the "polysulfide-diffusion effect" results in low cyclic stability. Though carbon encapsulation has proved effective in restricting polysulfide diffusion, it cannot be considered an efficient and cost-effective approach due to the involved complex procedures. Thus, other novel strategies based on simpler approaches need to be developed.

3.2 Oxide-Based Electrodes for LIC

Metal oxides have also emerged as reliable electrode materials for energy storage systems. Metal oxides such as $Li_4Ti_5O_{12}$ (LTO), $LiFePO_4$ (LFP), MnO, TiO_2, Co_3O_4, V_2O_3, Fe_3O_4, SnO_2, and $MnCo_2O_4$ have been used as anode for LIC applications [42–59]. Out of these oxides, the LTO and LFP are the most commonly used electrode materials for commercial applications due to their unique properties such as low cost, environmentally friendly, high coulombic efficiency, stable operating voltage (1.55 V vs. Li/Li^+), and zero volume change during Li insertion/de-insertion. However, the low electrical conductivity (10^{-9} Scm^{-1}) and the low Li-ion diffusivity result in low specific capacities and poor rate capabilities of these materials. Bokenfeld et al. [42] reported a lower rate capability of the LFP electrode with an attained capacity of 70 mAh/g at 50 C and 60 mAh/g at 100 C current density. Ye et al. [43] attempted to improve the LTO performance using a carbon composite structure (Fig. 12a). However, the strategy of using carbon composite did not prove so impressive as the LIC device fabricated using the LTO/C anode and porous graphene as cathode exhibited mediocre performance (ED, 72 Wh/kg; PD, 8.3 kW/kg; and 65% stability for 1000 cycles). Lin et al. [44] obtained the improved electrochemical performance of the LTO electrode using an ionic doping approach. The 3D structured spherical LTO particles were fabricated using a "spray-dry method" during which the metallic ions such as Mg^{2+} and Cr^{3+} were doped into its crystal structure. The 3D structured spherical shape of the LTO particles (Fig. 12b) provided high-density electro-active sites, highly desirable for attaining higher charge storage capacity. The ionic doping resulted in improved reaction kinetics and ionic mobility. Additionally, the thermal treatment under hypoxic conditions (inert atmosphere) further resulted in an oxygen-deficient structure, resulting in enhanced electrical conductivity. The LIC device fabricated using an LTO anode and porous carbon cathode yielded a higher electrical performance(ED, 142 Wh/kg; PD, 4.55 kW/kg; and 87% stability for 10,000 cycles). Thus, the above studies confirm the influence of the electrode intrinsic properties on electrochemical performance.

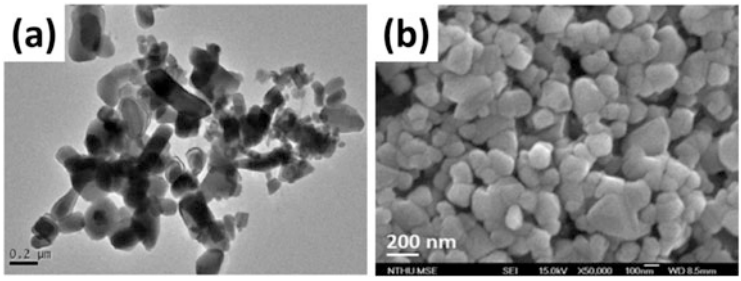

Fig. 12 The FESEM images of the (**a**) carbon-coated LTO microparticles and (**b**) the Mg^{2+}- and Cr^{3+}-doped LTO microspheres. (Reprinted with copyright permission from Refs. [43, 44])

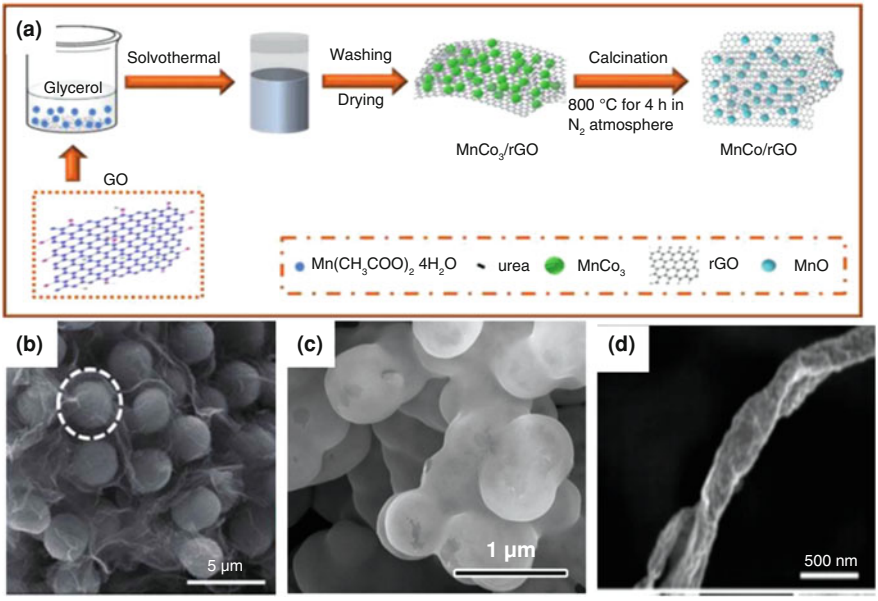

Fig. 13 (**a**) The schematics of the multistep fabrication process of RGO-encapsulated 3D MnO microspheres, (**b**–**d**) the FESEM images of the MnO/RGO composite, S-N-doped MnO/graphene composite, and 1D MnO/graphene composite, respectively. (Reprinted with copyright permission from Refs. [45–47])

Recently, transitional metal oxides such as MnO have garnered importance for energy storage systems due to various advantages such as low cost, high abundance, environmentally friendly, low voltage hysteresis, and high theoretical capacity (756 mAh/g) which is almost twice the theoretical capacity of graphite (372 mAh/g) [45]. However, the conversion reactions during the charge-discharge process result in high volume expansion of MnO structure. As a result, the pulverization effect is more prominent, resulting in high capacity loss. Additionally, the lower electrical conductivity of MnO results in poor rate capability. As a solution to address these issues, various literature reports have suggested MnO encapsulation with carbon material [45–47]. Jia et al. [45] fabricated RGO-encapsulated 3D MnO microspheres using a two-step process involving a solvothermal method followed by a calcination process (Fig. 13a). The RGO is uniformly encapsulated over MnO microspheres (Fig. 13b) and, as a result, provides a highly conductive framework for rapid charge transport. Moreover, the RGO encapsulation significantly improves the surface area of the composite electrode (63.1 m^2/g) than the pristine MnO electrode (18.1 m^2/g), thereby providing high-density electro-active sites. The LIC device fabricated using the composite electrode exhibited a high ED of 98 Wh/kg, PD of 10.35 kW/kg, and cyclic stability of 71% for 5000 cycles. The performance was further enhanced by Xiao et al. [46] through sulfur (S)

and nitrogen (N) doping in MnO/graphene composite electrode. The S and N doping generated additional pseudocapacitive charge generation in the composite electrode. The graphene encapsulation improved the overall electrical conductivity of the composite electrode (high rate capability), buffered the volume expansion of MnO, maintained the structural integrity, and provided stupendous electro-active sites for high charge generation/storage. Thus, the collective effect of ionic doping and carbon encapsulation resulted in superior electrochemical performance of the composite electrode despite exhibiting similar morphology (Fig. 13c) to the one reported in Fig. 13b. The morphology also plays a vital role in influencing the electrochemical performance of the electrode. Chen et al. [47] demonstrated further improved performance by fabricating 1D MnO nanorods encapsulated with graphene scrolls (Fig. 13d). The LIC device exhibited superior performance such as high ED of 179.3 Wh/kg, PD of 11.7 kW/kg, and long-term cyclic stability of 80.8% for 5000 cycles. The 1D structure is highly beneficial as it provides a large surface area (high surface-to-volume ratio) and high mechanical strength, prevents self-aggregation, and promotes rapid ionic transport. The combined benefits of a 1D structure with graphene encapsulation resulted in improved performance. Other carbon materials such as "hard carbon coating" on MnO have also been reported for attaining enhanced electrochemical performance [48]. A novel approach such as "alkali metal doping" in MnO structure has also proved very efficient in enhancing electrochemical performance. The study conducted by Zhang et al. [49] on potassium (K) doping in MnO structure improved kinetics, enhanced redox activity, and restricted volume expansion. Other alkali metals such as Li, Na, Rb, and Cs could also be considered for doping in MnO.

Transitional metal oxides such as TiO_2 have attracted significant research interest due to their applications in versatile fields such as photocatalysis, solar cells, water splitting, and the semiconductor industry [50, 51]. It has also emerged as reliable electrode material in energy storage systems due to various intriguing properties such as good theoretical capacity (335 mAh/g), reasonable redox potential (1.75 V vs. Li), low cost, and environmentally friendly nature [50–52]. Calcagno et al. [50] fabricated fast-charging anatase-structured TiO_2 microspheres (Fig. 14a) using a two-step method (solvothermal + calcination) as an anode for LIC. The LIC device delivered a high capacity of 37 mWh/g at the current density of 0.5 A/g and retained a capacity of 10 mWh/g at the ultra-high current density of 20 A/g. Furthermore, the LIC device exhibited high cyclic stability for 10,000 charge-discharge cycles with no reduction in a specific capacity. Such an improved performance was attributed to the formation of irreversible lithium-rich titanate ($LiTiO_2$) on the surface of TiO_2 microspheres that significantly counterbalanced the capacity decay at higher potentials. However, the performance was restricted due to the poor electrical conductivity of TiO_2 microspheres. Kim et al. [51] succeeded in improving the electrical properties of TiO_2 microspheres using an RGO composite. The uniformly distributed TiO_2 microspheres on RGO sheets (Fig. 14b) enabled faster reaction kinetics with high-density electro-active sites. Additionally, the combined role of TiO_2 and RGO resulted in a high specific capacity of 258 Wh/kg. TiO_2 has also

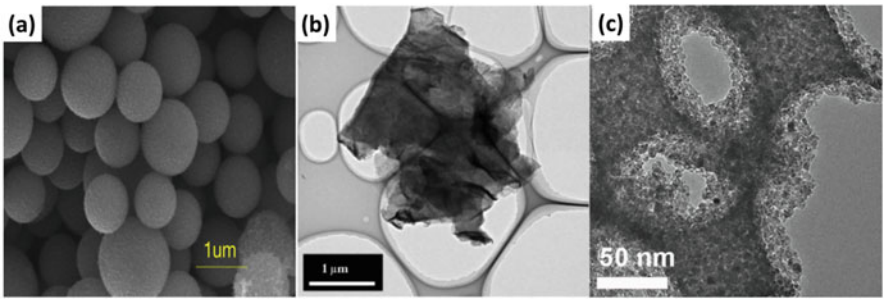

Fig. 14 The FESEM images of (**a**) TiO_2 microspheres, (**b**) TiO_2/RGO composite, and (**c**) TiO_2/Co_3O_4 composite. (Reprinted with copyright permission from Refs. [50], [51], and [52])

been used as an encapsulant for other active electrode materials such as Co_3O_4. The Co_3O_4 has emerged as the ideal electrode material due to its good electrochemical corrosion stability and high theoretical capacity (890 mAh/g). However, the structural collapse due to high volume expansion and particle aggregation results in lower performance. Peng et al. [52] fabricated TiO_2-encapsulated interconnected Co_3O_4 microspheres (Fig. 14c) using a template-based strategy. The TiO_2 encapsulation proved to be beneficial as it promoted fast ionic diffusion, offered high surface area, and prevented Co_3O_4 from falling off the electrode. As a result, a high discharge capacity of 944.1 mAh/g was obtained after 100 cycles. The LIC device also displayed a good performance with an ED of 87.9 Wh/kg, PD of 10.20 kW/kg, and cyclic stability of 88.1% for 6000 cycles.

Metal oxides exhibiting extremely high theoretical capacities such as Fe_3O_4 (924 mAh/g), SnO_2 (994 mAh/g), and V_2O_3 (1070 mAh/g) have also been used as electrode materials for LIC application [53–55]. However, the lower electrical conductivity (low ionic diffusion) and the high volume expansion of these electrodes limit their performance. The high volume expansion is a serious issue as it completely ruptures the electrode's crystal structure, leading to a sudden capacity drop. This issue is more profound in Sn-based electrodes (SnO_2, SnS) as there is 300% volume expansion during the lithiation process. Therefore, carbon encapsulation is done on these electrodes as it improves the electrical conductivity and buffers the volume expansion. Huang et al. [53], Arnaiz et al. [54], and Ren et al. [55] obtained improved performance of Fe_3O_4, SnO_2, and V_2O_3 electrodes, respectively, using carbon coating (RGO). The performance of other metal oxides such as $MnCo_2O_4$ [56] and Li_3VO_4 [57] has also been improved using such carbon encapsulation. The LIC device performance of the reported metal oxides is summarized in Table 2. Indeed, metal oxides have shown promising performance in LICs. The basic problem of metal oxides such as high volume expansion and low electrical conductivity still needs to be addressed decisively for their large-scale integration into the electronics industry.

Table 2 The electrochemical performance of the reported metal oxides for LIC application

Anode	Energy density (Wh/kg)	Power density (kW/kg)	Cyclic stability	References
$Li_4Ti_5O_{12}$ (LTO)/C	72	8.3	65% for 1000 cycles	[43]
LTO/porous carbon	142	4.55	85.7% for 10,000 cycles	[44]
MnO/RGO	98	10.35	71% for 5000 cycles	[45]
MnO/graphene sphere	126.7	5.72	81% for 10,000 cycles	[46]
MnO/graphene scroll	179.3	11.7	80.8% for 5000 cycles	[47]
N-doped MnO/C	125.3	19.9	83.2% for 5000 cycles	[48]
$K_{1.04}Mn_8O_{16}$	127.6	0.99	97% for 10,000 cycles	[49]
TiO_2	27	–	–	[50]
TiO_2/RGO	258	–	90% for 1000 cycles	[51]
TiO_2/Co_3O_4	87.9	10.20	88.1% for 6000 cycles	[52]
Fe_3O_4/RGO	98.8	3.4	78.9% for 1000 cycles	[53]
SnO_2/RGO	60	10.6	55% for 10,000 cycles	[54]
V_2O_5/C	116.5	32	81.2% for 5000 cycles	[55]
$MnCO_2$/RGO	78.8	3	76.9% for 1000 cycles	[56]
Li_3VO_4/graphene	122.9	17.6	95% for 300 cycles	[57]

3.3 Silicon-Based Electrodes for LIC

Recently, silicon (Si) has emerged as a reliable electrode material because of its unique advantages such as low cost, low lithiation potential (0.2 V vs. Li^+/Li), and high theoretical capacity (4200 mAh/g) [58, 59]. The Si anode holds great promise in the development of energy storage systems as it can outperform the existing commercial electrodes. However, the Si electrode exhibits serious drawbacks of high volume expansion (300%), pulverization, low electrical conductivity, formation of unstable solid electrolyte interphase (SEI) layer, and Li-ion trapping during the Li intercalation/de-intercalation processes (Fig. 15). As a result, the capacity is significantly reduced, resulting in poor cyclic stability.

Eguchi et al. [58] fabricated a LIC device based on Si anode and Ac cathode exhibiting an ED of 183 Wh/kg and a PD of 10 kW/kg with low cyclic stability of 86.6% for 1000 cycles. The majority of research work is focused on improving the cyclic stability of the Si anode by buffering its volume expansion. Shao et al. [59] attempted to improve the performance by encapsulating the Si with carbon coating. A two-step method comprising "gelation" followed by "carbonization" was opted to achieve uniform carbon encapsulation on the Si surface (Fig. 16a). The encapsulation resulted in the formation of an enhanced dual interface with a highly conductive network, suitable for efficient ionic diffusion (Fig. 16b). Additionally, carbon encapsulation provided a flexible framework for buffering volume expansion (Fig. 16c). As a result, improved electrochemical performance in terms of enhanced ED (213 Wh/kg), and PD (22.3 kW/kg), and high cyclic stability of 76.3% for 5000 cycles was obtained. Furthermore, a higher volume expansion buffering was

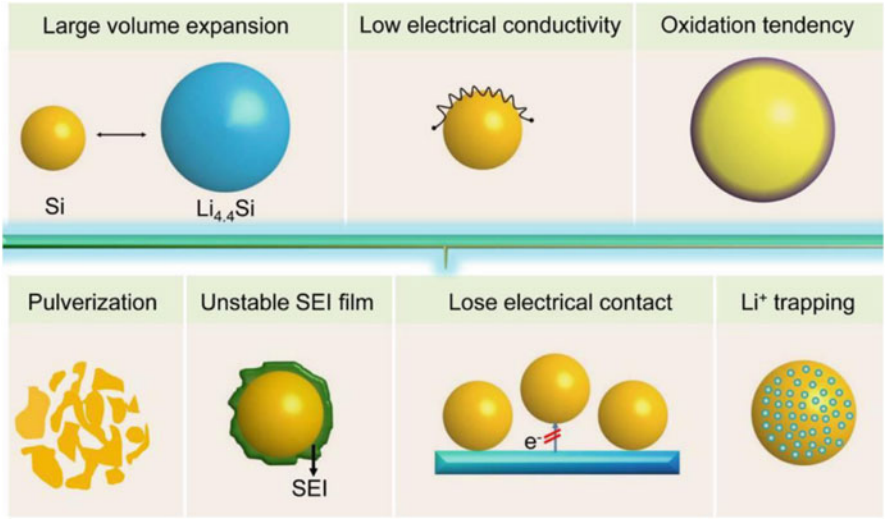

Fig. 15 The schematic illustrations of the various drawbacks of Si in Li-ion energy storage system. (Reprinted with copyright permission from Ref. [61])

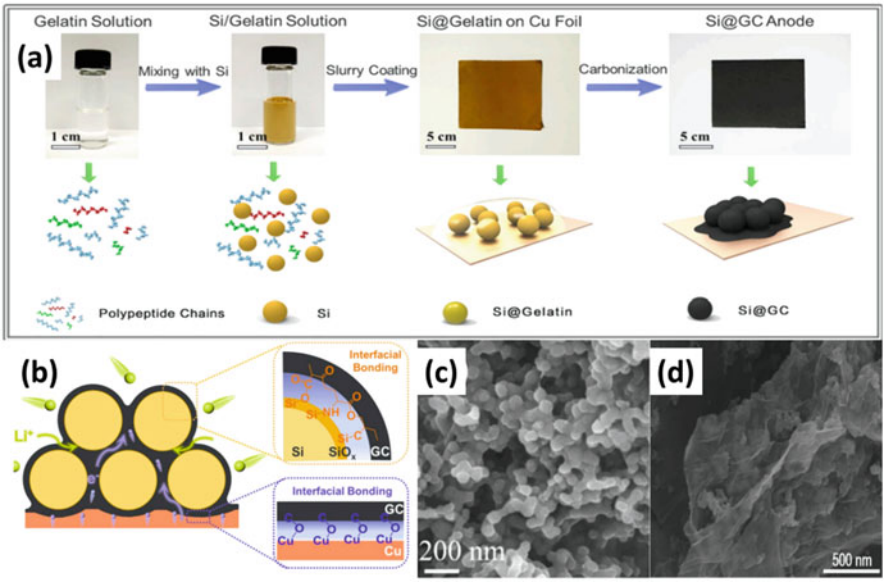

Fig. 16 (**a**) The schematics of the multistep fabrication process of the carbon-encapsulated Si particles, (**b**) the schematics depicting the enhanced interfacial bonding between the Si particles and carbon coating, and (**c**, **d**) the FESEM images of the carbon-encapsulated Si and the GO-encapsulated Si particles, respectively. (Reprinted with copyright permission from Refs. [59, 60])

demonstrated by Su et al. [60] by encapsulating boron-doped Si microspheres with a carbon layer followed by a GO layer (Fig. 16d). Due to such double carbon layer encapsulation, ultra-high cyclic stability of 74.4% for 10,000 cycles was attained. The reports based on the use of Si in LICs are very limited, and thus, extensive studies are needed to achieve further improved performance.

It should be noted that carbon encapsulation on Si is accomplished in two steps. The two steps are carbon precursor coating and carbonization. In the first step of carbon precursor coating, organic materials containing carbon compounds such as polymers, glucose, sucrose, polydopamine, etc. are coated on Si. Then in the next step (carbonization), the carbon compound-coated Si is heated in an inert atmosphere (Ar or N) to form a highly electrically conductive carbon layer. These multiple steps increase the cost and complexity, and hence, developing a single-step method of carbon encapsulation on Si is essential. The fabrication of Si material is also an important aspect to be considered. Generally, Si is synthesized using the "magnesiothermic reduction method" followed by acid etching. In the "magnesiothermic reduction method," silicon dioxide (SiO_2) is reduced to silicon (Si) using magnesium powder as the thermal moderator. The magnesium powder is highly flammable and can cause health hazards. The obtained Si is further purified by acid etching that involves highly harmful acids such as hydrochloric acid (HCl) and hydrofluoric acid (HF). Therefore, there is an urgent need to explore and develop safe methods of fabricating Si material.

Sun et al. [61] suggested some of the following strategies through which the Si performance could be enhanced (Fig. 17).

(a) *Structure Regulation*: The precise control of structure can contribute to improved electrochemical performance. For instance, it is reported that zero-dimensional (0D) Si nanoparticles with a size less than 150 nm can accommodate the extreme volume change without breaking the crystal structure [62]. 1D Si nanostructures such as nanotubes and nanowires can easily counter volume expansion due to the presence of space between the nanowires' vertical growth. Additionally, 1D nanostructures can promote rapid charge transport and provide numerous electro-active sites. 2D nanosheets provide superior ionic transport capabilities with sufficient room for volume expansion. It has been reported that 2D calcium silicide ($CaSi_2$) has emerged as an effective material for energy storage due to the stacking of alternate layers of Ca and Si.
(b) *Interface Modulation*: The interface modulation relates to surface coating and the metal/nonmetal doping approach. The surface coating is usually carbon coating on Si nanostructures. The carbon coating enhances the electrical, structural, and mechanical properties of the electrode. Additionally, the carbon coating prevents direct contact between the electrolyte and active material, thereby preventing the occurrence of undesirable side reactions. Conductive polymers and metal oxides can be used for coating Si nanostructures. Sun et al. [63] demonstrated coating of self-healing polymer that restricted volume expansion of Si nanostructures. Similarly, Yang et al. [64] also demonstrated amorphous TiO_2 coating for restricted volume expansion of Si nanostructures.

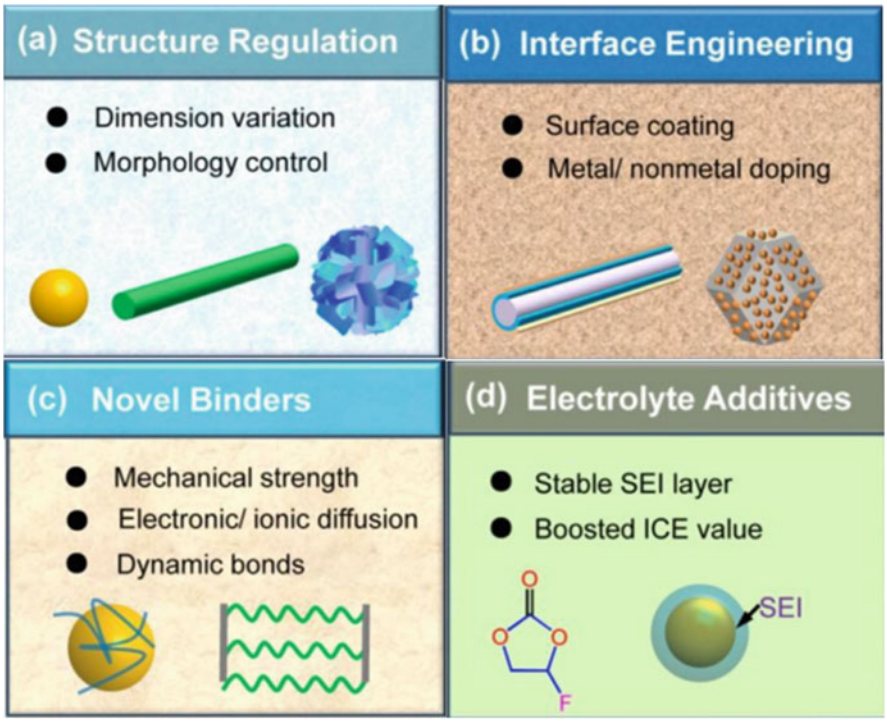

Fig. 17 (**a–d**): The various strategies used to enhance the performance of Si anode in Li-ion-based energy storage system. (Reprinted with copyright permission from Ref. [61])

The heteroatom doping has also been found useful in Si nanostructures. It has been found that Ge doping improves the Si initial coulombic efficiency (ICE) value by 94% [64]. Additionally, Ge doping expands the Si crystal lattice, promoting easy transport of Li ions and reducing Li trapping effect [64].

(c) *Novel Binders*: The function of the binder is to hold the active electrode components intact. Additionally, the binder should exhibit some characteristics such as high elastic strength, high electric conductivity, and strong adhesion [65]. Generally linear and nonlinear binders are used for electrode fabrication. Sodium carboxymethylcellulose (CMC), guar gum (GG), chitosan, sodium alginate (SA), polyvinyl alcohol (PVA), and polyacrylic acid (PAA) are commonly used linear binders [66–71]. Nonlinear binders include conjugated, branched, and 3D cross-linked structures [72–74]. Binders with high flexibility and larger resistance to deflection should be explored. Recently, Choi et al. [75] fabricated a cross-linked binder by adding 5 wt% polyrotaxane (PR) to a PAA binder that performed well in the cyclic stability study. Polyelectrolyte binders promoting high mass loadings and nature polymer binders with abundant edge groups should be focused on. Research based on developing nontoxic and cost-effective binders should be of prime interest.

(d) *Electrolyte Additives*: The SEI formation on the electrode plays an important role in influencing electrochemical performance. In the case of Si electrodes, the large volume expansion results in the breakage of the SEI film, leading to capacity degradation [76]. As a possible solution to prevent breakage of SEI, an additive such as fluoroethylene carbonate (FEC) can be mixed in the electrolyte which enhances the elastic strength and LIF content in the SEI layer through rapid defluorination and polymerization process [77]. Some other functional electrolyte additives based on nitrogen, silane, and multivalent ions have also been used. These additives include N-acetylcaprolactam (NACA), trans-difluoroethylene carbonate (DFEC), lithium difluorophosphate (LiDFP), pentafluorophenyl isocyanate (PFPI), lactic acid O-carboxyanhydride (lacOCA), trifluoropropylene carbonate (TFPC), lithium difluoro(oxalato)borate (LiFOB), mesylethyl-methyl-pyrrolidinium (MEMP-DFOB), succinic anhydride, and mixed salt electrolytes (M(TFSI)x, M = Mg, Zn, Al and Ca) [61].

3.4 MXene-Based Electrodes for LIC

In recent years, 2D transition metal carbide-based materials, named "MXenes," have attracted significant research attention due to their applications in versatile fields including energy storage and conversion, catalysis, biomedicine, electromagnetic shielding, sensors, and membrane systems [78–81]. The MXenes are fabricated by selective etching of "A" layer atoms from the MAX phase ceramics using HCl and HF solutions. The "A" layer atoms are group 13 or 14 elements (Al, Si, Ga). The MXenes are represented by the formula $M_{n+1}X_nT_x$ where M is a transition metal (Cr, Ti, V), X is a carbon (C) and nitrogen (N), n is the integer (between 1 and 4), and T_x is the surface moieties (OH^-, O^-, F^-) [79–82]. The metal carbide inner layers of MXenes exhibit good electrical conductivity and promote efficient electron transport, while the surface moieties impart a redox charge storage mechanism. As a result, MXenes can be effectively used in energy storage systems. The Ti_3C_2 is the most common MXene employed in energy storage systems due to its excellent properties such as high electrical conductivity, high hydrophilicity, good pseudocapacitive charge characteristic, and low Li-ion diffusion barrier (0.07 eV). However, the low theoretical capacity (320 mAh/g) and the reduced electro-active surface area due to restacking of Ti_3C_2 nanosheets result in limited performance in Li-ion-based energy storage systems [78–83].

So far, attempts have been made to improve the electrochemical performance of the Ti_3C_2MXene by restoring the electro-active surface area. This is usually achieved by preventing the restacking of nanosheets using the ionic intercalation and composite fabrication approach. Xia et al. [78] enlarged the interplanar lattice distance from 11.6 Å to 11.9 Å by intercalating Ti_3C_2 nanosheets with Sn^{4+} ions and forming an in-plane amorphous SiO_2 layer (Fig. 18a, b). The Sn^{4+} ions generated additional charge storage capacity through alloy reactions and also promoted faster

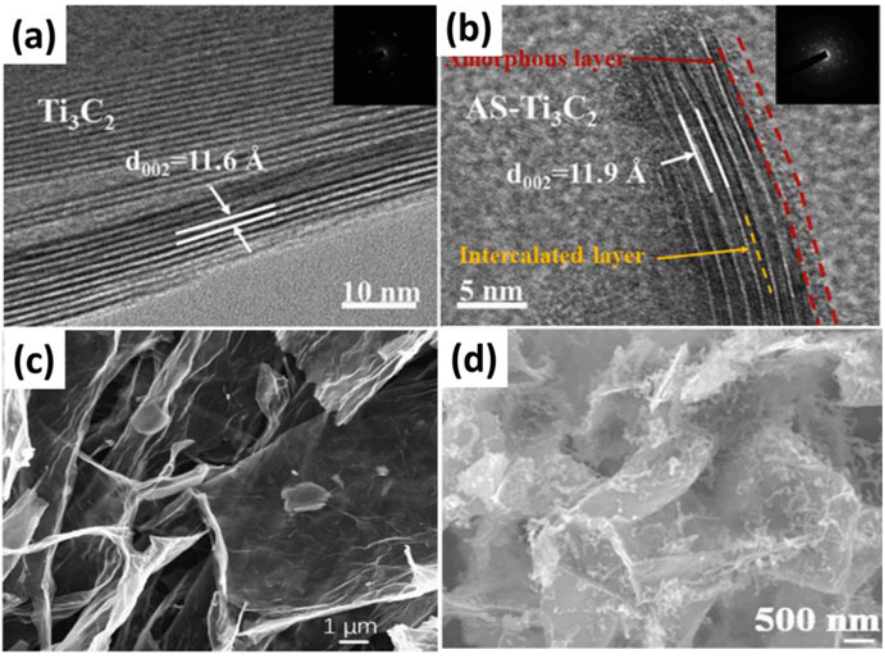

Fig. 18 The HRTEM image showing the interplanar lattice distance of the (**a**) pristine MXene nanosheets and (**b**) the Sn^{4+} ion-doped MXene nanosheets with in-plane amorphous SiO_2 layer, (**c**, **d**) the FESEM images of the MXene/RGO and MXene/CNT nanosheets, respectively. (Reprinted with copyright permission from Refs. [78–80])

Li-ion diffusion between the neighboring Ti_3C_2 nanosheets. The amorphous SiO_2 layer provided numerous resistance-free channels for Li diffusion. The synergistic effects of Sn^{4+} ions and amorphous SiO_2 resulted in lowered energy barrier for Li-ion diffusion and prevented nanosheets restacking, resulting in improved electrochemical performance. Yi et al. [79] reported improved electrochemical performance of Ti_3C_2/RGO composite for LIC application. The RGO nanosheets avoided restacking of Ti_3C_2 nanosheets, thereby restoring the electro-active surface area (Fig. 18c). Additionally, the RGO improved the electrical conductivity and provided a larger interplanar space for maximum Li-ion accommodation and resistance-free diffusion. Likewise, a similar approach was reported for the 3D Ti_3C_2/CNT composite by Yang et al. [80] for attaining improved LIC performance (Fig. 18d). The CNTs avoided the restacking by acting as a spacer between the Ti_3C_2 nanosheets. Besides avoiding the restacking of Ti_3C_2 nanosheets, some composites are used to exploit their charge storage mechanism for obtaining additional improved performance. Yu et al. [81] fabricated SnO_2/SnS_2@Ti_3C_2 composite. The battery-type insertion mechanism of SnO_2/SnS_2 combined with the pseudocapacitive mechanism of Ti_3C_2 resulted in good electrochemical performance for LIC in terms of high ED of 145.2 Wh/kg, PD of 11.25 kW/kg, and larger cyclic stability

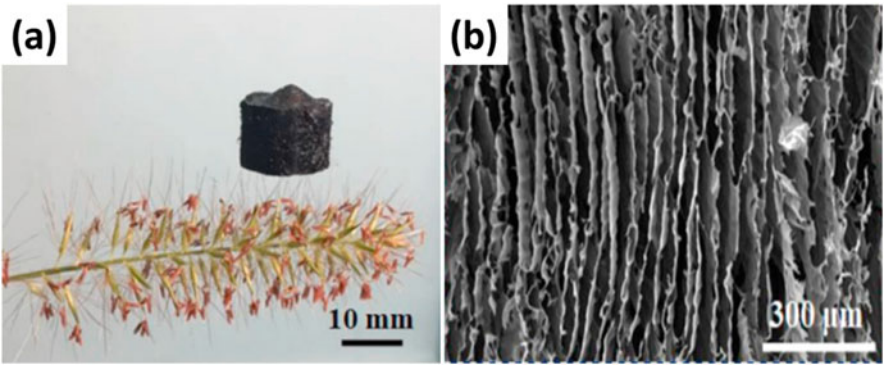

Fig. 19 (**a**) The photo image and (**b**) the corresponding FESEM image of the MXene aerogel prepared using the freeze casting method. (Reprinted with copyright permission from Ref. [83])

Table 3 The electrochemical performance of the reported MXene-based composites for LIC application

Anode	Energy density (Wh/kg)	Power density (kW/kg)	Cyclic stability	References
MXene/RGO	114	3.12	80% for 5000 cycles	[79]
MXene/CNT	201	21	87% for 3500 cycles	[80]
MXene/SnO_2@SnS_2	145.2	11.25	93.6% for 2000 cycles	[81]
MXene/Co_3O_4@ZnO	196.8	3.5	75% for 6000 cycles	[82]

(93.6% for 2000 cycles). A further improved performance (ED (196.8 Wh/kg), PD (3.5 kW/kg), and 75% cyclic stability for 6000 cycles) was reported for the alloy mechanism-type Co_3O_4-ZnO metal-organic framework (MOF) combined with the pseudocapacitive-type Ti_3C_2MXene [82]. Besides ionic intercalation and composite fabrication, Orangi et al. [83] reported a unique approach for preventing the restacking of Ti_3C_2 nanosheets by preparing aerogel using the unidirectional freeze casting method. As seen in Fig. 19, the fabricated Ti_3C_2 aerogel contained well-aligned separated nanosheets. As a result, the nanosheet restacking is avoided, and the electro-active surface area is maintained.

The LIC device performance based on MXene anode is shown in Table 3. Clearly, MXene has great potential to be developed as an ideal electrode material. However, more efficient approaches are still required to solve their restacking issues that lead to reduced electrochemical performance.

3.5 Carbon-Based Electrodes for LIC

Carbon-based electrodes have shown reliable performance in energy storage systems. Carbon-based electrodes exhibit two types of charge storage mechanisms,

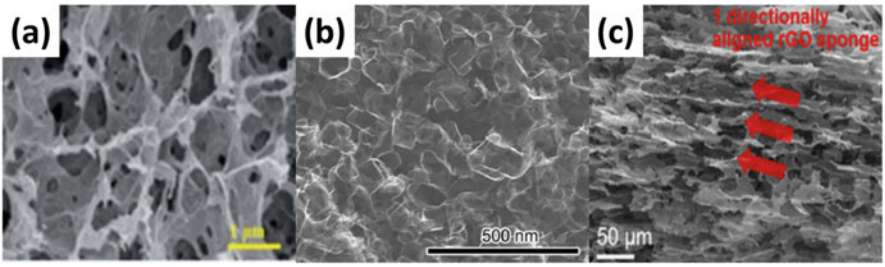

Fig. 20 The FESEM images of (**a**) porous graphene, (**b**) S-doped graphene, and (**c**) RGO sponge. (Reprinted with copyright permission from Refs. [90–92])

that is, insertion or EDLC when used as an anode and a cathode. Till now, various carbon-based electrodes, namely, graphite, graphene, graphdiyne, CNTs, and graphitic carbon, have been as electrode materials for LICs [84].

Graphite exhibits a 2D layered structure composed of individual carbon layers (graphene) stacked together in a hexagonal mesh structure. As the interlayer space between the graphite sheets (0.335 nm) is greater than Li ions (0.076 nm), it promotes easy insertion/de-insertion of Li ions with the least resistance [85]. The high theoretical capacity (372 mAh/g) combined with low Li-insertional potential (0.1 V) makes graphite an ideal material for Li-ion storage [86]. Usually, graphite anode has a working potential window of 3 V (1.5–4.5 V); thus, energy density as high as 100–105 Wh/kg can be attained for LICs [87].

Graphene is a 2D material composed of single atom thick sp^2 hybridized carbon atoms arranged in a hexagonal honeycomb lattice [88]. Graphene exhibits intriguing properties such as high electrical conductivity, high surface area (2630 m^2/g), high electron mobility (200,000 $cm^2\ V^{-1}\ s^{-1}$), and excellent mechanical strength with Young's modulus around 1 TPa [89]. As a result, graphene has been widely in energy storage systems. However, the face-to-face restacking of graphene nanosheets results in a reduced surface area, thereby leading to limited electrochemical performance. To avoid the restacking issue, pores are generated in their basal planes (Fig. 20a). The pores act as a spacer and prevent the nanosheets from restacking. Additionally, the pores increase the surface area for high-density charge accommodation and promote resistance-free ionic diffusion. Heteroatom doping has also proved to be useful in enhancing the electrochemical performance of the graphene electrode. Heteroatoms such as S, N, P, B, and Cl have been doped as they are found to improve the structural, electrical, chemical, and mechanical properties of graphene [88]. Recently, Xiao et al. [90] reported S-doped graphene electrode-based LIC that attained an excellent performance of high ED of 249.9 Wh/kg, PD of 2.16 KW/kg, and larger cyclic stability of 84.3% for 10,000 cycles. The porous structure of the S-doped graphene nanosheets results in enhanced Li-ion diffusivity (Fig. 20b). The S doping improved the electrical conductivity and enhanced the Li-ion storage of the graphene nanosheets.

Graphene oxide (GO), recued graphene oxide (RGO), and graphdiyne are the allotropes of graphene. GO exhibits various oxygen functional groups such as hydroxyl, epoxy, hydrolysis, carbonyl, and carboxyl groups [88, 91]. These functional groups are advantageous as they prevent the nanosheets from restacking and act as active charge storage sites for high charge generation and accommodation. However, GO exhibits the drawback of low electrical conductivity due to these functional groups. This drawback is addressed by converting GO into RGO as it exhibits lower functional groups. The RGO performance can be enhanced by assembling it into a 3D structured sponge form using the free-drying method (Fig. 20c). The unique 3D sponge structure provides high surface area electroactive sites and promotes easy Li-ion transport. The LIC based on a 3D sponge structure anode delivered a high ED of 231.7 Wh/kg and a PD of 0.57 KW/kg [92]. To avoid restacking, single-walled carbon nanotubes (SWCNTs) have been as a spacer between the RGO nanosheets. The LIC fabricated with SWCNTs/RGO composite electrode exhibited a high ED of 222 Wh/kg at the PD of 0.410 KW/kg [92]. Graphdiyne exhibits a structure slightly different from graphene. Graphdiyne has $sp.^{-}$ and sp^2 hybridized carbon atoms and exhibits uniformly arranged 18C cavities [84]. As a result, the graphdiyne can be fabricated in the bulky nonporous form that is beneficial for obtaining short diffusion pathways for Li ions. The LIC device fabricated using graphdiyne electrode delivered excellent electrochemical performance [84].

CNTs are also widely used in energy storage systems. CNTs exhibit better electrical conductivity than graphene. The 1D structure enables CNTs to form a self-supported structure that enables the formation of binder-free electrodes [93]. Additionally, the functional groups attached to the CNTs contribute to additional charge generation and storage [94]. Heteroatom doping (N) also proved beneficial in enhancing the electrochemical performance of the CNT electrode. N-doped CNTs' electrode demonstrated an outstanding charge storage capacity of 81 mAh/g at the ultrahigh current density of 60C (1C = 1 h charge/discharge) [94]. Biomass-derived carbon (graphitized carbon) has attracted significant attention in recent years due to its advantages such as cost-effectiveness, environmentally benign, and easy processability [95–99]. Biomass-derived carbon is fabricated from agricultural products using the carbonization process. Generally, biomass-derived carbon exhibits a high surface area (>2000 m^2/g) and high electrical conductivity that is suitable for achieving improved electrochemical performance. Biomasses such as fish skin [95], animal bone [96], teak wood sawdust [97], coffee waste [98], rice husk [99], etc. have been used in the fabrication of graphitized carbon. The biomass-derived (fish skin) carbon exhibiting a surface area of 2192 m^2/g delivered a high ED of 106.4 Wh/kg and a PD of 88.8 kW/kg in LIC. A further improved performance (ED of 184 Wh/kg and PD of 78.1 kW/kg) was reported by Liu et al. [95] by co-doping oxygen and nitrogen in the biomass-derived (fish skin) carbon. The co-doping improved electrical conductivity (111 Sm-1), resulting in high charge storage. Some of the reported performances of the biomass-derived carbon in LICs are tabulated in Table 4.

Table 4 The electrochemical performance of biomass-derived carbon for LIC application

Anode	Energy density (Wh/kg)	Power density (kW/kg)	Cyclic stability	References
Fish skin-derived carbon	184	78.1	70% for 10,000 cycles	[95]
Animal bone-derived carbon	106.4	88.8	88.3% for 8000 cycles	[96]
Teak wood sawdust-derived carbon	111	–	100% for 2000 cycles	[97]
Coffee waste-derived carbon	100	9	80% for 3000 cycles	[98]
Rice husk-derived carbon	45	4.3	92% for 2000 cycles	[99]

4 Conclusions

This chapter provides a brief outlook on the current status of LICs. Electrode properties such as charge storage mechanism, electrical conductivity, redox activity, active surface area, and morphology significantly influence the LIC performance. Various electrode materials along with their requirements and their electrochemical performance have been discussed in the chapter. Electrode materials based on sulfides, oxides, silicon, MXene, and carbon have shown outstanding electrochemical performance. However, no exact electrode material can be claimed to be an ideal material for LIC applications due to some drawbacks associated with them. Metal sulfides exhibit high charge storage capacity but exhibit poor cyclic stability due to high volume expansion and polysulfide diffusion effect. Metal oxides have high cyclic stability but suffer from lower charge storage capacity. Silicon exhibits an exceptional charge storage capacity that surpasses most of the reported electrode materials. However, the high volume expansion (300%) leads to lower cyclic stability. Electrode materials such as MXene and carbon (graphene, RGO) suffer from nanosheet restacking issues that result in lower charge storage capacity. Therefore, there is a great need to conduct extensive work to overcome these drawbacks for the development of LICs. Additionally, all the reported studies have been performed in a controlled manner at a lab scale. The mass-scale production and the practical implementation of LICs in our daily chores need to be studied.

Acknowledgments We gratefully acknowledge the financial support from Korea-UAE Joint R&D Technical Center (KUTC), under Award No. 8474000259.

References

1. M. Suberu, M. Mustafa, N. Bashir, Renew. Sust. Energ. Rev. **35**, 499 (2014)
2. A. Jagadale, X. Zhou, R. Xiong, D. Dubal, J. Xu, S. Yang, Energy Storage Mater. **19**, 314 (2019)

3. B.E. Conway, Springer Science & Business Media, 2013
4. J.B. Goodenough, K.-S. Park, J. Am. Chem. Soc. **135**, 1167 (2013)
5. A.F. Burke, Proc. IEEE **95**, 806 (2007)
6. A. Khaligh, Z. Li, IEEE Trans. Veh. Technol. **59**, 2806 (2010)
7. G.G. Amatucci, F. Badway, A. Du Pasquier, T. Zheng, J. Electrochem. Soc. **148**, A930 (2001)
8. W. Zuo, R. Li, C. Zhou, Y. Li, J. Xia, J. Liu, Adv. Sci. **4**, 1600539 (2017)
9. V. Etacheri, J.E. Yourey, B.M. Bartlett, ACS Nano **8**, 1491 (2014)
10. L.L. Zhang, X. Zhao, Chem. Soc. Rev. **38**, 2520 (2009)
11. Q. Dou, Y. Wang, A. Wang, M. Ye, R. Hou, Y. Lu, L. Su, S. Shi, H. Zhang, X. Yan, Sci. Bull. **65**, 1812 (2020)
12. H. Kim, J. Hong, K. Park, H. Kim, S. Kim, K. Kang, Chem. Rev. **114**, 11788 (2014)
13. X. Yanga, F. Chenga, O. Kaa, L. Wena, X. Gua, W. Houa, W. Lua, L. Da, Energy Storage Mater. **46**, 431 (2022)
14. A. Lokhande, S. Teotia, A. Shelke, T. Hussain, I. Qattan, V. Lokhande, S. Patole, J. Kim, C. Lokhande, Chem. Eng. J. **399**, 125711 (2020)
15. S. Patole, M. Arif, R. Susantyoko, S. Almheiri, S. Kumar, Sci. Rep. **15:8**(1), 12188 (2018)
16. H. Kim, M. Cho, M. Kim, K. Park, H. Gwon, Y. Lee, K. Roh, K. Kang, Adv. Energy Mater. **3**, 1500 (2013)
17. H. Song, J. Fu, K. Ding, C. Huang, K. Wu, X. Zhang, B. Gao, K. Huo, X. Peng, P. Chu, J. Power Sources **328**, 59 (2016)
18. B. Deng, T. Lei, W. Zhu, L. Xiao, J. Liu, Adv. Funct. Mater. **28**, 1704330 (2018)
19. L. Gao, D. Huang, Y. Shen, M. Wang, J. Mater. Chem. A **3**, 23570 (2015)
20. V. Aravindan, M. Reddy, S. Madhavi, S. Mhaisalkar, G. Rao, B. Chowdari, J. Power Sources **196**, 8850 (2011)
21. X. Wang, G. Shen, Nano Energy **15**, 104 (2015)
22. G. Yu, X. Xie, L. Pan, Z. Bao, Y. Cui, Nano Energy **2**, 213 (2013)
23. Y. Wang, M. Liu, J. Cao, H. Zhang, L. Kong, D. Trudgeon, X. Lid, F. Walsh, ACS Appl. Mater. Interfaces **12**, 3709 (2020)
24. V. Aravindan, W. Chuiling, S. Madhavi, J. Mater. Chem. A **22**, 16026 (2012)
25. V. Aravindan, W. Chuiling, M. Reddy, G. Rao, B. Chowdari, S. Madhavi, Phys. Chem. Chem. Phys. **14**, 5808 (2012)
26. F. Chen, R. Li, M. Hou, L. Liu, R. Wang, Z. Deng, Electrochim. Acta **51**, 61 (2005)
27. Z. Chen, V. Augustyn, J. Wen, Y. Zhang, M. Shen, B. Dunn, Y. Lu, Adv. Mater. **23**, 791 (2011)
28. X. Lu, T. Liu, T. Zhai, G. Wang, M. Yu, S. Xie, Y. Ling, H. Yu, Y. Tong, Y. Li, Adv. Energy Mater. **4**, 1300994 (2014)
29. H. Sun, L. Mei, J. Liang, Z. Zhao, C. Lee, H. Fei, M. Ding, J. Lau, M. Li, C. Wang, X. Xu, Science **356**, 599 (2017)
30. K. Karthikeyan, S. Amaresh, S. Lee, V. Aravindan, Y. Lee, Chem. Asian J. **9**, 852 (2014)
31. K. Chen, F. Zhang, J. Sun, Z. Li, L. Zhang, A. Bachmatiuk, Z. Zou, L. Zhang, H. Rummeli, F. Liu, Z. Liu, Energy Storage Mater. **12**, 110 (2018)
32. X. Liu, H. Jung, S. Kim, H. Choi, S. Lee, J. Moon, J. Lee, Sci. Rep. **3**, 3183 (2013)
33. R. Yi, S. Chen, J. Song, M. Gordin, A. Manivannan, D. Wang, Adv. Funct. Mater. **24**, 7433 (2014)
34. A.C. Lokhande, K. Gurav, E. Jo, C. Lokhande, J. Kim, J. Alloys Compd. **656**, 295 (2016)
35. J. Ju, L. Zhang, H. Shi, Z. Li, W. Kang, B. Cheng, Appl. Surf. Sci. **484**, 392 (2019)
36. R. Wang, S. Wang, D. Jin, Y. Zhang, Y. Cai, J. Ma, L. Zhang, Energy Storage Mater. **9**, 195 (2017)
37. F. Yin, P. Yang, W. Yuan, A. Semencha, C. Zhang, P. Ji, G. Wang, J. Power Sources **488**, 229452 (2021)
38. J. Huang, J. Chen, L. Ma, Q. Liu, M. Wang, L. Liao, T. Rujiralai, L. Xu, Electrochim. Acta **365**, 137350 (2021)
39. A.C. Lokhande, T. Hussain, A.R. Shelke, P.T. Babar, J.H. Kim, D. Choi, J. Energy Storage **50**, 104251 (2022)

40. T. Xing, Y. Ouyang, L. Zheng, X. Wang, H. Liu, M. Chen, R. Yu, X. Wang, C. Wu, J. Energy Chem. **42**, 108 (2020)
41. Y. Wang, M. Liu, J. Cao, H. Zhang, L. Kong, D. Trudgeon, X. Li, F. Walsh, ACS Appl. Mater. Interfaces. https://doi.org/10.1021/acsami.9b10990
42. N. Böckenfeld, R. Kühnel, S. Passerini, M. Winter, A. Balducci, J. Power Sources **196**, 4136 (2011)
43. L. Ye, Q. Liang, Y. Lei, X. Yu, C. Han, W. Shen, Z. Huang, F. Kang, Q. Yang, J. Power Sources **282**, 174 (2015)
44. Y. Lin, C. Jian, T. Hsieh, J. Huang, H. Weng, Y. Hsiao, W. Syu, C. Chen, Appl. Surf. Sci. **543**, 148717 (2021)
45. Y. Jia, Z. Yang, H. Li, Y. Wang, X. Wang, New Carbon Mater. **36**(3), 573 (2021)
46. Z. Xiao, Z. Yu, M. Ayub, S. Li, X. Ma, C. Xu, Chem. Eng. Sci. **245**, 116968 (2021)
47. P. Chen, W. Zhou, Z. Xiaoa, S. Li, H. Chena, Y. Wanga, Z. Wang, W. Xi, X. Xia, S. Xie, Energy Storage Mater. **33**, 298 (2020)
48. Y. Luan, J. Yin, K. Cheng, K. Ye, J. Yan, K. Zhu, G. Wang, D. Cao, J. Electroanal. Chem. **852**, 113515 (2019)
49. Y. Zhanga, L. Chena, C. Hao, X. Zheng, Y. Guo, L. Chen, K. Lai, Y. Zhang, L. Ci, J. Energy Chem. **46**, 53 (2020)
50. G. Calcagno, A. Lotsari, A. Dang, S. Lindberg, A.E.C. Palmqvist, A. Matic, C. Cavallo, Mater. Today Energy **16**, 100424 (2020)
51. H. Kim, D. Mhamane, M. Kim, H. Roh, V. Aravindan, S. Madhavi, K. Roh, K. Kim, J. Power Sources **327**, 171 (2016)
52. Y. Peng, H. Liu, Y. Li, Y. Song, C. Zhang, G. Wang, J. Colloid Interface Sci. **596**, 130 (2021)
53. J. Huang, L. Fan, Y. Gu, C. Geng, H. Luo, Y. Huang, J. Lin, J. Wu, J. Alloys Compd. **788**, 1119 (2019)
54. M. Arnaiz, C. Botas, D. Carriazo, R. Mysyk, F. Mijangos, T. Rojo, J. Ajuria, E. Goikolea, Electrochim. Acta **284**, 542 (2018)
55. X. Ren, A. De, R. Lv, F. Kang, Z. Huang, New Carbon Mater. **36**(6), 1103 (2021)
56. L. Fana, J. Huanga, Y. Wanga, C. Genga, S. Suna, Y. Huang, J. Wu, J. Energy Storage **30**, 101427 (2020)
57. M. Zhang, R. Bai, S. King, F. Yin, H. Penga, G. Wang, Energy Storage Mater. **43**, 482 (2021)
58. T. Eguchi, K. Sawada, M. Tomioka, S. Kumagai, Electrochim. Acta **394**, 139115 (2021)
59. R. Shao, J. Niu, F. Zhu, M. Dou, Z. Zhang, F. Wang, Nano Energy **63**, 103824 (2019)
60. J. Su, S. Lin, C. Cheng, P. Cheng, S. Lu, J. Power Sources **531**, 231345 (2022)
61. L. Sun, Y. Liu, R. Shao, J. Wu, R. Jian, Z. Jin, Energy Storage Mater. **46**, 482 (2022)
62. X. Liu, L. Zhong, S. Huang, S.X. Mao, T. Zhu, J.Y. Huang, ACS Nano **6**, 1522 (2012)
63. Y. Sun, J. Lopez, H.W. Lee, N. Liu, G. Zheng, C.L. Wu, J. Sun, W. Liu, J.W. Chung, Z. Bao, Y. Cui, Adv. Mater. **28**, 2455 (2016)
64. J. Yang, Y. Wang, W. Li, L. Wang, Y. Fan, W. Jiang, W. Luo, Y. Wang, B. Kong, C. Selomulya, H.K. Liu, S.X. Dou, D. Zhao, Adv. Mater. **29**, 1700523 (2017)
65. C. Jin, T. Liu, O. Sheng, M. Li, T. Liu, Y. Yuan, J. Nai, Z. Ju, W. Zhang, Y. Liu, Y. Wang, Z. Lin, J. Lu, X. Tao, Nat. Energy **6**, 378 (2021)
66. X. Qu, X. Zhang, Y. Gao, J. Hu, M. Gao, H. Pan, Y. Liu, ACS Sustain. Chem. Eng. **7**, 19167 (2019)
67. L. Ling, Y. Bai, Z. Wang, Q. Ni, G. Chen, Z. Zhou, C. Wu, ACS Appl. Mater. Interfaces **10**, 5560 (2018)
68. S.H. Lee, J.H. Lee, D.H. Nam, M. Cho, J. Kim, C. Chantha, Y. Lee, ACS Appl. Mater. Interfaces **10**, 16449 (2018)
69. Z. Wang, T. Huang, A. Yu, J. Power Sources **489**, 229530 (2021)
70. K.L. Browning, R.L. Sacci, M. Doucet, J.F. Browning, J.R. Kim, G.M. Veith, ACS Appl. Mater. Interfaces **12**, 10018 (2020)
71. X. Shan, Z. Cao, G. Zhu, Y. Wang, Q. Qu, G. Liu, H. Zheng, J. Mater. Chem. A **7**, 26 (2019)
72. H. Zhong, J. He, L. Zhang, Polymer **215**, 123 (2021)
73. S. Chen, H.Y. Ling, H. Chen, S. Zhang, A. Du, C. Yan, J. Power Sources **450**, 227671 (2020)

74. K. Minnici, Y.H. Kwon, L.M. Housel, G.D. Renderos, J.F. Ponder, C. Buckley, J.R. Reynolds, K.J. Takeuchi, E.S. Takeuchi, A.C. Marschilok, E. Reichmanis, ACS Appl. Energy Mater. **2**, 7584 (2019)
75. S. Choi, T.W. Kwon, A. Coskun, W. Choi Jang, Science **357**, 279 (2017)
76. I.A.J. Gordon, S. Grugeon, H. Takenouti, B. Tribollet, M. Armand, C. Davoisne, A. Débart, S. Laruelle, Electrochim. Acta **223**, 63 (2017)
77. Q. Li, X. Liu, X. Han, Y. Xiang, G. Zhong, J. Wang, B. Zheng, J. Zhou, Y. Yang, ACS Appl. Mater. Interfaces **11**, 1406 (2019)
78. Y. Xia, L. Que, F. Yu, L. Deng, C. Liu, X. Sui, L. Zhao, Z. Wang, Chem. Eng. J. **404**, 127116 (2021)
79. S. Yi, L. Wang, X. Zhang, C. Li, W. Liu, K. Wang, X. Su, Y. Xu, Z. Yang, Y. Cao, J. Sun, Y. Ma, Sci. Bull. **9**, 914 (2021)
80. B. Yang, B. Liu, J. Chen, Y. Ding, Y. Sun, Y. Tang, X. Yan, Chem. Eng. J. **429**, 132392 (2022)
81. L. Yua, Z. Xionga, W. Zhanga, D. Wang, H. Shi, C. Wang, X. Niu, C. Wang, L. Yao, X. Yan, Electrochim. Acta **409**, 139981 (2022)
82. W. Wu, C. Zhao, T. Hao Liu, L. Liu, J.Z. Wang, J. Colloid Interface Sci. **623**, 216 (2022)
83. J. Orangi, H. Tetik, P. Parandoush, E. Kayali, D. Linm, M. Beidaghi, Mater. Today Adv. **9**, 100135 (2021)
84. X. Wang, L. Lu, Z. Niu, Mater. Chem. Front. **3**, 1265 (2019)
85. L. Liu, Z. Niu, L. Zhang, X. Chen, Small **10**, 2200 (2014)
86. S.R. Sivakkumar, A. Pandolfo, Electrochim. Acta **65**, 280 (2012)
87. V. Khomenko, E. Pinero, F. Beguin, J. Power Sources **177**, 643 (2008)
88. C. Long, X. Chen, L. Jiang, L. Zhi, Z. Fan, Nano Energy **12**, 141 (2015)
89. X. Wang, F. Wan, L. Zhang, Z. Zhao, Z. Niu, J. Chen, Adv. Funct. Mater. **28**, 1707247 (2018)
90. Z. Xiao, Z. Yu, Z. Gao, B. Li, M. Zhang, C. Xu, J. Power Sources **535**, 231404 (2022)
91. A.C. Lokhande, I.A. Qattan, C.D. Lokhande, S.P. Patole, J. Mater. Chem. A **8**, 918–977 (2020)
92. W. Ahn, D.U. Lee, G. Li, K. Feng, X. Wang, A. Yu, G. Lui, Z. Chen, ACS Appl. Mater. Interfaces **8**, 25297 (2016)
93. C. Chen, J. Cao, X. Wang, Q. Lu, M. Han, Q. Wang, H. Dai, Z. Niu, J. Chen, S. Xie, Nano Energy **42**, 187 (2017)
94. S.R. Sivakkumar, A.G. Pandolfo, J. Appl. Electrochem. **44**, 105 (2013)
95. M. Liu, Z. Zhang, M. Dou, Z. Li, F. Wang, Carbon **151**, 28 (2019)
96. J. Niu, R. Shao, M. Liu, J. Liang, Z. Zhang, M. Dou, Y. Huang, F. Wang, Energy Storage Mater. **12**, 145 (2018)
97. A. Jain, S. Jayaraman, M. Ulaganathan, R. Balasubramanian, V. Aravindan, M. Srinivasane, S. Madhavi, Electrochim. Acta **228**, 131 (2017)
98. J. Urbano, G. Fernandez, M. Arnaiz, J. Ajuria, T. Rojo, D. Carriazo, Carbon **162**, 273 (2020)
99. B. Babu, P. Lashmi, M. Shaijumon, Electrochim. Acta **211**, 289 (2016)

Advances in Fabricating Mn_3O_4 and Its Carbon Composite for Electrochemical Energy Storage Applications

Agnes Chinecherem Nkele, Chinedu P. Chime, and Fabian I. Ezema

1 Introduction to Electrochemical Energy Storage

Increased population encourages people to look for alternative energy sources that are environmentally friendly with minimal pollution and available upon demand. Electrochemical energy storage includes every kind of secondary battery or supercapacitors. Electrochemical cells are fabricated with relatively cheap and less poisonous materials. However, the materials are nonrecyclable, suffer leakages, and have short life span, low power density values, and fluctuating current values. Their low energy densities can be increased through carbon incorporation [1]. Although the electric efficiency of an electrochemical system is above 60%, the power density has been recorded to be low. Reverse electrochemical oxidation-reduction reactions aid the conversion of chemical energy in batteries to electric energy. The different sizes of batteries encourage varying application areas [1]. The various energy storage processes of supercapacitors or electrochemical capacitors as distinguished

A. C. Nkele
Department of Physics & Astronomy, University of Nigeria, Nsukka, Enugu, Nigeria
e-mail: chinecherem.nkele@unn.edu.ng

C. P. Chime
Department of Agricultural & Bioresources Engineering, University of Nigeria, Nsukka, Enugu, Nigeria
e-mail: chinedu.chime@unn.edu.ng

F. I. Ezema (✉)
Department of Physics & Astronomy, University of Nigeria, Nsukka, Enugu, Nigeria

Nanosciences African Network (NANOAFNET), iThemba LABS-National Research Foundation, Somerset West, Western Cape Province, South Africa

Africa Centre of Excellence for Sustainable Power and Energy Development (ACE-SPED), University of Nigeria, Nsukka, Enugu, Nigeria
e-mail: Fabian.ezema@unn.edu.ng

F. I. Ezema et al. (eds.), *Chemically Deposited Metal Chalcogenide-based Carbon Composites for Versatile Applications*, https://doi.org/10.1007/978-3-031-23401-9_6

in Fig. 1 include electric double layer capacitors (EDLCs) and pseudocapacitors, depending on their energy storage mechanism [2]. Supercapacitors, also called ultracapacitors are good energy storage devices whose performances are determined by the combined effort of the electrolyte and electrode used. They exhibit quick charging and discharging features, long life cycle, high specific capacitance values, and wide range of operating temperature [3]. The electrodes to be used include transition metal oxides, carbon-based materials, and conductive polymers, while the electrolytes could be in ionic, aqueous, or organic form. Electric double layers formed at the interface between the electrode and electrolyte aid reversible charge storage in EDLCs. The electrostatic charges are stored by accumulating at the interface between the electrode and electrolyte. The surface features of the electrode like size of the pore and surface-to-volume ratio accelerate the charges and electrolytic ions. Pseudocapacitors are faradic systems of redox reactions that have high power storage and increased load discharge rates [4–6]. The quick surface redox reaction and electrode intercalation of ions are mechanisms for storing energy in EDLCs. Pseudocapacitors have higher energy density and charge storage capacity than EDLCs. Hybrid supercapacitors possess higher energy density and charge storage ability owing to the combined features of EDLCs and pseudocapacitors. Electrochemical energy storage systems (EESSs) are able to positively contribute to sustainable energy development [7, 8]. The kind of electrochemical storage device to be used should strongly depend on the energy requirement, fund available, duration of life span, and safety conditions.

In harnessing electrochemical energy, galvanic/voltaic and electrolytic cells are used in converting the electrochemical energy [9]. Galvanic/voltaic cells adopt spontaneous reactions for the conversion of chemical to electrical energy. Electrolytic cells convert electrical to chemical energy. Electrochemical cells enhance the limitation in emitting greenhouse gases, control of pollutants, management, conservation, and storage of energy. Energy can be stored electrochemically in various forms like compressed air, batteries, pumped hydroelectric storage, thermal energy storage, fly wheels, chemical energy (biofuels), electrical energy (capacitor), etc. Batteries comprise at least one electrochemical cell connected in series. During charging, electrical energy obtained from an external source is stored and utilized in supplying energy to a load during the discharging process. Similar to batteries, electrochemical energy is usually potential energy in the absence of an applied force that transforms the energy to kinetic. Different kinds of energy storage systems include batteries (rechargeable and flow) and fuel cells [10]. Rechargeable batteries have at least one electrochemical cell connected in series like lithium system, lead-acid system, etc. The electrical energy (from an external source) stored while charging is usefully supplied to an external load while discharging energy. Flow batteries are conventional batteries that require repetitive charging and discharging, with the energy storage material dissolved in the electrolyte and stored in external tanks. Fuel cells are electrochemical cells whose energy-supplying reactants are stored externally and supplied continuously to the electrodes. Fuel cells could be combined with electrolysers to enhance their energy storage ability [10].

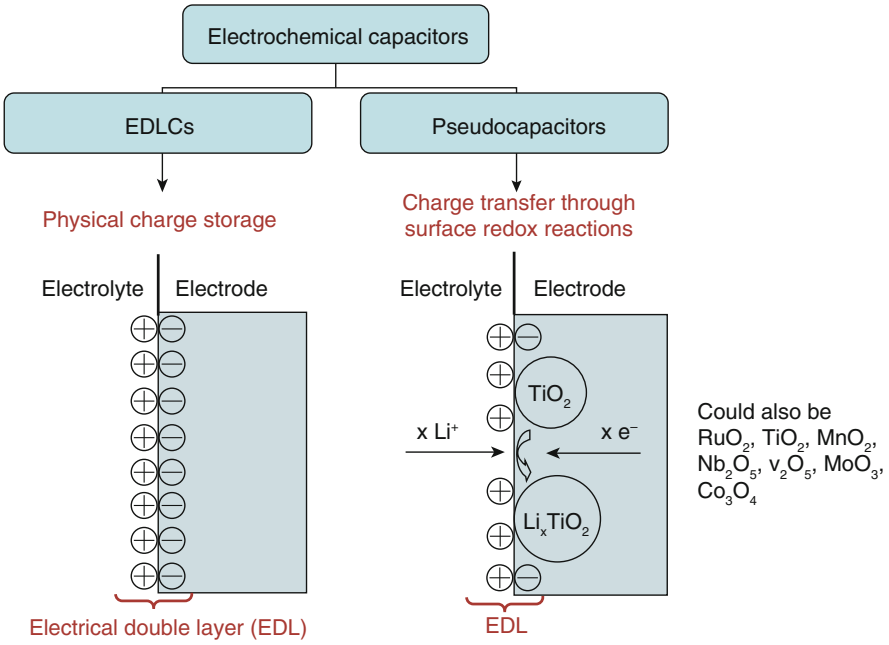

Fig. 1 Categories of electrochemical capacitors and their charge storage mechanism [2]

2 Mn_3O_4 as an Electrochemical Energy Storage Material

Manganese oxide (Mn_3O_4) is a crystalline material with a spinel structure where the tetrahedral and octahedral sites are occupied respectively by Mn^{2+} and Mn^{3+} [3]. The hausmannite phase is a very steady phase especially under high temperature conditions. It can be found naturally in ores, sediments, and soils. The crystal structure and properties of the Mn_3O_4 material in the hausmannite phase are as seen in Fig. 2. As a transition metal oxide, it has varying oxidation states [11–13], increased performance property, good catalytic activity, chemically stable nature, fast mobile carriers, and high charge storage ability that makes it useful as an electrode in supercapacitive devices [14]. Mn_3O_4 exhibits unique electrical features, high theoretical capacity, and stable crystalline phase. It also has available raw materials and increased specific capacitance value and is environmentally friendly [15]. The magnetic property of manganese oxide makes it useful for applications in batteries, adsorbents, catalytic systems, etc.

Setbacks on single Mn_3O_4 materials like low electroconductivity and reduced cyclic stability led to the development of Mn_3O_4 in its nanoparticle form and other composite forms. Reduced electroactive sites and low surface area of manganese oxide account for the large particle size and reduced charge storage capacity [16]. Mn_3O_4 in its nanoparticle form exhibits better features optically, electrically, and magnetically [14]. These nanoparticles have supercapacitive characteristics

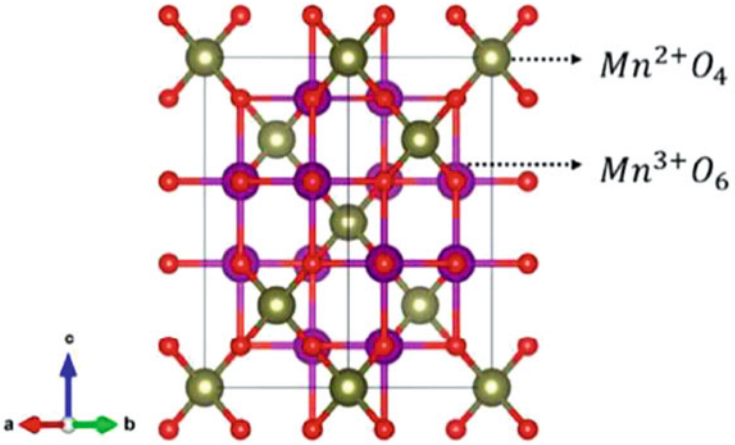

Fig. 2 Schematic of a unit hausmannite cell of the Mn_3O_4 phase with tetrahedral Mn^{2+} and octahedral Mn^{3+} lattice sites

owing to their environmentally friendly nature, high charge storage capacity, and wide potential window. Nanosheets of Mn_3O_4 exhibit morphological anisotropy and unique structural buildup [17]. Materials like graphene, reduced graphene oxide (rGO), etc., are useful agents in improving the electrical conduction and stable nature of manganese oxide. The inclusion of rGO to the Mn_3O_4 material widens the surface area and flexible nature of the electrode [17]. Energy storage devices fabricated from the Mn_3O_4 electrode are usually light in weight and flexible with high power density. Mn_3O_4 can be usefully applied as an electrode material in wastewater management, sensing devices, catalytic systems, batteries, and supercapacitors [3].

3 Recent Advances in Fabrication Techniques for Mn_3O_4

Mn_3O_4 has different fabrication techniques that usually account for their properties and increased performance. Some of these techniques include microwave-assisted combustion method.

3.1 Microwave-Assisted Combustion Method

Microwave-assisted combustion method is a synthesis technique that involves applying microwave radiation during film preparation by heating the solvents in contact with a sample. It allows materials to be processed within a short

time with high purity percentage [14]. The films produced are of good quality and homogeneity through a simple and convenient process. Manganese oxide nanoparticles were prepared by mixing manganese nitrate and glycine in a 1:1 ratio, dissolving in double distilled water, and keeping at 2450 MHz frequency for about 3 min in an oven [14]. Nanoparticles with a tetragonal hausmannite nanoparticle, a 28-nm crystallite size, spongy aggregates, an energy band gap of 1.97 eV, and good supercapacitive nature were produced. Nanoclusters of Mn_3O_4 were dispersed on rGO via a microwave technique for high-performance supercapacitive use [16]. The graphite flakes were oxidized by irradiating with microwave for several minutes. The fabricated electrodes exhibited high specific capacitance and cyclic stability.

Sankar et al. studied the effect of reaction time on the properties of Mn_3O_4 nanoparticles synthesized at varying reaction times [18]. Reduced resistance during charge transport, a high specific capacitance of 135 F/g, and increased charge retention were obtained. Reduced graphene oxide/Mn_3O_4 composites exhibited a specific capacitance of 344.8 F/g, a power density of 1 kW/kg, improved cyclic reversibility, and an energy density of 47.8 Wh/kg [19]. Depositing gold nanoparticles on Mn_3O_4 serves as a useful catalyst for oxidizing carbon oxide at low temperature [20]. The oxidation reaction occurring in the carbon oxide served as a model in studying the relationship between the catalyst and sample.

3.2 Thermal Decomposition

Preparing Mn_3O_4 from manganese (II) glycerolate at varying temperatures yields nanoparticles of small sizes [21]. Mn_3O_4/carbon composites doped with nitrogen yield a cell voltage of 1.8 V, an energy density of 44.5 Wh/kg, and a power density of 5.6 kW/kg [22]. Mn_3O_4 nanoparticles were properly dispersed on graphene and gave rise to improved catalytic effects and synergy between the materials [23]. Mn_3O_4 nanoparticles were prepared with a bid to controlling the size of the nanoparticle [24]. Yang et al. fabricated MnO/Mn_3O_4 nanocomposite tetrahedrons from the Mn(II) oleate complex, precipitated using methanol and collected by centrifugation [25]. These complex urchins as illustrated in Fig. 3 gave rise to structural pores, wide surface area, and excellent stable and charge storage capacity.

3.3 Hydrothermal Technique

Hydrothermal technique is a method of synthesizing single crystals that depend on heat application under high pressure while the crystal growth is performed in an autoclave [26]. It is an efficient, facile, energy-saving, and commercializable technique of synthesizing films. This method enhances the chemical and physical features of the material to be deposited. The mechanism of this method is characterized by the reactions between the chemical entities in the liquid phase. A one-step

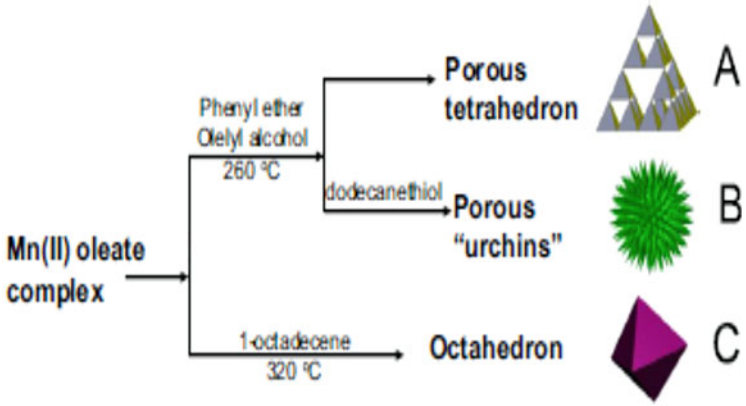

Fig. 3 Illustration showing manganese oxide preparation as tetrahedron urchins [25]

hydrothermal method assisted by sucrose was used to synthesize $MnCO_3/Mn_3O_4$ hybrid materials with the hybrid material and active carbon acting respectively as the positive and the negative electrode [26]. Homogeneous nanooctahedrons were formed after 12 h at a temperature of 180 °C. Specific current of 1 Ag^{-1} produced highest specific capacitance of 191 Fg^{-1}, good cyclic stability, and 97.8% retention of charge after several cycles at 1.5 Ag^{-1} were obtained. The fabricated device was practically applied as a pseudocapacitor material. Nanoclusters of Mn_3O_4 were fabricated with graphene as the hybrid electrode for use in supercapacitor materials [16]. They obtained a high charge retention of 95%, enhanced surface characteristics, and a specific capacitance value of 181 F/g at 0.3 A/g current density. Investigating a Mn_3O_4-mesoporous carbon composite produced a better conducting anode material for charge storage systems [27].

Mn_3O_4-anchored reduced graphene oxide (rGO) nanocomposites exhibited strong synergy and better specific capacitance value at 153 F/g at 10 mV/s [28]. The oxidation and electrochemical activation processes gave rise to better stability and good electrochemical features of the fabricated electrode. Porous Mn_3O_4 micro/nanocuboids encapsulated into a carbon matrix yielded 879 mAh/g at a current density of 100 mA/g [29]. Introducing glucose as a carbon source and reducing agent to the carbon matrix encouraged particle size control and cyclic stability. Decorating Mn_3O_4 nanoparticles with rGO nanosheets produced a specific capacitance of 457 F/g and increased charge retention in one molar concentration of sodium sulfate as electrolyte [30]. Annealing microspheres of Mn_3O_4 fabricated on carbon has produced aggregates of nanoparticles with homogeneous coatings and a discharge capacity of 913.8 $mAhg^{-1}$. The homogeneous carbon microsphere formed is illustrated in Fig. 4. The synthesized electrodes maintained high cyclic stability, increased electrical conductivity, and enhanced electrochemical characteristics due to the carbon-shell structure.

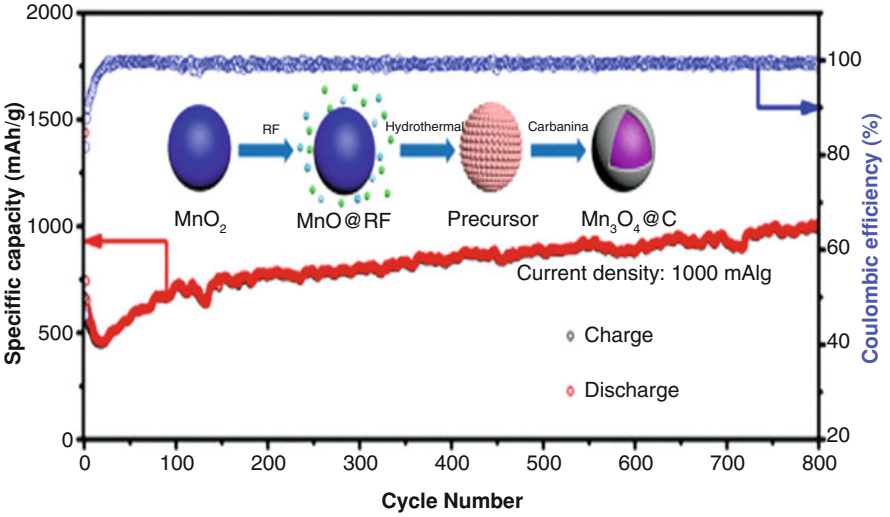

Fig. 4 Plot showing the relationship between specific capacitance and coulombic efficiency versus cycle number with an inset showing the preparation stages [31]

3.4 Chemical Route

Chemical route deals with simple processes that involve chemical reactions and methods in film synthesis. The ternary nanocomposite of graphene oxide-ferrocene/Mn_3O_4/PANI was obtained by physically mixing the constituents as illustrated in Fig. 5 [32]. Morphological and structural studies showed an aggregated nanofiber with a tetragonal crystal structure. At a current density of 2.5 A/g, a specific capacitance of 233 mAh/g, an energy density of 42.6 Wh/kg, a power density of 5.56 kW/kg, and 80% charge retention were obtained. The fabricated electrodes are potentially useful in battery-type supercapacitors. A sonochemical method was utilized in synthesizing Mn_3O_4/MnOOH nanocomposite for supercapacitive use [33]. The nanocomposite recorded a specific capacitance of 307.8 F/g, long stable cycles, a power density of 7.4 kW/kg, and an energy density of 10.6 Wh/kg. Introducing Mn_3O_4 into activated carbon through a sonochemical process enhances redox reaction rate, improves precursor permeability, and leads to uniform distribution of the nanocomposites [34]. The nanostructures exhibited specific capacitance, energy density, and power density values of 150 F/g, 68 Wh/kg, and 210 W/kg, respectively.

A successive ionic layer adsorption and reaction method was utilized in synthesizing Mn_3O_4 electrodes at different deposition cycles [35]. Homogeneous films with a maximum specific capacitance of 786.2 F/g, a solution resistance of 3.85 Ω, and cyclic stability over 1000 cycles were obtained. A one-pot chemical method of synthesizing nanostructures of Mn_3O_4 yields a specific capacitance of 210 F/g,

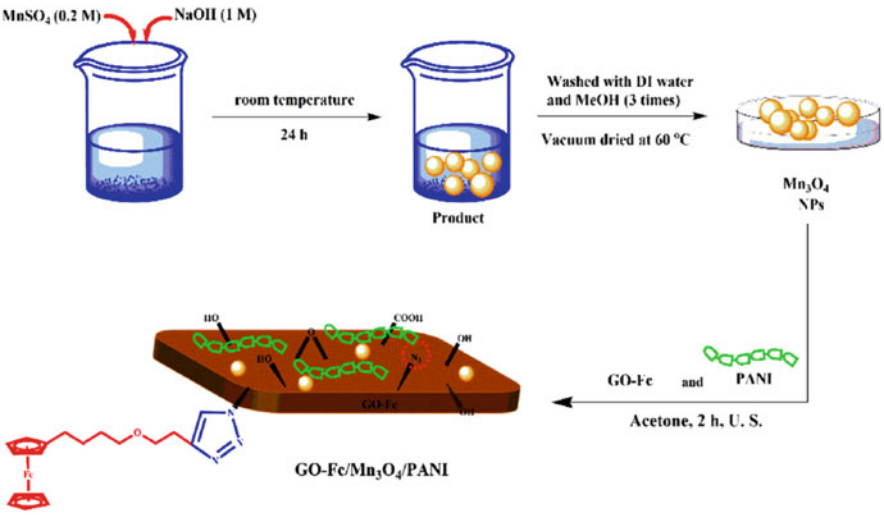

Fig. 5 Schematic illustration of the synthesis procedures for the ternary nanocomposite [32]

increased conducting power, and wider area available for electrochemical reactions [36]. An affordable synthesis method was used to prepare nanocomposites of Mn_3O_4 dipped into several electrolytes [37]. The fabricated electrodes exhibited excellent cyclic feature, a discharge capacity of 1813 $mAhg^{-1}$, and a specific capacitance of 194.8 Fg^{-1} and served as useful anode materials for use in lithium-ion batteries. Wang et al. adopted a chemical route involving ultrasonication, filtration, and hydrolysis stages to produce binder-free Mn_3O_4/rGO nanosheets [17]. The reduced graphene oxide (rGO) served as an electron conductor, agglomeration suppressant, and mechanically flexible substrate. Electrochemical studies showed a specific capacitance value of 409 F/g obtained at 0.5 A/g current density and a cyclic stability of 92% recorded after 300 cycles. Highly crystalline peaks with an irregular sheet-like surface homogeneously distributed and with minimal agglomerates were obtained. The highly performing nature of the fabricated electrode makes it useful in electronic and energy storage devices.

3.5 Self-Assembly

Self-assembly associates individual elements into highly ordered patterns through noncovalent interactions. It depends on weak covalent bonds in fabricating various nanostructures that exhibit unique features. Dubal and Holze adopted a scalable self-assembly strategy shown in Fig. 6 for fabricating Mn_3O_4 nanosheets using varying concentrations of hexamethylenetetramine (HMT) as complexing agent [38]. They

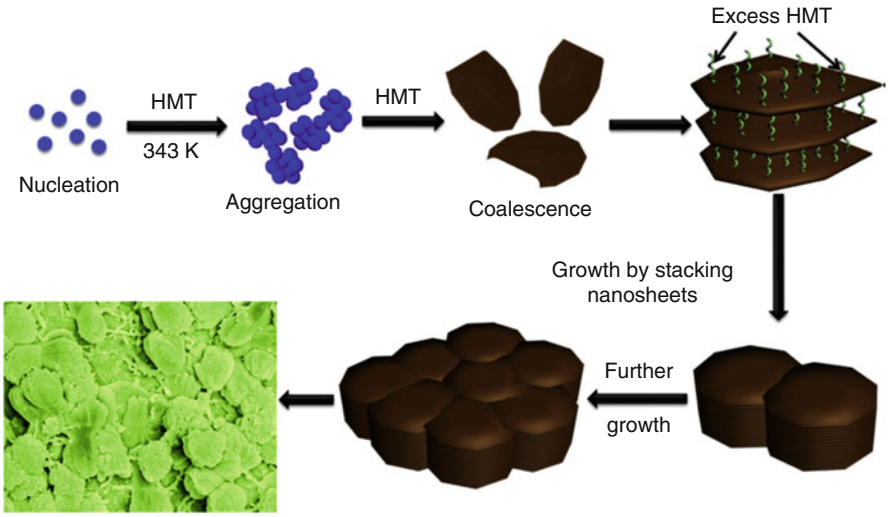

Fig. 6 Illustration of the stages involved in forming stacks of Mn_3O_4 nanosheets on the substrate surface [38]

observed that preparing the nanosheets at lower concentrations of the complexing agent gave better pore distribution, stable cycles, and improved specific capacitance.

Decorating graphene oxide with Mn_3O_4 nanocrystals produced electrodes that are electrochemically stable with improved charge retention, an energy density of 34.1 Wh/kg, a specific capacitance of 225 F/g, and a power density of 251 W/kg [39]. MnO_2 was reduced to a α-MnO_2/Mn_3O_4 structure upon dissolution in $NaBH_4$ and later deposited on a carbon cloth substrate [40]. α-MnO_2/Mn_3O_4 fabricated on CC was assembled with activated carbon to give higher charge retention, cyclic stability, reduced agglomeration, and improved energy density. This structure encourages further development of wearable energy storage systems. Mn_3O_4 tetragonal bipyramids deposited on a porous carbon composite as anode material were homogeneously dispersed and yielded a capacitance value of 279 F/g at 10 A/g [41]. This design was carried out at a potential of 1.8 V and is illustrated in Fig. 7. Easily controlled morphology, an energy density of 34.7 Wh/kg, high capacity retention, and a power density of 450 W/kg were achievable from this structural buildup.

Hiremath, Cho, and Seo synthesized Mn_3O_4 nanoclusters over carbon nanotube threads via self-assembly with acetylacetone acting as a chelating agent [42]. Porous morphology with better electroactive sites, a specific capacitance of 81.9 F/g, and better conductive nature were obtained. Liu assembled Mn_3O_4 composite fabricated on graphitic carbon and produced porous nanodandelions with better SO_2 resistance and improved conductivity [43]. The sequential buildup involving in the composite fabrication is illustrated in Fig. 8.

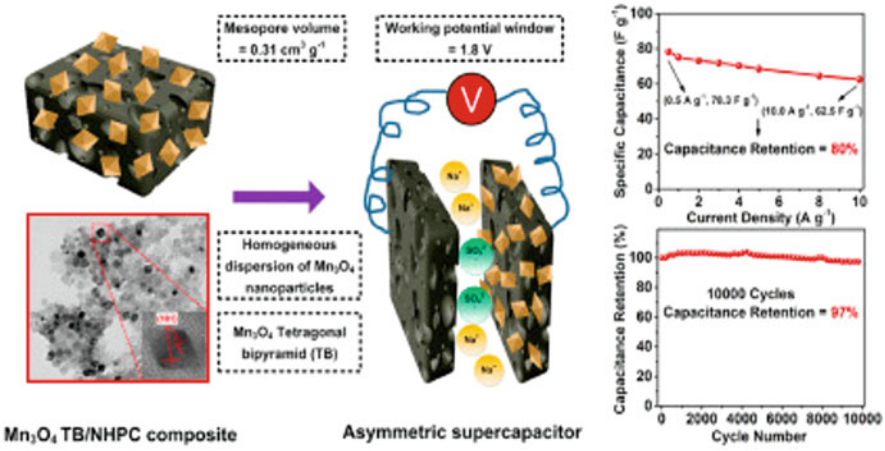

Fig. 7 Synthesis processes involved in preparing Mn_3O_4 tetragonal bipyramids and the obtained electrochemical feature [41]

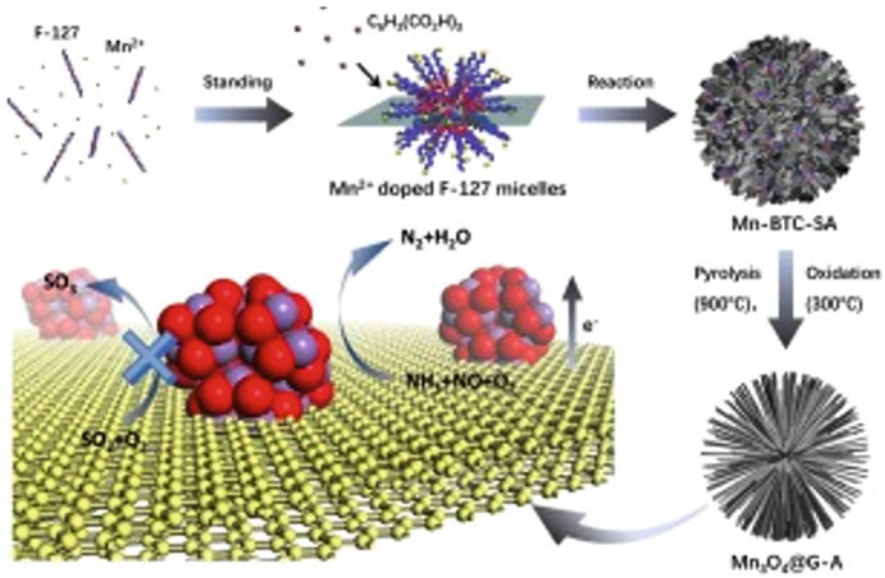

Fig. 8 Schematic showing the step-by-step processes involved in fabricating Mn_3O_4 composite fabricated on graphitic carbon porous nanodandelions [43]

3.6 Sol-Gel Technique

Sol-gel is a wet chemical method that involves forming an inorganic colloidal suspension/sol and gelation of the sol in a continuous liquid phase/gel to form

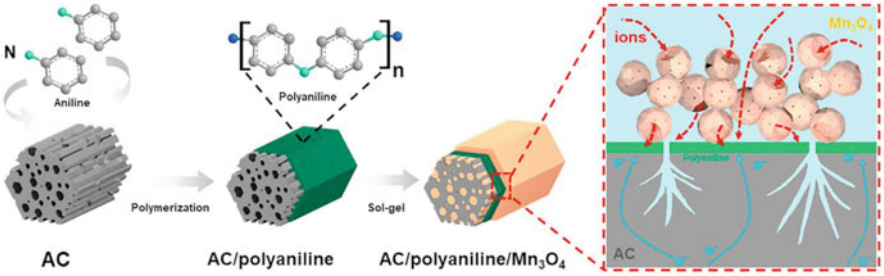

Fig. 9 Stages involved in fabricating Mn_3O_4 nanoparticles on activated carbon using polyaniline as a conductive bridge [15]

a three-dimensional gel structure [44]. It is a versatile and simple technique that produces materials that are chemically, mechanically, and thermally stable. A sol-gel reduction process was adopted to prepare a Mn_3O_4/rGO hybrid composite in 1 M of potassium hydroxide as electrolyte [45]. A specific capacitance of 427 F/g with an enhanced electrochemical feature was obtained. Incorporating Mn_3O_4 into nitrogen-doped porous carbon fibers is a good step toward enhancing the electrochemical performance of charge storage electrodes [46]. The electrodes exhibited cyclic stability, minimal electrode degradation, improved electrical conductivity, and environmentally compatible. Nanocomposite of (α-Mn_3O_4/MnO) fabricated on rGO produced a specific capacitance value of approximately 237 F/g and an energy density of 10.8 Wh/kg. The electrochemical properties of CPAC/Mn_3O_4 yielded a specific capacitance of 277 F/g at a calcine temperature of 500 °C for 3 h [47]. Mn_3O_4 nanoparticles were coupled on activated carbon using polyaniline as a conductive bridge as illustrated in Fig. 9 [15]. The electrode exhibited wide area of surface, ion mobility, and an enhanced specific capacitance value of 352 F/g. Good stability after 10^4 cycles, 90% charge retention, an energy density of 33.8 Wh/kg, and a power density of 152 W/kg were obtained at 0.5 A/g.

4 Conclusions

This chapter has successfully discussed recent advancements in fabricating Mn_3O_4 electrodes and their carbon composites for electrochemical energy storage devices. This chapter encompasses an overview of electrochemical energy storage systems, supercapacitors, and Mn_3O_4. Recent advancements in synthesis methods for Mn_3O_4 fabrication have been discussed with their results pointed out. Some of the synthesis methods include microwave-assisted combustion, thermal decomposition, hydrothermal technique, chemical route method, and sol-gel methods. The Mn_3O_4 electrodes find useful application in energy storage systems.

References

1. S. Sagadevan et al., Chapter two – Fundamental electrochemical energy storage systems, in *Advances in Supercapacitor and Supercapattery*, ed. by N. Arshid, M. Khalid, A.N. Grace, (Elsevier, Amsterdam, 2021), pp. 27–43. https://doi.org/10.1016/B978-0-12-819897-1.00001-X
2. P. Sharma, T.S. Bhatti, A review on electrochemical double-layer capacitors. Energy Convers. Manag. **51**(12), 2901–2912 (2010). https://doi.org/10.1016/j.enconman.2010.06.031
3. S.G. Sayyed, A.V. Shaikh, D.P. Dubal, H.M. Pathan, Paving the way towards Mn_3O_4 based energy storage systems. ES Energy Environ. **14**, 3–21 (2021)
4. A.C. Nwanya, D. Obi, R.U. Osuji, R. Bucher, M. Maaza, F.I. Ezema, Simple chemical route for nanorod-like cobalt oxide films for electrochemical energy storage applications. J. Solid State Electrochem. **21**(9), 2567–2576 (2017). https://doi.org/10.1007/s10008-017-3520-8
5. A.C. Nwanya et al., Electrochromic and electrochemical supercapacitive properties of room temperature PVP capped Ni(OH)2/NiO thin films. Electrochim. Acta **171**, 128–141 (2015). https://doi.org/10.1016/j.electacta.2015.05.005
6. A.C. Nwanya et al., Nanoporous copper-cobalt mixed oxide nanorod bundles as high performance pseudocapacitive electrodes. J. Electroanal. Chem. **787**, 24–35 (2017)
7. R.M. Obodo et al., Radiations Induced Defects in electrode materials for energy storage devices. Radiat. Phys. Chem. **191**, 109838 (2022)
8. R.M. Obodo et al., Effect of annealing on hydrothermally deposited Co_3O_4-ZnO thin films for supercapacitor applications. Materials Today: Proceedings (2020)
9. A.C. Nkele, F.I. Ezema, Voltammetric sensors for diverse analysis, in *Voltammetry for Sensing Applications* (2022), p. 103.
10. D.N. Buckley, C. O'Dwyer, N. Quill, R.P. Lynch, Electrochemical energy storage, in *Energy Storage Options and Their Environmental Impact*, (The Royal Society of Chemistry, London, 2018), pp. 115–149. https://doi.org/10.1039/9781788015530-00115
11. A.C. Nkele, S. Ezugwu, M. Suguyima, F.I. Ezema, Structural and electronic properties of metal oxides and their applications in solar cells, in *Chemically Deposited Nanocrystalline Metal Oxide Thin Films*, (Springer, New York, 2021), pp. 147–163
12. A.C. Nkele, S. Ezugwu, M. Suguyima, F.I. Ezema, Earth-abundant materials for solar cell applications, in *Electrode Materials for Energy Storage and Conversion*, (CRC Press, New York, 2021), pp. 397–409
13. A.C. Nkele et al., Enhanced electrochemical property of SILAR-deposited Mn_3O_4 thin films decorated on graphene. J. Mater. Res. Technol. **9**(4), 9049–9058 (2020). https://doi.org/10.1016/j.jmrt.2020.06.031
14. T. Patra, J. Panda, T.R. Sahoo, Synthesis of Mn_3O_4 nanoparticles via microwave combustion route for electrochemical energy storage application. Mater. Today Proc. **41**, 247–250 (2021). https://doi.org/10.1016/j.matpr.2020.08.802
15. R. Zhuang et al., Polyaniline-mediated coupling of Mn_3O_4 nanoparticles on activated carbon for high-performance asymmetric supercapacitors. J. Alloys Compd. **851**, 156871 (2021). https://doi.org/10.1016/j.jallcom.2020.156871
16. S. Daripa, S.M. Zaeem, B.K. Kuila, S. Das, Mn_3O_4 nanocluster-graphene hybrid for energy storage and electrochemical sensing application. Ionics **26**(5), 2623–2631 (2020). https://doi.org/10.1007/s11581-019-03349-y
17. W. Wang et al., Flexible Mn_3O_4 nanosheet/reduced graphene oxide nanosheet paper-like electrodes for electrochemical energy storage and three-dimensional multilayers printing. Mater. Lett. **213**, 100–103 (2018)
18. K.V. Sankar, S.T. Senthilkumar, L.J. Berchmans, C. Sanjeeviraja, R.K. Selvan, Effect of reaction time on the synthesis and electrochemical properties of Mn_3O_4 nanoparticles by microwave assisted reflux method. Appl. Surf. Sci. **259**, 624–630 (2012). https://doi.org/10.1016/j.apsusc.2012.07.087

19. H. Zhang et al., Microwave-assisted in situ synthesis of reduced graphene oxide/Mn_3O_4 composites for supercapacitor applications. RSC Adv. **5**(56), 45061–45067 (2015). https://doi.org/10.1039/C5RA05946A
20. M. Morad, M.A. Karim, H.M. Altass, A.E.R.S. Khder, Microwave-assisted synthesis of gold nanoparticles supported on Mn_3O_4 catalyst for low temperature CO oxidation. Environ. Technol. **42**(17), 2680–2689 (2021)
21. O. Jankovský, D. Sedmidubský, P. Šimek, Z. Sofer, P. Ulbrich, V. Bartůněk, Synthesis of MnO, Mn_2O_3 and Mn_3O_4 nanocrystal clusters by thermal decomposition of manganese glycerolate. Ceram. Int. **41**(1), 595–601 (2015)
22. X. Liu et al., From hierarchically porous carbon to Mn_3O_4/Carbon composites for high voltage aqueous supercapacitors. J. Power Sources **485**, 229111 (2021)
23. N. Li et al., Well-dispersed ultrafine Mn_3O_4 nanoparticles on graphene as a promising catalyst for the thermal decomposition of ammonium perchlorate. Carbon **54**, 124–132 (2013)
24. F. Davar, M. Salavati-Niasari, N. Mir, K. Saberyan, M. Monemzadeh, E. Ahmadi, Thermal decomposition route for synthesis of Mn_3O_4 nanoparticles in presence of a novel precursor. Polyhedron **29**(7), 1747–1753 (2010)
25. J. Yang, X. Yang, Y.L. Zhong, J.Y. Ying, Porous MnO/Mn_3O_4 nanocomposites for electrochemical energy storage. Nano Energy **13**, 702–708 (2015)
26. A.S. Keshari, P. Dubey, Sucrose-assisted one step hydrothermal synthesis of $MnCO_3$/Mn_3O_4 hybrid materials for electrochemical energy storage. Electrochim. Acta **402**, 139486 (2022)
27. M. Manoj, K.M. Anilkumar, A. Abhilash, S. Jayalekshmi, Li-ion full cell using $LiFePO_4$ and Mn_3O_4-mesoporous carbon composite as electrodes for energy storage applications. Low-Dimens. Mater. Device **11085**, 136–141. https://doi.org/10.1117/12.2529192
28. L. Li, K.H. Seng, H. Liu, I.P. Nevirkovets, Z. Guo, Synthesis of Mn_3O_4-anchored graphene sheet nanocomposites via a facile, fast microwave hydrothermal method and their supercapacitive behavior. Electrochim. Acta **87**, 801–808 (2013)
29. Y. Jiang et al., Highly porous Mn_3O_4 micro/nanocuboids with in situ coated carbon as advanced anode material for lithium-ion batteries. Small **14**(19), 1704296 (2018). https://doi.org/10.1002/smll.201704296
30. H. UllahShah, F. Wang, M. SufyanJahed, N. Shaheen, M. Saleem, Y. Li, Hydrothermal synthesis of reduced graphene oxide-Mn_3O_4 nanocomposite as an efficient electrode materials for supercapacitors (2017). https://www.sciencedirect.com/science/article/pii/S027288421732518X. Accessed 30 May 2022.
31. P. Chen et al., Hydrothermal synthesis of core-shell Mn_3O_4@C microspheres as superior anode materials for high-performance lithium-ion storage. Solid State Ionics **338**, 121–126 (2019). https://doi.org/10.1016/j.ssi.2019.05.021
32. E. Payami, A. Aghaiepour, K. Rahimpour, R. Mohammadi, R. Teimuri-Mofrad, Design and synthesis of ternary GO-Fc/Mn_3O_4/PANI nanocomposite for energy storage applications. J. Alloys Compd. **829**, 154485 (2020). https://doi.org/10.1016/j.jallcom.2020.154485
33. G.-R. Xu, X.-P. Min, Q.-L. Chen, Y. Wen, A.-P. Tang, H.-S. Song, Sonochemical synthesis of a Mn_3O_4/MnOOH nanocomposite for electrochemical energy storage. J. Alloys Compd. **691**, 1018–1023 (2017)
34. C. Liu et al., Coherent Mn_3O_4-carbon nanocomposites with enhanced energy-storage capacitance. Nano Res. **8**(10), 3372–3383 (2015)
35. M.C. Nwankwo et al., Electrochemical supercapacitive properties of SILAR-deposited Mn_3O_4 electrodes. Vacuum **158**, 206–214 (2018). https://doi.org/10.1016/j.vacuum.2018.09.057
36. Z. Qi, A. Younis, D. Chu, S. Li, A facile and template-free one-pot synthesis of Mn_3O_4 nanostructures as electrochemical supercapacitors. Nano-micro letters **8**(2), 165–173 (2016)
37. P. Rosaiah, J. Zhu, D.P. Shaik, O.M. Hussain, Y. Qiu, L. Zhao, Reduced graphene oxide/Mn_3O_4 nanocomposite electrodes with enhanced electrochemical performance for energy storage applications. J. Electroanal. Chem. **794**, 78–85 (2017)
38. D.P. Dubal, R. Holze, Self-assembly of stacked layers of Mn_3O_4 nanosheets using a scalable chemical strategy for enhanced, flexible, electrochemical energy storage. J. Power Sources **238**, 274–282 (2013)

39. C. Zhang, L. Wang, Y. Zhao, Y. Tian, J. Liang, Self-assembly synthesis of graphene oxide double-shell hollow-spheres decorated with Mn_3O_4 for electrochemical supercapacitors. Carbon **107**, 100–108 (2016). https://doi.org/10.1016/j.carbon.2016.05.057
40. J. Jia, X. Lian, M. Wu, F. Zheng, Y. Gao, H. Niu, Self-assembly of α-MnO_2/Mn_3O_4 hierarchical structure on carbon cloth for asymmetric supercapacitors. J. Mater. Sci. **56**(4), 3246–3255 (2021). https://doi.org/10.1007/s10853-020-05475-9
41. Y. Cheng et al., Mn_3O_4 tetragonal bipyramid laden nitrogen doped and hierarchically porous carbon composite as positive electrode for high-performance asymmetric supercapacitor. J. Power Sources **451**, 227775 (2020). https://doi.org/10.1016/j.jpowsour.2020.227775
42. V. Hiremath, M. Cho, J.G. Seo, Self-assembled Mn_3O_4 nano-clusters over carbon nanotube threads with enhanced supercapacitor performance. New J. Chem. **42**(24), 19608–19614 (2018). https://doi.org/10.1039/C8NJ04850A
43. Z. Liu et al., Design of assembled composite of Mn_3O_4@Graphitic carbon porous nano-dandelions: A catalyst for Low–temperature selective catalytic reduction of NOx with remarkable SO_2 resistance. Appl. Catal. B Environ. **269**, 118731 (2020). https://doi.org/10.1016/j.apcatb.2020.118731
44. A. Sharmin, M.S. Bashar, S. Tabassum, Z.H. Mahmood, Low cost and sol-gel processed earth abundant Cu_2ZnSnS 4 thin film as an absorber layer for solar cell: Annealing without sulfurization. IJTFST **8**(2), 65–74 (2019)
45. M. Mohamed Ismail, S. Hemaanandhan, D. Mani, M. Arivanandhan, G. Anbalagan, R. Jayavel, Facile preparation of Mn_3O_4/rGO hybrid nanocomposite by sol–gel in situ reduction method with enhanced energy storage performance for supercapacitor applications. J. Sol-Gel Sci. Technol. **93**(3), 703–713 (2020). https://doi.org/10.1007/s10971-019-05184-z
46. Z. Li, B. Tang, Mn_3O_4/nitrogen-doped porous carbon fiber hybrids involving multiple covalent interactions and open voids as flexible anodes for lithium-ion batteries. Green Chem. **19**(24), 5862–5873 (2017). https://doi.org/10.1039/C7GC02786A
47. H.-M. Luo, F.-B. Zhang, P. Yang, Preparation and electrochemical properties of CPAC/Mn_3O_4 nanocomposite electrode. J. Mater. Sci. Mater. Electron. **24**(2), 601–606 (2013). https://doi.org/10.1007/s10854-012-0992-2

Porous Hybrid Electrode Materials for High Energy Density Li-Ion and Li-S Batteries

Saiful Islam, Mahbuba Khanom, Md. Al-Amin, S. Mosaddeq Ahmed, Farzana Khalil, Mohammad Mahbub Rabbani, Mohammad Tariqul Islam, and Md. A. R. Jamil

1 Introduction

Inevitable advancement of technologies has created huge energy demand. In this situation, energy storage system is required to mitigate the energy crisis. Till now, rechargeable lithium-ion batteries are commercially available for storing energy. At first, it is obvious to know the function of secondary lithium-ion batteries (LIBs). In a rechargeable lithium-ion battery, lithium ions (Li^+) drift from the negative electrode called the anode to the opposite electrode known as the cathode during discharge and return to the anode during charging. Carbonaceous material, e.g., graphite, is used as anode, and metal oxides like lithium cobalt oxide ($LiCoO_2$) and iron phosphate ($LiFePO_4$) are used as cathode. And of course, electrolyte is required to transport lithium ions. The types of lithium-ion battery differ in chemistry, functionality, price, and reliability. Lithium-ion batteries, particularly non-rechargeable batteries (which are removable), use an interpenetrating lithium compound as the electrode material rather than metallic lithium [1]. Scheme 1 shows the charge-discharge function of a Li-ion battery. The reaction mechanism in an LIB consisting of graphite anode and $LiCoO_2$ cathode is as follows:

S. Islam (✉) · S. M. Ahmed · F. Khalil · M. T. Islam · M. A. R. Jamil
Department of Chemistry, American International University Bangladesh, Dhaka, Bangladesh

M. Khanom
Department of Chemical Engineering, University of Louisville, Louisville, KY, USA

M. Al-Amin
Department of Chemistry, University of Louisville, Louisville, KY, USA

M. M. Rabbani
Department of Chemistry, American International University Bangladesh, Dhaka, Bangladesh

Center for Nanotechnology Research, American International University Bangladesh, Dhaka, Bangladesh

F. I. Ezema et al. (eds.), *Chemically Deposited Metal Chalcogenide-based Carbon Composites for Versatile Applications*, https://doi.org/10.1007/978-3-031-23401-9_7

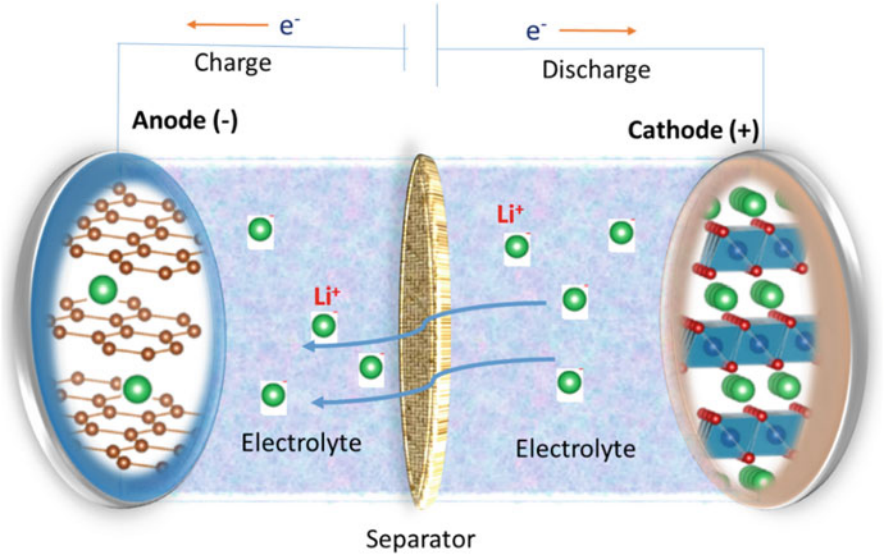

Scheme 1 Basic skeleton of a Li-ion battery

At anode:

$$C_n + xLi^+ + xe^- \underset{\text{Discharge}}{\Longrightarrow} C_nLi_x \tag{1}$$

$$C_nLi_x \overset{\text{Charge}}{\Longrightarrow} C_n + xLi^+ + xe^- \tag{2}$$

At cathode:

$$LiCoO_2 \overset{\text{Charge}}{\Longrightarrow} Li_{1-x}CoO_2 + xLi^+ + xe^- \tag{3}$$

$$Li_{1-x}CoO_2 + xLi^+ + xe^- \underset{\text{Discharge}}{\Longrightarrow} LiCoO_2 \tag{4}$$

In home appliances, lithium-ion batteries are widely used. If not used, they have one of the best power generation ratios, a robust open circuit, a reduced self-rate, a negligible memory effect, and a slow drop of charge. They are among the most prominent examples of rechargeable batteries for smartphones, laptops, and tablets.

Because of their high energy density, LIBs are being used more and more frequently in space applications, electric vehicles, and the military [2].

In 1970, M. S. Whittingham of Binghamton University proposed lithium-ion batteries as an energy storage system. Lithium metal is utilized as the anode and titanium disulfide (TiS_2) as the cathode in Whittingham's model. At the point when they disclosed the unhindered insertion of lithium into graphite in a designated lithium cell in 1980, Yazami et al. [3] first developed a functional graphite anode to take the role of lithium metal batteries. Therefore, graphite has become an ideal anode for rechargeable lithium-ion batteries. In 1991, Sony launched the first ever commercial announcement of a lithium-ion battery, replacing cathode research by a group under the direction of John B. Goodenough. Their cells used layered oxide chemistry, particularly layered lithium cobalt oxide ($LiCoO_2$). Using manganese-based spinel structured compound as a cathode material, Dr. Michael Thackeray, John B. Goodenough, and colleagues first reported it in 1983. Spinel holds a lot of potential because of its low price, strong electronic and Li^+-ion conductivity, and 3D geometry, which ensures dimensional support. While cycling degrades pure manganese spinel, this can be addressed by chemically altering the material. Industrial cells currently have been using a manganese spinel [4]. Nobel laureate John B. Goodenough showed in 1989 that the inductive effect of polyanions, such as sulfates, causes cathodes to produce higher voltages than oxides. However, in 1996, John B. Goodenough, Akshaya Padhi, and colleagues discovered highly stable lithium cobalt oxide and other phospho-olivines (lithium metal phosphates with an olivine structure) used as cathodes. Yet-Ming Chiang and his team at MIT demonstrated in 2002 that increasing the conductivity of lithium batteries by treating them with aluminum, niobium, and zirconium boosted their performance significantly [5]. The exact process that induced the rise became a point of disputation. A further improvement in quality was made by Chiang et al. in 2004 by utilizing iron phosphate particles with a diameter of less than 100 nm [6]. This resulted in a nearly 100-fold reduction in particle density, a rise in cathode surface area, and enhanced performance and effectiveness [7]. The anode, cathode, and electrolyte are three fundamental center parts of a lithium-particle battery. In a standard lithium-ion cell, the cathode is a metal oxide, the anode is carbon, and the electrolyte is lithium salt in an organic solvent. In the industry, graphite is the most often utilized anode material. A layered lithium cobalt oxide, an olivine structured polyanion (such as lithium iron phosphate, $LiFePO_4$), or spinel lithium manganese oxide ($LiMn_2O_4$) is the most common cathode material [8].

There have been increasing efforts to improve advanced batteries in rechargeable hybrid, plug-in hybrid, and battery-operated vehicles in the latest days. Li^+-ion batteries, which use a lithium metal oxide as the cathode and a carbon substance as the anode, have sparked the most fascination. However, the Li-ion battery cannot provide a sufficiently long driving range for pure electrically powered vehicles due to Li^+-ion intercalation materials (PEVs). To compete with gasoline-powered cars, next-generation alternative fuels require improved batteries with higher energy density and lower cost [9–11]. The conversion-type cathode materials, which have more than threefold the energy density of the Li^+-ion intercalation

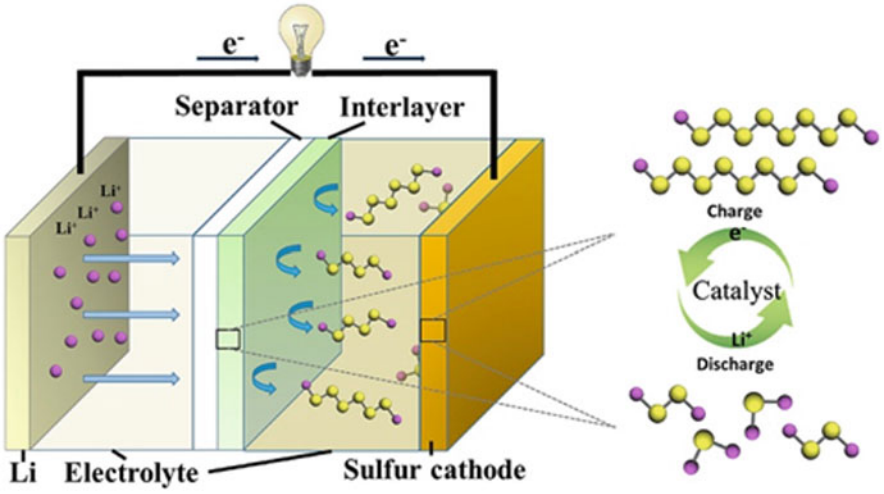

Fig. 1 An illustration of an Li-S battery. (Reproduced with the permission from Ref. [17]. Copyright © 2019, Elsevier)

cathode materials, might theoretically fulfill these criteria. Lithium-sulfur (Li-S) batteries are a good candidate for reaching high energy density. They have recently received considerable attention because of their high theoretical energy density of around 2600 W h/kg [12, 13]. The sulfur cathode is made up of elemental sulfur, a conducting agent, and a binder that is deposited on an aluminum current collector. A separator immersed in an organic electrolyte separates the cathode from the Li anode. Figure 1 depicts the function of a conventional Li-S battery. Li metal acts as an anode and S_8 acts as cathode and lithium-sulfur complex is used as electrolytes. While discharging, oxidation of Li happened, and it releases an electron [14]. The produced Li^+-ion eventually migrated to the cathode side where sulfur hosts lithium ion by forming lithium sulfide (Li_2S) [15]. That means each sulfur can host two sulfurs, whereas only 0.5–0.7 mole of Li can be hosted in LIB. Actually, it is going through some complex reactions, such as it may form intermediate products, namely, Li_2S_8, Li_2S_6, Li_2S_4, etc. [16]. And S_8 regain at cathode and Li metal deposits at anode side upon charging.

Although Li-S batteries have some advantages over Li-ion batteries, the porous hybrid structured materials for Li-ion and Li-S batteries have shown some promising possibilities for improving battery life cycle stability and performance (Scheme 2).

The preceding discussions obviously say the importance of improving electrode materials for high energy next-generation batteries. Since porous hybrid materials have tremendous applications in batteries, this chapter will focus on the hierarchical electrode materials for Li-ion and Li-S batteries.

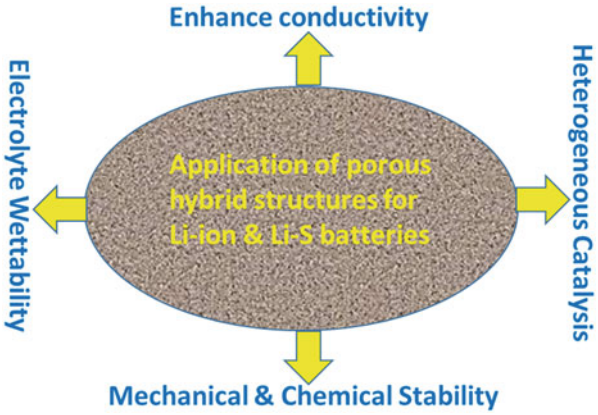

Scheme 2 Application of porous hybrid structures for Li-ion and Li-S batteries

2 Potential Application of Porous Morphology in Lithium-Ion and Lithium-Sulfur Batteries

Recently, lithium-ion batteries have long been used as the major source of power for various transportable high-tech devices. Yet the productivity of intercalation-type electrode materials for Li-ion batteries has hit its optimum. As a result, high-capacity conversion reaction-type energy storage systems, such as sulfur (Li-S batteries) and oxygen (Li-ion batteries), have received a lot of attention [4, 18, 19]. In addition, aqueous rechargeable batteries, which are moderate and reliable, are also attractive prospects for massive electrical energy storage systems. As the primary ingredient of any electrochemical energy storage unit, electrode materials are crucial to ensuring high energy densities. Therefore, researchers have developed and consolidated one-dimensional (1D) (nanoribbons, nanotubes, and nanowires), two-dimensional (2D) (nanoplates, nanosheets, and nanomembranes), and three-dimensional (3D) architectures into electrode materials throughout the last two decades to build strong electrode materials. However, even though solid 1D and 2D electrode materials with improved charge routes have also been demonstrated [20, 21], they nevertheless struggle to cope with aggregation, hindering facile electrolyte penetration and accelerated electrochemical reaction kinetics. For this purpose, one of the most effective techniques for resolving the issues mentioned above is to build 3D structural arrangements with highly porous channels. Furthermore, the electrode materials will then be compressed during the functional manufacturing of electrodes for application in consumer batteries and supercapacitors, producing irregular 3D structures. Electrolyte transfer and ion diffusion will benefit from these 3D structures in commercial bulk electrodes. Compressed architecture of 3D materials throughout advanced manufacturing produces double 3D structures in electrodes, allowing for better electrolyte transit and ion diffusion.

The 3D ordered porous (3DOP) structure is one of the most preferred 3D architectures for building high-performance electrode materials in electrochemical device systems. Colloidal crystal synthesizing methodologies are commonly used to create 3DOP materials. Here is the importance of porous materials for electrode materials [20–28].

- Pores allow the electrolyte to reach the electrode surface easily.
- Because a porous material's surface area is significantly larger, electron transfer across the electrode/electrolyte contact is enhanced.
- The active material walls near the pores can be skinny (nanometers to tens of nanometers), lowering ion diffusion travel time.
- The minimum feature size distribution allows for improved active material efficiency (needed in larger volume, profound cycling), allowing for better specific capacities, particularly at higher charge/discharge rates.
- In a permeable electrode, the partitions and apertures can sometimes be bicontinuous, enabling efficient transfer channels via the initial stage (walls) and the electrolyte phase (permeability) (pores).
- While porosity usually diminishes an electrode's capacity per unit volume (volumetric capacity), a few samples of porous electrodes have been demonstrated to have higher volumetric capacity than crammed nanoparticles.
- Porous solids have nanoscale characteristics accessible inside a more extensive material that can be managed and manipulated relatively simply than individual nanoparticles.
- Sometimes, the active phase can be held together with little or no adhesive.

3 Hybrid Materials

Nature-derived hybrid material has persisted for long periods. Nature created complex hybrid organic-inorganic materials with extraordinary mechanical performance and structural qualities [29]. Bone and large skeletons are natural types of combination organic-inorganic compounds. Hybrid materials are made up of organic and inorganic components that vary in size from a few nanometers to tens of nanometers [30]. In addition, the characteristics of organic and inorganic materials differ. Therefore, the possibilities for blending organic and inorganic components to create hybrid composites are endless [31]. As a result, a new combination can result in a new hybrid material.

Organic materials are recoverable, less expensive, more environmentally friendly, and simple to process [32]. On the other hand, inorganic materials excel in terms of dielectric constant, thermal properties, and charge mobility [33]. Mollusk shells, crustaceans, and bones, including human bones, are products of different organic-inorganic materials [34]. Since the dawn of time, artificial hybrid materials have been developed. Maya blue, an intercalated organic pigment found in clay minerals, shows that mixed material was used in the past [35].

On a molecular level, hybrid materials are defined as combining different components. Furthermore, hybrid materials are commonly referred to as parts produced in place. According to the *International Union of Pure and Applied Chemistry (IUPAC)*, hybrid materials are structures composed of a variety of inorganic and organic components or a mixture of both. Structure adaptability, manufacturing ease, semiconducting potential, changeable electrical characteristics, photocatalytic activity, and effective luminescence are all advantages of organic materials [36, 37]. On the other hand, the inorganic substance exhibits thermomechanical durability and magnetic and electric properties [38]. Hybrid material systems are classified into two types: homogeneous and heterogeneous. The probable molecular interaction among organic and inorganic type materials provides a complete overview of hybrid materials [39]. Hybrid materials are very often divided into two classes: class A and class B (class A: van der Waals and hydrogen bonding are examples of weak molecular contacts; class B: covalent, ionic, noncovalent, and coordinate bonding are examples of strong molecular interactions). Hybrid materials still present many opportunities and challenges; thus, research and development are always underway. However, it usually depends on synthetic procedures. In addition, heterostructures have fascinating and vital features for functional material applications such as photo-sensing devices, semiconductor materials, and supercapacitors. Rechargeable batteries have gotten a lot of consideration over the last few spans because of their high efficiency, cheapness, and low toxicity. Preparing improved active materials is a crucial technology for improving electrocatalytic battery activity. The idea of building hybrid materials for electrode materials has been deemed a viable system strategy in recent years. Several effective synthesis techniques are available for fabricating different types of hybrid materials such as chemical vapor depositions, chemical doping, and carbonization [40, 41]. The application of hybrid materials in energy storage devices will be discussed in this chapter.

3.1 Porous Hybrid Materials for Li-Ion Batteries

The electrochemical energy storage (EES) area faces enormous prospects and problems as a result of the fast-paced economic development and increased environmental responsibility. Rechargeable batteries, in particular, have received much interest in recent years owing to their benefits such as high power density, low price, and environmentally friendly nature. Nonetheless, the ever-increasing expectations for better electrochemical properties and durability have created many problems for them. The electrode material, which comprises cathodes and anodes, mostly determines how well batteries work [42]. Through the numerous methods of synthesis and recent innovative advancements, such as insulating conductive materials [43], doping heteroatoms [44], developing particular morphological feature nanostructures [45], hollow constructions [46], core-shell frameworks [47], and frameworks [48], scientists have developed significant effort to manufacture

Scheme 3 Schematic illustration of porous $LiNi_{1/3}Co_{1/3}Mn_{1/3}O_2$ and morphological effects. (Reproduced with permission from Ref. [45]. Copyright © 2015, American Chemical Society)

superior electrode materials. For example, Li and his group have developed a method for hybrid porous Li-ion battery as illustrated in Scheme 3.

As a result, building heterostructures made up of two or more separate components has only recently become famous and widely explored, mainly since they can combine the benefits of individual elements or even provide additional activities to enhance their properties further [49, 50]. This section will give recent advancement in electrode materials (anode and cathode) for improving the energy density and cyclic life of Lithium-ion batteries. Yin et al. [51], for example, demonstrated that porous TiO_2/C nanocomposite shells maintained good capacity, cycle stability, and rate performance. The cross-linked resorcinol-formaldehyde (RF) polymer correlates to the shells' excellent morphological strength and porous character (Fig. 2). In addition, a strong relationship between capability and the proportion of carbon inserted has been established, letting the electrode configuration be tailored for increased cell performance.

The structural stability of porous TiO_2/C nanoshells can be related to their solid accommodation to bulk or stress fluctuations during lithium insertion-extraction, which explains their improved cycling performance. Porous TiO_2/C nanoshells outperform several other TiO_2 hollow or porous nanostructures, even those with carbon coatings, in terms of performance [51]. Similar to the bulk counterpart, Chen et al. [45] revealed that the $LiNi_{1/3}Co_{1/3}Mn_{1/3}O_2$ cathode material exhibits significantly improved electrochemical performances with larger capacity, superior cycling stability, and considerable rate capability. They prepared hierarchal cathodes by using spherical $Ca_{0.2}Co_{0.4}MnCO_3$ with a uniform diameter of 1.5 μm (Fig. 3a,

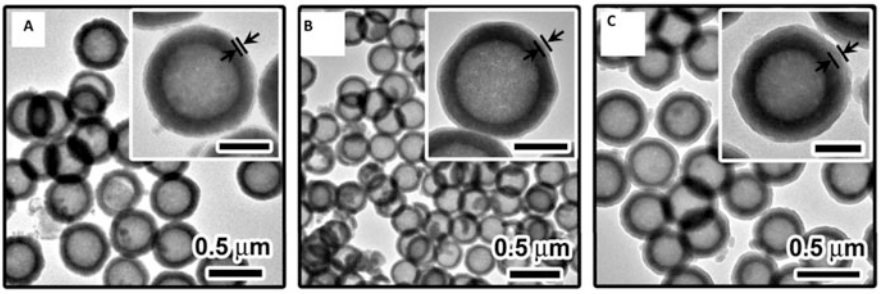

Fig. 2 TEM images of amorphous TiO_2/RF nanoshells with varying RF layer thicknesses were produced using (**a**) 100 mg resorcinol and 140 μL formaldehyde as precursors, (**b**) 250 mg resorcinol and 350 μL formaldehyde as precursors, and (**c**) two cycles of the RF coating technique. The RF layers have been identified in the insets for clarity. Inset scale bar: 200 nm. (Reproduced with permission from [51]. Copyright © 2013, American Chemical Society)

b) and $CoMnO_3$ template (Fig. 3c, d). Porous $LiNi_{1/3}Co_{1/3}Mn_{1/3}O_2$ microsphere with 25 nm width confirm by SEM analysis (Fig. 3e). As shown in Fig. 4, highly porous $LiNi_{1/3}Co_{1/3}Mn_{1/3}O_2$ has a high discharge capacity of 159.6 mAh g^{-1} at 0.2 C, with 98.7% charge-discharge repetitions after 75 cycles and 90% after 100 cycles while running the cell at 1 C. The cathodes with a large surface area of 51.77 m^2g^{-1} help to reach such a high capacity and long cycle life.

Though at a high current rate of 5 C applied, a high discharge capacity of 135.5 mAh g^{-1} is attained. The nano etching-template technique is used to increase the structural stability of the cathode materials for archiving long cycles and large capacity. Figure 4a, b shows galvanostatic charge/discharge profile of hierarchical $LiNi_{1/3}Co_{1/3}Mn_{1/3}O_2$ at 0.1 C rate (1C = 150 mA g^{-1}) within 2.8 and 4.3 V to show electrochemical efficiency at high current rates. Around 3.8 V is the middle of the charge and discharge curves' peaks. The voltage decline is relatively gradual until the abrupt fall at roughly 3.5 V in the discharge curves, ensuring excellent energy density. Long charge and discharge curve platforms, on the other hand, are helpful for electrode durability in reality. Similar capacity is retained even after 50 cycles.

The traces of the 25 cycles are nearly identical. After 50 cycles, a slight capacity loss of 3% is noticed. The more extensive the voltage range, the more noticeable the capacity/voltage decaying becomes. Transition metal ion dissolution, crystal disintegration, and electrolyte decomposition may occur at high voltage, resulting in substantial performance degradation. Figure 4c, d depicts that the discharge capacities of p-NCM are 159.6 mAh g^{-1} at 0.2 C after 75 cycles and 133.2 mAh g^{-1} at 1 C after 100 cycles. b-NCM, on the other hand, yields only 139.8 mAh g^{-1} at 0.2 C following 75 cycles and 112.8 mAh g^{-1} at 1 C following 100 cycles. Although both have a high coulombic efficiency of between 97% and 99%, p-NCM provides greater electrical power under such conditions. The lower slopes of p-NCM discharge capacity curves, on the other hand, imply superior cycling stability as contrasted to b-NCM [45]. Xia et al. [52] have demonstrated hierarchical macro-

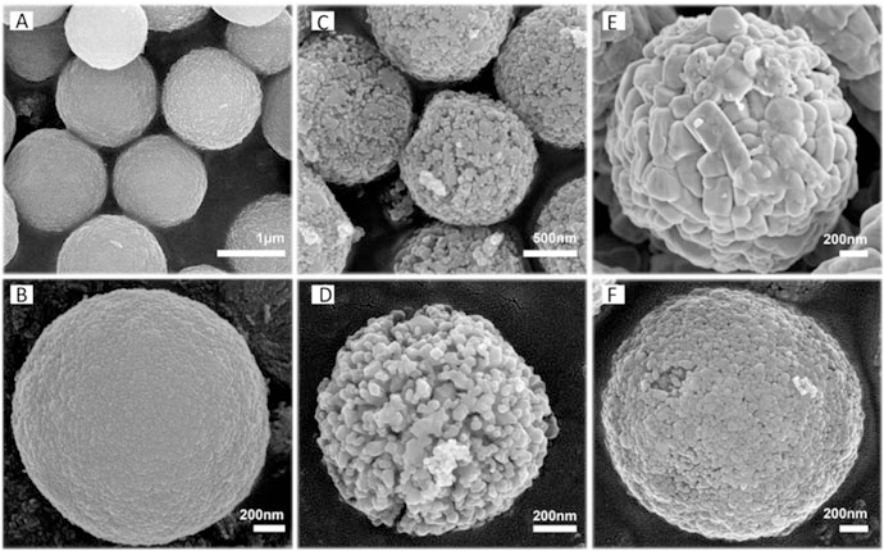

Fig. 3 SEM images of $Ca_{0.2}Mn_{0.4}Co_{0.4}CO_3$ microsphere precursors (**a**, **b**) and porous $CoMnO_3$ microspheres (**c**, **d**) after a 5-h calcination at 600 °C; SEM images of a single bulk $LiNi_{1/3}Co_{1/3}Mn_{1/3}O_2$ microsphere (**e**) and a porous nanomicro hierarchical $LiNi_{1/3}Co_{1/3}Mn_{1/3}O_2$ microsphere (**f**). (Reproduced with permission from Ref. [45]. Copyright © 2015, American Chemical Society)

/mesoporous silicon with tunable pore size and wall thickness was suitable for stress management and durable for capacity retention (Scheme 4).

Here, they treated the silicon with hydrochloric (HCl) and hydrofluoric acid (HF) to improve the mechanical stability and electrochemical performance of the silicon anode. Figure 5 shows the mesoporous silicon obtained by etching with HF at different times. HF-4h treated highly porous materials with pore size of 387 nm with a thickness of 37 nm exhibits a high capacity retention of 72.9%. Thus, the cyclability enhanced tremendously by controlling the porosity of the electrode materials.

Manthiram et al. developed a new alloying nanostructured composite foil (NCF) framework for high-capacity anode materials in lithium-ion batteries [53]. The model Sn/Cu NCF system has a volumetric capability range of 1000–1720 mAh cm^{-3}, which translates to a predicted 20–50% improvement in cell-level volumetric energy density. The first electrochemical cycle was linked to an excellent formation phase (88.92%) that dramatically enhanced transport kinetics, resulting in rapid lithiation (>8 mA cm^{-2}) in future cycles. Since both systems showed identical generation efficiency at this utilization, the cycling performance of the pewter and composite materials was assessed in the capacity-limited regime to understand the consequences of the copper matrix on lengthy cyclic stability (Fig. 6). Pewter had a forming efficiency of 78% during the first cycle, whereas the composite material

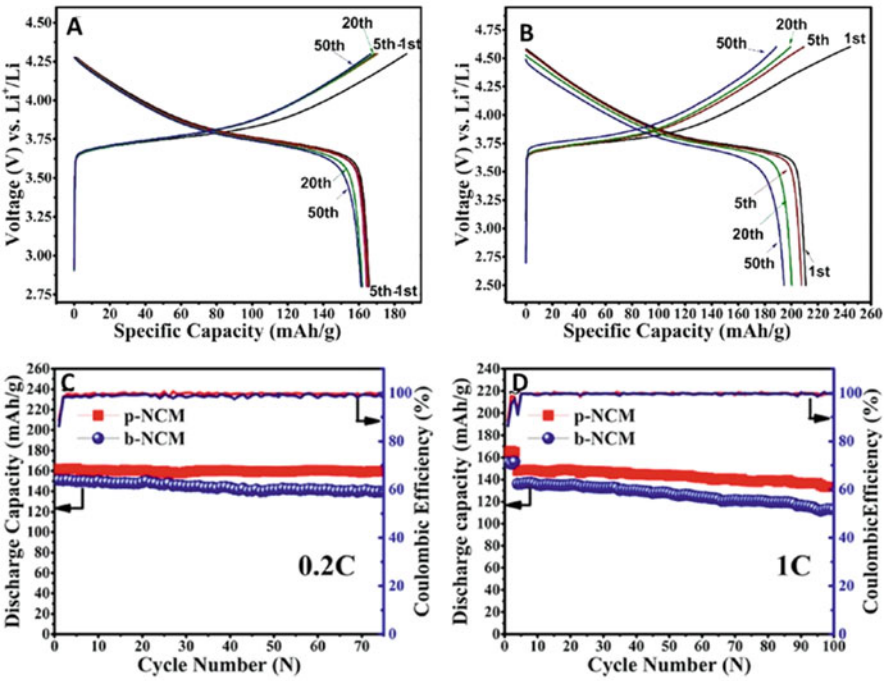

Fig. 4 Charge/discharge curves of hierarchical $LiNi_{1/3}Co_{1/3}Mn_{1/3}O_2$ at 0.1 C and voltages ranging from 2.8 to 4.3 V (**a**) and 2.5 to 4.6 V (**b**). At 0.2 C (**c**) and 1 C, the cycle performances of hierarchical (p-NCM) and bulk (b-NCM) $LiNi_{1/3}Co_{1/3}Mn_{1/3}O_2$ microsphere electrodes were compared (**d**). (Reproduced with permission from Ref. [45]. Copyright © 2015, American Chemical Society)

had an efficiency of 82%. The composite retrieved a small amount of lithium during the second cycle, bringing the overall formation efficiency to 88%.

While the trapped capacity of the pewter material improved slightly with time, it never reached the same level of accessible lithium as the composite. In the first cycle, the composite's polarization was higher than the unreinforced pewter foil, but in the following cycles, it was equivalent. In addition, the pewter system showed substantial voltage fluctuations after the early recovery phase, and the charge storage capacity was quickly depleted [53]. The first investigation on a 3D boron topological metal utilized as a Li or Na anode material was published by Sun et al. [54]. They observed 3D topological metal H-boron consisting of a B4 cluster has a relatively low density (0.91 g cm^{-3}) with numerous adsorbent surfaces for Li and Na ions due to the electron-deficient characteristic of boron, resulting in an ultrahigh specific capacity of 930 mAh g^{-1}. The fast charge-discharge of a battery system depends on the diffusion pathway of metal ions through electrode materials. Figure 7a, b represents the diffusion pathway of Li and Na ions in 3D B4 cluster materials. For the Li-ion-based system, the activation energies are 0.15 eV and 0.42 eV for P1

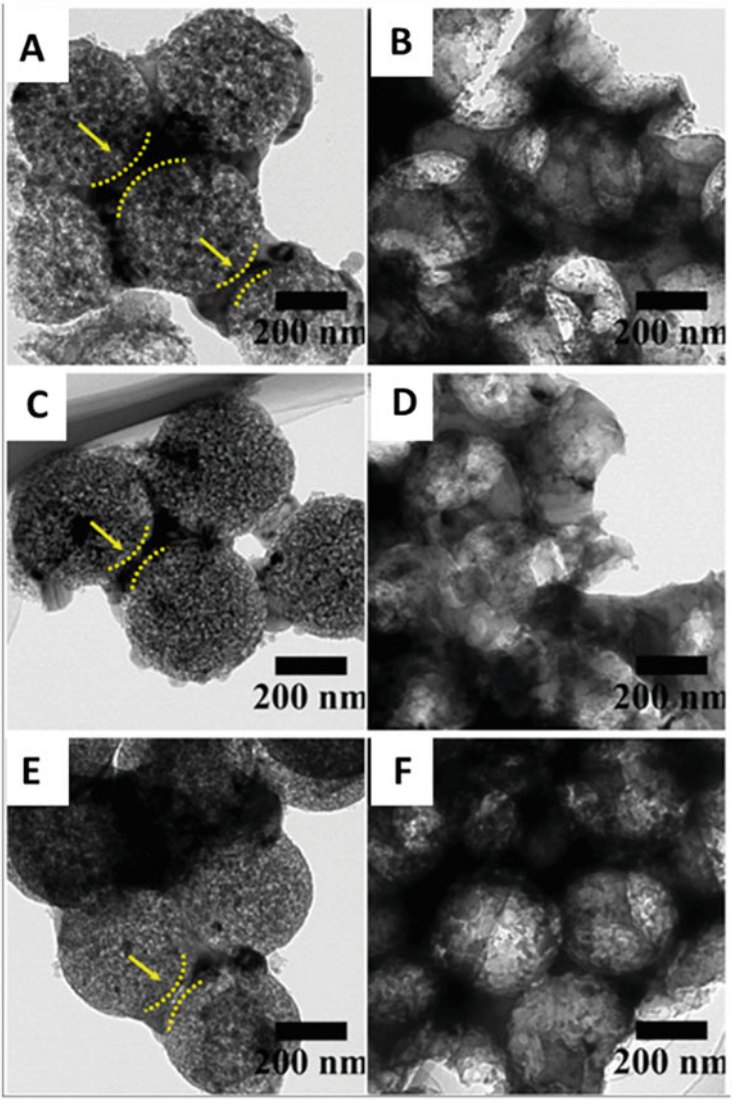

Fig. 5 TEM images of porous silicon samples. (**a**) HCl-4h, (**b**) HF-4h, (**c**) HCl-8h, (**d**) HF-8h, (**e**) HCl-16h, and (**f**) HF-16h (the arrows point out the interconnected part between the adjacent spheres). (Reproduced with permission from Ref. [52]. Copyright © 2020, American Chemical Society)

and P2 pathways, respectively. Since reaction kinetic is mainly based on activation energy, the P1 pathway for Li is more favorable. In the case of a Na-ion-based system, the activation energy for P1 is 0.22 eV, which is comparable to graphite (Fig. 7c, d). Thus, metal ion diffusion mostly depends on the thermal energy and

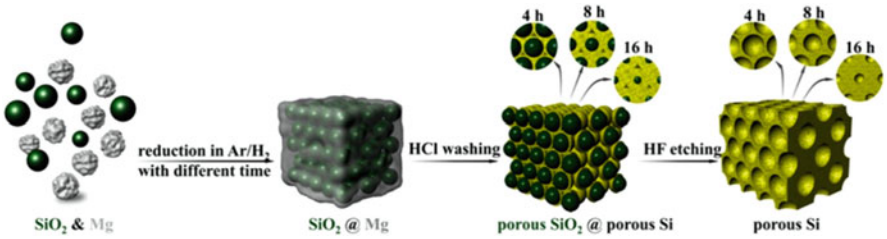

Scheme 4 Self-templating construction and morphology tuning of the 3D hierarchical macro-/mesoporous silicon. (Reproduced with permission from Ref. [52]. Copyright © 2020, American Chemical Society)

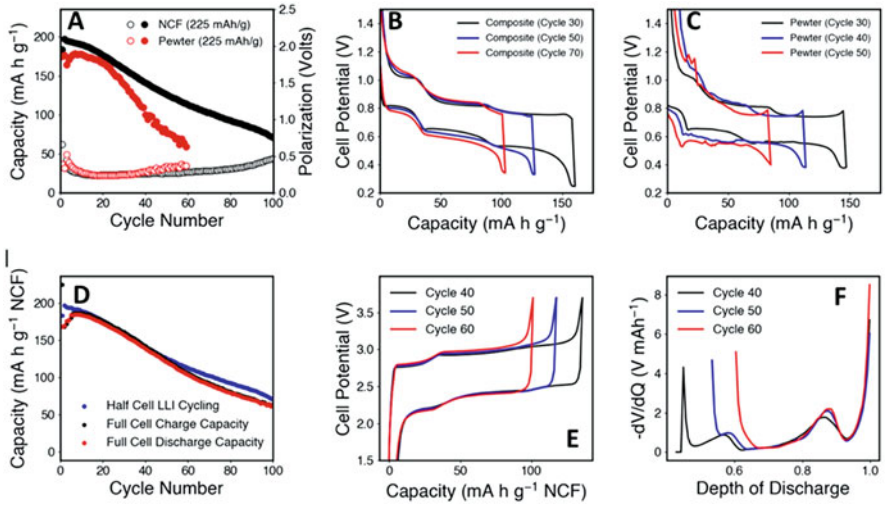

Fig. 6 (**a**) Long-term cycling stability of NCF anodes cycled at a rate of C/3. (**b**) Evolution of the voltage profiles for the composite foil anode. (**c**) Evolution of voltage profiles for the pewter foil anode. (**d**) Comparison of the LFP full cell with LLI cycling in a half-cell. (**e**) Evolution of voltage profiles during cycling of the full cell. (**f**) Evolution of differential capacity plots for the LFP full cell during cycling. Capacities and currents are normalized to the weight of the entire foil electrode. (Reproduced with permission from Ref. [53]. Copyright © 2022, American Chemical Society)

can be calculated by the following equation:

$$D = A\exp\left(-\frac{E_a}{K_b T}\right) \tag{5}$$

Here, D is for diffusivity, A represents the Arrhenius constant, E_a is for activation energy, K_b is a Boltzmann constant, and T is the temperature of the system.

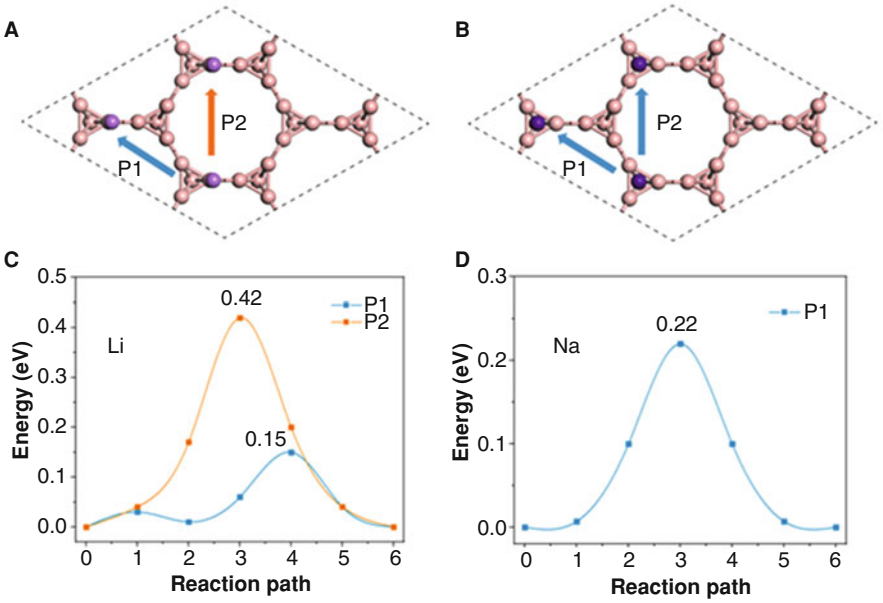

Fig. 7 Migration pathways for the (**a**) Li and (**b**) Na ion and (**c**, **d**) their respective energy barriers. (Reproduced with permission from Ref. [48] Copyright © 2021, American Chemical Society)

These fascinating properties show that B-based 3D topological quantum porous materials are deserving of future investigation as battery materials [54]. Gallei et al. [55] found porous mixed-metal oxide Li-ion battery electrodes with a specific capacity of 335 mAh g^{-1} at a rate of 10 mA g^{-1}.

Highly controlled 2D porous and hybrid materials with different morphology can be prepared through various synthetic ways. From the preceding discussion, it is to be noted that the hybrid materials open up a new possibility to develop highly efficient electrodes for Li/Na/K/Al/Zn ion batteries.

3.2 Porous Hybrid Materials for Li-S batteries

Lithium-sulfur (Li-S) batteries promise to surpass the storage drawbacks of current LIBs. However, they continue to face challenges that impede cyclic stability and efficiency. First, sulfur (5×10^{-30} S·c^{-1} at 25 °C) insulating properties result in low consumption and rate capability [4, 45, 56]. Furthermore, the polysulfides formed throughout cycling are converted to Li_2S_2 and Li_2S, dramatically lowering the electrode kinetics and cycling capacities [7], Second, the polysulfides generated during cycling disintegrate quickly in the carbon-based electrolyte, where they have high ionic mobility. The electrochemical use of sulfur in Li-S batteries is

all impacted by the dissipation of dissolved polysulfide anions into the spacer to the anode, where they interact with the lithium metal to form complexes. As a result, there is a sulfur deficit at the positive electrode, the lithium metal rusts, and the battery self-discharges [15]. A shuttle effect will occur from such disintegration and permeability. At the sulfur electrode, elemental sulfur is broken down to form soluble highly ordered polysulfides, resulting in a concentration gradient within the cell. The diffusion of well-ordered polysulfides toward the anode is detected containing large amounts of high-order polysulfides at the positive electrode, allowing the ordered polysulfides to react with the lithium anode to create low-order polysulfides. As a result, the anode of the cell produces a high concentration of low-order polysulfides, which migrate down to the cathode and are oxidized back to high-order polysulfides. The "polysulfide shuttle" [57] refers to the phenomenon of polysulfide diffusion back and forth between the two electrodes. Due to this shuttle phenomenon, coulombic efficiency will be exceedingly low, and capacity will disappear fast [15]. Another critical issue is caused by the dissolving of the polysulfides in the extreme auto-discharge seen in Li-S systems. Sulfur-based species may travel to the anode side and be transformed into polysulfides, lowering the potential window and Li-ion storage capacity. Last but not least, the substantial volume/morphology change of the S electrode throughout cycling is another major impediment to massive Li-S battery development. The poor cycle life of Li-S batteries will result from the degradation of electrode surface morphology or decoration caused by volume expansion/contraction (76%) and altered morphology of the S electrode material throughout cycling, as the volume expansion of the electro-active material could perhaps impact the electrical interconnection of the carbon host there at the cathode [15]. Moreover, hybrid materials like a combination of carbon and sulfur retain structure, enhance the electron transfer, and increase the surface area [58].

To increase the adsorption of polysulfide species, researchers have developed a number of strategies. These strategies include embedding sulfur in porous and hollow-muffled carbon [53], limiting and controlling the polysulfide shuttle using interlayers [54], fabricating sulfur electrodes with conductive carbon and polymers [55], and modifying the carbon hosts with metal oxides (e.g., TiO_2, MnO_2, ZnO). For example, Hailiang Wang and his group [59] have shown this method for preparing porous hybrid structure for Li-S battery as shown in Scheme 5.

Wang et al. [59] demonstrated that a ternary hybrid material structure containing (CNT) and $NiFe_2O_4S$ had comparatively high specific capacity, rate capability, and cycling stability, as well as an exceptionally high coulombic efficiency (Fig. 8). At low rates of 0.1 and 1 C, alterable specific capacities of 1350 and 900 mAh g^{-1} are attained, with a remarkable cycling stability of 0.009% capacity deterioration for each cycle over more than 500 cycles. Figure 8a depicts the typical charging and discharging voltage trends. At 0.1 C, the cell had a high reversible specific capacity of 1350 mAh g^{-1} (reached full theoretical capacity in 10 h). The rise in polarization that followed the increase in the charging/discharging rate (Fig. 8a) demonstrates the high efficiency of the electrode material's kinetics. At varying current densities of 0.1, 0.2, 0.5, 1, and 2 C, reversible specific capacities were 1350, 1200, 1050,

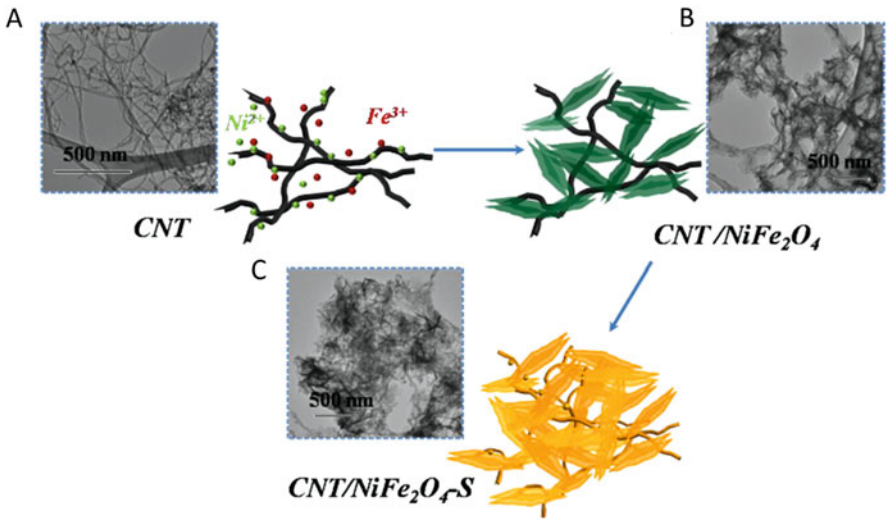

Scheme 5 Schematic of the preparation process for C-HPCM/S composites. (Reproduced with permission from Ref. [59].Copyright © 2015, American Chemical Society)

900, and 700 mAh g^{-1}, respectively. Fig. 8b depicts the battery's electrochemical performance over the first 100 cycles. The reversible capacity of the Li-S battery maintained at 1350 mAh g^{-1} after a minor capacity degradation during the first three cycles at 0.1 C and thereafter demonstrated firm capacity retention through each charging/discharging rate up to 2 C with coulombic efficiency nearly 100% (Fig. 8b). Another cell with a CNT/$NiFe_2O_4$-S hybrid as the working electrode was energized at 0.2 and 0.5 C for 30 cycles before cycling at 1 C for 500 cycles to examine the long-term cyclability of this ternary material (Fig. 8c).

The same cell was cycled at 2 C for another 150 cycles after more than 500 cycles at 1 C. Figure 8d shows a reversible capacity of 690 mAh g^{-1}, with 98.1% retention after 150 cycles, equivalent to a low capacity loss of 0.013% per cycle. The shape of the CNT/$NiFe_2O_4$S material was retained after this prolonged cycling test [59]. It is demonstrated that a three-dimensionally (3D) hierarchical Ni/Ni_3S_2/S cathode with high electronic conductivity and robust polysulfide adsorption capability could mitigate the shuttle effect and provide a desirable electrochemical environment with reduced interfacial resistance, enabling the redox kinetics of anchored polysulfides. As a result, the Ni/Ni_3S_2/S cathode produced with a sulfur dosage of 4.0 mg cm^{-2} exhibited good electrochemical properties. Cheng et al. [60] showed that CeF_3-doped porous carbon nanofibers have good electrochemical characteristics and stable capacity retention, with an initial discharge capacity of 1395.0 mAh g^{-1} and a capacity retention of 901.2 mAh g^{-1} after 500 cycles at 0.5 C. The discharge capacity of the Li-S battery with the electrode slowed right down during the rate capability testing of the battery, from 1284.6 mAh g^{-1} at 0.5 C to 1038.6 mAh g^{-1} at 1 C to 819.3 mAh g^{-1} at 2 C, respectively. When the current density

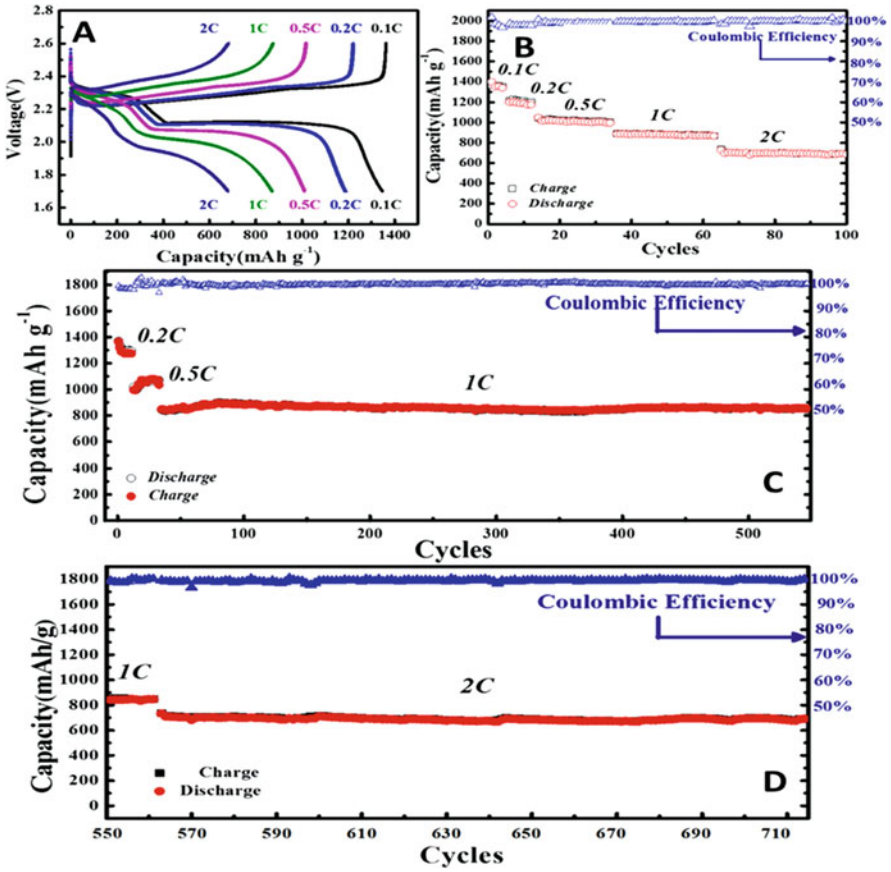

Fig. 8 Electrochemical performance of Li-S batteries using the CNT/$NiFe_2O_4$-S ternary hybrid material as the cathode. (**a**) Representative charging/discharging voltage profiles of the CNT/$NiFe_2O_4$-S ternary hybrid at various C rates from 0.1 to 2 C. Specific capacity values were calculated on the basis of the mass of sulfur. (**b**) Rate performance of CNT/$NiFe_2O_4$-S with corresponding coulombic efficiency. (**c**) Long-term cycling stability test showing unprecedentedly high capacity retention with excellent coulombic efficiency over 500 cycles at 1 C. (**d**) Continued cycling performance of the CNT/$NiFe_2O$-S electrode (the same cell as for C) over 150 cycles at 2 C. (Reproduced with permission from Ref. [59]. Copyright © 2015, American Chemical Society)

recovers to 0.5 C, the battery may still provide a tremendous discharge capacity of 1269.73 mAh g^{-1} with a high retention of 99.2%. In addition, the hierarchically porous carbon composites were an excellent host matrix for sulfur encapsulation, increasing sulfur use and preventing polysulfide dissolution in lithium-sulfur battery electrolytes. Moreover, doping of heteroatom like addition of nitrogen/phosphorus atom or nitrogen-MXene in C-S can play a pivotal role to improve the conductivity by increasing surface area and thereby bring the sulfur close to carbon [61–63]. Another interesting material, namely, sulfurized polyacrylonitrile, with various

heteroatoms like nitrogen, oxygen, and phosphorus, is used as a hybrid material for developing high-performance Li-S battery [64–66]. Since hybrid materials offer high conductivity, more active sites with a sufficient surface area, adsorption capacity, and structural stability, they can be advantageous for high performance Li-S batteries. In addition, the hybrid materials can be useful in other metal-sulfur batteries.

4 Conclusion

In conclusion, hybrid porous materials and nanocomposites are frequently used as electrode materials in various energy sources. Hybrid porous materials with material characteristics are beneficial. These characteristics enable us to overcome issues connected to material restructuring during electrochemical processes, enhance electrochemical performance, and implement them in more demanding energy applications by using them. Natural-source materials are particularly appealing, but their permeability is constrained, and researchers are indeed working to improve them.

Many academic and industrial research groups are actively interested in lithium-ion batteries. They are currently most commonly employed as energy sources in portable electrical gadgets, but as they grow, it is projected that the range of their uses will increase, including electric vehicles, autonomous devices, and much more. Nonetheless, many aspects of the cells necessitate the resolution of numerous issues, and the area thus offers a diverse range of research and development options for such technologies. Progress in it, though, frequently necessitates inter-disciplinary abilities in physics, materials engineering, supercapacitors, chemical engineering, computer simulations, and other fields. Nonetheless, the materials indicated previously offer solutions for the manufacture of high-power lithium-ion cell batteries. Many factors, such as temperature, electrolyte type, and others, can alter the structural development of a Li-ion battery, affecting charging/discharging capacity and cycle stability. Hybrid materials have achieved extensive use in several energy sources as electrode materials. Porous mixed materials with functional properties are beneficial. These materials allow you to overcome issues connected to material structure changes during electrochemical processes, boost electrochemical efficiency, and employ them in more demanding power generation. Natural-source materials attract attention, but their conductivity is restricted, and researchers are still working to improve them. Similar to Li-ion batteries, porous hybrid materials for Li-S batteries have significantly impacted specific capacity and cyclic stability. However, this research is still in the developing phase.

Acknowledgments Dr. Saiful Islam planned the whole outlines of the chapter and being rewritten the chapter after written by Mahbuba Khanom and Md. Al-Amin. Thankful to Dr. S. Mosaddeq Ahmed, Dr. Farzana Khalil, Dr. Mohammad Mahbub Rabbani, Dr. Mohammad Tariqul Islam, and Dr. Md. A. R. Jamil for their contribution.

References

1. J.-G. Wang, K. Xie, B. Wei, Advanced engineering of nanostructured carbons for lithium–sulfur batteries. Nano Energy **15**, 413–444 (2015). https://doi.org/10.1016/j.nanoen.2015.05.006
2. Z. Yang, J. Zhang, M.C.W. Kintner-Meyer, et al., Electrochemical energy storage for green grid. Chem. Rev. **111**, 3577–3613 (2011). https://doi.org/10.1021/cr100290v
3. G.L. Xu, R. Amine, A. Abouimrane, et al., Challenges in developing electrodes, electrolytes, and diagnostics tools to understand and advance sodium-ion batteries. Adv. Energy Mater **8** (2018)
4. P.G. Bruce, S.A. Freunberger, L.J. Hardwick, J.-M. Tarascon, Erratum: Li–O2 and Li–S batteries with high energy storage. Nat. Mater. **11**, 172 (2012). https://doi.org/10.1038/nmat3237
5. S.-Y. Chung, J.T. Bloking, Y.-M. Chiang, Electronically conductive phospho-olivines as lithium storage electrodes. Nat. Mater. **1**, 123–128 (2002). https://doi.org/10.1038/nmat732
6. Y.-N. Xu, S.-Y. Chung, J.T. Bloking, et al., Electronic structure and electrical conductivity of undoped $LiFePO_4$. Electrochem. Solid-State Lett. **7**, A131 (2004). https://doi.org/10.1149/1.1703470
7. X. Gu, S. Zhang, Y. Hou, Graphene-based sulfur composites for energy storage and conversion in Li-S batteries. Chin. J. Chem. **34**, 13–31 (2016). https://doi.org/10.1002/cjoc.201500675
8. Y. Yang, G. Zheng, Y. Cui, Nanostructured sulfur cathodes. Chem. Soc. Rev. **42**, 3018–3032 (2013). https://doi.org/10.1039/C2CS35256G
9. B. Scrosati, J. Garche, Lithium batteries: Status, prospects and future. J. Power Sources **195**, 2419–2430 (2010). https://doi.org/10.1016/j.jpowsour.2009.11.048
10. B. Scrosati, J. Hassoun, Y.-K. Sun, Lithium-ion batteries. A look into the future. Energy Environ. Sci. **4**, 3287–3295 (2011). https://doi.org/10.1039/C1EE01388B
11. M.S. Whittingham, Electrical energy storage and intercalation chemistry. Science **80**(192), 1126–1127 (1976). https://doi.org/10.1126/science.192.4244.1126
12. B. Dunn, H. Kamath, J. Tarascon, For the grid: A battery of choices. Science **80**(334), 928 (2011). https://doi.org/10.1126/science.1212741
13. Y. Yang, G. Zheng, S. Misra, et al., High-capacity micrometer-sized Li2S particles as cathode materials for advanced rechargeable lithium-ion batteries. J. Am. Chem. Soc. **134**, 15387–15394 (2012). https://doi.org/10.1021/ja3052206
14. T. Ould Ely, D. Kamzabek, D. Chakraborty, M.F. Doherty, Lithium–sulfur batteries: State of the art and future directions. ACS Appl. Energy Mater. **1**, 1783–1814 (2018). https://doi.org/10.1021/acsaem.7b00153
15. M.-K. Song, E.J. Cairns, Y. Zhang, Lithium/sulfur batteries with high specific energy: Old challenges and new opportunities. Nanoscale **5**, 2186–2204 (2013). https://doi.org/10.1039/C2NR33044J
16. Z. Lin, C. Liang, Lithium–sulfur batteries: From liquid to solid cells. J. Mater. Chem. A **3**, 936–958 (2015). https://doi.org/10.1039/C4TA04727C
17. J. He, A. Manthiram, A review on the status and challenges of electrocatalysts in lithium-sulfur batteries. Energy Storage Mater. **20**, 55–70 (2019). https://doi.org/10.1016/j.ensm.2019.04.038
18. Q. Pang, X. Liang, C.Y. Kwok, L.F. Nazar, Advances in lithium–sulfur batteries based on multifunctional cathodes and electrolytes. Nat. Energy **1**, 16132 (2016). https://doi.org/10.1038/nenergy.2016.132
19. Y. Sun, D. Wang, Z. Shuai, Indirect-to-direct band gap crossover in few-layer transition metal dichalcogenides: A theoretical prediction. J. Phys. Chem. C **120**, 21866–21870 (2016). https://doi.org/10.1021/acs.jpcc.6b08748
20. J. Wei, Z. Sun, W. Luo, et al., New insight into the synthesis of large-pore ordered mesoporous materials. J. Am. Chem. Soc. **139**, 1706–1713 (2017). https://doi.org/10.1021/jacs.6b11411

21. C. Tan, X. Cao, X.-J. Wu, et al., Recent advances in ultrathin two-dimensional nanomaterials. Chem. Rev. **117**, 6225–6331 (2017). https://doi.org/10.1021/acs.chemrev.6b00558
22. X. Wu, Y. Xiang, Q. Peng, et al., Green-low-cost rechargeable aqueous zinc-ion batteries using hollow porous spinel $ZnMn_2O_4$ as the cathode material. J. Mater. Chem. A **5**, 17990–17997 (2017). https://doi.org/10.1039/C7TA00100B
23. J. Zhang, C.M. Li, Nanoporous metals: fabrication strategies and advanced electrochemical applications in catalysis, sensing and energy systems. Chem. Soc. Rev. **41**, 7016–7031 (2012). https://doi.org/10.1039/C2CS35210A
24. S. Liu, F. Wang, R. Dong, et al., Dual-template synthesis of 2D mesoporous polypyrrole nanosheets with controlled pore size. Adv. Mater. **28**, 8365–8370 (2016). https://doi.org/10.1002/adma.201603036
25. S. Liu, F. Wang, R. Dong, et al., Soft-template construction of 3D macroporous polypyrrole scaffolds. Small **13**, 1604099 (2017). https://doi.org/10.1002/smll.201604099
26. Y. Lei, S. Yang, M. Wu, G. Wilde, Surface patterning using templates: Concept, properties and device applications. Chem. Soc. Rev. **40**, 1247–1258 (2011). https://doi.org/10.1039/B924854B
27. A. Stein, B.E. Wilson, S.G. Rudisill, Design and functionality of colloidal-crystal-templated materials—Chemical applications of inverse opals. Chem. Soc. Rev. **42**, 2763–2803 (2013). https://doi.org/10.1039/C2CS35317B
28. L. Zhang, K. Zhao, W. Xu, et al., Integrated SnO_2 nanorod array with polypyrrole coverage for high-rate and long-life lithium batteries. Phys. Chem. Chem. Phys. **17**, 7619–7623 (2015). https://doi.org/10.1039/C5CP00150A
29. U.G.K. Wegst, H. Bai, E. Saiz, et al., Bioinspired structural materials. Nat. Mater. **14**, 23–36 (2015). https://doi.org/10.1038/nmat4089
30. F. Mammeri, B.E. Le, L. Rozes, C. Sanchez, Mechanical properties of hybrid organic–inorganic materials. J. Mater. Chem. **15**, 3787–3811 (2005). https://doi.org/10.1039/B507309J
31. G. Kickelbick, Hybrid materials—Past, present and future. Hybrid Mater **1**, 39–51 (2014). https://doi.org/10.2478/hyma-2014-0001
32. L. Zhang, L. Chen, X. Zhou, Z. Liu, Towards high-voltage aqueous metal-ion batteries beyond 1.5 V: The zinc/zinc hexacyanoferrate system. Adv. Energy Mater. **5**, 1–5 (2015). https://doi.org/10.1002/aenm.201400930
33. T. Krasia-Christoforou, Organic–inorganic polymer hybrids: Synthetic strategies and applications BT, in *Hybrid and hierarchical composite materials*, ed. by C.-S. Kim, C. Randow, T. Sano, (Springer, Cham, 2015), pp. 11–63
34. Y.-P. Zhu, Z.-Y. Yuan, History and classification of non-siliceous hybrid materials BT, in *Mesoporous organic-inorganic non-siliceous hybrid materials: basic principles and promising multifunctionality*, ed. by Y.-P. Zhu, Z.-Y. Yuan, (Springer, Berlin, 2015), pp. 7–23
35. P. Gómez-Romero, C. Sanchez, Hybrid materials. Functional properties. From Maya Blue to 21st century materials. New J. Chem. **29**, 57–58 (2005). https://doi.org/10.1039/B416075B
36. T.S. Haddad, J.D. Lichtenhan, Hybrid organic−inorganic thermoplastics: Styryl-based polyhedral oligomeric silsesquioxane polymers. Macromolecules **29**, 7302–7304 (1996). https://doi.org/10.1021/ma960609d
37. J.H. Noh, S.H. Im, J.H. Heo, et al., Chemical Management for Colorful, Efficient, and Stable Inorganic–Organic Hybrid Nanostructured Solar Cells. Nano Lett. **13**, 1764–1769 (2013). https://doi.org/10.1021/nl400349b
38. A.O. Polyakov, A.H. Arkenbout, J. Baas, et al., Coexisting ferromagnetic and ferroelectric order in a $CuCl_4$-based organic–inorganic hybrid. Chem. Mater. **24**, 133–139 (2012). https://doi.org/10.1021/cm2023696
39. T.A. Saleh, Chapter 5—Hybrid materials: Fundamentals and classifications, in *Plastics design library*, ed. by T.A.B.T.-P.H.M. Saleh, (William Andrew Publishing, 2021), pp. 147–176
40. L. Peng, Y. Zhu, H. Li, G. Yu, Chemically integrated inorganic-graphene two-dimensional hybrid materials for flexible energy storage devices. Small **12**, 6183–6199 (2016). https://doi.org/10.1002/smll.201602109

41. P.T. Yin, S. Shah, M. Chhowalla, K.-B. Lee, Design, synthesis, and characterization of graphene–nanoparticle hybrid materials for bioapplications. Chem. Rev. **115**, 2483–2531 (2015). https://doi.org/10.1021/cr500537t
42. M. Armand, J.M. Tarascon, Building better batteries. Nature **451**, 652–657 (2008). https://doi.org/10.1038/451652a
43. J.S. Cho, J.-K. Lee, Y.C. Kang, Graphitic carbon-coated FeSe2 hollow nanosphere-decorated reduced graphene oxide hybrid nanofibers as an efficient anode material for sodium ion batteries. Sci. Rep. **6**, 23699 (2016). https://doi.org/10.1038/srep23699
44. C. Ling, F. Mizuno, Boron-doped graphene as a promising anode for Na-ion batteries. Phys. Chem. Chem. Phys. **16**, 10419–10424 (2014). https://doi.org/10.1039/C4CP01045K
45. L. Li, L. Wang, X. Zhang, et al., Structural and electrochemical study of hierarchical LiNi1/3Co1/3Mn1/3O2 cathode material for lithium-ion batteries. ACS Appl. Mater. Interfaces **7**, 21939–21947 (2015). https://doi.org/10.1021/acsami.5b06584
46. Y. Liu, Y. Qiao, X. Lou, et al., Hollow K0.27MnO2 nanospheres as cathode for high-performance aqueous sodium ion batteries. ACS Appl. Mater. Interfaces **8**, 14564–14571 (2016). https://doi.org/10.1021/acsami.6b03089
47. H. Hu, J. Zhang, B. Guan, X.W. Lou (David), Unusual formation of CoSe@carbon nanoboxes, which have an inhomogeneous shell, for efficient lithium storage. Angew. Chemie Int. Ed. **55**, 9514–9518 (2016). https://doi.org/10.1002/anie.201603852
48. Y. Li, Y. Bai, C. Wu, et al., Three-dimensional fusiform hierarchical micro/nano Li1.2Ni0.2Mn0.6O2 with a preferred orientation (110) plane as a high energy cathode material for lithium-ion batteries. J. Mater. Chem. A **4**, 5942–5951 (2016). https://doi.org/10.1039/C6TA00460A
49. T.D. Thanh, N.D. Chuong, H. Van Hien, et al., Recent advances in two-dimensional transition metal dichalcogenides-graphene heterostructured materials for electrochemical applications. Prog. Mater. Sci. **96**, 51–85 (2018). https://doi.org/10.1016/j.pmatsci.2018.03.007
50. L. Suo, O. Borodin, W. Sun, et al., Advanced high-voltage aqueous lithium-ion battery enabled by "water-in-bisalt" electrolyte. Angew. Chem. **128**, 7252–7257 (2016). https://doi.org/10.1002/ange.201602397
51. W. Wang, Q. Sa, J. Chen, et al., Porous TiO_2/C nanocomposite shells as a high-performance anode material for lithium-ion batteries. ACS Appl. Mater. Interfaces **5**, 6478–6483 (2013). https://doi.org/10.1021/am402350n
52. X. Zuo, Y. Wen, Y. Qiu, et al., Rational design and mechanical understanding of three-dimensional macro-/mesoporous silicon lithium-ion battery anodes with a tunable pore size and wall thickness. ACS Appl. Mater. Interfaces **12**, 43785–43797 (2020). https://doi.org/10.1021/acsami.0c12747
53. B.T. Heligman, K.P. Scanlan, A. Manthiram, Nanostructured composite foils produced via accumulative roll bonding as lithium-ion battery anodes. ACS Appl. Mater. Interfaces **14**, 11408–11414 (2022). https://doi.org/10.1021/acsami.1c23529
54. H. Xie, Y. Qie, I. Muhammad, Q. Sun, B4 cluster-based 3D porous topological metal as an anode material for both Li- and Na-ion batteries with a superhigh capacity. J. Phys. Chem. Lett. **12**, 1548–1553 (2021). https://doi.org/10.1021/acs.jpclett.0c03709
55. A.K. Boehm, S. Husmann, M. Besch, et al., Porous mixed-metal oxide Li-ion battery electrodes by shear-induced co-assembly of precursors and tailored polymer particles. ACS Appl. Mater. Interfaces **13**, 61166–61179 (2021). https://doi.org/10.1021/acsami.1c19027
56. J. Hassoun, K.-S. Lee, Y.-K. Sun, B. Scrosati, An advanced lithium ion battery based on high performance electrode materials. J. Am. Chem. Soc. **133**, 3139–3143 (2011). https://doi.org/10.1021/ja110522x
57. M.C. Lin, M. Gong, B. Lu, et al., An ultrafast rechargeable aluminium-ion battery. Nature **520**, 325–328 (2015). https://doi.org/10.1038/nature14340
58. Z. Li, L. Yin, Nitrogen-doped MOF-derived micropores carbon as immobilizer for small sulfur molecules as a cathode for lithium sulfur batteries with excellent electrochemical performance. ACS Appl. Mater. Interfaces **7**, 4029–4038 (2015). https://doi.org/10.1021/am507660y

59. Q. Fan, W. Liu, Z. Weng, et al., Ternary hybrid material for high-performance lithium–sulfur battery. J. Am. Chem. Soc. **137**, 12946–12953 (2015). https://doi.org/10.1021/jacs.5b07071
60. N. Deng, J. Ju, J. Yan, et al., CeF_3-doped porous carbon nanofibers as sulfur immobilizers in cathode material for high-performance lithium–sulfur batteries. ACS Appl. Mater. Interfaces **10**, 12626–12638 (2018). https://doi.org/10.1021/acsami.7b19746
61. H. Wu, L. Xia, J. Ren, et al., A high-efficiency N/P co-doped graphene/CNT@porous carbon hybrid matrix as a cathode host for high performance lithium–sulfur batteries. J. Mater. Chem. A **5**, 20458–20472 (2017). https://doi.org/10.1039/C7TA06504C
62. Q. Du, A. Fox, M. Benedikter, et al., High-performance cathode materials for lithium–sulfur batteries based on sulfurated poly(norbornadiene) and sulfurated poly(dicyclopentadiene). ACS Appl. Energy Mater. **5**, 7642–7650 (2022). https://doi.org/10.1021/acsaem.2c01113
63. W. Bao, L. Liu, C. Wang, et al., Facile synthesis of crumpled nitrogen-doped MXene nanosheets as a new sulfur host for lithium–sulfur batteries. Adv. Energy Mater. **8**, 1702485 (2018). https://doi.org/10.1002/aenm.201702485
64. Y. Liu, A.K. Haridas, K.-K. Cho, et al., Highly ordered mesoporous sulfurized polyacrylonitrile cathode material for high-rate lithium sulfur batteries. J. Phys. Chem. C **121**, 26172–26179 (2017). https://doi.org/10.1021/acs.jpcc.7b06625
65. T. Lebherz, M. Frey, A. Hintennach, M.R. Buchmeiser, Influence of morphology of monolithic sulfur–poly(acrylonitrile) composites used as cathode materials in lithium–sulfur batteries on electrochemical performance. RSC Adv. **9**, 7181–7188 (2019). https://doi.org/10.1039/C8RA09976F
66. J. Lee, J. Oh, Y. Jeon, Y. Piao, Multi-heteroatom-doped hollow carbon attached on graphene using $LiFePO_4$ nanoparticles as hard templates for high-performance lithium–sulfur batteries. ACS Appl. Mater. Interfaces **10**, 26485–26493 (2018). https://doi.org/10.1021/acsami.8b00925

Electrode Materials for High Energy Density Li-Ion

Satish Teotia and Anisha Chaudhary

1 Introduction

Lithium-ion batteries (LIBs) are the most advanced power source available for today's consumer electronics. LIBs are known for their high energy density, high specific capacity, and long cycle life [1]. These traits aided a significant advancement in portable electronics technology and the widespread adoption of information technology gadgets. Their growing use in hybrid electric vehicles (HEV) and power systems with high storage capacity makes them a possible solution to environmental and resource conservation problems. LIB research began in the early 1980s, and after its commercial launch (early 1990s), LIBs have made substantial progress [2].

The lithium–sulphur battery is a lithium-ion battery that is still being developed. Its advantage is its high energy density, which is several times higher than standard LIBs, having a theoretical capacity of 2600 Wh/kg and a 2 V open-circuit voltage. The real energy density, however, is far lower than the theoretical amount.

LIBs are widely employed in tiny electronic devices. The key components of these batteries are a cathode and a lithium-based anode immersed in an electrolyte solution separated by a selective membrane. The conductivity of the electrodes determines the final efficiency of LIBs. As a result, new hybrid materials with porous architecture are search and investigated to improve the electrochemical properties of electrodes through the design and application of a variety of innovative materials.

Many applications are increasing the demand for LIBs, which can store more energy in small volume so that better rate performance and higher energy density can be achieved in portable energy storage system. Similarly, in case of HEVs in

S. Teotia (✉)
Department of Physics, NIET, NIMS University Rajasthan, Jaipur, Rajasthan, India

A. Chaudhary
Department of Physics and Astrophysics, University of Delhi, New Delhi, India

F. I. Ezema et al. (eds.), *Chemically Deposited Metal Chalcogenide-based Carbon Composites for Versatile Applications*, https://doi.org/10.1007/978-3-031-23401-9_8

which higher energy is needed to accelerate a vehicle, the requirements for high energy density and rate performance becomes especially critical. Shorter recharge periods of vehicle for commercial applications would boost customer adoption of electric vehicle and HEV technology [3]. These requirements are also necessary for energy storage systems that store charges by using seasonal and intermittent renewable sources of energy like solar and wind energy.

However, the LIB's success in these applications is limited by several factors, including (1) insufficient power density, (2) difference between actually obtained capacity and theoretical capacity, (3) high polarisation losses during cycling that result in insufficient energy efficiency, (4) ageing that implies that capacity losses and sometimes battery failure occur with increasing the rate and number of cycling, and (5) solid electrolyte interface (SEI), which reduces the diffusion of Li-ions into the electrode surface when its thickness increased. The intrinsic features of electrode materials such as energy density, theoretical capacity, cell potential, and so forth also influence LIB performance. Furthermore, types of interfaces as well as their stability between the electrodes and the electrolyte also determine the cycle life and longevity.

As an alternate, supercapacitors possess high power density, which means they can deliver charges instantaneously at a quicker rate compared to traditional LIBs and are a frequent solution for high power requirements. They can store charges over the electrode surface, which enables them for quick delivery rate for short-term supply, and thus, they have low energy density [4]. A battery, on the other hand, holds a charge in the bulk and provides energy for a long time resulting in higher energy density. Unfortunately, Li-ion diffusion through the electrode interior surface limits the rate of charge transfer. Both capacitors and batteries have benefited from recent research. Supercapacitors with high energy densities are now being used to develop a combined redox charge storage (pseudo-capacitance) with double-layer storage. On the other hand, by properly designing the electrodes, the power density of LIBs can be enhanced. However, lithium-ion diffusion via electrode surface can limit the rate capability.

According to the relationship given below, the square of the typical diffusion length (l) determines how long it takes for lithium ions to diffuse through an electrode material (τ).

$$\tau \sim \left(\mathrm{l}^2/D\right) \tag{1}$$

where D is the coefficient of diffusion. As a result, techniques like doping with better Li-ion conductors or employing porous nanostructured electrode materials can be used to improve the Li-ion diffusion and shorten the diffusion length [5]. On decrease size to nanoscale level and employing porous architecture, the diffusion length (l) decreases, which significantly decrease the diffusion time (τ). It is usual practise to reduce the diffusion length in order to boost the rate performance of typical LIB materials. Many scholars have been paying close attention to this in recent years. In LIB applications, porous electrode materials have a lot of

potential for obtaining critical dimensions at the nanoscale scale. Thus, using porous electrode materials is one of the most alluring ways to significantly enhance the electrochemical features of LIBs, such as capacity, efficiency, stability in terms of cycle life, and importantly safety.

Furthermore, the majority of electrochemical reactions occur at the intersection of two or more phases. As a result, just as in any surface reaction, the reaction area is critical in determining the effectiveness of an electrochemical process. To enhance the available area for reaction in an electrochemical cell, a number of approaches are used such as multiple electrodes being alternately stacked, bipolar electrodes being employed, and the reaction surface occasionally changed by etching or coating with materials having a high surface area. A porous electrode is another effective approach to enhance the contact area between the electrode surface and the electrolyte so that the full electrode area can be made available for reaction.

2 Porous Electrode

A porous electrode is described as a composite material with interconnected void space that occupies a major fraction of the volume and differs from planar electrodes in terms of electrochemical behaviour. It is defined by a solid matrix with a suitably large fraction of vacancy and geometric dimensions that are tiny in relation to the electrode dimensions. Most of the holes that make up the void in an efficiently produced electrode are interconnected, allowing the electrolyte to flow freely. Thus, huge available surface area of the porous electrode, enhanced contact area between the electrolyte and electrode and more room to store dissolution products are some of the features of a porous electrode, which helps considerably to increases the charge-transfer process. The high specific surface area makes it possible to run a high current without experiencing a significant overpotential and maintain a high current since it influences the reduction of sensitivity to passivation [6]. The current dispersion from the electrode's outer surface to the interior is a distinguishing feature of porous electrodes. Because the lengths of the electrolyte paths vary, the current density near the electrode's outer surface and the current density inside the electrode differ significantly. The amount of current flowing between an electrode's surface and inside is determined by comparing the electrolyte resistance, R_e, to the polarisation resistance, R_p; porous electrodes provide a number of advantages, which are briefly described below:

- Because porous materials have a wide surface area, charge transmission at interfaces between the electrode and electrolyte is facilitated.
- Ion diffusion path lengths can be decreased by making the walls of the active material surrounding the pores exceedingly thin (nanometers to tens of nanometers).
- In some situations, the active phase can be held together with little or no binder.

- The vacant spaces between active material particles can aid to limit active material growth during cycling.
- Nanosized porous materials can inhibit irreversible phase shifts that take place in microcrystalline anodes. As a result, such particles can better accept volume variations caused by cycling-induced first-order phase variations. Composite electrodes with pores and a stabilising structure for active parts with limited cycle lifetimes can also be made (e.g. large volume changes disintegrate some components during cycles).

Furthermore, if the active material has a poor intrinsic conductivity, a second conductive phase may be added to porous composites to enhance electron transport and, consequently, the rate performance of the LIBs. The use of a conductive material reduces or otherwise eliminates the need for a conductive carbon additive at the end electrode. The use of porous electrodes allows for improved control of reaction distribution, active species transport, and heat distribution, as well as increased reaction efficiency and selectivity. A thorough understanding of various complicated mechanisms that underpin a porous electrode's performance is required for effective design. Several mathematical models and experimental research aid in the identification of attributes such as number of pore fraction, pore size and its distribution, electrolyte conductivity and viscosity and solid core characteristics.

3 Working of Lithium-Ion Battery

Nearly, all wearable digital gadgets are powered by lithium-ion batteries, among the most effective energy storage technologies. These batteries are used in a variety of industrial, military and consumer products as well as health care and industrial equipment. Cell capacities, on the other hand, have slowly improved over the last two decades of development, but the fundamental components, such as cathode and anode materials, have remained relatively unchanged.

The anode and cathode are the two electrodes that make up a battery. Both the electrodes are dipped in an electrolyte and are separated by a thin membrane. The positive terminal of the battery is the cathode, whereas the negative terminal is the anode. A lithium-ion battery's cathode is made up of lithium compounds, mostly in crystal structure of cathode materials such cobalt, nickel and manganese that combine to form a multi-metal oxide material, which is then combined with lithium. Lithium cobalt oxide ($LiCoO_2$) is most commonly used in LIBs; other materials used as cathode materials include lithium manganese oxide ($LiMn_2O_4$), lithium iron phosphate ($LiFePO_4$) and NMC cathode ($LiNi_xMn_yCo_{1-x}O_2$) containing three transition metal ions, etc. The anode's main component is graphite. Natural graphite is extracted from the earth, whereas artificial graphite is created synthetically. Both types of graphite are severely processed and then coated onto copper foil to act as anodes. Both electrodes are dipped in an organic electrolyte (e.g. $LiPF_6$, $LiBF_4$ or $LiClO_4$, etc.) [7]. In general battery setup, lithium ions tend to travel from the

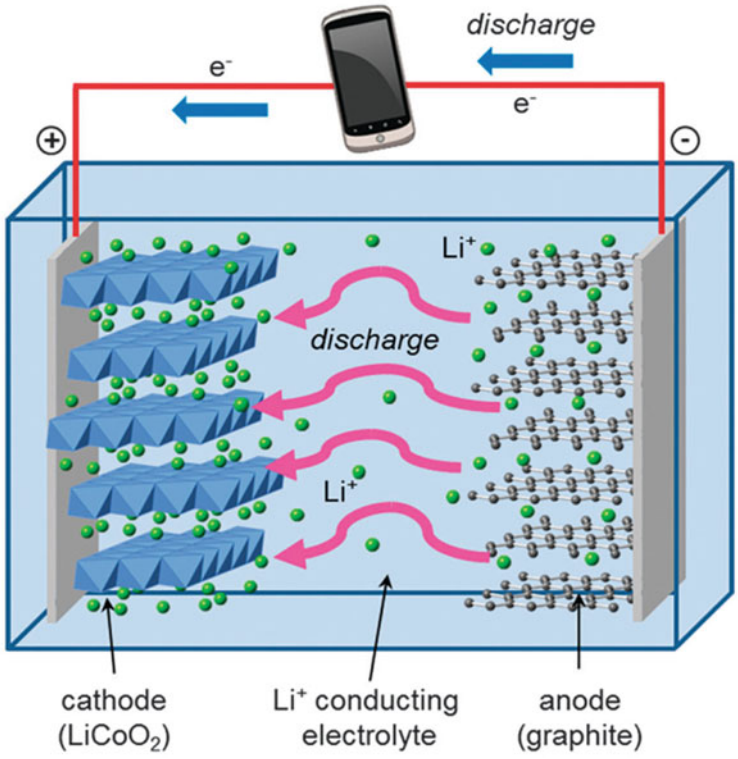

Fig. 1 First-generation rechargeable lithium-ion cell schematic diagram. Lithium ions travel via the electrolyte to the negative electrode during charging, whereas electrons travel from the external circuit. The directions are reversed during discharge, producing useable power that the gadget may utilise. Reproduced with permission from the Royal Society of Chemistry [8]

cathode to the anode, or from the positive terminal of the battery electrode to the negative terminal of the battery electrode when the battery is connected to an electric source. This is referred to as battery charging. The migration of lithium ions from the anode back to the cathode, meaning from the negative electrode to positive electrode, is reversed during the discharge phase of the battery, and the electrical energy is supplied to the attached load (Fig. 1). During charging, the movement of lithium ions and electrons reversed when an external voltage is being applied. Thus, battery is being charged, and electrical energy is converted to chemical energy by the reverse movement of lithium ions and electrons.

Lithium-sulphur (Li-S) batteries, which are distinguished by their high energy densities, typically consist of a sulphur cathode and a lithium-based anode that are submerged in a nonaqueous electrolyte and are separated by a separator. The separator allows diffusion of Li-ions in addition to preventing the short circuits of the battery. Despite being in the early phases of development and commercialisation, systems utilising Li-S batteries have the potential to deliver higher, safer amounts

of energy at a substantially lower cost. In comparison to Li-ion batteries, Li-S batteries require a complicated multistep process to operate. Sulphur creates the initial discharge product Li_2S_8, which then is disproportionate to form lower-order polysulfides, eventually resulting in Li_2S. During the charging of the battery, the process is reversed. All components of lithium-sulphur batteries (e.g. electrode materials, electrolytes or solvent, binder and additives to increase conducting) have a significant impact on the final battery performance. The cathode, on the other hand, transfers the active sulphur molecules, making it the most important part of Li-S batteries. The porous design of the sulphur substrate should be optimised to maximise sulphur usage.

4 Critical Issues that Limit the Performance of LIBs

LIBs have transformed the market for wearable digital gadgets, and currently, they are the focus of intense research for stationary storage and transmission of renewable energy like solar and wind. But some of the problems that prevent the LIB from being successful in these applications include insufficient power density, difference between practical and theoretical capacities, significant polarisation losses during charging and discharging that lead to poor energy efficiency and ageing, which leads to battery failure after repeated cycling during long run. Performances of LIBs in terms of capacity, energy density or battery efficiency are dependent on the inherent characteristics and architecture of the electrode materials. The design of the electrode's architecture affects the durability, cycle life and stability of the battery. The LIB's performance is constrained by a number of serious problems with active materials, which are simply summarised below.

4.1 Microstructure Change

When an electrode undergoes cycling, the form, size, distribution and connection of each electrode phase might vary, which could cause unintended phase segregation or redistribution, progressive degradation of capacity and insulation around active materials. Battery capacities have reportedly been increased by adjusting the shape or architecture of electrode material, thereby developing electrodes with porous structure and substantial surface area. For instance, mesoporous V_2O_5 aerogels had improved rate capability and specific capacity that were far more better than their nonporous form [9]. Consequently, high performance LIBs may be solved by porous electrodes.

4.2 Volume Expansion

Volume expansion and contraction due to volume changes brought on by lithiation and de-lithiation of Li^{-}ions inside the graphite architecture may lead to diffusion-induced tensions and a poor adhesion between the particles as well as between the electrode material and copper foil used as current collector. Because of this, few carbon particles that are active may get dissociated from the conducting electrode matrix and lose their functionality during cycling. It therefore causes rate performances and eventual capacity decline. For instance, $Li_{4.4}Si$ has a molar volume that is around four times more than Si [10]. The high cyclic volume shift that occurs when Li is alloyed with or removed from Si during cycling pulverises the electrode, causing capacity loss and poor rate performance. Superior cyclability can be achieved because of the hierarchical organisation, which keeps the solid-electrolyte interface (SEI) stable and spatially constrained. The microstructures also reduce contact area in between the electrode and electrolyte, which result in excellent volumetric capacitance and battery efficiency.

4.3 Phase Transformation

During the cycling of LIBs, the electrode materials undergo chemical reaction, which may alter their structure and result in the formation of insulating compounds. The flexibility for inserting and extracting Li-ions is reduced by these new phases. As a result, the LIB's capacity retention has decreased. For instance, $LiMnO_2$ experiences a phase transition during cycling, going from having a cubic structure to having a tetragonal structure [11]. However, the cathode of high-performance LIBs can be made of a nanoporous electrode, for example, $LiMn_2O_4$ nanowires (diameters <10 nm and lengths of several micrometres) in the form of very thin spinel. With strong capacity retention, the rapid structural transition to the cubic and tetragonal phases in a wide range of compositions was seen. The structural or phase shift in electrodes can be seen at increased cycling potential, which is responsible for the significant irreversible capacity loss.

4.4 Insulating Phase Formation

In passive electrode materials, the volume percentage of the phase is higher when an insulated layer develops at the electrode surface. Electrode reactions are slowed down by this insulating layer. The by-products of insulating processes may adhere to the surface of an active electrode, diminish the effectiveness of the protective layer and hinder the movement of electrochemically active electrode materials towards the active regions. The electrolyte degradation and subsequent creation

of an insulating layer on the electrode surface, which increases the resistance and uses up recyclable Li-ions, is one possible explanation of the above mechanism. The changes in lattice structure of the electrode are, however, rarely impacted by the degradation mechanisms. Researchers have used a number of techniques to reduce the likelihood of insulating phase production and also limit its impact on the performance of the electrode. These techniques include the inclusion of different stabilisers, strong electrolyte systems, and heat treatment.

5 Porous Hybrid Electrode Materials

Porous materials were first used in technical applications in the early twentieth century. The size of the pore in a porous materials determine the different categories of porous structures, as per the International Union of Pure and Applied Chemistry (IUPAC): there are three categories of porous structures, that is, microporous (pore size 2 nm), mesoporous (pore size 2–50 nm) and macroporous (pore size >50 nm) (Fig. 2) [12].

Numerous applications have used porous materials including vehicle body constructions, optical systems, biomedical implant manufacturing, water purification, biosensors, energy storage devices and aerospace. A nanoporous material should have special combination of different properties, such as lightweight with high effective surface area, high electrical conductivity, good thermal stability and efficient interconnected network. Energy conversion and its storage, sensing and gas separation can all benefit from porous materials [6]. Porous electrodes have several advantages, including the following:

1. Porous structure possesses relatively high surface area.
2. It allows electrolyte access to the electrode surface.

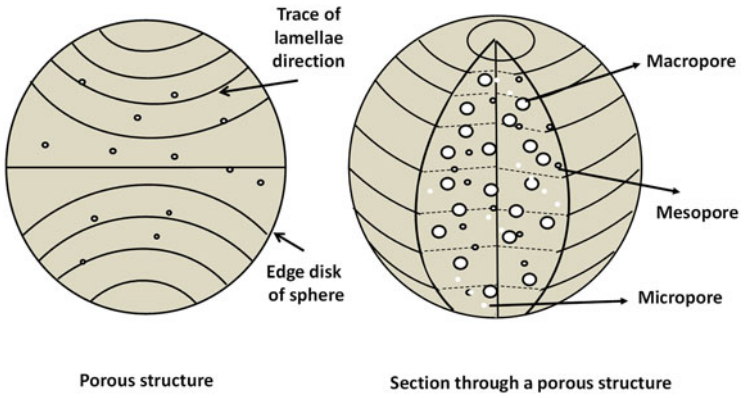

Fig. 2 Schematic illustration of the porous structure

3. It promotes high ionic movement depending upon the pore size, and it increases the Li ion diffusion rate and decreases the Li-ion diffusion length.
4. It allows whole area utilisation of electrode materials, resulting in increased energy density and capacity.
5. Porous structure promotes electrocatalytic activity due to improved ionic transport between the electrode and electrolyte filled in the nanosized pores.
6. Porous structure reduces or eliminates the requirement for a binder to hold the active components together.

In recent years, researchers have paid more attention to various porous materials as electrode for Li-ion batteries.

5.1 Porous Carbon

Porous carbon compounds are currently one of the most widely used electrode materials, appearing in capacitors and LIBs. They are preferred in applications where high power is needed to improve performance. Porous carbon electrode has advantages of membrane form in which there is no need of using a binder to support the electrode materials. It also permits high electrical conduction due the interconnected network of carbon particles. Deterioration in the connection between carbon particles and active materials, for example, could result in capacity fading, higher electrode polarisation and a slower rate of cycling.

Sony was the first to commercialise carbon-based anode materials in 1991. The energy density, specific capacity and cycle life along with cost of lithium insertion compounds have all improved dramatically since that time. Most typical LIBs still use graphite anode (theoretical capacity 372 $mAhg^{-1}$) [13]. The high surface areas and porous architectures make the porous carbon a desirable electrode materials for LIBs having diverse range of pore sizes such as microporous, mesoporous and macroporous. These materials have desirable properties such as effective Li-ion diffusion pathways because there are many active sites for Li storage, interconnected porous networks, which permit high electrical conductivity and avoid mechanical stresses over the electrode during Li intercalation and deintercalation. Porous carbons, in general, have high irreversible capacity and low volumetric energy density, despite typically high capacity. However, in order to improve overall performance, it must be hybridised with other high performance electrode materials (such as alloy or metal oxides).

5.2 Porous Carbon with Other Anode Materials (Si or Sn)

Porous carbon can be used in combination with other anode materials (Si or Sn or their oxides) for LIBs. When volume expansion happens during cycling as

a result of Li-ion intercalation and deintercalation, these high-capacity electrode materials benefit from the porous architecture. The porous electrode acts as a buffer against volume expansion and guards against electrode degradation. Carbon matrix is typically used to disperse these anode materials, resulting in excellent electrical conductivity and capacity.

5.2.1 Si/Porous Carbon Anode

Silicon (Si) is considered as efficient electrode materials for LIBs due to its high theoretical capacity (4100 mAh/g) and ease of availability. But the problem of volume expansion associated with silicon particles during cycling limits its effectiveness as anode materials. The silicon will be ground up, and electronic contact with other Si particles gets impaired as a result of the huge volume expansion, which will also lower the contact area with the current collector and decrease battery efficiency, and may result in sudden cell breakdown. In order to improve electrochemical performance of the silicon, coating of carbon-based porous materials is used, which not only increases the electrical conductivity but also stabilises the electrode against the volume expansion of the silicon particles. For instant, hybrid electrode of nanoporous silicon, graphite and pyrolyzed carbon is produced and studied up to the 120th cycle. It shows a reversible capacity of roughly 700 $mAhg^{-1}$ with minimal loss of capacity after long cycling [14]. Mesoporous and microporous carbon is studied to scatter Si nanoparticles, which demonstrated good capacity (450 $mAhg^{-1}$) after 50 cycles.[15] furthermore, to improve the electrochemical performance of the LIBs silicon coated on graphene surface, silicon grown on carbon microsphere, core shell silicon carbon porous spheres have been used to decrease the volume expansion/shrinkage problem, improving electronic transport properties and cycle life of the electrode. New preparation methods and techniques are adopted to combine superior properties and overcome negative aspects of electrode materials in order to obtain synergistic effects to enhance LIB performance, but high-capacity fading and electrolyte breakdown, along with instability related to SEI, are some of the limitations preventing these electrodes from being used.

5.2.2 Sn/Porous Carbon Anode

Tin (Sn) and its oxides (SnO, SnO_2) are a family of excellent high capacity anode materials that have received extensive study. It possesses theoretical capacity of 991 mAh g^{-1} and volumetric capacity of 2020 $mAhcm^{-3}$ comparable to silicon (2400 $mAhcm^{-3}$). Similar to silicon, tin too experiences the enormous volume shift that takes place during electrochemical cycling. A significant loss of capacity results from the large volumetric shift (about 300%), which causes the loss of electrical contact and failure of LIBs. Porous carbon and tin composites (Si/C) performed excellently electrochemically, just like porous Si/C electrodes. In general, high-

capacity materials (Sn, Si, Ge, etc.) face problem of capacity deterioration after repeated cycling, limiting their use as LIB electrodes in high energy demanding applications like in automobiles and grid systems. Furthermore, most high-capacity materials, such as C, Si and Sn, have a working potential of 0–0.5 V as compared to Li/Li^+ when used as anodes in LIBs. The electrolyte is prone to decomposition at such low working voltages, which result in formation of unstable SEI. A great deal of work has been put into constructing a hollow structure to enclose the components, an inert supporting material matrix and coating surface with conducting carbon materials such as carbon nanotube (CNT) as ways to solve this problem.

5.3 Metal Oxides

Metal oxides are among the most efficient alternative for replacing graphite anodes in long-term high energy, high-power requirements, such as HEVs, EVs and grid systems. Metal oxides possess excellent reversible capacities (500–1000 $mAhg^{-1}$) and show diverse chemical and physical characteristics, which make them widely explored prospective anode materials for rechargeable LIBs [16]. Metal oxides are the most diverse of these anode materials and have been extensively investigated in recent years. Many metal oxides outperform graphite in terms of capacity, cost and ease of synthesis. Based on their reaction processes, three categories can be used to demonstrate metal oxide-based anodes: (1) alloying reaction mechanism involving reaction between Li and anode materials, (2) insertion/extraction reaction mechanism involving the intercalation/deintercalation of Li ions into and out of the crystal structure of transition metal oxide, and (3) conversion-type reaction mechanism involving the synthesis and deterioration of lithium oxide (Li_2O) in conjunction with metal reduction and oxidation.

5.4 Hierarchical Porosity in Electrode Materials

A pore size hierarchy allows for greater electrolyte permeability through a porous electrode. Ion diffusion routes via the electrode are further reduced by secondary mesopores within macropore walls to improve the region of the interfacial layer between the electrolyte and the electrode. Additionally, they permit the housing inside the constraints of a porous matrix of active electrode material, an electrically conducting component, or other stabilisers additive while still permitting the passage of the electrolyte. In general, macropores can be added to mesoporous materials (e.g. through etching) to create hybrid hierarchical porous materials, or mesopores can be added to macroporous materials (e.g. dual templating). The distribution of pores in the porous medium can be random or organised. If mass transportation is more critical and organised, the ideal system has a network of interconnected macropores and extra mesopores implanted further into membranes.

This is typically the case when solvents with high viscosity or electrolytes with poor diffusion coefficient ions are used (ionic or high molecular weight solvent). Diffusion of electrolytes into and out of the electrode material is facilitated by an organised, interconnected macropore system with reduced tortuosity. If mass transmission is less significant, the macropores within mesoporous material can be distributed randomly, but they often only function like internal stores that provide access of electrolyte to the neighbouring mesopores. If one takes into account morphological mesoporosity among nanostructures as being one of the size scales, many of the structures as discussed earlier have porosity on several length scales. Moreover, with more command on porous structure architecture, it is conceivable to build hierarchical porosity by utilising many hard/soft templates during synthesis process. The steps are the same as those for making macroporous composites; however, before macropore materials are infused into a precursor, surfactants, supramolecules or nanoparticles are added. Colloidal particles formed when polystyrene microspheres were placed inside of photoresist structures on a copper substrate, heated to harden such granules, and then a Sn-Ni alloy was electroplated inside these particles resulting in Sn/Ni alloy composite with complicated hierarchical structure [17]. This micro-patterned Sn-Ni alloy with porous architecture resulted in a large area capacity when used as anode in LIBs. The greater porous structure of the photoresist material resulted in rise of the areal discharge capacity (open pore ratio decreases with hexagonal, square and cylindrical design). Lithographically, patterning a solution of dip-coated TiO_2 precursor over a macrostructured polymer template is another noteworthy example of creating possible hierarchical pore structure for LIB applications. The use of aluminium oxide (AAO) substrate membrane as templates allows for the formation of various nanotube architectures, such as those relevant to high capacity LIBs. To make nanotubes with different pore sizes, this sort of macroporous templating (polymer materials) can be used in combination with mesotemplating (surfactant materials). Using a titanium alkoxide precursor and the P123 triblock copolymer as the structure-directing agent, mesoporous titanium nanotubes can be synthesised inside of AAO membranes. Because the polymeric gel and the hydrophilic alumina walls are attracted to one another, hollow tubes were produced when the solvent drained, resulting in a shrinkage of the gel perpendicular to the porous openings. The calcination procedure eliminates template through dissolving it in NaOH solution. After treatment in supercritical CO_2, nanotube arrays with a 200 nm outer diameter were developed. The nanotubes get tightly packed and entangled as a result of surface tension imposed by the nanotubes walls, without the supercritical drying step. The electrolyte was distributed more efficiently through mesoporous channels, thanks to the hierarchical pore structure, resulting in exceptional rate performance (150 $mAhg^{-1}$ at 240C rate) and strong cycle performance. Carbon systems are the most common examples of hierarchical electrode templating with colloidal crystals, but this method has also been used to produce Fe_2O_3 type oxide materials having hierarchical pore structure. Nanocasting with hierarchical porosity created with both surfactants and polymeric colloidal crystals can produce carbon structures. They can also be made using a colloidal crystal template and a tri-constituent precursor

(silicon alkoxide, resol, block-copolymer surfactant) or a combination of phenol-formaldehyde and a block-copolymer surfactant. The final technique removes the use of toxic materials during silica etching while still allowing considerable control on design of the mesopores. But at the same point, the tri-component approach yields the biggest mesopores with highly variable size distribution within carbon skeleton surrounding the macropores. Tri-constituent derived or nano-cast monoliths are best for preparing porous electrodes in which carbon host is ingested with an active material precursor due to the bigger mesopores [18]. When utilised as monolithic electrodes in a LIBs, carbon materials outperform materials without the templated mesopores.

5.5 Electrodes Made of Hollow Spheres

The high effective surface areas, shorter Li-ion diffusion pathways and excellent packing density make hollow micro or nanospheres as appealing electrode materials for LIBs. The hollow nanospherical structures are especially useful for alloyed anodes because the hollow interiors will serve as a spacer against considerable volume expansion or shrinkage that take place during reaction after repeated cycling, and thus the isotropic feature associated with hollow spheres aids in distributing tensions due to volumetric changes evenly throughout electrode surface. In the event that the hollow nanospheres' surface has pores, there is more buffering space available. Moreover, if the inner walls of the spheres consist of pores that are wide enough to accommodate the electrolyte to move through, the inner walls remain accessible, enhancing the available surface area that can be used. The target materials' precursor is deposited on the templating spheres, which is subsequently hardened by gelation/thermal treatment. The template spheres coating with active materials can be done in a way that keeps these spheres apart, such as using sonication, stirring or ultrasonic spray pyrolysis. To form finally hollow interior, spheres used for template are stripped away via heat treatment or solvent extraction methods. Hollow spheres made from ZnSe/C composite compositions have been obtained from Ostwald ripening processes. Carbon layers can be used to enhance the electronic transport and structural rigidity of hollow spheres [19]. Solvothermal seems to be another viable technique to synthesised hollow sphere of bimetal nitride $NiCO_2N$ material with interconnected nanosheets shell [20]. Hydrothermal synthesis method was used to make mesoporous hollow sphere of TiO_2 coated with N-doped carbon from a combination including polypyrrole coating and carbon [21].

The hard template method can also be employed for preparing hollow metal oxide spheres, for example, mesoporous silica is used as nanoreactors for producing hollow of SnO_2. Template-based approaches for hollow structure manufacturing can generate spheres with good thermal conductivity with a restricted size distribution. On the other hand, non-template techniques are more cost-effective and scalable. Electrodeposition, ultrasonication, intercalation, hydro- or solvothermal syntheses and other non-template ways are capable of producing porous electrodes. Although

these methods frequently result in electrode materials with wider pore size distributions, many of them seem to be simpler than others that needed a template and can result in composites with specific properties and vital dimensions that improve LIB effectiveness. Electrochemical properties of different porous electrode materials for LIBs are summarised in Table 1.

6 Porous Cathode Materials

LIB capacity, output voltage and cost are all influenced by cathode materials. In the area of digital electronic devices, LIBs utilising LiCoO2 as the counter electrode have prevailed. However, the low specific capacity of $LiCoO_2$ (140 $mAhg^{-1}$) and expansive cobalt resources limit their use in practical LIB applications, which needed high capacity. The need for high specific capacity, low price and guaranteed safety has been satisfied by a variety of hierarchically structured materials, including layered transition-metal oxide (LMO), Mn-based spinels and exceptionally highly stable polyanion-type compound materials.

The morphological variations with electron transport in bulk and 1D nanoporous Ni-rich layered transition metal oxides (LNMO) are schematically illustrated (Fig. 3) [34]. The protective solid electrolyte interface (SEI) layer may be damaged as a result of the bulk particles breaking or pulverising and the electrical contact being lost among the electrode material and current collector. Fast electrode kinetics is favoured by nanosized porous particles, which also reduce ion build-up on the LNMO surface. As a result, each of these elements helps to explain the porous nanostructures' exceptional cyclability.

6.1 Layered Transition-Metal Oxides

Owing to its unique structure, simplicity in processing, higher working potential, high capacity and ease in large-scale manufacturing, layered transition metal oxides (L-TMO) are perhaps the most viable cathode options for LIBs. General composition of L-TMO includes $LiMO_2$ (where M = Co, Ni, Mn). In $LiMO_2$, M and lithium ions are positioned at octahedral sites in a cubic close-packed oxygen array, and the lithium layers are positioned among layers of octahedra created by the M and oxygen atoms. However, one type of transition metal ion is less stable structurally and associated with safety risks, making it unsuitable for supporting high energy LIBs. Li-stoichiometric combination of metal oxides and Li-rich Mn-based oxides are currently thought as being the most attractive cathode material for LIBs especially in commercial sector where very large energy density LIBs being utilise for transport applications [15]. To put it another way, layered structure intercalation materials offer a two-dimensional interstitial space that can help Li-ions move quickly through host materials. High-capacity Ni-rich L-TMO

Table 1 Electrochemical properties of different porous electrode materials for Li-ion batteries

Porous electrode materials	Type of structure	Properties	Performance
3D porous electrodes Aligned Fe_3O_4/GO (AGF) electrodes [22]	Ice-templating method	Less polarisation, smaller interfacial resistance and reduced ionic transport impedance inside pore space due to low-tortuosity porous ionic transport channels, architecture Open pore space buffering volume expansion and large effective surface area	Excellent rate performance (724 $mAhg^{-1}$ @ 2 Ag^{-1}) compared with electrodes prepared via traditional slurry-casting method (162 $mAhg^{-1}$ @ 2 Ag^{-1}) achieve high areal capacity of 3.6 $mAh{\cdot}cm^{-2}$ under 10 mA cm^{-2}
$LiNi_{1/3}Mn_{1/3}Co_{1/3}O_2$ (NCM111) low tortuosity porous electrodes [23]	Tuneable wall thickness and channel width	Porous electrodes with larger d have smaller ion transport impedance inside the pore space and thinner lamellae lead to faster overall ion diffusion kinetics	The capacity retention capabilities under increasing C-rates are compared for thick electrodes (20–25 mg cm^{-2}) 101 $mAhg^{-1}$ under 2.5 C. 3D porous electrodes exhibit better capacity retention with higher C-rates
Hierarchically porous polylactic-acid (PLA)/$LiFePO_4$ (LFP)/carbon nanotube (CNT) [24]	Nanoscaleadditive manufacturing	Controlled nano- and micro-architected hierarchical porous structures will enable desired porosity, and thereby specific and areal capacities can simultaneously be enhanced	Exhibit a specific capacity of 155 and 127 $mAhg^{-1}$ and an area capacity of 1.7 and 4.4 mAh cm^{-2} for 100 and 300 μm thick electrodes, respectively, at 0.39 mA cm^{-2}
A nanostructured, porous NCM cathode material [25]	–	Crack formation and particle fragmentation does not occur throughout the complete cycling, high electrode porosities of 65–70%, higher surface area and enlarged interface to the electrolyte, eases delithiation	Improved C-rate capabilities cycling up to 1100 cycles for the nanostructured material in relation to the commercial original NCM

(continued)

Table 1 (continued)

Porous electrode materials	Type of structure	Properties	Performance
TiO_2-$FeTiO_3$@C ternary porous nanocomposites [26]	Solvothermal annealing method	Porous structure provides large contact surface between TiO_2–$FeTiO_3$@C and electrolyte and abundant diffusion path for Li ions and electrons	Reversible capacity of 494.5 $mAhg^{-1}$ after 150 cycles at a current density of 100 mAg^{-1}
Si@$Cu_3(HITP)_2$ Anode [27]	–	Possesses high porosity, high surface area and unique chemical stability $Cu_3(HITP)_2$ coating reduces volume expansion and pulverisation of SiNPs	Cu-MOF (5%) delivered a reversible capacity of 1039 $mAhg^{-1}$, after 1000 cycles, at 1C and 1039 $mAhg^{-1}$ after 1000 cycles at 1C
Hybrid NiO/ nitrogen doped porous carbon matrix (NiO@N–C) [28]	–	Shorten ion diffusion length and abundant exposed active sites for lithium-storage Carbon matrix function as a buffer layer to alleviate the volume expansion	Large reversible capacity of 1373 $mAhg^{-1}$ at 100 mAg^{-1} After 200 cycles and cycling stability up to 1000 cycles at 1 Ag^{-1} with a capacity of 877 $mAhg^{-1}$
Nano-Si/graphite composite electrode materials (SGNM) [29]	Molten salt electrolysis	In situ microstructure control possibilities, cheap affordability and scale-up process capability	Capacity of 733.2 $mAhg^{-1}$ and an initial coulombic efficiency of 86.8%, retained 74.1% of the initial discharging capacity after 50 cycles at 0.2C
Hybrid MoO_3@MoS_2 [30]	A one-pot hydrothermal approach	MoO_3 passivation surface layer on MoS_2 and reactive interfaces between the two phases, which facilitate the Li ion insertion/extraction, successively improving performance	Retains its capacity of 564 $mAhg^{-1}$ after 100 cycles, and maintains a capacity of 278 $mAhg^{-1}$ at 700 mAg^{-1} current density with 99% Coulombic efficiency (CE)
Hybrid Mn_3O_4/graphene electrode [31]	Binder free electrodes	Excellent flexibility of graphene and the rich voids in sandwiched structure improve structural integrity but also the unobstructed conductive network	High reversible specific capacity 880 $mAhg^{-1}$ at 0.1 Ag^{-1}), rate capability 678 $mAhg^{-1}$ at 5 Ag^{-1}) and cycling stability (neglectable capacity decay after 500 cycles at 1 Ag^{-1})
NiO-Ni/CNTs composite [32]	Electrodeposition method	Tiny NiO-Ni particles uniformly distributed on the surface of CNTs Improves overall Conductivity and structural stability	Reversible capacity of 851 $mAhg^{-1}$ at 50 mAg^{-1} after 50 cycles
Nanostructured rock-salt Nb_2O_5 electrode [33]	–	Cubic rock-salt framework, promotes low-energy migration paths	Retains a capacity of 191 $mAhg^{-1}$ at a high rate of 1 Ag^{-1}. It exhibits superb cycling stability with a capacity of 225 $mAhg^{-1}$ at 200 mAg^{-1} for 400 cycles, and a Coulombic efficiency of 99.93%

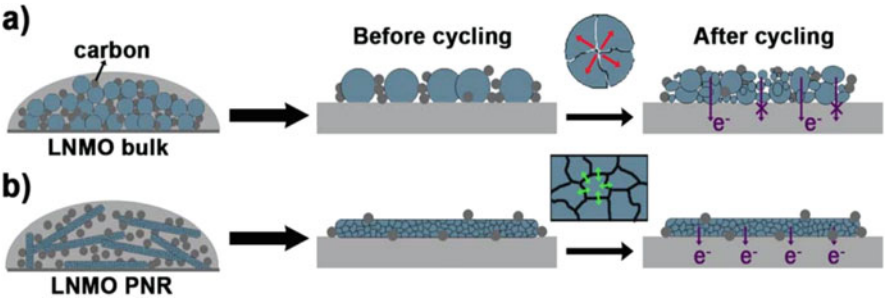

Fig. 3 Schematic showing the effect of electrochemical cycling on the morphological change and electron transport in bulk and 1D nanoporous LNMO electrodes. (a) The repeated Li-ion insertion/removal procedure would cause the bulk particle to deform, destroying the SEI layer that had been created on the electrode surface and resulting in poor particle-to-current collector contact. (b) A 1D nanoporous structure could easily tolerate the strain brought on by variations in the lattice properties due to slippage at the subunit wall borders. "Reprinted (adapted) with permission American Chemical Society" [34]

and highly stable Ni/Mn-based L-TMO are suggested to increase structural stability and practical capabilities.

6.1.1 Transition-Metal Oxides with Ni-Rich Layers

$LiNiO_2$ produces Ni-rich L-TMO. In comparison to $LiCoO_2$, its nickel-based electrode (LiNiO2) has a higher discharge capacity (>220 $mAhg^{-1}$) and is less expensive. Unfortunately, development of $LiNiO_2$ for commercial applications is hampered by its complex synthesis process, significant Li/Ni cationic blending as well as thermal instability. This occurs as a result of migration of Ni_3 ions to the Li layer; thus, $LiNiO_2$ suffers from structural deterioration and low capacity. Cation-substitution in L-TMO, and also structural doping, being researched to increase heat stability and performance of the electrode. A supersonic atomisation process was used to create $LiNi_{0.8}Co_{0.15}Al_{0.05}O_2$ spheres with uniformly distributed crumpled yolk–shell architectures, which were then heat treated [35].

6.1.2 Transition-Metal Oxides Based on Ni/Mn

Mn ions are very feasible to incorporate into the Ni cation layers to create Ni/Mn-rich L-TMO that is more stable and capable. $LiNi_{0.5}Mn_{0.5}O_2$ is the most structurally stable form of the binary Ni/Mn-based L-TMO $LiNi_{1-x}Mn_xO_2$ (0×1) family [36]. The $LiCoO_2$-$LiNi_{0.5}Mn_{0.5}O_2$ and Li_2MnO_3-$LiNi_{0.5}Mn_{0.5}O_2$ systems have been proposed to further stabilise the layered structure and increase capacity.

6.2 Mn-Based Spinels

The spinel structure is commonly represented by AB_2O_4, in which O_2 ions form a cubic densely packed structure while A and B ions, respectively, occupy the tetrahedral and octahedral positions. $LiMn_2O_4$ and $LiNi_{0.5}Mn_{1.5}O_4$ are the most common Mn-based spinels used in LIB cathodes. Because of their three-dimensional Li-ion diffusion pathway, theoretical capacity of Mn-based spinels is low compared to its greater rate performance than L-TMO, making them attractive cathode materials for high power batteries. Spinels made of Mn have a low cost and are environmentally friendly. High-rate capability and excellent specific capacity, with good cyclability of spinel-type Mn-based oxides, are achieved by using hollow or porous structures, which benefit from the fast Li diffusion routes.

6.3 Polyanion-Type Compounds

$LiMPO_4$ (M = Fe, Mn, Co and Ni), sodium superionic conductor (NASCION)-type $Li_3V_2(PO_4)_3$ and silicate-based Li_2MSiO_4 (M = Fe, Mn and Co) are the most common polyanion-type compounds. These materials have superior thermal stability and safety than layered lithiated transition-metal oxides, thanks to the O_2 ions experiencing strong covalent bonds. Polyanion-type compounds, on the other hand, have larger theoretical specific capabilities than Mn-based spinels. Nonetheless, the electrical and ionic conductivities of polyanion-type compounds are weak, resulting in poor rate performance. Carbon coating in combination with nanostructures and porous electrode design is a viable solution to this challenge.

7 Lithium-Sulphur Batteries

Lithium-sulphur batteries (Li-S batteries) will be among the foremost desirable upcoming electrochemical energy storage systems. The specific capacity and energy density of Li-S batteries are high 1672 $mAhg^{-1}$ and 2600 $Whkg^{-1}$, respectively. A Li-S battery is a complicated device that involves two common electrochemical processes using lithium metal and sulphur. Furthermore, elemental S is inexpensive, abundant in soil and environmentally favourable, making Li-S batteries highly suitable for advance applications (such as EVs and HEVs) [37, 38]. A conventional Li-S battery has four basic components, namely, Li metal anode, cathode, separator and organic electrolyte. Various reaction mechanisms involved during the widely acknowledged process for the complete reduction of element S are given below:

$$16Li + S_8 \rightarrow 8Li_2S \tag{2}$$

$$S_8 \leftrightarrow Li_2S_8 \leftrightarrow Li_2S_6 \leftrightarrow Li_2S_4 \leftrightarrow Li_2S_2 \leftrightarrow Li_2S \quad (3)$$

Sulphur is a possible electrode material for rechargeable lithium batteries; sulphur offers several appealing qualities, as well as a high theoretic capacity (1675 $mAhg^{-1}$) and a relatively low cost. Despite all of these advantages, Li-S batteries have had a difficult time developing, and numerous inherent problems must be resolved before they can be used in real life. Among these challenges are: (1) overall bulk electrical conductivity (at room temperature, 1030 S/cm) as well as ionic conductivity of sulphur and Li_2S, which are naturally insulative, which results in low active material consumption and high electrochemical polarisation. (2) The shuttle effect, which occurs when soluble lithium polysulfide (LiPS) intermediates dissolve in the electrolyte and migrate in between anode and cathode regions, can cause Li metal corrosion and the loss of cathode active S, resulting in a dramatic reduction in discharge capacity and cycle life. (3) The sluggish reaction kinetics due to the intrinsic insulating characteristics of elemental S, and the final discharge products (Li_2S_2/Li_2S) also decrease the discharge capacity. (4) The massive volume expands/shrinkage (up to 80%) caused by the conversion of elemental S to Li_2S, which places severe strain on the host structure, that frequently results in the failure of the electrode architecture. (5) The rapid deterioration of batteries and potential safety threat caused by the Li dendrite growth produced by the nonuniformity Li deposition and the passivation layer created by chemical interactions between active LiPSs and fresh Li.

More importantly, if the sulphur loading rises, all of these problems will become more problematic, especially in the pouch cells at the level of practical application. Massive efforts have been undertaken from the beginning to the present to address the problems with Li-S batteries that have been discussed. As a result, rational design of nanostructured conductive polar sulphur hosts, which is expected to reduce polysulfide diffusion via physical cavity confines or chemical covalence adsorption, is a potential technique for Li-S batteries to flourish. The use of nanostructured carbonaceous material, nanostructured transition metal compounds and their compounds as a host for Li-S batteries has been explored widely (Fig. 4).

7.1 Carbon-Based Hybrid Porous Materials

To accommodate the Li-ions, sulphur lacks a cage-like structure. Sulphur must therefore be allowed to exist in a host substance for Li to chemically react with it and generate Li_2S, which must then remain bonded to the host substance. Due to lithium polysulfides' potential for dissolution in the electrolyte, the attachment component is of highest significance. As this may results in the loss of the cathode's active material as well as disruption of the anode process. Hierarchical porous carbon materials have been discovered to be useful in Li-S batteries due to their large

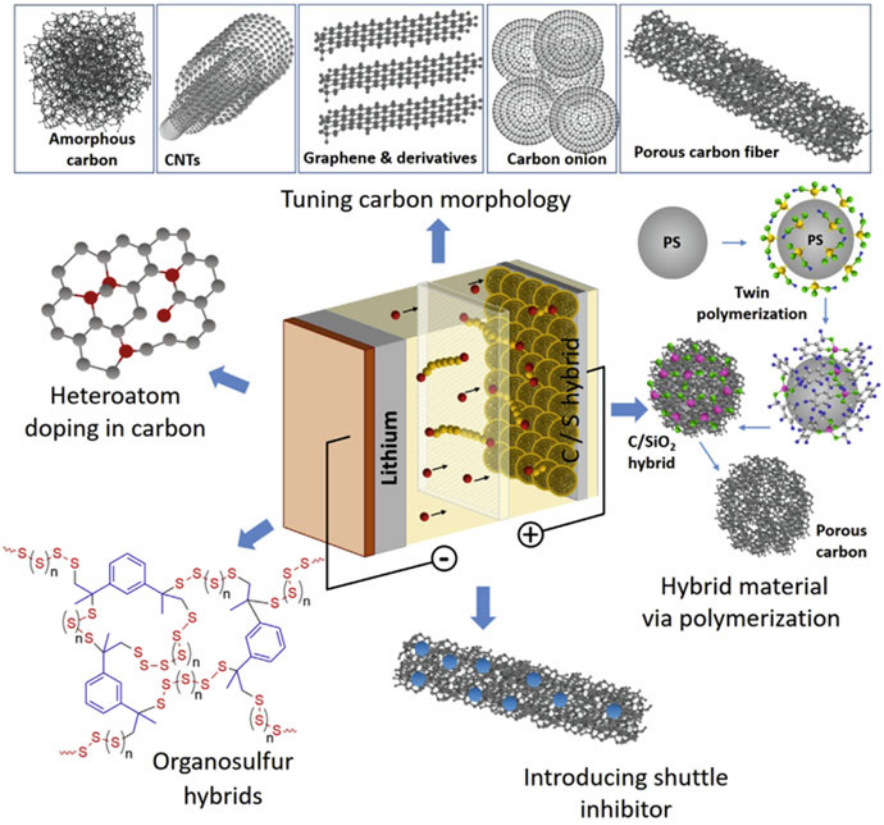

Fig. 4 Schematic illustration of carbon-sulphur hybrid material synthesised via different routes. PS: polystyrene, CNTs: carbon nanotubes, amorphous carbon. (Reproduced with permission from the Elsevier [39])

degrees of freedom to customise the porous microstructures, strong conductivities, high specific surface areas and electrochemical inertness.

Carbon has been investigated as the most potential sulphur host due to its light weight, mutual compatibility with sulphur, easy availability and ability to adjust the morphology at the nanoscale. Porous carbon black, mesoporous carbon, multiwalled carbon nanotubes, graphene, carbon nanofibers, metal organic framework (MOF), carbon aerogels, carbon composites, etc. have all been widely used as Li-S battery substrates. Choosing an appropriate carbon-sulphur hybrid can raise a number of important problems. (1) introduce sulphur as near as possible to carbon; (2) carbon material viability; (3) restraint effect in porous structure; (4) influence of pore volume, pore size and its distribution; (5) carbon purity; (6) strategies to control polysulfide shuttle; (7) effect of heteroatom doping in carbon; and (8) looking for an alternative sulphur feedstock.

The specific surface area, which can be attained through a variety of manufacturing processes, is one of the most important conditions for carbon to be an efficient sulphur host. Specific surface area can be up to 2000 m^2g^{-1} based on the processing methods [39]. Pore size and pore size distribution, on the other hand, play an essential role in bringing the majority of the sulphur to the carbon surface. In fact, most traditional porous carbon variations are amorphous in nature, with a low degree of graphitisation however and a wide range of porosity topologies. Because of their small pore spacing, micropores aid in the immobilisation of sulphur, resulting in fewer sulphur species. The shuttle effect is said to be mitigated by them.

Mesopores serve to aid in the trapping of sulphur and polysulfides, as well as to offer adequate pore volumes for high sulphur loading and sufficient ion transport channels for improved rate capability. Macropores are crucial at the nanoscale because they allow for rapid electrolyte transport. It would have a significant effect on the kinetics of ionic conduction. Furthermore, highly porous areas can hold a lot of sulphur and buffer volumetric changes during redox processes. Hierarchical porous carbon materials have been discovered to be useful in Li-S batteries due to their great degrees of freedom in tuning porous microstructures, strong conductivities, high specific surface areas and electrochemical inertness (Fig. 5) [40, 41].

7.2 Heteroatom Doping in Carbon-Sulphur Electrode

The electrical conductivity of a carbon substrate can be enhanced via heteroatom enrichment in the graphitic structure of the carbon material. Heteroatom doping (P, O and N) in porous carbon architecture aids in a distinct porous structure, a large superficial part and a high pore volume, allowing for robust physicochemical adsorption of polysulfides [42–44]. As a result, it is possible to achieve very high cycle stability. Polyacrylonitriles have also been reported to be used as a carbon source, so that nitrogen-containing carbon can be directly synthesised with higher cycle stability [45]. Because of the doping method's polarisation effect on an ordered host architecture and the material's high chemical sensitivity to polysulfides, polysulfide leaching is greatly reduced.

7.3 Dimensional Porous Nanostructured

For the substrate (or host) of non-conducting sulphur electrode, the use of a 3D porous architecture carbon is a successful strategy for addressing the challenges of extremely poor conductivity and substantial volume enlargement of the sulphur cathodes during cycling. A 3D porous carbon (DP) with mesopores (3–6 nm), for example, can operate as a scaffold to enclose transitional products and limit the shuttle influence of lithium polysulfide. In Li-S batteries, N-doped 3DP carbon

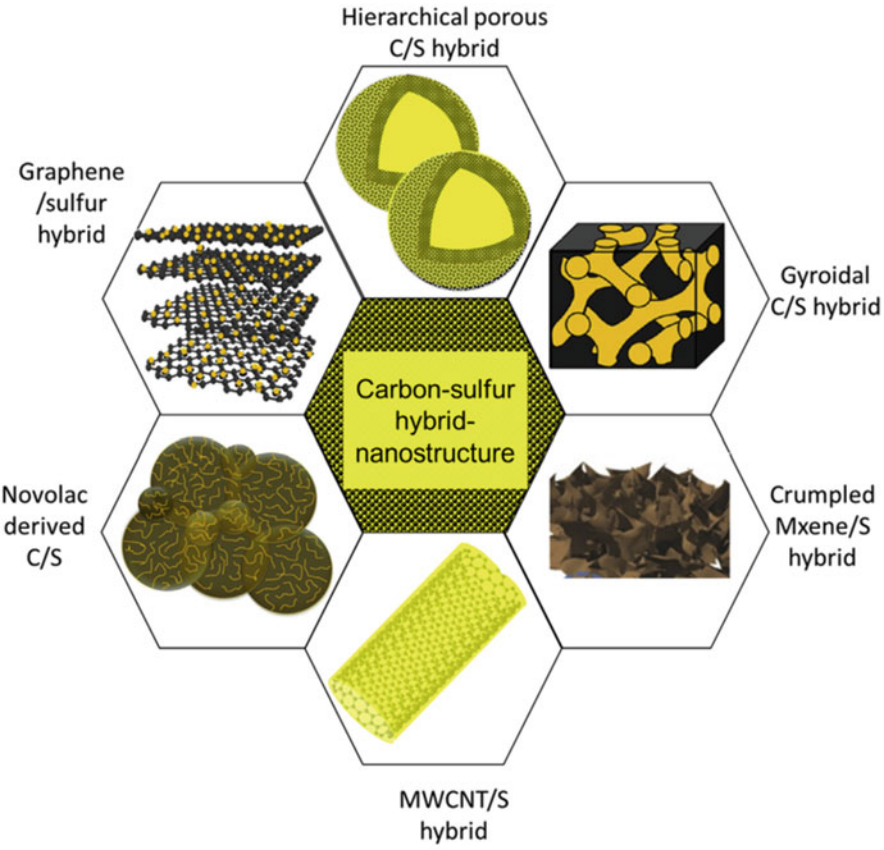

Fig. 5 Schematic representation of different carbon sulphur hybrids nanostructured used as electrode materials for Li-ion batteries. (Reproduced with permission from Elsevier [39])

serves as a host for sulphur cathodes. Soluble polysulfides are further trapped by N doping and the 3dP carbon, thereby stabilising sulphur [46]. Furthermore, metal oxides or metals can be incorporated into 3DP carbon materials functionalised by heteroatoms to boost the carbon hosts' cohesiveness with polysulfide molecules. It can also decrease the polysulfide shuttle effect and improve the polysulfide redox reaction kinetics.

7.4 Shuttle Inhibition in Inorganic Materials and Intercalation and Conversion in Li-S Cells

The shuttle effect is widely recognised as one among the key reasons that causes low charge efficiency and loss in capacity in Li-S battery. The soluble polysulfides react

irreversibly and travel to the lithium anode. The polysulphides break into shorter chains, and they retreat to the cathode. Yet, another approach to reduce and nullify the shuttle influence seems to incorporate several other supplementary additives that have an affinity for polysulfides. The migration of soluble polysulphides to the Li surface is stopped by either adsorbing or due to catalytic effect, which breaks polysulphides into short chains. Some examples of commonly employed shuttler inhibitors are oxides (e.g. SiO_2, Al_2O_3, TiO_2, MnO_2, MgO, CeO_2, Co_3O_4, ZrO_2) and hydroxides like $Ni(OH)_2$ and Ni/Fe [39]. Typically, these materials are decorated on porous carbon–sulphur hybrid electrodes, thus adding a shuttle resistor as a third hybrid ingredient that is properly dispersed.

Additionally, they can improve the cohesiveness of Li polysulphides, faster Li-ion transfer, improved electrical conductivity, and capacity share from both electrode's active materials, effectively immobilising soluble sulphur species.

7.5 Organosulphur Hybrids

The ideas outlined thus far have the potential to significantly increase battery performance. Neither of these attempts, however, were able to bridge the difference between small-scale study and genuine commercial execution. Each year, the petroleum refining industry produces a massive quantity of sulphur. Sulphur immobilisation is critical for hybrid electrodes. By using heat as a trigger, sulphur can go through ring-opening polymerisation, forming a metastable polymeric sulphur that eventually transforms back into the thermodynamically stable octasulphur form. Besides that, sulphur has been used in rubber vulcanisation to produce sulphur-rich copolymers through numerous condensation or radical processes, furthermost current of which being the reverse vulcanisation method.

Sulphur-containing copolymers can be made by mixing vinyl monomers with sulphur di-radicals. Based on number of vinyl units in each comonomer, linear, cross-linked and severely cross-linked copolymers can be produced. Sulphur content can also be adjusted depending on the ratio of input comonomer (sulphur:vinyl monomer). The sulphur copolymers swiftly gelled and vitrified, resulting in a hard material that can be combined with conductive carbon black to create a hybrid electrode material. But it's possible that the carbon and copolymer are not blended evenly, which would lead to a substantial loss of electrical conductivity and leave the capacity fading problem unresolved [47, 48]. The specific capacity is significantly affected by the incorporation of carbon anions into the sulphur copolymer because the copolymer efficiently stabilises and prevents sulphur species from recombination into the S8 configuration [49]. Furthermore, chemical polysulfides were limited by polar interactions with heteroatoms present in the linkers. In comparison to elemental sulphur cathodes, the significant challenge of Li diffusion kinetics was significantly eliminated. But more critically, these carbons needed high electrolyte/sulphur ratios (often >15 L/mg), which reduce the energy density at

the cellular level. These carbons also suffered from insufficient interaction with polysulfides and excessively high pore volumes, which led to low tap density.

7.6 Transition Metal Oxide

Because 3D metal oxides have higher specific capacity values, graphite anode is possibly replaced by transition metal oxides (TMOs) in LIBs. In addition, the lithium ion avoids the production of metal-lithium alloys by reacting reversibly with metal oxides as follows:

$$MO + xLi^{+} + xe^{-} \leftrightarrow Li_2O + M \qquad (M = Fe, Co, Ni, Cu) \tag{4}$$

The forward process, which involves several electron transfers for each metal atom, is thermodynamically advantageous and results in a large theoretical lithium storage capacity. The creation of Li-ions from Li_2O, which is a reaction going in the opposite direction, is a thermodynamically unfavourable process, although it is thought to be aided by metal nanoparticles (M) that are created during the reaction [50]. This shows that the reaction's reversibility is effectively preserved in the nanoscale system. Other limitations, such as poor conductivity, limited diffusion coefficient and production of extensive SEI layer, can be overcome by acquiring other combination of materials or by developing various hierarchical nanostructures. Tin oxide (SnO_2) was initially selected as the anode material among the TMOs because of its high value of theoretical capacity (790 $mAhg^{-1}$).

$$SnO_2 + 4Li^{+} + 4e^{-} \leftrightarrow Sn + 2Li_2O \tag{5}$$

$$Sn + xLi^{+} + xe^{-} \leftrightarrow 4Li_xSn \quad (0 \leq x \leq 4.4) \tag{6}$$

Notably, core-shell, hollow spheres or mesoporous architectures can tolerate the volume shift, while the nanowire or nanorods of SnO_2 offers the mechanical stability to persist during several cycles of the insertion-deinsertion activity [51]. Hydrothermal carbonisation approach is used to assemble nanoparticles to create mesoporous SnO_2 microspheres. It should be highlighted that porosity aids in both a quicker intercalation and deintercalation of lithium and a good network structure that makes surfaces available for electrolytes.

Another promising anode material in LIB is titanium dioxide (TiO_2), which is widely available and non-toxic as well as environmentally favourable. Different polymorphs of TiO_2 exist, including anatase, rutile, brookite, TiO_2 B (bronze) and TiO_2 H (Hollandite), and the electrochemical activity of these polymorphs is dependent on their inherent qualities as determined by their crystal structures. Anatase TiO_2 is the most electroactive polymorph of TiO_2 [52]. Similarly, due to its accessibility and environmental friendliness, many types of iron oxides,

including hematite (Fe_2O_3), magnetite (Fe_3O_4) and ferrous oxide (FeO), have been widely used in biological and industrial applications. Due to its high theoretical capacity value, Fe_2O_3 is used as a feasible anode in LIB because it is the most thermodynamically stable oxide among them (1007 $mAhg^{-1}$) [53]. Other promising candidates for the anode in LIB are the cobalt-based oxides, CoO and Co_3O_4. Effective anode materials in LIB also include diverse metal oxides or their mixed composites with carbon material. For example, solvothermal approach was used to create $CoSnO_3$/graphene nanohybrid materials, which were then dispersed on GO-reduced graphene nanosheets [54].

7.7 Transition-Metal Dichalcogenides (TMDs)

Layered metal dichalcogenides (MX_2) have a unique layered arrangement in their crystal structures, which contributes to their exceptional Li-ion storage capacity. The metal atoms in MX_2 are held together by weak van der Waal forces within two chalcogenide layers that are organised hexagonally in the order of X-M-X. The octahedral or tetrahedral interstitial sites, where the previous is actively more advantageous, can both be intercalated with lithium in this multilayer stacking structure. In addition, the lithium insertion through MX_2 includes a full charge transfer that converts the M^{4+} ion to the M^{3+} ion and diffusion of Li ion in the van der Waal's gap, which causes the volume to expand. Metal sulphides MS_2 of M = Co, Fe, Ni, Cu and Ti are thought to be cathode materials, and M = Nb, W, Ta, Mo and Ga are employed as anode materials in LIB, depending on the lithiation potential values [55].

Hollow MoS_2 nanoparticles were shown to be more stable than solid MoS_2 nanoparticles [56]. MoS_2 composites laminated with graphene had a high specific capacity of 1100 $mAhg^{-1}$ with current of 100 mAg^{-1} and 350 $mAhg^{-1}$ at a current of 2000 mAg^{-1}. The hydrothermal technique was used to create 3D MoS_2 flower-like nanostructure embedded on layers of graphene [57]. The spacing between the nanosheets of MoS_2, 13.8 Å in comparison with bulk MoS_2 6.2 Å, produced by such MoS_2 nanoflowers was advantageous for the insertion of Li-ions. In order to provide sulphur in lithium–sulphur batteries, a novel technique was used. A combination of elemental Li and MoS_2 is electrochemically transformed to Li_2S and elemental Mo to prevent the instability of Li_2S. According to the authors, the resulting cell is extremely stable. In a similar way, MoS_2 composite with single-walled carbon nanotubes and MoS_2 nanorods covered with amorphous carbon displayed relatively high capacity 992 $mAhg^{-1}$ in LIBs and 621 mAg^{-1} [58]. Mesoporous WS_2 has also been employed as an electrode in Li batteries. TiS_2, ZrS_2, $SnSe_2$ and their hybrid materials with carbon materials, among other transition metal chalcogenides, are also discovered to be particularly encouraging in the area of anode materials utilised in LIB. Li_xTiS_2 (x = 0.12, 0.52 and 1.0) is an intercalated chemical that is formed when lithium is intercalated into TiS_2, which shares the same layered structure as MoS_2 [59]. In LIBs, TiO_2 is primarily used as cathode rather than anode because it

has comparatively high discharge capacity value of 2.1 V. There are, however, few accounts of it being employed as an efficient anode material in a hybrid form with carbon materials.

8 Summary and Future Prospects

In a fairly broad spectrum of practical technologies, porous electrode materials and reactive flow are key components. The value of new capacities to depict and comprehend physical, chemical and electrochemical processes at the microscale is growing. Overall, it can be said that LIBs' performance is still subpar despite tremendous progress made thus far employing various types of materials as anodes.

Current challenges include the proper design of nanostructures and suitable combination of the materials. Additionally, low specific capacity (experimental) compared to theoretical ones, unexpected volume expansion, irreversible response of Li ion intercalation/deintercalation process, SEI layer formation, low electrical conductivity, etc. need to be investigated. Whereas the size, form, and design of innovative nanoarchitectures are crucial, it is also necessary to prevent harsh adverse effects caused by extremely large surface area. Additionally, it's important to take into account safety concerns, non-toxic properties and affordable materials. New knowledge can be upscaled to support the best design and control of whole devices and components at the macroscale in addition to increasing fundamental understanding.

Acknowledgments Author, Anisha Chaudhary expresses her thanks to DST for providing SERB-National Post-Doctoral Fellowship (file no**. PDF/2017/002601).**

References

1. K. Zhang et al., Nanostructured Mn-based oxides for electrochemical energy storage and conversion. Chem. Soc. Rev. **44**(3), 699–728 (2015)
2. B. Dunn, H. Kamath, J.-M. Tarascon, Electrical energy storage for the grid: A battery of choices. Science **334**(6058), 928–935 (2011)
3. J. Liang et al., Comparison of two energy management strategies considering power system durability for PEMFC-LIB hybrid logistics vehicle. Energies **14**(11), 3262 (2021)
4. H. Ji et al., Capacitance of carbon-based electrical double-layer capacitors. Nat. Commun. **5**(1), 1–7 (2014)
5. M. Winter, R.J. Brodd, What are batteries, fuel cells, and supercapacitors? Chem. Rev. **104**(10), 4245–4270 (2004)
6. F. Schüth, Engineered porous catalytic materials. Annu. Rev. Mater. Res. **35**, 209 (2005)
7. P.G. Bruce, B. Scrosati, J.M. Tarascon, Nanomaterials for rechargeable lithium batteries. Angew. Chem. Int. Ed. **47**(16), 2930–2946 (2008)
8. M.S. Islam, C.A. Fisher, Lithium and sodium battery cathode materials: Computational insights into voltage, diffusion and nanostructural properties. Chem. Soc. Rev. **43**(1), 185–204 (2014)

9. W. Dong, D.R. Rolison, B. Dunna, Electrochemical properties of high surface area vanadium oxide aerogels. Electrochem. Solid-State Lett. **3**(10), 457 (2000)
10. C.K. Chan et al., High-performance lithium battery anodes using silicon nanowires. Nat. Nanotechnol. **3**(1), 31–35 (2008)
11. Y. Shao-Horn et al., Structural characterization of layered LiMnO2 electrodes by electron diffraction and lattice imaging. J. Electrochem. Soc. **146**(7), 2404 (1999)
12. K.S. Sing, Reporting physisorption data for gas/solid systems with special reference to the determination of surface area and porosity (recommendations 1984). Pure Appl. Chem. **57**(4), 603–619 (1985)
13. J.L. Tirado, Inorganic materials for the negative electrode of lithium-ion batteries: State-of-the-art and future prospects. Mater. Sci. Eng. R. Rep. **40**(3), 103–136 (2003)
14. Y. Zheng et al., Nano-porous Si/C composites for anode material of lithium-ion batteries. Electrochim. Acta **52**(19), 5863–5867 (2007)
15. P. Lian et al., Electrochim. Acta **56**, 834 (2010)
16. L. Ji et al., Recent developments in nanostructured anode materials for rechargeable lithium-ion batteries. Energy Environ. Sci. **4**(8), 2682–2699 (2011)
17. J. Wang et al., Facile synthesis of nanocrystalline TiO2 mesoporous microspheres for lithium-ion batteries. J. Phys. Chem. C **115**(5), 2529–2536 (2011)
18. L. Li et al., [cu(dap)2Cl] as an efficient visible-light-driven photoredox catalyst in carbon–carbon bond-forming reactions. Chem.—Eur. J. **18**, 11417 (2012)
19. Z. Wang et al., Hollow-sphere ZnSe wrapped around carbon particles as a cycle-stable and high-rate anode material for reversible Li-ion batteries. New J. Chem. **41**(14), 6693–6699 (2017)
20. P. Wang et al., NiCo2N hollow sphere with interconnected nanosheets shell: A potential anode material for high performance lithium-ion batteries. Chem. Eng. J. **425**, 130607 (2021)
21. Y. Xing et al., N-doped hollow urchin-like anatase TiO2@ C composite as a novel anode for Li-ion batteries. J. Power Sources **385**, 10–17 (2018)
22. X. Zhang et al., Promoting transport kinetics in Li-ion battery with aligned porous electrode architectures. Nano Lett. **19**(11), 8255–8261 (2019)
23. X. Zhang et al., Tunable porous electrode architectures for enhanced Li-ion storage kinetics in thick electrodes. Nano Lett. **21**(13), 5896–5904 (2021)
24. V. Gupta et al., Additive manufacturing enabled, microarchitected, hierarchically porous polylactic-acid/Lithium iron phosphate/carbon nanotube nanocomposite electrodes for high performance Li-ion batteries. J. Power Sources **494**, 229625 (2021)
25. M. Müller et al., Effect of nanostructured and open-porous particle morphology on electrode processing and electrochemical performance of Li-ion batteries. ACS Appl. Energy Mater. **4**(2), 1993–2003 (2021)
26. S. Guo et al., Porous TiO2–FeTiO3@ carbon nanocomposites as anode for high-performance lithium-ion batteries. J. Alloys Compd. **858**, 157635 (2021)
27. A. Nazir et al., Si nanoparticles confined within a conductive 2D porous cu-based metal–organic framework (Cu3 (HITP) 2) as potential anodes for high-capacity Li-ion batteries. Chem. Eng. J. **405**, 126963 (2021)
28. K. Chu et al., NiO nanocrystals encapsulated into a nitrogen-doped porous carbon matrix as highly stable Li-ion battery anodes. J. Alloys Compd. **854**, 157264 (2021)
29. N. Wang et al., Electrolytic silicon/graphite composite from SiO2/graphite porous electrode in molten salts as a negative electrode material for lithium-ion batteries. Rare Metals **41**(2), 438–447 (2022)
30. M. Faizan et al., MoO3@ MoS2 core-shell structured hybrid anode materials for lithium-ion batteries. Nano **12**(12), 2008 (2022)
31. B.-L. Yan et al., A simplified electrophoretic deposition route for sandwiched structure-based Mn3O4/G composite electrodes as high-capacity anodes for lithium-ion batteries. J. Alloys Compd. **905**, 164121 (2022)
32. G. Yang et al., "Powder electrodeposition" synthesis of NiO-Ni/CNTs composites with high performances of lithium storage battery. J. Alloys Compd. **898**, 163005 (2022)

33. P. Barnes et al., Electrochemically induced amorphous-to-rock-salt phase transformation in niobium oxide electrode for Li-ion batteries. Nat. Mater. **21**, 1–9 (2022)
34. X. Zhang et al., LiNi0.5Mn1.5O4 porous nanorods as high-rate and long-life cathodes for Li-ion batteries. Nano Lett. **13**(6), 2822–2825 (2013)
35. H. Yang et al., Fabrication and characteristics of high-capacity LiNi0.8Co0.15Al0.05O2 with monodisperse yolk–shell spherical precursors by a facile method. RSC Adv. **4**(67), 35522–35527 (2014)
36. Y. Koyama et al., Systematic research on insertion materials based on superlattice models in a phase triangle of LiCoO[sub 2]-LiNiO[sub 2]-LiMnO[sub 2]. J. Electrochem. Soc. **151**(9), A1499 (2004)
37. Y. Huang et al., Recent advances and strategies toward polysulfides shuttle inhibition for high-performance Li–S batteries. Adv. Sci. **9**(12), 2106004 (2022)
38. L. Kong et al., Current-density dependence of Li 2 S/Li 2 S 2 growth in lithium–sulfur batteries. Energy Environ. Sci. **12**(10), 2976–2982 (2019)
39. S. Choudhury, Hybrid cathode materials for lithium-sulfur batteries. Curr. Opin. Electrochem. **21**, 303–310 (2020)
40. Z. Li et al., Engineered interfusion of hollow nitrogen-doped carbon nanospheres for improving electrochemical behavior and energy density of lithium–sulfur batteries. Adv. Funct. Mater. **29**(31), 1902322 (2019)
41. H. Chen et al., Electrode design with integration of high tortuosity and sulfur-philicity for high-performance lithium-sulfur battery. Matter **2**(6), 1605–1620 (2020)
42. M. Kopeć et al., Polyacrylonitrile-derived nanostructured carbon materials. Prog. Polym. Sci. **92**, 89–134 (2019)
43. X. Chen et al., Covalent organic framework derived boron/oxygen codoped porous carbon on CNTs as an efficient sulfur host for lithium–sulfur batteries. Small Methods **3**(11), 1900338 (2019)
44. M. Gao et al., Self-supporting N, P doped Si/CNTs/CNFs composites with fiber network for high-performance lithium-ion batteries. J. Alloys Compd. **857**, 157554 (2021)
45. S.-S. Yao et al., The electrochemical behavior of nitrogen-doped carbon nanofibers derived from a polyacrylonitrile precursor in lithium sulfur batteries. New Carbon Mater. **36**(3), 606–615 (2021)
46. J. Ren et al., A reduced graphene oxide/nitrogen, phosphorus doped porous carbon hybrid framework as sulfur host for high performance lithium-sulfur batteries. Carbon **140**, 30–40 (2018)
47. Z. Pan et al., Progress and perspectives of organosulfur for lithium–sulfur batteries. Adv. Energy Mater. **12**(8), 2103483 (2022)
48. X. Zhang et al., Structure-related electrochemical performance of organosulfur compounds for lithium–sulfur batteries. Energy Environ. Sci. **13**(4), 1076–1095 (2020)
49. S. Chen et al., 3D hyperbranched hollow carbon nanorod architectures for high-performance lithium-Sulfur batteries. Adv. Energy Mater. **4**(8), 1301761 (2014)
50. H.B. Wu et al., Nanostructured metal oxide-based materials as advanced anodes for lithium-ion batteries. Nanoscale **4**(8), 2526–2542 (2012)
51. R. Liu et al., Hydrothermal synthesis of hollow SnO2 spheres with excellent electrochemical performance for anodes in lithium ion batteries. Mater. Res. Bull. **96**, 443–448 (2017)
52. O. Eroglu, M.S. Kiai, H. Kizil, Glass fiber separator coated by boron doped anatase TiO2 for high-rate Li–S battery. Mater. Res. Bull. **129**, 110917 (2020)
53. S. Deng et al., Dipolar and catalytic effects of an Fe 3 O 4 based nitrogen-doped hollow carbon sphere framework for high performance lithium sulfur batteries. Inorg. Chem. Front. **8**(7), 1771–1778 (2021)
54. T. Kavinkumar, H.H. Lee, D.-H. Kim, Design of all-solid-state hybrid supercapacitor based on mesoporous CoSnO3@ RGO nanorods and B-doped RGO nanosheets grown on Ni foam for energy storage devices of high energy density. Appl. Surf. Sci. **541**, 148354 (2021)
55. M. Pumera, Z. Sofer, A. Ambrosi, Layered transition metal dichalcogenides for electrochemical energy generation and storage. J. Mater. Chem. A **2**(24), 8981–8987 (2014)

56. Z. Wan et al., Core–Shell structure of hierarchical quasi-hollow MoS2 microspheres encapsulated porous carbon as stable anode for Li-ion batteries. Small **10**(23), 4975–4981 (2014)
57. B. Ouyang et al., MoS2 anchored free-standing three dimensional vertical graphene foam based binder-free electrodes for enhanced lithium-ion storage. Electrochim. Acta **194**, 151–160 (2016)
58. X. Ning et al., In-situ construction of interconnected N-doped porous carbon-carbon nanotubes networks derived from melamine anchored with MoS2 for high performance lithium-ion batteries. J. Alloys Compd. **744**, 75–81 (2018)
59. K. Sun et al., Improvement of Li-S battery electrochemical performance with 2D TiS2 additive. Electrochim. Acta **292**, 779–788 (2018)

Emerging Novel Chalcogenide-Based Materials for Electro Water Splitting Applications

Vikas J. Mane, Vaibhav C. Lokhande, Abhishek C. Lokhande, Chandrakant D. Lokhande, and Dattatray S. Dhawale

1 Introduction

Environment and energy are the two urgent significant issues in current society for global commercial and social development. Nature provides a wide variety of sources of renewable energy such as solar energy, tidal energy, biomass energy, wind energy, and so on. However, due to regional or seasonal factors, renewable energy sources become inconsistent. Therefore, systematic energy conversion and storage systems are required for large-scale applications [1, 2]. Water is the most abundant source of hydrogen and oxygen on earth, and it can be split into oxygen and hydrogen using an electrolyzer. Electrochemical water splitting is a fascinating technology for renewable energy conversion into green hydrogen fuel. In electrochemical water splitting, hydrogen evolution reaction (HER) at the cathode and oxygen evolution reaction (OER) at the anode are the two half-cell reactions that take place [3]. Despite the merit of electrochemical water splitting, the reaction kinetics of OER is sluggish because the multistep electron transfer processes compared to HER are greatly affected by large overpotentials. Therefore,

V. J. Mane · C. D. Lokhande (✉)
Centre for Interdisciplinary Research, D. Y. Patil Education Society (Deemed to be University), Kolhapur, India

V. C. Lokhande
Department of Electrical, Electronic Communication and Computer Engineering, Chonnam National University, Gwangju, South Korea

A. C. Lokhande
Department of Mechanical Engineering, Khalifa University of Science and Technology, Abu Dhabi, United Arab Emirates

D. S. Dhawale (✉)
CSIRO Energy, Victoria, Australia
e-mail: dattatray.dhawale@csiro.au

F. I. Ezema et al. (eds.), *Chemically Deposited Metal Chalcogenide-based Carbon Composites for Versatile Applications*, https://doi.org/10.1007/978-3-031-23401-9_9

electrocatalysts are necessary to enhance the kinetics of both the OER and HER to ensure the overall energy-efficient process and minimize the energy barriers [4, 5]. In HER, water is reduced at the cathode to generate H_2, which requires a process of two electrons transfer, and the reaction is given as $[2H^+_{(aq)} + 2e^- \rightarrow H_{2(g)}]$. Similarly, OER is the reaction in which water is oxidized at the anode to generate O_2, involving a four-electron transport process that needs a significantly higher overpotential than HER [6]. The reaction pathway of alkaline OER is $2H_2O \rightarrow O_{2(g)} + 4H^+_{(aq)} + 4e^-$, and the overall reaction is represented as:

$$2H_2O \rightarrow 2H_2 + O_2 \tag{1}$$

Because of high overpotentials and slow kinetics in OER and HER, electrocatalyst plays a significant role to split the water. Therefore, the development of highly efficient electrocatalysts is essential for reducing OER and HER overpotentials to achieve efficient O_2 and H_2 generation.

Initially, platinum group metals such as palladium (Pd), platinum (Pt), iridium (Ir), and ruthenium (Ru) have been the choice of active electrocatalysts. However, their expensive nature and scarcity restrict their large-scale catalyst production for commercial applications. Hence, developing efficient, low-cost, and long-lasting electrocatalysts is vital for replacing expensive metals. Metal chalcogenides, such as sulfide, selenide, and telluride, have received extensive interest as an emerging material with superior performance due to their unique properties such as high surface area and better electrical conductivity compared to pure precious metals and metal oxides.

Several research strategies have been implemented to prepare a variety of transition metal chalcogenides for electrochemical water splitting. Figure 1 shows the summary of metal chalcogenide-based materials and their composites for overall water splitting application (reported using the data from Google scholar: 2001

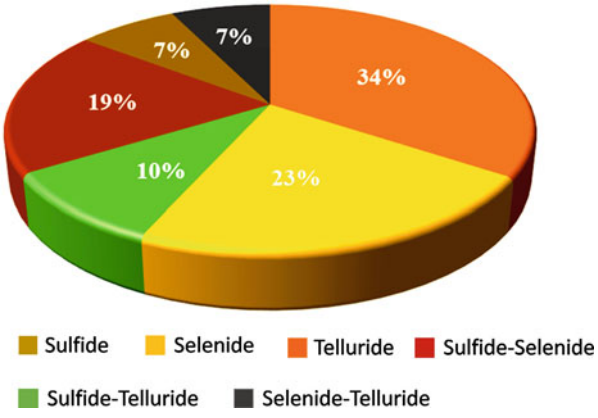

Fig. 1 Pie chart showing the summary of metal chalcogenide-based materials and their composites for overall water splitting application. (Reported using the data from google scholar: 2001 to 2022)

to 2022). Thus, this chapter is focused on various metal chalcogenides (sulfide, selenide, and telluride) and their composite electrodes for electrochemical water splitting [7].

2 Metal Chalcogenides (MCs) for Electro Water Splitting

The MCs are the emerging class of material for HER and OER activity and recently received more attention due to their good electrical conductivity and cost-effectiveness compared to metal oxides. MCs of S, Se, and Te to create binary constant crystalline structures utilized transition elements of VII to B IV merge with VI A group elements [8]. To enhance the catalytic activity of the MCs, different strategies have been explored such as rising active edge sites, constructing heterogeneous structures, doping heterogeneous atoms, and promoting electronic transmission [9]. The universal synthetic routes are summarized to synthesize MCs for improved electrocatalytic performance [10]. Figure 2 shows that several promising strategies are represented in the active and stable MC materials. The residual challenges in the research and growth of MCs and hopeful directions for upcoming research are also recapitulated.

The MCs can also be made into different heterostructures and nanocomposites, which can be applied in various electrochemical reactions such as fuel cells, sensors, lithium-ion batteries, light-emitting diodes, solar cells, thermoelectric devices, electrocatalysts, and supercapacitors as depicted in Fig. 3. In this section, we provide an overview of MCs for electro water splitting. First, we introduce current various types of synthesis methods for MC materials and their applications. In common, MCs can be synthesized through wet-chemical synthesis, solid-phase

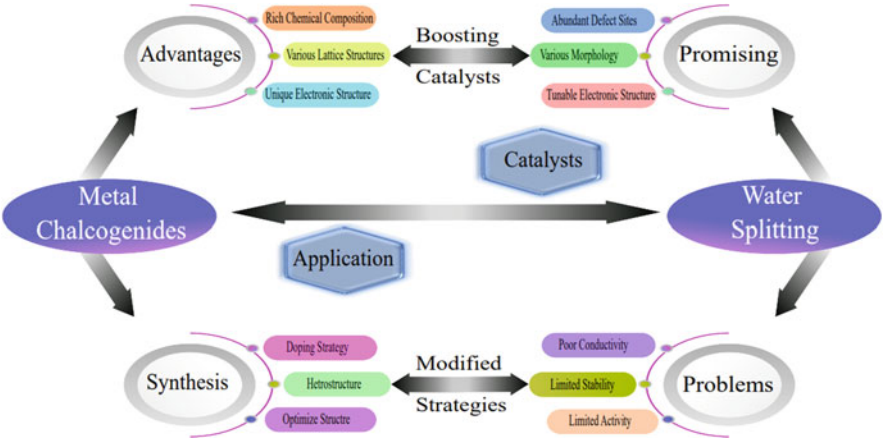

Fig. 2 The metal chalcogenides applied in water splitting [11]

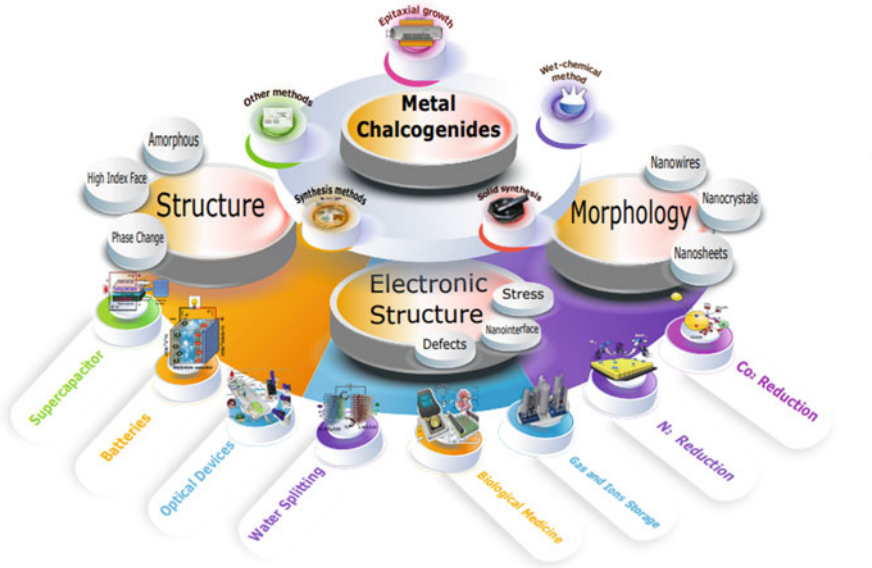

Fig. 3 Illustration of typical synthesis and application of metal chalcogenides [11]

chemical synthesis, and hydrothermal and chemical vapor deposition (CVD)-based epitaxial growth methods. Then we discuss various strategies employed to tune the morphology, crystal facets, crystallinity, phase, and heterostructures of MCs and their impact on water splitting performance. Lastly, we signify the faces in the research and improvement of MCs as the water splitting electrocatalysts and our viewpoints on the future directions to solve the energy-related problems.

2.1 Cobalt Sulfides (CoS) Electrocatalyst for OER

In the last few years, cobalt sulfide has attracted huge interest, owing to its applications in various fields like electrocatalysts, supercapacitors, alkaline rechargeable batteries, lithium-ion batteries, and magnetic materials [12–14]. However, due to the complicated phase diagram, controlled preparation of cobalt sulfide with high purity is very challenging. This may be owing to numerous chemical forms (CoS, $Co_{1x}S$, Co_9S_8, Co_3S_4, and CoS_2), and it can quickly change from one phase to another. Therefore, various synthetic methods have been used to deal with these parameters and synthesize high-purity cobalt sulfide nanostructures.

Liu and co-workers [15] revealed that electrodeposited CoS nanosheet films on Ti mesh illustrate high OER activity (Fig. 4). Figure 4a shows the SEM images of Ti mesh and CoS/Ti nanosheet films grown on Ti mesh. The CoS/Ti nanosheets require an overpotential of 361 mV to achieve 10 mA cm^{-2} and demonstrated

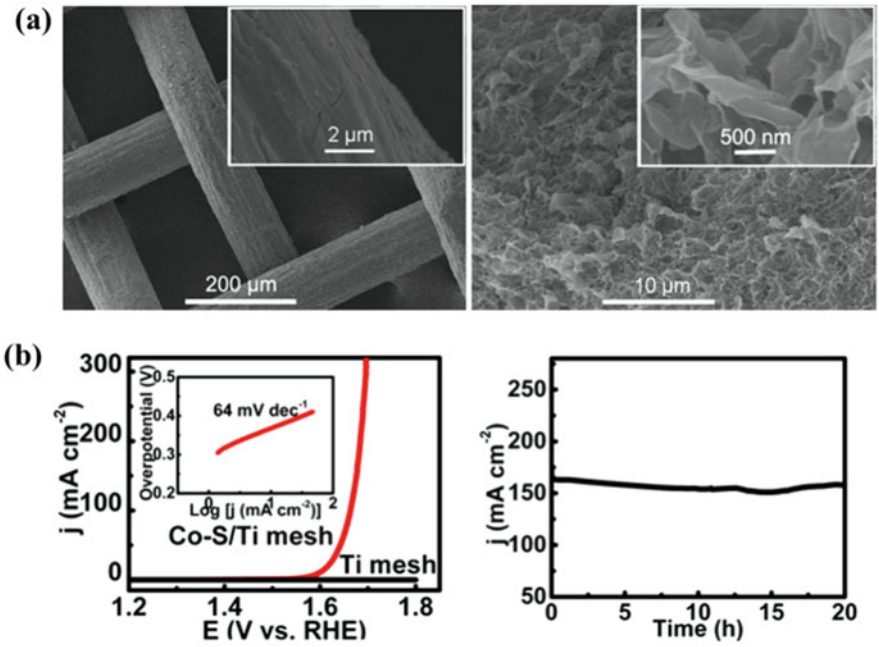

Fig. 4 (**a**) SEM images of Ti Mesh and CoS/Ti mesh nanosheets and (**b**) the OER polarization curves and time-dependent current density curves for 20 h of CoS/Ti mesh nanosheets [15]. (Copyright, 2015, Elsevier)

stable performance for 20 h as shown in Fig. 4b. The low overpotential and stable performance of CoS/Ti nanosheets suggest the ideal candidate for water oxidation (OER). The good electrocatalytic performance and durability, along with the simple and scalable fabrication procedure, of this architecture propose us useful features like a low-cost electrode for water splitting applications.

2.2 Molybdenum Disulfide (MoS_2) Electrocatalyst for HER

MoS_2 has received much attention in the last decade because of its unique physicochemical characteristics and applications in various fields such as catalysis, hydrogen storage, capacitors, batteries, and lubricants [16]. In addition, MoS_2 has been extensively used as an industrial catalyst for the sulfurization of petroleum and hence received particular attention as a catalyst [17].

Kibsgaard et al. [18] reported that the edge structure of MoS_2 nanoparticles could efficiently accelerate the HER process. A vast assortment of methods has been developed to improve the catalytic activity of MoS_2, centering mainly on the surface morphology, and electronic conductivity. Sun et al. [19] demonstrated that

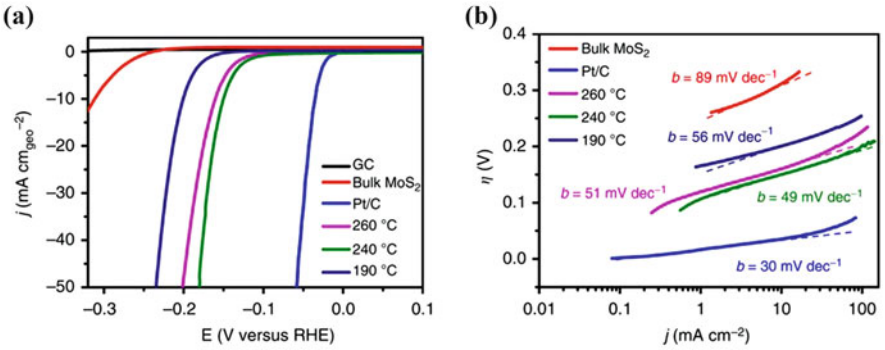

Fig. 5 (**a**) HER curves on bare glassy carbon electrode at 5 mV $s^{-1}$and MoS_2 synthesized from various temperatures and (**b**) Tafel slopes of MoS_2 and Pt/C catalyst from HER curves [20]. (Copyright, 2015, Nature Research)

Mn and N Co-doping optimized the electronic structure and allowed H adsorption and desorption, thereby increasing the HER performance of MoS_2 S-edge. In this study, a colloidal MoS_2 nanostructure and interlayer-expanded characteristics show increased HER activity and stability in acidic media. All the experimental work was carried out in Ar saturated 0.5 M H_2SO_4 solution. A superior catalytic activity with low overpotential of 103 mV and 49 mV dec^{-1} Tafel slope is attained as shown in Fig. 5a, b [20]. Furthermore, the advantage of an edge-completed structure, an interlayer extension, can enhance the electrical conductivity of the MoS_2 resulting in superior catalytic activity. This work indicates the scope of inexpensive and resourceful HER activity by transforming the interlayer distance in a 2D layered material. The practical challenges remain to enhancing the catalytic activity and durability of MoS_2-based electrocatalysts. Besides the edge-terminated structure, the expanded interlayer distance with modified electronic structure is due to dependability for the electrocatalytic performance enhancement. Other strategies to contain MoS_2 with conductive materials by synergetic coupling effects or transition metal ions doping into MoS_2 to optimize its electrocatalytic sites at S-edges due to improve HER performance.

3 Binary Metal Sulfides

While numerous transition metal sulphides have been investigated as catalytic electrodes, binary metal sulphides are more desirable due to their higher active redox sites and greater thermal and mechanical stabilities [21]. As a result, the Kirkendall effect was used to prepare the majority of binary metal sulphide nanostructures [22]. The motion of the interface between two metals that happens as a result of the variation in diffusion rates of the metal atoms is also known as the Kirkendall effect.

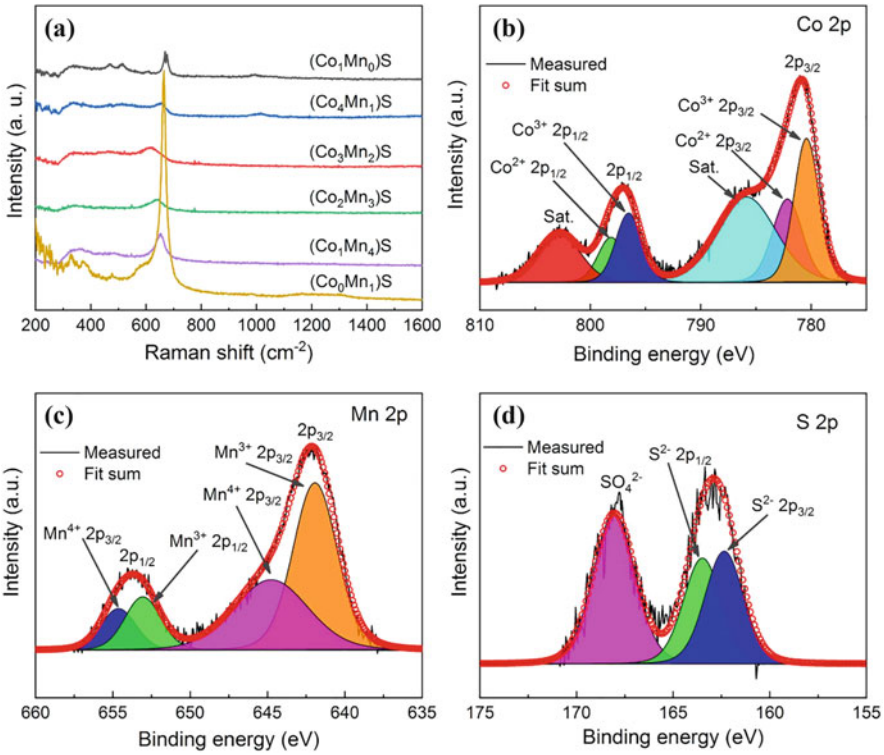

Fig. 6 (**a**) Raman spectra of $(Co_3Mn_2)S$ electrode catalysts. XPS spectra of (**b**) Co 2p, (**c**) Mn 2p, and (**d**) S 2p of $(Co_3Mn_2)S$ electrode catalyst [25]. (Copyright, 2021, Elsevier)

The result can be observed by incorporating insoluble indicators at the interface between a pure metal and alloy containing that metal and heating it to a temperature where atomic diffusion is feasible.

3.1 Manganese Cobalt Sulfides (MCS) Electrocatalyst for OER

MCS-based electrodes for electrocatalysts have received much attention in the last few years due to their eco-friendliness and strong redox characteristics. Recently, ultrathin mesoporous MCS nanosheets were electrodeposited on Ni foam and studied for OER application [23]. Zhang et al. [24] synthesized Ni–MnNPs@C, which showed high stability and better OER performance. The amorphous (Co-Mn)S electrodes fabricated using the SILAR method revealed nanosheet-like surface morphology beneficial for OER with good stability [25]. As shown in Fig. 6a, the chemical structure of (Co-Mn)S catalysts probed by Raman spectra consistent [26–28]. Chemical states of (Co-Mn)S electrodes were studied via XPS and are

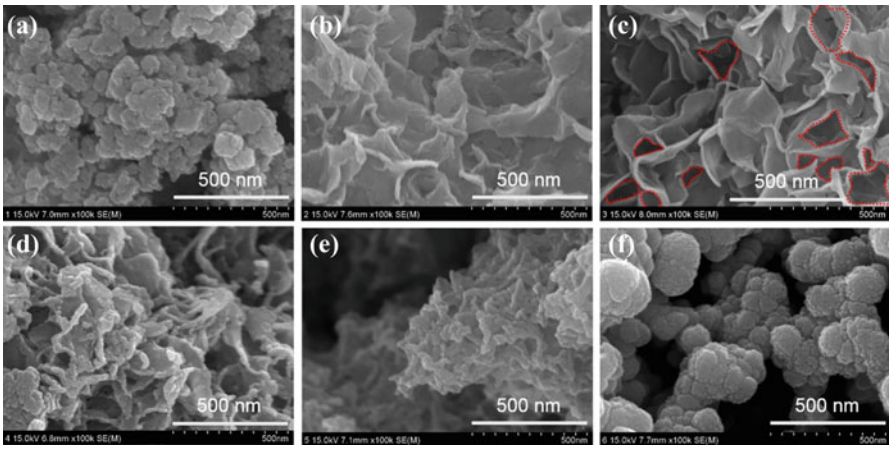

Fig. 7 FE-SEM images of $(Co_xMn_y)S$ electrode catalysts with various Co-Mn ratios, (**a**) $(Co_1Mn_0)S$, (**b**) $(Co_4Mn_1)S$, (**c**) $(Co_3Mn_2)S$, (**d**) $(Co_2Mn_3)S$, (**e**) $(Co_1Mn_4)S$, and (**f**) $(Co_0Mn_1)S$ at 100 k magnification [25]. (Copyright, 2021, Elsevier)

shown in Fig. 6b–d. The electrochemical activity of sulfide-based electrocatalysts is closely controlled by the redox chemical properties and valence states of comprising transition metal atoms. Consequently, to examine the oxidation states of elements present in amorphous (Co-Mn) electrocatalysts, it is clear that the different valence states of Co and Mn correspond to $(Co_3Mn_2)S$ catalyst, which could help to improve its OER performance [29, 30].

Figure 7a–f shows the morphology of (Co-Mn)S electrodes. The electrodes reveal a compact and nonporous structure (Fig. 7a, f). Further, ratios of dissimilarity of (Co-Mn)S catalyst change the chemical structure and transform the nature of electrodes. $(Co_3Mn_2)S$ electrode catalyst possesses open porous randomly interconnected nanosheets. As a result, many reaction sites at $(Co_3Mn_2)S$ offer superior electrocatalyst performance and higher OER activity [31].

(Co-Mn)S thin films deposited on SS substrates using the SILAR method showed stoichiometric composition adjustment and significant improvement in electrochemical OER activity by altered electronic structure, intermediates, and binding strength. Furthermore, modified nano-sheet surface morphology offered low overpotential at high current density. Figure 8a shows the polarization curves of $(Co_xMn_y)S$ electrocatalysts with various Co/Mn ratio (insert magnified view of iR-corrected). The binder-free deposition of $(Co_3Mn_2)S$ electrode showed low overpotential (243 mV) at 10 mA cm^{-2} current density as depicted in Fig. 8b. $(Co_3Mn_2)S$ electrode showed a low Tafel slope of 98 mV dec^{-1} for OER kinetics as compared to other electrodes (Fig. 8c). The experimentally measured and theoretically calculated oxygen evolution at an interval of 10 min for the $(Co_3Mn_2)S$ electrode is revealed in Fig. 8d. The $(Co_3Mn_2)S$ electrode demonstrates superior durability for 100 h with constant water oxidation. The (Co-Mn)S catalyst can be considered an excellent electrode for OER appliances due to its easy yet scalable preparation method and efficient OER performance. The overpotential and

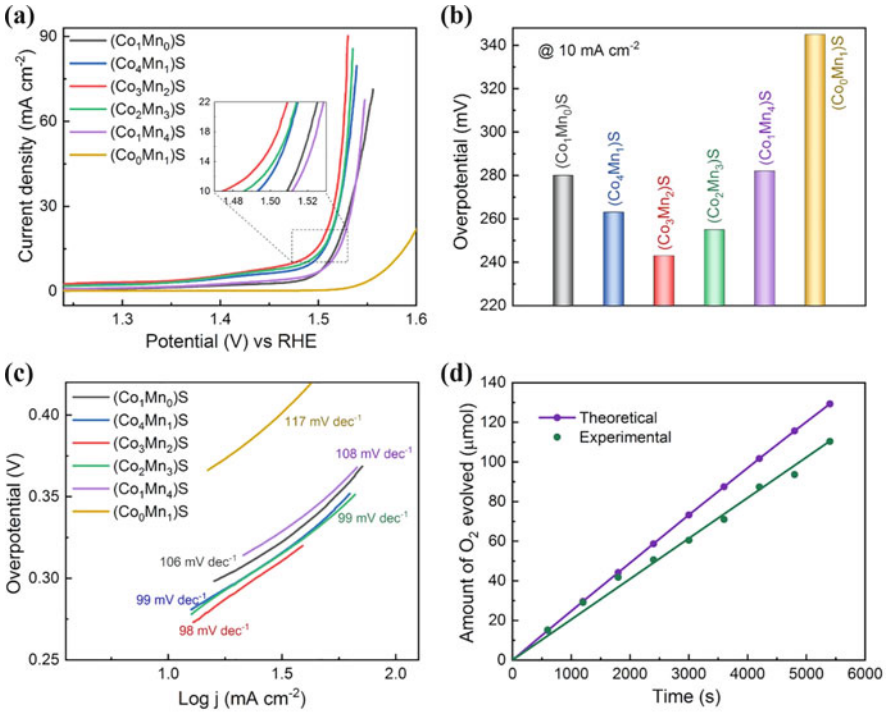

Fig. 8 (**a**) The LSV plots for $(Co_xMn_y)S$ electrodes (insert: magnified view of iR-corrected), (**b**) overpotential required at 10 mA cm^{-2} of $(Co_xMn_y)S$ catalyst, (**c**) Tafel plots of $(Co_xMn_y)S$ electrodes and various (Co-Mn) fractions, and (**d**) theoretically and experimentally measured O_2 gas versus time at a constant overpotential of 243 mV versus RHE [25]. (Copyright, 2021, Elsevier)

Tafel slope of $(Co_3Mn_2)S$ electrode compared with earlier reports on sulfide-based materials as illustrated in Table 1.

As given in Table 1, the OER activities of $(Co_3Mn_2)S$ catalysts showed low overpotential, low Tafel slope value, and excellent stability for OER application.

3.2 Molybdenum Disulfide/Conductive Polymer Polyaniline (MoS_2/PANI) Electrocatalyst for HER

Lukowski et al. [40] reported 187 mV overpotential at 10 mA cm^{-1} with a Tafel slope of 43 mV dec^{-1} for metallic nanosheets of MoS_2-PANI signifying increased HER activities. Zhang et al. [41] prepared 3D MoS_2 with PANI composite as an electrocatalyst. The SEM profile of MoS_2/PANI nanowires with uniform length and diameter is shown in Fig. 9a. The homogeneous and dense growth of MoS_2 nanosheets reveals excellent edge-rich sites in the vertical direction (insert of Fig.

Table 1 Comparative OER activities of $(Co_3Mn_2)S$ catalysts with previously reported works

Sr. no.	Catalyst	Methods	Electrolyte	Overpotential (η) (mV)	Stability (h)	Ref. No.
1.	$(Co_3Mn_2)S$	SILAR	1 M KOH	243	100	[25]
2.	Co-S/Ti mesh	Electrodeposition	1 M KOH	361	20	[32]
3.	Co_9S_8	Hydrothermal	1 M KOH	420	5	[33]
4.	CoS_2	Hydrothermal	1 M KOH	290	12	[34]
5.	Co_3S_4	Hydrothermal	1 M KOH	355	5000 cycles	[35]
6.	CoS	Solvent-less route	1 M KOH	325	18	[36]
7.	$NiCo_2S_4$	Hydrothermal sulfidation	1 M KOH	320	11	[37]
8.	$Co_xNi_{1-x}S_2$	Hydrothermal sulfurization	1 M KOH	290	10	[38]
9.	CoFeS	Solvothermal	1 M KOH	290	10	[39]

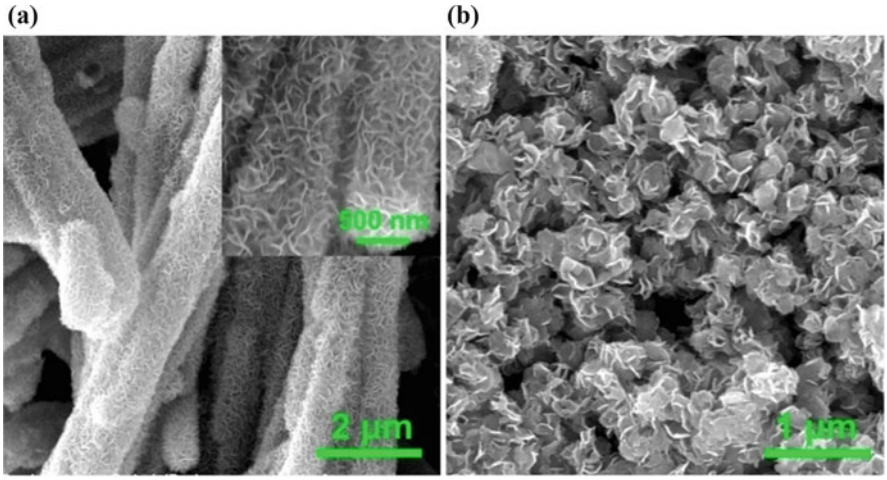

Fig. 9 (**a**) Surface morphology of MoS_2/PANI, insert shows elevated magnification and (**b**) SEM profile of MoS_2 [41]. (Copyright, 2015, Elsevier)

9a). Compared with the pure MoS_2 nanoclusters folding themselves with lots of active edges buried inside (Fig. 9b), the PANI exhibits stupendous active edges, thereby promoting higher electrochemical performance.

The polarization curve of Pt/C shows the higher HER electrocatalytic properties with a zero onset overpotential, while the PANI barely illustrates any HER performance (Fig. 10a, b). However, for MoS_2/PANI, superior HER activities were obtained with 100 mV and 45 mV dec^{-1} overpotential and Tafel slope, respectively. Figure 10c shows the Tafel slopes recorded with the linear regions fitted into the Tafel equation. MoS_2 with the composite percentage of 79.6 showed excellent performance as compared to other compositions of composite (62.6, 72.3, and 82.9%) (Fig. 10d). Herein, the MoS_2/PANI has achieved good stability over

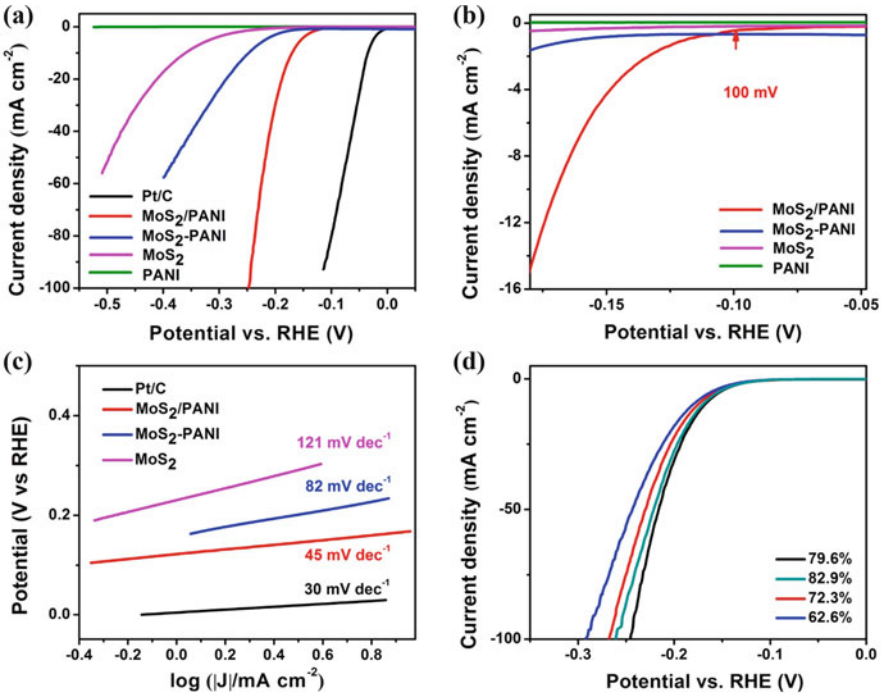

Fig. 10 (**a**) The HER curves, (**b**) the magnified version of HER plots, (**c**) Tafel graphs for Pt/C, MoS_2/PANI, MoS_2-PANI, and MoS_2 catalysts, and (**d**) various percentages of MoS_2 hybrid with MoS_2/PANI polarization plots [41]. (Copyright, 2015, Elsevier)

other MoS_2polymer-based HER electrocatalyst. The superior HER electrocatalytic performance of MoS_2/PANI confirmed the successful application of PANI in HER catalyst.

4 Transition Metal Selenides

Selenide-based MCs for electrochemical water splitting will be discussed in this section. Selenideis in the VI-A group and has an equal oxidation number as sulfur [42]. Therefore, metal selenides are expected to deliver similar electrochemical performance as that of metal sulfides.

4.1 Nickel Selenide for HER/OER Electrocatalyst

NiSe has gained significant attention in recent years due to its multiple oxidation states with tunable electronic properties [43, 44]. Swesi et al. [45] prepared Ni_3Se_2

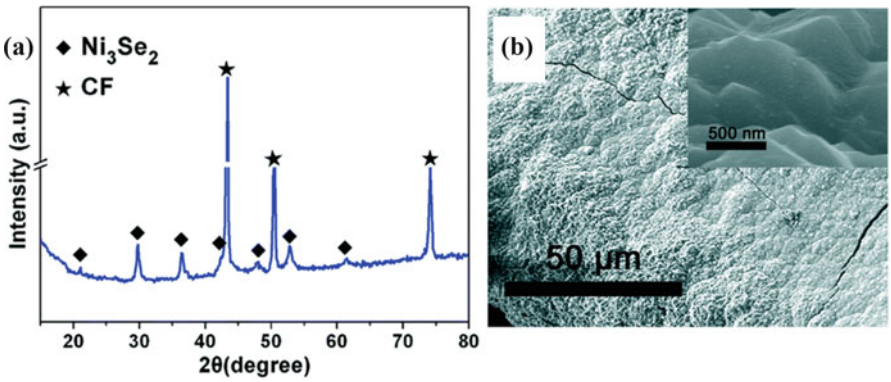

Fig. 11 (**a**) XRD diffraction analysis of Ni_3Se_2/CFand (**b**) SEM images of Ni_3Se_2/CF (Inset shows high-magnifications) [45]. (Copyright, 2015, Royal Society of Chemistry)

and showed the best OER and HER catalytic performance in alkaline conditions. The required 290 mV overpotential for 10 mA cm^{-2} signifies that this catalyst is efficient when compared with the oxide-based catalysts. The catalytic capability of Ni_3Se_2 was enhanced during the alteration of the Se-deficient phase in Ni_3Se_2. Furthermore, the electrodeposited Ni_3Se_2/CF on Cu foam as a bifunctional catalyst for OER and HER has exceptional stability. The XRD diffraction analysis as shown in Fig. 11a confirms the formation of trigonal Ni_3Se_2/CF. The smooth, compact, and homogeneous surface morphology of Ni_3Se_2/CF electrode is shown in Fig. 11b.

The HER catalytic activity of Ni_3Se_2/CF was investigated in a 1 M alkaline electrolyte with a three-electrode cell configuration. The polarization curve of Ni_3Se_2/CF (Ni_3Se_2 loading mass 3.0 mg cm^{-2}) is shown in Fig. 12a. The Ni_3Se_2/CF shows an efficient HER performance with a low overpotential (Fig. 12b), and it only needs 100 mV to reach 10 mA cm^{-2}. As predictable, the Pt/C shows superior HER activity, while bare CF reveals poor HER performance. The Tafel values of 98 and 63 mv dec^{-1} were for the Ni_3Se_2/CF and Pt/C catalysts, respectively (Fig. 12c). The low Tafel slope implies a rapid improvement in the HER kinetics. The time-dependent electrocatalytic durability for HER in 1 M KOH is presented in Fig. 12d. The results clearly show that Ni_3Se_2/CF is an appropriate electrode for the large-scale hydrogen production in alkaline electrolytes.

The OER catalytic properties of Ni_3Se_2/CF are being investigated in the 1 M KOH electrolyte. Figure 13a shows LSV curves of Ni_3Se_2/CF measured at 5 mV s^{-1} scan rate in the ambient atmosphere. The low onset potential of 1.51 V versus RHE for Ni_3Se_2/CF electrode is comparable to the value of 1.47 V versus RHE for RuO_2 (left panel of Fig. 13b). Also, at 50 mA cm^{-2}, the required potential for Ni_3Se_2/CF electrode is 1.57 V and 1.54 V for RuO_2 (right panel of Fig. 13b). The equivalent Tafel slope for Ni_3Se_2/CF (80 mV dec^{-1}) is close to the value of RuO_2 (72 mV dec^{-1}), signifying that Ni_3Se_2/CF is more active for OER as shown in Fig. 13c. The time-dependent chronoamperometric durability test of Ni_3Se_2/CF

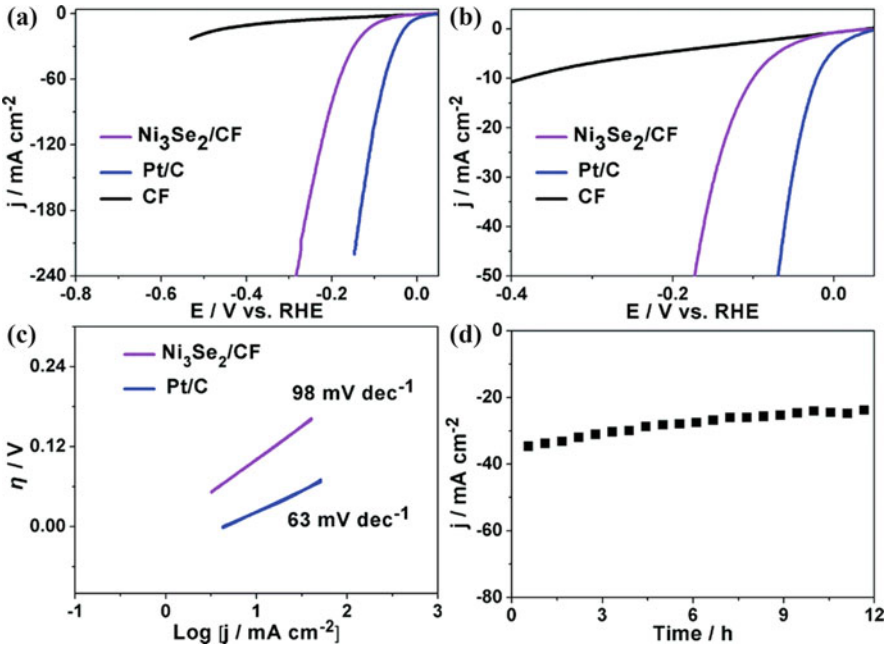

Fig. 12 (**a**) HER plots of CF, Pt/C and Ni_3Se_2/CF at5 mV s^{-1}, (**b**) high magnification of HER plots, (**c**) Tafel slopes for Pt/C and Ni_3Se_2/CF, and (**d**) stability for 12 h of 135 mV static overpotential for Ni_3Se_2/CF [45]. (Copyright, 2015, Royal Society of Chemistry)

electrode for 10 h (Fig. 13d) showed its bifunctional catalytic activity for both H_2 and O_2 evolution reactions. Thus, the above result certainly reveals the superior electrocatalytic performance of the Ni_3Se_2/CF electrode for practical applications.

4.2 Cobalt Selenide (CoSe) for HER/OER Electrocatalyst

Recently, CoSe has emerged as a suitable material for electrocatalysis due to its unique electrical and chemical properties. A multiplicity of these composites contains CoSe, $CoSe_2$, Co_3Se_4, Co_2Se_3, and $Co_{0.85}Se$ [46], prepared by different synthesis methods. Several results for CoSe and their composites in electrocatalyst OER and HER have been discussed in this section.

The OER catalytic performance of amorphous CoSe films electrodeposited on a Ti mesh (a-CoSe/Ti) increases dramatically beyond 1.54 V versus RHE. Figure 14a shows that a-CoSe/Ti electrode exhibits a low overpotential of 292 mV at 10 mA cm^{-2} in 1 M KOH solution. Figure 14b shows that the Tafel slope of a-CoSe/Ti of (69 mV dec^{-1}) is lower than that of RuO_2 (86 mV dec^{-1}) electrode, implying more helpful OER kinetics of the a-CoSe/Ti. Figure 14c shows that the

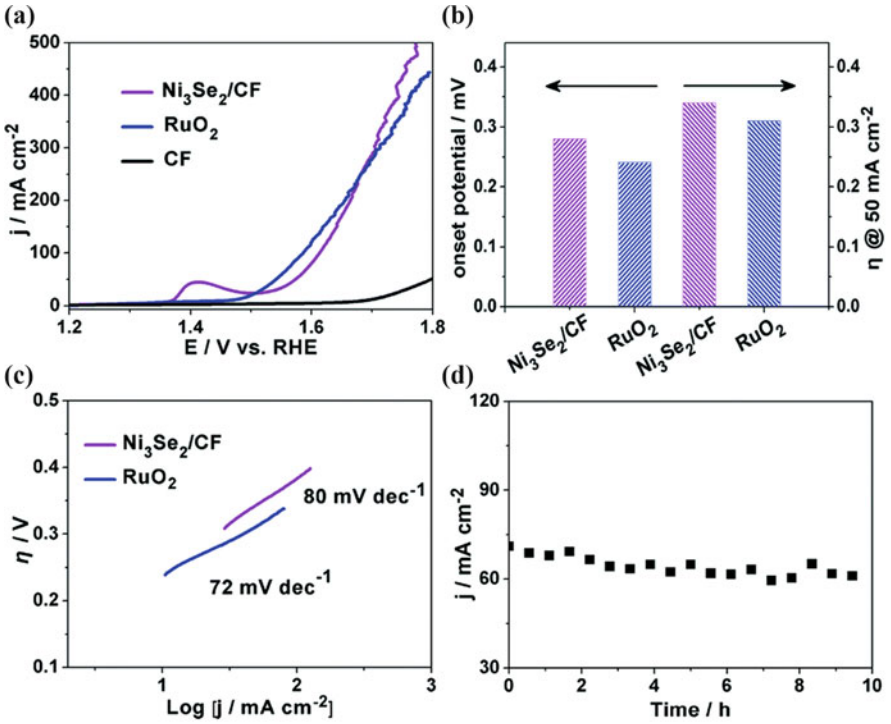

Fig. 13 (**a**) The LSV curves for CF, RuO_2 and Ni_3Se_2/CF at 5 mV s^{-1}, (**b**) plot of onset potentials (left) with overpotentials (right) at 50 mA cm^{-2} versus of Ni_3Se_2/CF electrocatalysts, (**c**) Tafel slopes of RuO_2 and Ni_3Se_2/CF electrodes, and (**d**) static curve of 10 h stability for Ni_3Se_2/CF at 70 mA cm^{-2} [45]. (Copyright, 2015, Royal Society of Chemistry)

as-prepared catalyst has superior durability with a small anodic current loss after 1000 cycles. These results illustrate the superior long-life chronoamperometric durability of 27 h for a-CoSe/Ti OER catalysts depicted in Fig. 14d.

The HER activity for a-CoSe/Ti, Pt/C, and Ti mesh were carried out in 1 M KOH electrolyte. The polarization curves of Pt/C reveal superior performance, and Ti mesh has poor performance as depicted in Fig. 15a. The a-CoSe/Ti required overpotential of 121 mV at 10 mA cm^{-2} signifies the superior HER activity of the catalysts. As shown in Fig. 15b, the Tafel slope of a-CoSe/Ti (84 mV dec^{-1}) suggests the HER occurs through a Volmer-Heyrosky mechanism. Figure 15c shows that the a-CoSe/Ti catalyst illustrates a slight decay after 1000 cycles for the HER. Time-dependent chronoamperometric stability of 27 h for CoSe/Ti with an overpotential of 145 mV shows its superior electrocatalytic activity (Fig. 15d). Ti mesh as a substrate for a catalyst has the obvious advantages of inexpensive, superior electric conductivity, poor electrochemical activity, and the ability to load more electrocatalyst than predictable electrodes. This amorphous a-CoSe/Ti electrode has an efficient bifunctional water splitting catalyst with superior durability in alkaline

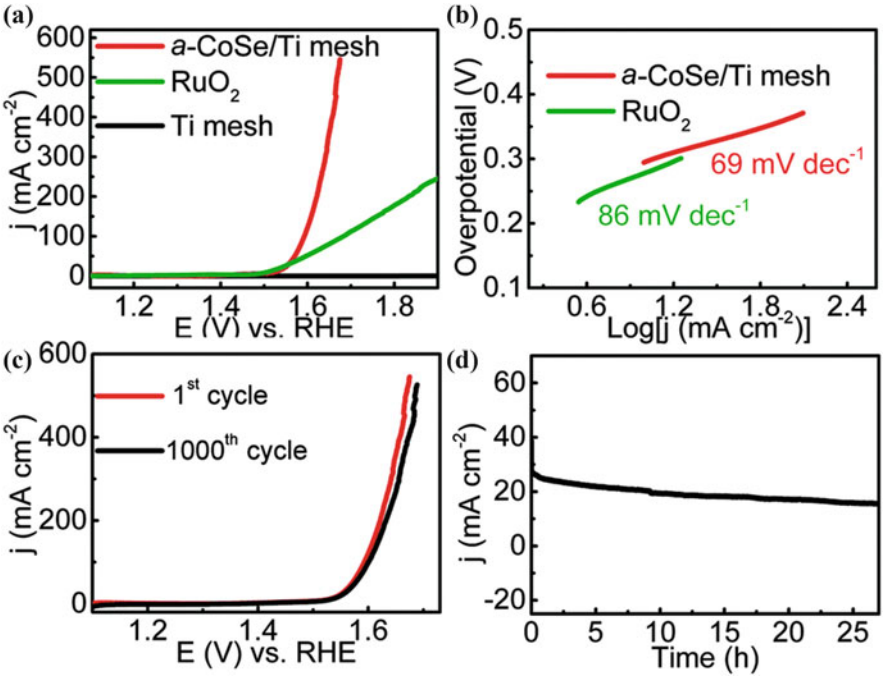

Fig. 14 (**a**) LSV plots for Ti mesh, $RuO_2$and a-CoSe/Ti catalyst at 5 mV s^{-1}, (**b**) Tafel slopes of RuO_2 and a-CoSe/Ti, (**c**) initial and after 1000 cycles examined LSV plots for a-CoSe/Ti, and (**d**) 155 mV static overpotential stability of 27 h for a-CoSe/Tisample [47]. (Copyright, 2015, Royal Society of Chemistry)

electrolytes. This as-prepared sample result of the critical defect concentration could lead to the exposure of considerably enhanced active sites, thus offering good electrochemical activities for water splitting applications.

5 Binary Metal Chalcogenides

Binary metal chalcogenides show huge potential for electrochemical activities. However, the reports based on their use as an electrocatalyst are very limited.

5.1 Te/FeNiOOH-NCs for Highly Efficient Overall Water Splitting

The improvement of efficient and stable non-noble nanomaterials as bifunctional HER/OER catalysts has the benefits of an easier electrolyzer procedure and

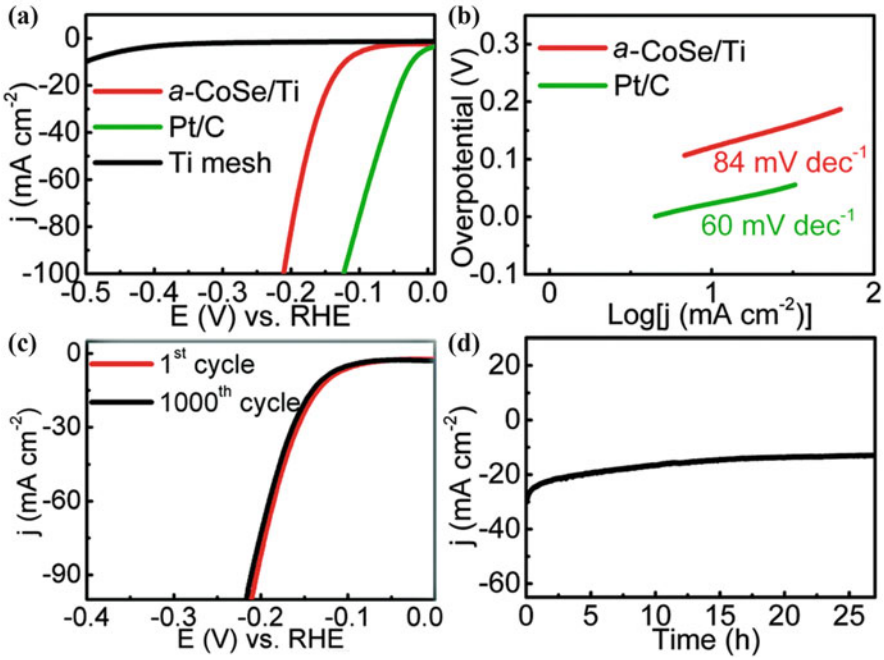

Fig. 15 (**a**) HER plots for Ti mesh, RuO_2 and a-CoSe/Ti electrodes at 5 mV s^{-1}, (**b**) Tafel curves of Pt/C and a-CoSe/Ti electrodes, (**c**) initial and after 1000 cycles examined LSV plots for a-CoSe/Ti, and (**d**) 145 mV static overpotential stability of 27 h for a-CoSe/Ti [47]. (Copyright, 2015, Royal Society of Chemistry)

dropping cost. The hydrothermally synthesized novel Te/FeNiOOH-NC cluster nanocubes as a highly active and durable catalyst show the best bifunctional electrocatalytic properties of both HER and OER in alkaline solution. OER catalytic performance of Te/FeNiOOH-NCs electrode was studied in the potential range from 1.23 to 1.8 V in 1 M KOH, and resultant LSV plots are revealed in (Fig. 16a). The lower Tafel slope value of the Te/FeNiOOH-NC catalyst (52 mV dec^{-1}) than other catalysts illustrates a good electron transfer rate and accelerated reaction kinetics of the Te/FeNiOOH-NC OER catalyst (Fig. 16b).

The bifunctional activity of the Te/FeNiOOH-NCs electrode was further studied. The Te/FeNiOOH-NCs were used as the cathode and anode (symmetric electrode configuration). The electrode obtained a cell voltage of 1.65 V at 10 mA cm^{-2} current density in 1 M KOH with continuous gas evolution on both electrodes (Fig. 17a) (inset reveals profile of water electrolysis). Furthermore, the electrode exhibited a long-life cyclic stability with negligible loss of 0.3% after 20 h electrolysis (Fig. 17b). It showed that the Te/FeNiOOH-NC-based catalyst has superior performance and durability than the Pt/C and IrO_2-based catalysts.

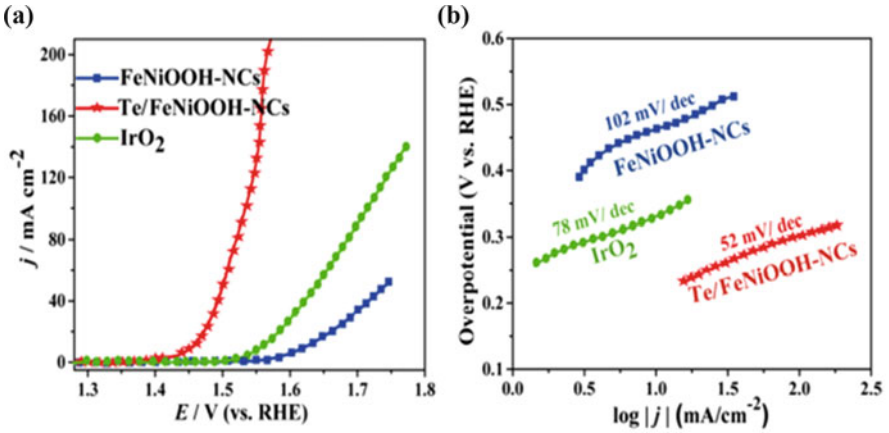

Fig. 16 (**a**) The iR corrected OER polarization curves at 10 mV s^{-1} scan rate, and (**b**) Tafel graphs of FeNiOOH-NCs, IrO_2, and Te/FeNiOOH-NCs catalysts [48]. (Copyright, 2018, American Chemical Society)

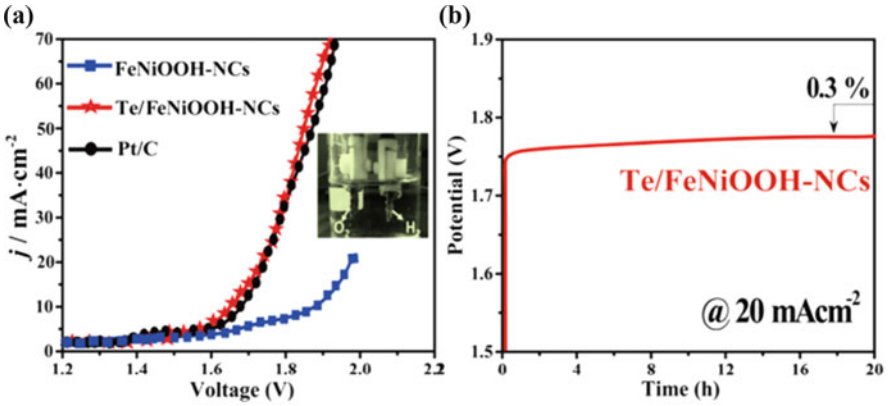

Fig. 17 (**a**) Polarization curve of Pt/C, Te/FeNiOOH-NCs, and FeNiOOH-NCs at 5 mV s^{-1} for water splitting device (Inset reveals profile of water electrolysis), and (**b**) chronoamperometric durability for 20 h at 20 mA cm^{-2} of Te/FeNiOOH-NC catalysts [48]. (Copyright, 2018, American Chemical Society)

5.2 Se-(NiCo)Sx/(OH)x Electrode for Electrocatalyst

Reports showed that $(Mo_{1-x})S_2$ coats could produce vacancies, edges, energy barriers, and point defects for increased HER activities [49]. Wang and coworkers [50] prepared $Co(S_xSe_{1-x})_2$ and revealed high HER and OER activities as compared to $CoSe_2$ and CoS_2 due to their high surface area and enhanced electron conductivity.

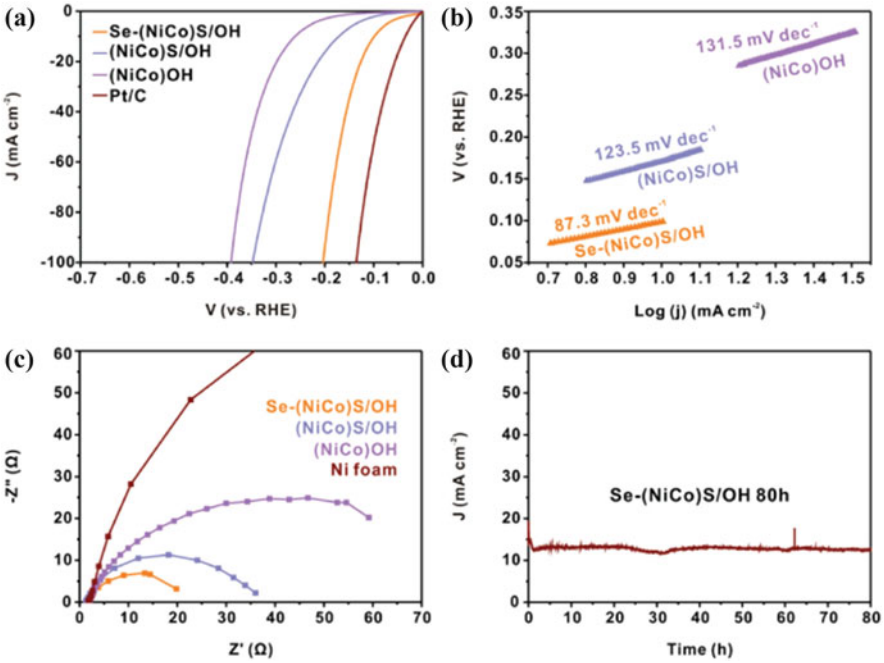

Fig. 18 (**a**) The HER plots, (**b**) Tafel graphs of Se-(NiCo)S/OH, (NiCo)S/OH, and (NiCo)OH, (**c**) Nyquiest graphs of nickel foam, (NiCo)OH,(NiCo)S/OH, and Se-(NiCo)S/OH electrodes, and (**d**) chronoamperometric stability for 80 h of Se-(NiCo)S/OH in 1 M KOH media [51]. (Copyright, 2018, Wiley, Wiley-VCH)

The electrocatalytic HER performance of Se-(NiCo)S/OH nanosheets was examined using polarization curves in 1 M KOH alkaline electrolyte (Fig. 18a). The HER curves of Se-(NiCo)S/OH nanosheets revealed a low overpotential of 103 mV at 10 mA cm^{-2} than that of (NiCo)S/OH, (NiCo)OH catalyst. The Tafel slope was 87.3 mV dec^{-1}, which is lower than that of other catalysts as shown in Fig. 18b. The initial adsorption of H_2O molecules was crucial for the subsequence process. The abundant defects and disorders might promote the adsorption of H_2O molecules and enhance the HER performance of the Se-(NiCo)S/OH catalyst. Figure 18c shows the EIS study carried out to gain further insight into the catalytic HER procedure. The Nyquist graphs depicted that Se-(NiCo)S/OH possessed rapid charge transfer capability. The durability test of Se-(NiCo)S/OH nanosheets showed no noticeable degradation after 80 h at 10 mA cm^{-2} current density (Fig. 18d).

The electrocatalytic OER performance of Se-(NiCo)S/OH nanosheets catalyst was invesigated in 1 M KOH solution. The Se-(NiCo)S/OH nanosheets at 10 mA cm^{-2} current density demonstrated a low overpotential of 155 mV than the (NiCo)S/OH,(NiCo)OH, RuO_2, and Ni foam catalysts (Fig. 19a). These results also showed the highly capable activity of Se-(NiCo)S/OH as an OER electrocatalyst. Further, the low Tafel slope of 33.9 mV dec^{-1}, which is lower than that of other

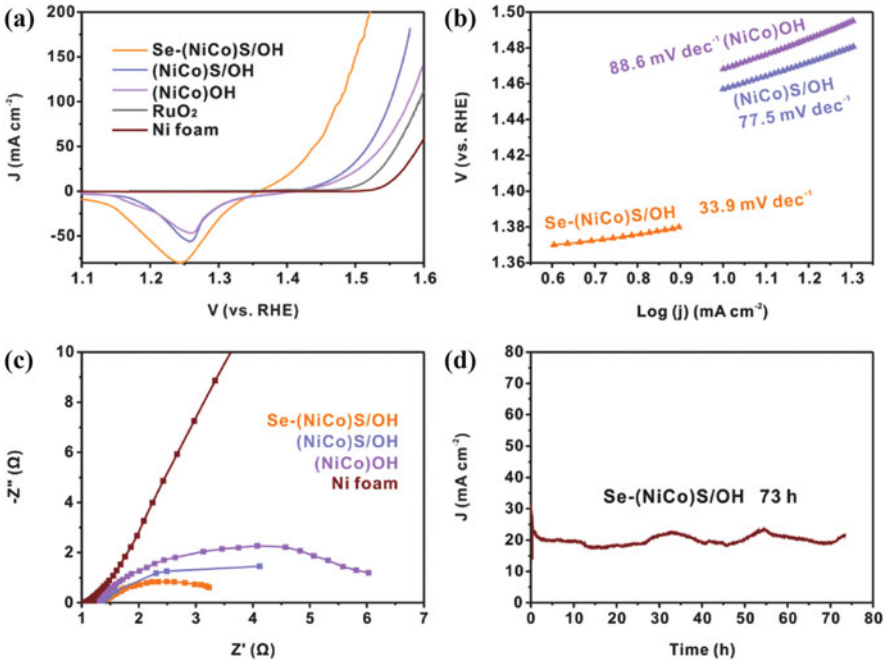

Fig. 19 (**a**) The LSV plots, (**b**) Tafel slopes (NiCo)OH, (NiCo)S/OH, and Se-(NiCo)S/OH electrodes, (**c**) Nyquist plots of nickel foam, (NiCo)OH, (NiCo)S/OH, and Se-(NiCo)S/OH electrodes, and (**d**) chronoamperometric durability of Se-(NiCo)S/OH [51]. (Copyright, 2018, Wiley, Wiley-VCH)

catalysts is shown in Fig. 19b, implies much fast OER kinetics for Se-(NiCo)S/OH nanosheets. Usually, it has been proposed that OH^- was primarily adsorbed on the surface of electrocatalysts during the catalytic OER. This fast process could be shown by the EIS test as revealed in Fig. 19c. While the total resistance of Se-(NiCo)S/OH is higher than the other catalysts, the charge transfer resistance was much lower than (NiCo)S/OH and (NiCo)OH catalysts. The electrocatalytic OER stability of Se-(NiCo)S/OH was conducted at 20 mA cm^{-2} in a 1 M KOH solution. Figure 19d shows that the Se-(NiCo)S/OH nanosheets retained stable OER activity with no obvious degradation for about 73 h.

The superior HER and OER activities of Se-(NiCo)S/OH anode and cathode electrode with fabricated water splitting device Fig. 20a show that the overall water splitting device required a low overpotential of 1.6 V at 10 mA cm^{-2} current density. Inset of Fig. 20a shows an optical image illustrating the production of H_2 and O_2 on the surface of Se-(NiCo)S/OH. The long-life electrochemical durability of 66 h for Se-(NiCo)S/OH electrode is shown in Fig. 20b. Also, the overall water splitting at 10 mA cm^{-2} current density for 66 h shows no degradation. The Se-(NiCo)S/OH nanosheets have extensive appliances in electrocatalysis, batteries, and supercapacitors of and would be worthy of further research in electrochemistry.

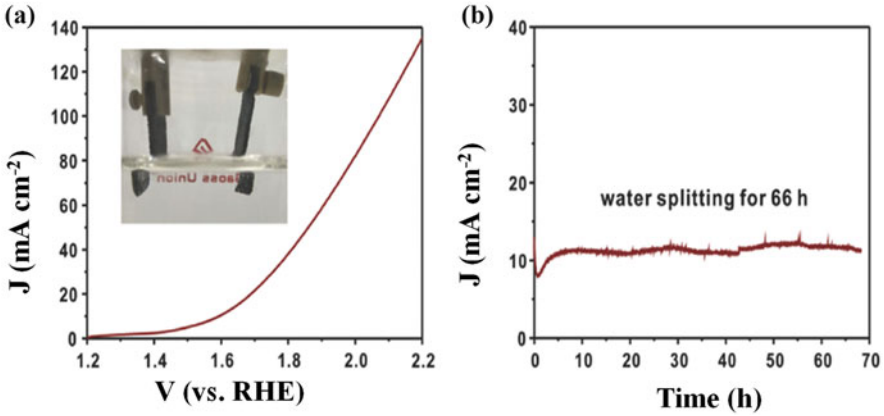

Fig. 20 (**a**) The LSV plot of water electrolysis as both OER and HER electrocatalytic in two-electrode cells. (Insert optical image illustrating the production of H_2 and O_2 evolve on surface of electrode), and (**b**) chronoamperometric stability for Se-(NiCo)S/OH [51]. (Copyright, 2018, Wiley, Wiley-VCH)

Table 2 Comparison of Se-(NiCo)S/OH electrode with previously reported electrocatalysts for overall water splitting

Sr. no.	Catalyst	Electrolyte	HER Overpotential (η) (mV)	OER Overpotential (η) (mV)	Overpotential (η) (mV)	Stability	Ref. No.
1.	Co_1Mn_1CH/NF	1 M KOH	184	294	1.68	14	[52]
2.	CoMnO@CN	1 M KOH	71	230	1.5	10	[53]
3.	Co_9S_8@NOSC	1 M KOH	320	340	1.74	10	[54]
4.	N-Ni_3S_2/N	1 M KOH	110	310	1.48	8	[55]
5.	Ni_5P_4	1 M KOH	150	300	1.7	20	[56]
6.	CoP NWs	1 M KOH	244	300	1.56	1000	[57]
7.	FeB_2 NPs	1 M KOH	61	296	1.57	24	[58]
8.	Co-B@CoO	1 M KOH	102	290	1.67	20	[59]
9.	Ni/Mo_2C-PC	1 M KOH	179	368	1.66	10	[60]
10.	NiCoFeLTHs/CFC	1 M KOH	200	239	1.55	19	[61]
11.	Ni_3S_2/NF	1 M KOH	170	260	1.76	150	[62]

The OER and HER performance of Se-(NiCo)S/OH electrode are compared with previously reported electrocatalysts for overall water splitting as shown in Table 2.

As given in Table 2, the OER activities of Se-(NiCo)S/OH catalysts showed low overpotential, Tafel slope and excellent stability representing a promising candidate for OER application.

6 Conclusions

This chapter describes a summary of the MCs, nanomaterials as new emerging electrocatalysts that have received huge attention in the field of electrocatalysis for HER, OER, and full water splitting. Due to its superior electrocatalytic activity, easily regulated structure, high electrical transport, large-scale synthesis, and predictability to replace noble metals. In outline, different types of MC electrodes with various overpotential values show different HER and OER performances. For HER, the required overpotential of 100 mV for Ni_3Se_2/CF catalyst while for OER, an overpotential of 135 mV is required for a-CoSe/Ti mesh catalyst to achieve at 10 mA cm^{-2} in 1 M KOH electrolyte, signifying superior performance for electro water splitting of MCs. Furthermore, improving earth-abundant and inexpensive resources using a simple preparation approach is necessary for extensive appliances. Additionally, various metal chalcogenide-based devices should be developed.

References

1. M. Khan, H. Zhao, W. Zou, Z. Chen, W. Cao, J. Fang, J. Xu, L. Zhang, J. Zhang, Recent progresses in electrocatalysts for water electrolysis. Energy Rev. **1**, 483–530 (2018). https://doi.org/10.1007/s41918-018-0014-z
2. A. Li, Y. Sun, T. Yao, H. Han, Earth-abundant transition-metal-based electrocatalysts for water electrolysis to produce renewable hydrogen. Chem. Eur. J. **24**, 18334–18355 (2018). https://doi.org/10.1002/chem.201803749
3. M. Kumar, P. Murugesan, S. Vivek, S. Ravichandran, $NiWO_3$ nanoparticles grown on graphitic carbon nitride (g-C_3N_4) supported on carbon as an efficient bifunctional electrocatalyst for oxygen and hydrogen evolution reactions. Part. Part. Syst. Charact. **34**, 1700043–1700053 (2017). https://doi.org/10.1002/ppsc.201700043
4. M. Arif, G. Yasin, M. Shakeel, M. Mushtaq, W. Ye, X. Fang, S. Ji, D. Yan, Hierarchical Co-Fe-layered double hydroxide and g-C_3N_4 heterostructures with enhanced bifunctional photo/electrocatalytic activity towards overall water splitting. Mater. Chem. Front. **3**, 520–531 (2019). https://doi.org/10.1039/C8QM00677F
5. T. Bhowmik, M. Kundu, S. Barman, Co-Fe-layered double hydroxide supported on graphitic carbon nitrides: An efficient and durable bi-functional electro-catalyst for oxygen evolution and hydrogen evolution reactions. ACS Appl. Energy Mater. **1**, 1200–1209 (2018). https://doi.org/10.1021/acsaem.7b00305
6. J. Gunjakar, B. Hou, A. Inamdar, S. Pawar, A. Ahmed, H. Chavan, J. Kim, S. Cho, S. Lee, Y. Jo, S. Hwang, Two-dimensional layered hydroxide nanoporous nanohybrids pillared with zero-dimensional polyoxovanadate nanoclusters for enhanced water oxidation catalysis. Small **14**, 1703481–1703491 (2018). https://doi.org/10.1002/smll.201703481
7. X. Zou, Z. Yu, Noble metal-free hydrogen evolution catalysts for water splitting. Chem. Soc. Rev. **44**, 5148–5180 (2015). https://doi.org/10.1039/C4CS00448E
8. P. Simon, Y. Gogotsi, Materials for electrochemical capacitors. Nat. Mater. **7**, 845–854 (2008). https://doi.org/10.1142/9789814287005_0033
9. G. Wang, L. Zhang, J. Zhang, A review of electrode materials for electrochemical supercapacitors. Chem. Soc. Rev. **41**, 797–828 (2012). https://doi.org/10.1039/C1CS15060J
10. R. Kötz, M. Carlen, Principles and applications of electrochemical capacitors. Electrochim. Acta **45**, 2483–2498 (2000). https://doi.org/10.1016/S0013-4686(00)00354-6

11. J. Yin, J. Jin, H. Lin, Z. Yin, J. Li, M. Lu, L. Guo, P. Xi, Y. Tang, C. Yan, Optimized metal chalcogenides for boosting water splitting. Adv. Sci. **7**, 1903070–1903097 (2020). https://doi.org/10.1002/advs.201903070
12. M. Otero-Leal, F. Rivadulla, J. Rivas, The magnetic phase transition of $CoS_{2-x}Se_x$. IEEE Trans. Magn. **44**, 4503–4505 (2008). https://doi.org/10.1109/TMAG.2008.2003239
13. M. Sadjadi, A. Pourahmad, S. Sohrabnezhad, K. Zare, Formation of NiS and CoS semiconductor nanoparticles inside mordenite-type zeolite. Mater. Lett. **61**, 2923–2926 (2007). https://doi.org/10.1016/j.matlet.2006.10.067
14. H. Behret, H. Binder, G. Sandstede, Electrocatalytic oxygen reduction with thiospinels and other sulphides of transition metals. Electrochim. Acta **20**, 111–117 (1975). https://doi.org/10.1016/0013-4686(75)90047-X
15. T. Liu, Y. Liang, Q. Liu, X. Sun, Y. He, A. Asiri, Electrodeposition of cobal tsulfide nanosheets film as an efficient electrocatalyst for oxygen evolution reaction. Electrochem. Commun. **60**, 92–96 (2015). https://doi.org/10.1016/j.elecom.2015.08.011
16. S. Ding, J. Chen, X. Lou, Glucose-assisted growth of MoS_2 nanosheets on CNT backbone for improved lithium storage properties. Chem. Eur. J. **17**, 13142–13145 (2011). https://doi.org/10.1002/chem.201102480
17. T. Jaramillo, K. Jørgensen, J. Bonde, J. Nielsen, S. Horch, I. Chorkendorff, Identification of active edge sites for electrochemical H_2 evolution from MoS_2 nanocatalysts. Science **317**, 100–102 (2007). https://doi.org/10.1126/science.1141483
18. J. Kibsgaard, Z. Chen, B. Reinecke, T. Jaramillo, Engineering the surface structure of MoS_2 to preferentially expose active edge sites for electrocatalysis. Nat. Mater. **11**, 963–969 (2012). https://doi.org/10.1038/nmat3439
19. T. Sun, J. Wang, X. Chi, Y. Lin, Z. Chen, X. Ling, C. Qiu, Y. Xu, L. Song, C. Su, Engineering the electronic structure of MoS_2 nanorods by N and Mn dopants for ultra-efficient hydrogen production. ACS Catal. **8**, 7585–7592 (2018). https://doi.org/10.1021/acscatal.8b00783
20. M. Gao, M. Chan, Y. Sun, Edge-terminated molybdenum disulfide with a 9.4-Å interlayer spacing for electrochemical hydrogen production. Nat. Commun. **6**, 7493–74100 (2015). https://doi.org/10.1038/ncomms8493
21. Z. Wang, L. Pan, H. Hu, S. Zhao, Co_9S_8 nanotubes synthesized on the basis of nanoscale kirkendall effect and their magnetic and electrochemical properties. CrystEngComm **12**, 1899–1904 (2010). https://doi.org/10.1039/b923206k
22. J. Pu, F. Cui, S. Chu, T. Wang, E. Sheng, Z. Wang, Preparation and electrochemical characterization of hollow hexagonal $NiCo_2S_4$ nanoplates as pseudocapacitor materials. ACS Sustain. Chem. Eng. **2**, 809–815 (2013). https://doi.org/10.1021/sc400472z
23. S. Sahoo, C. Rout, Facile electrochemical synthesis of porous manganese-cobalt-sulfide based ternary transition metal sulfide nanosheets architectures for high performance energy storage applications. Electrochim. Acta **220**, 57–66 (2016). https://doi.org/10.1016/j.electacta.2016.10.043
24. Y. Zhang, H. Zhang, J. Yang, Y. Bai, H. Qiu, Y. Wang, Unique sandwiched carbon sheets@Ni–Mn nanoparticles for enhanced oxygen evolution reaction. ACS Appl. Mater. Interfaces **8**, 11396–11402 (2016). https://doi.org/10.1021/acsami.6b00380
25. S. Kale, A. Bhardwaj, V. Lokhande, D. Lee, S. Kang, J. Kim, C. Lokhande, Amorphous cobalt-manganese sulfide electrode for efficient water oxidation: Meeting the fundamental requirements of an electrocatalyst. ChemEng J. **405**, 126993–1269104 (2021). https://doi.org/10.1016/j.cej.2020.126993
26. X. Cai, X. Shen, L. Ma, Z. Ji, L. Kong, Facile synthesis of nickel–cobalt sulfide reduced graphene oxide hybrid with enhanced capacitive performance. RSC Adv. **5**, 58777–58783 (2015). https://doi.org/10.1039/C5RA09447J
27. C. Chen, Z. Shih, Z. Yang, H. Chang, Carbon nanotubes cobalt sulfide composites as potential high-rate and high-efficiency supercapacitors. J. Power Sources **215**, 43–47 (2012). https://doi.org/10.1016/j.jpowsour.2012.04.075
28. A. Anastassiadou, E. Liarokapis, E. Anastassakis, A raman study of $Zn_{1-x}Mn_xS$ mixed crystals. Solid State Commun. **69**, 137–142 (1989). https://doi.org/10.1016/0038-1098(89)90378-5

29. Z. Dai, H. Geng, J. Wang, Y. Luo, B. Li, Y. Zong, J. Yang, Y. Guo, Y. Zheng, X. Wang, Q. Yan, Hexagonal-phase cobalt monophosphosulfide for highly efficient overall water splitting. ACS Nano **11**, 11031–11040 (2017). https://doi.org/10.1021/acsnano.7b05050
30. X. Wang, Q. Zhang, J. Sun, Z. Zhou, Q. Li, B. He, J. Zhao, W. Lu, C.P. Wong, Y. Yao, Facile synthesis of hierarchical porous manganese nickel cobalt sulfide nanotube arrays with enhanced electrochemical performance for ultrahigh energy density fiber-shaped asymmetric supercapacitors. J. Mater. Chem. A **6**, 8030–8038 (2018). https://doi.org/10.1039/C8TA01440J
31. Q. Kong, W. Feng, X. Xie, S. Zhang, X. Yuan, C. Sun, Morphology-controlled synthesis of Co_3O_4 materials and its electrochemical catalytic properties towards oxygen evolution reaction. Catal. Lett. **148**, 3771–3778 (2018). https://doi.org/10.1007/s10562-018-2574-2
32. T. Liu, Y. Liang, Q. Liu, X. Sun, Y. He, A. Asiri, Electrodeposition of cobalt-sulfide nanosheets film as an efficient electrocatalyst for oxygen evolution reaction. Electrochem. Commun. **60**, 92–96 (2015). https://doi.org/10.1016/j.elecom.2015.08.011
33. Y. Zhang, S. Chao, X. Wang, H. Han, Z. Bai, L. Yang, Hierarchical Co_9S_8 hollow microspheres as multifunctional electrocatalysts for oxygen reduction, oxygen evolution and hydrogen evolution reactions. Electrochim. Acta **246**, 380–390 (2017). https://doi.org/10.1016/j.electacta.2017.06.058
34. X. Ma, W. Zhang, Y. Deng, C. Zhong, W. Hu, X. Han, Phase and composition controlled synthesis of cobalt sulfide hollow nanospheres for electrocatalytic water splitting. Nanoscale **10**, 4816–4824 (2018). https://doi.org/10.1039/C7NR09424H
35. Y. Liu, C. Xiao, M. Lyu, Y. Lin, W. Cai, P. Huang, W. Tong, Y. Zou, Y. Xie, Ultrathin Co_3S_4 nanosheets that synergistically engineer spin states and exposed polyhedral that promote water oxidation under neutral conditions. Angew. Chem. Int. Ed. **54**, 11231–11235 (2015). https://doi.org/10.1002/ange.201505320
36. R. Akram, M. Khan, C. Zequine, C. Zhao, R. Gupta, M. Akhtar, J. Akhtar, M. Malik, N. Revaprasadu, M. Bhatti, Cobalt sulfide nanoparticles: Synthesis, water splitting and supercapacitance studies. Mater. Sci. Semicond. Process. **109**, 104925–104934 (2020). https://doi.org/10.1016/j.mssp.2020.104925
37. Z. Yu, Y. Bai, S. Zhang, Y. Liu, N. Zhang, K. Sun, MOF-directed templating synthesis of hollow nickel-cobalt sulfide with enhanced electrocatalytic activity for oxygen evolution. Int. J. Hydrog. Energy **43**, 8815–8823 (2018). https://doi.org/10.1016/j.ijhydene.2018.03.154
38. Y. Hong, S. Mhin, K. Kim, W. Han, H. Choi, G. Ali, K. Chung, H. Lee, S. Moon, S. Dutta, S. Sun, Y. Jung, T. Song, H. Han, Electrochemically activated cobalt nickel sulfide for an efficient oxygen evolution reaction: Partial amorphization and phase control. J. Mater. Chem. A **7**, 3592–3602 (2019). https://doi.org/10.1039/C8TA10142F
39. Y. Zhou, M. Luo, Z. Zhang, W. Li, X. Shen, W. Xia, M. Zhou, X. Zeng, Iron doped cobalt sulfide derived boosted electrocatalyst for water oxidation. Appl. Surf. Sci. **448**, 9–15 (2018). https://doi.org/10.1016/j.apsusc.2018.04.080
40. M. Lukowski, A. Daniel, F. Meng, A. Forticaux, L. Li, S. Jin, Enhanced hydrogen evolution catalysis from chemically exfoliated metallic MoS_2 nanosheets. J. Am. Chem. Soc. **135**, 10274–10277 (2013). https://doi.org/10.1021/ja404523s
41. N. Zhang, W. Ma, T. Wu, H. Wang, D. Han, L. Niu, Edge-rich MoS_2 naonosheets rooting into polyaniline nanofibers as effective catalyst for electrochemical hydrogen evolution. Electrochim. Acta **180**, 155–163 (2015). https://doi.org/10.1016/j.electacta.2015.08.108
42. M. Chhowalla, H. Shin, G. Eda, L. Li, K. Loh, H. Zhang, The chemistry of two-dimensional layered transition metal dichalcogenide nanosheets. Nat. Chem. **5**, 263–275 (2013). https://doi.org/10.1038/nchem.1589
43. Y. Jiao, Y. Zheng, M. Jaroniec, S. Qiao, Design of electrocatalysts for oxygen-and hydrogen-involving energy conversion reactions. Chem. Soc. Rev. **44**, 2060–2086 (2015). https://doi.org/10.1039/C4CS00470A
44. M. Xue, Z. Fu, Lithium electrochemistry of $NiSe_2$: A new kind of storage energy material. Electrochem. Commun. **8**, 1855–1862 (2006). https://doi.org/10.1016/j.elecom.2006.08.025

45. J. Shi, J. Hu, Y. Luo, A. Asiri, X. Sun, Ni_3Se_2 film as a non-precious metal bi-functional electro-catalyst for efficient water splitting. Cat. Sci. Technol. **5**, 4954–4958 (2015). https://doi.org/10.1039/C5CY01121C
46. Z. Wang, Q. Sha, F. Zhang, J. Pu, W. Zhang, Synthesis of polycrystalline cobalt selenide nanotubes and their catalytic and capacitive behaviors. CrystEngComm **15**, 5928–5934 (2013). https://doi.org/10.1039/c3ce40152a
47. T. Liu, Q. Liu, A. Asiri, Y. Luo, X. Sun, Amorphous CoSe film behaves as an active and stable full waters plitting electrocatalyst under strongly alkaline conditions. Chem. Commun. **51**, 16683–16686 (2015). https://doi.org/10.1039/C5CC06892D
48. S. Ibraheem, X. Li, S. Shoaib, A. Shah, T. Najam, G. Yasin, R. Iqbal, S. Hussain, W. Ding, F. Shahzad, Tellurium triggered formation of Te/Fe-NiOOH nanocubes as an efficient bi-functional electrocatalyst for overall water splitting. ACS Appl. Mater. Interfaces **13**, 10972–10978 (2021). https://doi.org/10.1021/acsami.0c22573
49. W. Zhang, K. Zhou, Ultrathin two-dimensional nanostructured materials for highly efficient water oxidation. Small **13**, 1700806–1700824 (2017). https://doi.org/10.1002/smll.201700806
50. L. Fang, W. Li, Y. Guan, Y. Feng, H. Zhang, S. Wang, Y. Wang, Tuning unique peapod-like $Co(S_xSe_{1-x})_2$ nanoparticles for efficient overall water splitting. Adv. Funct. Mater. **27**, 1701008–1701018 (2017). https://doi.org/10.1002/adfm.201701008
51. C. Hu, L. Zhang, Z. Zhao, A. Li, X. Chang, J. Gong, Synergism of geometric construction and electronic regulation: 3D Se-$(NiCo)S_x/(OH)_x$ nanosheets for highly efficient overall water splitting. Adv. Mater. **30**, 1705538–1705546 (2018). https://doi.org/10.1002/adma.201705538
52. T. Tang, W. Jiang, S. Niu, N. Liu, H. Luo, Y. Chen, S. Jin, F. Gao, L. Wan, J. Hu, Electronic and morphological dual modulation of cobalt carbonate hydroxides by Mn doping toward highly efficient and stable bifunctional electrocatalysts for overall water splitting. J. Am. Chem. Soc. **139**, 8320–8328 (2017). https://doi.org/10.1021/jacs.7b03507
53. J. Li, Y. Wang, T. Zhou, H. Zhang, X. Sun, J. Tang, L. Zhang, A. Al-Enizi, Z. Yang, G. Zheng, Nanoparticle superlattices as efficient bifunctional electrocatalysts for water splitting. J. Am. Chem. Soc. **137**, 14305–14312 (2015). https://doi.org/10.1021/jacs.5b07756
54. S. Huang, Y. Meng, S. He, A. Goswami, Q. Wu, J. Li, S. Tong, T. Asefa, M. Wu, N-, O-, and S-tridoped carbon-encapsulated Co_9S_8 nanomaterials: Efficient bifunctional electrocatalysts for overall water splitting. Adv. Funct. Mater. **27**, 1606585–1606595 (2017). https://doi.org/10.1002/adfm.201606585
55. P. Chen, T. Zhou, M. Zhang, Y. Tong, C. Zhong, N. Zhang, L. Zhang, C. Wu, Y. Xie, 3D nitrogen-anion-decorated nickel sulfides for highly efficient overall water splitting. Adv. Mater. **29**, 1701584–1701590 (2017). https://doi.org/10.1002/adma.201701584
56. M. Ledendecker, S. Calderón, C. Papp, H. Steinrück, M. Antonietti, M. Shalom, The synthesis of nanostructured Ni_5P_4 films and their use as a non-noble bi-functional electrocatalyst for full water splitting. Angew. Chem. **54**, 12361–12365 (2015). https://doi.org/10.1002/anie.201502438
57. Z. Liang, Z. Huang, H. Yuan, Z. Yang, C. Zhang, Y. Xu, W. Zhang, H. Zheng, R. Cao, Quasi-single-crystalline CoO hexagrams with abundant defects for highly efficient electrocatalytic water oxidation. Chem. Sci. **9**, 6961–6968 (2018). https://doi.org/10.1039/C8SC02294A
58. H. Li, P. Wen, Q. Li, C. Dun, J. Xing, C. Lu, S. Adhikari, L. Jiang, D. Carroll, S. Geyer, Earth-abundant iron diboride (FeB_2) nanoparticles as highly active bifunctional electrocatalysts for overall water splitting. Adv. Energy Mater. **7**, 1700513–1700525 (2017). https://doi.org/10.1002/aenm.201700513
59. W. Lu, T. Liu, L. Xie, C. Tang, D. Liu, S. Hao, F. Qu, G. Du, Y. Ma, A.M. Asiri, X. Sun, In situ derived Co-B nanoarray: A high-efficiency and durable 3D bi-functional electrocatalyst for overall alkaline water splitting. Small **13**, 1700805–1700813 (2017). https://doi.org/10.1002/smll.201700805
60. Z. Yu, Y. Duan, M. Gao, C. Lang, Y. Zheng, S. Yu, A one-dimensional porous carbon-supported Ni/Mo_2C dual catalyst for efficient water splitting. Chem. Sci. **8**, 968–973 (2017). https://doi.org/10.1039/C6SC03356C

61. A. Wang, H. Xu, G. Li, NiCoFe layered triple hydroxides with porous structures as high-performance electrocatalysts for overall water splitting. ACS Energy Lett. **1**(2), 445–453 (2016). https://doi.org/10.1021/acsenergylett.6b00219
62. L. Feng, G. Yu, Y. Wu, G. Li, H. Li, Y. Sun, T. Asefa, W. Chen, X. Zou, High-index faceted Ni_3S_2 nanosheet arrays as highly active and ultrastable electrocatalysts for water splitting. J. Am. Chem. Soc. **137**, 14023–14026 (2015). https://doi.org/10.1021/jacs.5b08186

Chemical Processing of Cu_2SnS_3 Nanoparticles for Solar Cells

A. C. Lokhande, V. C. Karade, V. C. Lokhande, C. D. Lokhande, and Jin Hyeok Kim

Abbreviations

CBD	Chemical Bath Deposition
CIGS	CuInGaS
CIS	$CuInS_2$
CTS	Cu_2SnS_3
CZTS	Cu_2ZnSnS_4
DBDCA	Dibutyldithiocarbamic acid
EDTA-Na_2	Ethylenediaminetetraacetic Acid Disodium Salt
MIT	Massachusetts Institute of Technology
NPs	Nanoparticles
OA	Oleic acid
ODE	Octadecene
OLA	Oleylamine
PCE	Power conversion efficiency
PEA	Polyetheramine

A. C. Lokhande (✉)
Optoelectronic Convergence Research Center, Department of Materials Science and Engineering, Chonnam National University, Gwangju, South Korea

Department of Mechanical Engineering, Khalifa University of Science and Technology (KUST), Abu Dhabi, United Arab Emirates

V. C. Karade · V. C. Lokhande · J. H. Kim (✉)
Optoelectronic Convergence Research Center, Department of Materials Science and Engineering, Chonnam National University, Gwangju, South Korea
e-mail: jinhyeok@chonnam.ac.kr

C. D. Lokhande
Centre for Interdisciplinary Research, D. Y. Patil Education Society (Deemed to be University), Kolhapur, India

F. I. Ezema et al. (eds.), *Chemically Deposited Metal Chalcogenide-based Carbon Composites for Versatile Applications*, https://doi.org/10.1007/978-3-031-23401-9_10

PEG	Polyethylene glycol
PET	Polyethylene terephthalate
PV	Photovoltaic
PVDF	Polyvinylidene fluoride
Si	Silicon
SILAR	Successive ionic layer adsorption and reaction
TFSC	Thin films solar cells
TOPO	Triphenylphosphine oxide
UNSW	University of New South Wales

1 Introduction

The search for low-cost and earth-abundant element-based photovoltaic (PV) materials continues for solar cell applications to satisfy the growing energy demands. Recently, the PV industry received enormous attention due to its clean and abundant energy source, which can reliably meet the current energy needs. It mainly relies on solar energy from the sun, which is considered an extensive, inexhaustible, and renewable energy source. Presently, the total electricity generated from the PV industry is close to 1% of that of total worldwide electricity production. The Joint Research Centre (Europe) anticipates that consumption will increase by 50% shortly. Hence, the dependence on solar energy led the scientific community to invest efforts and funds in producing solar cells with enhanced efficiencies [1].

The silicon (Si) solar cell technology (first generation solar cells) gained a huge boost as it achieved a record break efficiency of 25%, resulting in the dependence of 80% solar market on the Si industry in the last decade. However, the Si industry did not receive much attention as it had major drawbacks, for instance, the requirement of thicker absorber layers (200–300 μm), impurities, high production cost, and low power conversion efficiency (PCE) under low light intensity conditions [1, 2]. Hence, scientific research focused on developing novel PV materials that can overcome these drawbacks [3]. In the light of recent years, thin film solar cells (TFSCs), also referred to as second-generation solar cells, have been developed extensively. Like Si solar cells, these solar cells do not need thicker absorber layers and work efficiently at a lower thickness (1–2 μm) even in low-intensity conditions. The TFSCs based on CdTe and CIGS materials have already achieved reliable efficiencies up to 21.5% and 21.7%, respectively [4, 5]. Moreover, the ternary $CuInS_2$ (CIS)-based TFSCs have also achieved efficiencies up to 11.4% [6]. As these solar cells employ toxic, carcinogenic elements such as Cd and rare earth elements such as Te, Ga, and In, their use for large-scale solar cell device fabrication is not feasible. It has been reported that producing 1 GW of electricity requires nearly 30 tons of In in Japan [7]. Hence, considering the materials perspective, the use of toxic and costly rare earth elements seems highly unsuitable for electric power generation on a commercial basis.

The kesterite-based CZTS(Se) absorber material contains earth-abundant and nontoxic elements. It exhibits similar material properties to CIGS, such as P-type conductivity with a direct bandgap (1–1.5 eV) and a high absorption coefficient [1]. Though the recent PCE of CZTSSe-based TFSCs achieved ~13.0%, it is still low than CdTe and CIGS-based TFSCs [8]. This PCE is limited mainly due to the formation of a high density of defects and unfavorable secondary phases. The existence of nonideal recombination paths in the kesterite solar cells restricts the efficiency above 20%; hence, it remains a challenge [9]. The CTS, a ternary semiconductor compound, is formed as a secondary phase during CZTS compound growth. It also has a p-type conductivity and optimal optical properties, like a high optical absorption coefficient (10^5 cm^{-1}) and tunable bandgap (0.9–1.4 eV). The number of elements in the CTS compound is also less than in CZTS, resulting in lower production cost and a simplified structure with reduced defects depicting its suitability for PV application [1, 2]. According to the S-Q limit, the theoretically estimated PCE of CTS is close to 30% and practically demonstrated a linear increase from 0.11% to 6%, indicating much scope for further enhancement in efficiency [2]. The CTS-based absorber layers can be fabricated via both physical and chemical techniques. The commonly physical techniques employed for CTS syntheses are sputtering [10], electron beam evaporation [11], thermal evaporation [12], and pulsed laser deposition [13], which require a high vacuum, have complex operations, and are costly. On the other hand, chemical techniques such as chemical bath deposition (CBD) [14], successive ionic layer adsorption, and reaction (SILAR) [15], sol-gel [16], hot injection [17], solvothermal [18], hydrothermal [19], spray pyrolysis [20], electrodeposition [21], and microwave irradiation [22] used for CTS synthesis are easy and cheap, have low material wastage, and do not require high vacuum for the process. The chemical techniques possess the flexibility to control various experimental parameters, and hence the synthesized material properties can be controlled easily. Hence, chemical techniques can be the preferred choice considering from commercialization of PV material for a solar cell application. Combining cost-effective PV materials with low-cost processing techniques can reduce the overall manufacturing cost of solar cells.

As the particle size decreases, the size effect comes into play. The size effect influences the structural, chemical, optical, and electrical properties, which imparts intriguing properties to the nanoparticles (NPs). The NPs and their intrinsic properties derived from their sizes have attracted significant interest in the modern technological industry for versatile applications. Especially, the size-dependent NP applications have revolutionized the optical and electronics industry due to effective size control. Moreover, the effective size control of semiconductor NPs results in improved optical properties and has opened new doors in "bandgap" engineering. Semiconductor NPs exhibit high absorption coefficient and tunable bandgap, which is important in enhancing efficiency in solar cell application. However, effective size/shape control accompanied by mass scale NP production is still a big challenge. Intricate size/shape NPs could induce significant variation in their intrinsic properties, further altering the basic motivation of synthesizing NPs.

Hence, it is necessary to synthesize NPs without sacrificing their properties, which could be achieved by optimizing NP synthesis techniques.

Various innovative technologies have been considered in the race to cut down the manufacturing cost of solar cells. One of the most reliable and effective trends in the innovation stage is inkjet printable solar cells. Inkjet printing has advantages such as low production cost, low wastage of material, and the ability to coat ink on almost any surface. In the case of traditional solar cells, the substrate on which the absorber is deposited is costlier than the absorber itself. Inkjet printing will provide the flexibility to coat absorbers on flexible substrates, which will be cheaper and effectively reduce the manufacturing cost. This chapter illustrates the state-of-the-art of synthesis of CTS NPs by various chemical techniques and their further processing for printable solar cells.

2 Overview of Inkjet Solar Cell

As the name suggests, solar cells are manufactured through an inkjet printer by coating a semiconductor material over the substrate. This technique is independently established by the Massachusetts Institute of Technology (MIT), the University of New South Wales (UNSW), and Oregon State University. A private solar cell manufacturing company named "Konarka" also successfully constructed printed solar cells in 2008. Following the success of "Konarka," Oregon State University fabricated CIGS solar cell with a PCE of 5% in 2011. The photograph of the inkjet printer is shown in Fig. 1.

The inkjet printers can be employed to print both organic and inorganic types of solar cells. Flexible substrates such as paper, stainless steel, and polymer

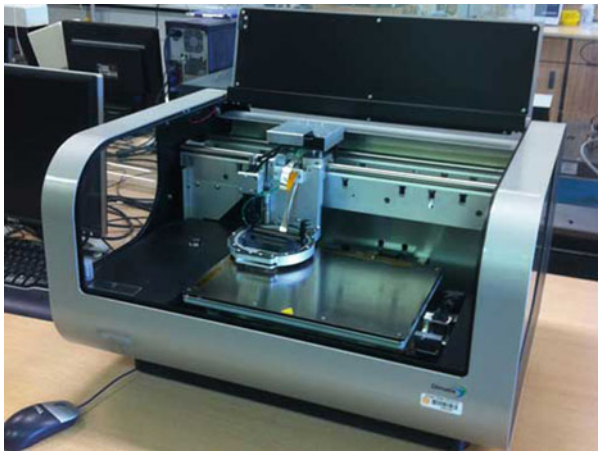

Fig. 1 The inkjet printer used to print CIGS-based solar panels [23]

(polyethylene terephthalate (PET)) can be used to print. The ink formulation of the PV material is a backbone of printable solar cells, which is used to coat the desired surface. Ink formulation is associated with a metal salt blend dissolved in solvents (solution processed) or the previously synthesized NPs dispersed in inorganic solvents (NP-based). The first approach of dissolving metal salts in a solvent to make the ink is a single-step approach similar to the spray pyrolysis technique and is quite easy. The latter approach of using NPs of absorber compound for printing is a multistep process where the NPs are synthesized using various chemical techniques such as hot injection, solvothermal, and hydrothermal and then dispersed in a solvent to make NPs ink for printing. After the ink formulation, the ink is coated on the desired substrate and subjected to annealing treatments (500–580 °C) to form a solar cell. The latency time and printing table temperature are the parameters that can be used to modulate the properties of the absorber layer. The major advantage of inkjet printing technology is its simple construction, low cost, very low wastage of material, and ability to coat any surface with controlled texture and thickness [23]. The cheap manufacturing cost of the inkjet printing approach opens up a new field of printable solar cell technological innovation.

It should be noted that the quality of the printed solar cells depends on the quality of the formulated ink. The ink can be prepared using NPs and a solution-based approach. Hence, this chapter discusses various chemical techniques employed for the high-quality ink formulation of the CTS absorber compound. Before focusing on the adopted chemical techniques for CTS synthesis, we take a brief outlook on the properties of the CTS compound.

3 Structural, Optical, and Electrical Properties of CTS

The CTS compound is considered to be biomorphic or polymorphic [24]. It exhibits different crystal structures such as cubic, tetragonal, mohite, wurtzite, orthorhombic, triclinic, and anorthic [2]. This structure formation depends upon cations distribution in the unit cell, which results from the applied annealing temperature. The CTS phases like tetragonal and monoclinic are stable at low temperature (<750 °C), while cubic and wurtzite are metastable (>750 °C) [1]. The isomorphic high-temperature CTS phase exhibits a cubic ZnS structure; at the same time, the low-temperature isomorphic phases come with the tetragonal stannite structure [25, 26]. Optimizing experimental conditions allows the high-temperature metastable phases to be made at a low temperature. This phase formation is also dependent on the Cu/Sn composition ratio. Figure 2 shows the theoretically estimated potential chemical stability region for Cu–Sn–S compound, where the Cu_2SnS_3 phase has a broad range.

As the composition becomes Cu rich, secondary phases of CuS, Cu_2S, Cu_3SnS_4, and Cu_4SnS_4 are formed, and at Cu poor conditions, SnS, SnS_2, and $Cu_4Sn_7S_{16}$ are formed. In addition, phase formation and its effect on solar cell performance should be considered. The first principle calculations study has suggested that cubic

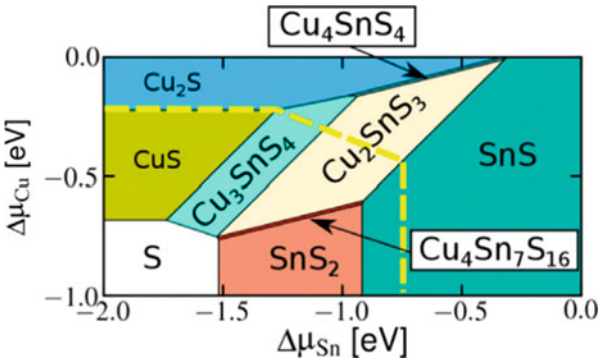

Fig. 2 Possible chemical potential phase Cu–Sn–S compound. (Reprinted with copyright permission from Ref. [27])

CTS carries several detrimental deep-level defects, while the monoclinic CTS phase has relatively low deep-level defects. Hence the monoclinic CTS phase should be preferred to fabricate CTS solar cells, which demonstrated the highest PCE.

The optical properties such as bandgap are also phase-dependent; the cubic phase has a bandgap around 1.0 eV, while the tetragonal and monoclinic structures exhibit 1.28 and 0.92 eV, respectively [28–30]. These distinct bandgap values are mainly observed owing to the unique cations-anions geometrical arrangement within the unit cell. The bandgap value can be altered through the doping impurities, which add sub-energy levels that lead to the generation and separation of charge carriers [2]. The quantum size confinement effect can also be one of the possible reasons for bandgap change in CTS NPs. The presence of secondary phases such as SnS and CuS also significantly affects the bandgap value and transmittance. Their presence leads to a decrease in transmittance value, resulting in decreased PCE [1].

The electrical properties of the CTS compound depend upon Cu/Sn ratio. Bodeux et al. [29] reported that the change in composition ratio affects the conductivity of CTS thin films. The increased Cu/Sn ratio from 1.9 to 2.2 caused the enhanced electrical conductivity from 0.1 S (S cm) to 0.8 S (S cm). The copper-rich phases like Cu_3SnS_4, Cu_4SnS_4, and Cu_2S exhibit relatively higher conductivity, and hence they enhance the overall conductivity of the CTS compound. Cu-rich composition in the CTS compound results in maximum charge carrier generation, which in turn increases the electrical conductivity and results in increased shunt losses. Hence, close control of the Cu/Sn ratio is important. The Cu oxidation state in CTS compound also significantly impacts electrical property control. Cu^{2+} state induces metallic character to CTS compound, which leads to shunt losses. Hence the suggested Cu oxidation state must be Cu^{1+} [27]. Temperature-dependent property of CTS, such as conductivity, reduces linearly with increasing temperature, and above 516 °C, CTS decomposes into CuS and SnS, indicating that the working temperature should not be above 516 °C [31]. Thus, the structural, optical, and electrical properties of CTS are significantly affected by factors such as Cu/Sn ratio

and secondary phases. Controlling these factors can help to maintain the absorber compound (CTS) properties.

4 The Device Structure of CTS-Based Thin Film Solar Cells

The chalcogenide-based TFSCs generally consist of multiple layers deposited on a substrate or soda lime glass (SLG). The typical device architecture for TFSCs is shown in Fig. 3; it consists of the back-contact layer, p-n junction, window layer, and front contact; different layers play their different part as they are called.

Briefly, the fabrication of a device starts with the deposition of metallic back contact on the substrate. Molybdenum (Mo)-coated SLG is commonly used to prepare the TFSCs with a thickness of around 500–1000 nm. The typical p-n junction in the solar cell can be fabricated by successfully fabricating the p-type absorber layer (CTS layer) and n-type CdS buffer layer through different techniques. The absorber layer exhibits an average thickness of around ~1000–1500 nm, whereas the n-type buffer layer has ~30–60 nm. Next, the window layer, also called the transparent conducting oxide layer (TCO), can be prepared by putting the i-ZnO and Al-ZnO layers by maintaining the thicknesses around 40–80 nm and 500–1000 nm, respectively, through the RF sputtering process. The device is completed by depositing top contact grids of Al or Ni/Al layers about 800–1000 nm.

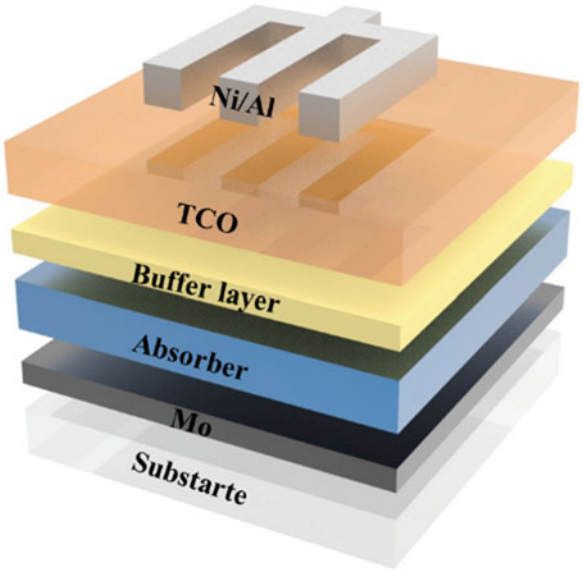

Fig. 3 The schematics device architecture of CTS-based TFSCs

Sometimes, the MgF_2-based coating layer is also used as an antireflection and a protective layer.

The selection process of materials for each layer is another important aspect of TFSCs. The substrate should be rigid to provide considerable stability in extreme environments and the mechanical strength of the solar cells. The SLG-based substrate is widely used as it satisfies the abovementioned requirements and provides additional Na supply to the absorber layer by diffusing through the Mo layer. This out-diffusion of Na atoms plays a decisive role in absorber growth and grain quality. To extract maximum charge carrier from the absorber layer, high-work function metals are typically preferred for the back contact. Mo is commonly referred as a rare contact material in chalcogenide-based TFSCs, since it controls the diffusion of Na atoms, has a high work function value, and has low sheet resistance ($0.2\ \Omega/cm^2$). Besides, chemically inert towards the absorber elements and provide good adhesion of absorber layer to the substrate.

The output parameters of the device strongly rely on the work function value of metals (Φ_m) and the back contact stability of TFSCs. Accordingly, optimizing the rare contact interface is of prime importance in developing TFSCs. The p-type absorber layer can be deposited through different techniques, which are discussed in the further sections of the chapter. The p-type absorber layer generates charge carriers, which are then separated through the different layers. Generally, a CdS buffer layer is deposited as an n-type buffer layer by the CBD technique. The CdS have a bandgap around ~2.4 eV, separating the minority charge carriers from the absorber layer and absorbing a considerable amount of light from the solar spectrum. The window layer, that is, the i-ZnO and Al-ZnO layer, has a wider bandgap than the p-n layers, which covers the rest of light from the solar spectrum. The window layer must possess higher transparency, minimal sheet resistance, and lower carrier recombination in the device. Besides, they must efficiently supply the extracted charge carriers from the p-n junction to the top electrode. The window layer is supported by the Ni or Ni-Al grids of the different areas as top contact, where the top contact collects the extracted charger carriers from the window layer. Ni and Al are low-cost materials generally used as some top contact materials to their industrialization perspective.

5 Synthesis of CTS NPs Using Chemical Techniques

This section will briefly explore various chemical techniques adopted for CTS NP synthesis. Apart from this, the influence of various experimental parameters on CTS NPs is also briefly discussed.

5.1 Solvothermal and Hydrothermal Techniques

Both solvothermal and hydrothermal techniques are close vessel reactions involving reactions under temperature and pressure. The generated pressure in the vessel depends upon the concentration of dissolved precursors and the subjected temperature [2]. The only difference in these techniques is the use of solvents. In solvothermal techniques generally, organic solvents like ethanol, ethylenediamine, ethylene glycol, and polyethylene glycol (PEG) are used; on the contrary, in the hydrothermal method, water is used as a solvent. All the chemical precursors are dissolved in the solvent and then placed in a closed vessel (Teflon) to initiate the reaction. Factors such as reaction time, temperature, solvent, pH, additivities, and precursors govern the experimental process [32]. Factors such as pH can affect the composition, size, and morphology of the NPs, while precursors stabilize the structure and affect the product's reactivity [33]. These methods are cheap, simple, and reproducible and involve low operating temperatures. They also have the advantage of producing NPs with controlled size and shapes.

The CTS NPs have been synthesized using the solvothermal and hydrothermal techniques in 120–300 °C temperature range, lasting 7–24 h. CTS NPs with various shapes such as microspheres, nanorods, micro flowers, and mesoporous spheres are synthesized by varying various experimental parameters. Chen et al. [34] investigated the effect of solvent on the morphology formation of CTS NPs. In the report, ethanol and water were used as solvents, whereas CTS NPs with nonuniform sizes and shapes were formed when only ethanol was used as a solvent. As 50 vol% water was mixed with ethanol, "flowerlike"-shaped CTS NPs were produced (Fig. 4a).

This effect of self-adjusting morphology was attributed to the use of mixed solvents (ethanol + water), which enhanced the reactivity of reactants. Hu et al. [16] evaluated the effect of varied sulfur precursor sources on the morphology formation of CTS particles. All the metal precursors (cationic) were dissolved in ethylene glycol solvent, and only two different sulfur sources (anionic) such as thiourea and thiosemicarbazide were used. CTS nanoshells (Fig. 4b) were formed for the thiourea sulfur sources. As thiosemicarbazide was used, the morphology transformed into "flakes"-like structure. This change in microstructure accounted for the higher chemical reactivity of thiosemicarbazide, which resulted in uncontrolled chemical reactions leading to irregular growth rates of the particles. Hence, the reactivity of the precursors drastically affects the morphology formation of CTS particles. The same study also determined the solvent variation effect using ethylene glycol, methanol, and benzene. Out of the three solvents, only ethylene glycol produced CTS particles as it acts as a solvent and reducing agent and favors anisotropic growth. Qu et al. [35, 36] also performed a similar study using thiourea and thiosemicarbazide sulfur sources on the morphology formation of CTS particles. In the study, PEG was used as a solvent instead of ethylene glycol as used in the former study. "Cabbage"-like and "mesoporous"-shaped CTS particles (Fig. 4c, d) were formed for thiourea and thiosemicarbazide sulfur sources, respectively. Hence,

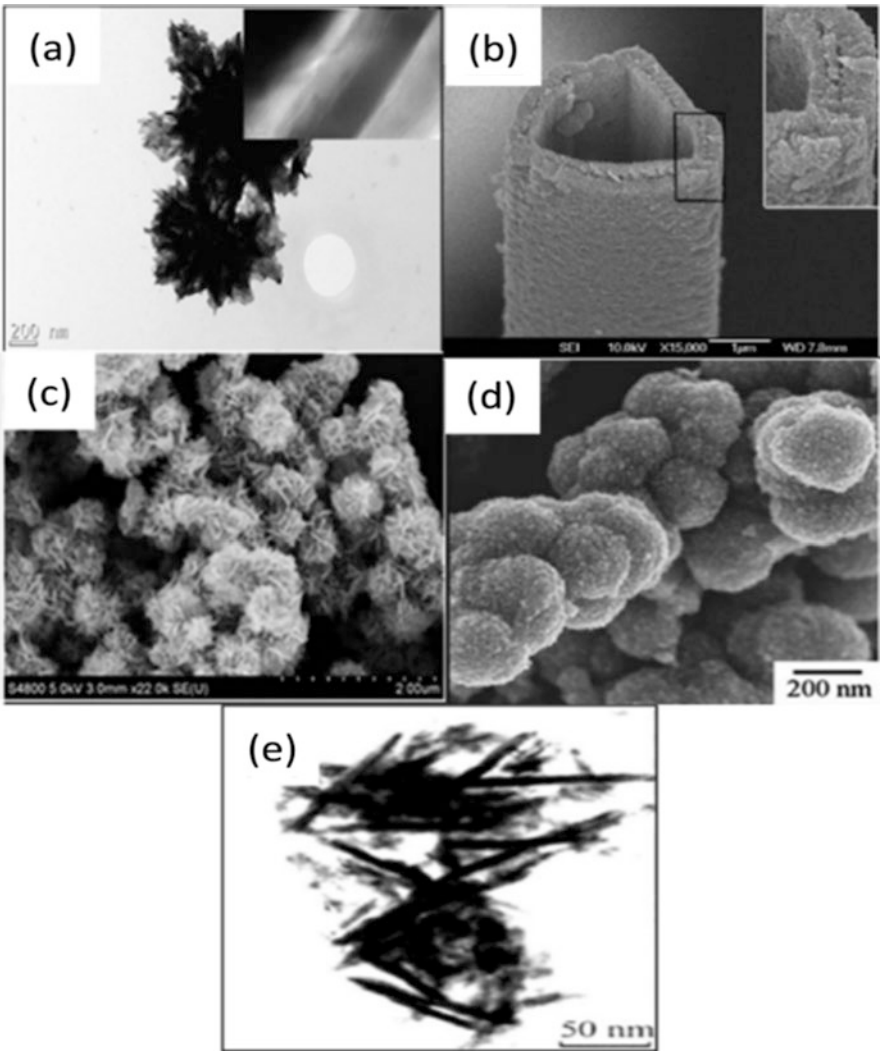

Fig. 4 (**a**) TEM image of CTS having flowerlike shape, (**b**) FESEM image of an individual Cu_3SnS_4 tubular nanoshell with its constituent spherical NPs, (**c**) Highly magnified image of the Cu_2SnS_3 cabbage-like nanostructures, (**d**) FESEM of the mesoporous CTS spheres and, (**e**) TEM image of CTS having 2-D nanorods shape. (**a**, **b**, **c**, **d**, and **e** reprinted with permission from Refs. [16, 31, 34–36], respectively)

solvents also significantly impact the morphology formation of CTS particles. The use of metal precursor sources also affects the structure and morphology formation of CTS particles. Xiong et al. [31] synthesized 2-D nanorods (Fig. 4e) in a mix solvent (water + ethanol) using a hydrated metal precursor source. The 2-D structure growth is associated with forming continuous hydrogen interlocking bonds

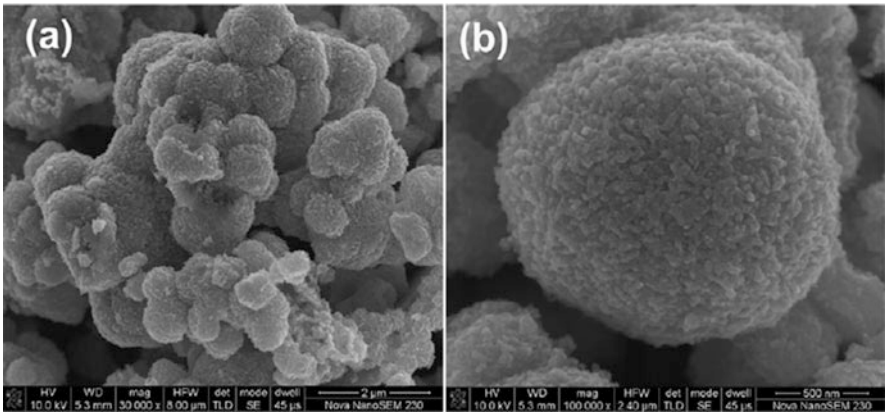

Fig. 5 FESEM images of CTS NPs with hollow spheres at (**a**) 2 μm and (**b**) 500 nm magnifications. (**a** and **b** reprinted with permission from Ref. [19])

between water and ethanol molecules. However, anhydrous metal sources (copper and tin), due to lack of H_2 bonding, did not produce the CTS compound, indicating that H_2 bonding plays a significant role in CTS compound and its morphology formation.

Compared to the solvothermal technique, hydrothermal is cheap as it involves using nontoxic and easily available water. Very limited work is conducted on the synthesis of CTS NPs by this technique. Reports include the influence of additive agents and sulfur precursor sources on the synthesis of CTS NPs. Zhang et al. [19] reported the formation of CTS NPs with hollow spheres (Fig. 5a, b) using ethylenediaminetetraacetic acid disodium salt (EDTA-Na_2).

The formation of CTS NPs is ascribed to the high chelating capacity of EDTA-Na_2, which controls the Cu^+ and Sn^{4+} release. It also acts as a template for forming a hollow structure. Li et al. [37] synthesized CTS NPs with tetragonal and cubic structures using thiourea and sodium sulfide, respectively. The excess use of thiourea suppressed the secondary phase formation. It produced phase pure tetragonal CTS NPs, while for cubic phase CTS synthesis, the process temperature was raised to 250 °C. It accelerated the reaction by increasing the release of S^{2-} ions from sodium sulfide. Hence, modulating the rate of a chemical reaction by sulfur sources and experimental temperature can produce CTS NPs with various phases. Table 1 indicates the experimental parameters and related properties of CTS NPs obtained by solvothermal and hydrothermal techniques [16, 18, 19, 31, 34–47].

The crystal structure and size distribution of CTS NPs are mostly determined by the selection of solvent and precursors reactivity. Table 2 indicates the influence of sulfur source and solvent on the CTS phase formation.

The coordinating, reducing, and chelating ability of the solvent decides the phase formation of CTS particles. As with the solvents, precursor reactivity affects the phase formation and size. Due to the unbalanced monomer's contribution,

Table 1 The experimental conditions and results of reported CTS NPs by solvothermal and hydrothermal techniques

Sr no.	Metal precursor	Sulfur source	Solvent	Time (h)	Temp (°C)	Phase	Size/shape	Ref. no.
1	$CuAC_2.H_2O$, $SnCl_4.5\ H_2O$	TH	DMF	12	200	Kuramite-Tetragonal	3D-flower microsphere	[18]
2	$CuAC_2.H_2O$, $SnCl_4.5H_2O$	TH	DMF	12	180	Kuramite-Tetragonal	Flower-like	[47]
3	$CuCl_2.2H_2O$, $SnCl_4.5H_2O$,	TH	Ethanol	24	190	Kuramite-Tetragonal	2-D nanorod	[31]
4	Cu and Sn	S	EDA	121010	250300250	Orthorhombic Anorthic Kuramite-Tetragonal	Nanorod Nanorod Nanoparticle	[38]
5	$CuCl_2.2H_2O$,$SnCl_4.5H_2O$	TH	Ethanol + water	7.5	200	Kuramite-Tetragonal	Flower like	[34]
6	$CuCl_2.2H_2O$,SnCl2.2H2O	TU	EGEDA	1616	180180	Cubic Wurtzite	Flower-like	[39]
7	$CuCl_2.2H_2O$, SnCl2.2H2O	TU	Ethanol	12	200	Kuramite-Tetragonal	Nanoparticle	[40]
8	$CuCl_2.2H_2O$,$SnCl_4.5H_2O$	TH	PEG	15	180	Cubic	2-D cabbage	[35]
9	CuCl, $SnCl_4.5H_2O$,	TU	PEG + Ethanol	20	180	Cubic	Mesaporous sphere	[36]
10	$CuAC_2.H_2O$,$SnCl_4.2H_2O$	TU	DMF	24	200	Cubic	Nanoparticle	[41]
11	$CuCl_2.2H_2O$, Sn	S	Ethylediamine	15	140–180	Triclinic	Nanocrystals	[42]
12	$CuCl_2.2H_2O$,$SnCl_4.5H_2O$	L-cysteine	Water	15	180	Mohite	Flower like	[43]
13	$CuCl_2.2H_2O$, Sn	S	Ethylediamine	20	170	Triclinic	Nanocrystals	[44]
14	$CuCl_2$,$SnCl_4$	TH	DMF	12	180	Hexagonal	Nanoparticle	[45]
15	CuCl, $SnCl_4.5H_2O$	L-cysteine	Water+EDTA-Na_2	24	180	Triclinic	Flower like	[19]
16	$CuCl_2.2H_2O$, $SnCl_2$	TH	Water	12	180	Tetragonal	Nanoparticle	[37]
17	$CuCl_2.2H_2O$, $SnCl_2$	Na_2S	Water	24	250	Cubic		[46]

Table 2 The dependence of CTS phase formation on a combination of the type of sulfur source and solvent used

Type of sulfur source	Type of solvent	Phase	Ref. no.
Highly reactive	Mild coordinating	Kuramite-tetragonal	[18, 31, 34, 38, 40]
Highly reactive	Strong coordinating	Triclinic	[44]
Mild reactive	Mild coordinating	Cubic	[35, 39, 41]
Mild reactive	Strong coordinating	Wurtzite	[39]

Table 3 The particle size distribution of NPs based on the reactivity of the precursors

Precursor reactivity	Particle distribution
High	Broad
Medium	Narrow
Low	Broad

highly reactive precursors provide broad particle size distribution. Meanwhile, mild reactive precursors have a balanced releasing rate of monomers, and control over nucleation and grain growth results in narrow particle size distribution. The nucleation process is prolonged for low reactive precursors, so monomers are produced after a long time, forming large-sized particles (spheres) [48]. Table 3 indicates the particle size distribution of NPs based on the reactivity of the precursors. Hence, the flexibility in tuning CTS NP properties (phase, shape, and particle size distribution) in the solvothermal and hydrothermal techniques provides a peculiar advantage for preparing high-quality NP ink for printable solar cells.

5.2 Hot Injection Technique

The hot injection is a facile and quick approach to producing the NPs and is widely adopted due to its ability to control the size, shape, composition, and phase of NPs. This technique involves the rapid insertion of cold precursors into hot complex precursors. The rapid injection of cold precursors lowers the temperature of a hot complex precursor, which terminates the nucleation due to a rapid drop in the solvent temperature and leads to reduced monomer concentration below the critical level. The newly generated nuclei grow slowly to form particles (Fig. 6).

The growth of the NPs is diffusion controlled, accompanying the slower growth rate of particles, followed by a reaction-controlled mechanism associated with the growth of larger particles due to the higher chemical potential of smaller particles (Ostwald's ripening), leading to the formation of NPs [49, 50]. In the synthesis of CTS NPs, cationic precursor sources (Cu and Sn) are initially mixed in a solvent and heated to initiate the reaction. After forming a metal complex at a certain temperature (140–160 °C), the reaction temperature is further raised (220–240 °C). Then an anionic precursor source (sulfur) is rapidly inserted in the metal complex precursor, followed by aging to form CTS NPs. Just like the solvothermal technique, factors such as reaction time, temperature, solvents,

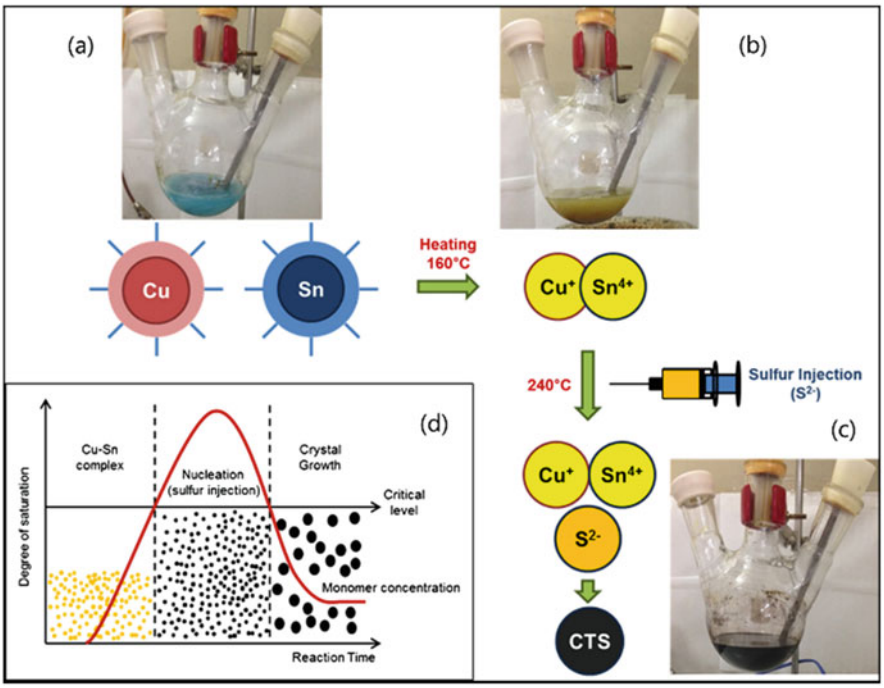

Fig. 6 (**a–c**) Reaction mechanism of CTS NPs and (**d**) schematics of NPs formation. (Reprinted with permission from Ref. [51])

and precursor sources also affect the structural and microstructural properties of CTS NPs. Cationic metal precursor sources commonly used are chloride, acetate, sulfate, acetate, acetylacetonate, and iodide [17, 51–57]. Sulfur sources such as thiourea, elemental sulfur powder, 1-dodecanethiol (DDT), dibutyldithiocarbamic acid (DBDCA), and solvents with high boiling point (<300 °C) such as oleylamine (OLA) and Octadecene (ODE) are used in NP synthesis. Various capping agents such as triphenylphosphine oxide (TOPO) and oleic acid (OA) are used to produce highly dispersed NPs by their effective role in stabilizing the free surface energy of the particles.

The chelating ability of solvent and reactivity of the precursor sources directly affects the size, shape, and phase formation of CTS NPs. Lokhande et al. [51] employed sulfate and chloride metallic precursor sources and synthesized CTS NPs in the size of 10 and 70 nm, respectively (Fig. 7a, b).

The increased NPs size (70 nm) is attributed to the higher chemical reactivity of the chloride precursor source. Compared to sulfate precursor sources, chloride precursors are highly reactive, resulting in rapid nucleation of the NPs followed by their growth and aggregation, resulting in increased particle size. The same authors [52] also demonstrated the effect of reactivity of the sulfur precursor source by synthesizing CTS NPs with two different phases, cubic and tetragonal, using

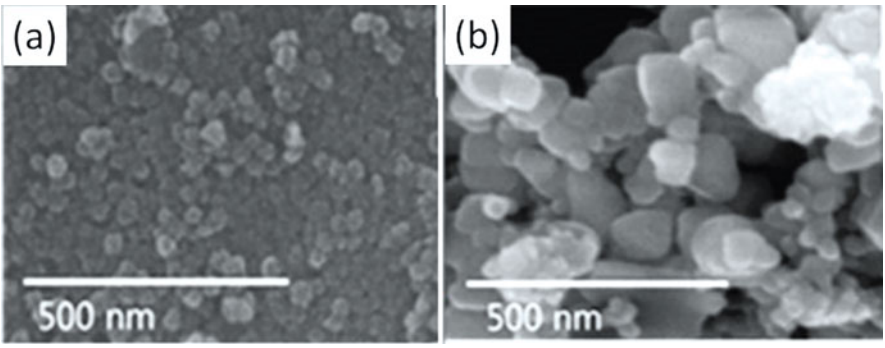

Fig. 7 FESEM images of CTS NPs produced from (**a**) sulfate and (**b**) chloride metal precursor source. (**a** and **b** reprinted with permission from Ref. [51])

two different sulfur sources, namely, sulfur powder and thiourea, respectively. The relatively higher reactivity sulfur source (i.e., elemental sulfur powder) results in the formation of cubic phase at low temperature (240 °C) owing to the faster-releasing rate of S^{2-} ions, which generally form at a higher temperature. Hence, CTS NP phase formation is mainly determined by the reactivity of the sulfur source (kinetics of S^{2-} ions).

Solvents also tune the phase, size, and shapes of the NPs. The coordinating and chelating properties of the solvents impart desired size and shape to the NPs. Chang et al. [53] explained the effects of solvents on the properties of CTS NPs. Cubic phase triangular-shaped CTS NPs (Fig. 8a) in the size of 150 nm were synthesized using ODE solvent.

As OLA was mixed with ODE solvent, wurtzite phase hexagonal-shaped particles (Fig. 8b) in the size range of 30–35 nm were formed. Similarly, CTS nanorods (Fig. 8c) in size range from 50 to 70 nm synthesized in ODE solvent transformed into hexagonal-shaped particles (Fig. 8d) in size ranging from 20 to 30 nm using OLA solvent [54]. Hence, the size reduction effect and shape tuning ability of OLA solvent is attributed to its strong coordinating capacity. Tin incorporation also affects the size and phase formation of the NPs. Wurtzite phase CTS NPs in the size of 10.4 nm were formed at 7:1 Cu: Sn ratio, and kesterite phase CTS NPs in the size of 3.5 nm were formed at an increased tin ratio (Cu: Sn = 1:7) [55]. Contrary to this result, tin incorporation in the synthesized CuS ($Cu_{31}S_{16}$) particles resulted in an increased size (31 nm) of the formed CTS particles due to the incorporation of tin in the CuS matrix resulting in overall increases in the volume of the unit cell and hence the size of particles [56]. Okano et al. [57] synthesized CTS NPs with a tetragonal phase by sequential injection of tin followed by sulfur in the Cu-Sn complex. However, NP cubic phase CTS NPs were formed when the same experimental conditions and precursors were used, and only sulfur was injected into the Cu-Sn complex [17]. Table 4 indicates the experimental conditions and results of reported CTS NPs by hot injection techniques.

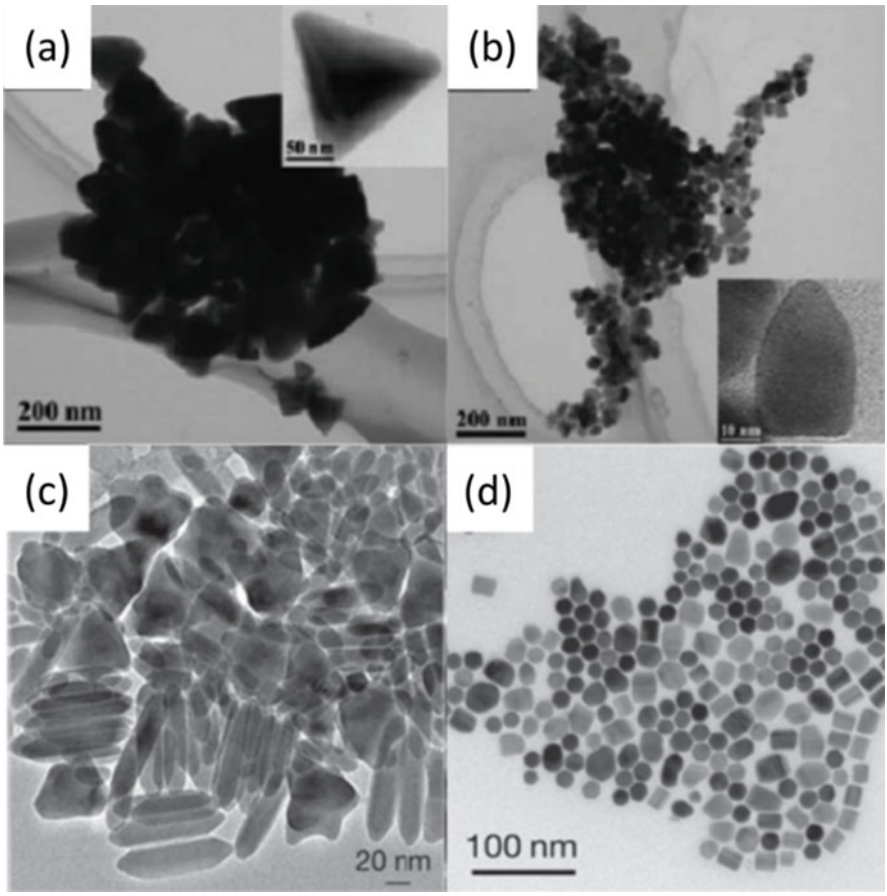

Fig. 8 TEM images of CTS NPs (**a**) triangular NPs with 150 nm from ODE solvent, (**b**) hexagonal NPs of 30 nm from OLA solvent (**c**) nanorod produced from ODE solvent and (**d**) hexagonal NPs produced from OLA solvent. (**a**, **b** reprinted with permission from Ref. [53] and **c**, **d** reprinted with permission from Ref. [54])

Hence, factors such as metallic precursor sources, solvents, capping agents, and sulfur precursor sources significantly affect the size, shape, and phase formation of CTS NPs. The advantage of controlled preparation of NPs with dispersibility and uniformity is beneficial for preparing NPs ink for printable solar cell fabrication.

5.3 One-Pot Chemical Synthesis Technique

"One-pot chemical technique," as the same suggests, means that all the precursors are initially mixed in the solvent. The reaction is initiated by steady heating

Table 4 The experimental conditions and results of reported CTS NPs by hot injection method

Metal precursor	Sulfur source	Solvent	Phase	Ref. no.
CuCl + $SnCl_2$	S	OLA	Tetragonal	[57]
CuCl + $SnCl_2$	S	OLA	Cubic	[17]
$CuCl_2$ + $SnCl_2$	DBDCA+DDT	OLA + ODE+TOPO+OA	Wurtzite	
CuCl + $SnCl_2$	S	OLA + TOPO+OA	Wurtzite	[55]
$Cu(acac)_2$ + $SnCl_4$	DDT		Orthorhombic	[56]
CuI + Sn(acac)	DDT	ODE	Cubic	[53]
CuI + Sn(acac)	DDT	ODE + OLA	Wurtzite	
$Cuacac_2$ + $Snac_4$	DDT	OLA + TOPO	Orthorhombic	[54]
$CuSo_4.XH_2O$	S	OLA	Kuramite-Tetragonal	[51]
$SnS0_4.XH_2O$				
$CuCl_2$ + $SnCl_2$	S	OLA	Tetragonal	
$CuCl_2$ + $SnCl_2$				
$CuCl_2$ + $SnCl_2$	Sthiourea	ODE	Cubic	[52]
		ODE	Tetragonal	

of solvent, which results in the thermal decomposition of precursors to undergo nucleation and grain growth. Like the hot injection technique, the solvents, capping agents, and precursors used in this technique are quite the same. The size of the NPs in this technique can be easily controlled by controlling the reaction time. In the synthesis of CTS NPs by Lin et al. [58], the size of the NPs increased from 10.7 to 16.4 nm with an increasing reaction time from 5 to 45 min (Fig. 9a, b).

The increased size with reaction time is attributed due to the crystallization and aggregation of particles. Simultaneous control of the phase and size of CTS NPs is also possible. Park et al. [59] synthesized CTS cubic and wurtzite phases by elemental sulfur powder and dodecanethiol (DDT) as a sulfur source. Also, the size of the NPs was reduced from 9 to 6.8 nm (Fig. 9c, d) with increased oleic acid to the cationic ratio from 6:1 to 18:1. The stabilization effect of oleic acid results in the restricted growth of the NPs and hence the size of NPs decreases. Hence, the easy control of NP properties by controlling various factors provides opportunities to synthesize NPs with desirable properties. Also, the major advantage of the "one-pot chemical technique" is that the yield of NP formation is more and hence best suitable for large-scale NP synthesis, which can be further used for ink formulation for printable solar cells [60].

One-pot multi-bubble sonoluminescence technique, similar to "one-pot chemical technique" has also been employed for CTS NP synthesis. Compared to "one-pot chemical method," the only difference is the working mechanism of this method, which is based on the emission of light due to the collapse of gas bubbles under the applied ultrasonic field. CTS NPs in the controlled size range of 5–6 nm have been synthesized by adjusting sonication time and frequency [61]. Rapid NP synthesis and precise control of NPs size make it an attractive technique for large-scale NP synthesis for ink formulation in printable solar cells.

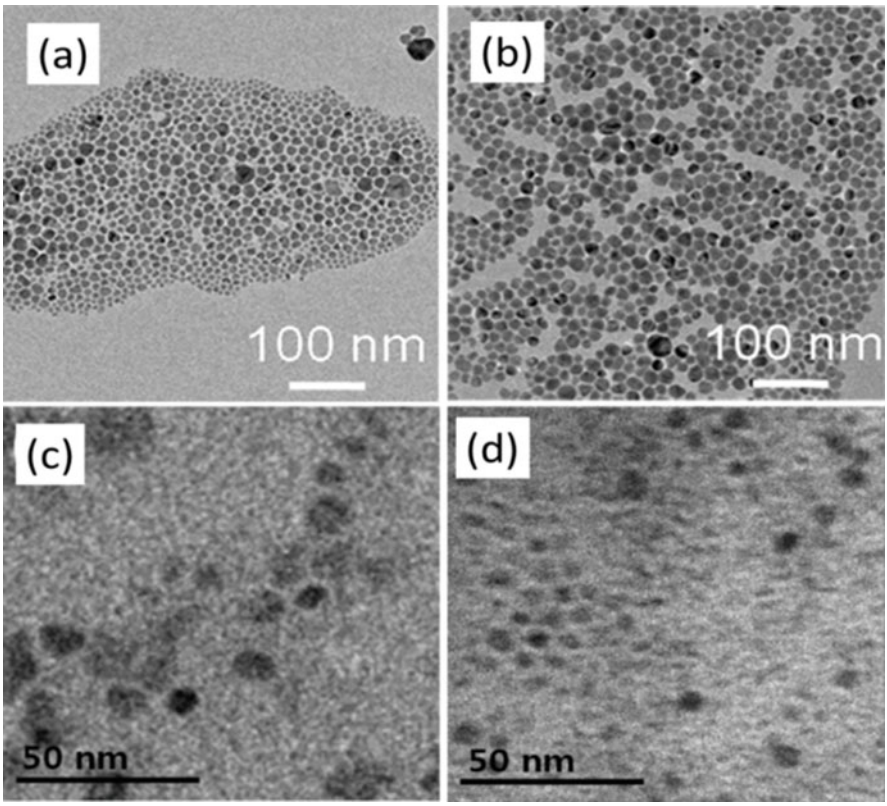

Fig. 9 TEM images of CTS NPs (**a**) and (**b**) at reaction stage of 5 and 45 min, respectively, (**c**) and (**d**) with increasing oleic acid content to cation molar ratio 6:1 and 18:1, respectively. (**a**, **b** reprinted with permission from Ref. [58] and **c**, **d** reprinted with permission from Ref. [59])

5.4 Microwave Irradiation Technique

The microwave technique is commonly used for NP synthesis as it is cheap, rapid, environmentally friendly, and scalable. Due to its highly polarizing nature, microwave radiations directly interact with the charged particles and form NPs. The microwave reflex involves rapidly heating particles under the vibrating electric field [22]. This technique is similar to one-pot chemical technique, where all the precursors are dissolved in the solvent, and the reaction is initiated, except the difference in this technique is the driving reaction force, that is, the microwaves. Parameters such as microwave reaction time and operating power can tune the NP properties (size, phase, and shape). Other well-known factors, such as solvent and sulfur precursor sources, influence NP formation [22, 62, 63]. Very limited reports are available on the microwave synthesis of CTS particles. A study based on the effect of varied sulfur sources on particle formation has been demonstrated by Wang

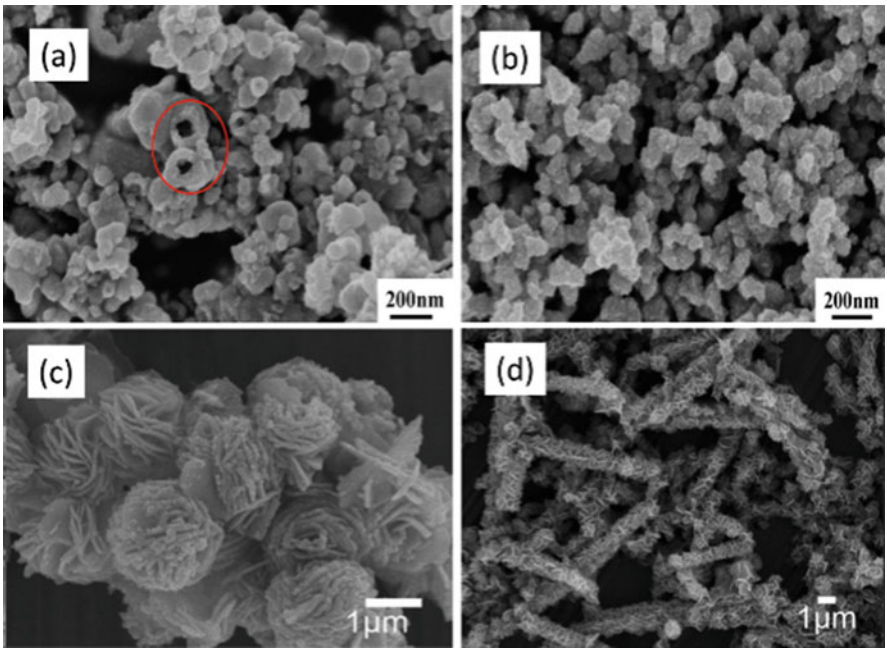

Fig. 10 (**a**) and (**b**) FESEM images of CTS NPs using sulfur sources as L-cysteine and thiourea, respectively, and (**c**) and (**d**) FESEM images of CTS NPs using the microwave reflux method and conventional reflux method, respectively. (**a**, **b** reprinted with permission from Ref. [62] and **c**, **d** reprinted with permission from Ref. [22])

et al. [62]. Sulfur sources such as L-cysteine and thiourea were used. Irregular-shaped hollow spheres (Fig. 10a) were formed for L-cysteine, and aggregated spherical NPs (Fig. 10b) were formed for the thiourea sulfur source.

The lower solubility of L-cysteine and its vesicle template formation lead to the agglomeration of smaller particles to form larger particles with hollow spheres. On the other hand, thiourea NPs, due to their higher solubility, did not form a vesicle template; hence, NPs in the spherical shape were formed. Hence, it is clear that the solubility of the sulfur sources drastically affects the morphology of CTS NP formation. The influence of microwave and conventional reflux on CTS particle formation has been evaluated by Tipcompor et al. [22]. "Aggregated flowerlike" morphology (Fig. 10c) was formed due to the rapid heating of particles under the vibrating electric field for the microwave reflux method. The rapid heating accelerates the chemical reaction and forms particles that aggregate and form clusters along with the time-lapse. However, in the case of the conventional reflux method, due to the absence of a vibrating electric field, the formed particles aggregate continuously in a 2-D direction to form nanorods (Fig. 10d). Hence, the type of reflux system adopted for NP synthesis affects the morphology formation of CTS NPs. The microwave synthesis method, as mentioned before, is very rapid and

cheap. This technique can be very effective for NP synthesis and further processing as NP ink formulation for printable solar cells.

Hence as we discussed, various techniques employed for CTS NPs produce NPs with peculiar advantages and properties. The selectivity of the technique depends on the desired properties of NPs. Apart from these NP synthesis techniques, solution processing of CTS has also been employed to prepare ink for printable solar cells.

6 Solution Process

The solution process is a simple, cost-effective, and scalable method as it involves mixing and dissolving all the precursor salts in the solvent, followed by its coating on the substrate. The advantages, such as precise composition control and conformal coating with uniform thickness throughout the surface, make it one of the most attractive and reliable methods for TFSCs fabrication [64]. The pioneering work of the Mitzi group demonstrated the fabrication of 12.6% CZTSSe by a solution-based approach reflecting the potential capability of the method to produce high-efficiency solar cells [8]. The solution-based approach was hydrazine-based, which is associated with several challenges. The toxic, corrosive, and flammable nature of hydrazine solvent requires careful handling during the preparation of both ink and a thin film, which can deprive its use. In this regard, alternate nontoxic solvents received attention for the solution-based approach. Several reports [64–70] have demonstrated the synthesis of CTS thin film and their solar cell application using a nontoxic solution-based approach.

The solution approach for CTS synthesis is associated with the formation of sol followed by spin coating. The sol is formed by dissolving all the precursor salts in the solvent. The sol is then spin-coated on the desired substrate, followed by annealing treatments. In the case of CTS, cationic precursors (Cu and Sn) and anionic precursors (S) are mixed and dissolved in a solvent. The commonly used metal precursor sources are chloride and acetate sources. The solvents employed are methanol, 2-methoxyethanol, and diethanolamine. Usually, the quality of the sol depends on the uniform mixing of the precursor salt and the stability of the solvent. The mixing of precursors is at the molecular level, enabling precise control over stoichiometry. After sol formation, the sol (ink) is spin-coated on the substrate, followed by annealing in the temperature range from 150 to 600 °C. Table 5 represents the reported results of the solution-processed CTS thin films. Efficiency as high as up to 2.10% for solution-processed CTS TFSCs is reported [69].

Hence, the solution prepared by dissolving all the precursors can be used as ink for printable solar cells. Solution-processed ink is easier, cheap, and more scalable than NP ink formulation. Also, the ink composition can be controlled simply by adjusting the concentration of chemical precursors. However, the preferred choice for ink preparation depends on the expected properties of the thin film.

Table 5 The reported results of the solution-processed CTS thin films

Precursors	Solvent	Annealing conditions	PCE (%)	Ref. no.
$Cu(OAc)_2$, $SnCl_2$	Aqueous precursor solution	600 °C for 10 min in S vapor	1.80	[64]
$CuCl_2$, $SnCl_2$, thiourea	Methanol	200 °C for 4 h in air	2.10	[69]
$CuCl_2$, $SnCl_2$, thiourea	Methanol	200 °C for 10 min in air	–	[68]
$Cu(OAc)_2$, $SnCl_2$, thiourea	Methanol	300 °C for 10 min in air	–	[65]
$Cu(OAc)_2$, $SnCl_2$, thiourea	2-Methoxyethanol, diethanolamine	550 °C for 2 h in S vapor	–	[66]
$Cu(OAc)_2$, $SnCl_2$, thiourea	Methanol	150–300 °C for 2 h in air	–	[67]
Cu, Sn, S powders	Hydrazine	600 °C for 20 min in excess S atmosphere	–	[70]

7 Post-Annealing Treatments

Apart from ink formulation, annealing treatments also significantly influence the quality of thin films. The printed films from the ink are subjected to annealing treatments to form the compound with enhanced crystallinity. In the case of the NP ink approach, the annealing treatment forms a compact microstructure with enhanced crystallinity. Noncompact microstructure leads to recombination losses, resulting in reduced power conversion efficiency (PCE) of the fabricated solar cells [1, 2]. As for the solution-based approach, an annealing treatment is needed to form a CTS compound from the film printed using ink. In the case of CTS, annealing can be done in the sulfur environment (sulfurization) and inert atmosphere (N_2 or Ar). CTS is highly temperature sensitive as its microstructure, phase, and composition change significantly with temperature. Elemental tin loss from CTS compound in tin sulfide (SnS/SnS_2) is dominant during annealing treatment. This elemental loss disrupts the microstructure and changes the composition and phase of the compound. If the elemental tin loss is more, the composition of CTS becomes copper-rich and results in increased shunt loss in the solar cells [1]. Hence, the elemental loss must be controlled by optimizing annealing conditions. Sulfurization in the tin environment, especially SnS_2 powder, can minimize tin loss from the compound.

Also, increasing the partial pressure (S/SnS_2) during sulfurization can effectively suppress the elemental losses. Sulfurization temperature is also the key factor affecting the thin film absorber quality. The temperature should not be too high as it promotes maximum elemental loss. The suggested sulfurization temperature for CTS thin film is in the range of 550–580 °C. High-efficiency CTS TFSCs with 4.67% PCE were sulfurized at 570 °C [12]. Apart from microstructural enhancement, optical properties such as bandgap can also be tuned by annealing

treatment. Selenization of films can tune the bandgap (narrow) of the printed films. Hence, annealing treatments have a significant role in modifying the properties of the thin film absorber compound.

8 Challenges and Solutions

The major requirement for printing the functional material is the formulation of stable ink. In the case of NP-based approach, the normal tendency of NPs to aggregate and precipitate formation affects the quality of the ink, which is solely responsible for inconsistent reproducible performance. The stability of the ink (NP dispersion) can be maintained using stabilizing agents. Stabilization can be achieved by electrostatic and steric mechanisms [71]. Electrostatic stabilization is associated with electrostatic repulsion between surrounding particles. The higher the electric potential (Zeta potential), the higher the repulsion will lead to higher stability of the particles. However, NP dispersion in polar media and organic solvents is not effective for electrostatic stabilization. Steric stabilization can be the alternative as the particles are covered by sterically bulky molecules (polymers). Combining electrostatic and steric mechanisms, usually referred to as electrostatic stabilization, can be effective in achieving particle stability in aqueous solvents. The stabilizers such as poly(N-vinyl-2-pyrrolidone) (PVP) can be used in both organic and aqueous media [72]. Other stabilizers include diethanolamine (DEA), ascorbic acid, carboxymethyl cellulose sodium salt, polynaphthalene sulfonate formaldehyde condensate, and poly(acrylic acid) salts [73, 74].

The size distribution of metal NPs is crucial. If the size distribution of the NPs is nonuniform, it may not form a uniform coating on the substrate, affecting the solar cell performance. Capping agents such as oleic acid and triphenylphosphine oxide (TOPO) can be used to maintain the size distribution. The adhesion of the NPs is also important. If adhesion is not well, NPs can detach from the substrate surface leading to nonuniform and noncompact coating resulting in decreased performance of solar cells. Binders such as ethyl cellulose, polyvinylidene fluoride (PVDF), and polyetheramine (PEA) can be used to enhance adherence. However, the use of binders introduces carbon impurities in the film, which increases the solar cell series resistance, leading to its decreased performance. Hence, carbon-free binders must be explored and employed as an alternative to the existing binders. In the case of solution-processed techniques, complexing agents (ethylenediamine and monoethanolamine) can be used to produce films with the desired composition and phase. A surfactant such as TritronX-100 can enhance the surface texture of the films. The ink's viscosity, wettability, and surface tension are also critical. Typical values of viscosity and surface tension should be in the range of 8–15 cP and 25–35 dyne/cm, respectively [71]. Viscosity can be tuned by adjusting ink concentration and using additives. The wettability between the ink and substrate also plays an important role in forming a uniform and homogeneous film. The contact angle of the ink droplet with the substrate must be as low as possible. Hence, identifying the

factors that hinder the quality and possible solutions for the same can effectively contribute to the increased performance and reliability of the printed solar cells.

9 Conclusions

Inkjet printing based on using functional material ink is an innovative technique for fabricating high-quality printable solar cells. The production of quality films at low cost, flexibility to produce films with desired properties, and its coating on almost any substrate have revolutionized the solar cell industry. Even though printable solar cells are in the early stage of innovation, extensive research and efforts have resulted in rapid development in this technology. The "ink," which decides the quality of the printable solar cell, is vital and should be formulated precisely. The NPs and solution-processed approach adopted for ink formulation in a printable solar cell involve various factors that directly affect the ink quality should be focused. Post-annealing treatments based on the desired properties in the printed film should be optimized. Efforts to understand the chemistry of ink formulation and its further processing by annealing treatments can transform the printable solar cell technology from a preliminary research stage to a developed stage. The combination of low-cost, functional material and ink formulation will realize high-performance printable solar cells in the near future.

Acknowledgments This work was supported by the National Research Foundation of Korea (NRF) grant funded by the Korea government (MSIT) (No.2022R1A2C2007219).

References

1. A.C. Lokhande, R.B.V. Chalapathy, M. He, E. Jo, M. Gang, S.A. Pawar, C.D. Lokhande, J.H. Kim, Sol. Energy Mater. Sol. Cells **153**, 84 (2016)
2. A.C. Lokhande, K.V. Gurav, C.D. Eunjin Jo, J.H.K. Lokhande, J. Alloys Compd. **656**, 295 (2016)
3. S.M. Shauddin, Energy Power **3**(6), 91 (2013)
4. PV Magazine, First Solar Raises Bar for CdTe with 21.5% Efficiency Record (6 February 2015)
5. M. Powalla, P. Jackson, D. Hariskos, S. Paetel, W. Witte, R. Wuerz, E. Lotter, R. Menner, W. Wischmann, *Proceedings of the 29th European Photovoltaic Solar Energy Conference* (3AO.4.2, Amsterdam, September 2014)
6. A.J. McEvoy, T. Markvart, L. Castaner (eds.), *Solar Cells: Materials, Manufacture, and Operation* (Elsevier, 2012)
7. H. Katagiri, K. Jimbo, W.S. Maw, K. Oishi, M. Yamazaki, H. Araki, A. Takeuchi, Thin Solid Films **517**, 2455 (2009)
8. W. Wang, M.T. Winkler, O. Gunawan, T. Gokmen, T.K. Todorov, Y. Zhu, D. Mitzi, Adv. Energy Mater. **4**, 201301465 (2014)
9. S. Siebentritt, Thin Solid Films **535**, 1 (2013)
10. P. Zhao, S. Cheng, Adv. Mater. Sci. Eng. **2013**, 1 (2013)

11. Z. Tang, K. Kosaka, H. Uegaki, J. Chantana, Y. Nukui, D. Hironiwa, T. Minemoto, Phys. Status Solidi A **212**, 2289 (2015)
12. M. Nakashima, J. Fujimoto, T. Yamaguchi, M. Izaki, Appl. Phys. Express **8**, 042303 (2015)
13. R.B. Ettlinger, A. Cazzaniga, S. Canulescu, N. Pryds, J. Schou, Appl. Surf. Sci. **336**, 385 (2015)
14. Y. Wang, J. Li, C. Xue, Y. Zhang, G. Jiang, W. Liu, C. Zhu, Mater. Lett. **178**, 104 (2016)
15. Z. Su, K. Sun, Z. Han, F. Liu, Y. Lai, J. Li, Y. Liu, J. Mater. Chem. **22**, 16346 (2012)
16. H. Hu, Z. Liu, B. Yang, X. Chen, Y. Qian, J. Cryst. Growth **284**, 226 (2005)
17. Q. Liu, Z. Zhao, Y. Lin, P. Guo, S. Li, D. Pan, X. Ji, Chem. Commun. **47**, 964 (2011)
18. F. Chen, J. Zai, M. Xu, X. Qian, J. Mater. Chem. A **1**, 4316 (2013)
19. Z. Zhang, Y. Fu, C. Zhou, J. Li, Y. Lai, Solid State Ionics **269**, 62 (2015)
20. G.M.M. Ilari, C.M. Fella, C. Ziegler, A.R. Uhl, Y.E. Romanyuk, A.N. Tiwari, Sol. Energy Mater. Sol. Cells **104**, 125 (2012)
21. D.M. Berg, R. Djemour, L. Gutay, G. Zoppi, S. Siebentritt, P.J. Dale, Thin Solid Films **520**, 6291 (2012)
22. N. Tipcompor, S. Thongtem, T. Thongtem, Superlattice. Microst. **85**, 488 (2015)
23. http://www.pbs.org/wnet/need-to-know/environment/inkjet-printing-solar-panels-cheap-and-almost-green/10348/
24. M. Onoda, X. Chen, A. Sato, H. Wada, Mater. Res. Bull. **35**, 1563 (2000)
25. S.R. Hall, J.T. Szymanski, J.M. Stewart, Can. Mineral. **16**, 13 (1978)
26. N. Wang, Neues Jahrb. Mineral. Monatshefte **9**, 424 (1974)
27. P. Zawadzki, L.L. Baranowski, H. Peng, E.S. Toberer, D.S. Ginley, W. Tumas, A. Zakutayev, S. Lany, Appl. Phys. Lett. **103**, 253902 (2013)
28. Y. Dong, J. He, X. Li, W. Zhou, Y. Chen, L. Sun, P. Yang, J. Chu, Mater. Lett. **160**, 468 (2015)
29. R. Bodeux, J. Leguay, S. Delbos, Thin Solid Films **582**, 229 (2015)
30. R. Chierchia, F. Pigna, M. Valentini, C. Malerba, E. Salza, P. Mangiapane, T. Polichetti, A. Mittig, Phys. Status Solidi C **13**, 35 (2016)
31. Y. Xiong, Y. Xie, G. Du, H. Su, Inorg. Chem. **41**, 2953 (2002)
32. G. Demazeau, Z. Naturforsch. **65b**, 999 (2010)
33. Q. Yu, X. Zhang, H. Bian, H. Liang, B. Zhao, S. Yan, D. Liao, Cryst. Growth Des. **8**, 1140 (2008)
34. Q. Chen, D. Ma, Int. J. Photoenergy **2013**, 5 (2013)
35. B. Qu, H. Li, M. Zhang, L. Mei, L. Chen, Y. Wang, Q. Li, T. Wang, Nanoscale **3**, 4389 (2011)
36. B. Qu, M. Zhang, D. Lei, Y. Zeng, Y. Chen, L. Chen, Q. Li, Y. Wang, T. Wang, Nanoscale **3**, 3646 (2011)
37. W. Li, X. Han, Y. Zhao, L. Liu, J. Wang, S. Yang, T. Tanaka, Mater. Lett. **125**, 167 (2014)
38. X. Chen, X. Wang, C. An, J. Liu, Y. Qian, J. Cryst. Growth **256**, 368 (2003)
39. X. Liang, Q. Cai, W. Xiang, Z. Chen, J. Zhong, Y. Wang, M. Shao, Z. Li, J. Mater. Sci. Technol. **29**(3), 231 (2013)
40. H. Wu, D. Liu, H. Zang, C. Wei, B. Zeng, J. Shi, S. Yang, Carbon **50**, 4847 (2012)
41. S. Rabaoui, H. Dahman, N.B. Mansour, L.E. Mir, J. Mater. Sci. Mater. Electron. **26**, 1119 (2015)
42. R.I. Walton, Chem. Soc. Rev. **31**, 230 (2002)
43. Y. Tan, Z. Lin, W. Ren, W. Ren, W. Long, Y. Wang, X. Ouyang, Mater. Lett. **89**, 240 (2012)
44. Q. Li, Y. Ding, X. Liu, Y. Qian, Mater. Res. Bull. **36**, 2649 (2001)
45. C. Wu, Z. Hu, C. Wang, H. Sheng, J. Yang, Y. Xie, Appl. Phys. Lett. **91**, 143104 (2007)
46. L. Essaleh, H. Chehouani, M. Belaqziz, K. Djessas, J.L. Gauffier, Superlattice. Microst. **85**, 806 (2015)
47. H. Liu, Z. Chen, Z. Jin, Y. Su, Y. Wang, Dalton Trans. **43**, 7491 (2014)
48. J.V.V. Embden, A.S.R. Chesman, J.J. Jasieniak, Chem. Mater. **27**, 2246 (2015)
49. G.H. Carey, A.L. Abdelhady, Z. Ning, S.M. Thon, O.M. Bakr, E.H. Sargent, Chem. Rev. **115**(23), 12732 (2015)
50. D.V. Talapin, A.L. Rogach, M. Haase, H. Weller, J. Phys. Chem. B **105**, 12278 (2001)

51. A.C. Lokhande, K.V. Gurav, E. Jo, M. He, C.D. Lokhande, J.H. Kim, Opt. Mater. **54**, 207 (2016)
52. A.C. Lokhande, S.A. Pawar, E. Jo, M. He, A. Shelke, C.D. Lokhande, J.H. Kim, Opt. Mater. **58**, 268 (2016)
53. J. Chang, E.R. Waclawik, Chem. Eng. Commun. **15**, 5612 (2013)
54. M. Kruszynska, J. Parisia, J. Kolny-Olesiaka, Z. Naturforsch. **69a**, 446 (2014)
55. X. Liu, X. Wang, M.T. Swihart, Chem. Mater. **27**, 1342 (2015)
56. L. Yi, D. Wang, M. Gao, Chem. Eng. Commun. **14**, 401 (2012)
57. S. Okano, S. Takeshita, T. Isobe, Mater. Lett. **145**, 79 (2015)
58. X. Lin, A. Steigert, M.C. Lux Steiner, A. Ennaoui, RSC Adv. **2**, 9798 (2012)
59. Y. Park, H. Jin, J. Park, S. Kim, CrystEngComm **16**, 8642 (2014)
60. Q. Liang, L. Han, X. Deng, C. Yao, J. Meng, X. Liu, J. Meng, CrystEngComm **16**, 4001 (2014)
61. J. Park, M. Song, W.M. Jung, W.Y. Lee, H. Kim, Y. Kim, C. Hwang, L.L.-W. Shim, Dalton Trans. **42**, 10545 (2013)
62. W. Wang, H. Shen, J. Li, Mater. Lett. **111**, 5 (2013)
63. M. Baghbanzadeh, L. Carbone, P.D. Cozzoli, C.O. Kappe, Angew. Chem. Int. **50**(48), 11312 (2011)
64. M.P. Suryawanshi, U.V. Ghorpade, S.W. Shin, S.A. Pawar, I.Y. Kim, C.W. Hong, M. Wu, P.S. Patil, A.V. Moholkar, J.H. Kim, ACS Appl. Mater. Interfaces **8**, 11603 (2016)
65. H. Dahman, S. Rabaoui, A. Alyamani, L. El Mir, Vacuum **101**, 208 (2014)
66. S. Yasar, S. Kahraman, S. Cetinkaya, I. Bilican, J. Alloys Compd. **618**, 217 (2015)
67. S. Rabaoui, H. Dahman, S. Dekhil, K. Omri, A. Alyamani, L. El Mir, J. Mater. Sci. Mater. Electron. **26**, 8588 (2015)
68. D. Tiwari, T.K. Chaudhuri, T. Shripathi, U. Deshpande, AIP Conf. Proc. **1447**, 1039 (2011)
69. D. Tiwari, T.K. Chaudhuri, T. Shripathi, U. Deshpande, R. Rawat, Sol. Energy Mater. Sol. Cells **113**, 165 (2013)
70. J. Han, Y. Zhou, Y. Tian, Z. Huang, X. Wang, J. Zhong, Z. Xia, B. Yang, H. Song, J. Tang, Front. Optoelectron. **7**, 37 (2014)
71. A. Kamyshny, J. Steinke, S. Magdassi, Open Appl. Phys. J. **4**, 19 (2011)
72. X. Zhang, D. Zhang, X. Ni, H. Zheng, Solid State Commun. **139**, 412 (2006)
73. L. Suber, I. Sondi, E. Matijevic, D.V. Goia, J. Colloid Interface Sci. **288**, 489 (2005)
74. I. Sondi, D.V. Goia, E. Matijevic, J. Colloid Interface Sci. **260**, 75 (2003)

Rational Engineering of Photocathodes for Hydrogen Production: Heterostructure, Dye-Sensitized, Perovskite, and Tandem Cells

Jasmin S. Shaikh, Meena Rittiruam, Tinnakorn Saelee, Victor Márquez, Navajsharif S. Shaikh, Pongsakorn Kanjanaboos, Chandrakant D. Lokhande, Supareak Praserthdam, and Piyasan Praserthdam

Abbreviations

APCE	Absorbed photon-to-current conversion efficiency
CB	Conduction band
CZTS	Copper zinc tin sulfide
D	Dimension
DSPECs	Dye-sensitized photo-electrochemical cells
DSC	Dye-sensitized solar cell
$E_{f,h}$	Quasi-Fermi levels of holes
$E_{f,n}$	Quasi-Fermi levels of electrons
$E_{F(EQ)}(H_2O/H_2)$	Fermi level of water/hydrogen redox reaction
ETM	Electron transporting material

J. S. Shaikh · M. Rittiruam · T. Saelee · S. Praserthdam (✉)
High-Performance Computing Unit (CECC-HCU), Center of Excellence on Catalysis and Catalytic Reaction Engineering (CECC), Chulalongkorn University, Bangkok, Thailand
e-mail: Supareak.P@chula.ac.th

V. Márquez · P. Praserthdam
Center of Excellence on Catalysis and Catalytic Reaction Engineering (CECC), Department of Chemical Engineering, Faculty of Engineering, Chulalongkorn University, Bangkok, Thailand

N. S. Shaikh
School of Materials Science and Innovation, Faculty of Science, Mahidol University, Nakhon Pathom, Thailand

Centre of Interdisciplinary Research, D. Y. Patil Education Society, Kolhapur, Maharashtra, India

P. Kanjanaboos
School of Materials Science and Innovation, Faculty of Science, Mahidol University, Nakhon Pathom, Thailand

C. D. Lokhande
Centre of Interdisciplinary Research, D. Y. Patil Education Society, Kolhapur, Maharashtra, India

F. I. Ezema et al. (eds.), *Chemically Deposited Metal Chalcogenide-based Carbon Composites for Versatile Applications*, https://doi.org/10.1007/978-3-031-23401-9_11

HER	Hydrogen evolution reaction
HTM	Hole transporting material
IPCE	Incident photon-to-current efficiency
OER	Oxygen evolution reaction
PSC	Perovskite solar cell
PEC	Photoelectrochemical
PMI-6 T-TPA	Perylenemonoimid-sexithiophene-triphenylamine dye
QDs	Quantum dots
STH	Solar to hydrogen conversion efficiency
VBM	Valence band maxima
VB	Valence band

1 Introduction

The use of solar energy for the production of chemical fuels is a sustainable retort to energy production. Photoelectrochemical (PEC) splitting of H_2O by the use of sun irradiation for hydrogen production is a renewable method [1–3]. A PEC cell is created on an electrode/liquid junction. Here, photocarriers (minority carriers) generated upon absorbing light via semiconductor electrode are transferred into the electrolyte via the electric field at the interface of semiconductor and solution, where the redox reaction can take place like reduction reaction of a proton (H^+) to H_2 [1, 4]. Figure 1a shows the schematic illustration of external bias requirement where theoretical voltage ($E = 1.23$ V), overpotential for HER and OER reaction, and bias required for water splitting with~10 mA/cm^2. Hydrogen production by PEC is very auspicious since high gravimetric energy (143 MJ/kg) and carbon-free characteristics of hydrogen are directly useful as a fuel in fuel cells and engine [1]. Many nanomaterials have been widely studied to attain the efficacy that could be for practical usage. A large effort has been dedicated to getting higher photocurrent density and stability by fabricating nanomaterials of having properties such as physical properties, heterostructure formation, and increased light absorption [5–8]. The physical properties are consisting of the presence of localized states, low-coordinated sites, anisotropic conductivity, high surface area, and tunable optical properties (Fig. 1b) [9–11]. The low-dimensional nanomaterials, which consist of a heterostructure of 0D-1D, 1D-2D, 0D-2D, and 2D-2D architectures, have strong van der Waals force of an attraction, which leads to the formation of stable electrochemical materials [12–14]. The nanomaterials show increased light absorption by plasmonic effect [15–17], field effect [18], doping or alloying [19], and defect grain boundary [20]. These phenomena are benefited to improve charge-transfer process and fast excitation of photocarriers and dissociation. However, many problems such as the narrow spectral ranges, fast recombination of carriers, and low quantum efficacy in the photocatalytic hydrogen evolution reaction (HER) have been faced. For the abovementioned problems, a variety of ways have been used to expand the catalytic activity to a greater range

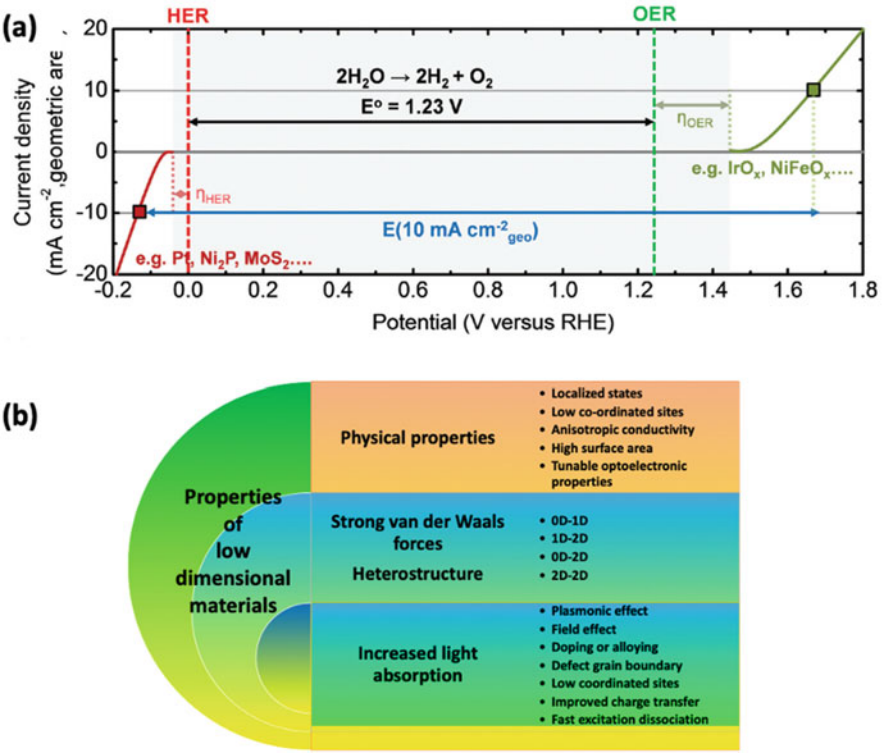

Fig. 1 (**a**) Schematic illustration of requirement of bias in addition to the theoretical voltage for the water splitting reaction ($E = 1.23$ V) [36]. Copyright 2019, The Royal Society of Chemistry. (**b**) Schematic representation of properties of low dimensional materials

such as (i) improving absorption by catalysts, (ii) improving the operation of photogenerated charges, and (iii) promoting the carrier separation and transfer of photogenerated carriers [21]. However, the key obstacle in the PEC is that it gets one semiconductor to attain all necessities. Visible light-absorbing semiconductor wrestle from corrosion, while broad bandgap materials are stimulated by UV light absorption. The high currents have been attained by integration of two materials having a type-II band level alignment. To expand the absorption of solar light, establishing heterojunctions with narrow bandgap, doping, surface plasmons, and DSC can be used. However, the obstacle of sluggish oxygen and hydrogen evolution reaction rate declines the performance of a material. Additional way to resolve this issue is to decorate the surface of semiconductor with a co-catalyst, which more decreases the overpotential via growing the kinetics of photogenerated electrons [22]. We represent to the development of heterostructural photocathode dye and perovskite-sensitized photocathode and tandem devices.

2 Literature Survey and State of the Art of PEC for Hydrogen Production and Photocathodes

The PEC consists of the decomposition of water into oxygen and hydrogen due to the absorption of light by photoelectrode (catalytic electrode). This process is important for the utilization of solar light for the production of H_2 gas for fuel. In 1972, Fujishima and Honda [23, 24] reported a light-driven PEC water splitting that is based on an open modern artificial photosynthesis approach. They used a single-crystalline TiO_2 as a photoanode and a Pt cathode. The current-voltage measurement under irradiation of light on TiO_2 electrode revealed the current passed through the load was directly proportional to the light intensity. From the direction of the current, it was discovered that the oxidation reaction happened at the photoanode (TiO_2), and the reduction process occurred at the photocathode. The oxidation reaction consists of oxygen evolution resulting from photoelectric water electrolysis. The schematic model of photosensitized electrolytic oxidation reaction at the photoanode was reported. The solar conversation efficiency for TiO_2 was less than 1% due to its high bandgap energy. The hydrogen is detected at the cathode (Pt electrode). In 1975, Mavroides et al. [25] reported photoelectrolysis of water using $SrTiO_3$ anode with maximum external quantum efficacy of 10%, and it is greater than the TiO_2-integrated anode PEC. This report revealed the small electron affinity material useful for getting high external quantum efficiency. In 1976, Nozik et al. [26, 27] reported the tandem-junction architecture, which was made by a photoanode (n-type) and photocathode (p-type) with highest STH conversion efficiency than a single photoelectrode. Difficulties to use direct PEC are the lack of light absorption (bandgap <2.0 eV), corrosion of the material, and obstacles of matching the semiconductor band-edge energies with the O_2 and H_2 evolution reactions.

Metal oxides are usually used due to its steadiness in an aqueous electrolyte but possess high bandgap (poor light absorption in the visible range) and poor semiconductor characteristics. Semiconductors are typically thermodynamically unstable for the oxidation process. However, p-type semiconductors have protection against photo corrosion because the surface is cathodically protected under the illumination of light [28, 29]. In 1986, theoretical studies showed that high-efficiency PEC can be obtained by low bandgap non-oxide photoanode [30]. In respect of this, in 1987, Kainthla et al. [27] reported self-driven PEC cell that is made by a p-InP with Pt as the photocathode and protected n-GaAs as a photoanode. The PEC measurement showed that STH of 8.2% with good stability (decrease of efficiency of about 10% throughout the first hour of the operation and later on as it is steady for further 10 h). In 1998, Khaselev et al. [28] reported the PEC cell integrated with photovoltaic device splits H_2O into H_2 and O_2 evolution directly upon light incident without bias applied. They fabricated a tandem cell of p/n GaAs junction (Eg = 1.42 eV) as a bottom cell designed for the absorption in the near-infrared range and the top p- $GaInP_2$ junction (Eg = 1.83 eV) designed for the absorption in visible light. The H_2 production efficacy of the tandem architecture was 12.4%.

In 2010, Domen's group [31] reported the CZTS-based photocathode for hydrogen evolution for the first time. Since 2012, dye-sensitized PECs (DSPECs) increased interest for H_2 generation as evidenced by the published articles. In 2012, Tong et al. [32] published the first report of the DSPEC fabricated by the perylenemonoimid-sexithiophene-triphenylamine dye coated on the photocathode. H_2 evolution at a rate of ca 80 nmol h^{-1} cm^{-2} was obtained in sodium sulfate electrolyte at an applied potential (0.197 V vs NHE) and under 600–800 mW cm^{-2} Xe light.

Semiconductor quantum dots (QDs) with broad absorption spectral range and good photostability are more for fabricating highly durable and efficient photocatalytic systems. In recent years, hybrid systems comprising QDs have been reported to be stable and active PEC [33]. In 2016, Quesada et al. first reported on the $CH_3NH_3PbI_3$ (perovskite)-based photocathode for the PEC. An InBiSn alloy was implemented to shield the perovskite from H_2O and letting the photoelectrons to get to a Pt electrode. The PEC exhibited high photocurrent density (9.8 mA cm^{-2} at 0 V vs RHE). The perovskite-based photocathode exhibited remarkable stability (80% retention of their initial current for 1 h under light) [34].

3 Principle, Charge Separation, Transportation, and Device Architecture of PEC Cells

The water splitting involves the process of charge separation of water into hydrogen and oxygen. Various ways for water splitting have been used like photocatalytic, photoelectrochemical (PEC), radiolysis, thermal decomposition, and photobiological. In PEC, the half-cell reaction consists of the production of H_2 at the cathode, and half-cell consists of O_2 evolution at the anode. The basic principle of PEC-integrated water splitting is the alteration of renewable solar energy to hydrogen by employing external bias to the two electrodes, which immersed in the electrolyte containing the redox couples. One electrode is made by photo-absorbing material (like semiconductor) called as photoelectrode, and another one is electrocatalyst either for oxygen evolution reaction (OER) or for hydrogen evolution reaction (HER) [35–37]. Mainly three types of device architecture have been investigated for water splitting: (i) The first type consists of fabrication of photoanode for OER reaction and use of electrocatalyst electrode (like Pt) for HER reaction, where different light-absorbing photoanode materials like high bandgap metal oxides (TiO_2, ZnO, and WO_3) have been investigated (Fig. 2a, b). (ii) The second type consists of the fabrication of the PEC device by developing photocathode material for HER reaction and using OER electrocatalyst material as anode material such as Pt electrode (Fig. 2d, e). (iii) The third method consists of the development of both photoelectrodes (photoanode and photocathode) for HER and OER reactions (Fig. 2g, h).

In these architectures, photoelectrode absorbs the photons and converts them to electron-hole pairs, in which further electrons are transferred to electrolyte

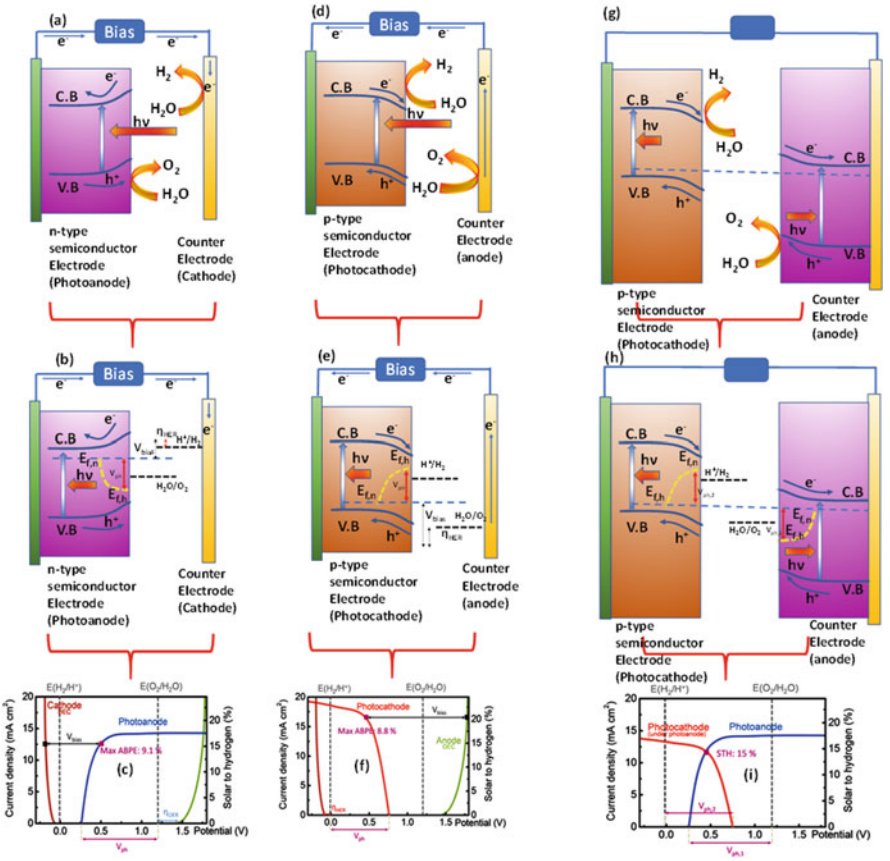

Fig. 2 The classification of PEC cells for water splitting. (**a**) Photoanode-HSC cathode. (**b**) Carrier transportation process in PEC device, which has fabricated by photoanode-HSC cathode combination. (**c**) The example of J-V curve and operating points getting from the device [36]. Copyright 2019, Royal Chemical Society. (**d**) Photocathode-OEC anode. (**e**) Carrier transportation process in PEC device, which has fabricated by photocathode-OEC anode. (**f**) The example of J-V curve of the photocathode-OEC anode device and operating point in the device. Max ABPE of the device [36]. Copyright 2019, Royal Chemical Society. (**g**) Photoanode-photocathode tandem cell. (**h**) Schematic of carrier transportation process in PEC device for tandem cell. (**i**) The example of J-V curve of the tandem cell and operating point in the device [36]. (Copyright 2019, Royal Chemical Society)

where redox reaction of reduction of protons into hydrogen molecule takes place. Furthermore, the hole is transferred through external circuit to an anode electrode where a redox reaction of oxidation of water to oxygen molecule takes place. The most significant device architecture feature consists of the formation of the semiconductor-electrolyte liquid junction at photoelectrode-electrolyte interface. In detail, photoelectrode is kept in interaction with an aqueous electrolyte, and carriers flow crossways the interface of semiconductor electrode-electrolyte owing

to differences in Fermi energy between semiconductor electrode and electrolyte. Once equilibrium is reached, the space-charge region that is the electric double layer (Helmholtz double layer) is generated at the semiconductor surface.

In the first step, consider p-type semiconductor (photocathode) having a bandgap energy Eg in connection with the electrolyte, charge carriers are exchanged between the semiconductor and the electrolyte. The negatively charged hole-depletion layer is generated at semiconductor part of the interface. This hole-depletion layer showed in the energy level diagram via downward bending of CB and VB edges in the direction of the bulk interface. In opposite to this in n-type semiconductor, the electron-depletion region formed at the surface and upward bending of CB and VB edges in the direction of the bulk interface takes place. In the second step, photoelectrode is illuminated by light having energy higher than Eg. The photon excites electrons from VB to CB and left holes in the VB. Under the illumination of light, the nonequilibrium condition comes, which leads to split quasi-Fermi levels of holes ($E_{f,h}$) and electrons ($E_{f,n}$) which showed that the concentration of the minority carrier is enhanced. The space-charge layer, which formed upon illumination of light, results into charge separation due to the formation of the electric field within the space-charge layer. Therefore, in a photocathode, electrons are taken away from the bulk toward the electrolyte to produce hydrogen due to the formation of electrical gradient and chemical gradient. Hence, for charge separation and transportation, the CB edge of the p-type semiconductor should lie above the Fermi level of water/hydrogen redox reaction ($E_{F(EQ)}(H_2O/H_2)$). Holes are transferred to counter electrode (OER catalyst-anode electrode) via external circuit for hole collection [36–38]. The collected holes are used to oxidize the water to oxygen; this reaction delivers electrons, which further pass via the external circuit from the counter electrode to the photoelectrode (photocathode). Figure 2c, f, i show the J-V curves and operating points.

The change in the Gibbs free energy ($\Delta G_0 = 237.2$ kJ/mol) is required for the splitting of H_2O into H_2 and ½ O_2. According to the Nernst equation, this attributed to the standard reversible electrode potential ΔE_0 (1.23 V). In water splitting process, the photon energy must be higher than 1.23 eV. The required equations for OER and HER are given below [39]:

$$H_2O\,(l) + 2h^+ \rightarrow 1/2O_2\,(g) + 2H^+\,(aq) \tag{1}$$

$$2H^+\,(aq) + 2e^- \rightarrow H_2\,(g) \tag{2}$$

$$H_2O\,(l) \rightarrow 1/2O_2\,(g) + H_2\,(g) \tag{3}$$

The four electron-hole pairs are required to produce for overall water splitting process.

4 The Conversion Efficiency Calculations

The standard STH can be deduced from the whole energy produced and applied overall energy sunlight (100 mW/cm^2) [35]:

$$\eta_{\mathrm{STH}} = \frac{\text{Total energy generated}}{\text{Total energy input}} = \frac{\Delta G \times \mathrm{r}_{\mathrm{H}_2}}{P_{\mathrm{light}} \times \mathrm{S}} \tag{4}$$

where rH is the rate of H_2 generation, ΔG is Gibbs free energy =237 kJ mol^{-1}, S is the area of the photoelectrode (cm^2), and P_{light} is the light intensity (100 mWcm^{-2}).

When external bias is supplied to the PEC system, applied bias photon-to-current efficacy (ABPE) at external voltage is calculated by Eq. 5:

$$\mathrm{ABPE} = \frac{J_{\mathrm{ph}}\left(V_{\mathrm{redox}} - V_{\mathrm{bias}}\right)}{P_{\mathrm{light}}} \tag{5}$$

where J_{ph} is the generated current density; V_{redox}-redox potential for H_2O splitting reaction, which is 1.23 V versus NHE; Vbias is the difference between voltage of the working and counter electrodes; P_{light} light intensity (100 mW cm^{-2}).

Calculation of Faradaic efficiency is the ultimate technique to confirm that produced photocurrent is attributed to the water splitting reaction and not due to corrosion of photoelectrodes or any adverse reactions. It is calculated by taking fraction of the actual evolved gas (based on the measured current) and the theoretically evolved gas:

$$\text{Faradaic efficiency} = \frac{\text{Experimental gas evolution}}{\text{Theoretical gas evolution}} \tag{6}$$

$$= \frac{\text{Oxygen evolution measured}}{\text{Gas evolution based on the photocurrent}} \tag{7}$$

$$= \frac{\text{Oxygen evolution measured}}{\left(\frac{J_{\mathrm{ph}} \times A \times T}{e}/4\right)/N_{\mathrm{A}}} \times 100\% \tag{8}$$

where J_{ph}- the photocurrent density (A/cm^2) generated during the measurement time (T in seconds), e represents the charge of an electron (1.62 × 10^{-19}C), A is the lighting area of the photoelectrode, and N_{A} is Avogadro constant (6.02 × 10^{23} mol^{-1}). Also, the amount of gas molecules (in moles) can be deduced by gas chromatog-

raphy (GC). But for oxygen, it can be deduced by using a fluorescence detector or using oxygen electrode.

5 Quantum Conversion Efficiency Calculations

The incident photon-to-current efficiency (IPCE) deduced at light wavelengths by Eqs. 9 and 10:

$$\text{IPCE}\,(\lambda) = \frac{\text{Total energy of converted electrons}}{\text{Total energy of incident photons}} \tag{9}$$

$$= \frac{\left(\frac{J_{\text{photo}}(\lambda)}{e}\right) \times \left(\frac{hc}{\lambda}\right)}{P\,(\lambda)} \times 100\% \tag{10}$$

where J_{photo} is photocurrent density at the incident light (mA/cm^2), e is the charge of an electron (1.602×10^{-19} C), h is Planck's constant (6.626×10^{-34} JS), λ is the wavelength of the light (nm), c is speed of light ($3.\,0 \times 10^8 \times 10^9$ nm s^{-1}), and $P(\lambda)$ is the light intensity at that particular wavelength (mW cm^{-2}).

In the calculation of IPCE, optical losses are not considered, in spite of it leads to the potential impression on the IPCE. To overcome these losses, the absorbed photon-to-current conversion efficiency (APCE) is applied. This is determined by following equation:

$$\text{APCE}\,(\lambda) = \frac{\text{IPCE}\,(\lambda)}{A\,(\lambda)} = \frac{\text{IPCE}\ (\lambda)}{1 - R - T} \times 100\% \tag{11}$$

where A is the absorption of light, R is the reflection, and T is the transmission of the light.

6 Photocathodes in PEC

Photocathodes that have been made up of p-type semiconductors evolve hydrogen at the interface between semiconductor and electrolyte. However, very few materials exhibit inherent p-type conductivity. Most nitride, sulphide, and metal oxide show n-type conductivity owing to the existence of anion defects [40]. Various techniques attained in order to enhance the efficiency of PEC including doping, heterojunction, dye sensitization, perovskite sensitization, tandem cell, etc. (Fig. 3) [41–46]. Often, Pt has used as a photocathode due to its high catalytic activity, that is, the high

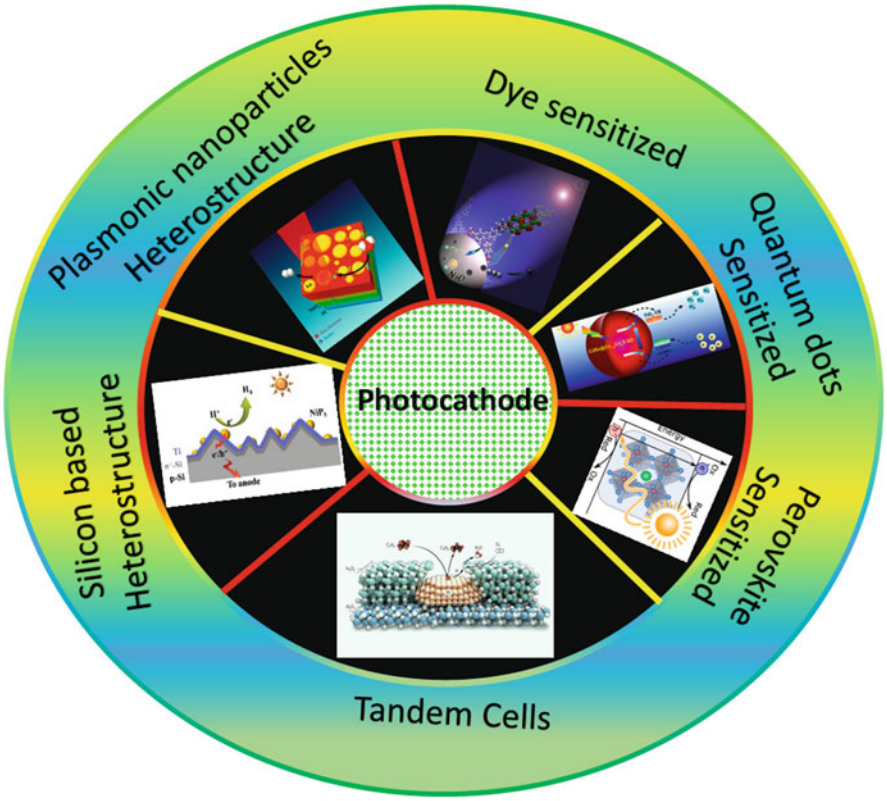

Fig. 3 Schematic diagram of photocathode fabrications by different methods such as silicon-based heterostructure [41]. Copyright 2016, American Chemical Society. Plasmonic nanoparticle heterostructures [42]. Copyright 2015, American Chemical Society. Dye-sensitized photocathode [43]. Copyright 2020, American Chemical Society. Quantum dot-sensitized photocathode [44]. Copyright 2020, Elsevier. Perovskite-sensitized photocathode [45]. Copyright 2020, American Chemical Society. Tandem cell photocathode [46]. Copyright 2021, Science

current density for the hydrogen evolution process. However, Pt is costly metal and hence replaced by other catalytic materials such as metal oxides, nitrides, and chalcogenides.

The p-type semiconductor is used as a photocathode with following desired properties. CB edge of the p-type electrode must be extra negative in NHE than the hydrogen evolution potential. The photovoltage generated must be high by way of applying outside bias or to remove the restriction on the choice of the counter electrode (anode electrode). Figure 4a, b displays the schematic diagram of the energy level positions of CB edge and VB edge for photocathode semiconductors. The p-type semiconductor (photocathode) ought to light absorptive (visible light) to reach high STH as high as possible. The photocathode necessity may be stable in the electrolyte under light to guarantee a long lifetime. And lastly, the material

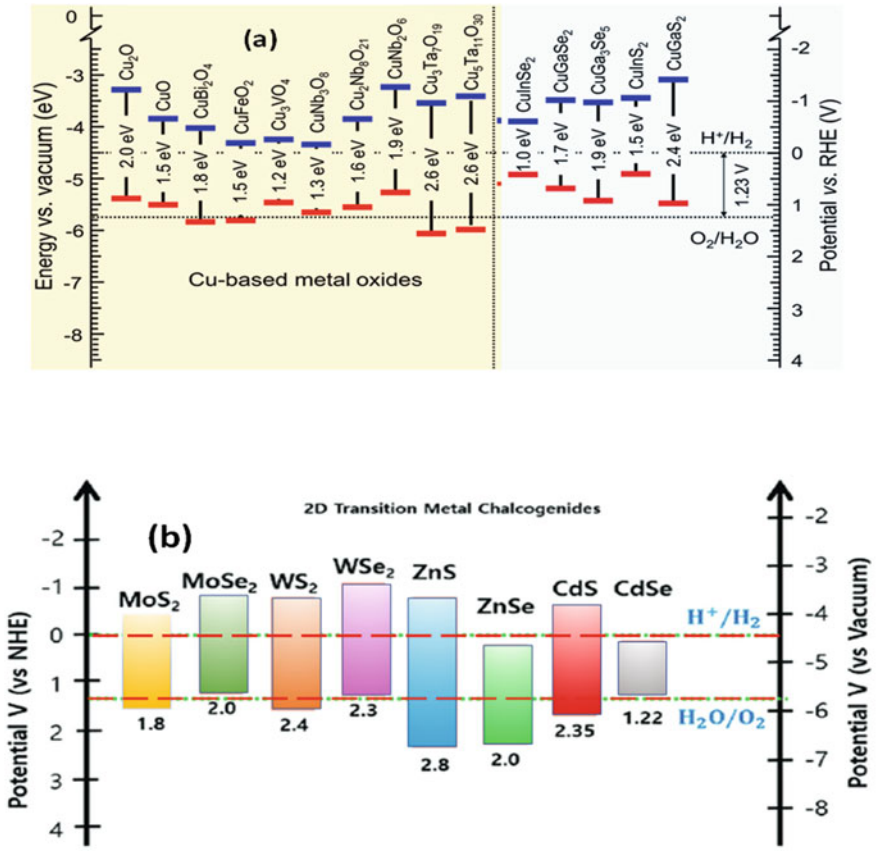

Fig. 4 Energy level diagram of photocathodes. (**a**) Cu-based metal oxides and chalcogenides [39]. Copyright 2020, The Royal Society of Chemistry. (**b**) 2D metal chalcogenide materials. Copyright 2019, MDPI

must be earth-abundant to get both feasibilities of wide application and get a high performance/price ratio. The cathodic photocurrent can be enhanced by fabricating the p-n heterojunction. The band-bending initiated in an n-type semiconductor on p-type semiconductor is the key to reach the high photocurrent and enhancing the onset potential of the cathodic current (photocurrent).

7 The P-N Heterojunction Photocathode for PEC

The use of a heterojunction photocathode is an auspicious method attempted to increase the efficiency of the PEC cell. There are four main types of heterostructure

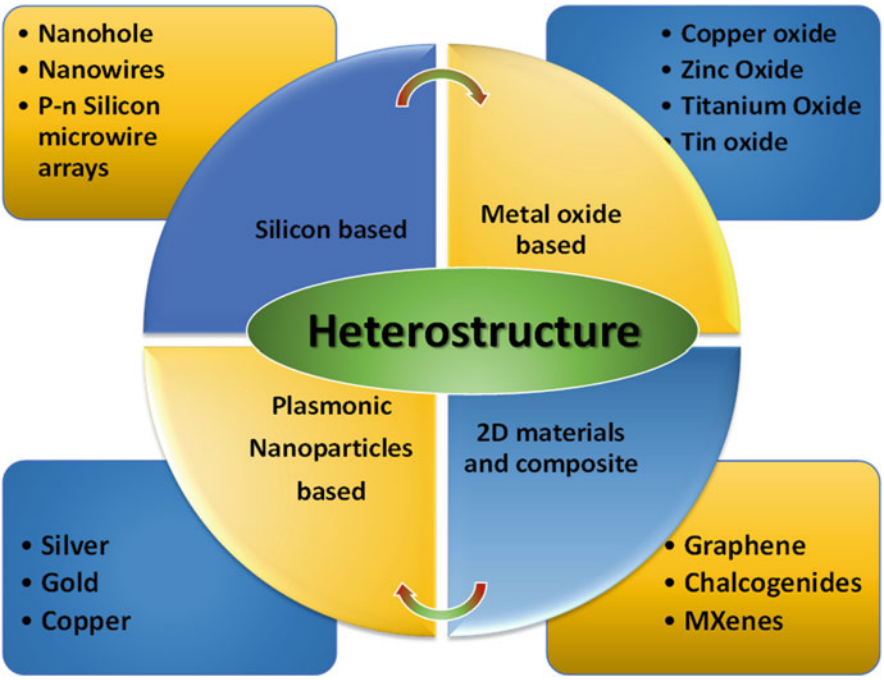

Fig. 5 Heterostructure is fabricated by different ways: (i) silicon-based heterostructure, (ii) metal oxide-based heterostructure, (iii) 2D materials and composite, and (iv) plasmonic nanoparticle-based heterostructure

fabrication: (i) metal oxide-based, (ii) 2D materials and composite-based, (iii) plasmonic nanoparticle-based, and (iv) silicon-based heterostructures. The detailed classification and materials used in the fabrication of heterostructure is shown in Fig. 5. Heterojunction photocathode is classified into two types: (i) Z-scheme and (ii) the Schottky junction [47, 48]. Often, a heterojunction has formed by using wide bandgap, and low bandgap semiconductor creates type-II band alignment (staggered band-edge alignment) in which the energy level of VB of one semiconductor is energetically positioned between the VB and CB of another semiconductor, and its CB is energetically positioned above the VB, and CB of other semiconductors can enhance separation of photocarriers resulting in improved photoactivity of photoelectrodes (photocathode). Schottky endorses the separation of photoelectron-hole pairs. It is formed by the integration of semiconductor and metallic nanoparticles, which results into the development of space charge region at the interface of semiconductor and nanoparticles [49].

8 Silicon Absorber-Based Heterostructure for Photocathode Fabrication

Silicon-based heterostructure materials have been extensively investigated in the past decade due to narrow bandgap (1.12 eV), earth abundance, low cost, and high theoretical photocurrent density (44 mA cm^{-2}) [50]. The pristine Si has disadvantages of sluggish carrier transportation at the interface of Si/electrolyte and exhibits deprived steadiness in an aqueous electrolyte; therefore, these limitations restrict the use of pristine Si in PEC for hydrogen evolution [51, 52]. In respect of these limitations, various Si-based nanocomposite photocathodes were investigated by coating the Si surface with various electrocatalysts that showed improvement in photogenerated electron transport kinetics and hydrogen evolution reaction (HER) at the electrode. For total water splitting process, HER at cathode and OER process at anode must be mutually compatible. The metal-based OER catalysts exhibit greater activity and better steadiness only in basic electrolytes. Hence, to protect corrosion of Si-based photocathodes in basic aqueous electrolytes, a covering layer with metal oxides such as the TiO_2 layer is used. An architecture of TiO_2/Au nanocoating (AuNR)/Si nanohole (SiNH) hetero-structure was constructed. Here, the SiNH arrays have been constructed via the amalgamation of nanoimprint lithography (NIL) besides reactive ion etching (RIE) process, respectively [53]. Figure 6a demonstrates the construction method of well-organized SiNH arrays. Then, poly(methyl methacrylate) (PMMA) (200 nm thick) has been deposited via spin coating on Si, and silicon-carrying UV-curable layer was deposited over PMMA layer via spin coating process. The hybrid PDMS was deposited by pressing over resist film and UV light exposing in nitrogen atmosphere. The PMMA layer was etched by RIE after removal of the mold. After that, Ni (30 nm) was deposited via electron-beam evaporation. The SiNH arrays were fabricated by RIE process via etching the Si substrate and removal of Ni via low-concentrated nitric acid. It demonstrates the construction of AuNR arrays immersed in SiNH arrays. Firstly, the oxidation layer on the prepared Si was detached by dipping it in the 5% solution of HF over 1 min. Then, Au metal was coated by ion beam sputtering method. Then, ion beam etching (IBE) process was adopted.

Also, it demonstrates the deposition of TiO_2 layer via e-beam evaporation method on AuNR arrays immersed in SiNH arrays. SEM of the AuNR/SiNH 310 arrays besides a pitch (600 nm) and a diameter 400 nm are showed in Fig. 6b. The electrochemical performance that means J-V curves of AuNR/SiNH, TiO_2/SiNH, and TiO_2/AuNR/SiNH samples was measured at100 mW/cm^2 illumination and without light in 0.5 M H_2SO_4. Figure 6c revealed TiO_2/SiNH sample has higher photocurrent with higher positive onset potential than AuNR/SiNH. The result revealed that the passivation process takes place by the TiO_2 layer. The TiO_2/AuNR/SiNH arrays showed higher photocurrent and positive onset potential than AuNR/SiNH and TiO_2/SiNH arrays. The higher work function of Au, which form an ohmic contact with SiNH tends to facile photoelectron transport process

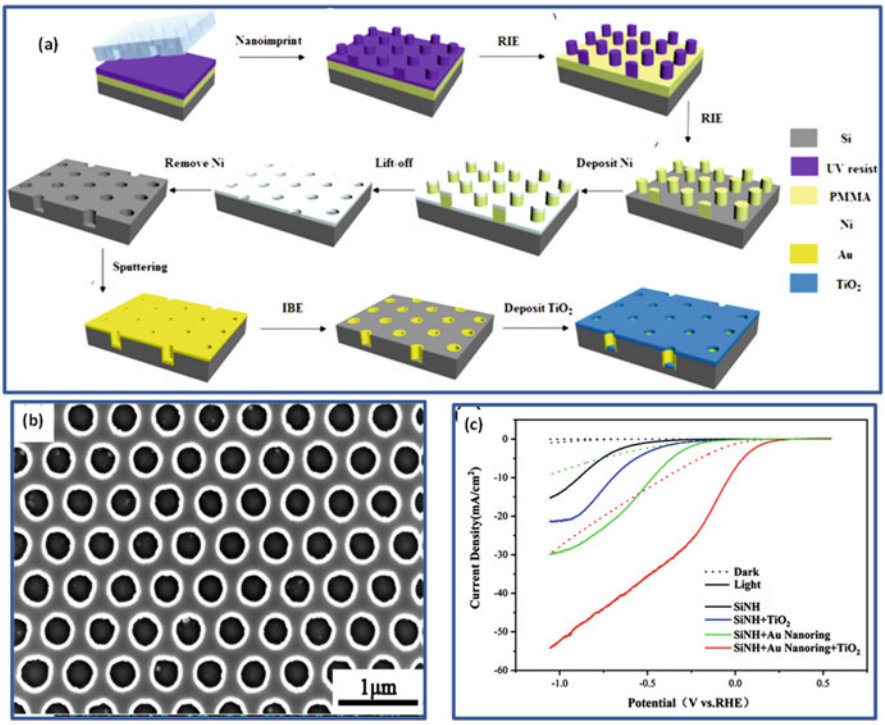

Fig. 6 (**a**) The schematic of the fabrication of TiO_2/AuNR/SiNH HN arrays. (**b**) SEM image of the AuNR/SiNH arrays (top view) after the IBE process. (**c**) J-V curves of (i) SiNH arrays, (ii) TiO_2/SiNH arrays, (iii) AuNR/SiNH arrays, and (iv) TiO_2/AuNR/SiNH arrays, which have measured with/without light illumination [53]. (Copyright 2019, American Chemical Society)

across the interfaces of Au and Si, causing the HER during the J-V measurements (electrochemical experiments).

Tekalgne et al. reported hydrothermal preparation of a photocathode of SnO_2@WS_2 nanoflowers (NF) on p-Si that has low recombination of photogenerated carriers and better light absorption for the HER. UV-vis spectral study revealed that SnO_2@WS_2 has Eg of 2.1 eV with higher absorbance in the visible range and absorption edge around 565 nm than that of bare SnO_2 (Fig. 7a) [54]. The photocatalytic HER activities of the bare SnO_2, bare WS_2, and SnO_2@WS_2 hybrid were examined in a H_2SO_4 electrolyte under irradiation of light having wavelength $\lambda > 420$ nm (visible light), as displayed in Fig. 7b. For bare WS_2, the current density at 0 V is very low indicating low performance for HER. Additionally, bare SnO_2 was low photocurrent density of -0.6 mA cm^{-2} at 0 V. The HER performance of the SnO_2@WS_2 nanocomposite was much higher than that of bare WS_2, and SnO_2 due to heterostructure improve the carrier transportation characteristics and suppression of the charge recombination process. For the synthesis of SnO_2@WS_2–1, the 0.02 M WS_2 was loaded on SnO_2 and shows the

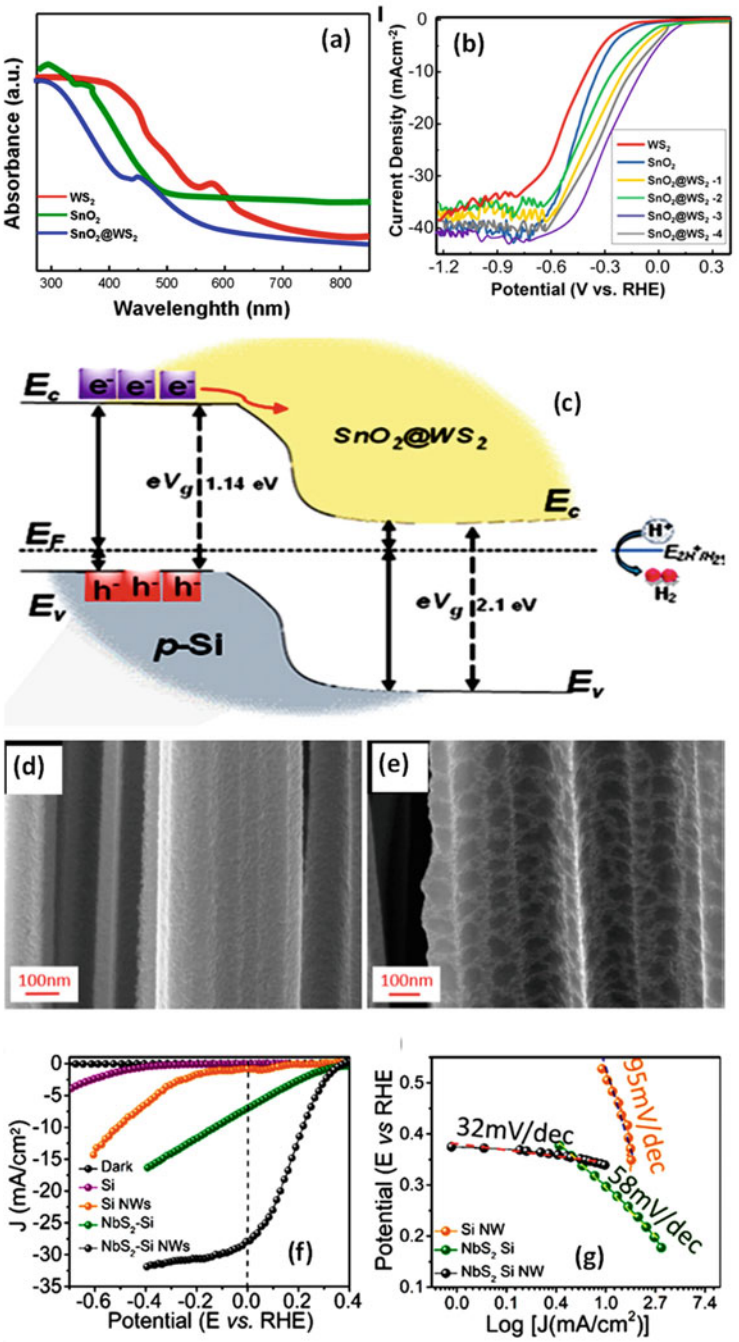

Fig. 7 (**a**) UV-vis spectra of WS_2, SnO_2, and $SnO_2@WS_2$. (**b**) HER polarization (in 0.5 M H_2SO_4. (**c**) Schematic of PEC device [54]. (**d**) FE-SEM image of the as-prepared Si NW. (**e**) FE-SEM image of NbS_2, which has grown by CVD. (**f**) J-V comparison of Si, NbS_2-Si, and NbS_2-Si NW at 0 V versus RHE. (**g**) Tafel slope of Si-NW, NbS_2-Si, and NbS_2-Si NW [55]. (Copyright 2019, American Chemical Society)

increased photocurrent density to -1.2 mA cm^{-2} at 0 V. Further, increased loading of the WS_2 (0.04 M) on SnO_2 for the synthesis of SnO_2@WS_2–2 exhibited high current density to -1.9 mA cm^{-2}. Loading amount of WS_2 increased to 0.06 M led to maximum HER rate of -3.5 mA cm^{-2} at 0 V for SnO_2@WS_2–3. Further increased of loading of WS_2 (0.08 M) on SnO_2 (SnO_2@WS_2–3) led to decreased current density to 2.4 mA cm^{-2}. The reduction of HER process could be occurred due to the high loading of WS_2 that hindered the light absorption process of SnO_2. The photocatalytic mechanism of the SnO_2@WS_2 nanocomposites was proposed based on the bandgap energy of SnO_2@WS_2 and p-Si (Fig. 7c). The photogenerated electrons and holes were produced by light absorption in SnO_2. However, high recombination process in bare SnO_2 took place and exhibited poor catalytic activity due to a large bandgap, which provides easy recombination of photogenerated carriers. However, after loading of WS_2 on SnO_2, the photogenerated electrons exhibited facile electron transportation from SnO_2 to WS_2 because of low bandgap energy of WS_2. In HER electrons are collected at WS_2 and reduced H^+. The H_2 evolution occurs due to the low electrochemical band potential of SnO_2@WS_2. Si nanowire arrays (NWs) have been demonstrated its capability as photocathode with wide absorption in the vis region and an appropriate bandgap of 1.12 eV. The Si NWs have aids like earth abundance, cost-effective, facile charge transportation, and light scattering, which is relevant for PEC. However, Si NWs suffer from rapid surface oxidation and poor acid steadiness that endures a questions. These difficulties can be overcome by improving the surface properties via coating the Si NWs with appropriate cocatalyst, which is an abundant approach for the prevention of surface oxidation and achieves efficient H_2 production. Nowadays, transition metal chalcogenides (TMDC) have appeared as PEC cocatalyst due to high acid stability and ultrahigh active sites for HER. The 2D MoS_2 is often studied as the cocatalyst due to its cost-effectiveness and dynamic edges of sulfur sites. The effective PEC water splitting in MoS_2 is constrained by inactive sulfur sites and deprived interlayer charge transportation process. However, theoretical studies greatly predicted that NbS_2 is an auspicious candidate for the water splitting owing to excellent acid stability, facile charge transportation between host material and electrolyte, and high HER active surface area. Gnanasekar et al. reported chemical vapor deposition method for coating of two-dimensional (2D) niobium disulfide (NbS_2) on high silicon NWs for the application in HER. Figure 7d shows the Si NW array has been used for the deposition of NbS_2 layer to prepare NbS_2/Si NW heterostructure [55]. The thickness of NbS_2 nanopatches is 0.55 nm, revealing the monolayer deposition of NbS_2 (Fig. 7e). The PEC measurement has been done for understand the HER performances of the NbS_2/Si NW heterostructure. The characteristics J-V plot of Si, Si NWs, NbS_2-Si, and NbS_2-Si NWs are shown in Fig. 7f. J-V plot revealed the Si photocathode has nearly zero current under dark conditions. Upon illumination, Si NW shows a maximum current density (J_{max}) (14 mA/cm^2) with the +0.06 V versus RHE turn-on potential. The NbS_2/Si NW shows 0.34 V versus RHE and a maximum current density of ~34 mA/cm^2. Figure 7g shows the Tafel slope of 32 mV/dev for NbS_2/Si NW. The NbS_2/Si and Si NWs

showed Tafel slope of 58 and 95 mV/dec, respectively. The J-V curves and Tafel slope proved that the presence of facile charge transportation between electrolyte-Si NW due to the existence of active sites in edges in NbS_2 hence consequential improved performance.

9 Metal Oxide-Based Heterostructure for Photocathode Fabrication

Although Si shows good performance as a photocathode, its high synthesis cost restricts commercialization. The Cu_2O materialemerged as earth-abundant and cost-effective material for the construction of photocathode. The Cu_2O exhibit p-type conductivity outcomes from copper vacancies [39, 56, 57]. The VB of Cu_2O is designed by the hybridized Cu 3d and O 2p energy bands. The uppermost of the VB is formed from fully occupied Cu $3d^{10}$ orbitals, subsequent into high mobility. The Cu_2O has bandgap energy of ~2.1 eV. The CB and VB favors the reduction (H_2 evolution) and oxidation (O_2 evolution) of water and resulted in j_{ph} of 14.7 mA/cm^2. Hence, Cu_2O is the promising metal oxide for PEC water splitting [39, 56–58]. However, Cu_2O is corroded instead of water splitting when it contacts with water, and light illumination due to its redox potential values (Cu^{II}/Cu^{I} and Cu^{I}/Cu^{0}) lies between the CB and VB. The heterostructures of Cu_2O-based materials have been investigated in order to get a high photocathode current and stability. An Au-sensitized Cu_2O-integrated heterostructure system (Z-scheme) was synthesized by coating a Cu_2O on Au-deposited TiO_2 nanorods [58]. Figure 8a shows the direct TiO_2-Cu_2O based Z-scheme, and Fig. 8b shows Au-mediated Z-Scheme (TiO_2-Au-Cu_2O). In TiO_2-Au-Cu_2O, Au nanoparticles act as a charge transportation arbitrator to increase the electron transportation process from the CB of TiO_2 to the VB of Cu_2O and holes were collected at the VB of TiO_2. The TiO_2-Au-Cu_2O heterostructure provides high redox capabilities for H_2 evolution process. The IPCE spectra of photocathodes (Cu_2O, TiO_2-Cu_2O, and TiO_2-Au-Cu_2O) are shown in Fig. 8c. The IPCE spectra revealed that the TiO_2-Au-Cu_2O have high photocurrent generation as compared to pure Cu_2O and TiO_2-Cu_2O. PEC measurement illustrates the photocurrents were − 0.15, −0.22, and − 0.38 mA/cm^2 for samples of pure Cu_2O, TiO_2-Cu_2O, and TiO_2-Au-Cu_2O, respectively, suggesting TiO_2-Au-Cu_2O surpass performance as a photoelectrode in H_2 production as equated to pure Cu_2O and TiO_2-Cu_2O. Wu et al. reported a novel heterojunction photocathode fabricated by NiO loaded with WO3 for PEC. The heterojunction NiO/WO_3 exhibited a higher current density up to −23.39 μA/cm^2 at 1.20 V versus RHE to the bare NiO photocathode, which exhibited only −5.93 μA/cm^2 [59]. Facile charge separation and transmission efficacy of the photocarriers (photocreated electron-hole pairs) and improved light absorption lead to this high PEC property of NiO/WO_3 heterojunction photocathode. The branched nanowire (b-NWs) heterostructures are very capable of PEC solar hydrogen production as compared to core/shell NW(cs-

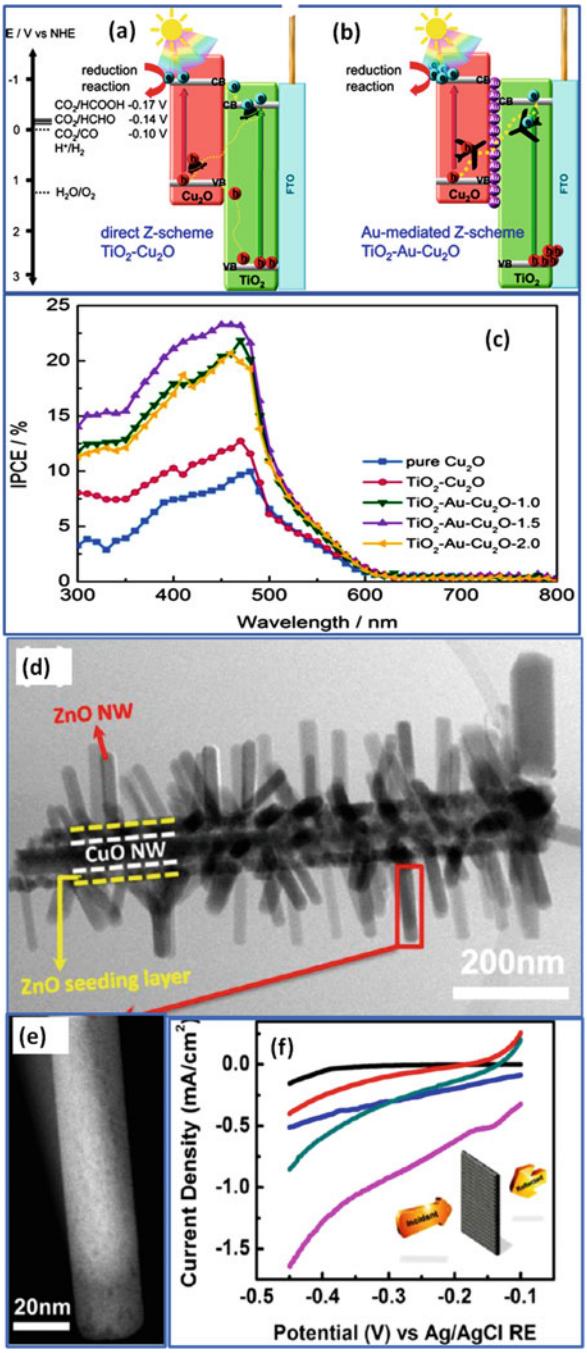

Fig. 8 (**a**) Energy level diagram and charge transfer process for (a) TiO_2-Cu_2O and (**b**) TiO_2-Au-Cu_2O. (**c**) IPCE spectra of Cu_2O, TiO_2-Cu_2O, and TiO_2-Au-Cu_2O [58]. Copyright 2018, American Chemical Society. (**d**) Low-magnification STEM image of a single nanowire of b(10 m-ZnO/4 h-400 °C-CuO). (**e**) STEM image of single ZnO NW. (**f**) J-V curves of b(10 m-ZnO/3 h-400 °C-CuO) NWs on Cu foil (black line-dark current, blue line-light current) and on Cu mesh (red line- dark current; dark cyan line-light current, magenta line-light current with the reflector [64]. (Copyright 2013, American Chemical Society)

NW) owing to enhanced light absorption, increased surface area, and improved gas evolution. Also, the smaller size of the NW branches can result in photogenerated electron-hole separation or/and collection owing to nearby closeness amid the semiconductor-electrolyte interface and the photogenerated carriers [60–63]. The 3D ZnO/CuO b-NW photocathode was fabricated for PEC solar H_2 production, where ZnO/CuO b-NWs were coated on copper mesh substrates and copper film with various CuO and ZnO NW sizes and densities. Figure 8d shows STEM image of the ZnO/CuO b-NW [64]. This image revealed the formation of three different regions: (i) CuO NW core, (ii) ZnO seeding layer, and (iii) ZnO NW branches. High-angle annular dark-field STEM image of individual ZnO NW shows the that diameter of ZnO NW is ~25 nm (Fig. 8e). The current densities of 3D ZnO/CuO b-NWs deposited on Cu foil substrate and Cu mesh substrate are shown in Fig. 8f. The 3D ZnO/CuO b-NWs deposited on Cu mesh substrate have high surface area as compared to 3D ZnO/CuO b-NWs grown on Cu foil. Owing to improved surface area, 3D ZnO/CuO b-NWs grown on mesh substrate exhibited higher dark and light currents as compared to 3D ZnO/CuO b-NWs grown on Cu foil. These results revealed the application of 3D ZnO/CuO b-NW mesh electrodes for potential high-efficacy and cost-effective solar fuel production.

Yang et al. [65] reported the Cu_2O/CuO by facile techniques such as an electrodeposition. The diffuse reflectance spectra of (i) Cu_2O, (ii) CuO, and (iii) Cu_2O/CuO films are shown in Fig. 9a. It revealed that the absorption edge for the pure Cu_2O film is at 600 nm, and Cu_2O/CuO film shows to 900 nm owing to CuO (low Eg material). Figure 9b shows the variation of photo-to-current efficiency (η) versus a function of cathodic potential for the CuO, Cu_2O, and Cu_2O/CuO nanocomposite cathodes. The Cu_2O,CuO, and Cu_2O/CuO show the conversion efficacy of 0.12, 0.43, and 0.55%, respectively, at 0.05 V versus RHE. This result revealed that Cu_2O/CuO film absorbs and uses the light more competently as related to Cu_2O and CuO films. And Cu_2O/CuO exhibited high photocurrent density for HER (3.15 mA/cm^2) at 0.40 V versus RHE. Figure 9c shows the energy level of Cu_2O/CuO in connection with Na_2SO_4 (0.5 M, pH 6.0) electrolyte in light. The CB levels of the CuO and Cu_2O are additional negative than H_2O/H_2, showing that the photoelectrons in the CB can be transferred into the H_2O and lead to the reduction of H_2O. This high performance of the Cu_2O/CuO film was credited to the subsequent advantages of the heterojunction: (i) It exhibited broadened light absorption band. (ii) The high space-charge potential and (iii) the more majority carriers that lead to a fast transportation rate.

10 Metal Chalcogenide-Based Heterostructure for Photocathode Fabrication

The Cu_2O/CuO/CuS was fabricated via electrodeposited Cu film. The Cu film was annealed in air in the order to produce heterostructure Cu_2O/CuO, and CuS loading on Cu_2O/CuO heterostructure has been done by a successive ion layer adsorp-

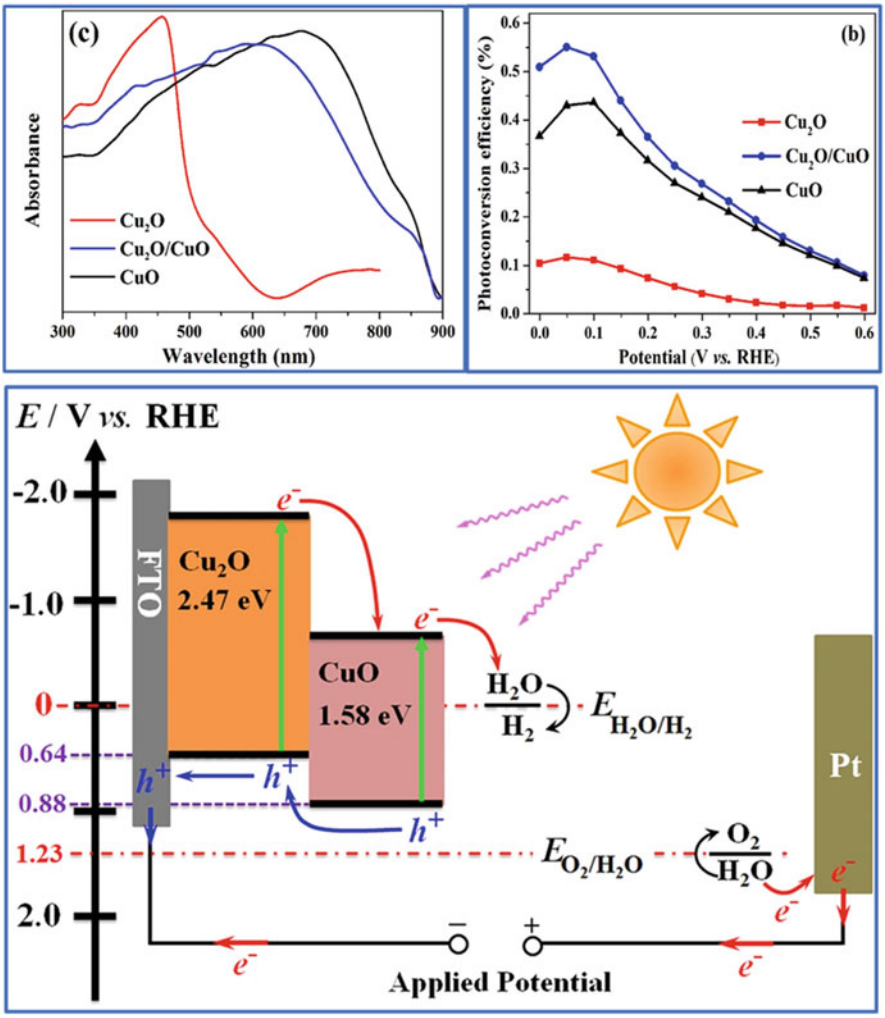

Fig. 9 (**a**) UV-vis diffuse reflectance spectra of the pure Cu_2O, CuO and Cu_2O/CuO composite films, (**b**) APCE as a function of applied potential (cathodic), (**c**) the schematic diagram of the energy band levels of the Cu_2O/CuO bilayered nanocomposite in contact with electrolyte during HER process in PEC [65]. (Copyright 2016, Nature Publishing Group)

tion and reaction (SILAR) method. The Cu_2O/CuO/CuS photocathode exhibited improved current density of -5.4 mA/cm^2 at 0 V versus RHE under standard AM 1.5 light. This is a highest photocurrent obtained as compared to Cu_2O/CuO photoelectrode for PEC. The steadiness of the Cu_2O/CuO electrode exhibited ~44% reduction in original current density within 1 h. This highly improved PEC property is resulted owing to the fast transportation of photoelectrons resulting to restrained electron-hole recombination, improved light absorption owing to heterojunction and

charge separation. The work showed a simple way and ability to use of CuS for PEC [66].

The ultrathin two-dimensional (2D) transition metal dichalcogenides (TMDs) with MX_2 (where M = Mo, W and X = S, Se) are layered coatings of X-M-X via van der Waals force of interactions. The 2D TMD nanosheets, such as [67–69], TiS_2 [70], SnS_2 [71–73], WS_2 [74–76], $MoSe_2$ [77, 78], WSe_2 [79–82], etc., are emerged as important 2D materials in PEC applications for hydrogen evolution owing to their attractive electric possessions and tailoring bandgap [83]. The nitride such as GaN displays prodigious potential as photocathode owing to its appropriate band energy level arrangements with the redox reaction potential of H_2O. However, a large Eg of GaN limits the absorption of the light in the visible range [84–87]. Therefore, heterostructure with 2D TMDs such as MoS_2 is predicted to be one promising choice to design efficient photoelectrodes. The heterostructure MoS_2/GaN exhibited visible light absorption and prevents the recombination of photocarriers along with lengthier carrier lifetime, which are advantages for engineering efficient photocathods. The P-GaN [p-GaN (Et)] with nanotextured hexagonal microwell was synthesized by wet chemical etching method. The heterostructure of p-GaN (Et) and MoS_2 was prepared for the fabrication of a photocathode. The FESEM image revealed the hexagonal well of GaN formation with well decorated by MoS_2 (Fig. 10a) [88]. The PEC measurement was done in 0.5 M H_2SO_4 (Fig. 10b). The LSV under chopped light having intensity of 100 mW cm^{-2} exhibited improvement in the current (1.52 mA/cm^2) for p-GaN/MoS_2 photocathode as compared to the p-GaN (-0.43 mA/cm^2) at 0 V vs RHE (Fig. 10c). The optimized p-GaN/MoS_2 photocathode exhibited the high applied bias photon-to-current conversion efficiency (ABPE) of ~3.18%, which is three times higher than p-GaN (~1.03%) with high hydrogen evolution rate (89.56 μmol/h), which measured at -0.3 V versus RHE (Fig. 10d).

Meng et al. reported the p-n multiple junctions for PEC by depositing p-type MoS_2 nano-platelets (size having 5–20 nm) on the nitrogen-doped rGO (n-rGO) (n-type) nanosheets [89]. Here, three types of photoelectrode fabricated by hydrothermal for comparisons: (i) MoS_2 nanoparticles (free standing); (ii) the MoS_2/rGO nanocomposite, here MoS_2 nanoplates, was decorated on rGO sheets; and (iii) the formation of p-MoS_2/n-rGO composite. The UV-visible spectrum displays that the MoS_2 has an absorbance tail, which occurs at 1020 nm, attributing to the formation of the indirect bandgap (Fig. 10e). The nanocomposite of MoS_2/rGO film showed absorption at 781 nm, while p-MoS_2/n-rGO film showed at 786 nm. Further, these three samples were investigated for hydrogen generation study by using the water/ethanol mixture (Fig. 10f). Here, ethanol acts as a hole scavenger. MoS_2 showed tiny photocatalytic activity. Though MoS_2 has the absorption properties and active edges for HER, the deficit of activity revealed the inefficient carrier separation, or the carriers cannot travel to the active edges. MoS_2/rGO film exhibited good photocatalytic performance with a H_2 generation rate of 7.4 μM g^{-1} h^{-1}. The sample p-MoS_2/n-rGO exhibited the uppermost H_2 generation of 24.8 μM g^{-1} h^{-1} with the respective abovementioned two samples. The high performance of p-MoS_2/n-rGO is attributed to the creation of many nanoscale p-n junctions and space charge layers at the junctions. Therefore, it suppresses

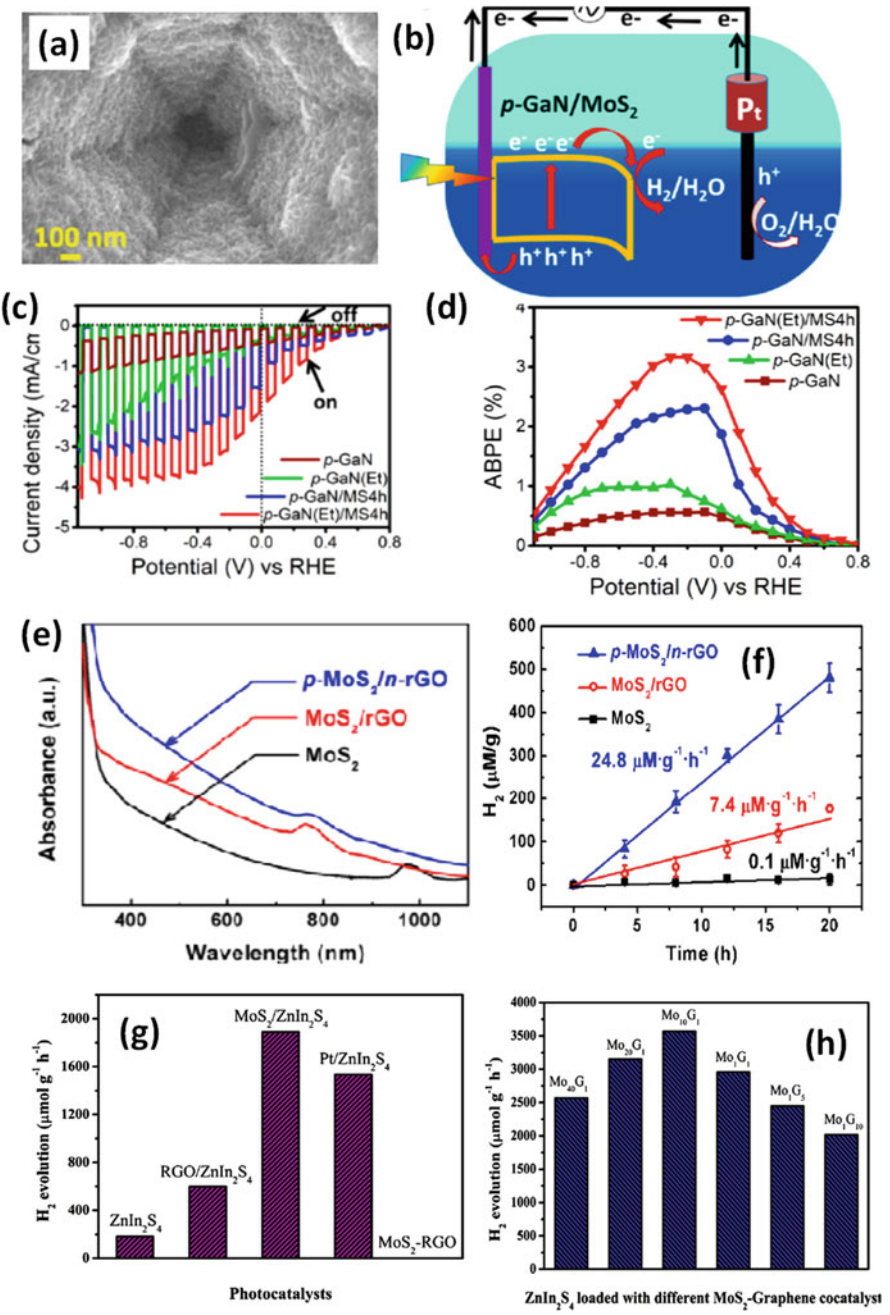

Fig. 10 (**a**) FE-SEM image of MoS_2 decorated p-GaN(Et) surface. (**b**) Schematic diagram of the PEC setup (**c**) LSV curves of p-GaN, p-GaN(Et), p-GaN/MS4h, and p-GaN(Et)/MS4h. (**d**) ABPE [88]. Copyright 2020, American Chemical Society. (**e**) The UV-Visible spectra of the MoS_2, the MoS_2/rGO and the p-MoS_2/n-rGO. (**f**) Hydrogen generated by photocatalysts [89]. Copyright 2013, American Chemical Society. (**g**) The rate of H_2 production over $ZnIn_2S_4$ loaded with different cocatalysts MoS_2/Graphene. (**h**) The rate of H_2 production over $ZnIn_2S_4$ loaded with different MoS_2-graphene [90]. (Copyright 2016, Elsevier)

the charge recombination and enhances the photocarriers. Here, MoS_2 acts as a electrocatalytic origin and also acts as an absorber to generate photocarriers. As a consequence, the p-n junction (p-MoS_2/n-rGO) enhances HER performance. The synthesis of MoS_2-graphene composite loaded with a highly efficient cocatalyst $ZnIn_2S_4$ to enhance the photocatalytic activity under light irradiation. The photocatalytic activity of H_2 production measurements was carried out in Na_2SO_3 and Na_2S as the sacrificial reagents under 300 WXe, $\lambda > 420$ nm [90]. Figure 10g illustrates that $ZnIn_2S_4$ sample has poor photocatalytic activity (H_2 evolution up to 183 μmol h^{-1} g^{-1}) owing to fast recombination process between electron-hole pairs. Graphene/$ZnIn_2S_4$ and MoS_2/$ZnIn_2S_4$ showed improved photocatalytic activity with 599 and 1889 μmol h^{-1} g^{-1} respectively under same conditions. The MoS_2-graphene composites were obtained by hydrothermal reaction of $Na_2MoO_4.2H_2O$ to graphene oxide with weight ratios of 40:1, 20:1, 1:1, 1:5, and 1:10, and the obtained powder referred as $Mo_{40}G_1$, $Mo_{20}G_1$, $Mo_{10}G_1$, Mo_1G_5, and Mo_1G_{10}, respectively. The ratio of MoS_2 to graphene co-catalysts was obtained by loading the $ZnIn_2S_4$ and study their photocatalytic activity for H_2 production. Figure 10h shows that with the increased amount of graphene in MoS_2-graphene cocatalyst, the nanocomposite MoS_2-graphene/$ZnIn_2S_4$ exhibited higher H_2 evolution activity. The $Mo_{10}G_1$ loaded with ZnIn2S4 shows the highest photocatalytic H_2 evolution activity (3567 μmol h^{-1} g^{-1}). Further increase of graphene content in MoS_2-graphene nanocomposite results in a decreasing photocatalytic H2 evolution activity. This result revealed that the activity enlarged with the increasing ratio of graphene in MoS_2-graphene nanocomposite and further decrease gradually. The improved activities resulted from excess active sites of graphene. However, further increasing graphene content resulted in low performance which is due to agglomeration of graphene.

Recently, many chalcopyrite semiconductors such as $CuGaSe_2$, Cu_2ZnSnS_4 (CZTS), Cu(In,Ga)Se2, $CuIn(S_{1-x}Se_x)_2$, and $Cu(In,Ga)(S,Se)_2$ have been studied as efficient photocathodes for HER, owing to their excellent properties such as suitable band structure, high absorption coefficient ~ 10^5 cm^{-1}, lengthy minority carrier diffusion length ~ 1 μm, and adjustable bandgap (1.0 ~ 2.4 eV) [91–95]. CZTS with In_2S_3/CdS coating photocathode exhibited 9 mA/cm^2 at 0 V/RHE [93]. Further, CZTS photocathode with TiO_2/CdS exhibited 13 mA/cm^2 at −0.2 V versus RHE [94]. The electrode stability in aqueous electrolyte represents important criteria for the development of PEC device. Firstly, Feng et al. [96] reported the use of MoSx-based catalyst for a CZTS-based photoelectrode. The MoSx-CdS/CZTS photocathode showed a good half-cell STH (>2.3%) and long-lasting steadiness (over 10 h) in neutral aqueous solution. MoSx-CdS/CZTS photocathode exhibited the highest half-cell STH (above 3%) in acidic buffer solution (pH 3), with a current density of 18 mA/cm^2 at 0 V_{RHE}. The flat band position of MoSx-CdS/CZTS was positively shifted, which facilitate the electron to lowering barrier between electrolyte and photocathode resulting in improving the water reduction efficiency. Yang et al. [94] reported a synthesis of CZTS by a hybrid ink, which is attained by restraint of precursor mixture to fabricate a highly efficient solution-processed (cost-

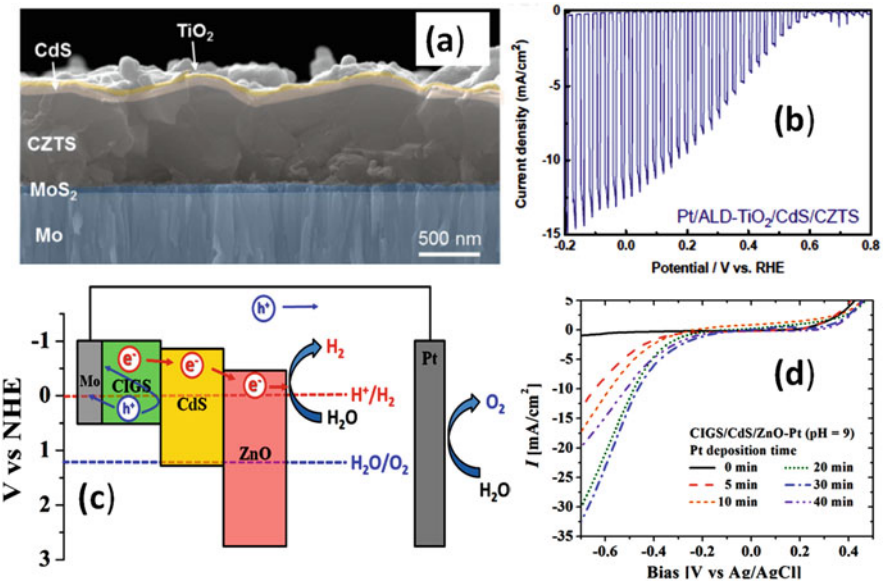

Fig. 11 (**a**) The cross-sectional SEM image of a Pt/AlD-TiO_2/CdS/CZTS photocathode. (**b**) J-V curves in aqueous electrolyte [94]. Copyright 2016, American Chemical Society. (**c**) Energy level diagram of charge transfer process in the CIGS/CdS/ZnO-Pt photocathode. (**d**) I-V curves for CIGS/CdS/ZnO-pt films [97]. (Copyright 2015, American Chemical Society)

effective method) CZTS photocathode. The ink-obtained CZTS films are redesigned by n-type TiO2/CdS double layer and followed by deposition of Pt. The SEM image confirms the thickness of TiO_2 (25 nm), CdS (35 nm) and covering over the CZTS film (Fig. 11a). The Pt/ALD-TiO_2/CdS/CZTS photoelectrode exhibited exceptional high current of 13 mA/cm^2 versus a RHE for 1 Sun illumination (Fig. 11b) and relatively stable H_2 production (the faradaic efficiency nearly one). The high photocurrent due to suitable band alignment and high absorption of light.

Mali et al. [97] reported the engineering of CIGS/CdS by depositing ZnO layer on the top. Further, Pt was deposited on the ZnO coating as a catalyst via electrodeposition method. Here, CIGS film was deposited by the co-evaporating deposition technique. The coating of CdS layer (n-type semiconductor) over the CIGS layer makes a space charge depletion area at the p-n junction interface, which leads to better separation of charges. Furthermore, the potential difference between CdS and CIGS layer results in further improvement in charge separation. The formation of powerful electric fields at the interface leads the facile electron transportation from CIGS to CdS, and the slightly positive band offset reduces the recombination process at the interface. The CdS/ZnO interface is formed; in this way, the position of CBM declines from CdS to ZnO, improving the transportation of the photoelectrons from CIGS to ZnO. The ZnO has bandgap of 3.3 eV (direct

bandgap), which is favorable for water reduction process keeping suitable CB and VB positions. The mechanism of charge separation and transportation over the CIGS/CdS/ZnO-Pt electrode is illustrated in Fig. 11c.

The influence of the Pt electrodeposition time (vary between 0, 5, 10, 20, 30, and 40) and the pH of the electrolyte (pH; 1, 7, and 9) was investigated to optimize the CIGS/CdS/ZnO-Pt photocathode. The maximum photocurrent density (-32.5 mA/cm^2) under light was reached with an electrodeposition time (30 min) (Fig. 11d). The high accomplishment of CIGS/CdS/ZnO-Pt was obtained due to its type II structure that leads to effectual carrier separation and transportation of photogenerated electrons at the interface junction. CIGSSe chalcopyrite photocathodes can efficiently absorb the incident light and create electron-hole pairs. However, the HER performance is poor due to the low charge separation and the high overpotential for hydrogen evolution. To reduce the overpotential for the HER, n-type semiconductor and HER catalysts (HEC) are required to deposit over the surface to get band bending [95].

CIGSSe photocathode with Cu_2S HEC enabling efficient water splitting in the absence of further coating of n-type semiconductor overlayers and HECs. Here, CIGSSe photocathode with Cu_xS catalyst has been achieved by the chalcogenization of CuInGa precursor films in the following steps: (i) synchronous sulfurization and selenization utilizing a mixture of H_2S gas and Se vapor, accompanied by further sulfurization process via H_2S. The above procedure creates Cu_xS at CIGSSe film. The controlled formation of Cu-based binary phase (Cu_xS, Cu_2Se) in the CIGSSe film has been done by using the abovementioned two step processes comprising of temperature at each step and a different proportion of chalcogen (Fig. 12a). The chopped LSV scans were carried out using a Cu_xS layer containing CIGSSe photocathode (shows photocurrent -25.7 mA cm^{-2} at -0.3 V vs RHE) and after removing surface Cu_xS (Fig. 12b). The LSV scans revealed that the rapid decrease of photocurrent density after removing Cu_xS surface of photocathode as compared to the Cu_xS covered photocathode. This result demonstrated that Cu_xS phase at CIGSSe photocathode reduced overpotential for HER, and the modified VBM level of photocathode is favorable for water splitting. The photoelectrochemical stability measurement of Cu_xS/CIGSSe photocathode was evaluated at 0 V versus RHE. The photocurrent (-8 mA cm^{-2}) was kept for 3 h with 100% Faraday efficiency (Fig. 12c). This study demonstrated that coating of Cu_xS on CIGSSe is useful for commercialization due to solution-processed chalcopyrite photocathode fabrication and high HER performance.

In 2016, Cu_2BaSnS_4 (CBTS) as a photocathode for PEC device was reported, exhibiting photocurrent of 4 mA/cm^2 at 0 V/RHE. Further, photocurrent improvement was carried out by using a Pt/TiO_2/ZnO/CdS coating on pure-sulfide CBTS (7 mA/cm^2 at 0 V/RHE) [98]. Also, as Se introduced in CBTS system (CBTSSe photocathode), the resultant PEC device showed improved photocurrent due to small bandgap to increase light absorption and large grain size to reduce recombination of the carriers at the grain boundaries. Zhou et al. [98] reported the fabrication of Pt/TiO_2/CdS/CBTSSe by chemical bath deposition of CdS, atomic-layer-deposition of TiO_2, and sputtering of CBTSSe. The Pt/TiO_2/CdS/CBTSSe-

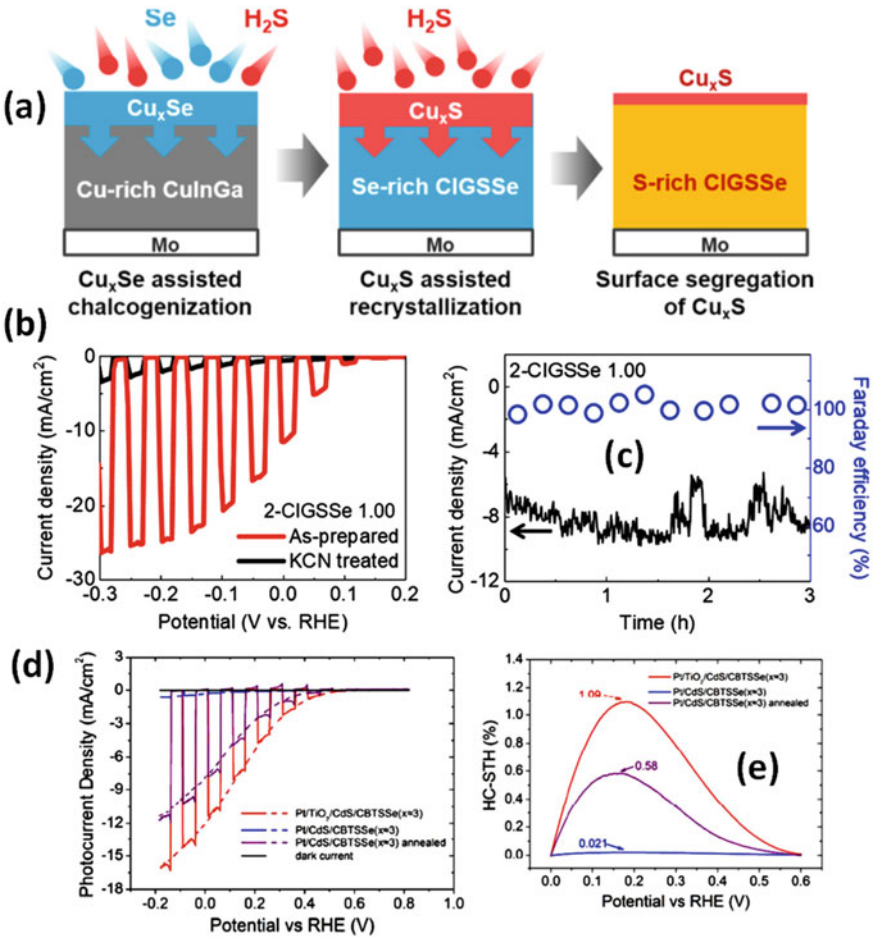

Fig. 12 (**a**) A schematic diagram of two-step chalcogenization process. (**b**) The chopped J-V curves of 2-CIGSSe photocathodes at 10 mV/s. (**c**) Photocurrent density versus time and Faradaic efficiency versus time plot for H_2 evolution of the 2-CIGSSe 1.00 photocathode at 0 V versus RHE [95]. Copyright 2019, American Chemical Society. (**d**) LSV of photocathodes [98]. (**e**) Plot of HC-STH (%) vs. Potential (in RHE). Copyright 2018, American Chemical Society

based photocathode showed ~12.08 mA/cm^2 photocurrent at 0 V/RHE highest reported for CBTSSe-contained PEC (Fig. 12d) and constant evolution for 10 h. The PEC device of Pt/TiO_2/CdS/CBTSSe exhibited a half-cell solar-to-hydrogen (HC-STH) efficacy over 1.09% at 0.183 V versus RHE (Fig. 12e). The high results of Pt/TiO_2/CdS/CBTSSe are attributed to the improved carrier isolation at the CdS/CBTSSe junction (p/n), high absorption of light by small bandgap CBTSSe and protection layer formed by TiO_2, which reduce recombination process and restrict

direct contact of electrode with electrolyte. Table 1 consists of heterostructure of photocathode for the fabrication of PEC device for hydrogen production.

11 Dye-Sensitized H_2 Evolving Photocathode Fabrication

The development of dye-sensitized PEC (DS-PEC) presenting molecular catalysts are capable for water splitting for hydrogen production owing to their easy remolding, assembly, and engineering flexibility [105–107]. Nowadays, molecular dyes or/and catalysts are embedded onto high bandgap materials such as NiO to construct DS-PEC for effective transformation of light into H_2 fuel. For the advancement of NiO holding cathodes, different approaches were employed to gather the molecular components with functional devices, which consist of photocathodes including with a catalyst in solution, layered architecture of the dye-catalyst, co-grafted dye/catalyst architecture, and supramolecular dye (covalent)/catalyst musters on the photoelectrode [108–110]. Li et al. [111] first time reported DS-PEC fabrication with a NiO photocathode, dye P1, and a cobalt catalyst (Co1). Kaeffer et al. [108] reported on covalent dye-catalyst and noble metal-free assembly grafted onto p-type NiO for photoelectrochemical light-assisted H_2 evolution in acidic electrolyte [108]. The dye catalyst accumulation was prepared by alkyne derivative terminal of the dye, which consists of electron-donor part (triarylamine) and electron-acceptor part (an ethyl cyanoacetate) parted by a thiophene unit. The energy level diagram of the NiO photocathode based on 4 at pH 5.5 is shown in Fig. 13a. When a light incident on dye 4, the photogenerated electron-hole pairs are generated. NiO is appropriate for hole insertion from HOMO of the excited 4 dye molecule. The photogenerated electron is transferred to a catalyst to convert protons into H_2 evolution. Here, an organic dye is attractive since it exhibits great absorption in the visible range and charge parting in the excited state of dye that restricts the recombination process from the dye to the photocathode (NiO electrode). Here, cobalt dimine-dioxime complex is applied as catalysts. The photocathodes ($F_{10}8$ templated, NiO) were fabricated and decorated by CH_3CN solution of dye 4 for 24 h. Further, chenodeoxycholic acid (CDCA) was used as co-adsorbent to improve the H_2 evolution process. Chronoamperometric employed at more negative potentials versus RHE exhibit constant cathodic photocurrent (Fig. 13b). The energy level diagram of the PEC device is displayed in Fig. 13c. The pristine and CDCA co-sensitized NiO electrodes show that the current is improved in the company of H_2 evolving catalyst (cobalt diamine-dioxime). The gas chromatographic analysis confirmed the H_2 evolution process with 8–10% faradic yield taken place during chronoamperometric measurements. The engineering of an original dye/catalyst assembly was done by axial coordination between cobalt-integrated catalyst (cobaloxime complex) to a pyridyl-functionalized Ru-diacetylide photosensitizer. This new supramolecular assembly was used for the construction of NiO-based photocathodes for subsequent H_2 generation under appropriate aqueous conditions. The energy level diagram of NiO-based photocathode including 6-Co

Table 1 The examples of heterostructure of photocathode for the fabrication of PEC device for the hydrogen generation

Sr.	Photocathode	Electrolyte	On set potential (V) versus RHE	Photocurrent (mA/cm^2)	Stability (h)	Hydrogen generation/Efficiency	References
1	n^+p-Si/5 nm, Ti/5 nm on Ni	1 M KOH	0.61	38.7	8 h	–	[99]
2	n-WS_2/p-Si	0.5 M H_2SO_4	+0.022 V	9.8	40	6.3 μmol/h [Faradaic efficiency of 86%]	[74]
3	p-Si wire arrays and NiMoZn	0.5 M H_2SO_4	0.27	1.45	3.5	Faradaic efficiency of 100%	[100]
4	2D-NbS_2-Si NWs	0.5 M $HClO_4$	0.34 V	28	20	STH: 2.6%	[55]
5	TiO_2/au Nanoring/p-Si Nanohole	0.5 M H_2SO_4	0.32	26.2	5	[Faradaic efficiency =100%]	[53]
6	CdS/Cu_2O	Na_2S and Na_2SO_3 mixture	–	4.2	7200 sec	161.2 μmol/h,	[101]
7	Cu_2O/$SrTiO_3$	0.1 M NaOH (pH 13)	–	2.52	–	ABPE = 1.% at 0.8 V versus SCE	[48]
8	Sb_2Se_3/In_2S_3	0.1 M H_2SO_4	0.20	27	90 min	STH = 2.6%	[102]
9	C60-decorated SnS_2/$CuInS_2$	0.5 M Na_2SO_4		4.51	3	IPCE = 4.8% at 400–600 nm	[72]
10	CuxS-covered CIGSSe	0.5 M H_2SO_4	0.2	26	3	STH = 0.29% Faraday efficiency~100%	[95]
11	Pt/CdS/$CuGa_3Se_5$/(Ag,Cu)$GaSe_2$ (ACGSe)	0.1 M Na_2HPO_4(pH 10)	0.62	8.79	20 days	IPCE.57% at range of 520–600 nm	[103]
12	MoSx-CdS/CZTS	Buffer solution (pH=3)	0.6	18	10	STH = 3%	[96]
13	$CuInS_2$/CdS/TiO_2/Pt	0.1 M Na2HPO4 (pH 10)	0.6	13	60 min	STH = 1.82%	[104]

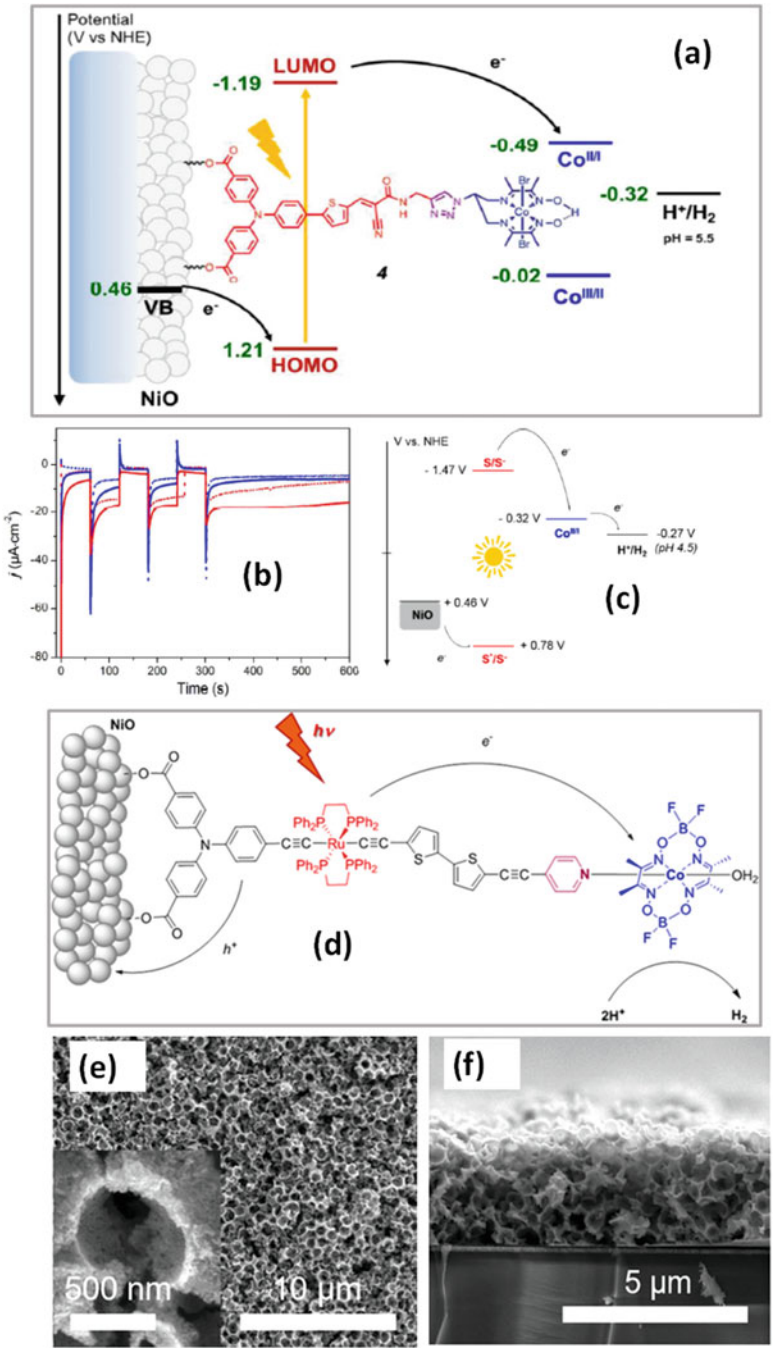

Fig. 13 (**a**) Energy level diagram and working principle of the photocathode. (**b**) Chopped-light chronoamperometric measurements. (**c**) Energy level diagram of a NiO-based photocathode including Ru-based dye (S) and 6-Co [108]. Copyright 2016, American Chemical Society. (**d**) Schematic representation of the Ru-diacetylide/cobaloxime assembly attached onto a mesoporous NiO nanoparticulate thin film [112]. Copyright 2019, American Chemical Society. (**e**) Top-down and (**f**) cross-sectional SEM image of IO-$CuCrO_2$ electrodes [118]. (Copyright 2019, American Chemical Society)

and Ru-based dye (denoted by S) is shown in Fig. 13d. After light excitation, hole injection takes place from the dye-excited state to the NiO VB; this process takes place very fast (from subpicosecond to a few tens of picoseconds) [112]. This process at the surface of the dye reduces the catalytic center via electron transportation [105]. The dye is reduced at the electrode (catalyst) surface due to the electron transfer and it help the protonation of Co^{I} state which generates a Co^{III}-H and subsequently reduction of to CoII-H species take place, the protonation the process leads H_2 generation and redevelops the initial C^{II} center. The representation of the design of the dye/catalyst (Ru-diacetylide/cobaloxime assembly) anchored onto a mesoporous NiO nanoparticulate thin film. The PEC generation of H_2 under appropriate aqueous conditions leads to a Faradaic efficiency of 27%. NiO is mostly studied as wide-bandgap semiconductor in DS-PEC due to possible facile synthesis. However, low hole mobility and presence of the high density of traps have been the lack of articles of H_2 generation.

Improved DS-PECs can be obtained through the advancement of substitute p-type semiconductors with wide bandgap [113–115]. Delafossite-structured materials are suitable owing to their high hole carrier mobility, solution effectivity, and metal oxide characteristics. $CuGaO_2$ and $CuCrO_2$ are studied in DS-PECs both aiding an early current onset owing to their anodic VB positions [116, 117]. The DS-PEC results are a similar NiO-integrated photocathode, but low catalyst and dye loadings inadequate H_2 formation. This was resolved via the synthesis of meso- and microporous architectures. Creissen et al. [118] reported a $CuCrO_2$ photocathode based on inverse opal (IO) structure. Figure 13e, f revealed the formation of the inverse opal architecture film with macropores of 600–700 nm in diameter, and thickness of the film is approximately 2 μm [118]. The inverse opal architecture of $CuCrO_2$ electrodes is sensitized with DPP-P and PMI-P dyes, respectively, with a Ni catalyst (NiP). PEC measurement was carried out in Na_2SO_4 electrolyte (0.1 M and pH 3) under chopped light illumination ($\lambda > 420$ nm) (visible range) and intensity 100 mW cm^{-2}. LSV measurement for photocathodes fabricated by IO-$CuCrO_2$/DPP-P/NiP and IO-$CuCrO_2$/PMP-P/NiP exhibited an onset potential ~0.8 V versus RHE. The improvement in photocurrent for PMP-P-based photocathode is attributed to the red-shift, broader absorption profile and more intensity.

12 Perovskite-Sensitized H_2 Evolving Photocathode Fabrication

The high performance of the PEC of perovskite-based devices for the H_2 evolution is due to their outstanding optoelectronic possessions of the semiconductors such as high light absorption coefficient, appropriate Eg, and high carrier mobility [119, 120]. The organometal halide perovskites (OHPs) have high performance of PEC devices with the high open circuit potential ($V_{oc} \geq 1$ V) and high photocurrent density Jph ≥ 20 mA/cm^2. However, PEC devices based on OHPs have limits of an instability problem due to intrinsic instability issue and intrinsic ionic defects, which

act as recombination centers and degrade the performance. Another major drawback originates from the hygroscopic vulnerability of OHPs to water and alcohols, which limits their application for PEC device fabrication. Reisner and co-workers [34] studied metal-encapsulated $CH_3NH_3PbI_3$ for stable hydrogen evolution reaction (HER). Here, fusible InBiSn alloy was taken to secure the perovskite layer from H_2O while allowing the photoelectrons to hit Pt. A highest photocurrent density (9.8 mA/cm^2 at 0 V vs RHE) through an onset potential of 0.95 V versus RHE was obtained with the stability of 80% of their initial photocurrent retention over ~1 h under illumination. Perovskite photocathode was developed to fabricate large-scale production. Figure 14a shows the schematic of the perovskite device arrangement of as-prepared sandwich-like photocathode. A planar $CH_3NH_3PbI_3$ solar cell having p-i-n configuration (inverted solar cells) was fabricated at the bottommost, and a conducting layer was covered on the topmost of the device [119]. Briefly, NiO was coated onto ITO substrate as hole-transporting material (HTM). On this layer, $CH_3NH_3PbI_3$ layer was prepared by antisolvent dripping strategy. Further, phenyl-C61-butyric acid methyl ester (PCBM) layer was deposited as an electron transporting material (ETM). Finally, conductive Ag layer was coated as a top electrode. Figure 14b showed the schematic energy level diagram of the $CH_3NH_3PbI_3$ solar cell having p-i-n configuration, which reveals the band positions are well for carrier separation and transportation. The current density-voltage (J-V) measurement showed that a short-circuit current density (Jsc) is ~20.38 mA cm^2, an open-circuit voltage (Voc) ~1.09 V, and a fill factor (FF) (72.9%), which yielded a PCE of at most ~16.1%. EQE was obtained more than 70% in a wide region (390–720 nm). After fabrication of $CH_3NH_3PbI_3$ solar cells, sandwich-like photocathodes were fabricated by Ti foil, and Pt deposited Ti foil by magnetron sputtering technique. The PEC performance of H_2 evolution process was estimated for $CH_3NH_3PbI_3$ photocathode by investigating in a three-electrode system, which is an SCE-reference electrode and a Pt plate counter electrode. The photocathode of sandwich-like Pt-Ti/$CH_3NH_3PbI_3$ exhibited an onset potential at~0.95 V versus RHE for H_2 evolution and showed a current density of ~18 mA/cm^2 at 0 V versus RHE. The perfect power-saved efficiency of ~7.63% and ~ 80% retention of initial current after 12 h in aqueous electrolyte (0.5 M H_2SO_4 electrolyte) was obtained under simulated AM 1.5 G solar illumination (100 mW/cm^2). Here, the onset potential and photocurrent density of perovskite photocathode were very close to V_{oc} and J_{sc} of the perovskite solar cell (inverted cell), indicating the usefulness of the perovskite-based PEC device for solar fuel production.

Kim et al. [121] reported a hybrid ETM, a $PC_{61}BM$-TiO_2 film (18–40 nm thickness) coated over the perovskite layer by atomic layer deposition, aids use as semitransparent photocathode for proton reduction process with acidic aqueous electrolytes. The semitransparent electrode with a Pt exhibit a nonstop reduction of H^+ to H_2 under light in 0.5 M H_2SO_4 solution. Figure 14c shows the schematic diagram of semitransparent photocathode, which consist of HTM (PEDOT: PSS) on ITO onto a triple-cation halide perovskite $(Cs_{0.05}\ MA_{0.17}FA_{0.83})_{0.95}Pb\text{-}(I_{0.83}Br_{0.17})_3$ layer, followed by deposition of ETM ($PC_{61}BM$ + ALD TiO_2). Finally, a Pt

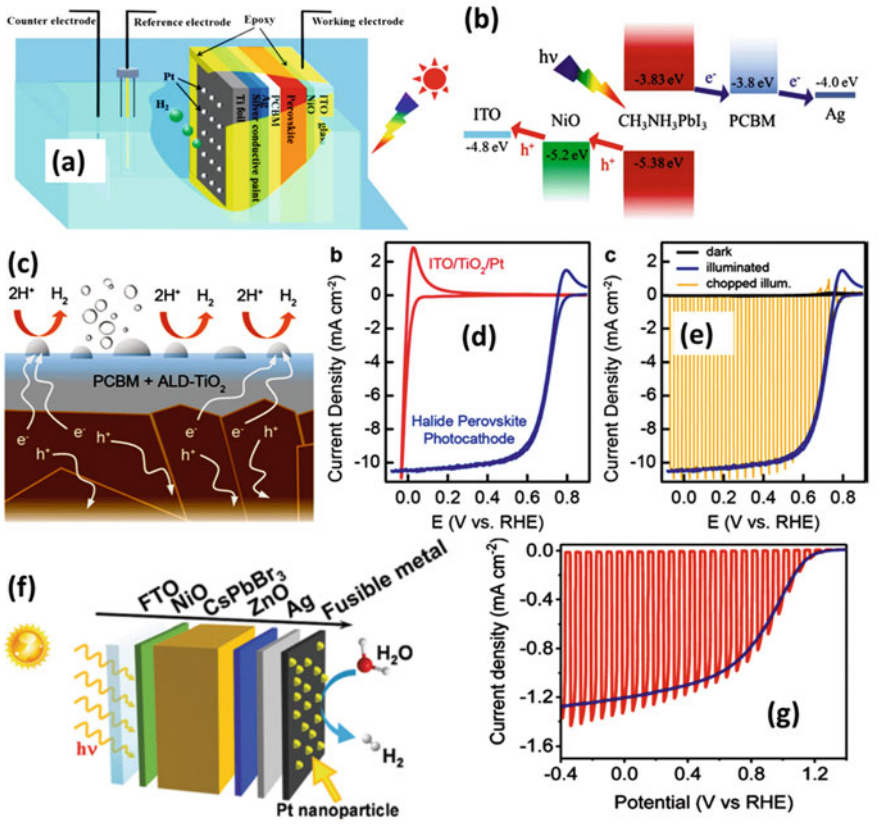

Fig. 14 (**a**) Schematic diagram of the sandwich-like perovskite ($CH_3NH_3PbI_3$) photocathode for PEC hydrogen evolution in a three-electrode system. (**b**) Schematic energy level diagram of all component in inverted perovskite solar cell [119]. Copyright 2018, Wiley publishing group. (**c**) Schematic cross-sectional image of photocathode stabilized against corrosion. (**d**) The photoelectrochemical properties of ITO/PEDOT: PSS/halide perovskite/$PC_{61}BM/TiO_2$/Pt photocathode. (**e**) The photoelectrochemical performance of the photocathode in the dark and under continuous and chopped illumination [121]. Copyright 2019, American Chemical Society. (**f**) The schematic diagram of the inorganic perovskite ($CsPbBr_3$)-based photocathode. (**g**) Current density-potential curves of inorganic perovskite-based photocathode [125]. (Copyright 2018, The Royal Society of Chemistry)

ultrathin film is deposited, which acts as a catalyst for HER. When photocathode was illuminated by light, the photocathode displays photoassisted reduction of 0.5 M H_2SO_4 @ pH = 0.32 with higher positive onset potential (0.68 V) than under dark (Fig. 14d). The photoelectrochemical behavior of the photocathode under chopped illumination exhibited >10 mA/cm^2 photocurrent (Fig. 14e).

Inorganic perovskites are promising materials in the field of solar cells due to their relatively high stability toward moisture. Among the inorganic perovskite, $CsPbBr_3$ is one of the capable materials. Although $CsPbBr_3$ is stable as compared

to organic lead halide perovskite in moisture and oxygen environments, direct use of $CsPbBr_3$ photocathode in water leads to dissolution in water and irreversible crystal structure breakdown. Hence, it is essential to find out a method to protect $CsPbBr_3$ from water for H_2 generation. There are two ways that are employed to get the waterproof effect: (i) compact layer deposition and (ii) bulk material-based encapsulation. In the compact layer way, a dense film of metal (like Ni) should be deposited by magnetron sputtering method or using a thermal evaporator technique to seal off the inorganic perovskite ($CsPbBr_3$) [122–124]. The presence of voids in the compact layer, aqueous electrolytes, can easily flow through the compact layer (Ni layer) and quickly breakdown the perovskite layer ($CsPbBr_3$). In contrast to this, bulk material-based encapsulation method (centimeter size metallic cover) is effective to protect the perovskite layer from water such as metallic foil (titanium foil) [119] and fusible alloys (InBiSn alloy) [34]. GaO et al. [125] reported deposition of a fusible InBiSn alloy (having low melting point 65 °C) to encapsulate the $CsPbBr_3$-based photocathode without ruining the perovskite layer and electron transport material (ZnO). The conductivity between alloy and ZnO has increased by depositing the layer of silver between it. Pt nanoparticles deposited on the alloy layer act as electrocatalysts for hydrogen generation. The schematic of $CsPbBr_3$-based photocathode is shown in Fig. 14f. When photocathode is irradiated, the absorption by $CsPbBr_3$ results into the formation of photocarriers (photogenerated electron hole pairs) and separates immediately. The holes are transferred to the HTM (NiO) and collected by FTO layer, whereas electrons are transported to the CB of ZnO and get the Pt nanoparticles to accomplish water reduction to hydrogen. The $CsPbBr_3$-based photocathode exhibited the photocurrent of ~1.2 mA/cm^2 at 0 V versus RHE (Fig. 14g). It shows retaining of opening photocurrent ~94% after incident of light for 1 h and Faradaic efficiency of 90%.

13 Tandem Cell for H_2 Evolving Photocathode

Often, the electrical potential required for water splitting process can be provided by PEC device. The modern electrolyzers require the potential for water splitting, and overpotential requires to conquer kinetics process of O_2 and H_2 evolution process. The alkaline electrolytes required the total operate voltage higher than 1.8 V. The utmost apparent way to create voltage with solar energy is by attaching multiple photovoltaics (PV) in series. In this section, the progress toward developing a tandem device for the generation of H_2 fuel is described. A simple photoanode (bandgap energy; E_{g1})/photocathode (bandgap energy; E_{g2}) tandem cell (where $E_{g1} > E_{g2}$) is useful for water splitting without the need for external bias [127]. In this approach, two photons are absorbed by a photoanode to create one electron-hole pair, and two photons are absorbed by photocathodes to create one electron-hole pair. Hence, a total of four photons must be absorbed by photoanode and photocathode to create one molecule of H_2. Further, a tandem device can be assembled by pairing a PV cell in tandem with a photoanode/photocathode. The

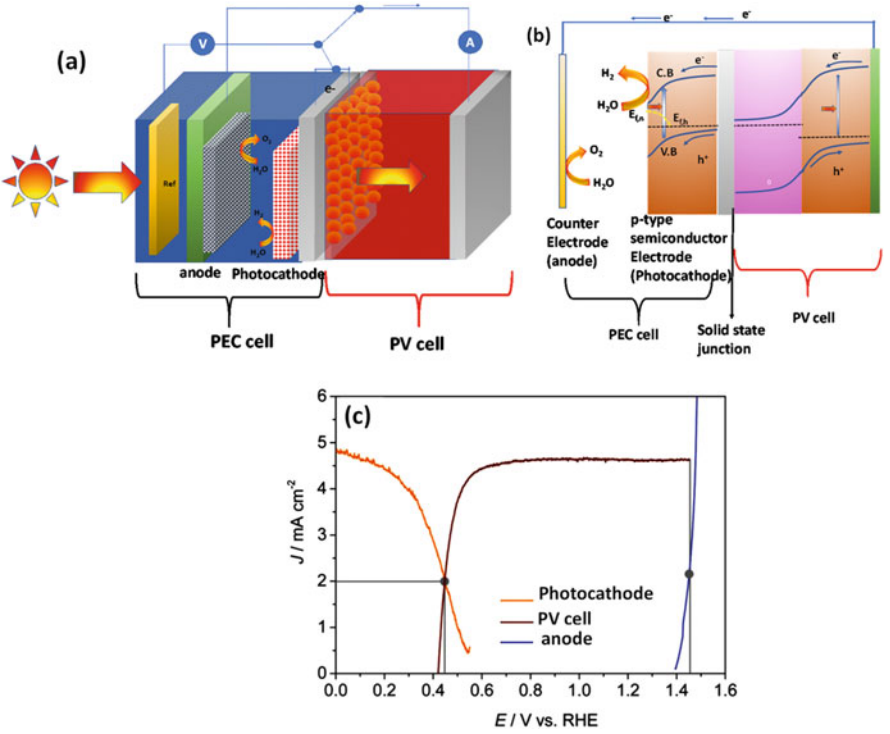

Fig. 15 (**a**) Schematic of tandem cell fabricated by compromising of PEC cell and PV cell. (**b**) Energy level diagram of tandem cell. (**c**) J-V characteristics of the tandem cell, photocathode and anode [128]. (Copyright 2015, Wiley publishing group)

ultimate goal in the fabrication of tandem devices is to make highly stable and efficient unassisted water splitting at an affordable cost [126–131].

In the fabrication of PEC-PV tandem for getting H_2O splitting, three factors are required: suitable transparent photocathode for hydrogen evolution reaction (proton reduction process), a photovoltaic cell working to the transmitted photons, and an anode for oxidation process (oxygen evolution reaction) (Fig. 15a). Figure 15b displays the energy level diagram of the PV-PEC device (tandem device). The J-V curves of the tandem device are displayed in Fig. 15c.

Copper oxide-based materials (like Cu_2O) have added significant effort for photocathode fabrication in a tandem cell due to their scalable synthesis techniques, elemental abundance, and natural p-type character. Also, Cu_2O exhibits Eg around 2.1 eV, and appropriate band energy position makes it an appropriate material for solar hydrogen production from PEC. To show the high performance of Cu_2O photocathode, the tandem device was fabricated by using Cu_2O-integrated photocathode and $BiVO_4$-integrated photoanode. Here, photocathode having the configuration of $RuO_x/TiO_2/Ga_2O_3/\ /Cu_2O/Au$ was fabricated, and photoanode was fabricated by $NiFeO_x$/reduced 1% Mo: $BiVO_4$. The details of the tandem device

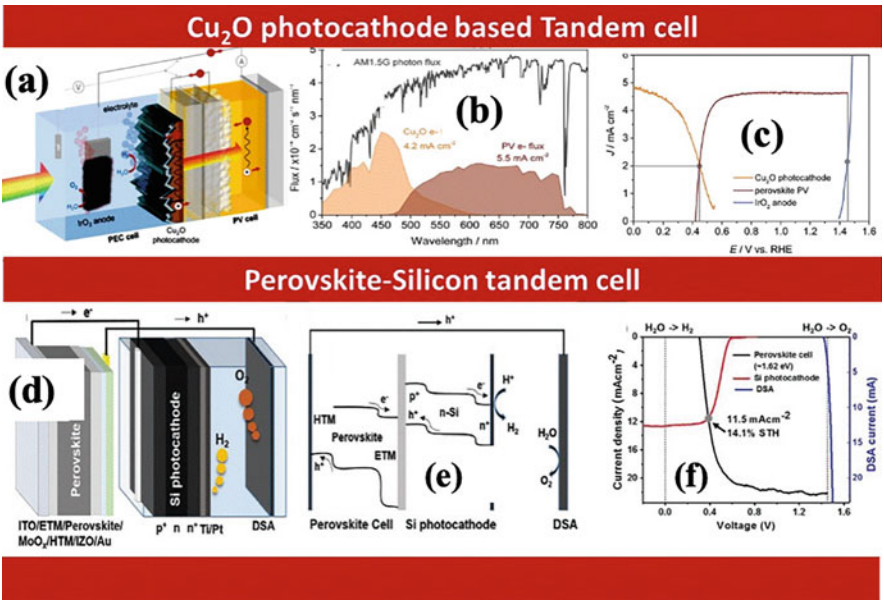

Fig. 16 (**a**) The schematic of the tandem cell fabricated by the Cu_2O-perovskite-IrO_2 configuration. (**b**) Graph of the spectral flux of photons (incident light) in the AM 1.5G spectrum and expected electron flux of PV and photocathode from multiplication of their IPCE responses respectively by the photon flux. (**c**) Plots of J-E curves of the anode and photocathode components with overlay of J-V response of the PV cell [128]. Copyright 2015, Wiley publishing group. (**d**) The tandem cell fabricated by perovskite-Si dual absorber for unassisted water splitting. (**e**) An energy level diagram of the abovementioned tandem cell. (**f**) The photocurrent of the two electrode during water splitting and the corresponding STH efficiency for the tandem cell [133]. (Copyright 2020, Wiley publishing group)

is displayed in Fig. 16a, where the light transferred via the photoanode absorber ($BiVO_4$) earlier reaching the photocathode (Cu_2O) absorber. In tandem device, the broad bandgap photoanode ($BiVO_4$; 2.4 eV) absorbs light at the low wavelength range, while high energy wavelength photons through photoanode are absorbed by Cu_2O (2. 0 eV bandgap) photocathode [132]. The steadiness test of device in 0.2 M potassium borate (pH 9.0) was studied and revealed that the device exhibited stable performance with only 10% losses take places under the illumination of light for 12 h (Fig. 16b). A topmost (peak) current density (~2.5 mA/cm^2) was reached after process for 1 h, which attributes to 3% STH. This is the uppermost STH efficiency reported for devices fabricated using metal oxide only. The current density of the tandem can be estimated by J-E curves of both photoelectrodes (photoanode and photocathode) in a front and back configuration illustrating the point at which they overlap (Fig. 16c). Dias et al. reported the Cu_2O-perovskite-IrO_2-based tandem cell for H_2 production from solar light-driven H_2O splitting. In this tandem device, IrO_2 has been used as photoanode, electrodeposited Cu_2O as photocathode, and formamidinium methylammonium lead iodide [$(MA)_x(FA)_{1-x}PbI_3$]-based PV cell

has been built. A schematic of PEC-PV is displayed in Fig. 16a [128]. Where the two absorbing electrodes are placed back to back, the hole collector is connected to anode, and electron collector is connected to the photocathode. In this tandem device (PEC-PV), the PV cell and photoelectrodes absorbed photons of different wavelength region of the solar spectrum to achieve broad sunlight harvesting (Fig. 16b). Figure 16c shows the J-E plot of all three components (anode, photocathode, and PV cell) tested individually. Comparison of the anode and photocathode curves discloses the current-dependent voltage needed to do complete electrolysis. Here, approximately 1 V is required for getting a current density of 2 mA/cm^2 between anode and photocathodes. The PV cell based on [$(MA)_x(FA)_{1-x}PbI_3$] exhibits a Voc of 1.13 V under on sun illumination. The operating current density for tandem configuration is 2 mA/cm^2, and corresponding STH is 2.5%. The tandem devices (two absorbers) have been investigated for solo water splitting for hydrogen production. The semiconductors having smaller bandgaps can absorb a larger fraction of solar spectrum accomplishing theoretical calculated STH efficiencies up to 25%. Tandem devices that have fabricated by using III-V semiconductors demonstrate STH up to 19%. However, the expensive equipment are required in fabricating these materials, which limits their applications in commercialization. Further, inexpensive materials demonstrated STH efficiencies well below 10% with fluctuating levels of durability. Variety of low-cost PV cells such as perovskite, dye, quantum dot -sensitized has been investigated to supply additional bias to the photoelectrodes made of low-cost semiconductors to achieve water splitting. Among the PV devices, perovskite cells are outstanding candidates for tandem devices with photoelectrodes owing to their low-cost processing, high efficiencies, optical transparency, and bandgap tunability. Despite an enormous capability of these perovskite cells, there are no reports showing STH efficiencies greater than 10% with inexpensive photoelectrode. Karuturi et al. published a buried p-n junction Si photocathode (p^+nn^+-Si/Ti/Pt) to minimize photovoltage losses from deprived band alignments and lessen the photocurrent losses by improving light absorption and separating light-absorbing material with reactive interfaces [133]. This photocathode showed high photocurrent density (39.7 mA/cm^2 at 0 V vs RHE) with an onset potential of 590 mV, exhibiting a remarkable applied bias photon-to-current efficiency (ABPE) (14.1%) and photostability of over 3 days. To enhance the PEC further, perovskite PV cell is connected where PV acts as a top absorber and Si photocathode as a bottom absorber in tandem. To accomplish the half reactions of water splitting, stable anode (Ir and Ru coated Ti) was employed as a counter electrode for OER reaction (Fig. 16d). The energy level schematic of the tandem device is shown in Fig. 16e. Here, PSC has fabricated by using Cs0.05Rb0.05FA0.765MA0.135PbI2.55Br0.45 integrated perovskite (bandgap ~1.62 eV) with an n-i-p architecture. This device exhibited a high PCE of up to 20%. The photocathode fabricated by Si positioned behind the PV cell exhibited a photocurrent density of 12.6 mA/cm2 at 0 V versus RHE. The properties of the tandem cell (PV-PEC) were evaluated by the J-V characteristics of the Si photelectrode in the back of the PSC, the redox potentials, and the perovskite solar cell as displayed in Fig. 16f. The intersections of the J-V characteristics of two absorbers (perovskite PV cell and Si photocathode) give the operating current of the

PV-PEC cell (tandem device). The tandem device shows the current of 11.5 mA/cm2 for solar water splitting, which attributes to an STH efficiency of 14.1%. This is the greatest reported STH efficiency device for non-III-V semiconductor materials.

14 Summary and Future Outlook

In the PEC field, developing an earth-abundant and low-cost photocathode that can provide high efficiency and long-term stability for practical appliances remains a substantial challenge. P-type silicon is a low-cost and earth-abundant semiconductor with a low bandgap (1.1 eV) and has been widely employed as a light absorber for the fabrication of photocathodes. The single Si photocathode has low electron-hole separation efficiency, and photocorrosion takes place. Thus, making heterostructure with other materials like metal oxides and chalcogenides has been investigated to increase the PEC performance and stability of the photocathode. Among the low-cost p-type semiconductors, metal oxide (Cu_2O) and metal chalcogenides (like MoS_2) have been used for fabrication p-n junction photocathode via coupling with n-type semiconductors. Recently, dye-sensitized and perovskite-sensitized photocathodes are studied in order to achieve high STH. The fabrication of tandem device with a different configuration of PEC-PV devices is investigated to achieve high STH efficiency, where PV cell can be a DSC or PSC or III-IV-based solar cells. Modeling of the tandem device suggested that further work required to substituting the noble-metal electrocatalyst with earth-abundant materials and upgrading of solar cell fill factor will cover the improvement in STH efficiency for getting the cost effective and high-efficacy tandem PEC system.

Acknowledgments Authors gratefully acknowledge the funding as the statement: this research is supported by the Second Century Fund (C2F), the CAT-REAC industrial project, Thailand Science Research and Innovation Fund Chulalongkorn University (CU_FRB65_ind (15)_163_21_29), the NSRF via the Program Management Unit for Human Resources and Institutional Development, Research and Innovation [grant number B16F640143]), and the Asahi Glass Foundation.

References

1. Q. Huang, Z. Ye, X. Xiao, Recent progress in photocathodes for hydrogen evolution. J. Mater. Chem. A **3**, 15824–15837 (2015). https://doi.org/10.1039/C5TA03594E
2. C. Ros, T. Andreu, J.R. Morante, Photoelectrochemical water splitting: A road from stable metal oxides to protected thin film solar cells. J. Mater. Chem. A **8**, 10625–10669 (2020). https://doi.org/10.1039/D0TA02755C
3. S. Chen, D. Huang, P. Xu, W. Xue, L. Lei, M. Cheng, et al., Semiconductor-based photocatalysts for photocatalytic and photoelectrochemical water splitting: Will we stop with photocorrosion? J. Mater. Chem. A **8**, 2286–2322 (2020). https://doi.org/10.1039/C9TA12799B

4. Y.J. Jang, J.S. Lee, Photoelectrochemical water splitting with p-type metal oxide semiconductor photocathodes. ChemSusChem **12**, 1835–1845 (2019). https://doi.org/10.1002/cssc.201802596
5. T. Su, Q. Shao, Z. Qin, Z. Guo, Z. Wu, Role of interfaces in two-dimensional Photocatalyst for water splitting. ACS Catal. **8**, 2253–2276 (2018). https://doi.org/10.1021/acscatal.7b03437
6. M. Faraji, M. Yousefi, S. Yousefzadeh, M. Zirak, N. Naseri, T.H. Jeon, et al., Two-dimensional materials in semiconductor photoelectrocatalytic systems for water splitting. Energy Environ. Sci. **12**, 59–95 (2019). https://doi.org/10.1039/C8EE00886H
7. A. Govind Rajan, J.M.P. Martirez, E.A. Carter, Why do we use the materials and operating conditions we use for heterogeneous (photo)electrochemical water splitting? ACS Catal. **10**, 11177–11234 (2020). https://doi.org/10.1021/acscatal.0c01862
8. J. Joy, J. Mathew, S.C. George, Nanomaterials for photoelectrochemical water splitting – Review. Int. J. Hydrog. Energy **43**, 4804–4817 (2018). https://doi.org/10.1016/j.ijhydene.2018.01.099
9. D. Wang, A. Pierre, M.G. Kibria, K. Cui, X. Han, K.H. Bevan, et al., Wafer-level photocatalytic water splitting on GaN nanowire arrays grown by molecular beam epitaxy. Nano Lett. **11**, 2353–2357 (2011). https://doi.org/10.1021/nl2006802
10. I. Oh, J. Kye, S. Hwang, Enhanced Photoelectrochemical hydrogen production from silicon nanowire Array photocathode. Nano Lett. **12**, 298–302 (2012). https://doi.org/10.1021/nl203564s
11. D. Voiry, H.S. Shin, K.P. Loh, M. Chhowalla, Low-dimensional catalysts for hydrogen evolution and CO_2 reduction. Nat. Rev. Chem. **2**, 105 (2018). https://doi.org/10.1038/s41570-017-0105
12. C.-H. Lee, G.-H. Lee, A.M. van der Zande, W. Chen, Y. Li, M. Han, et al., Atomically thin p–n junctions with van der Waals heterointerfaces. Nat. Nanotechnol. **9**, 676–681 (2014). https://doi.org/10.1038/nnano.2014.150
13. A. Pospischil, M.M. Furchi, T. Mueller, Solar-energy conversion and light emission in an atomic monolayer p–n diode. Nat. Nanotechnol. **9**, 257–261 (2014). https://doi.org/10.1038/nnano.2014.14
14. S.J.A. Moniz, S.A. Shevlin, D.J. Martin, Z.-X. Guo, J. Tang, Visible-light driven heterojunction photocatalysts for water splitting – A critical review. Energy Environ. Sci. **8**, 731–759 (2015). https://doi.org/10.1039/C4EE03271C
15. H. Yu, Y. Peng, Y. Yang, Z.-Y. Li, Plasmon-enhanced light–matter interactions and applications. npj Comput. Mater. **5**, 45 (2019). https://doi.org/10.1038/s41524-019-0184-1
16. J.R. Hendrickson, S. Vangala, N. Nader, K. Leedy, J. Guo, J.W. Cleary, Plasmon resonance and perfect light absorption in subwavelength trench arrays etched in gallium-doped zinc oxide film. Appl. Phys. Lett. **107**, 191906 (2015). https://doi.org/10.1063/1.4935219
17. M. Sabaeian, M. Heydari, N. Ajamgard, Plasmonic excitation-assisted optical and electric enhancement in ultra-thin solar cells: The influence of nano-strip cross section. AIP Adv. **5**, 87126 (2015). https://doi.org/10.1063/1.4928517
18. L. Ma, J. Zhao, J. Tan, L. Liu, Near-field effects on light absorption in nanoparticle system, in *2017 Progress in Electromagnetics Research Symposium – Fall (PIERS – FALL)*, (2017), pp. 2797–2801
19. Q. Xu, F. Liu, Y. Liu, K. Cui, X. Feng, W. Zhang, et al., Broadband light absorption enhancement in dye-sensitized solar cells with Au-Ag alloy popcorn nanoparticles. Sci. Rep. **3**, 2112 (2013). https://doi.org/10.1038/srep02112
20. Y. Chen, H. Zhou, Defects chemistry in high-efficiency and stable perovskite solar cells. J. Appl. Phys. **128**, 60903 (2020). https://doi.org/10.1063/5.0012384
21. J. Zhu, G. Cheng, J. Xiong, W. Li, S. Dou, Recent advances in cu-based Cocatalysts toward solar-to-hydrogen evolution: Categories and roles. Solar RRL **3**, 1900256 (2019). https://doi.org/10.1002/solr.201900256
22. M. Basu, Z.-W. Zhang, C.-J. Chen, P.-T. Chen, K.-C. Yang, C.-G. Ma, et al., Heterostructure of Si and $CoSe_2$: A promising photocathode based on a non-noble metal catalyst for Photoelectrochemical hydrogen evolution. Angew. Chem. Int. Ed. **54**, 6211–6216 (2015). https://doi.org/10.1002/anie.201502573

23. A. Fujishima, K. Honda, Electrochemical evidence for the mechanism of the primary stage of photosynthesis. Bull. Chem. Soc. Jpn. **44**, 1148–1150 (1971). https://doi.org/10.1246/bcsj.44.1148
24. A. Fujishima, K. Honda, Electrochemical photolysis of water at a semiconductor electrode. Nature **238**, 37–38 (1972). https://doi.org/10.1038/238037a0
25. J.G. Mavroides, J.A. Kafalas, D.F. Kolesar, Photoelectrolysis of water in cells with $SrTiO_3$ anodes. Appl. Phys. Lett. **28**, 241–243 (1976). https://doi.org/10.1063/1.88723
26. A.J. Nozik, p-n photoelectrolysis cells. Appl. Phys. Lett. **29**, 150–153 (1976). https://doi.org/10.1063/1.89004
27. R.C. Kainthla, B. Zelenay, J.O. Bockris, Significant efficiency increase in self-driven Photoelectrochemical cell for water Photoelectrolysis. J. Electrochem. Soc. **134**, 841–845 (1987). https://doi.org/10.1149/1.2100583
28. O. Khaselev, J.A. Turner, A monolithic photovoltaic-Photoelectrochemical device for hydrogen production via water splitting. Science **280**, 425 LP – 427 (1998). https://doi.org/10.1126/science.280.5362.425
29. E. Aharon-Shalom, A. Heller, Efficient p - InP (Rh - H alloy) and p - InP (Re - H alloy) hydrogen evolving photocathodes. J. Electrochem. Soc. **129**, 2865–2866 (1982). https://doi.org/10.1149/1.2123695
30. T.N. Veziroğlu, F. Barbir, Initiation of hydrogen energy system in developing countries. Int. J. Hydrog. Energy **17**, 527–538 (1992). https://doi.org/10.1016/0360-3199(92)90152-M
31. D. Yokoyama, T. Minegishi, K. Jimbo, T. Hisatomi, G. Ma, M. Katayama, et al., H_2 Evolution from water on modified Cu_2ZnSnS_4 photoelectrode under solar light. Appl. Phys. Express **3**, 101202 (2010). https://doi.org/10.1143/apex.3.101202
32. D.A. Hoogeveen, M. Fournier, S.A. Bonke, A. Nattestad, A. Mishra, P. Bäuerle, et al., Origin of photoelectrochemical generation of dihydrogen by a dye-sensitized photocathode without an intentionally introduced catalyst. J. Phys. Chem. C **121**, 25836–25846 (2017). https://doi.org/10.1021/acs.jpcc.7b08067
33. P. Meng, M. Wang, Y. Yang, S. Zhang, L. Sun, CdSe quantum dots/molecular cobalt catalyst co-grafted open porous NiO film as a photocathode for visible light driven H_2 evolution from neutral water. J. Mater. Chem. A **3**, 18852–18859 (2015). https://doi.org/10.1039/C5TA06255A
34. M. Crespo-Quesada, L.M. Pazos-Outón, J. Warnan, M.F. Kuehnel, R.H. Friend, E. Reisner, Metal-encapsulated organolead halide perovskite photocathode for solar-driven hydrogen evolution in water. Nat. Commun. **7**, 12555 (2016). https://doi.org/10.1038/ncomms12555
35. C. Jiang, S.J.A. Moniz, A. Wang, T. Zhang, J. Tang, Photoelectrochemical devices for solar water splitting – Materials and challenges. Chem. Soc. Rev. **46**, 4645–4660 (2017). https://doi.org/10.1039/C6CS00306K
36. J.H. Kim, D. Hansora, P. Sharma, J.-W. Jang, J.S. Lee, Toward practical solar hydrogen production – An artificial photosynthetic leaf-to-farm challenge. Chem. Soc. Rev. **48**, 1908–1971 (2019). https://doi.org/10.1039/C8CS00699G
37. L. Pan, N. Vlachopoulos, A. Hagfeldt, Directly Photoexcited oxides for photoelectrochemical water splitting. ChemSusChem **12**, 4337–4352 (2019). https://doi.org/10.1002/cssc.201900849
38. M.T. Mayer, Photovoltage at semiconductor–electrolyte junctions. Curr. Opin. Electrochem. **2**, 104–110 (2017). https://doi.org/10.1016/j.coelec.2017.03.006
39. C. Li, J. He, Y. Xiao, Y. Li, J.-J. Delaunay, Earth-abundant Cu-based metal oxide photocathodes for photoelectrochemical water splitting. Energy Environ. Sci. **13**, 3269–3306 (2020). https://doi.org/10.1039/D0EE02397C
40. T. Hisatomi, J. Kubota, K. Domen, Recent advances in semiconductors for photocatalytic and photoelectrochemical water splitting. Chem. Soc. Rev. **43**, 7520–7535 (2014). https://doi.org/10.1039/C3CS60378D
41. F. Chen, Q. Zhu, Y. Wang, W. Cui, X. Su, Y. Li, Efficient photoelectrochemical hydrogen evolution on silicon photocathodes interfaced with nanostructured NiP_2 cocatalyst films. ACS Appl. Mater. Interfaces **8**, 31025–31031 (2016). https://doi.org/10.1021/acsami.6b11197

42. H. Robatjazi, S.M. Bahauddin, C. Doiron, I. Thomann, Direct plasmon-driven photoelectrocatalysis. Nano Lett. **15**, 6155–6161 (2015). https://doi.org/10.1021/acs.nanolett.5b02453
43. L. Tian, R. Tyburski, C. Wen, R. Sun, M. Abdellah, J. Huang, et al., Understanding the role of surface states on mesoporous NiO films. J. Am. Chem. Soc. **142**, 18668–18678 (2020). https://doi.org/10.1021/jacs.0c08886
44. X. Liu, D. Wen, Z. Liu, J. Wei, D. Bu, S. Huang, Thiocyanate-capped CdSe@$Zn_{1-X}Cd_XS$ gradient alloyed quantum dots for efficient photocatalytic hydrogen evolution. Chem. Eng. J. **402**, 126178 (2020). https://doi.org/10.1016/j.cej.2020.126178
45. H. Huang, B. Pradhan, J. Hofkens, M.B.J. Roeffaers, J.A. Steele, Solar-driven metal halide perovskite photocatalysis: Design, stability, and performance. ACS Energy Lett. **5**, 1107–1123 (2020). https://doi.org/10.1021/acsenergylett.0c00058
46. H. Yan, K. He, I.A. Samek, D. Jing, M.G. Nanda, P.C. Stair, et al., Tandem In_2O_3-Pt/Al_2O_3 catalyst for coupling of propane dehydrogenation to selective H_2 combustion. Science **371**, 1257 LP-1260 (2021). https://doi.org/10.1126/science.abd4441
47. S. Choudhary, S. Upadhyay, P. Kumar, N. Singh, V.R. Satsangi, R. Shrivastav, et al., Nanostructured bilayered thin films in photoelectrochemical water splitting – A review. Int. J. Hydrog. Energy **37**, 18713–18730 (2012). https://doi.org/10.1016/j.ijhydene.2012.10.028
48. D. Sharma, S. Upadhyay, V.R. Satsangi, R. Shrivastav, U.V. Waghmare, S. Dass, Improved Photoelectrochemical water splitting performance of Cu_2O/$SrTiO_3$ heterojunction photoelectrode. J. Phys. Chem. C **118**, 25320–25329 (2014). https://doi.org/10.1021/jp507039n
49. J. Li, P. Jiménez-Calvo, E. Paineau, M.N. Ghazzal, Metal chalcogenides based heterojunctions and novel nanostructures for photocatalytic hydrogen evolution. Catalysts **10**, 89 (2020). https://doi.org/10.3390/catal10010089
50. X. Sun, J. Jiang, Y. Yang, Y. Shan, L. Gong, M. Wang, Enhancing the performance of Si-based photocathodes for solar hydrogen production in alkaline solution by facilely intercalating a sandwich N-doped carbon nanolayer to the interface of Si and TiO_2. ACS Appl. Mater. Interfaces **11**, 19132–19140 (2019). https://doi.org/10.1021/acsami.9b03757
51. D. Zhang, J. Shi, W. Zi, P. Wang, Liu S (Frank), Recent advances in photoelectrochemical applications of silicon materials for solar-to-chemicals conversion. ChemSusChem **10**, 4324–4341 (2017). https://doi.org/10.1002/cssc.201701674
52. S.-S. Yi, X.-B. Zhang, B.-R. Wulan, J.-M. Yan, Q. Jiang, Non-noble metals applied to solar water splitting. Energy Environ. Sci. **11**, 3128–3156 (2018). https://doi.org/10.1039/C8EE02096E
53. L. Zhang, X. Chen, Z. Hao, X. Chen, Y. Li, Y. Cui, et al., TiO_2/Au Nanoring/p-Si Nanohole photocathode for hydrogen generation. ACS Appl. Nano Mater. **2**, 3654–3661 (2019). https://doi.org/10.1021/acsanm.9b00590
54. M.A. Tekalgne, A. Hasani, D.Y. Heo, Q. Van Le, T.P. Nguyen, T.H. Lee, et al., SnO_2@WS_2/p-Si heterostructure photocathode for photoelectrochemical hydrogen production. J. Phys. Chem. C **124**, 647–652 (2020). https://doi.org/10.1021/acs.jpcc.9b09623
55. P. Gnanasekar, D. Periyanagounder, P. Varadhan, J.-H. He, J. Kulandaivel, Highly efficient and stable photoelectrochemical hydrogen evolution with 2D-NbS_2/Si nanowire heterojunction. ACS Appl. Mater. Interfaces **11**, 44179–44185 (2019). https://doi.org/10.1021/acsami.9b14713
56. E. Luévano-Hipólito, L.M. Torres-Martínez, D. Sánchez-Martínez, M.R. Alfaro Cruz, Cu_2O precipitation-assisted with ultrasound and microwave radiation for photocatalytic hydrogen production. Int. J. Hydrog. Energy **42**, 12997–13010 (2017). https://doi.org/10.1016/j.ijhydene.2017.03.192
57. I.V. Bagal, N.R. Chodankar, M.A. Hassan, A. Waseem, M.A. Johar, D.-H. Kim, et al., Cu_2O as an emerging photocathode for solar water splitting – A status review. Int. J. Hydrog. Energy **44**, 21351–21378 (2019). https://doi.org/10.1016/j.ijhydene.2019.06.184
58. J.-M. Li, C.-W. Tsao, M.-J. Fang, C.-C. Chen, C.-W. Liu, Y.-J. Hsu, TiO_2-Au-Cu_2O photocathodes: Au-mediated Z-scheme charge transfer for efficient solar-driven photoelectrochemical reduction. ACS Appl. Nano Mater. **1**, 6843–6853 (2018). https://doi.org/10.1021/acsanm.8b01678

59. P. Wu, Z. Liu, D. Chen, M. Zhou, J. Wei, Flake-like NiO/WO_3 p-n heterojunction photocathode for photoelectrochemical water splitting. Appl. Surf. Sci. **440**, 1101–1106 (2018)
60. C. Cheng, H.J. Fan, Branched nanowires: Synthesis and energy applications. Nano Today **7**, 327–343 (2012). https://doi.org/10.1016/j.nantod.2012.06.002
61. A. Kargar, K. Sun, Y. Jing, C. Choi, H. Jeong, G.Y. Jung, et al., 3D branched nanowire Photoelectrochemical electrodes for efficient solar water splitting. ACS Nano **7**, 9407–9415 (2013). https://doi.org/10.1021/nn404170y
62. A. Kargar, K. Sun, Y. Jing, C. Choi, H. Jeong, Y. Zhou, et al., Tailoring n-ZnO/p-Si branched nanowire Heterostructures for selective Photoelectrochemical water oxidation or reduction. Nano Lett. **13**, 3017–3022 (2013). https://doi.org/10.1021/nl304539x
63. H.S. Song, W.J. Zhang, C. Cheng, Y.B. Tang, L.B. Luo, X. Chen, et al., Controllable fabrication of three-dimensional radial ZnO nanowire/silicon microrod hybrid architectures. Cryst. Growth Des. **11**, 147–153 (2011). https://doi.org/10.1021/cg101062e
64. A. Kargar, Y. Jing, S.J. Kim, C.T. Riley, X. Pan, D. Wang, ZnO/CuO heterojunction branched nanowires for Photoelectrochemical hydrogen generation. ACS Nano **7**, 11112–11120 (2013). https://doi.org/10.1021/nn404838n
65. Y. Yang, D. Xu, Q. Wu, P. Diao, Cu_2O/CuO bilayered composite as a high-efficiency photocathode for photoelectrochemical hydrogen evolution reaction. Sci. Rep. **6**, 35158 (2016). https://doi.org/10.1038/srep35158
66. A.A. Dubale, A.G. Tamirat, H.-M. Chen, T.A. Berhe, C.-J. Pan, W.-N. Su, et al., A highly stable CuS and CuS–Pt modified Cu_2O/CuO heterostructure as an efficient photocathode for the hydrogen evolution reaction. J. Mater. Chem. A **4**, 2205–2216 (2016). https://doi.org/10.1039/C5TA09464J
67. Z. Li, Z. Jiang, W. Zhou, M. Chen, M. Su, X. Luo, et al., MoS_2 nanoribbons with a prolonged photoresponse lifetime for enhanced visible light photoelectrocatalytic hydrogen evolution. Inorg. Chem. **60**, 1991–1997 (2021). https://doi.org/10.1021/acs.inorgchem.0c03478
68. W. Xun, Y. Wang, R. Fan, Q. Mu, S. Ju, Y. Peng, et al., Activating the MoS_2 basal plane toward enhanced solar hydrogen generation via in situ photoelectrochemical control. ACS Energy Lett. **6**, 267–276 (2021). https://doi.org/10.1021/acsenergylett.0c02320
69. S. Zhang, X. Li, X. Zhang, X. Wang, W. Wang, R. Yu, et al., Enhancement of the photoelectrocatalytic H_2 evolution on a rutile-TiO_2(001) surface decorated with dendritic MoS_2 monolayer Nanoflakes. ACS Appl. Energy Mater. **3**, 5756–5764 (2020). https://doi.org/10.1021/acsaem.0c00682
70. Y. Liu, C. Liang, J. Wu, T. Sharifi, H. Xu, Y. Nakanishi, et al., Atomic layered titanium sulfide quantum dots as Electrocatalysts for enhanced hydrogen evolution reaction. Adv. Mater. Interfaces **5**, 1700895 (2018). https://doi.org/10.1002/admi.201700895
71. G. Liu, Z. Li, T. Hasan, X. Chen, W. Zheng, W. Feng, et al., Vertically aligned two-dimensional SnS_2 nanosheets with a strong photon capturing capability for efficient photoelectrochemical water splitting. J. Mater. Chem. A **5**, 1989–1995 (2017). https://doi.org/10.1039/C6TA08327G
72. F. Zhang, Y. Chen, W. Zhou, C. Ren, H. Gao, G. Tian, Hierarchical SnS_2/$CuInS_2$ Nanosheet Heterostructure films decorated with C_{60} for remarkable Photoelectrochemical water splitting. ACS Appl. Mater. Interfaces **11**, 9093–9101 (2019). https://doi.org/10.1021/acsami.8b21222
73. M. Cao, K. Yao, C. Wu, J. Huang, W. Yang, L. Zhang, et al., Facile synthesis of SnS and SnS_2 Nanosheets for FTO/SnS/SnS_2/Pt photocathode. ACS Appl. Energy Mater. **1**, 6497–6504 (2018). https://doi.org/10.1021/acsaem.8b01414
74. A. Hasani, Q. Van Le, M. Tekalgne, M.-J. Choi, S. Choi, T.H. Lee, et al., Fabrication of a WS_2/p-Si heterostructure photocathode using direct hybrid thermolysis. ACS Appl. Mater. Interfaces **11**, 29910–29916 (2019). https://doi.org/10.1021/acsami.9b08654
75. D. Chu, K. Li, A. Liu, J. Huang, C. Zhang, P. Yang, et al., Zn-doped hematite modified by graphene-like WS_2: A p-type semiconductor hybrid photocathode for water splitting to produce hydrogen. Int. J. Hydrog. Energy **43**, 7307–7316 (2018). https://doi.org/10.1016/j.ijhydene.2018.02.152

76. L. Zeng, Y. Liu, S. Lin, W. Qarony, L. Tao, Y. Chai, et al., High photoelectrochemical activity and stability of Au-WS_2/silicon heterojunction photocathode. Sol. Energy Mater. Sol. Cells **174**, 300–306 (2018). https://doi.org/10.1016/j.solmat.2017.07.042
77. G. Huang, J. Mao, R. Fan, Z. Yin, X. Wu, J. Jie, et al., Integrated $MoSe_2$ with n+p-Si photocathodes for solar water splitting with high efficiency and stability. Appl. Phys. Lett. **112**, 13902 (2018). https://doi.org/10.1063/1.5012110
78. S. Hong, C.K. Rhee, Y. Sohn, Photoelectrochemical hydrogen evolution and CO_2 reduction over MoS_2/Si and $MoSe_2$/Si nanostructures by combined Photoelectrochemical deposition and rapid-thermal annealing process. Catalysts **9**, 494 (2019). https://doi.org/10.3390/catal9060494
79. S. Seo, S. Kim, H. Choi, J. Lee, H. Yoon, G. Piao, et al., Direct in situ growth of centimeter-scale multi-heterojunction MoS_2/WS_2/WSe_2 thin-film catalyst for photo-electrochemical hydrogen evolution. Adv. Sci. **6**, 1900301 (2019). https://doi.org/10.1002/advs.201900301
80. Z. Ma, P. Konze, M. Küpers, K. Wiemer, D. Hoffzimmer, S. Neumann, et al., Elucidation of the active sites for monodisperse FePt and Pt nanocrystal catalysts for p-WSe_2 photocathodes. J. Phys. Chem. C **124**, 11877–11885 (2020). https://doi.org/10.1021/acs.jpcc.0c01288
81. X. Yu, N. Guijarro, M. Johnson, K. Sivula, Defect mitigation of solution-processed 2D WSe_2 Nanoflakes for solar-to-hydrogen conversion. Nano Lett. **18**, 215–222 (2018). https://doi.org/10.1021/acs.nanolett.7b03948
82. F. Bozheyev, K. Harbauer, C. Zahn, D. Friedrich, K. Ellmer, Highly (001)-textured p-type WSe_2 thin films as efficient large-area photocathodes for solar hydrogen evolution. Sci. Rep. **7**, 16003 (2017). https://doi.org/10.1038/s41598-017-16283-8
83. B. Luo, G. Liu, L. Wang, Recent advances in 2D materials for photocatalysis. Nanoscale **8**, 6904–6920 (2016). https://doi.org/10.1039/C6NR00546B
84. M.A. Hassan, M.-W. Kim, M.A. Johar, A. Waseem, M.-K. Kwon, S.-W. Ryu, Transferred monolayer MoS_2 onto GaN for heterostructure photoanode: Toward stable and efficient photoelectrochemical water splitting. Sci. Rep. **9**, 20141 (2019). https://doi.org/10.1038/s41598-019-56807-y
85. J. Liao, B. Sa, J. Zhou, R. Ahuja, Z. Sun, Design of high-efficiency visible-light photocatalysts for water splitting: MoS_2/AlN(GaN) heterostructures. J. Phys. Chem. C **118**, 17594–17599 (2014). https://doi.org/10.1021/jp5038014
86. H. Zhang, Y.-N. Zhang, H. Liu, L.-M. Liu, Novel heterostructures by stacking layered molybdenum disulfides and nitrides for solar energy conversion. J. Mater. Chem. A **2**, 15389–15395 (2014). https://doi.org/10.1039/C4TA03134B
87. Z. Zhang, Q. Qian, B. Li, K.J. Chen, Interface engineering of monolayer MoS_2/GaN hybrid heterostructure: Modified band alignment for photocatalytic water splitting application by nitridation treatment. ACS Appl. Mater. Interfaces **10**, 17419–17426 (2018). https://doi.org/10.1021/acsami.8b01286
88. D. Ghosh, P. Devi, P. Kumar, Modified p-GaN microwells with vertically aligned 2D-MoS_2 for enhanced photoelectrochemical water splitting. ACS Appl. Mater. Interfaces **12**, 13797–13804 (2020). https://doi.org/10.1021/acsami.9b20969
89. F. Meng, J. Li, S.K. Cushing, M. Zhi, N. Wu, Solar hydrogen generation by nanoscale p–n junction of p-type molybdenum disulfide/n-type nitrogen-doped reduced graphene oxide. J. Am. Chem. Soc. **135**, 10286–10289 (2013). https://doi.org/10.1021/ja404851s
90. Y.-J. Yuan, J.-R. Tu, Z.-J. Ye, D.-Q. Chen, B. Hu, Y.-W. Huang, et al., MoS_2-graphene/$ZnIn_2S_4$ hierarchical microarchitectures with an electron transport bridge between light-harvesting semiconductor and cocatalyst: A highly efficient photocatalyst for solar hydrogen generation. Appl. Catal. B Environ. **188**, 13–22 (2016). https://doi.org/10.1016/j.apcatb.2016.01.061
91. M. Moriya, T. Minegishi, H. Kumagai, M. Katayama, J. Kubota, K. Domen, Stable hydrogen evolution from CdS-modified $CuGaSe_2$ photoelectrode under visible-light irradiation. J. Am. Chem. Soc. **135**, 3733–3735 (2013). https://doi.org/10.1021/ja312653y
92. H. Kumagai, T. Minegishi, N. Sato, T. Yamada, J. Kubota, K. Domen, Efficient solar hydrogen production from neutral electrolytes using surface-modified Cu(In,Ga)Se_2 photocathodes. J. Mater. Chem. A **3**, 8300–8307 (2015). https://doi.org/10.1039/C5TA01058F

93. F. Jiang, H.T. Gunawan, Y. Kuang, T. Minegishi, K. Domen, et al., Pt/In_2S_3/CdS/Cu_2ZnSnS_4 thin film as an efficient and stable photocathode for water reduction under sunlight radiation. J. Am. Chem. Soc. **137**, 13691–13697 (2015). https://doi.org/10.1021/jacs.5b09015
94. W. Yang, Y. Oh, J. Kim, M.J. Jeong, J.H. Park, J. Moon, Molecular chemistry-controlled hybrid ink-derived efficient Cu_2ZnSnS_4 photocathodes for photoelectrochemical water splitting. ACS Energy Lett. **1**, 1127–1136 (2016). https://doi.org/10.1021/acsenergylett.6b00453
95. B. Kim, G.S. Park, Y.J. Hwang, D.H. Won, W. Kim, D.K. Lee, et al., Cu(In,Ga)$(S,Se)_2$ photocathodes with a grown-in CuxS catalyst for solar water splitting. ACS Energy Lett. **4**, 2937–2944 (2019). https://doi.org/10.1021/acsenergylett.9b01816
96. K. Feng, D. Huang, L. Li, K. Wang, J. Li, T. Harada, et al., MoSx-CdS/Cu_2ZnSnS_4-based thin film photocathode for solar hydrogen evolution from water. Appl. Catal. B Environ. **268**, 118438 (2020). https://doi.org/10.1016/j.apcatb.2019.118438
97. M.G. Mali, H. Yoon, B.N. Joshi, H. Park, S.S. Al-Deyab, D.C. Lim, et al., Enhanced photoelectrochemical solar water splitting using a platinum-decorated CIGS/CdS/ZnO photocathode. ACS Appl. Mater. Interfaces **7**, 21619–21625 (2015). https://doi.org/10.1021/acsami.5b07267
98. Y. Zhou, D. Shin, E. Ngaboyamahina, Q. Han, C.B. Parker, D.B. Mitzi, et al., Efficient and stable Pt/TiO_2/CdS/$Cu_2BaSn(S,Se)_4$ photocathode for water electrolysis applications. ACS Energy Lett. **3**, 177–183 (2018). https://doi.org/10.1021/acsenergylett.7b01062
99. C. Yu, Q. Jia, H. Zhang, W. Liu, X. Yu, X. Zhang, Enhancing photoelectrochemical hydrogen production of a n+p-Si hetero-junction photocathode with amorphous Ni and Ti layers. Inorg. Chem. Front. **6**, 527–532 (2019). https://doi.org/10.1039/C8QI01269E
100. S.K. Choi, G. Piao, W. Choi, H. Park, Highly efficient hydrogen production using p-Si wire arrays and NiMoZn heterojunction photocathodes. Appl. Catal. B Environ. **217**, 615–621 (2017). https://doi.org/10.1016/j.apcatb.2017.06.020
101. L. Wang, W. Wang, Y. Chen, L. Yao, X. Zhao, H. Shi, et al., Heterogeneous p–n junction CdS/Cu_2O Nanorod arrays: Synthesis and superior visible-light-driven Photoelectrochemical performance for hydrogen evolution. ACS Appl. Mater. Interfaces **10**, 11652–11662 (2018). https://doi.org/10.1021/acsami.7b19530
102. C. Liu, T. Liu, Y. Li, Z. Zhao, D. Zhou, W. Li, et al., A dendritic Sb_2Se_3/In_2S_3 heterojunction nanorod array photocathode decorated with a MoSx catalyst for efficient solar hydrogen evolution. J. Mater. Chem. A **8**, 23385–23394 (2020). https://doi.org/10.1039/D0TA08874A
103. L. Zhang, T. Minegishi, M. Nakabayashi, Y. Suzuki, K. Seki, N. Shibata, et al., Durable hydrogen evolution from water driven by sunlight using (Ag,Cu)$GaSe_2$ photocathodes modified with CdS and $CuGa_3Se_5$. Chem. Sci. **6**, 894–901 (2015). https://doi.org/10.1039/C4SC02346C
104. J. Zhao, T. Minegishi, L. Zhang, M. Zhong, N.M. Gunawan, et al., Enhancement of solar hydrogen evolution from water by surface modification with CdS and TiO_2 on porous $CuInS_2$ photocathodes prepared by an electrodeposition–sulfurization method. Angew. Chem. Int. Ed. **53**, 11808–11812 (2014). https://doi.org/10.1002/anie.201406483
105. D.L. Ashford, M.K. Gish, A.K. Vannucci, M.K. Brennaman, J.L. Templeton, J.M. Papanikolas, et al., Molecular chromophore–catalyst assemblies for solar fuel applications. Chem. Rev. **115**, 13006–13049 (2015). https://doi.org/10.1021/acs.chemrev.5b00229
106. Z. Yu, F. Li, L. Sun, Recent advances in dye-sensitized photoelectrochemical cells for solar hydrogen production based on molecular components. Energy Environ. Sci. **8**, 760–775 (2015). https://doi.org/10.1039/C4EE03565H
107. N. Queyriaux, N. Kaeffer, A. Morozan, M. Chavarot-Kerlidou, V. Artero, Molecular cathode and photocathode materials for hydrogen evolution in photoelectrochemical devices. J Photochem Photobiol C: Photochem Rev **25**, 90–105 (2015). https://doi.org/10.1016/j.jphotochemrev.2015.08.001
108. N. Kaeffer, J. Massin, C. Lebrun, O. Renault, M. Chavarot-Kerlidou, V. Artero, Covalent design for dye-sensitized H_2-evolving photocathodes based on a cobalt Diimine–Dioxime catalyst. J. Am. Chem. Soc. **138**, 12308–12311 (2016). https://doi.org/10.1021/jacs.6b05865

109. M.A. Gross, C.E. Creissen, K.L. Orchard, E. Reisner, Photoelectrochemical hydrogen production in water using a layer-by-layer assembly of a Ru dye and Ni catalyst on NiO. Chem. Sci. **7**, 5537–5546 (2016). https://doi.org/10.1039/C6SC00715E
110. Z. Ji, M. He, Z. Huang, U. Ozkan, Y. Wu, Photostable p-type dye-sensitized Photoelectrochemical cells for water reduction. J. Am. Chem. Soc. **135**, 11696–11699 (2013). https://doi.org/10.1021/ja404525e
111. L. Li, L. Duan, F. Wen, C. Li, M. Wang, A. Hagfeldt, et al., Visible light driven hydrogen production from a photo-active cathode based on a molecular catalyst and organic dye-sensitized p-type nanostructured NiO. Chem. Commun. **48**, 988–990 (2012). https://doi.org/10.1039/C2CC16101J
112. S. Lyu, J. Massin, M. Pavone, A.B. Muñoz-García, C. Labrugère, T. Toupance, et al., H_2-evolving dye-sensitized photocathode based on a ruthenium–Diacetylide/Cobaloxime supramolecular assembly. ACS Appl. Energy Mater. **2**, 4971–4980 (2019). https://doi.org/10.1021/acsaem.9b00652
113. C.J. Wood, G.H. Summers, C.A. Clark, N. Kaeffer, M. Braeutigam, L.R. Carbone, et al., A comprehensive comparison of dye-sensitized NiO photocathodes for solar energy conversion. Phys. Chem. Chem. Phys. **18**, 10727–10738 (2016). https://doi.org/10.1039/C5CP05326A
114. E.A. Gibson, M. Awais, D. Dini, D.P. Dowling, M.T. Pryce, J.G. Vos, et al., Dye sensitised solar cells with nickel oxide photocathodes prepared via scalable microwave sintering. Phys. Chem. Chem. Phys. **15**, 2411–2420 (2013). https://doi.org/10.1039/C2CP43592F
115. D. Dini, Y. Halpin, J.G. Vos, E.A. Gibson, The influence of the preparation method of NiOx photocathodes on the efficiency of p-type dye-sensitized solar cells. Coord. Chem. Rev. **304–305**, 179–201 (2015). https://doi.org/10.1016/j.ccr.2015.03.020
116. C.E. Creissen, J. Warnan, E. Reisner, Solar H_2 generation in water with a $CuCrO_2$ photocathode modified with an organic dye and molecular Ni catalyst. Chem. Sci. **9**, 1439–1447 (2018). https://doi.org/10.1039/C7SC04476C
117. H. Kumagai, G. Sahara, K. Maeda, M. Higashi, R. Abe, O. Ishitani, Hybrid photocathode consisting of a $CuGaO_2$ p-type semiconductor and a Ru(ii)–Re(i) supramolecular photocatalyst: Non-biased visible-light-driven CO_2 reduction with water oxidation. Chem. Sci. **8**, 4242–4249 (2017). https://doi.org/10.1039/C7SC00940B
118. C.E. Creissen, J. Warnan, D. Antón-García, Y. Farré, F. Odobel, E. Reisner, Inverse opal $CuCrO_2$ photocathodes for H_2 production using organic dyes and a molecular Ni catalyst. ACS Catal. **9**, 9530–9538 (2019). https://doi.org/10.1021/acscatal.9b02984
119. H. Zhang, Z. Yang, W. Yu, H. Wang, W. Ma, X. Zong, et al., A Sandwich-like Organolead halide perovskite photocathode for efficient and durable Photoelectrochemical hydrogen evolution in water. Adv. Energy Mater. **8**, 1800795 (2018). https://doi.org/10.1002/aenm.201800795
120. J.-H. Kim, S. Seo, J.-H. Lee, H. Choi, S. Kim, G. Piao, et al., Efficient and stable perovskite-based photocathode for Photoelectrochemical hydrogen production. Adv. Funct. Mater. **31**, 2008277 (2021). https://doi.org/10.1002/adfm.202008277
121. I.S. Kim, M.J. Pellin, A.B.F. Martinson, Acid-compatible halide perovskite photocathodes utilizing atomic layer deposited TiO_2 for solar-driven hydrogen evolution. ACS Energy Lett. **4**, 293–298 (2019). https://doi.org/10.1021/acsenergylett.8b01661
122. P. Da, M. Cha, L. Sun, Y. Wu, Z.-S. Wang, G. Zheng, High-performance perovskite Photoanode enabled by Ni passivation and catalysis. Nano Lett. **15**, 3452–3457 (2015). https://doi.org/10.1021/acs.nanolett.5b00788
123. M.T. Hoang, N.D. Pham, J.H. Han, J.M. Gardner, I. Oh, Integrated Photoelectrolysis of water implemented on organic metal halide perovskite Photoelectrode. ACS Appl. Mater. Interfaces **8**, 11904–11909 (2016). https://doi.org/10.1021/acsami.6b03478
124. C. Wang, S. Yang, X. Chen, T. Wen, H.G. Yang, Surface-functionalized perovskite films for stable photoelectrochemical water splitting. J. Mater. Chem. A **5**, 910–913 (2017). https://doi.org/10.1039/C6TA08812K

125. L.-F. Gao, W.-J. Luo, Y.-F. Yao, Z.-G. Zou, An all-inorganic lead halide perovskite-based photocathode for stable water reduction. Chem. Commun. **54**, 11459–11462 (2018). https://doi.org/10.1039/C8CC06952B
126. K. Zhang, M. Ma, P. Li, D.H. Wang, J.H. Park, Water splitting Progress in tandem devices: Moving photolysis beyond electrolysis. Adv. Energy Mater. **6**, 1600602 (2016). https://doi.org/10.1002/aenm.201600602
127. M.S. Prévot, K. Sivula, Photoelectrochemical tandem cells for solar water splitting. J. Phys. Chem. C **117**, 17879–17893 (2013). https://doi.org/10.1021/jp405291g
128. P. Dias, M. Schreier, S.D. Tilley, J. Luo, J. Azevedo, L. Andrade, et al., Transparent cuprous oxide photocathode enabling a stacked tandem cell for unbiased water splitting. Adv. Energy Mater. **5**, 1501537 (2015). https://doi.org/10.1002/aenm.201501537
129. Y. Chen, X. Feng, Y. Liu, X. Guan, C. Burda, L. Guo, Metal oxide-based tandem cells for self-biased Photoelectrochemical water splitting. ACS Energy Lett. **5**, 844–866 (2020). https://doi.org/10.1021/acsenergylett.9b02620
130. Y. Piekner, H. Dotan, A. Tsyganok, K.D. Malviya, D.A. Grave, O. Kfir, et al., Implementing strong interference in ultrathin film top absorbers for tandem solar cells. ACS Photonics **5**, 5068–5078 (2018). https://doi.org/10.1021/acsphotonics.8b01384
131. A. Vilanova, T. Lopes, C. Spenke, M. Wullenkord, A. Mendes, Optimized photoelectrochemical tandem cell for solar water splitting. Energy Storage Mater. **13**, 175–188 (2018). https://doi.org/10.1016/j.ensm.2017.12.017
132. L. Pan, J.H. Kim, M.T. Mayer, M.-K. Son, A. Ummadisingu, J.S. Lee, et al., Boosting the performance of Cu_2O photocathodes for unassisted solar water splitting devices. Nat. Catal. **1**, 412–420 (2018). https://doi.org/10.1038/s41929-018-0077-6
133. S.K. Karuturi, H. Shen, A. Sharma, F.J. Beck, P. Varadhan, T. Duong, et al., Over 17% efficiency stand-alone solar water splitting enabled by perovskite-silicon tandem absorbers. Adv. Energy Mater. **10**, 2000772 (2020). https://doi.org/10.1002/aenm.202000772

One-Step Solid-State Mechanochemical Synthesis of Metal Chalcogenides as a Perspecitve Alternative to Traditional Preparation Routes

Matej Baláž, Martin Stahorský, Peter Baláž, Erika Dutková, and Marcela Achimovičová

Abbreviations

CFTS	Copper iron tin sulfide
CTS	Copper tin sulfide
CZTS	Copper zinc tin sulfide
ED	Electron diffraction
EDS	Energy-dispersive X-ray spectroscopy
ESM	Eccentric vibratory mill
FFT	Fast Fourier transform
HRTEM	High-resolution transmission electron microscopy
ICDD-PDF	International Centre for Diffraction Data–Powder Diffraction File
INCOME	International Conference on Mechanochemistry
IUPAC	International Union of Pure and Applied Chemistry
JCPDS	Joint Committee on Powder Diffraction Standards
SAED	Selected area electron diffraction
S_{BET}	Brunauer-Emmett-Teller specific surface area
SEM	Scanning electron microscopy
TEM	Transmission electron microscopy
UV-Vis	Ultraviolet-visible
XRD	X-ray diffraction

M. Baláž (✉) · M. Stahorský · P. Baláž · E. Dutková · M. Achimovičová
Institute of Geotechnics, Slovak Academy of Sciences, Košice, Slovakia
e-mail: balazm@saske.sk

F. I. Ezema et al. (eds.), *Chemically Deposited Metal Chalcogenide-based Carbon Composites for Versatile Applications*, https://doi.org/10.1007/978-3-031-23401-9_12

1 Introduction to Mechanochemistry

Mechanochemistry is defined as a branch of chemistry that is concerned with chemical and physicochemical changes of substances of all states of aggregation due to the influence of mechanical energy [1]. According to the International Union of Pure and Applied Chemistry (IUPAC), which also recognizes it, a mechanochemical reaction is a chemical reaction that is induced by the direct absorption of mechanical energy [2]. In simple words, it is an alternative method to the traditional solution-based chemistry due to the availability to perform chemical reactions completely in solid state in the absence of toxic solvents and external elevation of temperature and pressure. It was defined as a separate research field at the beginning of twentieth century [3] and has been proven to be applicable in distinct research areas since then, as it is demonstrated in Fig. 1. Its applicability is mostly in chemistry, materials science, and environmental sciences.

1.1 High-Energy Milling

High-energy milling is a tool to perform mechanochemical reactions. Apart from conventional ball milling that delivers only limited amount of energy mainly to reduce the particle size of the treated material, additional effects like mechanical activation and defect formation are observed by applying high-energy mills. Conventional ball milling also most often does not lead to the occurrence of chemical reaction. Today, there is a number of high-energy ball mills that efficiently deliver the energy to the treated powders (examples are shown in Fig. 2). For less energy-demanding reactions like organic ones, mixer or shaker mills are usually employed (Fig. 2b). The effect of milling is achieved by an intensive shaking from one side to the other, and the milling chambers usually have the cylindrical shape with a

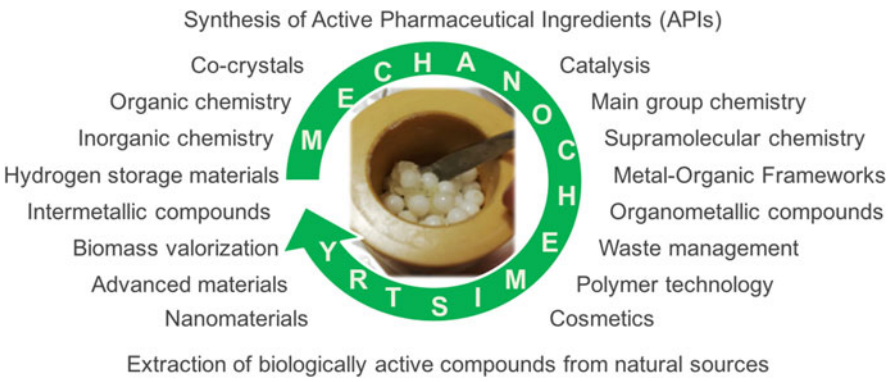

Fig. 1 Diverse applications of mechanochemistry [4]

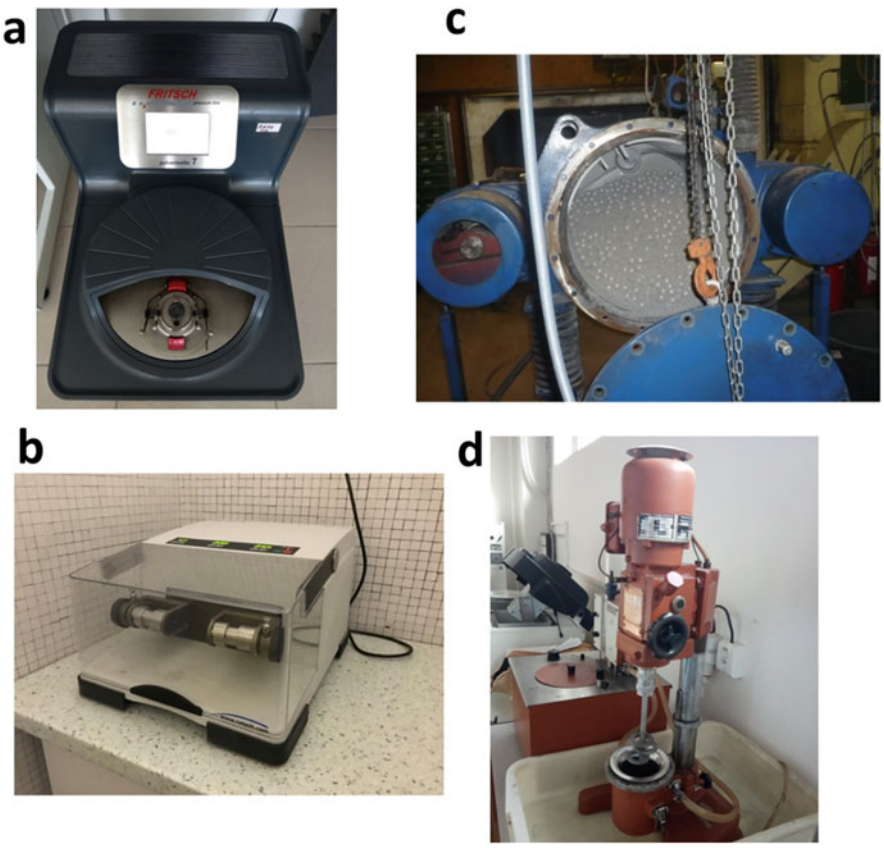

Fig. 2 Examples of high-energy mills used for mechanochemical processes: (**a**) planetary ball mill, (**b**) electric shaker mill, (**c**) eccentric vibratory mill, (**d**) attrition mill. (Adapted from Springer Nature Customer Service Centre GmbH: Springer Nature [5] [COPYRIGHT] (2021))

volume of up to 20 mL. However, to perform more energy-demanding inorganic synthesis, the planetary ball mills where the milling chamber is located on the disc and is being intensively rotated to the one side, while the disc is being rotated to the other one, are being used (Fig. 2a). The volumes of the chambers used in the planetary ball mills are usually up to 500 mL. Shaker/mixer and planetary mills are exhaustively applied for the lab-scale experiments, but they are not suitable for implementation on a larger scale. In order to scale up mechanochemical reactions, eccentric vibratory (Fig. 2c) or attrition mills (Fig. 2d) can be applied.

There are plenty of experimental conditions that can be changed when performing the high-energy milling treatment. The most common ones are presented in Fig. 3. Depending on the treated material, different conditions might be suitable. One of the greatest challenges in mechanochemistry is the abrasion of milling media, which contaminates the product. This problem can be overcome, or at least

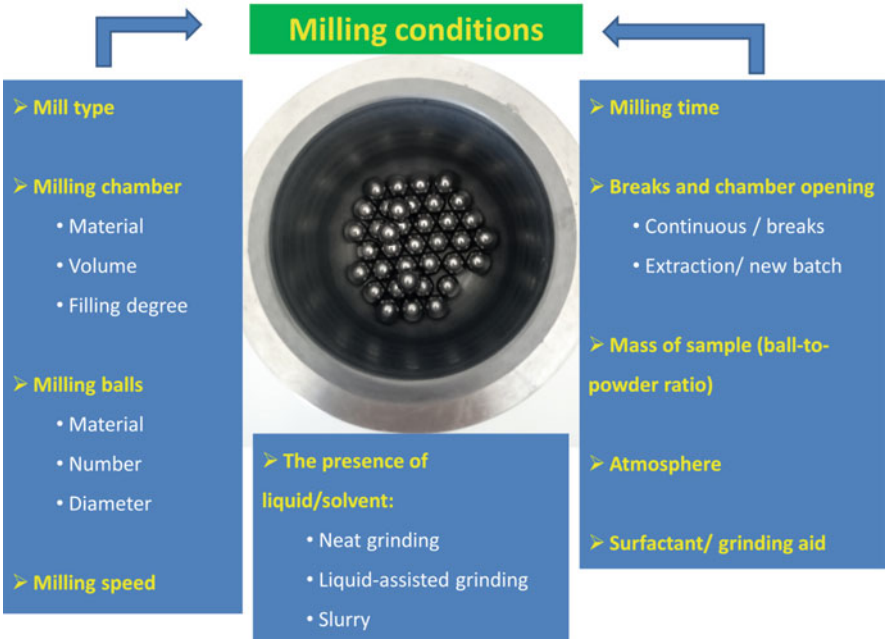

Fig. 3 Most commonly changed experimental conditions during high-energy milling. (Reprinted by permission from Springer Nature Customer Service Centre GmbH: Springer Nature [5] [COPYRIGHT] (2021))

significantly reduced, by changing the conditions like the material of milling media, revolution speed, or using the grinding aids.

The high-energy milling treatment of the powders can lead to two scenarios. Either just physicochemical characteristics of the treated solids (such as particle size or specific surface area) are changed, however, no clear chemical change is observed. In this case, the process can be defined as mechanical activation. On the other hand, when a clear chemical change occurs, we are talking about mechanochemical reaction. To illustrate this difference, Fig. 4 is shown. The two processes can take place in one system, and mechanical activation of the reactants is often necessary before they undergo the mechanochemical reaction.

In most research groups working with mechanochemistry around the world, it is being tested as an alternative to the procedures that are already established there (as an example, performing organic reactions via the traditional solution-based methods versus mechanochemical one can be mentioned). However, the authors of this chapter are part of the department, where mechanochemistry is the main research focus and the high-energy milling is being applied for the processing of a wide variety of materials (Fig. 5).

As it can be seen, one of the main research directions is the mechanochemical synthesis of chalcogenides. This has been a permanent agenda at the Department as manifested in the reviews [7, 8] and monographs from the years 2000–2021

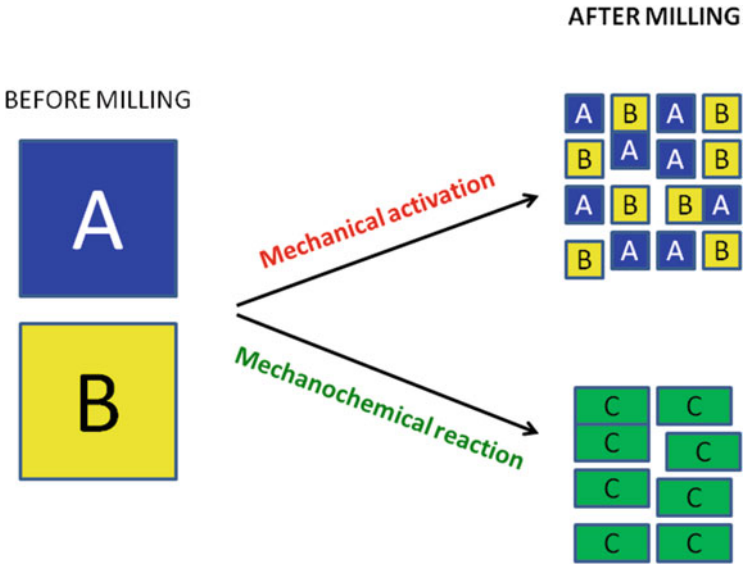

Fig. 4 Schematic illustration showing the difference between mechanical activation and mechanochemical reaction (A, B- reactants, C- product of mechanochemical reaction). (Reprinted by permission from Springer Nature Customer Service Centre GmbH: Springer Nature [5] [COPYRIGHT] (2021))

published by the authors of this chapter [5, 9, 10]. In the present work, the overview of recent works of our research group from the year 2018 is provided. This is complemented by providing overview tables on the mechanochemical syntheses of chalcogenides by other research groups around the world. As the mechanochemical synthesis can also be performed in the scale-up fashion, the text is subdivided into a lab-scale and scalable synthesis. Further structuring is based on the chemical composition of chalcogenides, namely to binary, ternary, and quaternary ones.

2 Laboratory-Scale Mechanochemical Synthesis of Chalcogenides

The simplicity of mechanochemical synthesis of chalcogenides in comparison with other methods can be well demonstrated by the fact that just high-energy milling of the solid precursors is satisfactory to obtain nanocrystalline products [8]. Most often, two methodologies are applied; either the elements or compounds are used as precursors. The second option became preferred with time, as the obtained nanoparticles are usually smaller and thus more suitable for advanced applications, for example, as quantum dots. The principle of the two methodologies is demonstrated in the example of sulfides synthesis below (Fig. 6). The concept

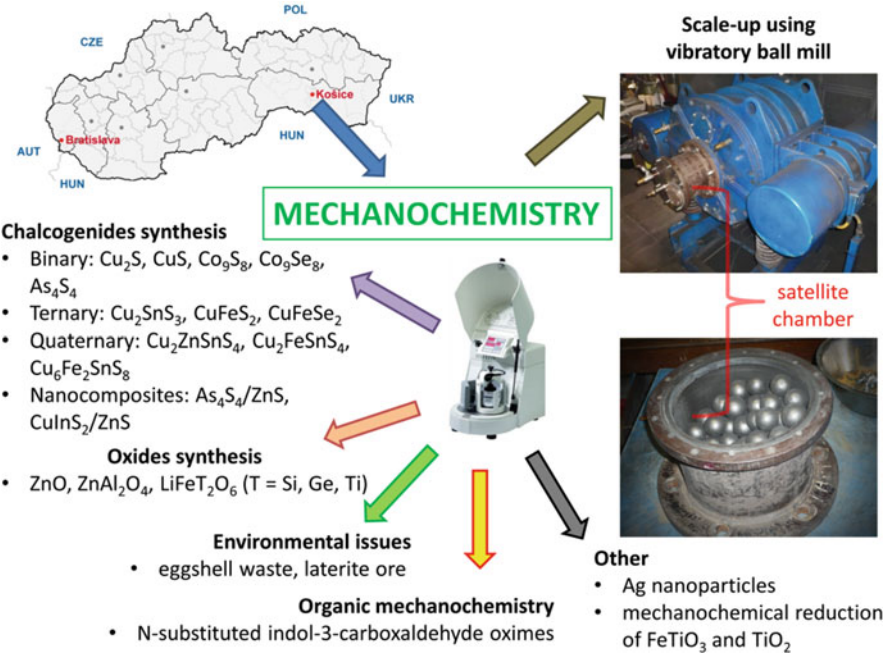

Fig. 5 Variety of research activities being performed at the Department of Mechanochemistry, Institute of Geotechnics, Slovak Academy of Sciences in Košice, Slovakia. (Reprinted from [6], Copyright (2020), with permission from Elsevier)

of using metal acetate and sodium sulfide as the precursor of metal and sulfur, respectively, has been introduced by the research group of the authors of this chapter already in [11]. This synthetic pathway is sometimes referred to as a wet one because sodium sulfide is used as nonahydrate and the resulting reaction mixture often resembles a slurry. As a side-product, sodium acetate, which can be easily washed out, is formed.

3 Binary Systems

3.1 Cobalt Pentlandite, Co_9S_8

Co_9S_8 nanoparticles from cobalt and sulfur in stoichiometric ratio in a planetary ball mill in an inert atmosphere were successfully prepared via mechanochemical synthesis in [12]. The cubic Co_9S_8 nanoparticles were nanocrystalline with crystallite size of about 16 nm, as confirmed by both Rietveld analysis and transmission electron microscopy. They consist of nanocrystals closely aggregated into spherical-like objects. The kinetics reaction studied by X-ray diffraction (XRD) is depicted

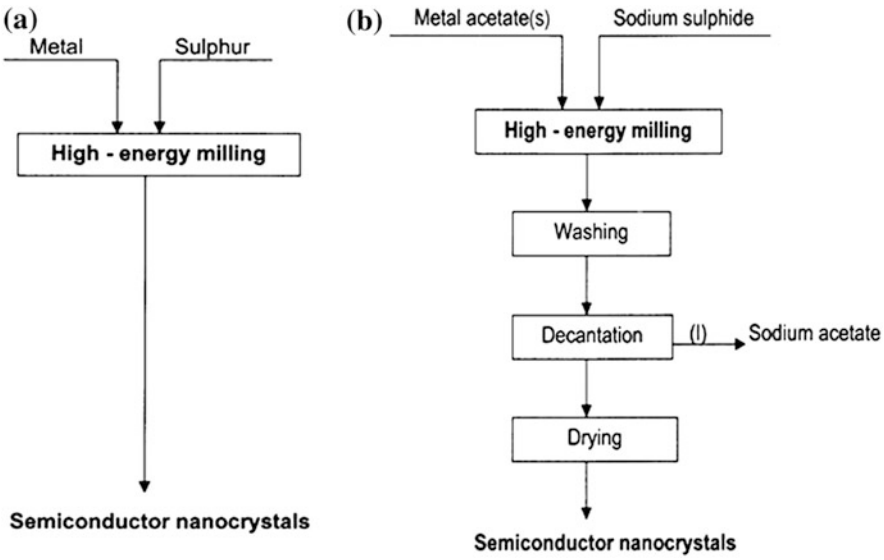

Fig. 6 Mechanochemical synthesis of sulfides using: (**a**) elemental precursors, (**b**) compounds (metal acetate and sodium sulfide). (Reprinted by permission from Springer Nature Customer Service Centre GmbH: Springer Nature [8] [COPYRIGHT] (2017))

in Fig. 7. The patterns were recorded after 60–180 min of milling. After the first 60 min, only small amounts of desired sulfide are visible next to the non-reacted cobalt and sulfur precursors. Another 60 min of milling was needed to obtain final product cobalt pentlandite Co_9S_8 (01-073-6395), which crystallized in the cubic face-centered structure. Further treatment until 180 min did not lead to any significant change in the phase composition.

The transition from paramagnetic to weak ferromagnetic or ferrimagnetic behavior by changing the magnetic field was proven by magnetic measurements (Fig. 8).

3.2 Copper Sulfides-Chalcocite Cu_2S and Covellite CuS

Copper sulfide is a semiconductor with multidisciplinary applications, the ones in biomedicine being of particular interest. In our older studies, we have shown the possibility to prepare this chalcogenide within a second range [13] and that despite the precursors are consumed, the phase transformations still go on for a couple of minutes [14]. The equilibrium was reached after 15 min and 30 min in the case of CuS and Cu_2S, respectively. The obtained products were properly characterized using a rich pallette of experimental techniques (SEM/EDS, FTIR, XPS, photoluminescence, nitrogen adsorption, thermal analysis) [15]. In addition, the optical properties by UV-vis spectroscopy were determined (Fig. 9). The optical bandgap of CuS (blue) and Cu_2S was calculated to be 1.92 eV and 3 eV, respectively. In the former case, a red shift in comparison with its bulk analogue was evidenced.

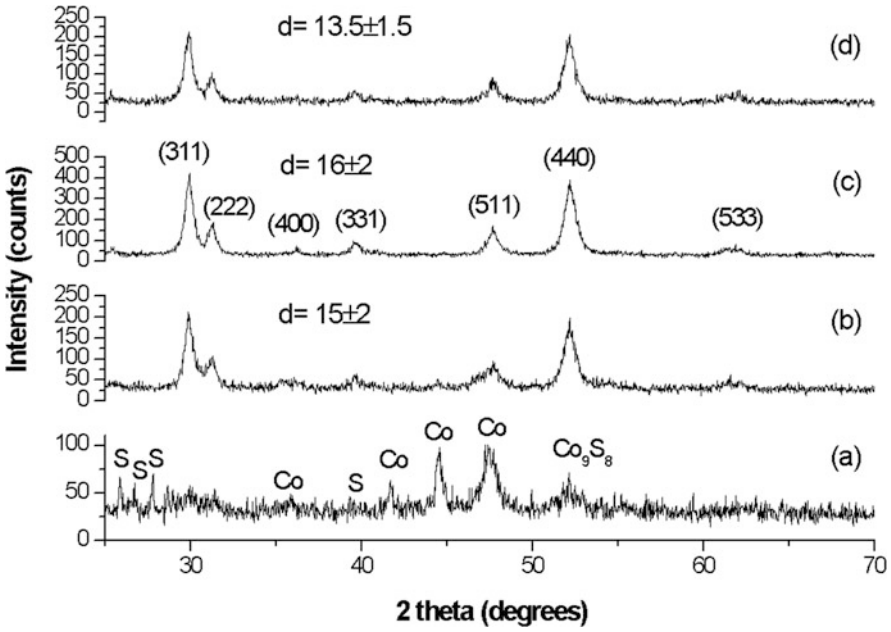

Fig. 7 XRD patterns of mechanochemically synthesized pentlandite Co_9S_8 after different milling time: (**a**) 60 min, (**b**) 90 min, (**c**) 120 min, and (**d**) 180 min. (Reprinted from [12], Copyright (2018), with permission from Elsevier)

The ability of both CuS and Cu_2S to photocatalytically degrade the methyl orange (MO) dye was tested, showing both materials being good photocatalysts. Better results were achieved using Cu_2S (Fig. 9b), as complete degradation of MO dye was observed within 150 min. Covellite (CuS) showed 80% MO degradation after the same duration. Interestingly, the results for the products were better than for the commercial TiO_2 (P25) or ZnO. It has to be noted that the adsorption stage was not considered in the experiments and all the decrease in the dye concentration was ascribed to the photocatalytic effect [15].

Mechanochemical synthesis of copper sulfide was also the main topic of the report [16], which was a common work with our Kazakh colleagues. The initial idea was to obtain copper sulfide/sulfur composite by combining the already explained acetate route (milling copper acetate and sodium sulfide) and simultaneously synthesize elemental sulfur (by using sodium thiosulphate as its source and citric acid as a catalyst). However, instead of obtaining CuS/S composite, the needle-like nanocrystals of CuS were obtained. This is of particular interest to mechanochemists, as the shape control is a large issue due to a constant supply of energy and stress to the milled solids, which hampers them from creating a well-crystallized structures. Simultaneously, the problem with synthesis of CuS using acetate route with the formation of oxidized products reported in the past, was also overcome by the proposed methodology. The whole paper is based on the comparison between CuS obtained using the traditional acetate route and the sample prepared by using also the additional sulfur source. The as-received CuS

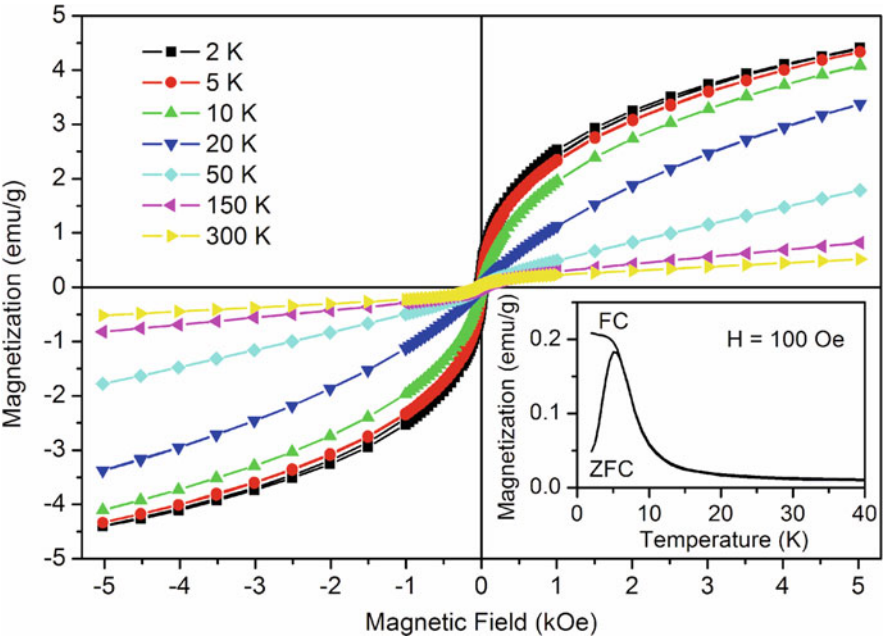

Fig. 8 Hysteresis loops measured at various temperatures and temperature dependence of magnetization (inset) of mechanochemically synthesized pentlandite Co_9S_8 after 120 min of milling. (Reprinted from [12], Copyright (2018), with permission from Elsevier)

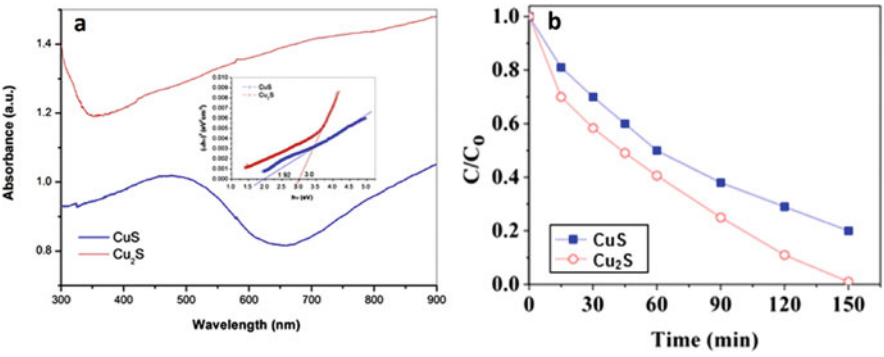

Fig. 9 (**a**) UV-vis absorption spectra (inset Tauc's plots) of CuS and Cu_2S products. (**b**) The irradiation time-dependent degradation efficiencies of MO solution in the presence of CuS and Cu_2S photocatalysts. (Reprinted from [15], Copyright (2018), with permission from Elsevier)

had a needle-like shape with a uniform thickness of around 6 nm length of up to 60 nm (aspect ratio 1:10), whereas the sample obtained using just copper acetate and sodium sulfide exhibited an isometric morphology with particle size around 20 nm. The formation of the specific morphology in the first case is most probably a result of the presence of elemental sulfur, which may in situ react with CuS by enhancing the S − S bonding and thus causing a preferential growth of CuS along

the basal planes. There was also a significant difference in the grain size (as very often when using the mechanochemical synthesis), the individual nanoparticles are assembled into larger grains, being significantly finer in the case of needle-like CuS, namely, the average grain size was around 340 nm for CuS prepared without using the additional sulfur source and 170 nm when using it. The obtained products were tested as antibacterial agents using the agar well diffusion method, and it was shown that the elongated CuS exhibited activity against both gram-negative *E. coli* and gram-positive *S. aureus*, whereas the other sample was active just against the gram-negative bacteria. The whole story of the paper is summarized in Fig. 10 below.

The mechanochemical synthesis of CuS was also the topic of the study [17]; however, the selected reaction was used just as a model to investigate the amount of iron wear by means of magnetometry. The CuS product was formed in 15 min (in this case, the reaction was much slower than in [13], because the atomized powder Cu with spherical morphology, neither electrolytically prepared Cu powder with needle-like one was used). The possibility to use the magnetization value to calculate the actual amount of iron (even if it is present in trace amounts) in powders treated in steel milling jars was proposed. The amount of iron has rapidly increased between 15 and 30 min of milling, when its content was 0.13 and 0.76%,

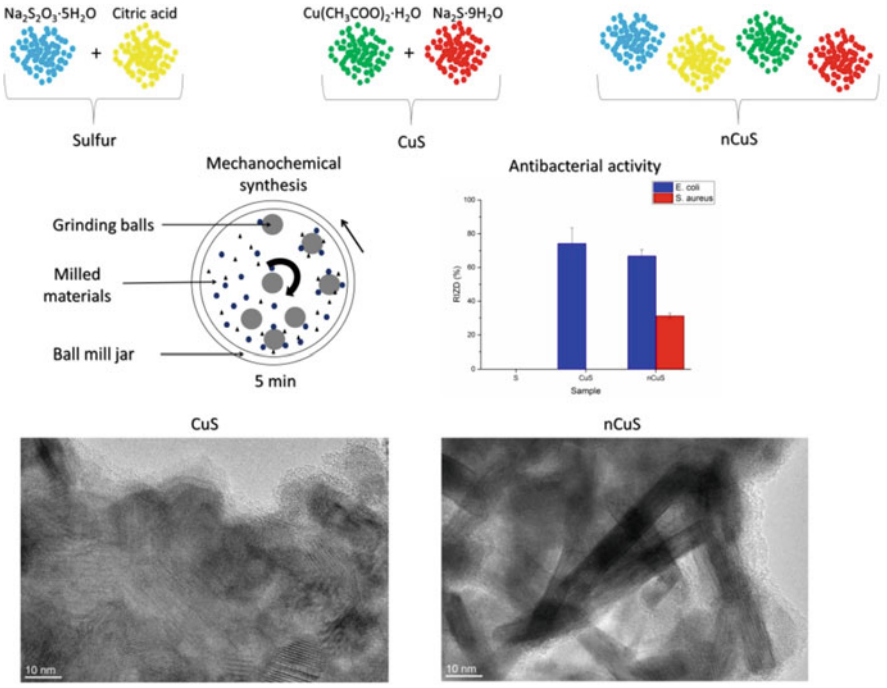

Fig. 10 Graphical abstract of the report [16] showing the possibility to prepare needle-like CuS nanocrystals using mechanochemical synthesis. (Reprinted with permission from [16]. Copyright 2019 American Chemical Society)

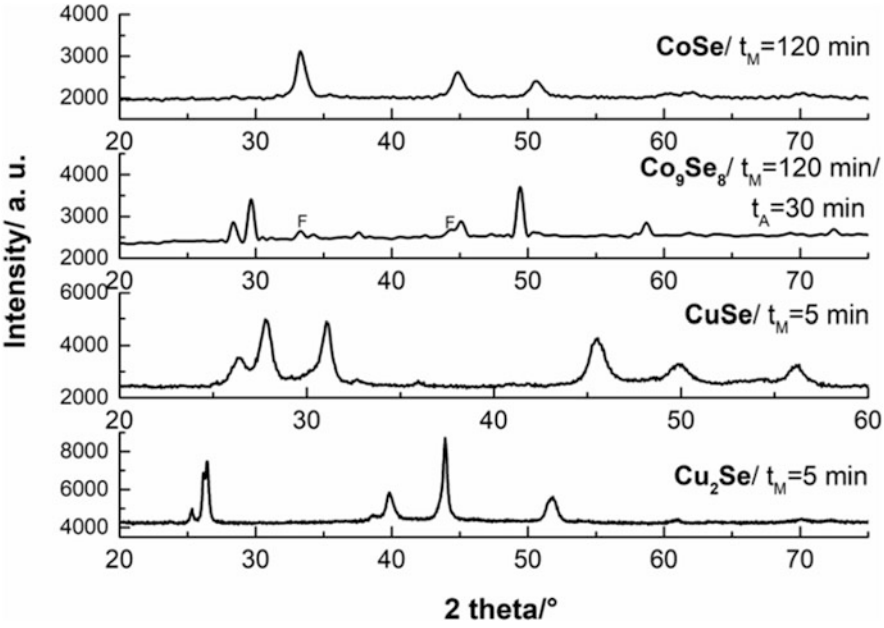

Fig. 11 X-ray diffraction patterns of synthesized cobalt and copper selenides; t_M: milling time, t_A: annealing time; F: freboldite-CoSe

respectively. This increase is ascribed to the fact that after 15 min, the reaction is finished and further energy input is used inefficiently.

3.3 Co, Cu-Transition-Metal Selenides

In our recent works, nanostructured CoSe, CuSe, and Cu_2Se semiconductors were successfully synthesized by simple, direct, and relatively inexpensive short-time solid-phase mechanochemical reactions in a high-energy planetary ball mill [18–20]. The synthetic Co_9Se_8 with the pentlandite structure, $(Fe,Ni)_9S_8$, was also prepared; however, in this case, also a short subsequent thermal annealing was necessary [21]. The X-ray diffraction patterns of the mechanochemically synthesized cobalt and copper selenides with the corresponding time of mechanochemical synthesis and subsequent thermal treatment, respectively, are shown in Fig. 11.

The diffraction peaks were identified based on the ICDD-PDF cards and correspond to CoSe (freboldite 01-077-7572), Co_9Se_8 (01-089-4180), CuSe (00-34-0171), and Cu_2Se (00-47-1448). Rietveld analyses confirmed that mechanochemical synthesis of CoSe is completed after 120 min of milling with an average crystallite size of 26 nm, and mechanochemical/thermal synthesis produced Co_9Se_8 nanoparticles with an average crystallite size of 67 nm. After 5 min of milling, CuSe and

Cu_2Se nanoparticles with an average crystallite size of 24 and 25 nm, respectively, were obtained.

TEM/HRTEM images of the agglomerated nanoparticles of prepared Co and Cu-containing transition metal selenides are shown in Fig. 12 and Fig. 13. The larger clusters composed of nanoparticles with tens of nanometer in size were observed in both cases. Within the single agglomerate of Co_9Se_8, the crystallites are in close contact, separated by distinct grain boundaries, almost like in sintered ceramics (see Fig. 12b)).

By comparing our mechanochemical synthesis results with the literature, only Campos and co-authors managed to prepare CoSe in more than 72 h by milling in a SPEX shaker mill [22], Co_9Se_8 has not been mechanochemically synthesized yet. With regard to copper selenides, Ohtani and co-authors were the only researchers who synthesized γ-CuSe by mechanical alloying for 60 min using a high-energy ball mill [23]. In 2017, Bulat with co-workers produced a single-phase material containing the α-Cu_2Se phase after 2 h of milling in a high-energy ball mill [24] and in 2018, Li and co-workers synthesized almost single-phase β-$Cu_{2-x}Se$ after 20 min of milling in a vibratory mill [25].

The overview table showing the precursors, necessary milling time, achieved particle size, and the application of the binary chalcogenides prepared recently by other research groups is shown below in Table 1.

4 Ternary Systems

4.1 Chalcopyrite, $CuFeS_2$

One of the most interesting chalcogenides in ternary systems is chalcopyrite $CuFeS_2$. The rapid mechanochemical synthesis of $CuFeS_2$ particles with good magnetic, optical, and electro-optical properties prepared by high-energy milling in a planetary mill from copper, iron, and sulfur precursors was firstly investigated by our research group [54]. The progress of the mechanochemical synthesis was studied by XRD (Fig. 14). Nanocrystalline $CuFeS_2$ with a tetragonal body-centered crystal structure and crystallite size around 38 nm could be prepared within 60 min of milling. No significant change, either in the lattice parameters or in the microstrain, was observed after prolonged milling until 120 min.

This mineral has been considered as a potential thermoelectric material due to the abundance of the constituting elements, as well as its environmental friendliness. Nanophase and defect formation via milling is a possible route to decrease the fairly high thermal conductivity by increasing phonon scattering. In this respect, mechanochemical pretreatment by high-energy milling in $CuFeS_2$ synthesis is an innovative procedure. Recently, a couple of papers to elucidate the thermoelectric properties of mechanochemically treated chalcopyrite have been published [55–57]. The influence of high-energy milling on structure as well as on the semiconducting

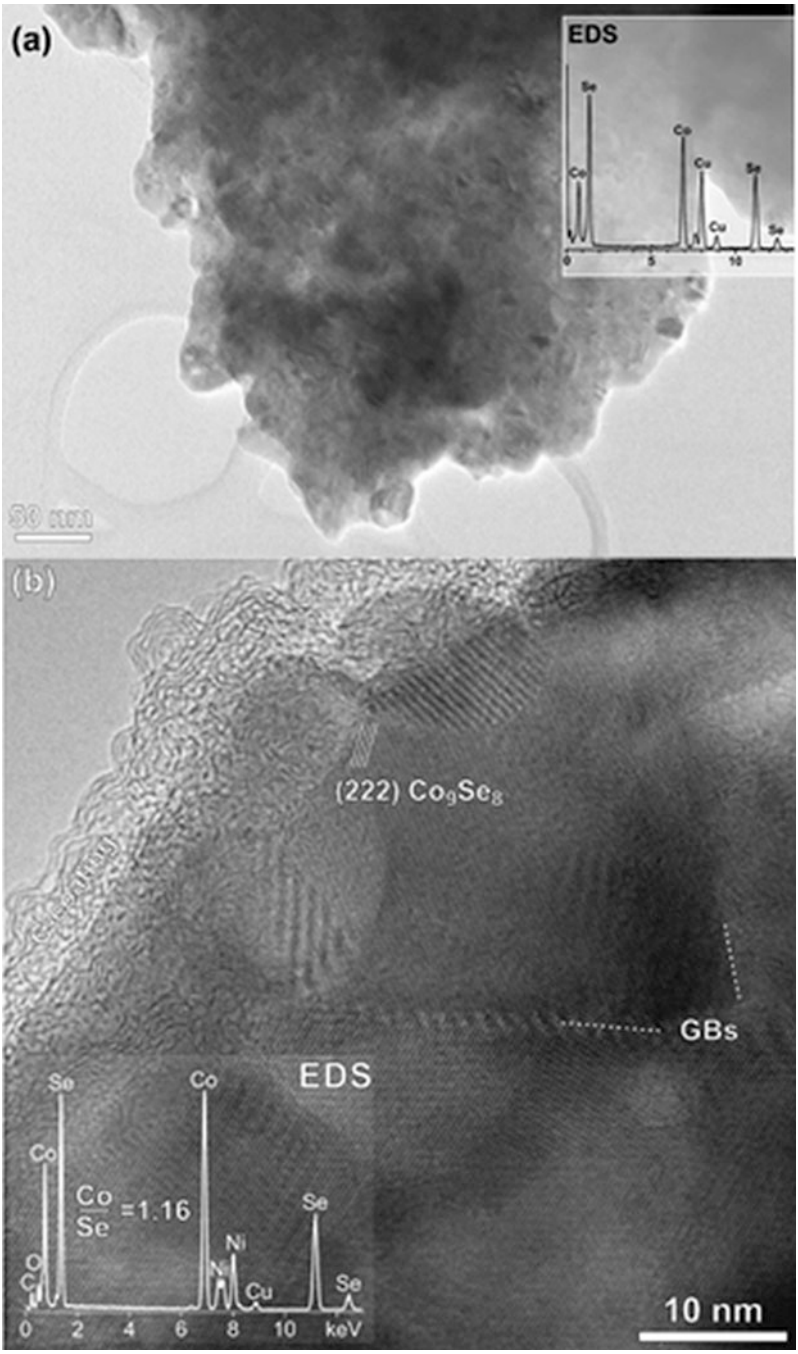

Fig. 12 (**a**) TEM image of an agglomerated cluster of CoSe nanoparticles with a typical EDS spectrum (inset). The Cu peaks stem from the copper TEM-grid. Reprinted by permission from Springer Nature Customer Service Centre GmbH: Springer Nature [20] [COPYRIGHT] (2017); (**b**) HRTEM image from the thin part of the agglomerate shows larger Co_9Se_8 crystallites in close contact (GBs = grain boundaries). EDS analysis from this region yielded Co/Se ratio of 1.16, which is close to 9:8 as expected. Reprinted by permission from Springer Nature Customer Service Centre GmbH: Springer Nature [21] [COPYRIGHT] (2019)

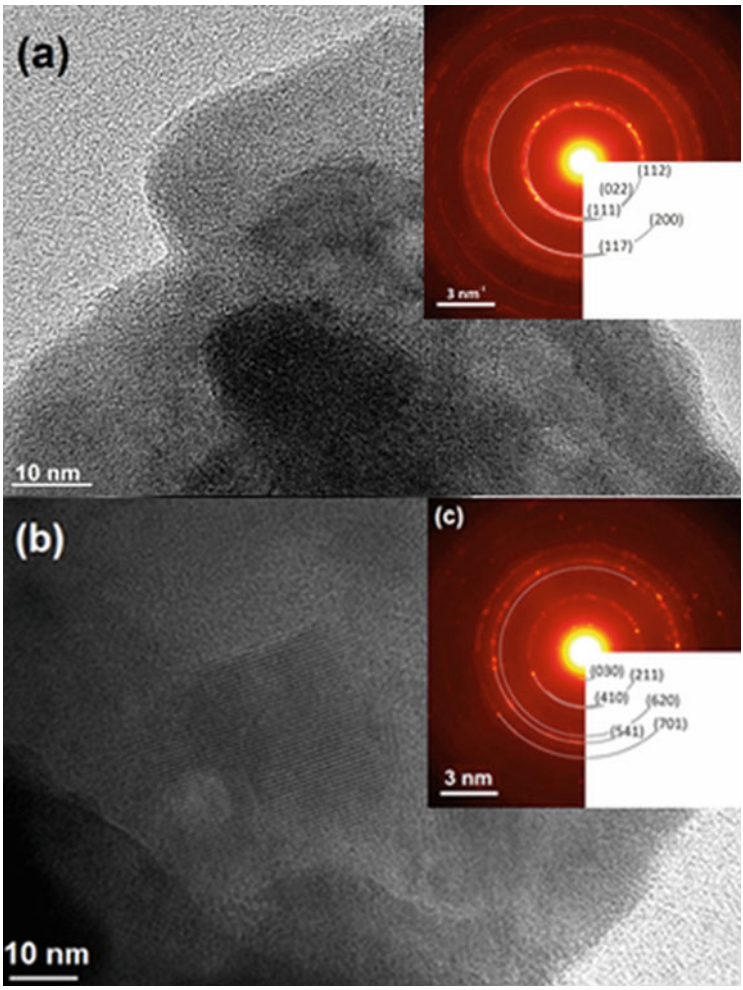

Fig. 13 (**a**) HRTEM image of agglomerated crystals of CuSe with selected area electron diffraction (SAED) pattern (inset); (**b**) TEM image of agglomerated Cu_2Se crystals; (**c**) SAED pattern of the same crystals. (Reprinted by permission from Springer Nature Customer Service Centre GmbH: Springer Nature [19] [COPYRIGHT] (2021))

properties was studied. While dependence of specific surface area S_{BET} and crystallinity X is already known and tested for several sulfides [10] (Fig. 15 left), a possibility to influence of bandgap is a totally new agenda. In Fig. 15 (right), the dependence of bandgap value on milling time is shown, which illustrates a possibility to manipulate with semiconducting properties (bandgap engineering) of chalcopyrite.

The progress of chalcopyrite synthesis from elements can be also investigated via observing the magnetization changes. This has been accomplished in the study [58].

Table 1 Overview of binary chalcogenides including selected mechanochemical conditions, obtained crystallite size, and application prepared by other research groups since 2018

Product	Precursors	Milling time	Particle size	Application	References
Sulfides					
CuS	CuO and S	22 min	–	Recovery treatment	[26]
CuSC, CuS-S-C, CuS-S	C (activated), S, and CuS	13 h	10–20 nm	Batteries	[27]
Cu_2S	$CuCl_2$, benzene-1,3,5-tricarboxaldehyde and 2,5-diaminobenzene sulfonic acid	45 min	40–70 nm	Catalyst	[28]
$Fe_{1-X}S$ (x = 0–0.2)	$FeCl_3$ and four different sulfur sources: $Na_2S•9H_2O$, CH_3CSNH_2, $Na_2S_2O_3$ and NH_2CSNH_2	2 h	10–20 nm	Catalyst	[29]
FeS_x (x = 1, 2)	Fe, S, $Li_2S·P_2S_5$	10 h and 30 h	1–3 μm	Batteries	[30]
$FeS_{1.92}$	Mackinawite (FeS) and S	3 h	Micron scale	Organic waste remediation and catalyst	[31]
Fe_9S_8	Fe and S	2 h	9–15 nm	Catalyst	[32]
Ga_2S_3	Ga and S	4 h	42–420 nm	–	[33]
MoS_3	MoS_2 and S	10 h	Micron scale	Batteries	[34]
$NiS_{1.03}$, NiS_2 and Ni_3S_2	Ni and S	1–8 h	10–20 nm	–	[35]
Ni_9S_8	Ni and S	2 h	9–15 nm	Catalyst	[32]
NiS-C	$NiCl_2$ and NH_2CSNH_2	3 h	20–50 nm	Catalyst	[36]
PbS	PbO and Na_2S	1 h	11–24 nm	–	[37]
RuS-C	$RuCl_3$ and NH_2CSNH_2	3 h	20–50 nm	Catalyst	[36]
SnS	$C_6H_{15}NO_3$, $SnCl_2·2H_2O$, C_2H_5NS and NH_3	1–3 h	20–100 nm	–	[38]

(continued)

Table 1 (continued)

Product	Precursors	Milling time	Particle size	Application	References
	Sn and S	2 h	10–13 nm	Batteries	[39]
	Sn and S	5 h	15 nm	Solar cells	[40]
ZnS	Zn and S	30 to 45 min	–	–	[41]
	Zn, S, and Mn	90 min	5–20 nm	–	[42]
	$Zn(OAc)_2 \cdot 2H_2O$, $Na_2S \cdot 9H_2O$ and sodium dodecyl benzene sulfonate	40 min	1–8 nm	–	[43]
	Zn and S	14–16 h	200 nm	–	[44]
	$ZnCl_2$, $AcCl_3$ and Na_2S	16 h	4–18 nm	Diodes	[45]
Selenides					
CdSe	Cadmium acetate, $FeCl_3.6H_2O$ and Na_2O_3Se	35 min	100–150 nm	–	[46]
$Cu_{2-x}Se$ ($0.03 \leq x \leq 0.23$)	Cu and Se	2 h	–	–	[47]
$Cu_{2-x}Se$	Cu and Se	5–60 min	–		[25]
Sb_2Se_3	Sb and Se	12 h	5–15 nm	Batteries	[48]
Tellurides					
NiTe, $NiTe_2$ and Ni_2Te_3	Ni and Te	1–12 h	10–20 nm	–	[49]
Ni_3Te_2	Ni and Te	3–20 h	4–10 nm	Sensors	[50]
$P_{0.8}Te_{0.2}$	P (red) and Te	0–80 h	–	–	[51]
$Pr_{3-x}Te_4$ ($x = 0 - 0.33$)	Pr and Te (shot)	10 h	43–61 nm	Thermoelectrics	[52]
Sc_2Te_3	Sc and Te (shot)	10 h	Micron scale	Thermoelectrics	[53]

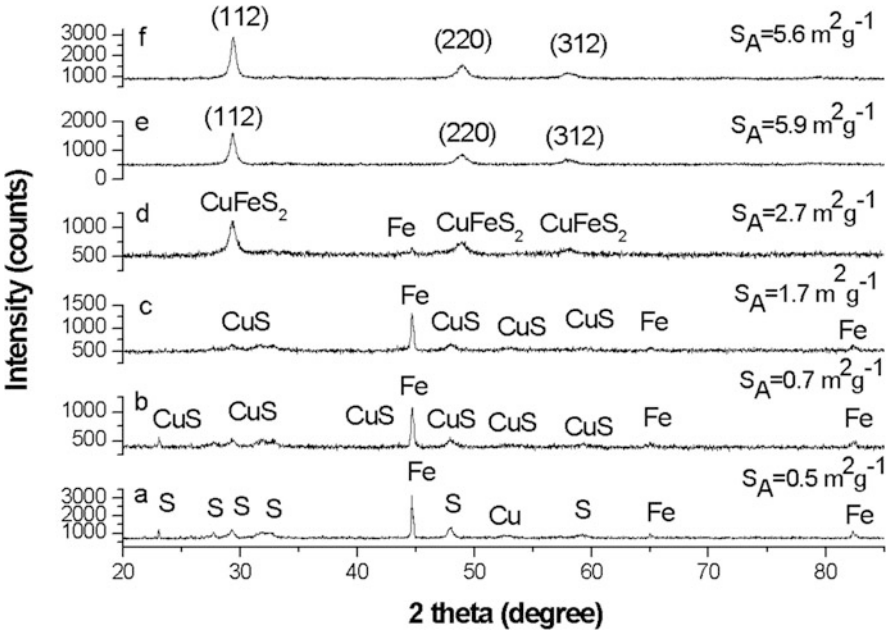

Fig. 14 XRD patterns of Cu-Fe-S powders before milling (**a**) and after 5 min (**b**), 15 min (**c**), 30 min (**d**), 60 min (**e**), and 120 min (**f**) of milling (the lines labelled by their Miller indexes alone belong to $CuFeS_2$ nanoparticles). (Reprinted with permission from Ref. [54]. Copyright 2018, Elsevier)

Namely, at the beginning, the magnetism is very high due to the presence of highly magnetic elemental iron. As it becomes incorporated into chalcopyrite structure, the magnetization value decreases rapidly (from around 65 Am^2/kg to around 2 Am^2/kg upon 120 min of milling).

4.2 Copper Antimony Sulfides-:Chalcostibite, $CuSbS_2$ and Famatinite, Cu_3SbS_4

$CuSbS_2$ nanocrystals were mechanochemically prepared in an argon atmosphere after only 30 min of milling in a laboratory planetary mill [59]. The progress of mechanochemical synthesis is illustrated in Fig. 16 by means of XRD. The analysis validated the formation of orthorhombic structure of $CuSbS_2$ with crystallite size around 25 nm determined by LeBail refinement. UV-vis spectrum revealed absorption of $CuSbS_2$ nanocrystals in the entire visible range with the determined optical bandgap 1.54 eV.

The formation of nanocrystalline chalcostibite $CuSbS_2$ was also validated by transmission electron microscopy (Fig. 17). The sample consists of small nanocrys-

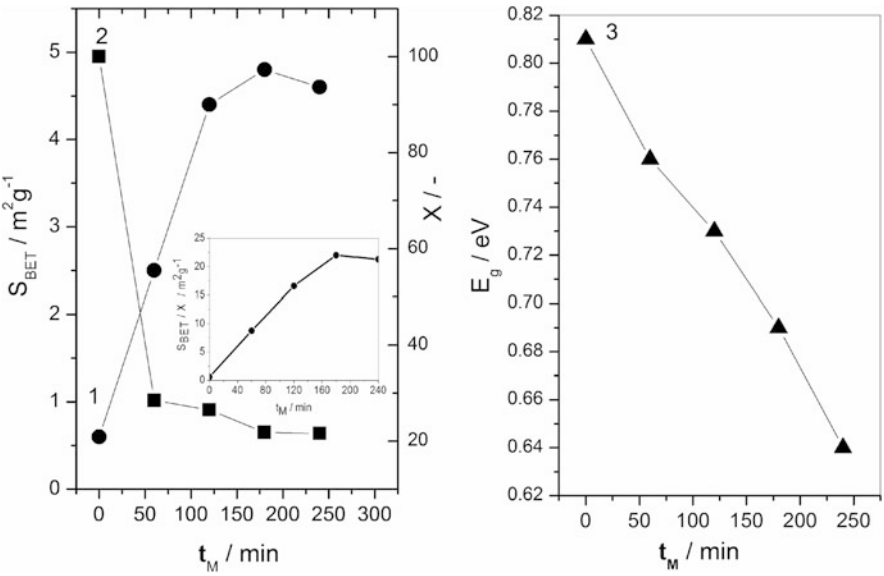

Fig. 15 The influence of milling time, t_M on specific surface area, S_{BET} (1), crystallinity, X (2) and bandgap, E_g (3) for chalcopyrite $CuFeS_2$. (Reprinted with permission from Ref. [57]. Copyright 2018, Elsevier)

talline domains, which aggregate giving rise to larger particles as can be observed in the TEM image (Fig. 17a). All the SAED rings (Fig. 17a (inset) could be indexed in the orthorhombic symmetry of the $CuSbS_2$, thus being in accordance with the XRD results (Fig. 16). HRTEM images (Fig. 17c, d) indicate nanocrystals directed along two distinct zone axes.

In addition to chalcostibite, $CuSbS_2$, also famatinite Cu_3SbS_4 was mechanochemically synthesized using copper, antimony, and sulfur in a stoichiometric ratio 3:1:4 in a planetary ball mill with the utilization of protective atmosphere without the next post-heating [60]. The progress of the mechanochemical synthesis of Cu_3SbS_4 for milling times 60–120 min is illustrated in Fig. 18.

The mechanochemical reaction was completed after 120 min of milling, when no other phases could be detected in the XRD pattern, indicating the high purity of the product. The crystallite size 14 nm of the prepared tetragonal famatinite was calculated by LeBail refinement.

The optical properties of Cu_3SbS_4 were studied using UV-vis spectroscopy (Fig. 19). The Tauc plot to deduce the direct bandgap from derived UV-vis spectrum is shown as an inset of Fig. 19. The determined direct optical bandgap 1.31 eV is blue-shifted relatively to the bulk Cu_3SbS_4. The observed blue shift could be attributed to the existence of very small nanocrystallites.

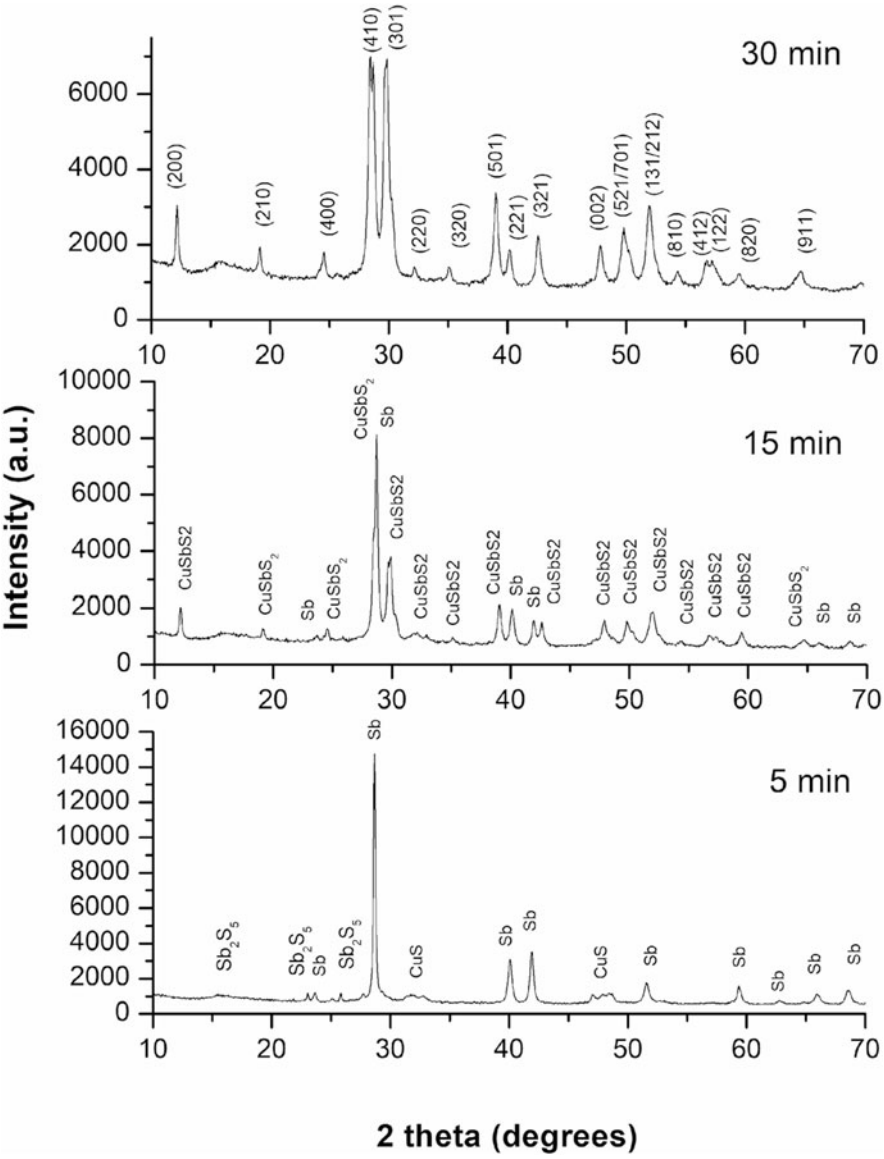

Fig. 16 XRD patterns of $CuSbS_2$ synthesized for different milling times (the Miller indices in the upper-most pattern belong to $CuSbS_2$ nanoparticles). (Reprinted by permission from Springer Nature Customer Service Centre GmbH: Springer Nature [59] [COPYRIGHT] (2021))

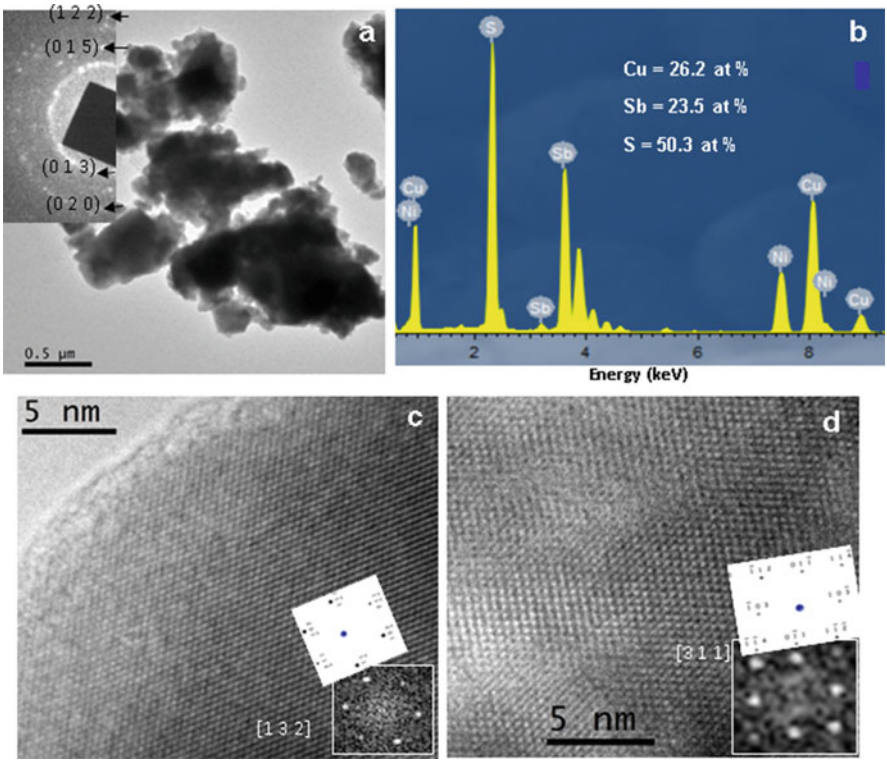

Fig. 17 TEM analysis of mechanochemically synthesized $CuSbS_2$: TEM image at low magnification with indexed SAED pattern (inset) (**a**), EDS spectrum (**b**), HRTEM images and the corresponding FFTs and simulated ED patterns (inset) (**c**, **d**). (Reprinted by permission from Springer Nature Customer Service Centre GmbH: Springer Nature [59] [COPYRIGHT] (2021))

4.3 Copper Tin Sulfide Mohite, Cu_2SnS_3

By means of mechanochemical synthesis, we managed to prepare Cu_2SnS_3 (mohite) phase in 15 min using planetary ball milling starting from elements [61]. The XRD patterns measured after 15 s, 5, 10, 15, and 30 min are shown in Fig. 20a. Already after a few seconds, the elemental Cu and S rapidly reacted to form CuS (already after 15 s, the diffractions of CuS are visible). The exothermic reaction of CuS formation is in line with the phenomena described in [13] and was corroborated by a significant increase of pressure in the milling chamber after about 13 s. Until 15 min, tin, together with additional sulfur, was subsequently incorporated into the crystal structure. Further milling did not bring about any changes in the phase composition, only the occurrence of agglomeration phenomenon. The product was in the form of nanocrystals embedded in large micron-sized agglomerates. The presence of small nanocrystals was confirmed by TEM (HRTEM), showing that the size of all the

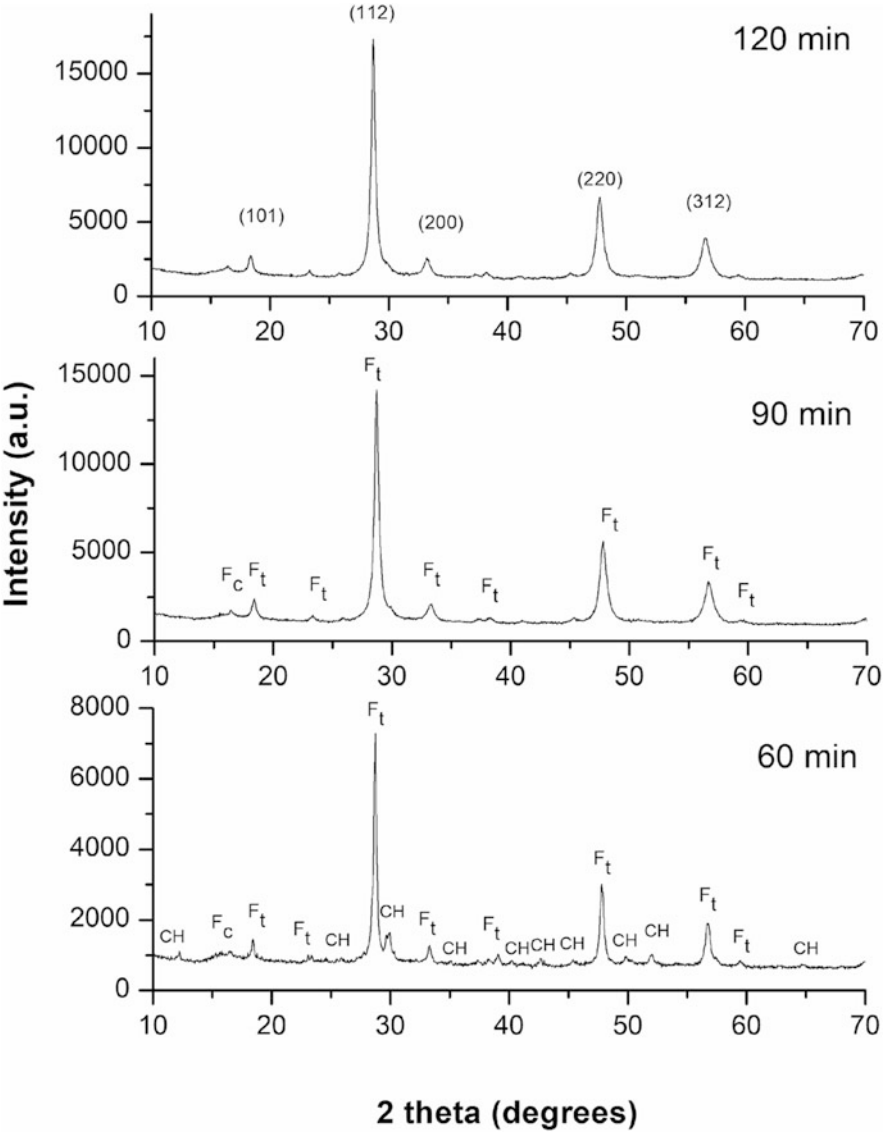

Fig. 18 XRD patterns of Cu_3SbS_4 synthesized in laboratory mill for different milling time. The identified phases are marked as follows: $CuSbS_2$ – chalcostibite (CH), Cu_3SbS_4 – tetragonal famatinite (F_t), Cu_3SbS_4 – cubic famatinite (F_c). (Reprinted with permission from Ref. [60]. Copyright 2021, Elsevier)

nanocrystals was below 20 nm (Fig. 20b). The obtained crystals were defective, and such planar defects are marked by an arrow in the figure. The electrical resistivity showing a clear negative correlation with the grain size was also discovered therein.

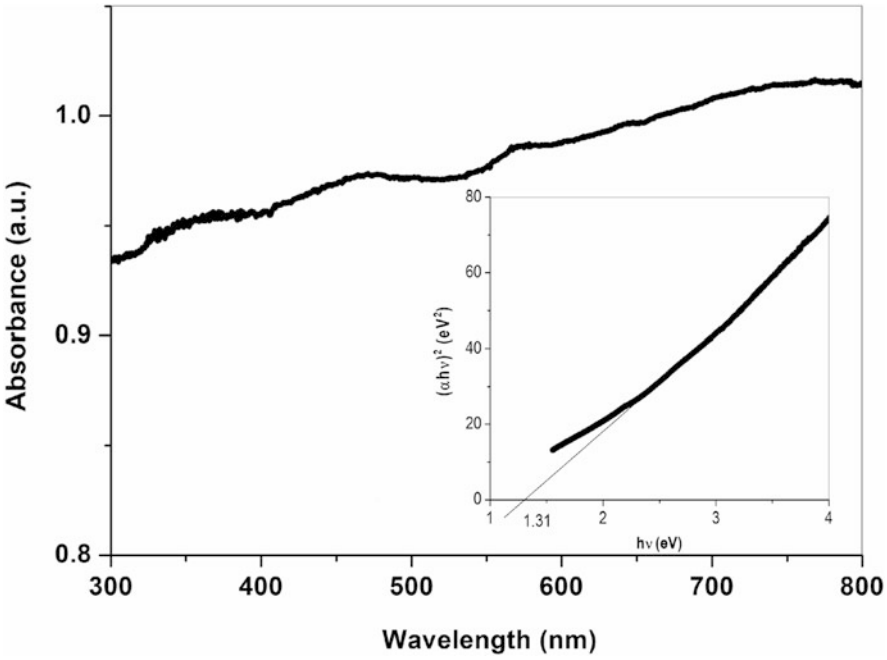

Fig. 19 UV-vis spectrum of mechanochemically synthesized Cu_3SbS_4 and Tauc plot (inset). (Reprinted with permission from Ref. [60]. Copyright 2021, Elsevier)

Very recently, an update to this study concentrating mainly on the Raman spectroscopy characterization of these samples was published. Due to the high sensitivity of Raman spectroscopy, an additional phase of copper sulfate was found, and its presence was postively correlated with the amount of CuS phase, which most probably serves as a precursor of its formation. Thus, the sample after 15 min was the most stable [62].

In our research, we also managed to obtain pure Cu_2SnS_3 phase after 60 min of milling in a laboratory planetary ball mill using covellite CuS and SnS (previously obtained by a mechanochemical synthesis) as precursors. The obtained nanocrystals exhibited size of approximately 10–15 nm. Reaction progress calculated from the Rietveld refinement of the XRD patterns is illustrated in Fig. 21a, where the dependence of conversion degree on milling time is shown. Since CTS phase exists in several polymorphs not detectable by XRD, the Raman spectroscopy was used for deeper inspection (Fig. 21b). There was a peak broadening due to the phonon confinement effect. The peak with a maximum at 335 cm^{-1} is undoubtedly assigned to the tetragonal CTS phase. The Raman spectroscopy revealed also the presence of impurities like CuS, SnS, and SnS_2, which are formed as intermediates during the mechanochemical synthesis.

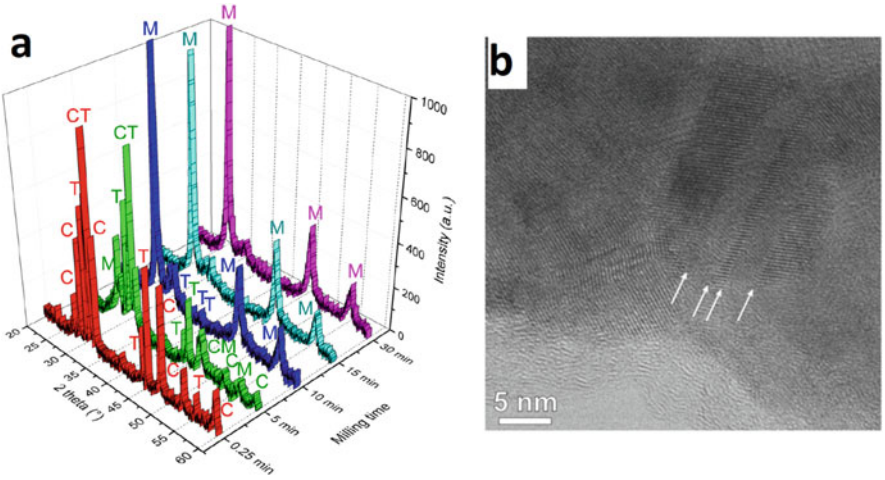

Fig. 20 (**a**) XRD patterns of the copper-tin-sulfur reaction mixtures milled for different time. The identified crystallographic phases are marked in the figure as follows: C—covellite (JCPDS 00–006-0464), T—tin (JCPDS 03–065-0296), M—mohite (JCPDS00–027-0198), (**b**) HRTEM image showing the Cu_2SnS_3 product obtained after 15 min of milling of the stoichiometric elemental mixture. The arrows point to the planar defects. (Reprinted by permission from Springer Nature Customer Service Centre GmbH: Springer Nature [61] [COPYRIGHT] (2018))

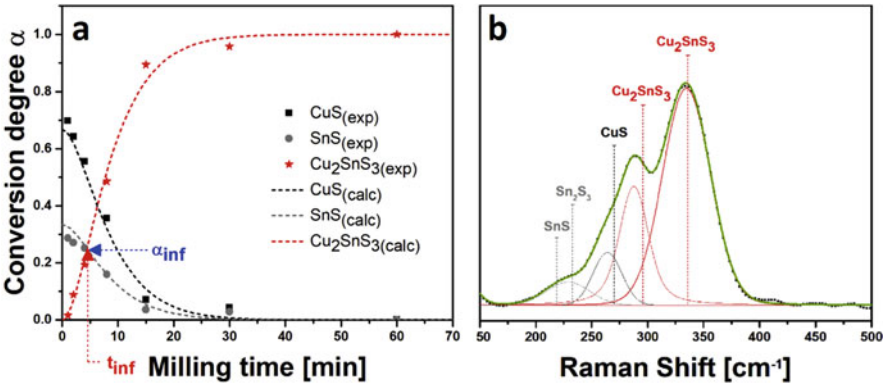

Fig. 21 (**a**) Reaction kinetics of Cu_2SnS_3 synthesis in a laboratory mill calculated from the XRD data using the Rietveld refinement, (**b**) fitted Raman spectra of the product synthesized after 60 min. (Reprinted with permission from Ref. [63]. Copyright 2018, Elsevier)

The overview table showing the precursors, necessary milling time, achieved particle size, and the application of the ternary chalcogenides prepared recently by other research groups is shown below (Table 2).

Table 2 Overview of ternary chalcogenides prepared by other research groups since 2018

Product	Precursors	Milling time	Particle size	Application	References
Sulfides					
$AgInS_2$	S, AgI, $In(ac)_3$, oleyl amine and 1-DDT (1-dodecanethiol)	2–4 min	2–5 nm	–	[64]
$CuInS_2$	S, CuBr, $In(ac)_3$, oleyl amine and 1-DDT (1-dodecanethiol)	2–4 min	2–5 nm	–	[64]
	Cu_2S and In_2S_3	1 h	9 nm	–	[65]
Cu_3SbS_4 Cu_3SbS_3	Cu, Sb and S	2 h	Micron scale	–	[66]
$Cu_{12}Sb_4S_{13}$	Cu_2S, CuS, Sb_2S_3	30 min to 6 h	–	Thermoelectrics	[67]
	Cu, Sb, and S	2 h	Micron scale	–	[66]
$Fe_xNi_{9-X}S_8$ (x = 0–9)	Fe, Ni, and S	2 h	9–15 nm	Catalyst	[32]
$Fe_{4.5}Ni_{4.5}S_8$	Fe, Ni, and S	15–60 min	250 nm	Catalyst	[68]
$Li_4P_2S_6$ and $xLi_2S.(100-x)P_2S_5$ (x = 50, 75 and 80)	S, P (red), Li_2S, and P_2S_5	10 h	–	Batteries	[69]
Li_2S-P_2S_5 and Li_2S-SiS_2	Li_2S, P_2S_5 or SiS_2	20 min – 20 h	5 nm	Batteries	[70]
Li_3SbS_4	Li_2S, Sb_2S_3 and S	100 h	Micron scale	Thermoelectrics	[71]
Li_4SnS_4 Li_3PS_4	Li_2S, SnS_2, P_2S_5 and LiI	10–60 h	–	Batteries	[72]
Na_2TiS_3	Na_2S and TiS_2	10 h	–	Batteries	[73]
PbS/Ni–Cr	Ni–Cr and PbS	3 h	15–25 nm	–	[74]
Ru-Ni-S	$NiCl_2$, $RuCl_3$ and NH_2CSNH_2	2 h	20–50 nm	Catalyst	[36]
Selenides					
$AgInSe_2$	Se, AgI, $In(ac)_3$, oleyl amine and 1-DDT (1-dodecanethiol)	2–4 min	2–5 nm	–	[64]
$CuInSe_2$	Se, CuBr, $In(ac)_3$, oleyl amine and 1-DDT (1-dodecanethiol)	2–4 min	2–5 nm	–	[64]

5 Quaternary Systems

From the quaternary systems, most of our work was devoted to Cu-Fe-Sn-S and Cu-Zn-Sn-S systems. Initially, we planned to apply the obtained materials as adsorber layer in the solar cells; however, the manufacturing of actual cell was necessary to test the performance, and this was not feasible, so therefore, we turned to testing these compounds as potential thermoelectric materials.

5.1 Stannite, Cu_2FeSnS_4

With regard to Cu-Fe-Sn-S (CFTS) system, we have intensively investigated the mechanochemical synthesis of stannite Cu_2FeSnS_4 phase in the past [75–77]. The synthesis included a rapid formation of CuS as the first step, then incorporation of tin and finally iron into the structure. However, there was always an admixture of rhodostannite $Cu_2FeSn_3S_8$ phase. More recently, two studies describing the spectroscopic properties of the CFTS nanocrystals were published. In the first one [78], the detailed far-infrared study on the prepared CFTS nanocrystals was conducted, and as demonstrated in the spectra obtained for the sample milled for different times, the signals corresponding to binary sulfides (reaction intermediates) disappear with time to reach only CFTS after 2 h of the treatment (Fig. 22). The same facts have been confirmed in another study utilizing Raman measurements [79].

5.2 Kesterite, Cu_2ZnSnS_4

We also succeeded in mechanochemically synthesizing the analogue with zinc (instead of iron), which is called kesterite, Cu_2ZnSnS_4 (CZTS) [80]. We have investigated an option to prepare it by using elemental precursors and also a mixture of compounds and elements (see equations below):

$$2\,Cu + Zn + Sn + 4\,S \rightarrow Cu_2ZnSnS_4 \tag{1}$$

$$2\,CuS + SnS + Zn + S \rightarrow Cu_2ZnSnS_4 \tag{2}$$

The reaction pathway is of course different depending on the option selected. Whereas when the combination of compounds and elements is used, CuS and SnS react to form Cu_2SnS_3, and the elements react to form ZnS (Fig. 23, left), the immediate formation of CuS and subsequent incorporation of Sn and Zn takes place in the other case (Fig. 23, right). In both cases, the pure kesterite phase was obtained after 60 min of milling, although in the last 30 min, just the incorporation of last traces of zinc takes place.

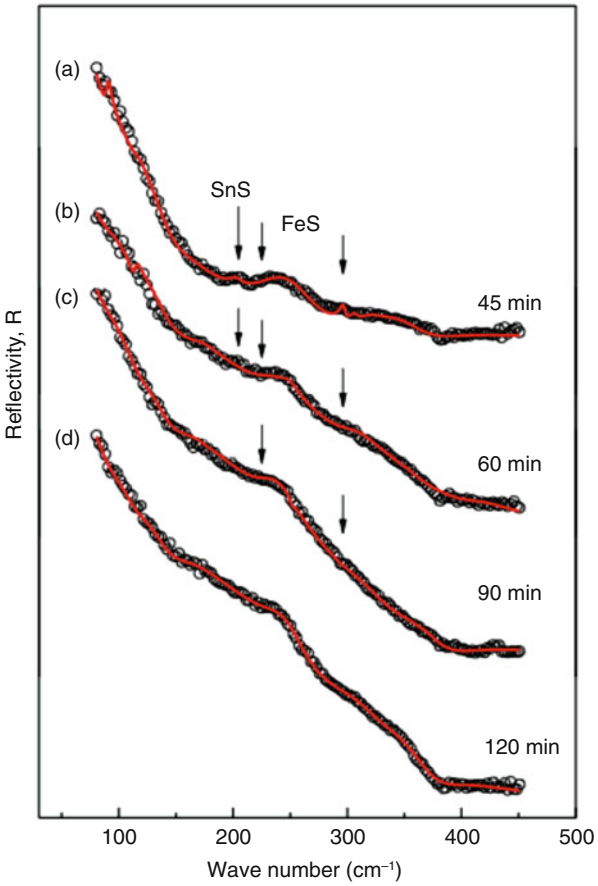

Fig. 22 Far-infrared reflection spectra of stannite Cu_2FeSnS_4 obtained after different milling times (given in the figure). Experimental spectra are presented by circles. The solid lines are calculated spectra obtained by a fitting procedure based on the Maxwell-Garnet mixing rule. (Reprinted with permission from Ref. [78]. Copyright 2018, Elsevier)

TEM analysis has shown that in both cases, the CZTS nanocrystals have the size ranging from 5 to 20 nm and that they contain defects. The elemental distribution seems to be slightly better in the case of the sample prepared by a combination of compounds and elements.

The overview table showing the precursors, necessary milling time, achieved particle size, and the application of quaternary chalcogenides prepared recently by other research groups is shown below (Table 3). Similarly to ternary chalcogenides, only the reports on sulfides were found.

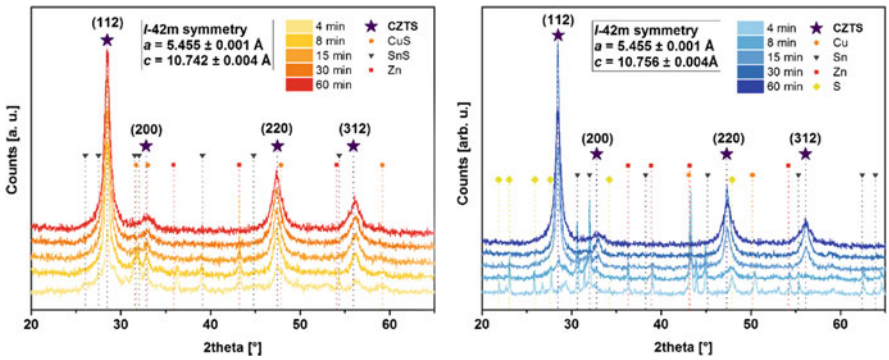

Fig. 23 X-ray diffraction patterns of stoichiometric mixtures milled according to Eq. 2 (from compounds/elements mixture) (**a**) and Eq. 1 (from elements) (**b**) for various times. (Reprinted with permission from Ref. [80]. Copyright 2019, Elsevier)

6 Scale-Up of Mechanochemical Synthesis of Chalcogenides

Although the lab-scale processing opens up new research pathways and leaves enough space for scientists to investigate interesting phenomena, the large-scale production is always questioned by the companies and the applied research. Mechanochemistry is well-scalable; however, only selected methods are suitable for it. In our research, we have shown that the synthesis of chalcogenides can be well-performed in a scalable manner by using eccentric vibratory milling. In this section, we provide a brief overview to show the feasibility of scalable mechanochemical synthesis of chalcogenides via this method.

The concept of eccentric vibratory mill (ESM) has been developed in Germany by the group of professor Gock [92, 93]. The schematic view of the ESM and its photograph is provided in Fig. 24a and b, respectively. The key difference in comparison with the traditional vibratory mills is that this mill produces elliptic, circular, and linear vibrations, which lead to unequalled amplitudes of vibration up to 20 mm and a high degree of disaggregation of the grinding media. This results in more intensive milling, and the specific energy consumption is reduced by 50%.

As it can be seen in Fig. 24b, there is a gray vessel in the middle of the front wall of the mill. This is called a "satellite" chamber and mirrors the exact events going on inside of the big mill (capable of the treatment of tens of kilograms) in a smaller volume. In this configuration, milling of the overall mass up to hundreds of grams is possible, and in our research, we have mostly used this satellite chamber.

The overview table showing various chalcogenides synthesized by our research group using an eccentric vibratory milling (in a satellite chamber) together with the information about the batch size and milling time is provided in Table 4. As

Table 3 Overview of quaternary chalcogenides prepared by other research groups since 2018

Product	Precursors	Milling time	Particle size	Application	References
Sulfides					
Ag_2FeGeS_4	Ag_2S, FeS_2, GeS_2, Fe	4 h	Micron scale	–	[81]
$Ag_2MgSn_3S_8$	MgS, SnS, S, and Ag_2S	4 h	4–36 nm	–	[82]
$Cu_2MgSn_3S_8$	MgS, SnS, S, and CuS	4 h	4–36 nm	–	[82]
$Cu_{1.92}ZnSnS_4$	Cu, Sn, ZnS, and S	2 h	11–13 nm	Solar cells	[83]
Cu_2ZnSnS_4	Cu, Zn, Sn, and S	1–10 h	12–14 nm	-	[84]
	Cu, Zn, Sn, and S or Cu_2S, ZnS, SnS, and S	4 h or 20 h	10–90 nm or 10–50 nm	–	[85]
	Cu, Zn, Sn and S	5 h	–	Solar cells	[86]
Cu_2ZnGeS_4	Cu, Zn, Ge and S	5 h	–	Solar cells	[86]
$Li_2MSn_3S_8$ (M = Mg, Mn, Fe or Ni)	Li_2S, SnS, CoS_2, S, and FeS_2 or MS (M = Mg, Mn, Ni)	4 h	–	Batteries	[87]
Na_2MgSnS_4	SnS, Na_2S, MgS, and S	4 h	Micron scale	–	[88]
$Na_{3-x}P_{1-x}W_xS_4$ ($0 \leq x \leq 0.24$)	Na_2S, P_2S_5, S and WS_2	15 h	Micron scale	Batteries	[89]
$Na_{3+x}Sb_{1-x}M_xS_4$ (M = Si, Ge, Sn; x = 0.03, 0.06, 0.09)	Na_2S, Sb_2S_3, S and SiS_2 or SnS_2 GeS_2	30 h	–	Batteries	[90]
$Na_{3-x}Sb_{1-x}Mo_xS_4$ (x = 0.06, 0.12, 0.18, 0.24)	Na_2S, Sb_2S_3, S, and MoS_2	30 h	–	Batteries	[90]
Selenides					
Cu_2ZnMSe_4 M = Ge, Sn	Cu, Zn, Sn, Ge, and Se	5 h	–	Solar cells	[86]
$Na_{11}Sn_2PSe_{12}$	Na, Sn, P, and Se	10–15 h	Micron scale	Batteries	[91]

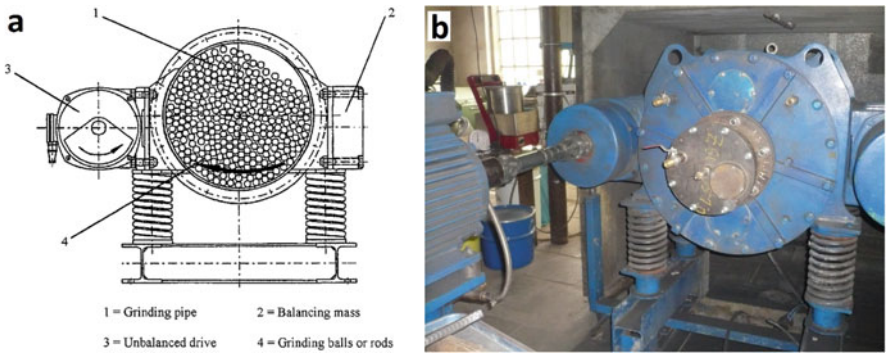

Fig. 24 Eccentric vibratory mill: (**a**) schematic view, (**b**) photograph. (Part A is reprinted with permission from Ref. [93]. Copyright 1999 Elsevier)

it can be seen, mainly copper-based chalcogenides were synthesized. The duration of milling was usually longer than in the case of lab-scale synthesis; however, the scalability of the process is of utmost importance. Finally, we managed to prepare covellite in 7.5 kg batch upon operating the ESM device in the full mode. In the majority of works, we have evaluated the thermoelectric performance of the prepared chalcogenides.

7 Conclusion

In this chapter, mechanochemical synthesis has been shown as a very perspective method to prepare nanocrystalline chalcogenides. The high-energy milling process and the events of mechanical activation and mechanochemical reaction play a decisive role in achieving the products with desired properties. The overview tables have shown that a rich plethora of binary, ternary, and quaternary chalcogenides have been recently prepared by research groups all around the world. The works of our research group focusing on the lab-scale preparation of mainly copper-based sulfides and selenides have been reviewed. The scalability of mechanochemical synthesis upon using eccentric vibratory milling was outlined in the last part of the chapter.

Table 4 Overview of recent studies of our research group reporting the scalable mechanochemical synthesis using eccentric vibratory mill

Targeted product	Precursors	Batch	Milling time (min)	Crystallite size	Tested application	References
Binary						
Covellite CuS	Cu, S	300 g	40	11 nm		[94]
	Cu, S	7.5 kg	60			[94]
Klockmannite CuSe	Cu, Se	90.25 g	10	64 nm	–	[18]
Ternary						
Mohite Cu_2SnS_3	Cu, Sn, S	100 g	180		Thermoelectrics	[95]
	CuS, SnS	100 g	240	10–15 nm		[63]
Tetrahedrite $Cu_{12}Sb_4S_{13}$	Cu, Sb, S	100 g	240	20 nm	Thermoelectrics	[95]
Bi-doped Tetrahedrite $Cu_{12}Sb_4S_{13}$	Bi, Cu, Sb, S	100 g	60		Thermoelectrics	[96]
Chalcopyrite $CuFeS_2$	Cu, Fe, S	100 g	720	10 nm	Thermoelectrics	[95]
Famatinite Cu_3SbS_4	Cu, Sb, S	100 g	180	10 nm		[60]
Quaternary						
Kesterite Cu_2ZnSnS_4	Cu, Zn, Sn, S	100 g	240			[97]
	Cu, Zn, Sn, S or CuS, SnS, Zn, S	100 g	360	15 nm		[80]
Stannite Cu_2FeSnS_4	$CuFeS_2$, CuS, SnS	100 g	240			[97]
	CuS, SnS, Fe, S	100 g	480			
	Cu, Fe, Sn, S	100 g	240			
Mawsonite $Cu_6Fe_2SnS_8$	Cu, Fe, Sn, S	100 g	240	< 1 μm	Thermoelectrics	[98]
Rhodostannite $Cu_2FeSn_3S_8$	Cu, Fe, Sn, S	100 g	360	12 nm	Thermal insulation	[99]
Colusite $Cu_{26}V_2Sn_6S_{32}$	Cu, V, Sn, S	100 g	720	< 1 μm	Thermoelectrics	[100]

Acknowledgments This work was supported by the projects of the Slovak Research and Development Agency APVV (contract no. 18-0357) and the Scientific Grant Agency of the Ministry of Education, Science, Research and Sport of the Slovak Republic and Slovak Academy of Sciences (2/0112/22, 2/0103/20).

References

1. G. Heinicke, *Tribochemistry* (Akademie-Verlag, Berlin, 1984), 495 p
2. A.D. McNaught, A. Wilkinson, *IUPAC Compendium of Chemical Terminology ("The Golden Book")*, 2nd edn. (Blackwell Scientific Publication, Oxford, 1997)
3. W. Ostwald, Die chemische Literatur und die Organisation der Wissenschaft, in *Handbuch der Allgemeinen Chemie*, ed. by W. Ostwald, C. Drucker, (Akademische Verlagesellschaft, Leipzig, 1919), pp. 70–77
4. M. Baláž, L. Vella-Zarb, J.G. Hernández, I. Halasz, D.E. Crawford, M. Krupička, et al., Mechanochemistry: A disruptive innovation for the industry of the future. Chim. Oggi **37**, 32–34 (2019)
5. M. Baláž, *Environmental Mechanochemistry: Recycling Waste into Materials Using High-Energy Ball* (Springer, Milling, 2021), 619 p
6. M. Baláž, M. Achimovičová, P. Baláž, E. Dutková, M. Fabián, M. Kováčová, Z. Lukáčová Bujňáková, E. Tóthová, Mechanochemistry as a versatile and scalable tool for nanomaterials synthesis: Recent achievements in Košice, Slovakia. Curr. Opin. Green Sustain. Chem. **24**, 7–13 (2020)
7. P. Baláž, M. Achimovičová, M. Baláž, P. Billik, Z. Cherkezova-Zheleva, J.M. Criado, et al., Hallmarks of mechanochemistry: From nanoparticles to technology. Chem. Soc. Rev. **42**, 7571–7637 (2013)
8. P. Balaz, M. Balaz, M. Achimovicova, Z. Bujinakova, E. Dutkova, Chalcogenide mechanochemistry in materials science: Insight into synthesis and applications (a review). J. Mater. Sci. **52**, 11851–11890 (2017)
9. P. Baláž, *Extractive Metallurgy of Activated Minerals* (Elsevier, Amsterdam, 2000), p. 278
10. P. Baláž, *Mechanochemistry in Nanoscience and Minerals Engineering* (Springer, Berlin/Heidelberg, 2008), p. 413
11. P. Baláž, E. Boldižárová, E. Godočíková, J. Briančin, Mechanochemical route for sulphide nanoparticles preparation. Mater. Lett. **57**, 1585–1589 (2003)
12. E. Dutková, M. Čaplovičová, I. Škorvánek, M. Baláž, A. Zorkovská, P. Baláž, Ľ. Čaplovič, Structural, surface and magnetic properties of chalcogenide Co_9S_8 nanoparticles prepared by mechanochemical synthesis. J. Alloys Compd. **745**, 863–867 (2018)
13. M. Baláž, A. Zorkovská, F. Urakaev, P. Baláž, J. Briančin, Z. Bujňáková, M. Achimovičová, E. Gock, Ultrafast mechanochemical synthesis of copper sulfides. RSC Adv. **6**, 87836–87842 (2016)
14. M. Baláž, A. Zorkovská, J.S. Blazquez, N. Daneu, P. Baláž, Mechanochemistry of copper sulphides: Phase interchanges during milling. J. Mater. Sci. **52**, 11947–11961 (2017)
15. M. Baláž, E. Dutková, Z. Bujňáková, E. Tóthová, N.G. Kostova, Y. Karakirova, J. Briančin, M. Kaňuchová, Mechanochemistry of copper sulfides: Characterization, surface oxidation and photocatalytic activity. J. Alloys Compd. **746**, 576–582 (2018)
16. Z. Shalabayev, M. Baláž, N. Daneu, E. Dutková, Z. Bujňáková, M. Kaňuchová, et al., Sulfur-mediated Mechanochemical synthesis of spherical and needle-like copper sulfide nanocrystals with antibacterial activity. ACS Sustain. Chem. Eng. **7**, 12897–12909 (2019)
17. M. Baláž, M. Rajňák, Z. Shalabayev, A. Zubrik, Detection of iron wear in mechanochemistry using magnetometry. Acta Phys. Pol. A **137**, 684–686 (2020)

18. M. Achimovicova, M. Balaz, V. Girman, J. Kurimsky, J. Briancin, E. Dutkova, K. Gaborova, Comparative study of nanostructured CuSe semiconductor synthesized in a planetary and vibratory mill. Nanomaterials **10**, 2038 (2020)
19. K. Gaborova, M. Achimovicova, M. Hegedus, V. Girman, M. Kanuchova, E. Dutkova, Advantageous mechanochemical synthesis of copper(I) selenide semiconductor, characterization, and properties. Front. Chem. Sci. Eng. **16**, 433 (2021)
20. M. Achimovičová, N. Daneu, E. Dutková, A. Zorkovská, Mechanochemically synthesized cobalt monoselenide: Structural characterization and optical properties. Appl. Phys. A Mater. Sci. Process. **123**, 154 (2017)
21. M. Achimovicova, N. Daneu, E. Tothova, M. Mazaj, E. Dutkova, Combined mechanochemical/thermal annealing approach for the synthesis of Co_9Se_8 with potential optical properties. Appl. Phys. A Mater. Sci. Process. **125**, 8 (2019)
22. C. Campos, J. de Lima, T. Grandi, K. Machado, P. Pizani, Structural studies of cobalt selenides prepared by mechanical alloying. Phys. B Condens. Matter **324**, 409–418 (2002)
23. T. Ohtani, M. Motoki, K. Koh, K. Ohshima, Synthesis of binary copper chalcogenides by mechanical alloying. Mater. Res. Bull. **30**, 1495–1504 (1995)
24. L. Bulat, V. Osvenskii, A. Ivanov, A. Sorokin, D. Pshenay-Severin, V. Bublik, N. Tabachkova, V. Panchenko, M. Lavrentev, Experimental and theoretical study of the thermoelectric properties of copper selenide. Semiconductors **51**, 854–857 (2017)
25. J. Li, G. Liu, X. Wu, G. He, Z. Yang, J. Li, Reaction mechanism in mechanochemical synthesis of Cu_2-xSe. Ceram. Int. **44**, 22172–22175 (2018)
26. M. Masdarian, A. Azizi, Z. Bahri, Mechanochemical sulfidization of a mixed oxide-sulphide copper ore by co-grinding with sulfur and its effect on the flotation efficiency. Chin. J. Chem. Eng. **28**, 743–748 (2020)
27. S.M. Hosseini, A. Varzi, S. Ito, Y. Aihara, S. Passerini, High loading CuS-based cathodes for all-solid-state lithium sulfur batteries with enhanced volumetric capacity. Energy Storage Mater. **27**, 61–68 (2020)
28. S. Kumar, M.B. Gawande, I. Medřík, M. Petr, O. Tomanec, V. Kupka, R.S. Varma, R. Zbořil, Mechanochemical synthesis of Cu_2S bonded 2D-sulfonated organic polymers: Continuous production of dimethyl carbonate (DMC) via preheating of reactants. Green Chem. **22**, 5619–5627 (2020)
29. A. Molla, H. Choi, H. Sakong, J.H. Youk, Sulfur-source dependent wet mechanochemical synthesis of pyrrhotite nanoparticles and evaluation of their sonocatalytic dye degradability. Mater. Res. Bull. **145**, 111519 (2022)
30. M. Pan, T. Hakari, A. Sakuda, A. Hayashi, Y. Suginaka, S. Mori, M. Tatsumisago, Electrochemical properties of all-solid-state lithium batteries with amorphous FeSx-based composite positive electrodes prepared via Mechanochemistry. Electrochemistry **86**, 175–178 (2018)
31. C. Guo, D. Yue, S. Wang, X. Qian, Y. Zhao, Mechanochemically sulfured $FeS_{1.92}$ as stable and efficient heterogeneous Fenton catalyst. Chin. Chem. Lett. **31**, 1978–1981 (2020)
32. H.M. Amin, M. Attia, D. Tetzlaff, U.P. Apfel, Tailoring the Electrocatalytic activity of Pentlandite $Fe_xNi_{9-X}S_8$ nanoparticles via variation of the Fe: Ni ratio for enhanced water oxidation. ChemElectroChem **8**, 3863–3874 (2021)
33. K. Denoue, F. Cheviré, C. Calers, L. Verger, D. Le Coq, L. Calvez, Mechanochemical synthesis and structural characterization of gallium sulfide Ga_2S_3. J. Solid State Chem. **292**, 121743 (2020)
34. G. Shirota, A. Nasu, M. Deguchi, A. Sakuda, M. Tatsumisago, A. Hayashi, Electrode performance of amorphous MoS_3 in all-solid-state sodium secondary batteries. J. Power Sources Adv. **10**, 100061 (2021)
35. M. Kristl, S. Gyergyek, J. Kristl, Nanostructured nickel sulfides with different Stoichiometries prepared by Mechanochemical synthesis. Chalcogenide Lett. **15**, 55–61 (2018)
36. T.L. Jin, X. Liu, H. Wang, X. Wu, Y. Zhang, Mechanochemical-assisted synthesis of ternary Ru-Ni-S pyrite analogue for enhanced hydrogen evolution performance. Carbon **162**, 172–180 (2020)

37. W. Meng, W. Yuan, Z. Wu, X. Wang, W. Xu, L. Wang, et al., Mechanochemical synthesis of lead sulfide (PbS) nanocrystals from lead oxide. Powder Technol. **347**, 130–135 (2019)
38. A. Kothari, K. Dave, Solution-based deposition of SnS nanostructures from mechanochemically prepared precursor bath. Mater. Lett. **236**, 299–302 (2019)
39. M. Dogrusoz, R. Demir-Cakan, Mechanochemical synthesis of SnS anodes for sodium ion batteries. J. Energy Res. **44**, 10809–10820 (2020)
40. B.-I. Park, Y.H. Jang, S.Y. Lee, D.-K. Lee, Mechanochemically synthesized SnS nanocrystals: Impact of nonstoichiometry on phase purity and solar cell performance. ACS Sustain. Chem. Eng. **6**, 3002–3009 (2018)
41. H. Petersen, S. Reichle, S. Leiting, P. Losch, W. Kersten, T. Rathmann, et al., In situ synchrotron X-ray diffraction studies of the Mechanochemical synthesis of ZnS from its elements. Chem. Eur. J. **27**, 12558 (2021)
42. M.A. Avilés, J. Córdoba, M.J. Sayagués, F. Gotor, Synthesis of Mn 2+-doped ZnS by a mechanically induced self-sustaining reaction. J. Mater. Sci. **55**, 1603–1613 (2020)
43. P. Hu, C. Xie, Z. Mao, X. Liang, A Mechanochemical route for ZnS nanocrystals, and batch sorting along size distribution. Nanomaterials **9**, 1325 (2019)
44. H.-Y. Ahn, W.J. Choi, S.Y. Lee, B.-K. Ju, S.-H. Cho, Mechanochemical synthesis of ZnS for fabrication of transparent ceramics. Res. Chem. Intermed. **44**, 4721–4731 (2018)
45. A. Alshahrie, A. Al-Ghamdi, L.M. Bronstein, Synthesis and characterization of $Zn_{1-x}Ac_xS$ ($0 \leq x \leq 0.1$) nanocrystalline quantum dots prepared via soft mechanochemical approach. Ceram. Int. **45**, 20929–20935 (2019)
46. N. Jafaripour, H. Omidvar, S. Saber-Samandari, R. Mohammadi, R. Shokrani Foroushani, B. Kamyab Moghadas, M. Soleimani, B. Noshadi, A. Khandan, Synthesize and characterization of a novel cadmium selenide nanoparticle with iron precursor applicable in hyperthermia of cancer cells. Int. J. Nanosci. Nanotechnol. **17**, 77–90 (2021)
47. A. Ivanov, I. Tarasova, V. Bublik, R.K. Akchurin, I. Shchetinin, N.Y. Tabachkova, D. Pshenay-Severin, V. Osvenskii, Temperature dependence of the lattice parameters of $Cu_{2-x}Se$ ($0.03 \leq x \leq 0.23$) powders fabricated by mechanochemical synthesis. Phys. Solid State **60**, 2295–2299 (2018)
48. J.-H. Choi, M.-H. Lee, H.-Y. Choi, C.-M. Park, S.-M. Lee, J.-H. Choi, Investigation of electrochemical reaction mechanism for antimony selenide nanocomposite for sodium-ion battery electrodes. J. Appl. Electrochem. **49**, 207–216 (2019)
49. M. Kristl, S. Gyergyek, S.D. Škapin, J. Kristl, Solvent-free mechanochemical synthesis and characterization of nickel tellurides with various Stoichiometries: NiTe, $NiTe_2$ and Ni2Te_3. Nanomaterials **11**, 1959 (2021)
50. U.K. de Fatima, J.P. Winiarski, C.L. Jost, C.E.M. de Campos, Mechanochemical synthesis of a Ni_3-xTe_2 nanocrystalline composite and its application for simultaneous electrochemical detection of dopamine and adrenaline. Compos. Part B Eng. **183**, 107649 (2020)
51. K. Itoh, Y. Mizuhara, T. Otomo, Mechanochemical synthesis of binary phosphorus telluride: Short range structure and thermal properties. J. Solid State Chem. **267**, 119–123 (2018)
52. D. Cheikh, B.E. Hogan, T. Vo, P. Von Allmen, K. Lee, D.M. Smiadak, et al., Praseodymium telluride: A high-temperature, high-ZT thermoelectric material. Joule **2**, 698–709 (2018)
53. D. Cheikh, K. Lee, W. Peng, A. Zevalkink, J.-P. Fleurial, S.K. Bux, Thermoelectric properties of scandium sesquitelluride. Materials **12**, 734 (2019)
54. E. Dutkova, Z. Bujnakova, J. Kovac, I. Skorvanek, M.J. Sayagues, A. Zorkovska, J. Kovac, P. Balaz, Mechanochemical synthesis, structural, magnetic, optical and electrooptical properties of $CuFeS_2$ nanoparticles. Adv. Powder Technol. **29**, 1820–1826 (2018)
55. P. Levinsky, J. Hejtmanek, K. Knizek, M. Pashchenko, J. Navratil, P. Masschelein, E. Dutkova, P. Balaz, Nanograined n- and p-type chalcopyrite $CuFeS_2$ prepared by mechanochemical synthesis and sintered by SPS. Acta Phys. Pol. A **137**, 904–907 (2020)
56. P. Balaz, E. Dutkova, P. Levinsky, N. Daneu, L. Kubickova, K. Knizek, et al., Enhanced thermoelectric performance of chalcopyrite nanocomposite via co-milling of synthetic and natural minerals. Mater. Lett. **275**, 128107 (2020)

57. P. Baláž, E. Dutková, M. Baláž, R. Džunda, J. Navrátil, K. Knížek, P. Levinský, J. Hejtmánek, Mechanochemistry for energy materials: Impact of high-energy milling on chemical, electric and thermal transport properties of chalcopyrite $CuFeS_2$ nanoparticles. ChemistryOpen **10**, 806–814 (2021)
58. P. Baláž, M. Baláž, E. Dutková, M. Hegedus, M. Rajňák, K. Knížek, et al., Magnetization as an effective tool for kinetic evaluation in Mechanochemical synthesis of chalcopyrite $CuFeS_2$. Acta Phys. Pol. A **137**, 647–649 (2020)
59. E. Dutkova, M.J. Sayagues, M. Fabian, J. Kovac, J. Kovac, M. Balaz, M. Stahorsky, Mechanochemical synthesis of ternary chalcogenide chalcostibite $CuSbS_2$ and its characterization. J. Mater. Sci. Mater. Electron. **32**, 22898–22909 (2021)
60. E. Dutkova, M. Sayagues, M. Fabian, M. Balaz, M. Achimovicova, Mechanochemically synthesized ternary chalcogenide Cu_3SbS_4 powders in a laboratory and an industrial mill. Mater. Lett. **291**, 129566 (2021)
61. M. Baláž, N. Daneu, M. Rajňák, J. Kurimský, M. Hegedűs, E. Dutková, M. Fabián, M. Kaňuchová, P. Baláž, Rapid mechanochemical synthesis of nanostructured mohite Cu_2SnS_3 (CTS). J. Mater. Sci. **53**, 13631–13642 (2018)
62. J. Trajic, M. Curcic, M. Casas Luna, M. Romcevic, M. Remesova, M. Baláž, L. Čelko, K. Dvorek, N. Romcevic, Vibrational properties of the mechanochemically synthesized Cu_2SnS_3: Raman study. J. Raman Spectrosc. **53**, 977–987 (2022)
63. M. Hegedüs, M. Baláž, M. Tešinský, M.J. Sayagués, P. Šiffalovič, M. Kruľáková, J. Briančin, M. Fabián, Scalable synthesis of potential solar cell absorber Cu_2SnS_3 (CTS) from nanoprecursors. J. Alloys Compd. **768**, 1006–10015 (2018)
64. A. Bera, S.S. Pathak, V. Kotha, B.L. Prasad, Lamellar bimetallic thiolates: Synthesis, characterization, and their utilization for the preparation of bimetallic chalcogenide nanocrystals through Mechanochemical grinding. Adv. Mater. Interfaces **8**, 2100898 (2021)
65. D. Delmonte, R. Manfredi, D. Calestani, F. Mezzadri, L. Righi, M. Mazzer, et al., An affordable method to produce $CuInS_2$ 'mechano-targets' for film deposition. Semicond. Sci. Technol. **35**, 045026 (2020)
66. F. Neves, L. Esperto, I. Figueira, J. Mascarenhas, R. Salgueiro, T. Silva, J. Correia, P.A. Carvalho, D. de Oliveira, Mechanochemical synthesis of tetrahedrite materials using mixtures of synthetic and ore samples collected in the Portuguese zone of the Iberian Pyrite Belt. Miner. Eng. **164**, 106833 (2021)
67. F.A. López Cota, J.A. Díaz-Guillén, O. Juan Dura, M.A. López de la Torre, J. Rodríguez-Hernández, A. Fernández Fuentes, Mechanosynthesis and thermoelectric properties of Fe, Zn, and Cd-Doped P-Type Tetrahedrite: $Cu_{12-x}M_xSb_4S_{13}$. Materials **14**, 3448 (2021)
68. D. Tetzlaff, K. Pellumbi, D.M. Baier, L. Hoof, H.S. Barkur, M. Smialkowski, et al., Sustainable and rapid preparation of nanosized Fe/Ni-pentlandite particles by mechanochemistry. Chem. Sci. **11**, 12835–12842 (2020)
69. M. Suyama, S. Yubuchi, M. Deguchi, A. Sakuda, M. Tatsumisago, A. Hayashi, Importance of Li-metal/sulfide electrolyte interphase ionic conductivity in suppressing short-circuiting of all-solid-state Li-metal batteries. J. Electrochem. Soc. **168**, 060542 (2021)
70. M. Tatsumisago, A. Hayashi, *Preparation of Solid Electrolyte Particles and Solid-Solid Interfaces for All-Solid-State Batteries*, Nanoparticle Technology Handbook (Elsevier, 2018), pp. 579–584
71. T. Kimura, A. Kato, C. Hotehama, A. Sakuda, A. Hayashi, M. Tatsumisago, Preparation and characterization of lithium ion conductive Li_3SbS_4 glass and glass-ceramic electrolytes. Solid State Ionics **333**, 45–49 (2019)
72. M. Otoyama, K. Kuratani, H. Kobayashi, Mechanochemical synthesis of air-stable hexagonal Li_4SnS_4-based solid electrolytes containing LiI and Li_3PS_4. RSC Adv. **11**, 38880–38888 (2021)
73. A. Nasu, M. Otoyama, A. Sakuda, A. Hayashi, M. Tatsumisago, Mechanochemical synthesis of cubic rocksalt Na_2TiS_3 as novel active materials for all-solid-state sodium secondary batteries. J. Ceram Soc. Jpn. **127**, 19086 (2019)

74. K.A. Ibrahimova, A.A. Azizov, O.O. Balayeva, R.M. Alosmanov, S.C. Mammadyarova, Mechanochemical synthesis of PbS/Ni–Cr layered double hydroxide nanocomposite. Mendeleev Commun. **31**, 100–103 (2021)
75. P. Baláž, M. Baláž, A. Zorkovská, I. Škorvánek, Z. Bujňáková, J. Trajić, Kinetics of solid-state synthesis of quaternary Cu_2FeSnS_4 (stannite) nanocrystals for solar energy applications. Acta Phys. Pol. A **131**, 1153–1155 (2017)
76. P. Baláž, M. Baláž, M.J. Sayagués, I. Škorvánek, A. Zorkovská, E. Dutková, et al., Mechanochemical solvent-free synthesis of quaternary semiconductor Cu-Fe-Sn-S nanocrystals. Nanoscale Res. Lett. **12**, 256 (2017)
77. P. Baláž, M. Baláž, M.J. Sayagués, A. Eliyas, N.G. Kostova, M. Kaňuchová, E. Dutková, A. Zorkovská, Chalcogenide quaternary Cu_2FeSnS_4 nanocrystals for solar cells: Explosive character of mechanochemical synthesis and environmental challenge. Crystals **7**, 367 (2017)
78. J. Trajic, M. Romcevic, N. Paunovic, M. Curcic, P. Balaz, N. Romcevic, Far-infrared study of the mechanochemically synthesized Cu_2FeSnS_4 (stannite) nanocrystals. Infrared Phys. Technol. **90**, 66–69 (2018)
79. J. Trajic, M. Romcevic, M. Petrovic, M. Gilic, P. Balaz, A. Zorkovska, N. Romcevic, Optical properties of the mechanochemically synthesized Cu_2FeSnS_4 (stannite) nanocrystals: Raman study. Opt. Mater. **75**, 314–318 (2018)
80. P. Baláž, M. Hegedus, M. Baláž, N. Daneu, P. Siffalovic, Z. Bujňáková, et al., Photovoltaic materials: Cu_2ZnSnS_4 (CZTS) nanocrystals synthesized via industrially scalable, green, one-step mechanochemical process. Prog. Photovolt. Res. Appl. **27**, 798–811 (2019)
81. E.M. Heppke, S. Mahadevan, T. Bredow, M. Lerch, Crystal structure of mechanochemically prepared Ag_2FeGeS_4. Z. Naturforsch., B: Chem Sci **76**, 607–614 (2021)
82. E.M. Heppke, S. Klenner, O. Janka, R. Pöttgen, M. Lerch, Mechanochemical synthesis of $Cu_2MgSn_3S_8$ and $Ag_2MgSn_3S_8$. Z. Anorg. Allg. Chem. **646**, 5–9 (2020)
83. F. Neves, A. Stark, N. Schell, M.J. Mendes, H. Aguas, E. Fortunato, R. Martins, J.B. Correia, A. Joyce, Investigation of single phase $Cu_2ZnSn_xSb_{1-x}S_4$ compounds processed by mechanochemical synthesis. Phys. Rev. Mater. **2**, 075404 (2018)
84. K. Kapusta, M. Drygas, J.F. Janik, Z. Olejniczak, New synthesis route to kesterite Cu_2ZnSnS_4 semiconductor nanocrystalline powders utilizing copper alloys and a high energy ball milling-assisted process. J. Mater. Res. Technol. **9**, 13320–13331 (2020)
85. K. Lejda, M. Drygaś, J.F. Janik, J. Szczytko, A. Twardowski, Z. Olejniczak, Magnetism of Kesterite Cu_2ZnSnS_4 semiconductor Nanopowders prepared by Mechanochemically assisted synthesis method. Materials **13**, 3487 (2020)
86. K. Tsuji, T. Maeda, T. Wada, Optical properties and electronic structures of Cu_2ZnSnS_4, Cu_2ZnGeS_4, and Cu_2Zn (Ge, Sn) S_4 and Cu_2Zn (Ge, Sn) Se_4 solid solutions. Jpn. J. Appl. Phys. **57**, 08RC21 (2018)
87. E.M. Heppke, S. Mahadevan, M. Lerch, New compounds of the $Li_2MSn_3S_8$ type. Z. Naturforsch., B: Chem Sci **75**, 625–631 (2020)
88. E.M. Heppke, M. Lerch, Na_2MgSnS_4–a new member of the A2IBIICIVX4 family of compounds. Z. Naturforsch., B: Chem Sci **75**, 721–726 (2020)
89. F. Tsuji, A. Nasu, A. Sakuda, M. Tatsumisago, A. Hayashi, Mechanochemical synthesis and characterization of $Na_{3-x}P_{1-x}W_xS_4$ solid electrolytes. J. Power Sources **506**, 230100 (2021)
90. F. Tsuji, N. Masuzawa, A. Sakuda, M. Tatsumisago, A. Hayashi, Preparation and characterization of cation-substituted Na_3SbS_4 solid electrolytes. ACS Appl. Energy Mater. **3**, 11706–11712 (2020)
91. R.P. Rao, X. Zhang, K.C. Phuah, S. Adams, Mechanochemical synthesis of fast sodium ion conductor $Na_{11}Sn_2PSe_{12}$ enables first sodium–selenium all-solid-state battery. J. Mater. Chem. A **7**, 20790–20798 (2019)
92. E. Gock, K.E. Kurrer, Eccentric vibratory mills-a new energy efficient way for pulverization. Erzmetall **49**, 434–442 (1996)
93. E. Gock, K. Kurrer, Eccentric vibratory mills – theory and practice. Powder Technol. **105**, 302–310 (1999)

94. M. Achimovicova, E. Dutkova, E. Tothova, Z. Bujnakova, J. Briancin, S. Kitazono, Structural and optical properties of nanostructured copper sulfide semiconductor synthesized in an industrial mill. Front. Chem. Sci. Eng. **13**, 164–170 (2019)
95. P. Balaz, M. Achimovicova, M. Balaz, K. Chen, O. Dobrozhan, E. Guilmeau, et al., Thermoelectric Cu-S-based materials synthesized via a scalable Mechanochemical process. ACS Sustain. Chem. Eng. **9**, 2003–2016 (2021)
96. P. Balaz, E. Guilmeau, M. Achimovicova, M. Balaz, N. Daneu, O. Dobrozhan, M. Kanuchova, Bismuth doping in nanostructured tetrahedrite: Scalable synthesis and thermoelectric performance. Nanomaterials **11**, 1386 (2021)
97. P. Baláž, M. Hegedüs, M. Achimovičová, M. Baláž, M. Tešinský, E. Dutková, M. Kaňuchová, J. Briančin, Semi-industrial green mechanochemical syntheses of solar cell absorbers based on quaternary sulfides. ACS Sustain. Chem. Eng. **6**, 2132–2141 (2018)
98. P. Baláž, M. Hegedüs, M. Reece, R.Z. Zhang, T.C. Su, I. Škorvánek, et al., Mechanochemistry for thermoelectrics: Nanobulk $Cu_6Fe_2SnS_8/Cu_2FeSnS_4$ composite synthesized in an industrial mill. J. Electron. Mater. **48**, 1846–1856 (2019)
99. M. Balaz, O. Dobrozhan, M. Tesinsky, R. Zhang, R. Dzunda, E. Dutkova, et al., Scalable and environmentally friendly mechanochemical synthesis of nanocrystalline rhodostannite ($Cu_2FeSn_3S_8$). Powder Technol. **388**, 192–200 (2021)
100. M. Hegedus, M. Achimovicova, H. Hui, G. Guelou, P. Lemoine, I. Fourati, et al., Promoted crystallisation and cationic ordering in thermoelectric $Cu_{26}V_2Sn_6S_{32}$ colusite by eccentric vibratory ball milling. Dalton Trans. **49**, 15828–15836 (2020)

Fundamentals of First-Principles Studies

Abhishek Sharan, Muhammad Sajjad, and Nirpendra Singh

1 Density Functional Theory

One of the most effective and promising approaches to understanding the electronic structure of materials is density functional theory (DFT), which has extensively been explored in understanding material properties [1]. Numerous simplifications and approximations have led this method to be used with an adequate balance of accuracy and computational costs. Walter Kohn was awarded Nobel Prize in Chemistry in 1998 for his vital contribution to DFT development. Since then, a swiftly growing number of publications utilizing this theory for understanding and predicting material properties advocate its significance in materials science and condensed matter physics research. DFT is a rigorous technique for resolving electronic features by mapping a many-body interacting system to a many-body non-interacting system. Its applications span is quite widespread, going beyond the conventional systems in materials science and physics to geology and biology. In subsequent sections, we address the difficulties involved in solving many-body (electron and nucleus) interacting systems that led to DFT development. We then provide an overview of DFT and the approximations that enable it to be applied to real systems.

A. Sharan · M. Sajjad · N. Singh (✉)
Department of Physics, Khalifa University of Science and Technology, Abu Dhabi, UAE
e-mail: Nirpendra.Singh@ku.ac.ae

F. I. Ezema et al. (eds.), *Chemically Deposited Metal Chalcogenide-based Carbon Composites for Versatile Applications*, https://doi.org/10.1007/978-3-031-23401-9_13

1.1 Many-Body Schrödinger Equation

The many-body time-independent Schrödinger equation, which establishes the fundamental basis for understanding the electronic character of solids, for a system of N electrons and K nuclei is given by

$$\hat{H}_{tot}\Psi\left(r_1, r_2, r_3 \ldots r_N, r_1', r_2' \ldots r_K'\right) = E_{tot}\Psi\left(r_1, r_2, r_3 \ldots r_N, r_1', r_2' \ldots r_K'\right), \tag{1}$$

where Ψ, E_{tot}, and $\hat{H}_{tot}$ correspond to wavefunction, total energy, and Hamiltonian, respectively, such that $\hat{H}_{tot}$ of the system is given as (in atomic units)

$$\hat{H}_{tot} = -\frac{1}{2}\sum_{i=1}^{N}\nabla_i^2 - \frac{1}{2}\sum_{k=1}^{K}\frac{1}{M_k}\nabla_k^2 - \sum_{i=1}^{N}\sum_{k=1}^{K}\frac{Z_k}{r_{ik}} + \sum_{i=1}^{N}\sum_{j>i}^{N}\frac{1}{r_{ij}} + \sum_{k=1}^{K}\sum_{l>k}^{K}\frac{Z_k Z_l}{r_{kl}'}, \tag{2}$$

where k and l (i and j) stand for K nuclei (N electrons). M denotes the mass of an atom possessing the atomic number Z. r_{ik}, r_{ij}, and r_{kl}' correspond to the distance between electron i and nucleus k, electrons i and j, and nuclei k and l, respectively. A solution to this equation results in the ground state of particles occupying the lowest eigenstates of the system, which eventually governs the equilibrium properties of the material. However, the complexity of the equation hinders its exact solution in most cases, except only in simple atomic systems. The level of complexity grows exponentially as the size of the system increases and making it practically impossible for this equation to be solved and leading to approximations and simplifications that need to be adopted for the solution of the equation in a realistic system, with a reasonable balance between the accuracy and computational cost. We will discuss the approximations and simplifications involved in the next few sections.

1.2 Born–Oppenheimer Approximation

An electron is substantially lighter in mass than a nucleus of an atom, resulting in a significantly small kinetic to potential energy ratio. Therefore, the spread in the electron wavefunction for a given potential is much greater than that for nuclei, as seen in Fig. 1 for a toy model with an Au atom in a parabolic potential. Therefore, the total wavefunction Ψ can be written as the product of electron-only and nuclear-only wavefunctions ($\psi_{r'}$ and χ_r) as

$$\Psi\left(r_1, r_2 \ldots, r_N; r_1', r_2' \ldots, r_K'\right) = \psi_{r'}(r_1, r_2 \ldots, r_N)\chi_r\left(r_1', r_2', \ldots, r_K'\right), \tag{3}$$

and Eq. (2) can be resolved into electronic and nuclear components as

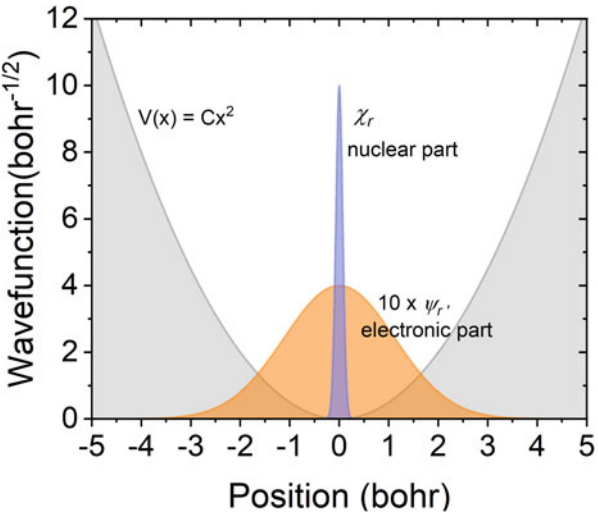

Fig. 1 Wavefunction showing the ground state of a toy model of Gold (Au) electron and nucleus in parabolic potential. The larger spread for electrons than nucleus is attributed to the larger mass of nucleus compared to electron

$$\left[-\sum_{i=1}^{N}\frac{\nabla_i^2}{2}+\sum_{i=1}^{N}V_n(r_i;r')+\frac{1}{2}\sum_{i=1}^{N}\sum_{j>i}^{N}\frac{1}{|r_i-r_j|}\right]\psi_{r'}=E_{r'}\psi_{r'} \tag{4}$$

$$\left[-\frac{1}{2}\sum_{k}^{K}\frac{\nabla_k^2}{M_k}+\frac{1}{2}\sum_{k=1}^{K}\sum_{l>k}^{K}\frac{Z_kZ_l}{r'_{kl}}+E(r'_1,r'_2\ldots,r'_K)\right]=E_{tot}\chi. \tag{5}$$

The electronic component of the wavefunction is specified for a particular nuclear configuration; hence, the subscript r' in $\psi_{r'}$. $V_n(r_i;r')$ indicates the potential caused by electrons and nuclei interactions. The electronic energy $E_{r'}$ acts as an effective potential for the nuclei. The combination of Coulomb contact and nuclear configuration electron energy gives the nuclei their overall potential. This decoupling of Eq. (2) into electron and nucleus parts is known as *Born–Oppenheimer approximation*.

According to Fig. 1, the nuclear component of the wavefunction is more localized than the electronic component for a parabolic potential. To a first approximation, it can be said that while electrons behave like waves, nuclei behave like point particles. Thus classical mechanics should be capable of adequately describing the nuclear dynamics. This approximation is excellent for the investigation of equilibrium structures. Nuclei are modeled in current DFT implementations using classical mechanics equations, which are relatively well-known and computationally less costly than solving the Schrödinger equation. According to the approximation, as electrons evolve from the initial to the final ground state upon changing nuclear

coordinates, no energy exchange occurs between the nuclear and electronic systems, suggesting the adiabatic development of the system. Hence, this approximation is also referred to as *adiabatic approximation*.

Solving Eq. (4) remains very difficult to solve due to the presence of a large number of electrons in the system. Here, rewriting the equation more succinctly leads to

$$\hat{H}\psi = E\psi, \tag{6}$$

where $\hat{H}$ and ψ are electronic parts of Hamiltonian and wavefunction, respectively, such that the former quantity can be written as

$$\hat{H} = \hat{G} + \hat{V}_{ext} + \hat{V}_{ee}, \tag{7}$$

where $\hat{G}$, $\hat{V}_{ext}$, and $\hat{V}_{ee}$ correspond to kinetic energy operator, potential contribution from electron–nuclei interaction, and potential energy operator for electron–electron repulsion, respectively. Furthermore, these terms are expanded as

$$\hat{G} = -\sum_{i=1}^{N} \frac{\nabla_i^2}{2} \tag{8}$$

$$\hat{V}_{ext} = \sum_{i=1}^{N} V_n(r_i; r') \tag{9}$$

$$\hat{V}_{ee} = \frac{1}{2} \sum_{i=1}^{N} \sum_{j>i}^{N} \frac{1}{|r_i - r_j|}. \tag{10}$$

Electrons behave according to Fermi–Dirac statistics and the Pauli exclusion principle. The ground-state wavefunction ψ can be approximated as an antisymmetrized product of N orthonormal single-particle wavefunctions, φ_i, and the Slater determinant

$$\psi_{HF} = \frac{1}{\sqrt{N!}} \begin{vmatrix} \varphi_1(r_1) & \varphi_2(r_1) & \ldots & \varphi_{N-1}(r_1) & \varphi_N(r_1) \\ \varphi_1(r_2) & \varphi_2(r_2) & \ldots & \varphi_{N-1}(r_2) & \varphi_N(r_2) \\ . & . & & . & \\ . & . & & . & \\ . & . & & . & \\ \varphi_1(r_N) & \varphi_2(r_N) & \ldots & \varphi_{N-1}(r_N) & \varphi_N(r_N) \end{vmatrix}, \tag{11}$$

where product of spatial and spin parts constitutes each $\varphi_i(r)$.

In the case of *Hartree–Fock approximation*, one needs to employ the variational principle in obtaining $\varphi_i's$ to minimize the system energy, *i.e.*,

$$E_{HF} = min_{\psi} E[\psi] \tag{12}$$

subject to the orthonormalization conditions

$$\int \varphi_i^*(r)\varphi_j(r)dr = \delta_{ij}, \tag{13}$$

where Kronecker delta function δ_{ij} holds 0 and 1 values for $i \neq j$ and $i = j$, respectively. The Hartree–Fock equation derived from the combination of variational principle and orthonormalization constraint is

$$\left[-\frac{\nabla^2}{2} + V_n(r) + V_H(r)\right]\varphi_i(r) + \int ds V_X(r,s)\varphi_i(s) = \epsilon_i \varphi_i(r). \tag{14}$$

In the above equation, the quantities V_n and V_H are referred to the external potential and the Hartree potential, respectively, such that the later quantity is dependent on electron density $n(r)$ as

$$\nabla^2 V_H(r) = -4\pi n(r), \tag{15}$$

$$n(r) = \sum_{i=1}^{N} |\varphi_i(r)|^2. \tag{16}$$

On the other hand, the Fock exchange potential V_X is given by

$$V_X(r,s) = -\sum_j \frac{\varphi_j^*(s)\varphi_j(r)}{|r-s|}. \tag{17}$$

The summation runs over the occupied single-particle states.

Significant simplifications have been made while going from Eq. (4) (describing 3N-dimensional interacting particles) to Eq. (14) (N 3-dimensional single non-interacting particles). However, certain limitations exist in the Hartree–Fock approximation. It consistently underestimates equilibrium bond lengths and atomization energy and also incapable of accurately describing the electronic character of molecular systems (e.g., ozone and diatomic fluorine). Besides, it does not account for electronic correlation effects, so the energy predicted with this approach is always larger than the precise energy. Furthermore, the electronic wavefunction represented by a single Slater determinant fails to account for electron correlation. Therefore, it is necessary to engage a more sophisticated theory to take electron correlation effects into account to describe such systems accurately.

1.3 Hohenberg–Kohn Theorem

Hohenberg and Kohn established two theorems that serve as the foundation for DFT and apply to any system of interacting particles, having a Hamiltonian given in Eq. (7).

Theorem 1 *Ground-state density $n_o(r)$ of an interacting system uniquely determines the external potential $V_{ext}(r)$ to which this system is subjected. Proof of the theorem is straightforward. Assume that there are two distinct external potentials $V^1_{ext}(r)$ and $V^2_{ext}(r)$ that vary by more than a constant for a particular ground-state density $n_o(r)$. These potentials are subject to provide two distinct Hamiltonians ($\hat{H}_1$ and $\hat{H}_2$) of Eq. (7), with distinct ground-state wavefunctions ϕ_1 and ϕ_2, respectively, which should result in the identical ground-state density $n_o(r)$. The ground-state energies associated with the Hamiltonians $\hat{H}_1$ and $\hat{H}_2$ are as follows:*

$$E_1 = \langle \phi_1 | \hat{H}_1 | \phi_1 \rangle \qquad \text{and} \tag{18}$$

$$E_2 = \langle \phi_2 | \hat{H}_2 | \phi_2 \rangle. \tag{19}$$

ϕ_2 not being the ground-state wavefunction for $\hat{H}_1$, suggests that

$$E_1 < \langle \phi_2 | \hat{H}_1 | \phi_2 \rangle. \tag{20}$$

According to Hohenberg and Kohn, the inequality holds for non-degenerate ground state. The equations shown above can alternatively be expressed as follows:

$$\langle \phi_2 | \hat{H}_1 | \phi_2 \rangle = \langle \phi_2 | \hat{H}_2 | \phi_2 \rangle + \langle \phi_2 | \hat{H}_1 - \hat{H}_2 | \phi_2 \rangle \qquad \text{and} \tag{21}$$

$$\langle \phi_2 | \hat{H}_1 | \phi_2 \rangle = E_2 + \int dr \left[V^1_{ext}(r) - V^2_{ext}(r) \right] n_o(r). \tag{22}$$

Following Eqs. (20) and (22),

$$E_1 < E_2 + \int dr \left[V^1_{ext}(r) - V^2_{ext}(r) \right] n_o(r). \tag{23}$$

If we started with E_2 instead of E_1 in Eq. (20), we would get

$$E_2 < E_1 + \int dr \left[V^2_{ext}(r) - V^1_{ext}(r) \right] n_o(r). \tag{24}$$

Combining the above two equations leads to a contradiction that $E_1 + E_2 < E_1 + E_2$. Therefore, the same non-degenerate ground-state density cannot be represented by two distinct external potentials. Up to a constant, $V_{ext}(r)$ and $n_o(r)$ (ground-state density) uniquely map into each other.

Theorem 2 *Ground-state density $n(r)$ of an interacting system subjected to an external potential $V_{ext}(r)$ reduces the energy functional $E[n]$ to its ground-state value. According to the first theorem, $n_o(r)$ defines $V_{ext}(r)$ and the system energy, and, hence, all of the ground-state properties.*

$$E[n] = G[n] + E_{ee}[n] + E_{Ne}[n] = L[n] + \int dr\, V_{ext}(r) n(r). \tag{25}$$

The quantities E_{Ne} and E_{ee} are referred to the energy contribution from electron–nuclei interaction and from electron–electron repulsion, respectively. The functional $L[n]$

$$L[n] = G[n] + E_{ee}[n] \tag{26}$$

is independent of $V_{ext}(r)$. The proof of this theorem lies in the variational principle. For example, there exist Hamiltonian $\hat{\overline{H}}$ and wavefunction $\overline{\phi}$ for a trial density $\overline{n}(r)$. If Hamiltonian $\hat{H}$, generated by a true V_{ext}, takes $\overline{\phi}$ and $\overline{n}(r)$ as trail functions, then

$$\langle \overline{\phi} | \hat{H} | \overline{\phi} \rangle = E[\overline{n}] \geq E_o[n] = \langle \phi_o | \hat{H} | \phi_o \rangle. \tag{27}$$

Hence, Eq. (25) reflects energy for $n_o(r)$, which is lower than $n(r)$ (any other density). In case of known $L[n]$, minimizing the total system energy as a function of $n(r)$ gives rise to the ground-state density and energy.

1.4 Kohn–Sham Equation

The Hohenberg–Kohn theorem proves that the total energy of a many-electron system is a functional of electron density. However, a clear expression of the energy functional is still unknown. Many useful approximations have been employed, but its precise form is still a mystery. Rewriting Eq. (25) leads to

$$E[n] = \int dr\, n(r)\, V_{ext}(r) + \langle \Phi[n] | \hat{G} + \hat{V_{ee}} | \Phi[n] \rangle, \tag{28}$$

where $\hat{G}$ and $\hat{V_{ee}}$ represent the kinetic energy and potential energy operators, respectively, owing to electron–electron interaction. The first and second terms are explicitly and implicitly density-dependent, respectively. With reference to the concept behind Kohn and Sham equations, splitting the second component gives Hartree and kinetic energies of the independent electrons, followed by an additional factor to account for the difference.

$$E[n] = \int dr\, n(r) V_{ext}(r) - \sum_i \int \Phi_i^*(r) \frac{\nabla^2}{2} \Phi_i(r) + \frac{1}{2} \int \int dr\, ds \frac{n(r)n(s)}{|r-s|} + E_{xc}[n]. \tag{29}$$

The above equation contains four terms: energy due to external potential, kinetic energy of an independent electron system, Hartree energy, and an additional term known as *exchange and correlation* energy E_{xc}.

The ground-state density, n_o, is the function that minimizes the energy functional, $E[n]$,

$$\left. \frac{\partial E[n]}{\partial n} \right|_{n_o} = 0. \tag{30}$$

Similar to Eqs. (12) and (14) under the orthonormalization condition, solution is based on a variational equation. The Kohn–Sham equations here are derived in the same way.

$$\left[-\frac{1}{2}\nabla^2 + V_{ext}(r) + V_H(r) + V_{xc}(r) \right] \Phi_i(r) = \epsilon_i \Phi_i(r), \tag{31}$$

where the exchange–correlation potential V_{xc} is given by

$$V_{xc}(r) = \left. \frac{\partial E_{xc}[n]}{\partial n} \right|_{n(r)}. \tag{32}$$

These equations serve as the foundation for first-principles calculations, and the complexity of Schrödinger equations has been significantly lowered from 3N dimensions to 3 dimensions in terms of electron charge density. An initial guess on charge density leads to calculated eigenvalues and, hence, provides eigenenergies and single-particle wavefunctions. Following that, the density employed in the first stage is determined. As a result, equations are self-consistently solved, as seen in Fig. 2. The inner loop searches for the minimal energy and ground-state density using self-consistent solutions of the Kohn–Sham equations. The outer loop, which is addressed classically, iterates through structural relaxation until the lowest-energy configuration is achieved.

1.5 Bloch Theorem

For periodic systems, such as crystalline solids in solid-state systems, it is advantageous to use the *Bloch theorem*. According to the theorem, the wavefunction of periodic systems can be written as the product of a plane wave and a function that has the same periodicity as the crystal.

$$\varphi_i(\vec{r}) \rightarrow \varphi_{ik}(\vec{r}) = e^{i\vec{k}.\vec{r}} w_{ik}(\vec{r}), \tag{33}$$

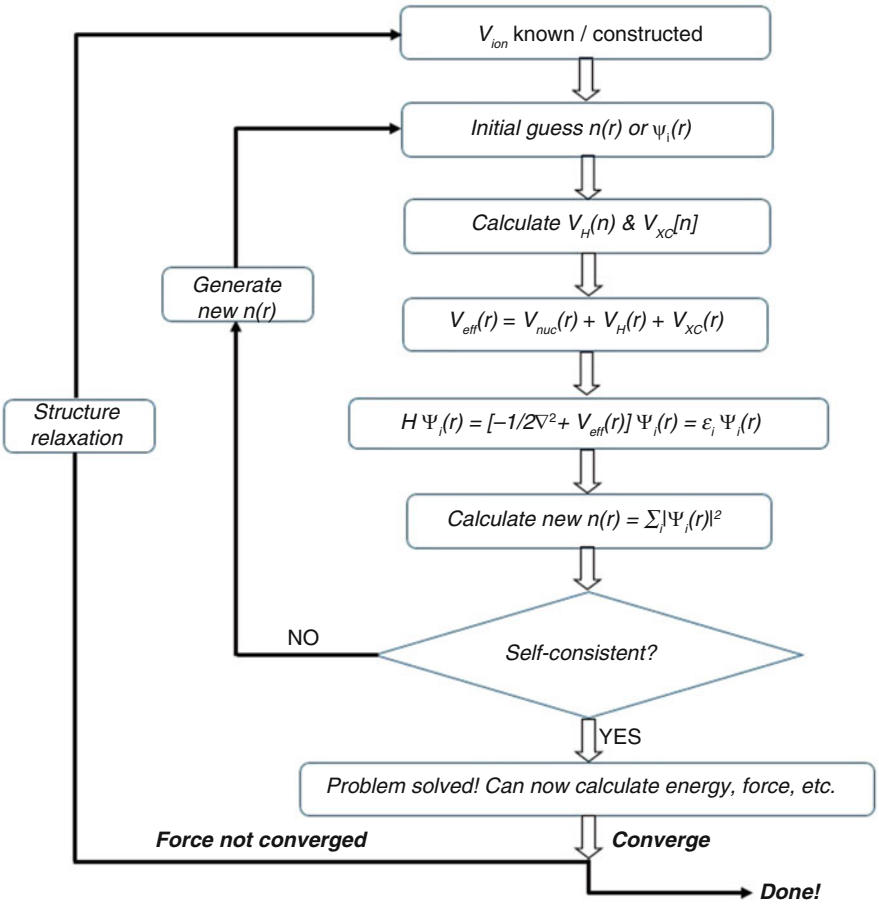

Fig. 2 A schematic of work flow of self-consistent loop for solving Kohn–Sham equations in first-principles calculations

where $w_{ik}(\vec{r})$ is the periodic function in the unit cell with wavevector $\vec{k}$ such that

$$w_{ik}(\vec{r} + \vec{R}) = w_{ik}(\vec{r}), \quad \text{for} \quad \tilde{R} = m_1\tilde{a_1} + m_2\tilde{a_2} + m_3\tilde{a_3}, \tag{34}$$

where (m_1, m_2, m_3) are integers. It is to be noted here that "i" in $e^{i\vec{k}.\vec{r}}$ is the imaginary unit, while "i" in φ_{ik} is the index. Implementing the Bloch wavefunction into Koh–Sham equation, Eq. (31) reduces to

$$\left[-\frac{1}{2}(\nabla + ik)^2\right] + V_{ext}(r) + V_H(r) + V_{xc}(r)]w_{ik}(r) = \epsilon_{ik}w_{ik}(r). \tag{35}$$

The normalization condition on the periodic part of the single-particle wavefunction suggests that each wavefunction can accommodate one electron per unit cell.

$$\int_{UC} |w_{ik}(r)|^2 dr = 1, \tag{36}$$

and the electron density is

$$n(r) = \sum_i \int_{BZ} \frac{dk}{\Omega_{BZ}} f_{ik} |w_{ik}(r)|^2, \tag{37}$$

where Ω_{BZ} and f corresponds to the Brillouin zone volume and the Fermi–Dirac distribution function, respectively.

2 Exchange and Correlation Functionals

Since the creation of Kohn–Sham equations, much effort has been spent on developing precise exchange and correlation functionals. Today under a variety of approximations, different functionals exist. Several prominent functionals in the solid-state domain have been addressed here.

2.1 Local Density Approximation (LDA)

As Kohn and Sham proposed, solids may often be regarded as being near to homogeneous electron gas. Because the exchange and correlation are local in the case of the homogeneous electron gas, this is referred to as the local density approximation. This approximation assumes that N non-interacting electrons are enclosed in a big box of volume V, such that the potential owing to nuclei is constant. For the said situation, a solution to the Schrödinger equation results in plane wave eigenstates with wavevectors ($\vec{k}$) and eigenvalues like

$$\Phi_k = \frac{1}{\sqrt{V}} exp(i\vec{k}.\vec{r}) \qquad \text{and} \tag{38}$$

$$\epsilon_k = \frac{|\vec{k}|^2}{2}. \tag{39}$$

The Fermi energy ϵ_F and the corresponding wavevector k_F are related as $\epsilon_F = k_F^2/2$. The electron density $n = N/V$ determines all the physical properties of the system, and the density-dependent k_F is

$$k_F = (3\pi^2 n)^{\frac{1}{3}}. \tag{40}$$

The exchange energy E_X is given by (in Hartree units)

$$E_X = -\frac{3}{4}\left(\frac{3}{\pi}\right)^{\frac{1}{3}} n^{\frac{4}{3}} V, \tag{41}$$

and the corresponding exchange potential is given by

$$V_x(r) = -\left(\frac{3}{\pi}\right)^{\frac{1}{3}} n^{\frac{1}{3}}(r). \tag{42}$$

The correlation energy of a homogeneous electron gas does not have a simple analytic expression. The correlation energy, on the other hand, was estimated for this basic model by solving the many-body Schrödinger equation using stochastic numerical techniques and parametrizing it with the Wigner–Seitz radius r_s

$$\frac{V}{N} = \frac{4\pi}{3} r_s^3 = \frac{1}{n}. \tag{43}$$

The exchange and correlation energy in local density approximation, E_{xc}^{LDA}, is given as

$$E_{xc}^{LDA}[n] = \int_r n(r)\ V_{xc}(n(r))dr = \int_r n(r)[V_x(n(r)) + V_c(n(r))]dr. \tag{44}$$

2.2 Generalized Gradient Approximation (GGA)

LDA, as discussed above, is dependent on the local electron density. However, GGA takes local density n and gradient ∇n into account to address how exchange and correlation function is affected. The mathematical expression of E_{xc}^{GGA} is

$$\begin{aligned} E_{xc}^{GGA} &= \int_r n(r)\varepsilon_{xc}(n, |\nabla n|, \ldots)dr \\ &\equiv \int_r n(r)\varepsilon_x^{hom}(n)L_{xc}(n, |\nabla n|, \ldots)dr, \end{aligned} \tag{45}$$

where L_{xc} is dimensionless and $\varepsilon_x^{hom}(n)$ is the exchange energy analogous to the term V_x in Eq. (42). The expansion of $L_x(n)$ in terms of reduced density gradient (s_k) of various orders is given by

$$L_x = 1 + \frac{10}{81}s_1^2 + \frac{146}{2025}s_2^2 + \ldots, \tag{46}$$

whereas

$$s_k = \frac{|\nabla^k n|}{(2k_F)^k n} = \frac{|\nabla^k n|}{2^k (3\pi^2)^{k/3} (n)^{1+k/3}}. \tag{47}$$

Numerous flavors of GGA exist as Perdew and Wang (PW91), Perdew, Burke, and Ernzerhof (PBE), and PBE for solids (PBEsol)) [2–4] to accurately predict material properties.

The contribution of correlation energy functional to total energy is often considerably less than the exchange energy but still significant. The lowest order gradient expansion at high density was established by Ma and Brueckner [5]. The variation in correlation energy is in such a way that it drops in magnitude and eventually dissipates at high density. Such behavior is understandable with the fact that significant density gradients correlate to strong confining potentials, which enhance the allowed energy level separation and decrease the interactions in comparison to terms relating to independent electrons.

2.3 Hybrid Functionals

The GGA functionals use semi-local approximations of the exchange–correlation energy. However, they are not without flaws. They routinely underestimate the band gaps of semiconductors and insulators in comparison to experimental values [6–8]. Additionally, these functionals overstate the effects of electron delocalization and fall apart for certain systems with partly occupied d and f electrons. Hybrid functionals, on the other hand, have been proven to somewhat overcome the constraints of semi-local functionals [9–13].

Hybrid functionals are constructed by combining a portion of the actual Hartree–Fock exchange with LDA or GGA exchange energy. However, these energy functionals have a substantially higher computational cost than LDA or GGA functionals, owing to the non-local nature of the Hartree–Fock exchange. Numerous formulations of hybrid functionals have been proposed, and some of them are addressed below. PBE0 hybrid functionals combine 25% of the Hartree–Fock exchange energy with 75% of the PBE exchange energy in order to calculate the overall exchange energy [14]. The correlation component of the functional is identical to the PBE correlation component

$$E_{xc}^{PBE0} = \frac{1}{4} E_x^{HF} + \frac{3}{4} E_x^{PBE} + E_c^{PBE}. \tag{48}$$

The Hartree–Fock exchange has a substantial computing cost and cannot be used on bigger systems. The screened hybrid functional of Heyd, Scuseria, and Ernzerhof (HSE) [15–17] is an alternative to standard hybrid functionals. In HSE, the decay of the Hartree–Fock exchange interaction is accelerated by substituting a screened

Coulomb interaction for the complete $1/r$ Coulomb interaction. The exchange component of HSE functionals is classified as short range (SR) or long range (LR) as follows:

$$\frac{1}{r} = \frac{1 - erf(\nu r)}{r} + \frac{erf(\nu r)}{r}, \tag{49}$$

where ν is the screening parameter and $erf(y)$ is the error function defined as $erf(y) = \frac{2}{\sqrt{\pi}} \int_0^y e^{-k^2} dk$. Both the first and second parts define the short-range (SR) and the long-range (LR) components, respectively. The exchange–correlation energy E_{xc} is therefore calculated as

$$E_{xc}^{HSE} = aE_x^{HF,SR}(\nu) + (1-a)E_x^{PBE,SR}(\nu) + E_x^{PBE,LR}(\nu) + E_c^{PBE}. \tag{50}$$

The terms $E_x^{HF,SR}$, $E_x^{PBE,SR}$, $E_x^{PBE,LR}$, and E_c^{PBE} correspond to the SR Hartree–Fock exchange, SR PBE exchange, long-ranged PBE exchange, and PBE correlation energy, respectively. The perturbation theory [14] derives the mixing parameter $a = 1/4$, and its value is sometimes altered in order to fine-tune the estimated electronic properties (i.e., band gap) of semiconductors. The optimal value of ν is between 0.2 $Å^{-1}$ (for HSE06) and 0.3 $Å^{-1}$ (for HSE03) [15, 16, 18, 19]. Besides, $\nu = 0$ and $\nu \to \infty$ correspond to PBE0 and PBE functional, respectively.

References

1. A. Sharan, *Electronic Properties of Semiconductors and Energy Materials from Density Functional Theory* (University of Delaware, Newark, 2019)
2. J.P. Perdew, Y. Wang, Accurate and simple analytic representation of the electron-gas correlation energy. Phys. Rev. B **45**, 13244–13249 (1992)
3. J.P. Perdew, K. Burke, M. Ernzerhof, Generalized gradient approximation made simple. Phys. Rev. Lett. **77**(18), 3865–3868 (1996)
4. G.I. Csonka, J.P. Perdew, A. Ruzsinszky, P.H.T. Philipsen, S. Lebègue, J. Paier, O.A. Vydrov, J.G. Ángyán, Assessing the performance of recent density functionals for bulk solids. Phys. Rev. B **79**, 155107 (2009)
5. S.K. Ma, K.A. Brueckner, Correlation energy of an electron gas with a slowly varying high density. Phys. Rev. **165**, 18–31 (1968)
6. J.P. Perdew, M. Levy, Physical content of the exact Kohn-Sham orbital energies: Band gaps and derivative discontinuities. Phys. Rev. Lett. **51**, 1884–1887 (1983)
7. J.P. Perdew, Density functional theory and the band gap problem. Int. J. Quantum Chem. **28**(S19), 497–523
8. M. Grüning, A. Marini, A. Rubio, Density functionals from many-body perturbation theory: the band gap for semiconductors and insulators. J. Chem. Phys. **124**(15), 154108 (2006)
9. R.L. Martin, F. Illas, Antiferromagnetic exchange interactions from hybrid density functional theory. Phys. Rev. Lett. **79**, 1539–1542 (1997)
10. T. Bredow, A.R. Gerson, Effect of exchange and correlation on bulk properties of MgO, NiO, and CoO. Phys. Rev. B **61**, 5194–5201 (2000)

11. J. Muscat, A. Wander, N.M. Harrison, On the prediction of band gaps from hybrid functional theory. Chem. Phys. Lett. **342**(3), 397–401 (2001)
12. P.J. Hay, R.L. Martin, J. Uddin, G.E. Scuseria, Theoretical study of CeO2 and Ce2O3 using a screened hybrid density functional. J. Chem. Phys. **125**(3), 034712 (2006)
13. K.N. Kudin, G.E. Scuseria, R.L. Martin, Hybrid density-functional theory and the insulating gap of uo_2. Phys. Rev. Lett. **89**, 266402 (2002)
14. J.P. Perdew, M. Ernzerhof, K. Burke, Rationale for mixing exact exchange with density functional approximations. J. Chem. Phys. **105**(22), 9982–9985 (1996)
15. J. Heyd, G.E. Scuseria, M. Ernzerhof, Hybrid functionals based on a screened Coulomb potential. J. Chem. Phys. **118**(18), 8207 (2003)
16. J. Heyd, G.E. Scuseria, M. Ernzerhof, Erratum: "Hybrid functionals based on a screened Coulomb potential" [J. Chem. Phys. **118**, 8207 (2003)]. J. Chem. Phys. **124**(21), 219906 (2006)
17. J. Heyd, G.E. Scuseria, M. Ernzerhof, Erratum: Hybrid functionals based on a screened Coulomb potential (J. Chem. Phys. (2003) 118 (8207)). J. Chem. Phys. **124**(21), 2005–2006 (2006)
18. J. Heyd, G.E. Scuseria, Efficient hybrid density functional calculations in solids: assessment of the Heyd–Scuseria–Ernzerhof screened Coulomb hybrid functional. J. Chem. Phys. **121**(3), 1187–1192 (2004)
19. A.V. Krukau, O.A. Vydrov, A.F. Izmaylov, G.E. Scuseria, Influence of the exchange screening parameter on the performance of screened hybrid functionals. J. Chem. Phys. **125**(22), 224106 (2006)

Rare Earth Element-Based Nonenzymatic Glucose Sensor

Yogesh M. Chitare, Vikas V. Magdum, Satish B. Jadhav, Shirin P. Kulkarni, Chandrakant D. Lokhande, and Jayavant L. Gunjakar

Abbreviations

AA	Ascorbic acid
ACM	Activated chemisorption model
CV	Cyclic voltammetry
DA	Dopamine
FE-SEM	Field emission scanning electron microscope
Fru	Fructose
GCE	Glassy carbon electrode
IHOAM	Incipient hydrous oxide adatom mediator model
Lac	Lactose
LOD	Limit of detection
MOH	Metal hydroxide
PBS	Phosphate buffer solution
PVP	Polyvinyl pyrrolidone
REEs	Rare earth elements
RGO	Reduced graphene oxide
RSD	Relative standard deviation
SWV	Square wave voltammetry
UA	Uric acid

Y. M. Chitare · V. V. Magdum · S. B. Jadhav · S. P. Kulkarni · C. D. Lokhande (✉) · J. L. Gunjakar (✉)
Centre for Interdisciplinary Research, D. Y. Patil Education Society (Institution Deemed to be University), Kolhapur, India

F. I. Ezema et al. (eds.), *Chemically Deposited Metal Chalcogenide-based Carbon Composites for Versatile Applications*, https://doi.org/10.1007/978-3-031-23401-9_14

1 Introduction

Today's fast-moving world has a rose the lifestyle of the human being to a significantly level causing a tremendous change in habits, daily routines, and eating as well as drinking patterns. This has resulted in the spreading of various kinds of diseases in humans irrespective of their age. As a result, nowadays, there is an enormous increment in the death rates of adults and nonadults due to stroke, heart attack, asthma, different types of cancer, etc. [1]. Along with these diseases, diabetes has spread its root so strong all over the world that every country has a tremendously larger number of diabetic patients that includes people of all age groups [2–4]. According to a survey, in 2017, 425 million people were diagnosed with diabetes and by 2045, 48% hike in the number is expected with 629 million diagnosed patients. According to the World Health Organization, an individual consuming more than 25 g of sugar per day for a prolonged time period possesses higher possibility to diagnose with diabetes [5]. The diabetes patient is characterized by measuring the glucose level in their blood sample. The glucose level for a normal person is 3.9–6.2 (empty stomach) or 3.9–7.8 (2 h after food) mM above which is considered a diabetic patient. These numbers are very scary that many medical field experts are worrying about the uncontrollable growth rate in the number of diabetic patients because diabetes is one of the major causes behind deaths as well as disability. In addition, numerous worsening effects of diabetes result in heart failure, blindness, kidney failure, stroke, birth defects, etc. [6–8].

This furious condition of diabetes has recently turned considerable attention toward the research and development in the field of glucose sensing that can help early detection of glucose concentration in the blood. It is well known that glucose is one of the important constituents of the blood, and diabetes is checked by evaluating the glucose level in the blood [9–11]. However, currently available glucose-monitoring techniques are costly that it is not possible for everyone to check the glucose level on daily basis. This may result in a sudden hike or deprivation in the glucose level of the patient depending on their health. Therefore, it is of prime importance to continuously monitor the glucose level in the blood sample of the patient.

So far, many techniques are being used for the detection of glucose levels in the blood such as optical, electrochemical, colorimetry, and conductometry, where recently electrochemical glucose sensors are largely explored due to their fast response, higher sensitivity, excellent stability, and lower limit of detection (LOD) [12]. There are some important requirements that need to be accomplished by an electrode to become an ideal glucose-sensing electrode. The sensor should exhibit good sensitivity even at LOD. It should have fast and relevant changes toward the changing glucose concentration, low cost of fabrication, easy to use, and noninvasive and possess long cycle life [13].

Despite having such fascinating properties that are useful for electrochemical applications, very scarce literature is found on the application of rare earth elements (REEs) for electrochemical glucose sensing. Therefore, this chapter focuses on the

electrochemical nonenzymatic glucose sensor (NEGS) performance exhibited by various REEs. Their mechanism, working, and sensing performance are presented.

2 History of Glucose Sensor

The first ever electrochemical glucose sensing dates back to 1962 when Clarke and Lyons [14] demonstrated enzyme-based glucose-sensing performance of an oxygen electrode. Later, their patent showed the effective utilization of enzymes for the conversion of electro-inactive substance to electro-active surface, which can sense glucose. This glucose sensor has been considered as first-generation glucose sensor. This sensor was based on a semipermeable dialysis membrane sandwiched between two electrodes. One electrode contained at least one enzyme that could convert electro-inactive-interfering species into electro-active. On the other hand, the other electrode was used to measure the reading of interfering species that afterward subtracted from the reading of the first electrode to obtain the current originated due to the enzyme-based glucose-sensing electrode [15].

The first-generation glucose sensors were based on the production of H_2O_2 during enzymatic processes, which required high operating potentials for the sensing. In addition, the solubility of oxygen is restricted in the biomolecules that resulted in the fluctuation in the amperometric measurement creating oxygen tension [16]. The abovementioned drawbacks of first-generation glucose sensors were overcome by mediator-based second-generation glucose sensors where mediator worked as an electron acceptor. In this case, mediator was used to replace the oxygen of first-generation glucose sensor. The mediator worked as redox mediator, which could take electrons from enzyme to transfer them to the surface of the working electrode. Due to these redox reactions, amperometric signals are generated, which were used to detect the presence of glucose molecules [17]. Various materials employed as redox mediator include tetracyanoquinodimethane, ferricyanide, tetrathialfulvalene, ferrocene, and quinines. The first report on mediator-based glucose sensors was published in 1970 [18].

The leakage from the mediator hindered the applicability of the second-generation glucose sensor and brought forward the third generation of glucose sensors, which were independent of the electron mediator [12]. This resulted in the direct electron transfer between the enzyme and the electrode. Due to this, third-generation glucose sensors enabled implementable needle-like sensors for in vivo glucose monitoring. The mediatorless assembly resulted in the enhanced sensitivity of the sensor material [19–21].

Apart from these generations, the currently used continuous glucose-monitoring system has found way more advancement in the field of real-time glucose monitoring and control. This system is primarily based on the insulin release system in the body and is very advantageous to controlling diabetes [22]. The timeline of the development of the glucose sensor is listed in Table 1.

Table 1 Timeline of glucose sensor

S. n.	Year	Timeline
1	1962	Concept of biosensor by Clarke and Lyons
2	1967	First enzyme-based electrode by Updike and Hicks
3	1973	H_2O_2-based glucose enzyme-mediated electrode
4	1975	First commercial biosensor (Yellow Springs Instrument analyzer)
5	1982	First needle-like enzyme electrode
6	1984	First ferrocene-mediated amperometric electrode
7	1987	MediSense ExacTech blood glucose biosensor
8	1999	Commercial in vivo glucose meter
9	2000	Wearable noninvasive glucose sensor

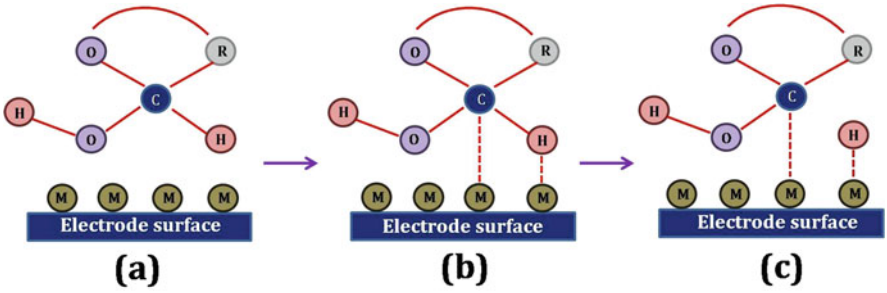

Fig. 1 Schematic representation of ACM, where M is metal atom, O is oxygen, H is hydrogen, C is hemiacetalic carbon atom, and R is other glucose molecule component

3 Mechanism of Glucose Sensor

The enzyme-based glucose sensors suffer from various disadvantages like chemical and thermal stability, pH, humidity, and costliness. Therefore, NEGS are introduced in which nanostructured inorganic materials are employed for the electrooxidation of glucose molecules upon adsorption on the surface of the active electrode [23]. The glucose sensing by NEGS can be explained using two different mechanisms, namely. Activated chemisorption model (ACM) and incipient hydrous oxide adatom mediator model (IHOAM).

The ACM is based on the adsorption of glucose molecules on the surface of the active material (Fig. 1a). When glucose molecules are adsorbed on the surface of the active materials, abstraction of hydrogen occurs, which allows chemical adsorption of glucose molecules that enhance the rate of glucose oxidation as shown in Fig. 1(b and c). Various nanostructured materials with high surface area possess higher density of chemically active sites, which oxidize the glucose molecules. However, this model could not explain the role of hydroxyl radicals generated during the oxidation process [24, 25].

In that context, the role of hydroxyl radicals generated during the oxidation of glucose molecules is explained by IHOAM. In this model, it is explained that a pre-

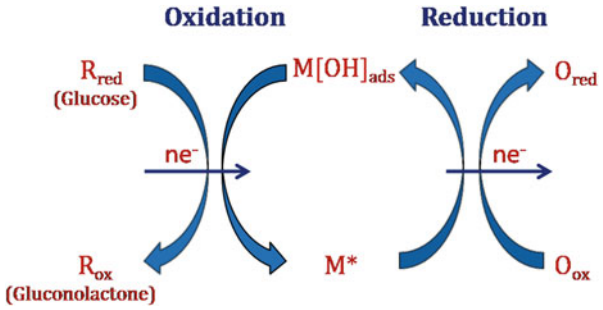

Fig. 2 Schematic representation of IHOAM, where $M[OH]_{ads}$ and M* are adsorbed hydroxide anion and reductive metal adsorption site, R is glucose molecule, and O is oxygen, respectively

monolayer of surface-oxidized metal atoms is formed on the surface of the active material, which further generates hydroxyl radicals [26]. The [OH]ads layer acted as mediator in oxidation and inhibitors in reduction reaction as shown in Fig. 2. It is well known that hydroxide ions are formed upon the dissociation of water. Therefore, metal ion forms bond with hydroxide anions to form metal hydroxide, which is helpful for the oxidation of glucose [6, 27]. In addition, an alkaline medium can provide plenty of hydroxide anions; therefore, a higher oxidation rate of glucose can be achieved when the reaction is carried out in an alkaline medium. The schematic of IHOAM model is shown in Fig. 2.

4 Rare Earth Elements (REEs)

REEs are a class of chemical elements in the periodic table belonging to the lanthanide series containing a total of 17 elements. Out of 17 elements, 15 elements are in between 57 and 71 atomic numbers, and remaining two elements, scandium and yttrium having atomic numbers of 21 and 39, respectively, are also commonly considered as REEs due to their physicochemical characteristics associated with the lanthanides. The lanthanide series contains many of the most important elements that are widely used in our modern-day technological devices and various electronic equipment. The demand for REEs is increasing worldwide as these possess some important characteristics such as large atomic magnetic moments, 4f-electron structures, and strong spin-orbit coupling. When REEs react with other elements to form complexes, their coordination number can be varied from 3 to 12, and it can acquire various oxidation states. Also, they are more inexpensive than other noble metals like Au and Pt. Therefore, REEs are commonly applied in every aspect of life. In recent years, various research institutes and industrialists are jointly working together on REEs to increase their applicability in the field of energy storage, electronics, high-tech military components, etc. REEs are being used in large scale in the electrochemical field as it possesses multiple transition energy levels [28–30].

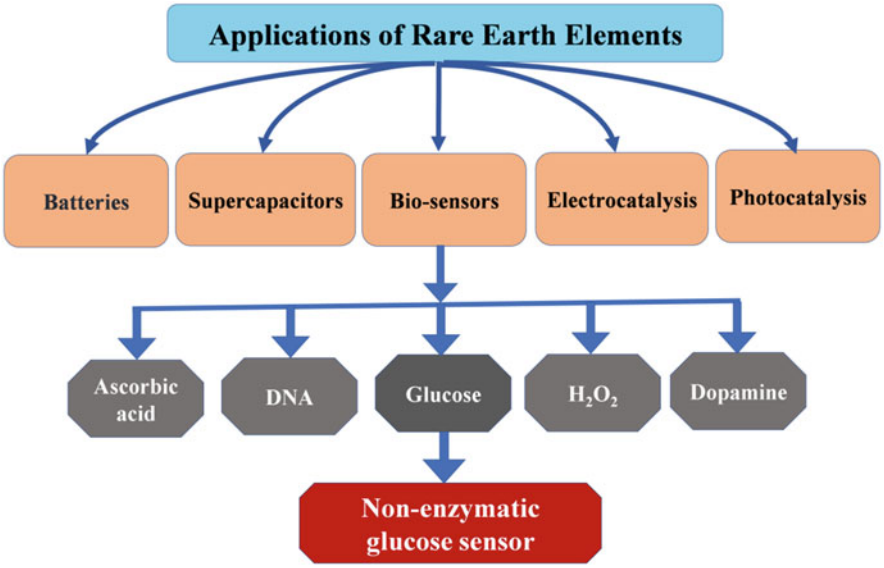

Fig. 3 Applications of REEs in various fields (particularly NEGS)

The electrochemical behavior of REEs depends on their shape, size, structure, morphology, and composition with other materials. REEs and their derivative components have received noticeable attention in the field of batteries [31], supercapacitor [32, 33], sensors [34], electrocatalyst [35], and photocatalyst [36] represented in Fig. 3. It also shows the use of REEs toward NEGS.

5 Rare Earth Elements for Nonenzymatic Glucose Sensor

All REEs have stable chemical states of 3+ except Ce and Tb. Their excellent electrochemical properties help to fabricate efficient and low-cost NEGS. Below literature review explains the work done so far using REEs for the NEGS.

The electrodeposition method was applied for the deposition of various metal oxide thin films on different substrates. Potentiostatic electrodeposition method was applied to deposit lanthanum oxide (La_2O_3) thin film on a stainless-steel substrate. For this, 0.01 M lanthanum nitrate hexahydrate ($La(NO_3)_3.6H_2O$) electrolyte was prepared and applied constant working potential of −1.0 V for 1 h to obtain whitish-colored La_2O_3 thin film on the desired substrate. The deposited film showed a monoclinic structure with vertically aligned interconnected irregular nanosheets-like morphology of an average length of 1.1 μm. Such nanosheet-like morphology is beneficial to decrease the contact resistance and enhance the performance due to the large surface area and appropriate surface-to-volume ratio. The specific surface area

was found to be 14.17 $m^2\ g^{-1}$. The electrocatalytic performance toward the glucose oxidation was studied in the potential between 0 and 0.5 V in an aqueous 1 M KOH solution. The La_2O_3 electrode showed good linear response toward glucose concentration in the range between 1.25 and 3.75 mM and exhibited maximum sensitivity of 616 $\mu A\ mM^{-1}\ cm^{-2}$, quick response within 1 s, and LOD of 0.27 mM. The selectivity test was examined toward various interfering species like fructose (Fru), lactose (Lac), and ascorbic acid (AA), which showed less current response to the interfering species than that of glucose. The reproducibility and stability tests have shown acceptable reproducibility with relative standard deviation (RSD) of 2.5% and long stability retaining 8% over 4000 s at 1 mM glucose concentration [37].

The nanoflake-like morphology with an average length of 1.3 μm and thickness from 50 to 130 nm was observed for Ag-composited La_2O_3 synthesized by electrodeposition method. To deposit Ag-composited La_2O_3 thin film, 10 mM solution of $AgNO_3$ and $(La(NO_3)_3.6H_2O)$ were mixed in the volumetric ratio of 10:90. A schematic representation of the electrodeposition method of La_2O_3 and Ag-La_2O_3 is shown in Fig. 4i. From x-ray diffraction study, no significant difference occurred between pristine La_2O_3 and Ag-La_2O_3. With Ag-La_2O_3 thin-film electrode, the specific surface area was enhanced to 22.45 $m^2\ g^{-1}$ from the pristine La_2O_3 (14.17 $m^2\ g^{-1}$), which results in enhancement of sensitivity toward glucose oxidation. The staircase-like graph shown in Fig. 4ii is produced due to the injection of increasing concentration of glucose in NaOH electrolyte. The Ag-La_2O_3 electrode showed maximum sensitivity of 1677 $\mu A\ mM^{-1}\ cm^{-2}$, which was greater than pristine La_2O_3 (616 $\mu A\ mM^{-1}\ cm^{-2}$). The maximum response was gained between 0.1 and 0.6 mM glucose concentration. The enhancement in sensitivity was due to Ag, which facilitates the fast transport of charge carriers and large number of active sites due to higher specific surface area. The LOD was obtained to be 0.62 μM. The selectivity test to check the effect of different interfering species such as Lac, Fru, AA, and dopamine (DA) on the glucose-sensing performance was conducted. Moreover, composite electrode showed long-term stability over 3600 s [38].

Physical method such as pulsed laser deposition was used to deposit CeO_2/Au nanostructured electrode on carbon paper substrate. The CeO_2 electrodes were synthesized by using different background gas pressure. It was observed that background gas pressure affects the surface morphology of Au-deposited CeO_2 electrodes where smooth and closed topography structure was obtained under vacuum conditions. Two different techniques, namely, cyclic voltammetry (CV) and square wave voltammetry (SWV), were used to check the electrocatalytic performance of glucose by synthesizing CeO_2/Au electrodes under various background gases. Among all these electrodes, CeO_2/Au electrode deposited under 10 mTorr of oxygen showed maximum current response through the CV technique. Such optimized electrode showed maximum sensitivity of 27 $\mu A\ mM^{-1}\ cm^{-2}$ in the concentration range of 0.01–15 mM and LOD of 10 μM. To explore improvements in the sensitivity, the SWV technique was also used. It was found that, as glucose

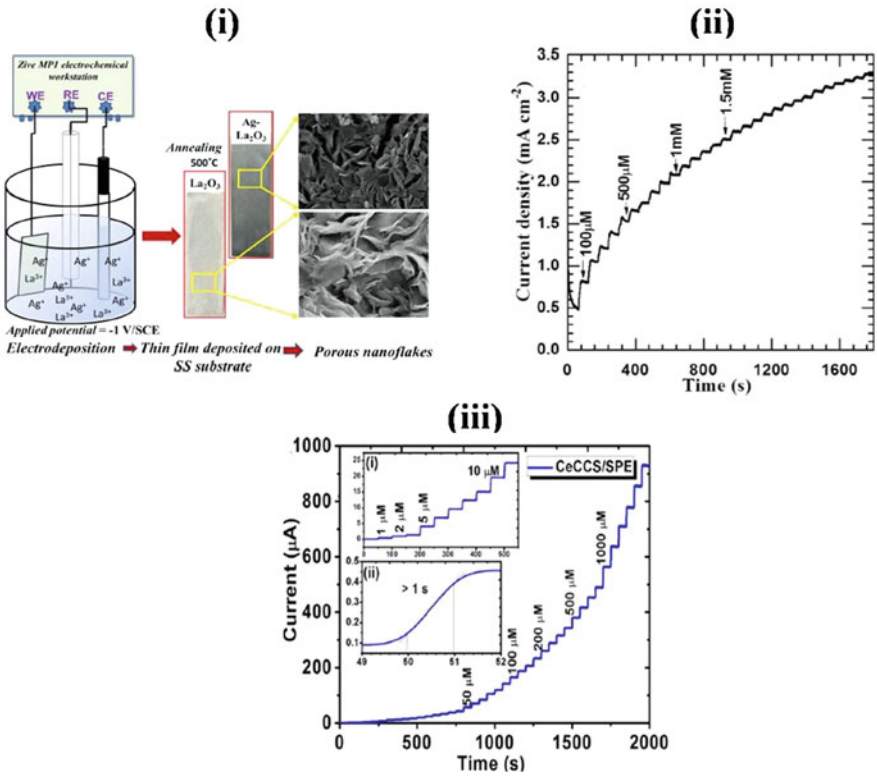

Fig. 4 (i) Schematic of electrodeposition method of La_2O_3 and Ag-doped La_2O_3, (ii) current versus time (i-t) graph of addition of various concentrations of glucose at a time interval of 60 s. (Reprinted with permission from ref. [38]. Copyright 2021, Elsevier). (iii) Steady-state amperometric current-time (i-t) curve for CeO_2@CuO core-shell nanostructures (inset: 1–10 μM glucose concentration). (Reprinted with permission from ref. [41]. Copyright 2018, Elsevier)

concentration changes, the current response also changes linearly up to 20 mM and sensitivity enhances to 44 μA mM^{-1} cm^{-2}, which was larger than the above reported CV techniques [39].

A glassy carbon electrode (GCE) was used to cast Au nanoparticles on CeO_2-modified electrode by electrochemical (chronoamperometry) method between −0.6 and 0.6 V potential for 60 min at 50 mV s^{-1} scan rate. Initially, CeO_2 crystals were dropped on GCE followed by chitosan (0.2 wt %) addition. Then, CeO_2-modified electrode (CTS/CeO_2) was immersed in 0.01 M $HAuCl_4$ to deposit Au nanoparticles. The surface morphology of CeO_2 electrode showed crystals of CeO_2 aggregated in irregular lumps (average size 2 μM), and Au modified CeO_2 (Au/CTS/CeO_2) electrode showed a layer of Au nanoparticles on the aggregated CeO_2 crystals. The Au/CTS/CeO_2 electrode showed well linearity between 0.02 and 0.6 mM, maximum sensitivity of 1076.71 μA mM^{-1} cm^{-2}, and LOD of 6.89 μM. It showed good selectivity toward various interfering species as well as excellent

stability above 95% of the current response to its original after 30 days. The stability test checked for various temperatures (0, 25, 60, and 80 °C) indicated temperature independency of the electrode [40].

Core-shell nanostructured CeO_2@CuO electrode synthesized by bio-mediated method was used to evaluate the NEGS properties. For the synthesis of CeO_2@CuO, at first, *Ocimum tenuiflorum* leaf extract was added to cerium nitrate solution at 393 K for half an hour. Different wt% of copper nitrate was added: at a temperature of 393 K to get CeO_2@CuO core-shell nanostructure and calcinated at 450 °C to obtain crystalline shell. The CeO_2@CuO core-shell nanostructured electrode synthesized with 0.4 wt % showed maximum current response in 0.1 M NaOH as well as maximum electrocatalytic activity of core CeO_2 and shell CuO. The amperometric current response of glucose sensing at various concentrations (1–1000 μM) is shown in Fig. 4iii. The optimized electrode displayed a good linear response between 0.001 and 0.0089 mM concentration, 0.019 μM LOD, and 3319.83 μA mM^{-1} cm^{-2} sensitivity. The maximum sensitivity was ascribed due to core-shell morphology that possesses higher surface area, which enhanced the electrocatalytic activity by providing enough number of active sites. The synthesized electrode showed good selectivity toward AA, DA, and uric acid (UA) with RSD of 2.66. The electrode used to evaluate glucose concentration in human blood samples showed good agreements with data measured by volunteer's sample (Accu-Check performa), indicating its promising candidature for NEGS [41].

CuO-decorated CeO_2 nanocomposites were developed by wet-impregnation method on conducting glass substrate. The TEM study showed the size of nanoparticles found to be approximately 20–50 nm. The highest current response toward oxidation of glucose was observed for CuO/CeO_2 nanocomposite. The amperometric response of the developed sensor was checked in 0.1 M phosphate buffer solution (PBS) at 0.4 V working potential. The CuO/CeO_2 nanocomposite exhibited a sensitivity of 2.77 μA mM^{-1} cm^{-2}, response time of 5–8 s, and LOD of 10 μM. The sensitivity was obtained toward only CuO/CeO_2 nanocomposite by considering that the role of CeO_2 and CuO was only to accelerate the electron and dominate redox reaction of glucose, respectively. It also showed acceptable stability with 80% retention of its original value (after 20 days) and good performance in recovery toward real sample analysis [42].

The hydrothermal method was employed for the synthesis of ZnO-CeO_2 nanocomposite electrode using petal carbon as template. The nanocomposites were immobilized on GCE. The ZnO nanoparticles (5 nm diameter) were anchored on the whiskers body. The length and diameter of whiskers were several hundreds and 10–15 nm, respectively. The ZnO-CeO_2 nanocomposites exhibited higher specific surface area of 550.9 m^2 g^{-1}. The differential pulse voltametric technique applied to evaluate the glucose sensing performance in 0.1 M PBS solution showed an excellent linear response between 0.5 and 300 μM concentrations and LOD of 0.224 μM [43].

The hybrid nanocomposite of a nanoceria-nanoplatinum-graphene (nCe-nPt-RGO) electrode was synthesized by sonoelectrodeposition followed by spin coating method for mediator-free enzymatic biosensors. Amorphous-natured nanoplatinum

(nPt) clusters were formed on the electrode surface by the sonoelectrodeposition method. A suspension consisting mixture of CeO_2 nanoparticles and graphene was coated on nPt-modified electrode using spin coating. The hybridized nCe-nPt-RGO nanocomposite developed sandwich-like structure showed the highest electrocatalytic activity. The sensitivity of nCe-nPt-RGO nanocomposite electrode was found to be 66.2 ± 2.6 μA mM^{-1} cm^{-2}. The response time and LOD were 6.3 ± 3.4 s and 1.3 ± 0.6 μm, respectively. The performance of this hybridized nanocomposite was lower than the previously discussed CeO_2-modified electrode with Au nanoparticles [44].

It is noteworthy to mention that the perovskite with general formula ABO_3 containing REEs has been widely explored for the application of NEGS. Perovskites possess unique structural features that changing the element of A site can significantly affect the performance of the material. For example, the perovskite-structured $LaNiO_3$ nanofibers and $NdNiO_3$ nanoparticles were synthesized by electrospinning and hydrothermal method, respectively. No difference occurs in their morphology of $La(NO_3)_3$/$Ni(Ac)_2$/PVP nanofibers and calcinated $LaNiO_3$ nanocomposites, but the average diameter of nanofibers was reduced from 400 nm to 140 nm due to decomposition of $La(NO_3)_3$ and $Ni(Ac)_2$ as well as degradation of polyvinyl pyrrolidone (PVP) after calcination. The electrode exhibited linear response in the range between 1 and 1000 μM. It showed sensitivity, response time, and LOD of 42.321 μA mM^{-1} cm^{-2}, 4 s, and 0.32 μM, respectively [45].

The $NdNiO_3$ nanoparticles were synthesized by using different concentrations (5, 10, and 15 mM) of $NiCl_2$. The high- and low-resolution field emission scanning electron microscope (FE-SEM) images of synthesized samples are shown in Fig. 5a–f. Figure 5 displays low (a, b), equal (c, d), and high (e, f) distribution of nanoparticles on Nd surface. It was found that $NdNiO_3$ synthesized with 10 mM concentration of $NiCl_2$ ($NdNiO_3$–2) showed higher response toward glucose oxidation than that of the other two synthesized electrodes due to uniform distribution of nanoparticles of size ranges between 60 and 120 nm. The chronoamperometry method was used to study the glucose-sensing performance of $NdNiO_3$-2 electrode. It showed good linear response in the concentration between 0.5 μM and 4.6 mM with correlation coefficient of 0.9985 displayed in Fig. 5g. The sensor showed maximum sensitivity and LOD of 1105.1 μA mM^{-1} cm^{-2} and 0.3 μM, respectively. The superior performance of $NdNiO_3$ electrode was due to high electrical conductivity as well as improved rate of electron transfer between electrolyte and electrode. The $LaNiO_3$ and $NdNiO_3$–2 electrodes demonstrated current response of 92.9% (after 4 weeks) and 94.46% (after 15 days) of its initial current, respectively, indicating high stability of both electrodes. The $LaNiO_3$ (RSD 5.23%) and $NdNiO_3$–2 (RSD 3.2%) also showed superior reproducibility. The $NdNiO_3$–2 was used for the evaluation of human blood sample, which indicated suitability for the practical applications of the glucose sensor [46].

The non-stiochiometric $LaNi_{0.6}Co_{0.4}O_3$ (LNC) and $Co_{0.4}Fe_{0.6}LaO_3$ (CFL) nanoparticles were synthesized by the sol-gel method. To make the gel of LNC and CFL, the solution mixture consists of 0.1 M lanthanum nitrate and cobalt nitrate added with 0.1 M nickel nitrate and iron nitrate, respectively. The mixture

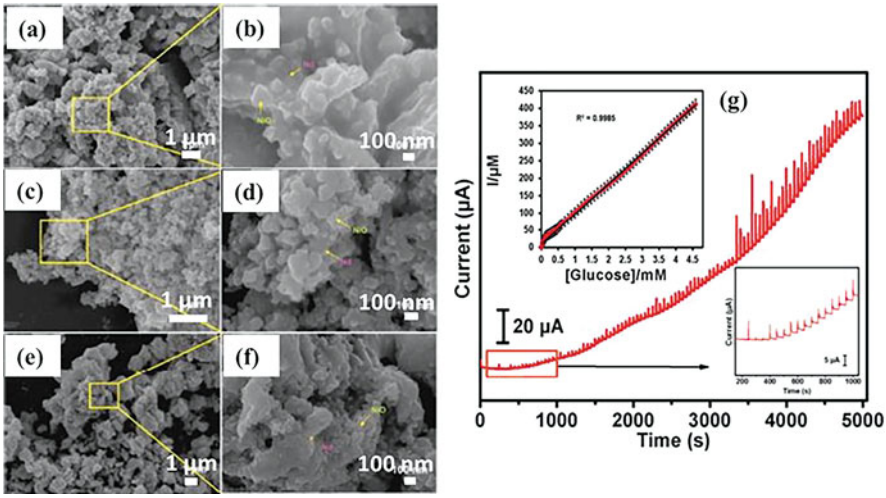

Fig. 5 FE-SEM images for (**a**, **b**) $NdNiO_3$–1, (**c**, **d**) $NdNiO_3$–2 and (**e**, **f**) $NdNiO_3$–3. (**g**) amperometric i-t curve for $NdNiO_3$–2. (Reprinted with permission from ref. [46]. Copyright 2017, Royal Society of Chemistry)

was heated at 80 °C for 12 h, and then the resulted gel was dried at 200 °C. Finally, the prepared products were calcinated at different temperatures. After optimizing the conditions, the LNC and CFL electrodes showed maximum current response within 3 s and 4 s, respectively. The current-time plot of LNC electrode obtained from the addition of different glucose concentrations is shown in Fig. 6i. The current response had only one linear relationship between 0.05 and 200 μM concentration for LNC electrode, while two linear relationships (0.05–5 μM and 5–500 μM) were obtained for CFL electrode, which may be due to adsorption of intermediates. The LNC electrode displayed maximum sensitivity of 642.78 μA mM^{-1} cm^{-2}, which is lower than CFL electrode (1013.8 μA mM^{-1} cm^{-2}), and LOD was lower for LNC (0.008 μM) than CFL (0.01 μM) electrode. The highest sensitivity of CFL electrodes may be due to higher surface area as well as presence of highly active sites. Both electrodes showed long-term stability over a period of 3 weeks as well as reproducibility with calculated RSD of 2.7. Moreover, the LNC electrode was employed to check that the glucose level in human blood serum showed not much difference between the values determined by a standard instrument and synthesized electrode [47, 48].

The perovskite-type oxide of $La_{0.6}Sr_{0.4}FeO_{3-\delta}$ (LSF) and $La_{0.6}Sr_{0.4}Co_{0.2}Fe_{0.8}O_{3-\delta}$ (LSCF) was synthesized by sol-gel technique. Carbon screen-printed electrode was used to fabricate sensors. The surface morphology for both electrodes appeared to be highly porous structures with agglomerates composed of about 100 nm particle size. The electrocatalytic activity of both electrodes was tested in 0.1 M KOH. Both electrodes showed enhanced response than that of bare carbon electrode. The LSCF electrode showed improved electrocatalytic activity due to the addition of cobalt on

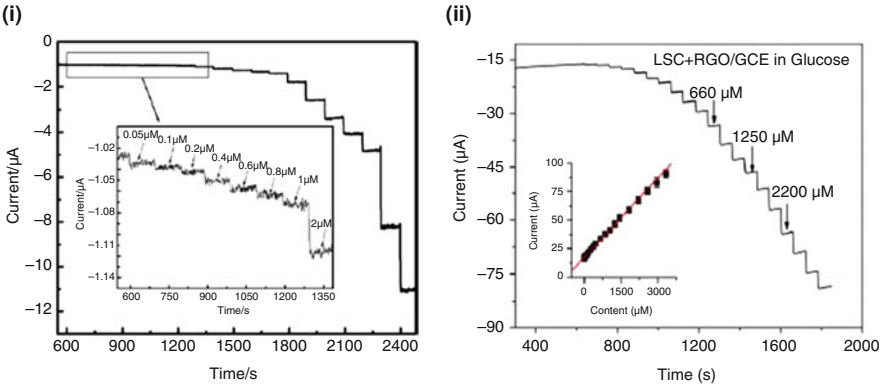

Fig. 6 Typical i-t response of (i) LNC and (ii) LSC + RGO electrodes in 0.1 M NaOH upon addition of glucose at various concentration (inset: linear range for glucose detection). (Reprinted with permissions from ref. [47] and [50]. Copyright 2012 and 2016, Elsevier)

the ferrite structure. It exhibited good linearity curve in the concentration range of 0–200 μM, maximum sensitivity of 285 μA mM^{-1} cm^{-2}, and 7 μM LOD [49].

Moreover, La0.6Sr0.4CoO3-δ (LSC), LaNi0.6Co0.4O3 (LNC), and LSCF materials were also synthesized using ethylenediamine tetraacetic acid and citric acid as a complexing agent with CA:EDTA:metal ion molar ratio of 2:1:1. The LSC electrode showed excellent response between 0.005 and 1.500 mM, LOD of 0.15 μM, and sensitivity of 275 μA mM^{-1} cm^{-2}, which was higher than other electrodes. The higher sensitivity of LSC was due to the larger oxygen non-stoichiometry, larger oxygen diffusion coefficient, and highly oxidative oxygen species. The higher oxidation activity in LNC (0.55×10^{-12} cm^2 s^{-1}) was likely related to higher oxygen ion diffusion coefficient than LSCF (0.21×10^{-12} cm^2 s^{-1}). Moreover, reduced graphene oxide (RGO) into LSC improved its catalytic performance in terms of linear range, LOD, and sensitivity. Figure 6ii shows i-t response of LSC + RGO electrode upon successive injection of glucose. The linear response, improved sensitivity, and LOD were found to be 0.002–3.3 mM, 330 μA mM^{-1} cm^{-2}, and 0.063 μM, respectively. The enhanced performance was due to the large surface area and high conductivity of graphene. The RGO incorporated in LSC was highly selective toward AA, UA, and DA [50].

The electrospinning followed by calcination was applied to fabricate $La_{0.88}Sr_{0.12}MnO_3$ (LSMO) electrode on the smooth surface of carbon paste electrode. The randomly oriented nanofibers with 300–400 nm average diameter and several micrometers in length were obtained. The maximum current response within 4 s was obtained for LSMO electrode. The highest performance was due to the doping of strontium in the perovskite structure. The electrode showed maximum sensitivity of 1111.1 μA mM^{-1} cm^{-2} and LOD of 0.031 μM. The electrode showed excellent reproducibility and high stability over a period of 15 days with current response of 94.8% of its original value. Moreover, it demonstrated high selectivity

Table 2 REEs for NEGS

S. n.	Electrode material	Synthesis method	Morphology (dimension)/surface area ($m^2\ g^{-1}$)	Sensitivity ($\mu A\ mM^{-1}\ cm^{-2}$)	Linear range (mM)	LOD (μM)	Response time (s)	Working potential (V)	Electro-lyte	Ref
1	La_2O_3	Electro-deposition	Nanosheets (length ~ 1.1 μm)/14.17	616	1.25–3.75	270	1	0.43	1 M KOH	[37]
2	Ag-La_2O_3	Electro-deposition	Nanoflakes (length 1.3 μm and thickness 50 to 130 nm)/22.45	1677	0.1–0.6	0.62	5	0.43	0.1 M NaOH	[38]
3	CeO_2/Au	Pulsed laser deposition	Jigsaw/–	44	0.01–20	10	–	–	0.01 M PBS	[39]
4	Au/CTS/CeO_2	Electro-chemical	Nanoparticles/–	1076.71	0.02–0.6	6.89	–	–	0.1 M NaOH	[40]
5	CeO_2@CuO	Bio-mediated	Core-shell (size 23–26 nm)/–	3319.83	0.001–0.0089	0.019	>1	0.4	0.1 M NaOH	[41]
6	CuO/CeO_2	Wet-impregnation	Nanoparticles (size 20–50 nm)/–	2.77	–	10	5–8	0.4	0.1 M PBS	[42]
7	ZnO-CeO_2	Hydro-thermal	Whickers (diameter 10–15 nm)/550.9	–	0.000–0.300	0.224	–	0.5	0.1 M PBS	[43]
8	nCe-nPt-RGO	Electro-deposition and spin coating	Spherical (diameter 20 nm)/–	66.2 ± 2.6	–	1.3 ± 0.6	6.3 ± 3.4	0.3	PBS	[44]
9	$LaNiO_3$	Electro-spinning	Nanofibers (diameter 140 nm)/–	42.321	0.001–1	0.32	4	0.6	0.1 M NaOH	[45]
10	$NdNiO_3$	Hydro-thermal	Nanoparticles (size 60–120 nm)/–	1105.1	0.0005–4.6	0.3	–	0.54	0.1 M NaOH	[46]
11	$LaNi_{0.6}Co_{0.4}O_3$	Sol-gel	Nanoparticles/–	642.78	0.00005–0.2	0.008	3	0.5	0.1 M NaOH	[47]
12	$Co_{0.4}Fe_{0.6}LaO_3$	Sol-gel	Nanoparticles (size 30–70 nm)/–	1013.8	0.00005–0.005 and 0.005–0.5	0.01	4	0.55	0.1 M NaOH	[48]
13	$La_{0.6}Sr_{0.4}Co_{0.2}Fe_{0.8}O_{3-\delta}$	Sol-gel	Nanoparticles (size 100 nm)/–	285	0–0.2	7	5	0.5	0.1 M KOH	[49]
14	$La_{0.6}Sr_{0.4}CoO_{3-\delta}$ + RGO	Sol-gel	–	330	0.002–3.350	0.063	–	0.6	0.1 M NaOH	[50]
15	$La_{0.88}Sr_{0.12}MnO_3$	Sol-gel	Nanofibers (diameter 200–300 nm)/–	1111.11	0.00005–0.1	0.031	4	0.6	0.1 M NaOH	[51]
16	$LaTiO_3$-Ag0.2	Sol-gel	Spherical/–	784.14	0.0025–4	0.21	6	0.7	0.2 M NaOH	[52]

toward various interfering species and is used in clinical diagnosis of the real blood sample [51].

The $LaTiO_3$-Ag0.2 (LTA) perovskite structured electrode was fabricated with the help of GCE and tested as a glucose sensor. The sensor showed linear response between 2.5 μM and 4 mM concentration. It exhibited maximum sensitivity of 784.14 μA mM^{-1} cm^{-2}, LOD of 0.21 μM, and response time of 6 s. The interference and blood serum sample test were carried out at 0.7 V in alkaline solution. The tested value of real blood samples was well matched with hospitalized determined one with 101.3–102.6 recovery value. The sensor exhibited high stability with 92% of its original current value after one month [52].

In short, perovskite-structured materials have shown promising potential for glucose sensing. However, the process comprises multiple steps including synthesis by sol-gel method and calcination at higher temperature to achieve phase purity. Then synthesized material was cast on the desired substrate by using an appropriate binder and used as a glucose sensor. Table 2 summarizes the study of glucose sensing for various rare earth metal-based electrodes synthesized with various physical and chemical methods.

Table 2 and Fig. 7 summarize the applicability of a wide range of REEs for the NEGS. In addition, the table contains overall information regarding the synthesis method, morphology, glucose-sensing sensitivity, linear range, LOD, response time, and working potential. A general trend seen from Table 2 is that almost all electrodes are in their oxide form with some of them composited with a suitable material like rGO. The effect of doping has also been tested by several researchers where doping has resulted in the increased glucose-sensing performance. In addition, ample study has been carried out using perovskite structures composed of REEs.

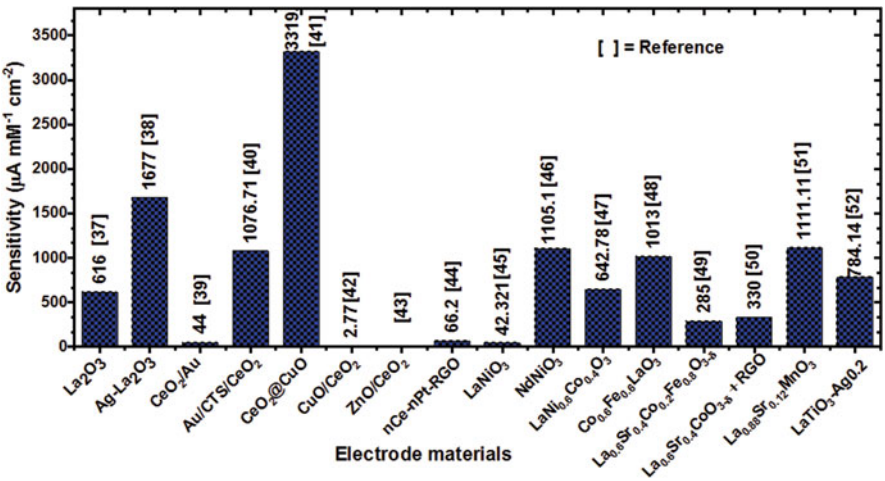

Fig. 7 Plot of various REEs with sensitivity

From Table 2, it is seen that sol-gel and electrodeposition methods have been widely used for material synthesis and to obtain morphologies including nanoparticles, nanofibers, nanoplates, spherical, and nanosheets. Specifically, bio-mediated CeO_2@CuO exhibited the highest sensitivity among all other reported materials. As a whole, it can be concluded that the above literature displays the potential applicability of REEs for the NEGS as well as highlights the scarce literature available on the same.

6 Conclusions

In this chapter, the potential of REEs for NEGS application has been highlighted. Literature displays the excellent glucose-sensing performances of various REEs and reflects the scientific hindrance toward their vast applicability. REEs show relatively lower performance than reported materials, but the earth's abundance of REEs allows cost-effective fabrication of NEGS. In addition, as long as performance is considered, the performance of REEs can be enhanced using different strategies like doping, composite, or hybridization. As a result of effective composite, REE-based nanostructured composites and CeO_2@CuO core-shell structure showed maximum response with sensitivity of 3319.83 $\mu A\ mM^{-1}\ cm^{-2}$, lowest LOD of 0.019, and excellent linear response in the concentration range of 0.001–0.0089 mM. These results show excellent applicability of REEs in the field of glucose sensors. In addition, this review compiles the available literature by means of their synthesis parameters as well as glucose sensing measurements.

From a future perspective, it is important to employ REEs in the continuous glucose monitoring system. The results stated in the table are reliable and possess potential to commercialize in the near future. Their commercialization could result into the fabrication of robust, low-cost glucose-sensing electrodes reasonable enough that every diabetic patient could be able to use it.

Acknowledgments The authors would like to thank the Science and Engineering Research Board (SERB), a statutory body of the Department of Science and Technology (DST), Government of India for awarding the Ramanujan Fellowship (SB/S2/RJN-090/2017) and core research grant (CRG/2019/006059).

Conflict of Interest The authors declare no conflict of interest.

References

1. W. Raghupathi, V. Raghupathi, An empirical study of chronic diseases in the United States: A visual analytics approach to public health. Int. J. Environ. Res. Public Health **15**, 431 (2018). https://doi.org/10.3390/ijerph15030431
2. K. Ghosh, P. Dhillon, G. Agrawal, Prevalence and detecting spatial clustering of diabetes at the district level in India. J. Public Health **28**, 535–545 (2020). https://doi.org/10.1007/s10389-019-01072-6

3. J. Mattei, V. Malik, N.M. Wedick, F.B. Hu, D. Spiegelman, W.C. Willett, H. Campos, Reducing the global burden of type 2 diabetes by improving the quality of staple foods: The global nutrition and epidemiologic transition initiative. Glob. Health **11**, 1–20 (2015). https://doi.org/10.1186/s12992-015-0109-9
4. K.M. Pike, P.E. Dunne, The rise of eating disorders in Asia: A review. J. Eat. Disord. **3**, 1–14 (2015). https://doi.org/10.1186/s40337-015-0070-2
5. K.L. Leong, M.Y. Ho, X.Y. Lee, M.S.L. Yee, A review on the development of non-enzymatic glucose sensor based on graphene-based nanocomposites. Nano **15**, 2030004 (2020). https://doi.org/10.1142/S1793292020300042
6. C. Chen, Q. Xie, D. Yang, H. Xiao, Y. Fu, Y. Tan, S. Yao, Recent advances in electrochemical glucose biosensors: A review. RSC Adv. **3**, 4473–4491 (2013). https://doi.org/10.1039/C2RA22351A
7. Z. Haghparas, Z. Kordrostami, M. Sorouri, M. Rajabzadeh, R. Khalifeh, Highly sensitive non-enzymatic electrochemical glucose sensor based on dumbbell-shaped double-shelled hollow nanoporous CuO/ZnO microstructures. Sci. Rep. **11**, 1–12 (2021). https://doi.org/10.1038/s41598-020-79460-2
8. M. Adeel, M.M. Rahman, I. Caligiuri, V. Canzonieri, F. Rizzolio, S. Daniele, Recent advances of electrochemical and optical enzyme-free glucose sensor operating at physiological conditions. Biosens. Bioelectron. **165**, 112331 (2020). https://doi.org/10.1016/j.bios.2020.112331
9. E. Bonora, M. Muggeo, Postprandial blood glucose as a risk factor for cardiovascular disease in type II diabetes: The epidemiological evidence. Diabetologia **44**, 2107–2114 (2001). https://doi.org/10.1007/s001250100020
10. S.F. Clarke, J.R. Foster, A history of blood glucose meters and their role in self-monitoring of diabetes mellitus. Br. J. Biomed. Sci. **69**, 83–93 (2012). https://doi.org/10.1080/09674845.2012.12002443
11. Advance Collaborative Group, Intensive blood glucose control and vascular outcomes in patients with type 2 diabetes. New. Eng. J. Med. **358**, 2560–2572 (2008). https://doi.org/10.1056/NEJMoa0802987
12. Y.M. Chitare, S.B. Jadhav, P.N. Pawaskar, V.V. Magdum, J.L. Gunjakar, C.D. Lokhande, Metal oxide-based composites in nonenzymatic electrochemical glucose sensors. Ind. Eng. Chem. Res. **60**, 18195–18217 (2021). https://doi.org/10.1021/acs.iecr.1c03662
13. N.S. Oliver, C. Toumazou, A.E.G. Cass, D.G. Johnston, Glucose sensors: A review of current and emerging technology. Diabet. Med. **26**, 197–210 (2009). https://doi.org/10.1111/j.1464-5491.2008.02642.x
14. L.C. Clark, C. Lyons, Electrode systems for continuous monitoring in cardiovascular surgery. Ann. NY Acad. Sci. **102**, 29–45 (1962). https://doi.org/10.1111/j.1749-6632.1962.tb13623.x
15. V.B. Juska, M.E. Pemble, A critical review of electrochemical glucose sensing: Evolution of biosensor platforms based on advanced nanosystems. Sensors **20**, 6013 (2020). https://doi.org/10.3390/s20216013
16. J. Liu, J. Wang, A novel improved design for the first-generation glucose biosensor. Food Technol. Biotechnol. **39**, 55–58 (2001)
17. A.P. Turner, B. Chen, S.A. Piletsky, In vitro diagnostics in diabetes: Meeting the challenge. Clin. Chem. **45**, 1596–1601 (1999). https://doi.org/10.1093/clinchem/45.9.1596
18. A. Chaubey, B. Malhotra, Mediated biosensors. Biosens. Bioelectron. **17**, 441–456 (2002). https://doi.org/10.1016/S0956-5663(01)00313-X
19. F. Palmisano, P.G. Zambonin, D. Centonze, M. Quinto, A disposable, reagentless, third-generation glucose biosensor based on overoxidized poly (pyrrole)/tetrathiafulvalene-tetracyanoquinodimethane composite. Anal. Chem. **74**, 5913–5918 (2002). https://doi.org/10.1021/ac0258608
20. J. Wang, Electrochemical glucose biosensors. Chem. Rev. **108**, 814–825 (2008). https://doi.org/10.1021/cr068123a
21. H. Teymourian, A. Barfidokht, J. Wang, Electrochemical glucose sensors in diabetes management: An updated review (2010–2020). Chem. Soc. Rev. **49**, 7671–7709 (2020). https://doi.org/10.1039/D0CS00304B

22. E.H. Yoo, S.Y. Lee, Glucose biosensors: An overview of use in clinical practice. Sensors **10**, 4558–4576 (2010). https://doi.org/10.3390/s100504558
23. P. Si, Y. Huang, T. Wang, J. Ma, Nanomaterials for electrochemical non-enzymatic glucose biosensors. RSC Adv. **3**, 3487–3502 (2013). https://doi.org/10.1039/C2RA22360K
24. S. Park, H. Boo, T.D. Chung, Electrochemical non-enzymatic glucose sensors. Anal. Chim. Acta **556**, 46–57 (2006). https://doi.org/10.1016/j.aca.2005.05.080
25. G. Amala, S.M. Gowtham, Recent advancements, key challenges and solutions in non-enzymatic electrochemical glucose sensors based on graphene platforms. RSC Adv. **7**, 36949–36976 (2017). https://doi.org/10.1039/C7RA02845H
26. L.D. Burke, Premonolayer oxidation and its role in electrocatalysis. Electrochim. Acta **39**, 841–1848 (1994). https://doi.org/10.1016/0013-4686(94)85173-5
27. G. Wang, X. He, L. Wang, A. Gu, Y. Huang, B. Fang, B. Geng, X. Zhang, Non-enzymatic electrochemical sensing of glucose. Microchim. Acta **180**, 161–186 (2013). https://doi.org/10.1007/s00604-012-0923-1
28. T. Kegl, A. Kosak, A. Lobnik, Z. Novak, A.K. Kralj, I. Ban, Adsorption of rare earth metals from wastewater by nanomaterials: A review. J. Hazard. Mater. **386**, 121632 (2020). https://doi.org/10.1016/j.jhazmat.2019.121632
29. H. Huang, J.J. Zhu, The electrochemical applications of rare earth-based nanomaterials. Analyst **144**, 6789–6811 (2019). https://doi.org/10.1039/C9AN01562K
30. V. Balaram, Rare earth elements: A review of applications, occurrence, exploration, analysis, recycling, and environmental impact. Geosci. Front. **10**, 1285–1303 (2019). https://doi.org/10.1016/j.gsf.2018.12.005
31. R. Indhrajothi, I. Prakash, M. Venkateswarlu, N. Satyanarayana, Lanthanum ion (La^{3+}) substituted $CoFe_2O_4$ anode material for lithium ion battery applications. New J. Chem. **39**, 4601–4610 (2015). https://doi.org/10.1039/C5NJ00791G
32. S.B. Ubale, R.N. Bulakhe, V.J. Mane, D.B. Malavekar, I. In, C.D. Lokhande, Chemical synthesis of nano-grained ytterbium sulfide thin films for supercapacitor application. Appl. Nanosci. **10**, 5085–5097 (2020). https://doi.org/10.1007/s13204-020-01495-8
33. P.P. Bagwade, D.B. Malavekar, T.T. Ghogare, S.B. Ubale, V.J. Mane, R.N. Bulakhe, I. In, C.D. Lokhande, A high performance flexible solid-state asymmetric supercapacitor based on composite of reduced graphene oxide@ dysprosium sulfide nanosheets and manganese oxide nanospheres. J. Alloys Compd. **859**, 157829 (2021). https://doi.org/10.1016/j.jallcom.2020.157829
34. F. Charbgoo, M. Ramezani, M. Darroudi, Bio-sensing applications of cerium oxide nanoparticles: Advantages and disadvantages. Biosens. Bioelectron. **96**, 33–43 (2017). https://doi.org/10.1016/j.bios.2017.04.037
35. N. Fujiwara, T. Nagai, T. Ioroi, H. Arai, Z. Ogumi, Bifunctional electrocatalysts of lanthanum-based perovskite oxide with Sb-doped SnO_2 for oxygen reduction and evolution reactions. J. Power Sources **451**, 227736 (2020). https://doi.org/10.1016/j.jpowsour.2020.227736
36. M. Ghiasi, A. Malekzadeh, Synthesis, characterization and photocatalytic properties of lanthanum oxy-carbonate, lanthanum oxide and lanthanum hydroxide nanoparticles. Superlattice. Microst. **77**, 295–304 (2015). https://doi.org/10.1016/j.spmi.2014.09.027
37. S.B. Jadhav, U.M. Patil, R.N. Bulakhe, I. In, C.D. Lokhande, P.N. Pawaskar, Vertically aligned nanosheets of an electrodeposited lanthanum oxide electrode for non-enzymatic glucose sensing application. J. Electron. Mater. **50**, 675–685 (2021). https://doi.org/10.1007/s11664-020-08605-w
38. S.B. Jadhav, D.B. Malavekar, R.N. Bulakhe, U.M. Patil, I. In, C.D. Lokhande, P.N. Pawaskar, Dual-functional electrodeposited vertically grown Ag-La_2O_3 nanoflakes for non-enzymatic glucose sensing and energy storage application. Surf. Interfaces **23**, 101018 (2021). https://doi.org/10.1016/j.surfin.2021.101018
39. M. Gougis, A. Tabet-Aoul, D. Ma, M. Mohamedi, Nanostructured cerium oxide catalyst support: Effects of morphology on the electroactivity of gold toward oxidative sensing of glucose. Microchim. Acta **181**, 1207–1214 (2014). https://doi.org/10.1007/s00604-014-1283-9

40. L. Jian, Q. Xue, C. Jiao, H. Liu, Y. Zhou, H. Ma, Q. Yang, A non-enzymatic nanoceria electrode for non-invasive glucose monitoring. Anal. Methods **10**, 2151–2159 (2018). https://doi.org/10.1039/C8AY00433A
41. T. Dayakar, K.V. Rao, K. Bikshalu, V. Malapati, K.K. Sadasivuni, Non-enzymatic sensing of glucose using screen-printed electrode modified with novel synthesized CeO_2@CuO core shell nanostructure. Biosens. Bioelectron. **111**, 166–173 (2018). https://doi.org/10.1016/j.bios.2018.03.063
42. P. Guan, Y. Li, J. Zhang, W. Li, Non-enzymatic glucose biosensor based on CuO-decorated CeO_2 nanoparticles. Nanomaterials **6**, 159 (2016). https://doi.org/10.3390/nano6090159
43. J. Qian, Y. Wang, J. Pan, Z. Chen, C. Wang, J. Chen, Z. Wu, Non-enzymatic glucose sensor based on ZnO-CeO_2 whiskers. Mater. Chem. Phys. **239**, 122051 (2020). https://doi.org/10.1016/j.matchemphys.2019.122051
44. P. Chaturvedi, D.C. Vanegas, M. Taguchi, S.L. Burrs, P. Sharma, E.S. McLamore, A nanoceria–platinum–graphene nanocomposite for electrochemical biosensing. Biosens. Bioelectron. **58**, 179–185 (2014). https://doi.org/10.1016/j.bios.2014.02.021
45. B. Wang, S. Gu, Y. Ding, Y. Chu, Z. Zhang, X. Ba, Q. Zhang, X. Li, A novel route to prepare $LaNiO_3$ perovskite-type oxide nanofibers by electrospinning for glucose and hydrogen peroxide sensing. Analyst **138**, 362–367 (2013). https://doi.org/10.1039/C2AN35989H
46. M. Sivakumar, K. Pandi, S.M. Chen, Y.H. Cheng, M. Sakthivel, Facile synthesis of perovskite-type $NdNiO_3$ nanoparticles for an effective electrochemical non-enzymatic glucose biosensor. New J. Chem. **41**, 11201–11207 (2017). https://doi.org/10.1039/C7NJ02156A
47. Z. Zhang, S. Gu, Y. Ding, J. Jin, A novel nonenzymatic sensor based on $LaNi_{0.6}Co_{0.4}O_3$ modified electrode for hydrogen peroxide and glucose. Anal. Chim. Acta **745**, 112–117 (2012). https://doi.org/10.1016/j.aca.2012.07.039
48. Z. Zhang, S. Gu, Y. Ding, F. Zhang, J. Jin, Determination of hydrogen peroxide and glucose using a novel sensor platform based on $Co_{0.4}Fe_{0.6}LaO_3$ nanoparticles. Microchim. Acta **180**, 1043–1049 (2013). https://doi.org/10.1007/s00604-013-1012-9
49. L.F. Liotta, F. Puleo, L.V. Parola, S.G. Leonardi, N. Donato, D. Aloisio, G. Neri, $La_{0.6}Sr_{0.4}FeO_{3-\delta}$ and $La_{0.6}Sr_{0.4}Co_{0.2}Fe_{0.8}O_{3-\delta}$ perovskite materials for H_2O_2 and glucose electrochemical sensors. Electroanalysis **27**, 684–692 (2015). https://doi.org/10.1002/elan.201400589
50. J. He, J. Sunarso, Y. Zhu, Y. Zhong, J. Miao, W. Zhou, Z. Shao, High-performance non-enzymatic perovskite sensor for hydrogen peroxide and glucose electrochemical detection. Sensors Actuators B Chem. **244**, 482–491 (2017). https://doi.org/10.1016/j.snb.2017.01.012
51. D. Xu, L. Luo, Y. Ding, P. Xu, Sensitive electrochemical detection of glucose based on electrospun $La_{0.88}Sr_{0.12}MnO_3$ naonofibers modified electrode. Anal. Biochem. **489**, 38–43 (2015). https://doi.org/10.1016/j.ab.2015.08.013
52. Y.Z. Wang, H. Zhong, X.M. Li, F.F. Jia, Y.X. Shi, W.G. Zhang, Z.P. Cheng, L.L. Zhang, J.K. Wang, Perovskite $LaTiO_3$-$Ag_{0.2}$ nanomaterials for nonenzymatic glucose sensor with high performance. Biosens. Bioelectron. **48**, 56–60 (2013). https://doi.org/10.1016/j.bios.2013.03.081

Surface-Functionalized Iron Oxide (Fe_3O_4) Nanoparticles for Biomedical Applications

Rutuja P. Gambhir, Anuja A. Vibhute, Tejaswini P. Patil, and Arpita P. Tiwari

Abbreviation

ab@IONP	Antibody functionalized IONP
AC	Alternating current
APTES	3-aminopropyltriethyloxysilane
AuNPs	Gold nanoparticles
BBB	Blood-brain barrier
BSA	Bovine serum albumin
CEA	Carcinoembryonic antigen
CMC	Carboxymethylcellulose
CNT	Carbon nanotube
CT	Computed tomography
DNA	Deoxyribonucleic acid
GET	Glycosaminoglycan binding-enhanced transduction
GFP	Green fluorescent protein
HA	Hyaluronic acid
HEK	Human embryonic kidney cell
IgG	Immunoglobulin G
IONP	Iron oxide nanoparticle
LDH	Layered double hydroxide
MNP	Magnetic nanoparticle
MPA	Mercaptopropionic acid
MPTES	Mercaptopropyltriethoxysilane
MR	Magnetic resonance

R. P. Gambhir · A. A. Vibhute · T. P. Patil · A. P. Tiwari (✉)
Department of Medical Biotechnology, D Y Patil Education Society, (Deemed to be University), Kolhapur, Maharashtra, India

F. I. Ezema et al. (eds.), *Chemically Deposited Metal Chalcogenide-based Carbon Composites for Versatile Applications*, https://doi.org/10.1007/978-3-031-23401-9_15

MRI	Magnetic resonance imaging
PC	Poly (amino ester) with carboxyl groups
PEG	Polyethylene glycol
PEI	Polyethylenimine
PLA	poly(D, L-lactide)
PVA	Polyvinyl alcohol
RNA	Ribonucleic acid
ROS	Reactive oxygen species
SARS-CoV-2	Severe acute respiratory syndrome coronavirus 2
SiRNA	Small interfering RNA

1 Introduction

Iron oxide (Fe_3O_4) nanoparticles (IONPs) own unique physicochemical as well as biomedical properties like superparamagnetism, larger surface area, easy and cost-effective synthesis, magnet-responsive nature, etc. These properties could be extensively useful for various biological or biomedical applications [1]. There are commonly three types of iron oxide compounds present in nature: magnetite, maghemite, and hematite. Structural formulae for magnetite, maghemite, and hematite are Fe_3O_4, γ- Fe_2O_3, and α- Fe_2O_3, respectively. They possess properties of biomolecule immobilization, biomolecule delivery, drug delivery, cell-specific cytotoxicity, gene therapy, etc. [2]. Some of the reported biomedical functions of surface-functionalized iron oxide nanoparticles were mentioned in Table 1 and Fig. 1.

Iron oxide nanoparticles are synthesized by co-precipitation, hydrothermal reaction, thermal decomposition, solvothermal reaction, template synthesis, electrochemical synthesis, polyol synthesis, microemulation, and sol-gel methods. The IONPs are utilized for various biomedical applications such as tumor treatment (chemotherapy), delivery of biomolecules inside the body, diagnostic imaging, etc. These applications are interlinked with each other. IONPs are loaded with drugs or genes for the detection of specific bio-entities, and thereby it leads to diagnosis as well as therapy of diseases like cancer. Likewise, IONPs are targeted at specific locations, and magnet-responsive diagnostic imaging is performed [33].

However, IONPs possess certain limitations such as toxicity due to the presence of metal, immunogenic response when entered inside an organ, biocompatibility issues, restricted membrane permeability, etc. To address and overcome mentioned limitations, IONPs are surface functionalized with different chemical and biological moieties. Surface functionalization or modification or fabrication minimizes the abovementioned limitations of IONPs and eases their entry into the body [34].

Surface functionalization or fabrication provides biomolecule-specific targeting to IONPs as illustrated in Fig. 2. Nanoparticles (IONPs) are surface functionalized by ligands that possess an affinity for a target molecule. As illustrated in the figure, when ligand-functionalized IONPs are incorporated in a sample, affinity interactions

Table 1 Literature for biomedical applications of surface-functionalized iron oxide nanoparticles (IONPs)

Sr. No	Nanoparticle	Surface fabrication	Biomedical application	References
1	IONP	Graphene oxide	Drug delivery for cancer	[3]
2	IONP	Gelatin and BSA	Drug delivery for tuberculosis	[4]
3	IONP	Citric acid	Drug delivery for cancer	[5]
4	IONP	–	Drug delivery for antimicrobial action	[6]
5	IONP	Poly(3,4-ethylenedioxythiophene):poly(styrenesulfonate)	Biosensing for cancer detection	[7]
6	IONP	PEGylated bilirubin	ROS biosensing from whole blood	[8]
7	IONP	–	Aminoaldehyde biosensing from alcoholic beverages	[9]
8	IONP	Biotin	NMR biosensing for *Salmonella* detection from milk	[10]
9	IONP	Chitosan	Urea and glucose biosensing	[11]
10	IONP	LDH	Chemotherapy of tumors	[12]
11	IONP	PEGylated phospholipid	Chemotherapy of glioma	[13]
12	IONP	Alginate	Chemotherapy and hyperthermia of cancer	[14]
13	IONP	Polyethylenimine	Chemotherapy of tumor	[15]
14	IONP	CMC	Chemotherapy of brain cancer cells	[16]
15	IONP	Polyethylenimine	Gene delivery of SiRNA	[17]
16	IONP	Cetuximab	Gene therapy of glioma	[18]
17	IONP	Polyacrylamide	Antimicrobial action against *E. coli*	[19]
18	IONP	–	Antimicrobial activity against bacteria	[20]
19	IONP	–	Antibacterial and antioxidant action	[21]
20	IONP	Dextran and trypsin	Antibacterial activity	[22]
21	IONP	–	Antimycotic action against fungal pathogens	[23]
22	IONP	MPA	Detection of dengue virus	[24]
23	IONP	Glycine and citric acid	Antiviral activity against influenza virus	[25]
24	IONP	Gold(Au)/CNT	Antiviral activity against influenza virus	[26]
25	IONP	PC	SARS-CoV-2 RNA extraction from sample	[27]
26	IONP	Polyethylenimine	Magnetofection in breast cancer cell	[28]
27	IONP	GET	Magnetofection in fibrablast cell	[29]
28	IONP	Polyethylenimine	Magnetofection and isolation of plasmid DNA	[30]
29	IONP	Positively charged polymer	Magnetofection in HEK cell	[31]
30	IONP	Polyethylenimine	Magnetofection in osteoblast cell	[53]

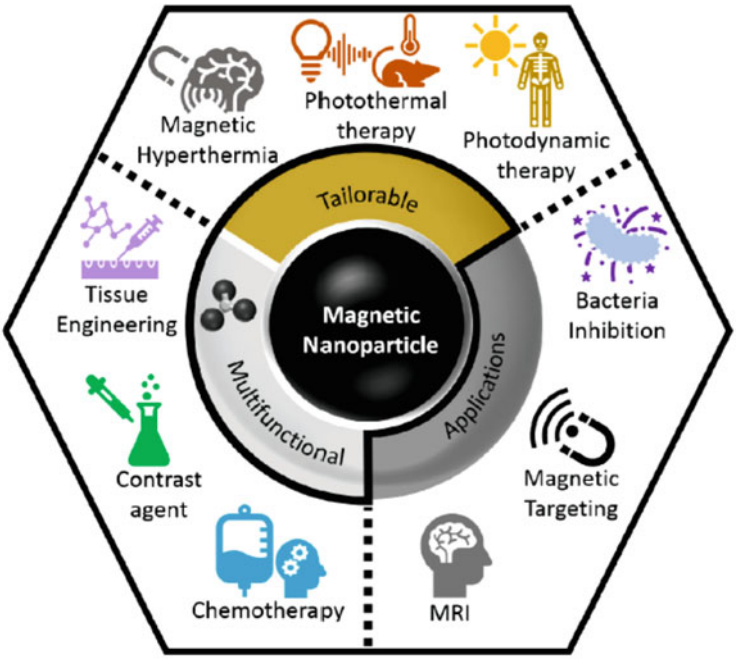

Fig. 1 Biomedical applications of iron oxide (Fe_3O_4) nanoparticles. (Reprinted by permission from reference [32]. Copyright 2021 ACS Applied Bio Materials)

between ligand and target molecules take place. This results in the formation of a molecule-IONP complex. The complex is separated from undesired molecules by using an external magnet. Hence, desired or targeted molecules are separated from a sample with the help of surface-functionalized IONPs [35].

The chapter summarizes biomedical applications of IONPs, drug delivery, biosensing, chemotherapy, gene therapy, antimicrobial activity, cytotoxicity, pathogen detection, virus detection, and magnetofection. A detailed explanation of each application has been provided within.

2 Surface Functionalization of Iron Oxide Nanoparticles for Biomedical Applications

The major challenge in the use of magnetic nanoparticles for biological applications is the long-term inherent instability of the iron oxide nanoparticles in biological systems. This occurs due to two main reasons first due to dispersibility loss, where nanoparticles agglomerate, and second owing to magnetism loss where the oxidation of nanoparticles occurs. These problems can be overcome by functionalizing the surface with an appropriate functional group. It enhances the biocompatibility

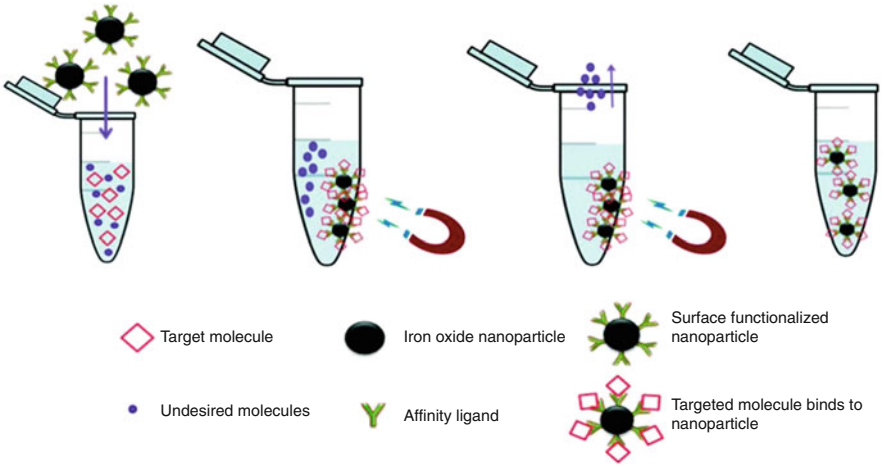

Fig. 2 Surface functionalization of iron oxide nanoparticles provides biomolecule specific targeting. (Reprinted by permission from reference [35]. Copyright 2015 RSC Publication)

of iron oxide nanoparticles, increases hydrophilicity, and prevents agglomeration. Also, it helps in retaining the magnetic characteristics of magnetic nanoparticles**.**

Organic polymers are the most common surface-functionalizing agents for iron oxide nanoparticles. Both natural and synthetic polymers are extensively used in cancer therapy and imaging applications. Polymers are sensitive to temperature and pH due to which they are extensively used for drug release systems at the targeted site. One of the most exploited materials for surface functionalization of magnetic nanoparticles is silica. Dextran, poly(D, L-lactide) (PLA), polyethylene glycol (PEG), polyethyleneimine (PEI), and starch are also commonly used in surface functionalization. PH-responsive bovine serum albumin-functionalized iron oxide nanoparticles are used for pathogenic DNA detection [36]. Also, chitosan and silica-functionalized IONPs are reported for possessing around 80% DNA adsorption and 98% DNA elution efficiency from human saliva samples [37].

Surface functionalization with reactive groups like –COOH, –NH2,-OH, and –SH is also reported, which have a potential for further modifications with various bioactive molecule attachments. It has been reported that a facile technique to synthesize 3-aminopropyltriethyloxysilane (APTES)-coated magnetite with tailored surface functional groups to be applied in the biological field. Hemolytic assay and cytotoxicity results showed that the acetylation of amine groups on the surface of MNPs notably ameliorates hemocompatibility and cytocompatibility. In addition, as observed in past research, mercaptopropyltriethoxysilane (MPTES)-modified MNPs trigger a minute decline in magnetic properties, while APTES helps maintain the morphology of MNPs [38].

Polyethylenimine (PEI) is another molecule that provides better functionalization on the surface of IONP and is hence used for various applications. It possesses luminescence hence widely used in transfection experiments [39].

Another approach to exert therapeutic application for the treatment of cancer was reported by oleic acid functionalized magnetic iron oxide nanoparticle-based hyperthermia. It was observed that the material possessed efficient tumor destruction [40].

Surface functionalization by using biomolecules has gained much attention recently and has been used in applications like biosensing [41]. Biomolecules like nucleic acids, biotin-avidin, proteins, enzymes, antibodies, and serum albumin and polypeptides are being used as functionalizing agents frequently [9, 42, 43].

Surface functionalization with inorganic materials like manganese or cobalt provides better magnetic moment, whereas functionalization with gold or silver gives robust visual adsorption and higher electron density. Hence, multicomponent nanoparticle term is offering new insights for diagnostic applications such as magnetic resonance imaging (MRI) and computed tomography (CT) diagnosis [44]. Carbon-functionalized IONPs are exploited for biosensing. Graphite-activated carbon-functionalized IONPs are used to develop screen-printed electrode sensors, which show rutin (Vitamin P) detection with high reproducibility, sensitivity, and selectivity [45]. It was also reported that surface functionalization of IONPs prevents their oxidation due to air and makes them efficient for related applications [46].

3 Biomedical Applications of Iron Oxide Nanoparticles

3.1 IONP-Based Drug Delivery

Engineered nanoparticles improve significant medicinal applications. Nanotechnology-mediated drug delivery overcomes certain barriers to conventional delivery such as site-specific targeting. Drug delivery to the targeted site has been inculcated through different modes of administration. Recently, IONP-responsive drug delivery has shown promising results. Such delivery could be controlled externally by an induced magnetic field. Moreover, suitable functionalization on the surface of IONP often restrains its toxicity inside the human body. Various biopolymers such as carbohydrates, proteins, antibodies, enzymes, lipids, etc. were used for functionalization. This process provides better binding efficiency for drug adsorption. Once the drug loading on IONP is achieved successfully, the assembly is administered in the human body through various modes like intravenous blood circulation, pulmonary administration, subcutaneous injection, etc. Some interacting moieties were functionalized on the surface of IONP to execute cell-specific targeting. These moieties were in the form of antibodies, transporter molecules, integrins, glucose, etc. and possess the ability to achieve binding with the targeted site. For example, a specific antibody-functionalized IONP reached a specific receptor of a cell. Binding between receptor and antibody-functionalized IONP (ab@IONP) was enforced at a specific location. As ab@IONPs was already loaded with the desired drug, eventually delivery of the drug at a specific location was achieved [47, 48].

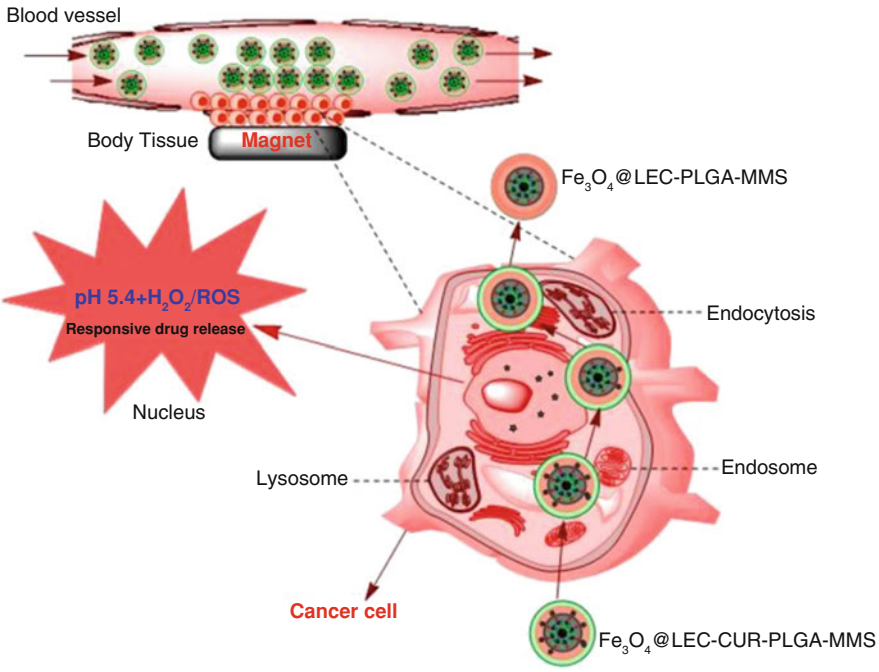

Fig. 3 Iron oxide nanoparticle-mediated drug delivery in cancerous cell. (Reprinted by permission from reference [51] Copyright 2020 Elsevier Publication)

Recent advancements showed that iron oxide nanoparticles enhanced the biological activity of drugs inside bacterial cells. Binding and release of the drug Lasioglossin III from IONP significantly generated the cytotoxic behavior against *Escherichia coli* [6]. Likewise, drug delivery was effective against diseases like cancer. IONPs were functionalized by polyvinyl alcohol and acted as a drug carrier. Later, the Sorafenib drug was loaded on polyvinyl-functionalized IONPs. Sorafenib is considered a kinase inhibitor effective against cancer. When this assembly was incubated with liver cancer cells, cytotoxicity was obtained. However, same assembly could not show cytotoxicity for fibroblast cells, which concluded that drug delivery was achieved at specifically targeted cancer cells using functionalized IONPs [49]. IONP-medicated delivery of neuronal drugs has been reported for targeting the ear and central nervous systems as well [50].

IONP-mediated drug delivery has been illustrated in Fig. 3. Mechanism or mode of delivery was observed in a cancerous cell. Drug-loaded iron oxide (Fe_3O_4) nanoparticles entered the blood vessels of body tissue by providing an external magnetic field. Specifically, they were targeted at the tumor region by a moving magnet. Once they reached to target, tumor cells were assimilated into them and delivered to the nucleus. Responsive drug release occurred, and IONPs were

engulfed by an endosome. They were released outside the cell by endocytosis. The released drug bound to a specific biomolecule and mediated a cytotoxic mechanism [51].

3.2 IONP-Based Biosensing

IONPs were extensively engineered for biosensing applications. The quantity of various biomolecules such as enzymes, nucleic acids, proteins, and aptamers was traced with the help of magnet-responsive IONP biosensors. Surface fabrication on IONPs provided stability, sensitivity, and biocompatibility. Basically, a biosensor was made up of a receptor and transducer. Initially, the receptors conjugated with IONP were used as targeting agents of the interested biomolecule and followed by transducer converted these events into assessable signals. Recent achievements in magnet-responsive nanotechnology were beneficial for the preparation of biosensing assembly. Magnetic IONPs led to electrochemical biosensing of biomolecules due to their high surface area and electron-conducting capacity [52].

IONP biosensors possess several advantages due to the presence of nanosize particles, less manufacturing cost, and their reusability. Reports suggested that functionalized IONPs are used to detect cancer biomarkers like carcinoembryonic antigen (CEA). Functionalized IONPs were immobilized with CEA, and thereby cancer detection was achieved from serum samples [7]. Likewise, reactive oxygen species (ROS) detection was done by constructing an IONP biosensor. PEG-coated bilirubin IONPs were loaded with fluorescent dye. Obtained fluorescence transformed into assessable signals. Hence, a fluorescence-based IONP biosensor was constructed that detects ROS generation from blood samples [8].

The mechanism of action of IONP-based biosensors is illustrated in Fig. 4. Magnetic iron oxide nanoparticles were functionalized by biomolecular moieties to achieve a specific target. It was called a surface modification or fabrication of nanoparticles. Such modified nanoparticles were used for capturing analytes (specific biomolecule) that need to be detected from the sample. The analyte was deposited on top of an electrode by using a magnet. Electrode was attached to a magnet for efficient sensing of a biomolecule. Electrochemical signals were generated with the help of a transducer. The amount of analyte or biomolecule deposited on the electrode was directly proportional to the intensity of electrochemical signals. Hence, a biosensing technique based on magnetic iron oxide nanoparticles was developed [53].

3.3 IONP-Based Chemotherapy

The development of magnet-responsive platforms for the treatment of cancer was enhanced in recent decades. IONP-based chemotherapy protocol was developed

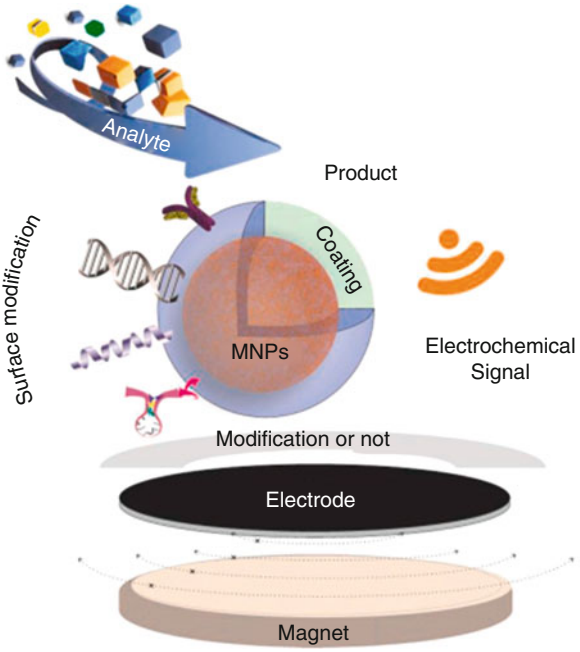

Fig. 4 Mechanism of magnetic iron oxide nanoparticle-based biosensor. (Reprinted by permission from reference [53] Copyright 2021 Elsevier Publication)

in combination with different techniques such as magnetic resonance imaging (MRI). Layered double hydroxide (LDH) functionalized IONPs were used for chemotherapy applications. They were conjugated with hyaluronic acid (HA), which was a targeting agent for cancerous cells. However, the LDH molecules act as a drug carrier. Anticancerous drug (doxorubicin) delivery is achieved by the mentioned assembly. Specific anticancerous effects were observed by functionalized IONPs leading to remarkable chemotherapy application [12].

Likewise, IONPs were effective against glioma brain tumors. The advantage of IONP-based chemotherapy was that the drug was passed through the blood-brain barrier (BBB) with the help of IONPs. Hydrophobic functionalization on IONPs was carried out with several chemical moieties. Doxorubicin drug was then loaded on functionalized IONPs. The anticancer ability was recorded by fluorescence and MR imaging. Doxorubicin-loaded IONPs could penetrate BBB, and site-specific drug delivery was observed in glioma tumors [13].

Chemotherapy for cancer cure tends to possess several side effects such as specific targeting is lacking, possess high toxicity for nontumor cells, etc. Hence, magnetic IONP-based drug delivery could be an effective approach in chemotherapy application. The reduced high toxicity on nontumor cells and tumor cell-specific targeting was achieved. Functionalized IONPs with biopolymer alginate acted

as drug carriers. Further, doxorubicin was added to them. The evaluation of efficient drug delivery was performed with a commercial generator. Magnet-responsive hyperthermia and cytotoxicity had confirmed the affectivity of IONPs for chemotherapy application [14].

Adsorption and release of drugs from functionalized IONPs could be pH-influenced. This property was incorporated in MRI-dependent chemotherapy. It was observed that the release of doxorubicin at the targeted tumor site occurred efficiently in an acidic medium [15].

In combination with magnetic hyperthermia, IONPs were used for chemotherapy. This technology-induced heat generation at a specific targeted site by applying an external magnetic field. Due to the generation of heat, the targeted cells were damaged. For example, doxorubicin-loaded IONPs were delivered at the glioblastoma brain tumor site. Due to the magnetic nature of IONPs, hyperthermia-induced heat was generated and that led to glioblastoma cell damage [16].

Nanoparticle-based chemotherapy is illustrated in Fig. 5. Functionalized nanoparticles were targeted at specific cells. Functionalization consisted of an imagined agent, targeting moiety, drug carrier, and drug. Targeting moieties were antibodies, proteins, small molecules, or oligonucleotides for specific cell recognition. They recognized specific receptors present on a cancer cell. The whole assembly was entered into the cell through the endosome. Drug release occurred inside the cell and initiated its mode of action, which led to cell death [54].

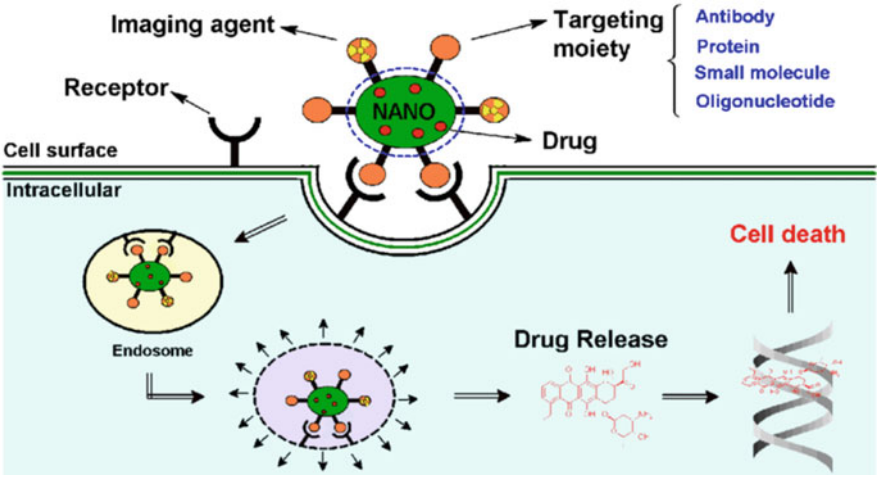

Fig. 5 Mechanism of nanoparticle-based chemotherapy. (Reprinted by permission from reference [54] Copyright 2015 MDPI Publication)

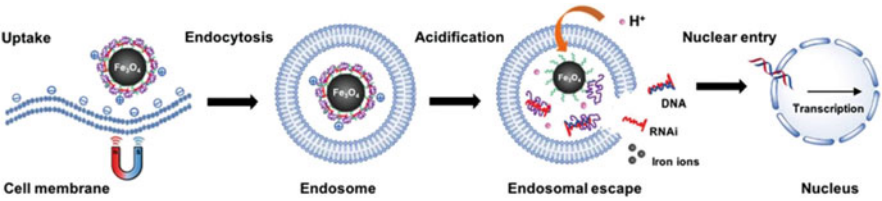

Fig. 6 Gene uptake of IONPs by endocytosis process. (Reprinted by permission from reference [56] Copyright 2020 Wiley Online Library Publication)

3.4 IONP-Based Gene Therapy

IONP-based gene therapy provided nonviral gene transfer inside the targeted cell. IONPs gave stability to therapeutic genes against degrading enzymes. They additionally possessed biocompatibility due to the functionalization of biomolecules on their surface. Later, they were loaded with a gene that had to be delivered to specific location for gene therapy. IONPs provided magnet-responsive gene delivery and therapy by applying or inducing a magnetic field [55].

Biodistribution and biocompatibility of IONPs decided by loading small interfering RNA (SiRNA) on polyethyleneimine (PEI)-functionalized IONPs. SiRNA provided biocompatibility to nanoparticles as no toxicity was observed in vitro and in vivo. Additionally, the biodistribution of IONPs could be seen in liver and spleen tissues. However, no shreds of evidence of nanoparticles were observed in tissues of lungs and kidneys when SiRNA-loaded IONPs were injected in mice. No tissue damage was occurred in any organ, which proves the biocompatibility of particles. Biodistribution in the spleen and liver suggested the specificity of SiRNA gene delivery [17].

The mechanism of gene delivery is illustrated in Fig. 6. Functionalized IONPs were loaded with a specific gene and were transported to the targeted site by an inducing magnetic field. Cellular uptake took place during the endocytosis process. Nanoparticles were separated from the gene (DNA/RNA) in slightly acidic conditions. Later entry of gene occurred inside nucleus, which led to transcription. Hence, functionalized IONPs have the capacity to overcome membrane barriers and mediated the gene delivery process [56].

3.5 IONP-Based Antimicrobial Activity

IONPs were extensively effective against microorganisms. Contamination of microbes in water or any source leads to major concerns. Hence, magnetic IONP-responsive detection and killing of microorganisms were needed. Surface-functionalized IONPs (with polyacrylamide) showed efficient antimicrobial properties against *Escherichia coli* [19].

For effective antimicrobial activity, another feasible approach to IONP synthesis was used. Green synthesis of IONPs is a method in which plant extract is used as a solvent. The advantage of this approach was that no separate biomolecule functionalization is required on the surface of the nanoparticle. As plant proteins and other biological entities are present in the extract, the synthesized nanoparticles were self-functionalizing and showed better antimicrobial action. For example, IONPs prepared using *Withania coagulans* plant extract were reported for antimicrobial activity [20].

Another biological synthesis method for IONPs was effective against certain microorganisms. Fungal species were preliminarily isolated from the soil. Later, particularly *Penicillium* species were identified and isolated from the mixture. Biosynthesis of IONPs was carried out from *Penicillium* extract. The reports suggested that synthesized nanoparticles possess antioxidant and antibacterial actions [21].

Likewise, trypsin- and dextran-functionalized IONPs were used as screening agents for protease inhibitors. It was a novel technique for antimicrobial analysis as nanoparticles have gained protease inhibitor activity [22].

Surface-functionalized IONPs showed antifungal activity as well. These particles were effective against *Trichothecium roseum*, *Penicillium chrysogenum*, *Aspergilus niger*, etc. IONPs inhibited the spore formation of fungal pathogens [23].

The mechanism of antimicrobial activity of surface-functionalized IONPs has been described in Fig. 7. Iron oxide nanoparticles were functionalized with chitosan molecules. The interaction between functionalized IONP and the cell membrane of bacteria could show more free radical formation. This indicated membrane damage led to the death of bacteria. However, the interaction between IONP and membrane showed less free radical formation. This phenomenon suggested that surface fabrication of IONP provides higher antimicrobial efficiency to the particle [57].

3.6 IONP-Based Virus Detection

Surface-functionalized IONPs were used for extraction as well as detection of many viruses. IONP-based virus detection mainly reported for dengue, influenza, and the recently emerged SARS-CoV-2 virus.

For the detection of the dengue virus, mercaptopropionic acid (MPA)-functionalized IONPs were reported. Later, they were conjugated with gold nanoparticles (AuNPs) and specific aptamers. The whole assembly formed chemical bonding with four serotypes of the dengue virus. Due to the presence of IONPs, magnetic separation of viral particles could achieve. AuNPs provided visual or calorimetric analysis without the requirement of high maintenance types of equipment [24].

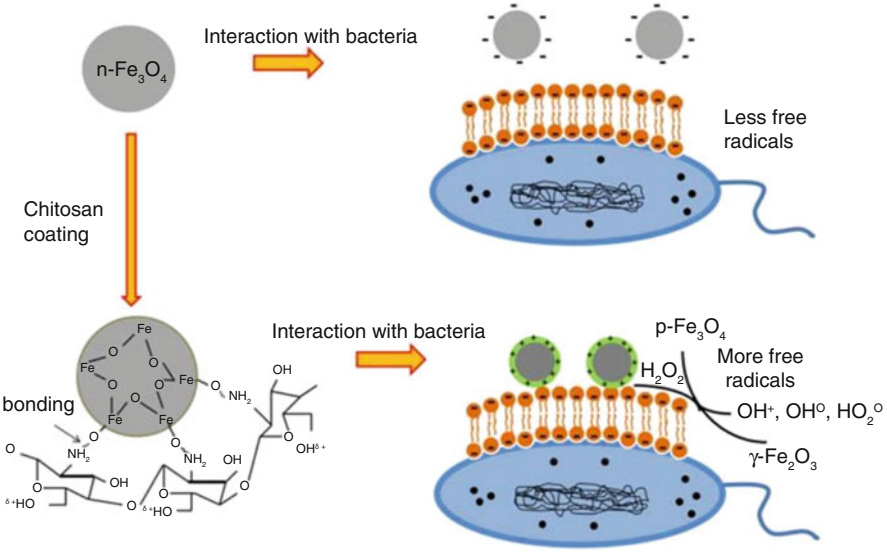

Fig. 7 Mechanism of antimicrobial activity of surface-functionalized IONPs. (Reprinted by permission from reference [57] Copyright 2015 Macmillan Publication)

Newly emerged IONP nanozymes showed antiviral ability against the influenza virus. These nanozymes targeted the lipid envelope of the virus. The mechanism of antiviral activity suggested that these nanozymes were catalyzing lipid peroxidation of the viral lipid envelope and led to the inhibition of transmission and infectivity of the virus [25].

Likewise, IONPs functionalized with glycine and citric acid were reported for detection and antiviral activity against the influenza virus. Also, gold (Au)/CNT-functionalized IONPs provided antiviral activity against influenza [26].

Surface-functionalized IONPs were effective for extraction and detection of the recently emerged SARS-CoV-2 virus. IONPs functionalized with poly amino ester with carboxylic groups (PC) gained the ability to extract SARS-CoV-2 RNA from a clinical sample [27]. Hence, IONP-mediated strategy helped to detect and diagnose viral pathogens from a sample.

IONP-mediated virus extraction and detection is illustrated in Fig. 8. They were surface functionalized with specific chemical or biological moieties. Later, functionalized IONPs were incorporated into a patient viral sample. Here, nanoparticle-based virus capture occurred, and the immediately captured complex was separated by an externally induced magnetic field. A targeted biomolecule of a virus (such as RNA) was separated from nanoparticles and detected with the help of different technologies [58].

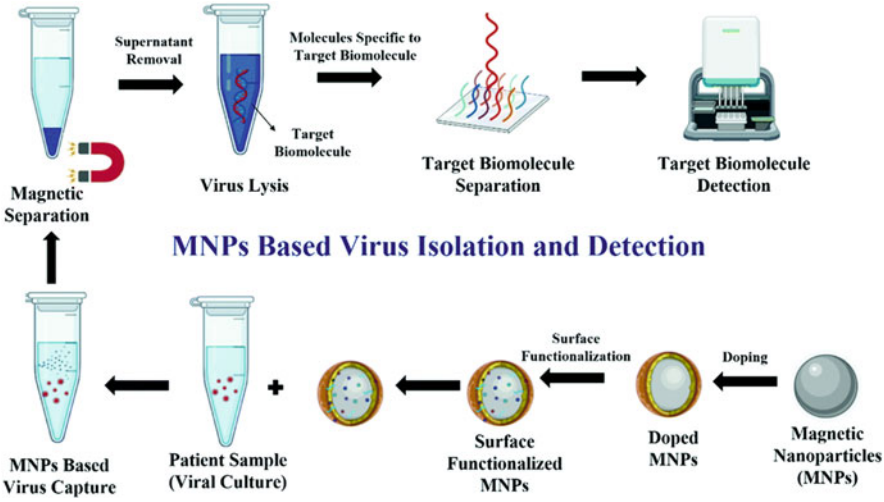

Fig. 8 Mechanism of surface-functionalized IONP-based virus extraction and detection. (Reprinted by permission from reference [58] Copyright 2021 RSC Publication)

3.7 IONP-Based Magnetofection

Magnetofection is a process in which gene-loaded IONPs are transported to the target cell for magnet-responsive gene delivery and therapy. Basically, gene possesses a negative surface charge. Hence, usually cationic polymer-functionalized IONPs are being incorporated for magnetofection. Gene binding occurred efficiently due to the positive surface charge of functionalized IONPs. Further, the gene-loaded IONP assembly entered a cell by endocytosis. Reports suggested that polyethyleneimine (PEI) functionalized IONPs are efficient for the magnetofection of GFP encoded DNA in breast cancer cells [28].

A major advantage of magnetofection is the nonviral gene delivery. It was reported that IONPs loaded with glycosaminoglycan-binding enhanced transduction (GET) peptides showed efficient DNA transfection in mouse embryonic fibroblast cells [29].

Genomic DNA on the surface of PEI-functionalized IONP adsorbed in high amount than that of the plasmid DNA. Binding and elution of gene from IONP was carried out by changing buffer conditions [30].

Furthermore, an AC magnet plate was developed for efficient IONP-assisted magnetofection. Efficient magnetofection was carried out in HEK cells [31]. Likewise, PEI-functionalized IONPs were suitable for gene delivery in osteoblast cell lines [59].

The mechanism of IONP-assisted magnetofection is represented in Fig. 9. Primarily IONPs were functionalized with suitable chemical or biological entities due to which DNA-IONP complex formation occurred. The assembly was transported

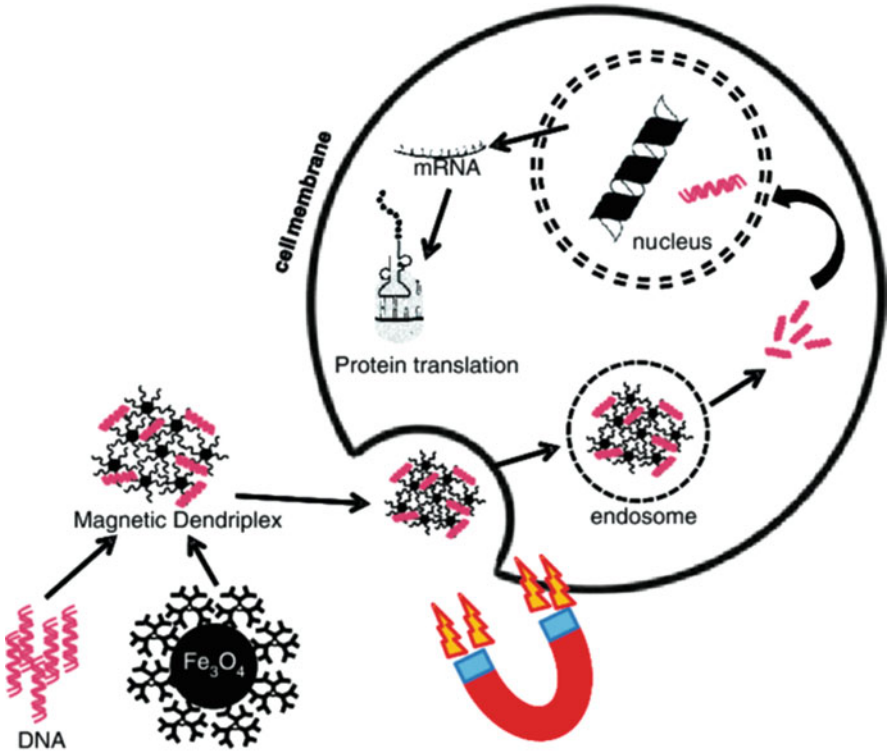

Fig. 9 Mechanism of surface functionalized IONP-responsive magnetofection of DNA into the cell. (Reprinted by permission from reference [60] Copyright 2014 ASP Publication)

to the target cells by moving an external magnetic field. Further, DNA-IONP uptake was carried out inside the cell through endocytosis. Endosome delivered the complex to the nucleus and thereby DNA was delivered to the nucleus. Followed by translation of desired protein, it was occurred through mRNA transcription. The respective protein was utilized by the cell for the purpose of gene therapy [60].

3.8 IONP-Based Bioseparation

In order to carry out disease-specific diagnosis or theranostics, different strategies are being considered, for example, bioseparation. As the name suggests, it is a process of separating desired biomolecules from a sample for biomedical purposes. Aiming to optimize the Bioseparation strategy, the magnetic nanotechnology platform is summarized in this section. Although research is being continuously performed with respect to the particular subject, there is very little success obtained in terms of commercialization. It was reported that biosepa-

ration is performed for different biomolecules such as proteins, nucleic acids, peptides, etc. Magnetic nanoparticle-based bioseparation and biosensing technology began to achieve increasing attention. Recent experiment efforts denoted that the surface-functionalized magnetic iron oxide nanoparticles evaluate for the bioseparation process. It was reported that IONPs functionalized with SiO_2, gold, and poly(vinylpyrrolidone) were utilized for the bioseparation of glucagon-like-peptide 1 from the solution. The separated peptide was analyzed by UV-vis spectroscopy. The focus of the study was to notice the design and synthesis of magnetic nanoparticles, which provides efficient adsorption ability to nanoparticles [61].

Additionally, it was already reported that magnetic antibody separation is by using IONPs. As we are aware of the demand for purified antibodies, the study presented a magnetic nanoparticle-based method for separating an immunoglobulin G (IgG) antibody. In this sense, the method benefited from a cost-effective strategy. Iron oxide nanoparticles were immobilized with protein domain A and a peptide tag with iron oxide affinity. In this way, the immobilized nanoparticles were adsorbed with the IgG antibody from the serum sample [62]. Nevertheless, a novel strategy to make hydrogen peroxide biosensors with the help of functionalized iron oxide nanoparticles was reported. Fe_3O_4 nanocomposites functionalized with silica and chitosan have been used to separate hydrogen peroxide from the solution [63].

Another reported bioseparation was of genomic DNA by IONPs. The magnetic adsorption property of polymer-functionalized iron oxide nanoparticles showed the separation of genomic DNA from biological samples because of their changing “on and off” phase of magnetization. Functionalization on nanoparticles was provided with silica for specific research [37].

3.9 IONP-Based Multifunctional Approaches

Previous sections revealed that IONPs have prominent use in the biomedical field. The last few years have been an innovative period in synthesizing magnetic nanoparticles with interesting multifunctional approaches. As it was already revealed, magnetic IONPs were applied to drug delivery, biosensing, chemotherapy, hyperthermia, gene therapy, magnetofection, theranostic purpose, bioseparation, and many more biomedical applications. Researchers began to study multifunctional approaches to iron oxide nanoparticles in these years. It was reported that the interplay between several biomedical applications leads to strong and powerful multifunctional magnet-based nanoplatforms to face emergencies in the biomedical field. This section highlights the multifunctional approaches of IONPs for various applications. Superparamagnetic IONPs were reported to use in combination therapy consisting of chemotherapy and hyperthermia. These particles were functionalized with phospholipid-polyethylene glycol. Later, anticancer drug doxorubicin was loaded on prepared particles to exhibit cancer therapy. The combined effect of chemotherapy (due to doxorubicin) and magnet-induced hyperthermia has helped to destruct tumors [64].

Designing of multifunctional material was reported for collaborative cancer therapy, which includes photodynamic therapy (PDT), bioimaging, and hyperthermia [65].

Multifunctional platforms were reported in many flexible manners to match particular biomedical requirements. In this sense, antibacterial and imaging approaches were developed with magnetic nanoparticles using multifunctional platforms. IONPs were synthesized and functionalized with silica and silver nanoparticles. This setup was used to capture bacteria at the surface in a combination of two approaches: antibacterial property and bioimaging, providing the composition of different proteins, and fatty acids present in bacteria that lead to metabolic analysis [66].

4 Summary and Future Perspective

The chapter summarizes the use of surface-functionalized IONPs for biomedical applications. The surface functionalization provides an advantage of biocompatibility along with the reactive groups, which make the nanoparticles suitable for biological applications. Numerous polymers and ligands are reported for surface functionalization. Also, the ranges of applications are not restricted to a narrow domain. Surface-functionalized iron oxide nanoparticles are being used in cancer therapy, drug delivery, MRI contrast agents, disease diagnostics, biosensing, gene therapy, and magneto-separation of nucleic acids and proteins.

Despite the promising concepts and applications of surface-functionalized IONPs, there lies a narrow gap, which needs to be addressed for the widespread use of surface-functionalized IONPs in biomedical applications.

The challenges are there at each step from synthesis to application. The application-oriented synthesis of nanoparticles with careful tailoring of size, morphology, and magnetic properties along with biocompatibility is crucial. Sustainable methods of synthesis of surface-functionalized IONPs are another important aspect to be paid attention to. Apart from this, scalability, reusability, and reproducibility of the synthesis method are pertinent. Surface functionalization aims to address the challenge pertaining to the toxicity of nanoparticles to biological systems, renal clearance, and accurate targeting.

Also, it is significant to notice that the multifunctional approaches are mostly based on combining materials fetch undesired physical-chemical and adverse secondary biological responses. These points should be addressed before the translation of the proof of concept to real application. Although the magnetic nanoparticle-based drug delivery shows promising results in theoretical experiments, there are challenges of accuracy and precision magnetic penetration that the AC magnetic field needs to reach the delivery site with adequate strength. More research is required in this area.

Another challenge in this area is biosafety and disposal. Various studies have reported that by controlling the properties such as size, shape, quantities, oxidation state, and surface functionalities, the problems can be mitigated.

IONP-based cancer therapy is still at the foundation stage and holds a great expectation due to the potential to eliminate the most chemotherapeutic side effects and increase survival rate (first of animals and later of human beings). Regardless of many successful studies using IONPs for cancer therapy being reported in small animal models, there are still many important issues to address such as loading capacity, specificity, and affinity optimization to target cancer cells.

By addressing the challenges of surface functionalization of iron oxide nanoparticles and working on the optimized clinical outcomes, one can pave a sustainable future and consumer market for novel MNP-based biomedical products.

Acknowledgments The research acknowledges the Internal University Project entitled as "Targeted destruction of cancer stem cells by surface functionalized magnetic nanoparticles" (project no. DYPES DUR&D/2021/274), D. Y. Patil Education Society, Kolhapur.

References

1. A. Ali, H. Zafar, M. Zia, I. ul Haq, A.R. Phull, J.S. Ali, Synthesis, characterization, applications, and challenges of iron oxide nanoparticles. Nanotechnol. Sci. Appl. **9**, 49 (2016)
2. K. Jiang, L. Zhang, G. Bao, Magnetic iron oxide nanoparticles for biomedical applications. Curr. Opin. Biomed. Eng. **20**, 100330 (2021)
3. R. Gonzalez-Rodriguez, E. Campbell, A. Naumov, Multifunctional graphene oxide/iron oxide nanoparticles for magnetic targeted drug delivery dual magnetic resonance/fluorescence imaging and cancer sensing. PLoS One **14**, 0217072 (2019)
4. M.S. Miranda, M.T. Rodrigues, R.M. Domingues, R.R. Costa, E. Paz, C. Rodríguez-Abreu, P. Freitas, B.G. Almeida, M.A. Carvalho, C. Gonçalves, C.M. Ferreira, Development of inhalable superparamagnetic iron oxide nanoparticles (SPIONs) in microparticulate system for antituberculosis drug delivery. Adv. Healthc. Mater. **7**, 1800124 (2018)
5. P. Kumar, S. Agnihotri, I. Roy, Preparation and characterization of superparamagnetic iron oxide nanoparticles for magnetically guided drug delivery. Int. J. Nanomedicine **13**, 43 (2018)
6. C. Turrina, S. Berensmeier, S.P. Schwaminger, Bare iron oxide nanoparticles as drug delivery carrier for the short cationic peptide lasioglossin. Pharmaceuticals **14**, 405 (2021)
7. S. Kumar, M. Umar, A. Saifi, S. Kumar, S. Augustine, S. Srivastava, B.D. Malhotra, Electrochemical paper based cancer biosensor using iron oxide nanoparticles decorated PEDOT: PSS. Anal. Chim. Acta **1056**, 135 (2019)
8. D.Y. Lee, S. Kang, Y. Lee, J.Y. Kim, D. Yoo, W. Jung, S. Lee, Y.Y. Jeong, K. Lee, S. Jon, PEGylated bilirubin-coated iron oxide nanoparticles as a biosensor for magnetic relaxation switching-based ROS detection in whole blood. Theranostics **2020**, 10 (1997)
9. M. Magro, D. Baratella, G. Miotto, J. Frömmel, M. Šebela, M. Kopečná, E. Agostinelli, F. Vianello, Enzyme self-assembly on naked iron oxide nanoparticles for aminoaldehyde biosensing. Amino Acids **51**, 679 (2019)
10. T. Li, L. Jin, K. Feng, T. Yang, X. Yue, B. Wu, S. Ding, X. Liang, G. Huang, J. Zhang, A novel low-field NMR biosensor based on dendritic superparamagnetic iron oxide nanoparticles for the rapid detection of Salmonella in milk. Lebensm.-Wiss. Technol. **133**, 110149 (2020)

11. M.W. Akram, M.F. Alam, H.N. Ji, A. Mahmood, T. Munir, M.Z. Iqbal, M.R. Saleem, N. Amin, A.G. Wu, Chitosan blend iron oxide nanostructure-based biosensor for healthy & malignant tissue glucose/urea detection. Mater. Sci. Eng. **474**, 012060 (2019)
12. N. Zhang, Y. Wang, C. Zhang, Y. Fan, D. Li, X. Cao, J. Xia, X. Shi, R. Guo, LDH-stabilized ultrasmall iron oxide nanoparticles as a platform for hyaluronidase-promoted MR imaging and chemotherapy of tumors. Theranostics **10**, 2791 (2020)
13. C. Shen, X. Wang, Z. Zheng, C. Gao, X. Chen, S. Zhao, Z. Dai, Doxorubicin and indocyanine green loaded superparamagnetic iron oxide nanoparticles with PEGylated phospholipid coating for magnetic resonance with fluorescence imaging and chemotherapy of glioma. Int. J. Nanomedicine **14**, 101 (2019)
14. T.T. Le, T.Q. Bui, T.M. Ha, M.H. Le, H.N. Pham, P.T. Ha, Optimizing the alginate coating layer of doxorubicin-loaded iron oxide nanoparticles for cancer hyperthermia and chemotherapy. J. Mater. Sci. **53**, 13826 (2018)
15. Y. Zou, D. Li, Y. Wang, Z. Ouyang, Y. Peng, H. Tomás, J. Xia, J. Rodrigues, M. Shen, X. Shi, Polyethylenimine nanogels incorporated with ultrasmall iron oxide nanoparticles and doxorubicin for MR imaging-guided chemotherapy of tumors. Bioconjug. Chem. **31**, 907 (2020)
16. S.M. Carvalho, A.G. Leonel, A.A. Mansur, I.C. Carvalho, K. Krambrock, H.S. Mansur, Bifunctional magnetopolymersomes of iron oxide nanoparticles and carboxymethylcellulose conjugated with doxorubicin for hyperthermo-chemotherapy of brain cancer cells. Biomater. Sci. **7**, 2102 (2019)
17. Q. Yu, X.Q. Xiong, L. Zhao, T.T. Xu, H. Bi, R. Fu, Q.H. Wang, Biodistribution and toxicity assessment of superparamagnetic iron oxide nanoparticles in vitro and in vivo. Curr. Med. Sci. **38**, 1096 (2018)
18. A.C. Freeman, S.R. Platt, S. Holmes, M. Kent, K. Robinson, E. Howerth, J. Eagleson, A. Bouras, M. Kaluzova, C.G. Hadjipanayis, Convection-enhanced delivery of cetuximab conjugated iron-oxide nanoparticles for treatment of spontaneous canine intracranial gliomas. J. Neuro-Oncol. **137**, 653 (2018)
19. M. Mukherje, In vitro antimicrobial activity of polyacrylamide doped magnetic iron oxide nanoparticles. Int. J. Mater. Mech. Manuf. **2**, 64 (2014)
20. S. Qasim, A. Zafar, M.S. Saif, Z. Ali, M. Nazar, M. Waqas, A.U. Haq, T. Tariq, S.G. Hassan, F. Iqbal, X.G. Shu, Green synthesis of iron oxide nanorods using *Withania coagulans* extract improved photocatalytic degradation and antimicrobial activity. J. Photochem. Photobiol. B Biol. **204**, 111784 (2020)
21. N.A. Zakariya, S. Majeed, W.H. Jusof, Investigation of antioxidant and antibacterial activity of iron oxide nanoparticles (IONPS) synthesized from the aqueous extract of *Penicillium* SPP. Sens. Int. **3**, 100164 (2022)
22. S.M. Mandal, W.F. Porto, D. De, A. Phule, S. Korpole, A.K. Ghosh, S.K. Roy, O.L. Franco, Screening of serine protease inhibitors with antimicrobial activity using iron oxide nanoparticles functionalized with dextran conjugated trypsin and in silico analyses of bacterial serine protease inhibition. Analyst **139**, 464 (2014)
23. S. Parveen, A.H. Wani, M.A. Shah, H.S. Devi, M.Y. Bhat, J.A. Koka, Preparation, characterization and antifungal activity of iron oxide nanoparticles. Microb. Pathog. **115**, 287 (2018)
24. C.R. Basso, B.P. Crulhas, M. Magro, F. Vianello, V.A. Pedrosa, A new immunoassay of hybrid nanomater conjugated to aptamers for the detection of dengue virus. Talanta **197**, 482 (2019)
25. R. Kumar, M. Nayak, G.C. Sahoo, K. Pandey, M.C. Sarkar, Y. Ansari, V.N. Das, R.K. Topno, M. Madhukar, P. Das, Iron oxide nanoparticles based antiviral activity of H1N1 influenza A virus. J. Infect. Chemother. **25**, 325 (2019)
26. J. Lee, M. Morita, K. Takemura, E.Y. Park, A multi-functional gold/iron-oxide nanoparticle-CNT hybrid nanomaterial as virus DNA sensing platform. Biosens. Bioelectron. **102**, 425 (2018)
27. Z. Zhao, H. Cui, W. Song, X. Ru, W. Zhou, X. Yu, A simple magnetic nanoparticles-based viral RNA extraction method for efficient detection of SARS-CoV-2. BioRxiv **1**, 1 (2020)

28. M. Zuvin, E. Kuruoglu, V.O. Kaya, O. Unal, O. Kutlu, H. Yagci Acar, D. Gozuacik, A. Koşar, Magnetofection of green fluorescent protein encoding DNA-bearing polyethyleneimine-coated superparamagnetic iron oxide nanoparticles to human breast cancer cells. ACS Omega **4**, 12366 (2019)
29. L.A. Blokpoel Ferreras, S.Y. Chan, S. Vazquez Reina, J.E. Dixon, Rapidly transducing and spatially localized magnetofection using peptide-mediated non-viral gene delivery based on iron oxide nanoparticles. ACS Appl. Nano Mater. **4**, 167 (2020)
30. A.N. Danthanarayana, D.C. Manatunga, R.M. De Silva, N.V. Chandrasekharan, K.M. Nalin De Silva, Magnetofection and isolation of DNA using polyethyleneimine functionalized magnetic iron oxide nanoparticles. R. Soc. Open Sci. **5**, 181369 (2018)
31. M.K. Yapici, A. Al Nabulsi, N. Rizk, S.M. Boularaoui, N. Christoforou, S. Lee, Alternating magnetic field plate for enhanced magnetofection of iron oxide nanoparticle conjugated nucleic acids. J. Magn. Magn. Mater. **469**, 598 (2019)
32. P.M. Martins, A.C. Lima, S. Ribeiro, S. Lanceros Mendez, P. Martins, Magnetic nanoparticles for biomedical applications: From the soul of the earth to the deep history of ourselves. ACS Appl. Bio Mater. **4**, 5839 (2021)
33. S. Zhao, X. Yu, Y. Qian, W. Chen, J. Shen, Multifunctional magnetic iron oxide nanoparticles: An advanced platform for cancer theranostics. Theranostics **10**, 6278 (2020)
34. S.O. Aisida, P.A. Akpa, I. Ahmad, T.K. Zhao, M. Maaza, F.I. Ezema, Bio-inspired encapsulation and functionalization of iron oxide nanoparticles for biomedical applications. Eur. Polym. J. **122**, 109371 (2020)
35. G.S. Demirer, A.C. Okur, S. Kizilel, Synthesis and design of biologically inspired biocompatible iron oxide nanoparticles for biomedical applications. J. Mater. Chem. B **3**, 7831 (2015)
36. A.P. Tiwari, S.S. Rohiwal, M.V. Suryavanshi, S.J. Ghosh, S.H. Pawar, Detection of the genomic DNA of pathogenic α-proteobacterium *Ochrobactrum anthropi* via magnetic DNA enrichment using pH responsive BSA@ Fe_3O_4 nanoparticles prior to in-situ PCR and electrophoretic separation. Microchim. Acta **183**, 675 (2016)
37. A.P. Tiwari, R.K. Satvekar, S.S. Rohiwal, V.A. Karande, A.V. Raut, P.G. Patil, P.B. Shete, S.J. Ghosh, S.H. Pawar, Magneto-separation of genomic deoxyribose nucleic acid using pH responsive Fe_3O_4@ silica@ chitosan nanoparticles in biological samples. RSC Adv. **5**, 8463 (2015)
38. K. Marycz, K. Kornicka-Garbowska, A. Patej, P. Sobierajska, A. Kotela, E. Turlej, M. Kepska, A. Bienko, R.J. Wiglusz, Aminopropyltriethoxysilane (APTES)-modified nanohydroxyapatite (nHAp) incorporated with iron oxide (IO) nanoparticles promotes early osteogenesis, reduces inflammation and inhibits osteoclast activity. Materials **15**, 2095 (2022)
39. C.A. Albornoz, M.A. Paulin, A.A. Cristóbal, D.R. Vega, A.G. Leyva, C.P. Ramos, Microwave-assisted hydrothermal nanoarchitectonics of polyethyleneimine-coated iron oxide nanoparticles. Appl. Phys. A **128**, 1 (2022)
40. O.A. Kulikov, M.N. Zharkov, V.P. Ageev, D.E. Yakobson, V.I. Shlyapkina, A.V. Zaborovskiy, V.I. Inchina, L.A. Balykova, A.M. Tishin, G.B. Sukhorukov, N.A. Pyataev, Magnetic hyperthermia nanoarchitectonics via iron oxide nanoparticles stabilised by oleic acid: Anti-tumour efficiency and safety evaluation in animals with transplanted carcinoma. Int. J. Mol. Sci. **23**, 4234 (2022)
41. J.M. George, A. Antony, B. Mathew, Metal oxide nanoparticles in electrochemical sensing and biosensing: A review. Microchim. Acta **185**, 1 (2018)
42. A.P. Tiwari, S.J. Ghosh, S.H. Pawar, Biomedical applications based on magnetic nanoparticles: DNA interactions. Anal. Methods **7**, 10109 (2015)
43. N.V. Vallabani, S. Singh, Recent advances and future prospects of iron oxide nanoparticles in biomedicine and diagnostics. 3 Biotech **8**, 1 (2018)
44. C. Chen, J. Ge, Y. Gao, L. Chen, J. Cui, J. Zeng, M. Gao, Ultrasmall superparamagnetic iron oxide nanoparticles: a next generation contrast agent for magnetic resonance imaging. Wiley Interdiscip. Rev. Nanomed. Nanobiotechnol. **14**, 1740 (2022)

45. M. Elancheziyan, S. Ganesan, K. Theyagarajan, M. Duraisamy, K. Thenmozhi, C.H. Weng, Y.T. Lin, V.K. Ponnusamy, Novel biomass-derived porous-graphitic carbon coated iron oxide nanocomposite as an efficient electrocatalyst for the sensitive detection of rutin (vitamin P) in food and environmental samples. Environ. Res. **211**, 113012 (2022)
46. J. Darson, M. Mohan, *Iron Oxide Nanoparticles and Nano-Composites: An Efficient Tool for Cancer Theranostics*, vol 1 (Interchopen, 2022), p. 1
47. M.J. Mitchell, M.M. Billingsley, R.M. Haley, M.E. Wechsler, N.A. Peppas, R. Langer, Engineering precision nanoparticles for drug delivery. Nat. Rev. Drug Discov. **20**, 101 (2021)
48. I.K. Herrmann, M.J. Wood, G. Fuhrmann, Extracellular vesicles as a next-generation drug delivery platform. Nat. Nanotechnol. **16**, 748 (2021)
49. M. Ebadi, K. Buskaran, S. Bullo, M.Z. Hussein, S. Fakurazi, G. Pastorin, Drug delivery system based on magnetic iron oxide nanoparticles coated with (polyvinyl alcohol-zinc/aluminium-layered double hydroxide-sorafenib). Alex. Eng. J. **60**, 733 (2021)
50. C. Guigou, A. Lalande, N. Millot, K. Belharet, G.A. Bozorg, Use of super paramagnetic iron oxide nanoparticles as drug carriers in brain and ear: State of the art and challenges. Brain Sci. **11**, 358 (2021)
51. S. Ayyanaar, M.P. Kesavan, C. Balachandran, S. Rasala, P. Rameshkumar, S. Aoki, J. Rajesh, T.J. Webster, G. Rajagopal, Iron oxide nanoparticle core-shell magnetic microspheres: Applications toward targeted drug delivery. Nanomedicine **24**, 102134 (2020)
52. M. Hasanzadeh, N. Shadjou, M. de la Guardia, Iron and iron-oxide magnetic nanoparticles as signal-amplification elements in electrochemical biosensing. TrAC Trends Anal. Chem. **72**, 1 (2015)
53. F. Mollarasouli, E. Zor, G. Ozcelikay, S.A. Ozkan, Magnetic nanoparticles in developing electrochemical sensors for pharmaceutical and biomedical applications. Talanta **226**, 122108 (2021)
54. M. Srinivasan, M. Rajabi, S.A. Mousa, Multifunctional nanomaterials and their applications in drug delivery and cancer therapy. Nanomaterials. **5**, 1690 (2015)
55. C. Liu, N. Zhang, Nanoparticles in gene therapy: Principles, prospects, and challenges. Prog. Mol. Biol. Transl. Sci. **104**, 509 (2011)
56. T. Zhang, Q. Xu, T. Huang, D. Ling, J. Gao, New insights into biocompatible iron oxide nanoparticles: A potential booster of gene delivery to stem cells. Small **16**, 2001588 (2020)
57. M. Arakha, S. Pal, D. Samantarrai, T.K. Panigrahi, B.C. Mallick, K. Pramanik, B. Mallick, S. Jha, Antimicrobial activity of iron oxide nanoparticle upon modulation of nanoparticle-bacteria interface. Sci. Rep. **5**, 1 (2015)
58. S.K. Jat, H.A. Gandhi, J. Bhattacharya, M.K. Sharma, Magnetic nanoparticles: An emerging nano-based tool to fight against viral infections. Mater. Adv. **2**, 4479 (2021)
59. C. Cen, J. Wu, Y. Zhang, C. Luo, L. Xie, X. Zhang, X. Yang, M. Li, Y. Bi, T. Li, T. He, Improving magnetofection of magnetic polyethylenimine nanoparticles into MG-63 osteoblasts using a novel uniform magnetic field. Nanoscale Res. Lett. **14**, 1 (2019)
60. S. Chandra, S. Nigam, D. Bahadur, Combining unique properties of dendrimers and magnetic nanoparticles towards cancer theranostics. J. Biomed. Nanotechnol. **10**, 32 (2014)
61. S.A. Adams, J.L. Hauser, A.L. Allen, K.P. Lindquist, A.P. Ramirez, S. Oliver, J.Z. Zhang, Fe_3O_4@ SiO_2 nanoparticles functionalized with gold and poly (vinylpyrrolidone) for bio-separation and sensing applications. ACS Appl. Nano Mater. **1**, 1406 (2018)
62. Y. Kaveh-Baghbaderani, R. Allgayer, S.P. Schwaminger, P. Fraga-García, S. Berensmeier, Magnetic separation of antibodies with high binding capacity by site-directed immobilization of protein A-domains to bare iron oxide nanoparticles. ACS Appl. Nano Mater. **4**, 4956 (2021)
63. R.K. Satvekar, S.S. Rohiwal, A.P. Tiwari, A.V. Raut, B.M. Tiwale, S.H. Pawar, Sol–gel derived silica/chitosan/Fe_3O_4 nanocomposite for direct electrochemistry and hydrogen peroxide biosensing. Mater. Res. Exp. **2**, 015402 (2015)
64. C.A. Quinto, P. Mohindra, S. Tong, G. Bao, Multifunctional superparamagnetic iron oxide nanoparticles for combined chemotherapy and hyperthermia cancer treatment. Nanoscale **7**, 12728 (2015)

65. H. Bi, Y. Dai, P. Yang, J. Xu, D. Yang, S. Gai, F. He, B. Liu, C. Zhong, G. An, J. Lin, Glutathione mediated size-tunable UCNPs-Pt (IV)-$ZnFe_2O_4$ nanocomposite for multiple bioimaging guided synergetic therapy. Small **14**, 1703809 (2018)
66. V. Vedarethinam, L. Huang, W. Xu, R. Zhang, D.D. Gurav, X. Sun, J. Yang, R. Chen, K. Qian, Detection and inhibition of bacteria on a dual-functional silver platform. Small **15**, 1803051 (2019)

Index

F. I. Ezema et al. (eds.), *Chemically Deposited Metal Chalcogenide-based Carbon Composites for Versatile Applications*, https://doi.org/10.1007/978-3-031-23401-9